Implications of Seismic Data for the Structural Evolution and Numerical Modelling of the Eastern Mediterranean Basin

Simon Austin Libby

Submitted for the degree of Doctor of Philosophy

in Applied Geoscience at Heriot-Watt University

Shell Centre of Exploration, Applied Geoscience Unit

School of Energy, Geoscience, Infrastructure and Society

October 2017

Abstract

The Eastern Mediterranean region includes several diverse tectonic domains. Their complexity and interaction have led to competing theories for the region's evolution. This study aims to resolve some of these issues by using interpretations of regional seismic reflection data located in the offshore waters of Cyprus, Syria, Lebanon and Israel. The extent of the available data is unprecedented for a single study in the area, and the academic nature of the study means the remit is not constrained by political boundaries. The interpretations facilitated a new regionally consistent understanding of the tectonic evolution of the area that included several key conclusions.

On the basis of literature review and regional seismic data, the western boundary of the 'Sinai Plate' that underlies the Eastern Mediterranean was concluded to run further west than is commonly drawn. However, the 'Sinai Plate' may not represent a true tectonic plate as it is not fully rifted at the Gulf of Suez.

This study had access to a seismic data set from offshore Syria that only a single published paper had previously investigated. This allowed numerous new observations of a relic subduction zone beneath the Cyprus Arc to be made. The structural restoration constrained by these observations required a restructured plate evolution that included the arrival of the subduction zone in the latest Cretaceous, and provided the keystone to a new explanation for a set of normal faults mapped in the Levantine Basin. These layer-bound normal faults exist spatially and temporally where one might expect compressional features. The interpretation of the regional seismic data more than doubled the area documented as being affected by this deformation, and highlights a set of anticlines that are perpendicular and contemporaneous to the faults. Numerical analysis was conducted on detailed 3D interpretations of the faults using purpose-written software. In combination with observations from seismic data, this analysis provided evidence that contradicted previously published explanations, and suggested the shear system associated with the formation of the neighbouring Levant Shear Zone could have generated the deformation. Both Wilcox-strain-ellipse and extension associated with tectonic indentation of Eurasia contributed to the deformation.

Seismic lines over the enigmatic Eratosthenes Seamount with a significantly higher fidelity than those in previously published work showed features that included prograding foresets and an erosive escarpment. These previously undocumented features formed the basis for an updated evolution of carbonate growth on the feature. A depression surrounding the bathymetric high is defined by an external escarpment. Numerical modelling of halokinetic deformation supports inflation of an evaporite body as the explanation for the formation of this depression. Well-imaged internal salt reflectors also indicate an episode of halokinesis immediately after evaporite deposition, contrary to some published interpretations.

The new regional insights and detailed interpretations of localised features observed in the newly available 3D datasets are summarised in a series of maps detailing the evolution of the area.

Acknowledgements

It was thanks to Prof. John Underhill that this PhD was orchestrated; devising, assembling and managing the components of a three-year project is no small task and so I am indebted for these efforts. In conjunction with Dr Rachel Jamieson the provision of advice, knowledge and proofreading has elevated the work carried out for the project, thank you for your help with this.

This PhD was funded by, and conceived in partnership with, Shell. This funding was part of a larger agreement that provided the facilities in which the PhD was undertaken: the Wouter Hoogeven seismic laboratory. Thus, Shell has been doubly instrumental in enabling this PhD to occur, and is acknowledged accordingly. Thanks go to particular Shell staff for their contributions, Dr Ceri Powell for authorising funding, and Dr Jeroen Peters, Dr Keith Gerdes, Dr Andy Bell and Jack Russell for sharing their advice and knowledge.

Spectrum ASA provided the majority of the seismic data available to this study. This included exclusive access to the Syria data set and rare access to the LEB3D and EMED00 PSDM data. This generosity permitted the vast majority of the key conclusions of this study, thanks to Dr Neil Hodgson, Howard Nicholls and Karyna Rodriguez for their parts in allowing data access.

The interpretation of the seismic data available to this study was accomplished using Petrel software donated by Schlumberger. This software package permitted efficient interrogation of the seismic data and was crucial in timely submission of this thesis.

Midland Valley donated their Move software. The restorations in this study could not have been achieved in the same fashion without it.

Assessment of the suitability of Cyprus fieldwork was undertaken in part by attending the Edinburgh University Undergraduate fieldtrip to Cyprus. Prof. Alastair Robertson was key in facilitating this.

Dr. Tim Kinnaird kindly gave access to the structural data he collected as part of his PhD onshore Cyprus. This allowed comparison with structural trends onshore.

Open source software packages including GeoMapApp, GPlates, and Cartopy all played integral roles in the formation of this Thesis. The authors of this software are thanked for writing and then giving open access to this software.

To write the software that produced the figures, analysed faults and simulated the flow of salt I had to learn how to do some programming. The community behind the programming Q&A website Stack Overflow (.com) helped significantly with this.

Finally, thanks to Heriot-Watt University for providing the ideal environment in which to undertake the work.

ACADEMIC REGISTRY

Research Thesis Submission

Name*:*	Simon Libby		
School:	School of Energy, Geoscience, Infrastructure and Society		
Version: *(i.e. First, Resubmission, Final)*	Final	Degree Sought:	Doctor of Philosophy

Declaration

In accordance with the appropriate regulations I hereby submit my thesis and I declare that:

1) the thesis embodies the results of my own work and has been composed by myself
2) where appropriate, I have made acknowledgement of the work of others and have made reference to work carried out in collaboration with other persons
3) the thesis is the correct version of the thesis for submission and is the same version as any electronic versions submitted*.
4) my thesis for the award referred to, deposited in the Heriot-Watt University Library, should be made available for loan or photocopying and be available via the Institutional Repository, subject to such conditions as the Librarian may require
5) I understand that as a student of the University I am required to abide by the Regulations of the University and to conform to its discipline.
6) I confirm that the thesis has been verified against plagiarism via an approved plagiarism detection application e.g. Turnitin.

* *Please note that it is the responsibility of the candidate to ensure that the correct version of the thesis is submitted.*

Signature of Candidate*:*		Date:	

Submission

Submitted By *(name in capitals):*	
Signature of Individual Submitting:	
Date Submitted:	

For Completion in the Student Service Centre (SSC)

Received in the SSC by *(name in capitals):*			
Method of Submission *(Handed in to SSC; posted through internal/external mail):*			
E-thesis Submitted ***(mandatory for final theses)***			
Signature:		Date:	

Table of Contents

Table of Figures

Included with this thesis is also a supplementary figure intended to give the reader a reference to locations mentioned in the text.

Chapter 1 Introduction

1.1 Research Rationale

The Eastern Mediterranean region, defined here as the easternmost offshore section of the Mediterranean Sea and the nearshore areas of the bordering countries, lies at the junction of the European and African tectonic plates (Figure 1.1). As a result, this region includes several closely spaced but diverse tectonic domains, including subduction and collision zones, passive continental margins, deep basins and shear zones (Figure 1.1). Consequently, the region provides world class examples of interaction between different geological domains, including records of past geological processes. Access to a suite of modern industry seismic data provided this study with the means to study, interpret and describe the record of tectonic deformation. These industry seismic data sets provided regional coverage, which included previously poorly studied areas and imaging to depths rarely achieved in previous seismic data collected for academic purposes. By studying these data, insight was gained into how these geological processes evolved and interacted over time. These new observations have furthered our understanding of the Eastern Mediterranean, but may also be used to inform our understanding of the evolution of other areas.

The part of the he Eastern Mediterranean region subject to this study (EMR) is shown in Figure 1.1. Some of the terminology used for sub-areas of the EMR later in this Thesis are also labelled on this figure.

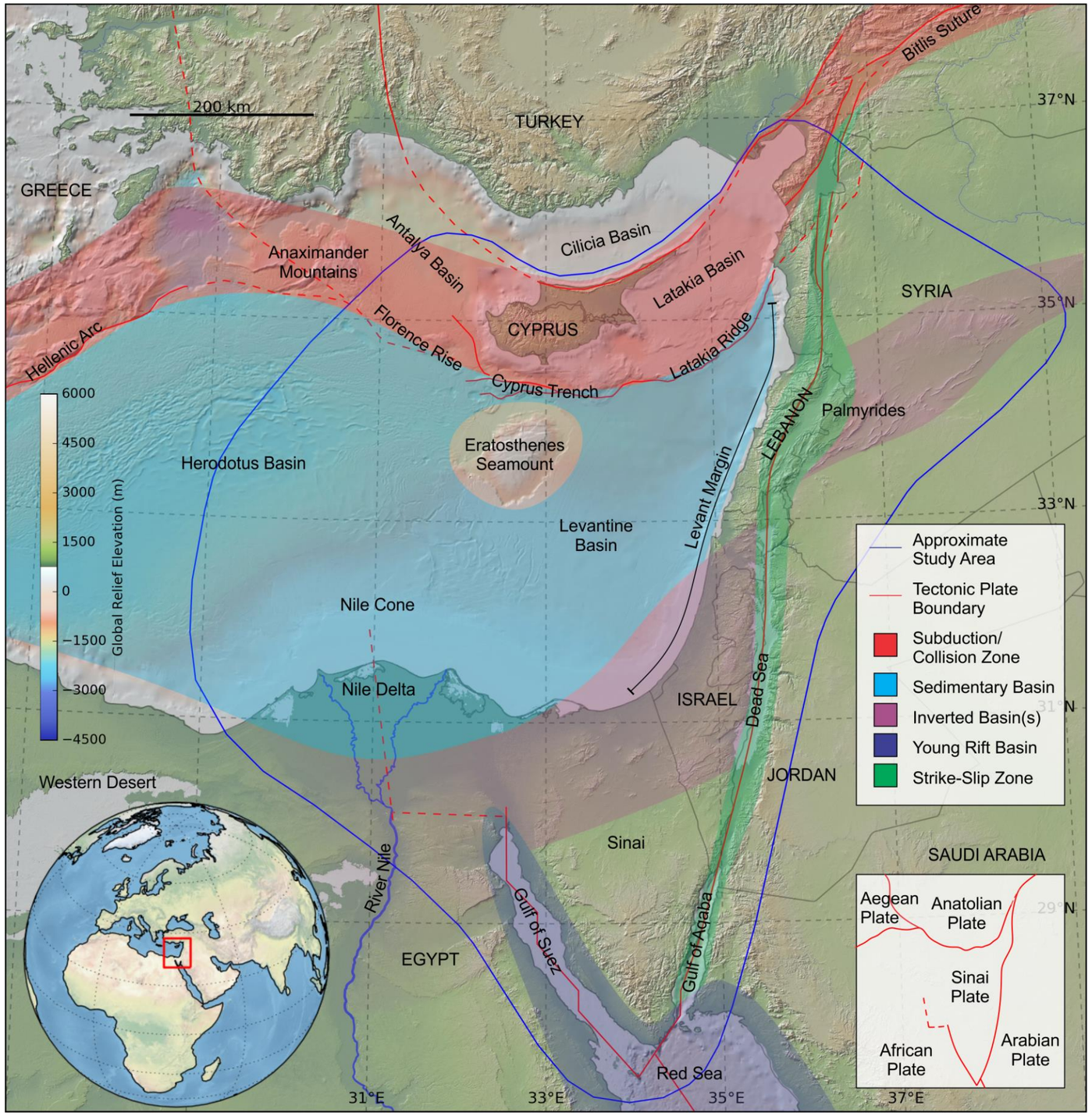

Figure 1.1-Map showing the area relevant to this study and tectonic plate boundaries. Country names (capitalised) and some geological features discussed later in this document are labelled. The insets show the global location and plate names. The global relief data used in this figure and the rest of those in this study is the Global Multi-Resolution Topography Synthesis (Ryan et al., 2009). The global relief colour scale used in this figure is the same as for the rest of the figures in this study and is from GeoMapApp.

Offshore investigations into the regional tectonics of the EMR have been largely driven by national energy resource and economic exploration efforts. Consequently, many previous studies focus within the borders of a single country. This focus has resulted in a varied depth of investigation across the region, with the differing levels of investigation divided by political boundaries as opposed to geological boundaries. An example of this is Israel; it has a large amount of publically available detailed studies but the regional context of some studies is often not fully realised (e.g. Gardosh et al., 2008b). Whilst the geological understanding for an individual country may be internally consistent, a greater or more broadly focused understanding may be provided by utilising information that transcends political boundaries. This is because the remit of many of the studies have hard perimeters; a view of a tectonic map indicates that the geological features do not follow the same limits, and intra-plate forces mean that tectonism in one area affects another. This is especially true offshore where distance-to-shore often defines the maritime borders, in contrast to terrestrial borders that, for historical geographic reasons, often follow trends in the landscape.

This country specific remit of previous studies combined with the structural complexity of the area means that the timing and nature of the interaction between different structural domains in the EMR has not been definitively established. The aim of this project has been to use the full range of geoscience databases available to create an internally consistent model of the tectonic evolution of the region, a model exhibited in Chapter 8. More localised aspects of this model were constructed using the components of this study outlined in Chapters 4-7. This model can also act as a regional framework to underpin subsequent more focused studies on specific aspects of the geology of the region. The seismic data available to this study spans the majority of the offshore EMR, a study area larger than any previously published seismic studies in the area. This scope therefore provides further confidence in the conclusions of this study.

1.2 Research Strategy

The study was undertaken by first reviewing existing knowledge and testing current interpretations against the newly available dataset. This identified controversies, unknowns and inchoate areas in the published understanding of the region. A first-pass interpretation of the data available to the study then permitted assessment of what further work could address these specific issues. This also avoided duplication of work that has been previously published. The possibility of obtaining original data from field work was considered, however current political instabilities and access to published field data made this impractical.

For specific areas and processes, the work was divided into sub-studies, which were collated as chapters. As many aspects of each sub-study have implications or foci that overlap with other sub-studies, it is not possible to order the chapters such that no reference is made to implications or understanding from work that is not yet described. Significant effort has been made to reduce this as much as possible and the selected chapter order is the closest to this sequential ideal that may be reasonably achieved.

A key example of the ordering selection is the placement of Chapter 5; it focuses on a different tectonic plate to the other chapters. It might therefore be considered logical to locate it prior to the Thesis conclusion. However, the findings of Chapter 6 are heavily dependent on observations made in Chapter 5, hence the selected chapter. Where implications and understanding in a later chapter is pertinent, a reference (with the prefix 'see') and brief explanation is given.

1.3 Chapter Outlines

The content of each chapter is outlined below.

Chapter 2 Geological Background

This chapter serves as both a literature review pertinent to this study, and an introduction to the geology of the EMR. Controversies are also summarised. This provided the context for the studies described later in this document. As this chapter is intended as an introduction of the literature in the area, no major original interpretations or observations are shown. Instead, the figures and discussion are comparative or collationary.

Chapter 3 Seismic Interpretation

This study has access to a suite of seismic datasets that cover a large area, in addition to other publically available geoscience data. By outlining the data and defining the conventions and constraints used to carry out the interpretations it permits later descriptions of these interpretations to be carried out succinctly. An overview of the seismic interpretations is presented, and those areas not the focus of later chapters are discussed. Highlights include an updated history for an enigmatic bathymetric high (the Eratosthenes Seamount) and regional observations of the occurrence of seismically resolvable salt throughout the EMR.

Chapter 4 The Sinai-Levantine Crustal Promontory

The Sinai Sub-Plate represents the northeast tip of the African Plate (Figure 1.1). It is bounded to the east by the Levant Shear Zone (Figure 1.1) but its other borders are less certain. By evaluating documented hypotheses on the limits of the plate with observations made using the regional seismic data a critical assessment of the validity of the different plate boundaries was made. The discussion encompasses the crustal type of the Sinai Plate and its proximal surroundings. Outlining the underlying tectonic plates prior to investigation of the overlying geology is necessary to understand the large scale geological context. This study concludes that the Sub-Plate might better be considered a crustal promontory of the African Plate. This chapter was included after the data introduction as its focus forms the literal and figurative foundation of much of the later work.

Chapter 5 Cypriot Subduction and Collision

The uplift involved in continent-continent collision means that mature convergent plate boundaries are often terrestrial, and thus facilitate field study (e.g. Andersen et al., 1991; Krogh, 1977; Lewry et al., 1994; McGregor et al., 1991; Sandvol et al., 2003). The transition from oceanic-continent collision to continent-continent collision means that incipient continent-continent collision is marine and comparatively short lived, and is therefore generally less well studied (e.g. Bry et al.,

2004; Kinnaird and Robertson, 2012; Ten Veen and Kleinspehn, 2003). The collisional boundary between the Sinai (African) Plate and Anatolian (Eurasian) Plate at the Cyprus Arc provides an opportunity to study boundary this further. This study had access to seismic data that had been the subject of a single previous publication. These data permitted kinematic restorations of the Cyprus Arc that produced a series of original observations, highlighting that subduction ceased at the southern edge of the Arc around the end of the Cretaceous, and a key new observation that there was a hiatus in compression across the Arc during the end of the Miocene. The hiatus in compression was a key component of the investigation in Chapter 6, hence the selected chapter order.

Chapter 6 The Piano Key Faults

In the central basin of the EMR, a swarm of over 400 normal faults was documented where the regional tectonic configuration means convergent stresses might be expected, both spatially and temporally. These faults transect contemporaneous folds, an observation that is largely ignored in previous literature. Large scale geological features that have been clearly imaged by multiple seismic data sets, but the genesis of which remain controversial, are unusual in academic literature. Identifying the genesis of these faults therefore represented an opportunity to generate original insight into the evolution of the area and more general observations on how faults may form. The observation of previously undocumented normal faults, consideration of the implications of folds contemporaneous and perpendicular to the normal faults, and the hiatus in compression across the Cyprus Arc observed in Chapter 5 led to the conclusion that the normal faults are a manifestation of the shear forces associated with the northward propagation of the nearby Levant Shear Zone (Figure 1.1).

Chapter 7 Forward Modelling of Halokinesis

The Eratosthenes Seamount is a bathymetric high located ~100 km south of Cyprus (Figure 1.1). It is surrounded on three sides by a moat-like depression circular to elliptical in shape that is defined by an external escarpment. Multiple hypotheses have been suggested for the formation of this feature, however critical consideration reveals the only hypothesis that is compatible with the observations made on seismic data in this study is flow of an underlying evaporite horizon (Libby and Underhill, 2015; Reiche et al., 2015). Numerical modelling was used to further test this hypothesis, using software written for purpose as no suitable pre-existing software was available. The numerical modelling suggests that solely evaporite flow can form simulated feature geometries that match, but are smaller than, the true geometries of the feature. Feedbacks suggest supra-salt translation would enhance the height of the moat escarpment, so it is likely that this process is occurring in the EMR. This analysis could have been grouped with other aspects of the evaporites and Eratosthenes Seamount in Chapter 3, however the numerical modelling focus and the contrasting form of discussion this requires means it was separated as a standalone chapter.

Chapter 8 Summary and Conclusions

The final chapter draws together all the points of the preceding chapters into a unified model for the tectonic evolution of the EMR. This affirms the compatibility of new insights which in turn lends

credence to the interpretations and the preferred model presented. General evaluation points and recommendations for future studies are also discussed.

Chapter 2 Geological Background

2.1 Introduction

This chapter serves to introduce the reader to the geological configuration and evolution of the EMR by review and summary of published literature. In doing so, it also identifies controversies and unknowns in the published understanding of the area. The diverse range of tectonic regimes within the EMR, the interaction between elements of these regimes, and the varying coverage of sequential events affecting a given location, means that describing the structural elements of the EMR in a spatially sequential fashion would lead to either large amounts of repetition or inadequate linking between connected events. To circumvent this issue, the review of literature is undertaken so that geological events are described in a temporally sequential fashion. This description of the EMRs tectonic evolution, Section 2.5, forms the bulk of this chapter.

Prior to Section 2.5, Sections 2.2, 2.3 and 2.4 introduce the tectonic configuration, structural elements and stratigraphy of the EMR respectively. These sections are intended to give the reader a greater awareness of the features and locations referred to in Section 2.5. Consequently, the descriptions of the structural elements in Section 2.3 serve as introductions to features; the full details of which are given later in Section 2.5. To permit the reader greater awareness of the geological context, and to avoid repetition of pertinent but subsequent events, controversies are referenced in Section 2.5 but discussed subsequently in Section 2.6.

The land areas surrounding the EMR have been subject to much study. The North African margin, Hellenic Arc, Syrian continental interior, Levant Shear Zone, Bitlis Suture and Anatolia are all complex areas, and there are links between these areas and the concepts discussed in this literature review. Consequently, these periphery areas are described where pertinent in the following sections. The choice of how much detail to include for the description of each area was made with reference to the work undertaken for this study. Thus, the omission of a full literature review for these adjacent areas does not negatively impact the context given for the work or conclusions of this study. The reader is referred to the references in the pertinent descriptions if further details of these areas are desired.

2.2 Current Tectonic Configuration

The Eastern Mediterranean region lies at the intersection of three tectonic plates, the European and African Plates and the Arabian Sub-Plate (Figure 1.1). The details of the interaction between these plates is complex and forms the crux of this thesis. However, before considering regional and local scales it is important to summarise our understanding of the interactions of these plates at the global scale.

The Mediterranean Sea is thought to be the last remnant of a Mesozoic oceanic domain called the Tethys (Van der Voo, 2005), classifying it as being at the terminal subduction phase on the Wilson Cycle (Wilson, 1966). If follows that the greater Mediterranean area shares a common tectonic history of continental rifting through to spreading, divergence and convergence. The

foundation of what defines the tectonic history of a given area is its underlying tectonic plate. Thus, before exploring the specific aspects of the EMRs tectonic history it is necessary to define the tectonic plates of the area.

Global relief and earthquake foci has defined the African, Arabian and Eurasian continental landmasses as separate tectonic plates since the inception of the theory of plate tectonics (e.g. McKenzie, 1970). Marking consistent trends in lateral changes of global relief, earthquake data, GPS data, and gravity anomalies permits more precise delineation of these plates (Figure 2.1). In conjunction with other geophysical studies these consistent trends also permit definition of several sub-plate boundaries; isolating the Anatolian and Aegean Sub-Plates from the greater Eurasian Plate and what has been termed the Sinai Sub-Plate from the African and Arabian Plates (Figure 2.1). The limits of the Sinai Sub-Plate are uncertain (see Section 2.6.5), and the critical consideration documented in Chapter 4 concludes that it may be better considered a crustal promontory of the African Plate, although ‘Sinai Plate’ remains a convenient label (see Section 4.1).

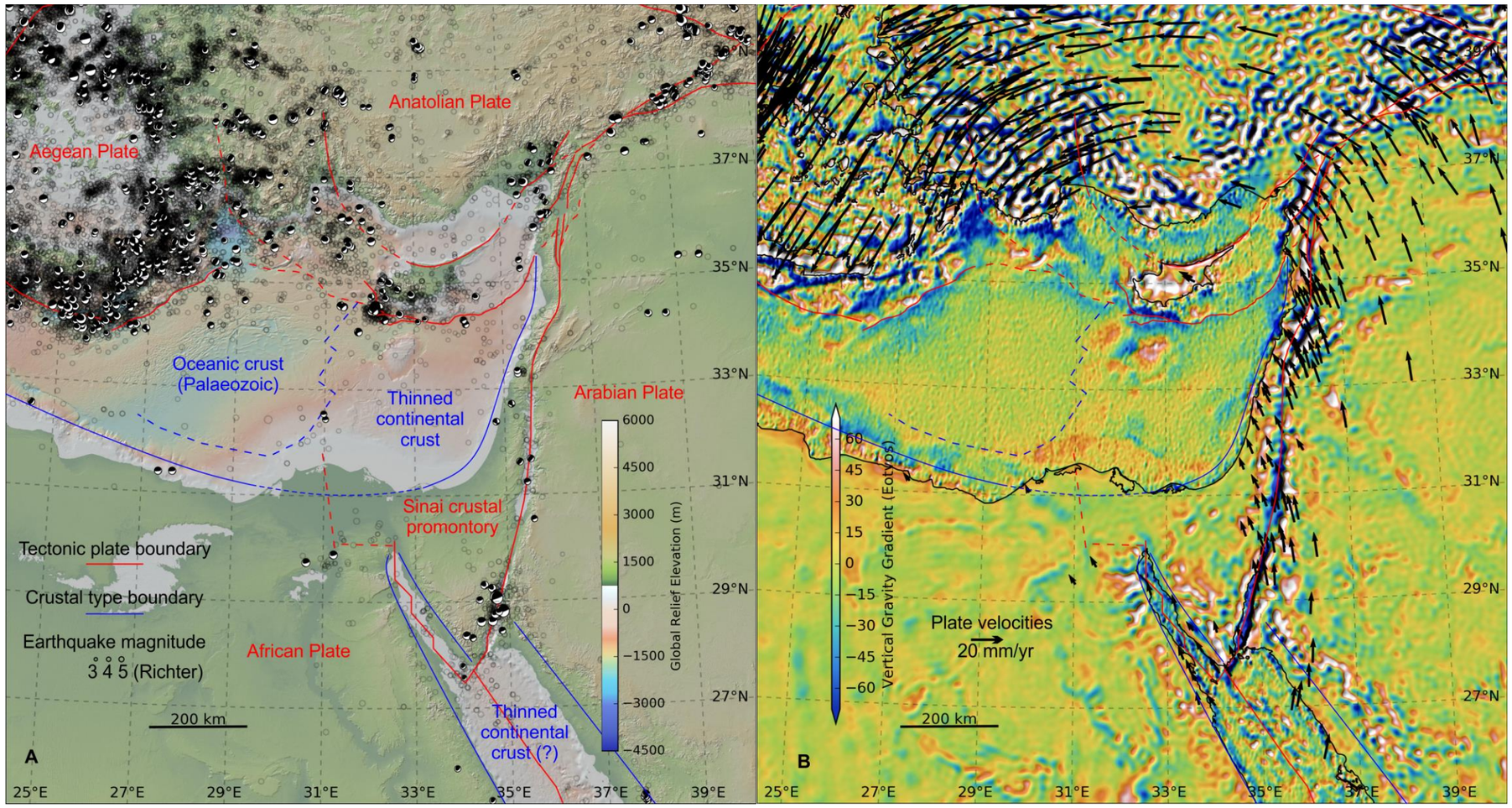

Figure 2.1-Maps showing the plate boundaries of the EMR and delineation of different crustal types (Bosworth, 2015; Bosworth and McClay, 2001; Cowie and Kusznir, 2012a; Longacre et al., 2007) according to discussion in Chapter 4, overlain on some of the data used to define these boundaries. (A) global relief (Ryan et al., 2009) and earthquake data (focal mechanisms plotted with: Beyreuther et al., 2010; focal mechanism data: Dziewoński et al., 1981; Ekström et al., 2012; unorientated earthquake data: U.S. Geological Survey, 2015), oceanic crust age estimate is from Granot (2016). (B) vertical gravity gradient (Sandwell et al., 2014, 2013; Sandwell and Smith, 2009) and GPS velocities relative to Eurasia (Reilinger et al., 2006). Some Anatolian and Aegean plate boundaries are omitted for clarity.

Currently the African and Arabian Plates are moving broadly northward, with the Arabian Plate moving faster (Figure 2.1B) as the Arabian Plate and African Plates diverge along the rift that forms the Red Sea (Figure 2.1A). Magnetic anomalies reveal this divergence has recently switched from continental rifting to oceanic spreading in the central and southern Red Sea (Bosworth, 2015). The northern Arabian Plate is a continental promontory that has collided with the Anatolian Plate, forming the Bitlis Suture (Dewey et al., 1973; Sengör and Yilmaz, 1981). Thus it is a step ahead on the Wilson cycle (Wilson, 1966) compared to the rest of the EMR. The Anatolian Plate is undergoing western tectonic escape from this collision, pushing the Aegean Plate before it which is escaping south (Reilinger et al., 2006), together setting up an anticlockwise set of relative plate motions (Figure 2.1B).

Originally named the 'Turkish' Plate (McKenzie, 1970), further work has revealed the Anatolian sub-Plate as a structurally complex zone of terranes accreted onto the northern margin of the Tethys during subduction of the Tethys oceanic lithosphere (e.g. Robertson et al., 2013).

Although the morphology and seismicity of the Gulf of Suez allowed earlier workers to consider the Sinai Peninsula as having moved separately to the African Plate (see Section 2.6.5), the limits of the 'Sinai Plate' are uncertain and several competing outlines have been proposed. These are described in Section 2.6.5 and discussed as the focal subject of Chapter 4. As with other microplates the Sinai Sub-Plate is often omitted from large scale plate models (e.g. DeMets et al., 2010).

Rybakov and Segev (2004) integrated borehole, seismic, gravity and magnetic data to produce a map of the top of the crystalline basement in the Levant. This map provides a useful overview of the basement relief at the regional scale, although on the basis of the data and published literature discussed in this study many areas are demonstrably inaccurate at finer resolutions.

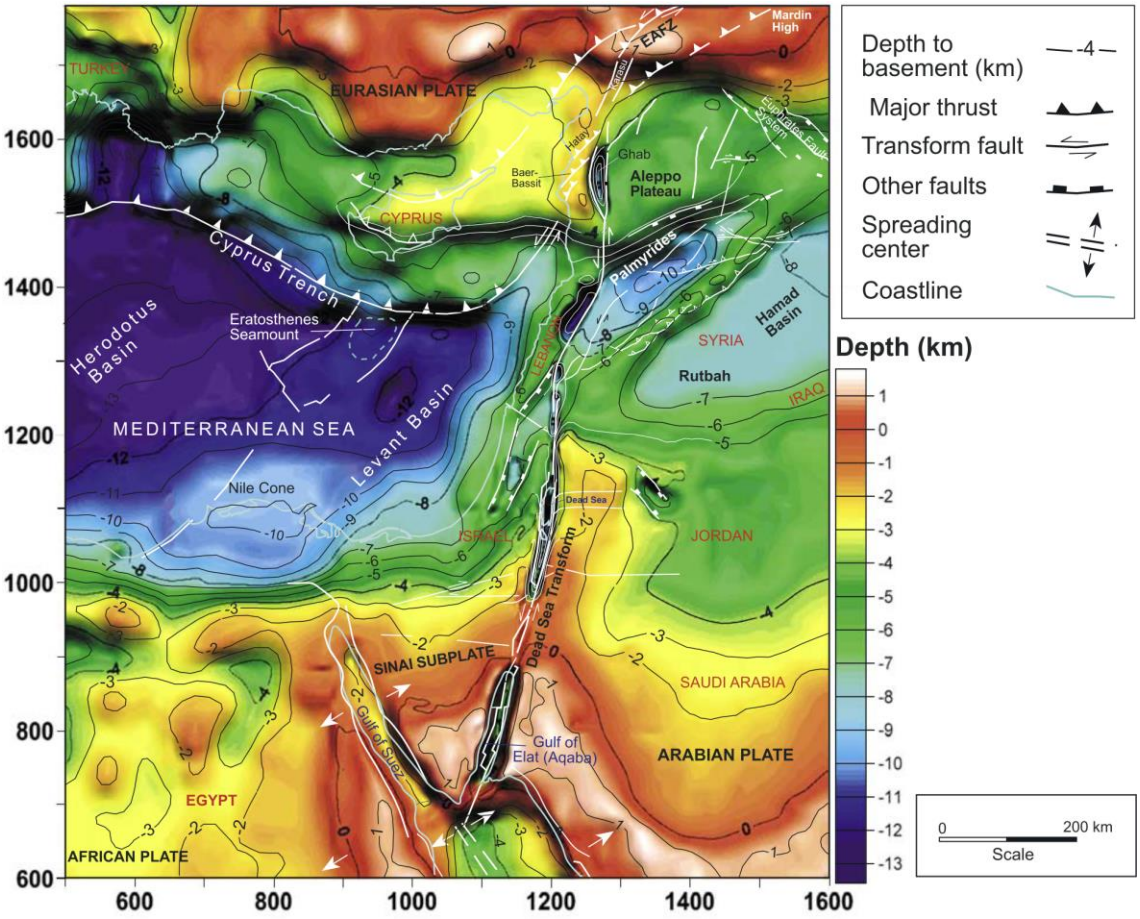

Figure 2.2-Depth to crystalline basement in the EMR (Rybakov and Segev, 2004).

The distribution of different lithospheric types in the offshore EMR has been the source of some controversy (Cowie and Kusznir, 2012a). Whether the Levantine Basin is floored by oceanic crust (Garfunkel, 1998; Ginzburg and Ben-Avraham, 1987; Woodside, 1977) or not (Ben-Avraham et al., 2002; Gardosh and Druckman, 2006; Hirsch et al., 1995; Robertson et al., 1996) has been debated, however consensus now converges around thinned continental lithosphere (Bentham et al., 2007; Cowie and Kusznir, 2012a; Gardosh and Druckman, 2006; Netzeband et al., 2006a; Sagy et al., 2015). This is largely based on analysis of seismic refraction profiles of the Levantine Basin showing velocity profiles consistent with thinned continental crust (Ben-Avraham et al., 2002; Netzeband et al., 2006a; Welford et al., 2015), and corroborated by interpretations of seismic reflection data (Gardosh et al., 2010, 2008b; Sagy et al., 2015; this study). It is also supported by refraction data onshore Israel (Makris et al., 1983) and gravity data onshore Syria and Lebanon (Beydoun, 1977; Khair et al., 1997) which appear to show thinning of the continental lithosphere. The presence of Triassic deep-water sediments and extensive volcanism including mid-ocean-ridge type in northern Syria, SW Turkey and the Mamonia Complex of western Cyprus (Robertson, 2007, 1998a) but not in the Levantine margin area indicates that a Tethyan ocean did not extend as far as this region (Gardosh et al., 2010). This corroborates the interpretation for thinned continental crust underlying the Levantine Basin. However, some authors continue to draw oceanic crust underlying the Levantine Basin (Bosworth, 2015; Eppelbaum and Katz, 2015; Montadert et al., 2014; Morris et al., 2015).

It is widely accepted that the Herodotus Basin is underlain by the last remnants of Tethyan oceanic lithosphere (Granot, 2016 and refs. within), with a passive continental margin along north Africa. The location of the boundary between the oceanic lithosphere of the Herodotus Basin and continental lithosphere of the Levantine Basin is uncertain, and discussed further in Section 2.6.4.

The preferred interpretation of crustal type north of the Latakia Ridge comes from extrapolation of field data exposed in onshore Cyprus and Turkey (Robertson et al., 2013; Vidal et al., 2000a), extrapolation of well data offshore SE Turkey (Bowman, 2011), and geophysical studies (Ben-Avraham et al., 1995; Woodside, 1977), all of which suggest an ophiolitic basement. Gravity models by Ergün et al. (2005) concur with these interpretations. North of the Kyrenia thrust system the basement is largely unknown (Calon et al., 2005a), although indirect evidence suggests it is a back-arc or foredeep basin (Aksu et al., 2005a; Mart and Ryan, 2002), both of which would be underlain by thinned continental crust, and an early gravity based study interpreted densities indicating continental crust (Gass and Masson-Smith, 1963, via Harrison et al., 2012). Evidence presented in Chapter 5 concurs with ophiolitic basement east and west of Cyprus, and more speculatively, thinned continental crust north of Cyprus.

2.3 Structural Elements

The complex geological history of the EMR has resulted in an array of geological features (Figure 1.1). A review of our understanding of the tectonic history of the region is given in Section 2.5 and describes the evolution of these features as documented in published literature. The interdependent formation of many of these features causes circular dependencies to arise when attempting to introduce the formation of the features in a chronological order. To circumvent this issue and retain clarity, some of these features are highlighted below to give introduction to Section 2.5. To minimise repetition these highlights do not include the full description of the evolution given later in Section 2.5, but instead focus on the morphology of the feature.

Up-to-date published cross section(s) do not exist that include and show the relationships between all the different features in this study. This is likely due in part to an absence of a convenient ‘line’ along which such a section could be drawn. Figure 2.3 shows a broadly N-S striking composite cross section, and the maps include the locations of other cross section figures included in this section. Figure 3.14 in the following chapter shows regional seismic lines across the whole of the EMR that serve as more contiguous cross sections.

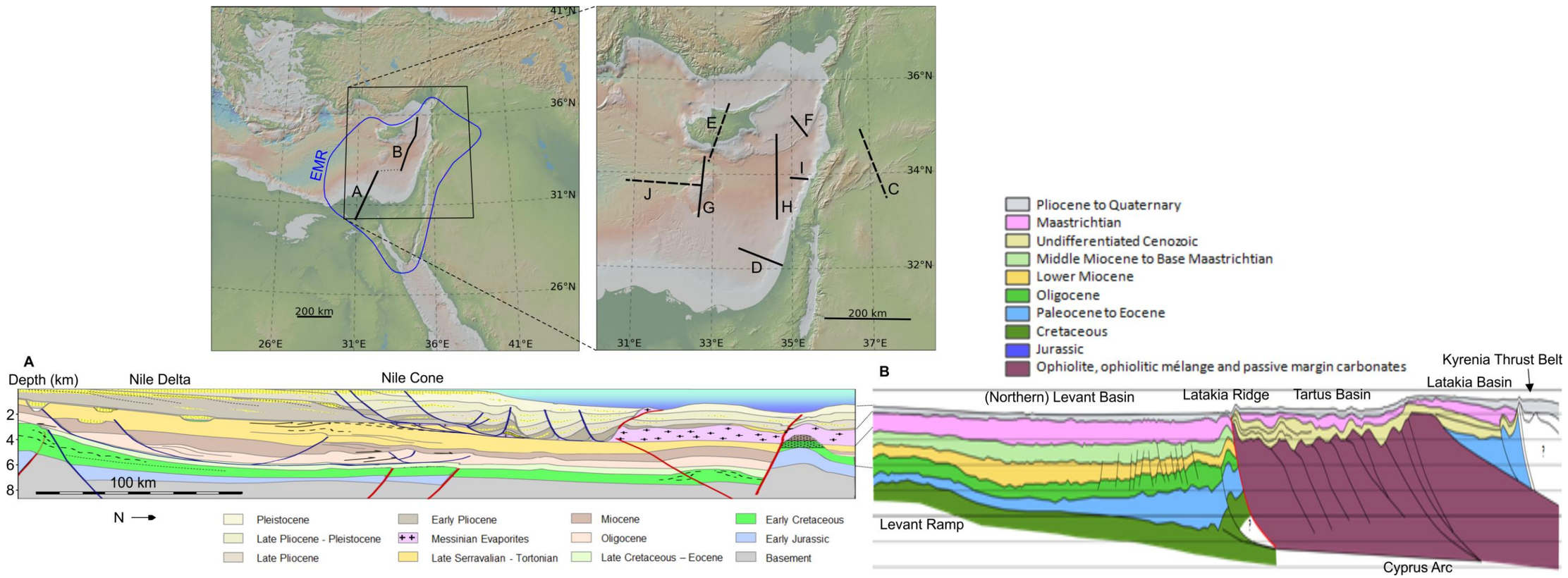

C	Figure 2.4
D	Figure 2.5
E	Figure 2.12
F	Figure 2.13
G	Figure 2.8B
H	Figure 2.6A
I	Figure 2.7
J	Figure 2.10

Figure 2.3- A) Cross section across the Nile Cone (adapted from Bertello et al., 2016) and B) cross section across the Cyprus Arc and Northern Levant Basin (adapted from Plummer et al., 2013) with scales matched, together providing a N-S cross section across the EMR. The maps show the locations of the cross-sections included in this section, and the table links the cross-section letter to the figure number. The global relief (Ryan et al., 2009) vertical scale on the maps is shown on Figure 1.1 and the supplementary figure.

2.3.1 Levant Shear Zone

The Levant Shear Zone (LSZ), often called the Dead Sea Transform or variations thereof, is a strike-slip fault system that runs for c. 1000 km linking extension in the Red Sea with collision in Southern Turkey (Figure 1.1). Displacement is thought to have started in the early Miocene (Eyal and Reches, 1983; Garfunkel et al., 1974; Ginzburg and Kashai, 1981; Hurwitz et al., 2002; Zak and Freund, 1981) and is active today (Figure 2.1B). The Palmyride Mountains (Section 2.3.2) are associated with a restraining bend on the LSZ (Gomez et al., 2007). Several pull-apart basins exist along the LSZ south of the Palmyride Mountains (Figure 1.1), for example the Gulf of Aqaba, Dead Sea and Sea of Galilee (Hardy et al., 2010).

2.3.2 Palmyride Mountains

The Palmyride mountains is a fold and thrust belt in Lebanon and southern Syria. It is understood to be an NE-SW Palaeozoic and Mesozoic Rift Basin that has been inverted in the Late Cretaceous and Cenozoic (Brew et al., 2001; Figure 2.4). The folds represent the northern limit of the Syrian Arc (see Section 2.3.3).

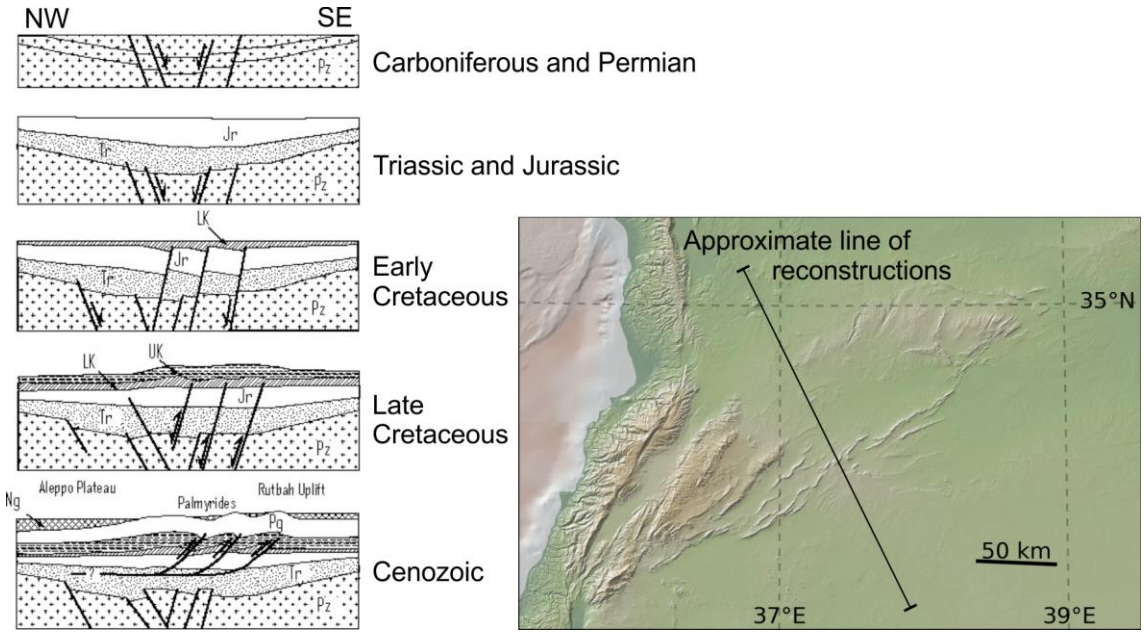

Figure 2.4-Sketch cross sections illustrating the evolution of the Palmyride Mountains (adapted from Sawaf et al., 2001). The global relief (Ryan et al., 2009) vertical scale is shown on Figure 1.1 and the supplementary figure.

2.3.3 Syrian Arc

The Syrian Arc comprises a series of Late Cretaceous to Miocene compressional features that may be traced across Syria, Lebanon, Israel and onshore into NE Egypt (Figure 1.1; Figure 2.5; Hardy et al., 2010). Its name is not currently geographically representative of this feature as it is based on now outdated geographical terminology (Krenkel, 1924; Walley, 1998), and it has be The western edge of the Syrian Arc offshore NE Egypt and Israel was originally interpreted as a transcontinental shear zone by Neev (1977) and termed the Pelusium Line. This is now

understood to represent the same change in basement properties that defined the location of the western edge of the Syrian Arc fold belt (Netzeband et al., 2006a).

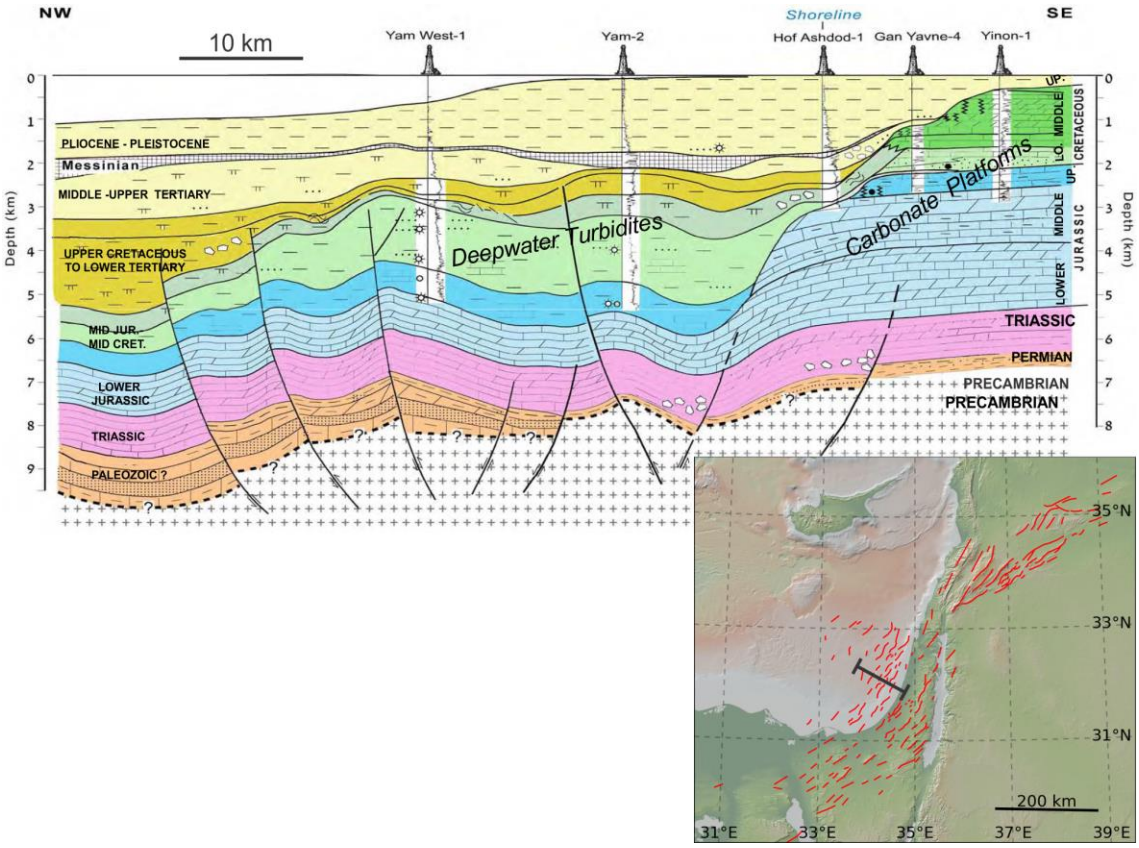

Figure 2.5-Folds showing cross section geometry of the Syrian Arc folds offshore Israel (adapted from Gardosh et al., 2008b) and map showing the axial traces of Syrian Arc folds marked in red (adapted from Walley, 1998 and others). The global relief (Ryan et al., 2009) vertical scale on the minimap is shown on Figure 1.1 and the supplementary figure.

2.3.4 Levantine Basin

The Levantine Basin (sometimes called the Levant Basin) is located between the southern edge of the Cyprus Arc, the Syrian Arc and the Eratosthenes Seamount (Figure 1.1). It may be divided into Northern and Southern sections along a feature called the Levant Ramp (Hodgson, 2012). This linear slope is more pronounced on deeper stratigraphic horizons and divides the deeper northern basin from the shallower southern basin, and is described in detail in Section 3.6.4. Up to c. 9 s TWTT of Cenozoic sediments exist in the northern part of the basin, and up to c. 7 s TWTT of equivalent stratigraphy in the southern part (Figure 2.6). These sediments have remained relatively undisturbed in comparison to the severe tectonic deformation in the surrounding regions, but are segmented by a series of anomalous strata bound normal faults which are outlined in Section 2.6.6 and discussed in detail in Chapter 6. These sediments are fairly planar at the regional scale in the northern Levantine Basin, but in the southern Levantine Basin several features break up the Palaeogene to early Miocene sediments, including structural inversion and drape folds which form hydrocarbon traps (Figure 2.6B), carbonate mounds including the Jonah High (Figure 2.6B), and a basement high protruding from the margin called the Saida-Tyr Plateau (Figure 2.6A). Along the eastern margin of the southern Levantine Basin the Cretaceous-Palaeogene sediments are folded by Syrian Arc deformation (Figure 2.6B). In the

Southern Levantine Basin NE-SW trending Mesozoic rift faults are widespread (Gardosh et al., 2010, 2008b). Equivalent age rift faults are less well resolved in the Northern Levantine Basin, however Reiche et al. (2014a, fig. 2a) interpret a series of normal faults deforming the Mesozoic sediments. These are discussed in Section 6.6.8.

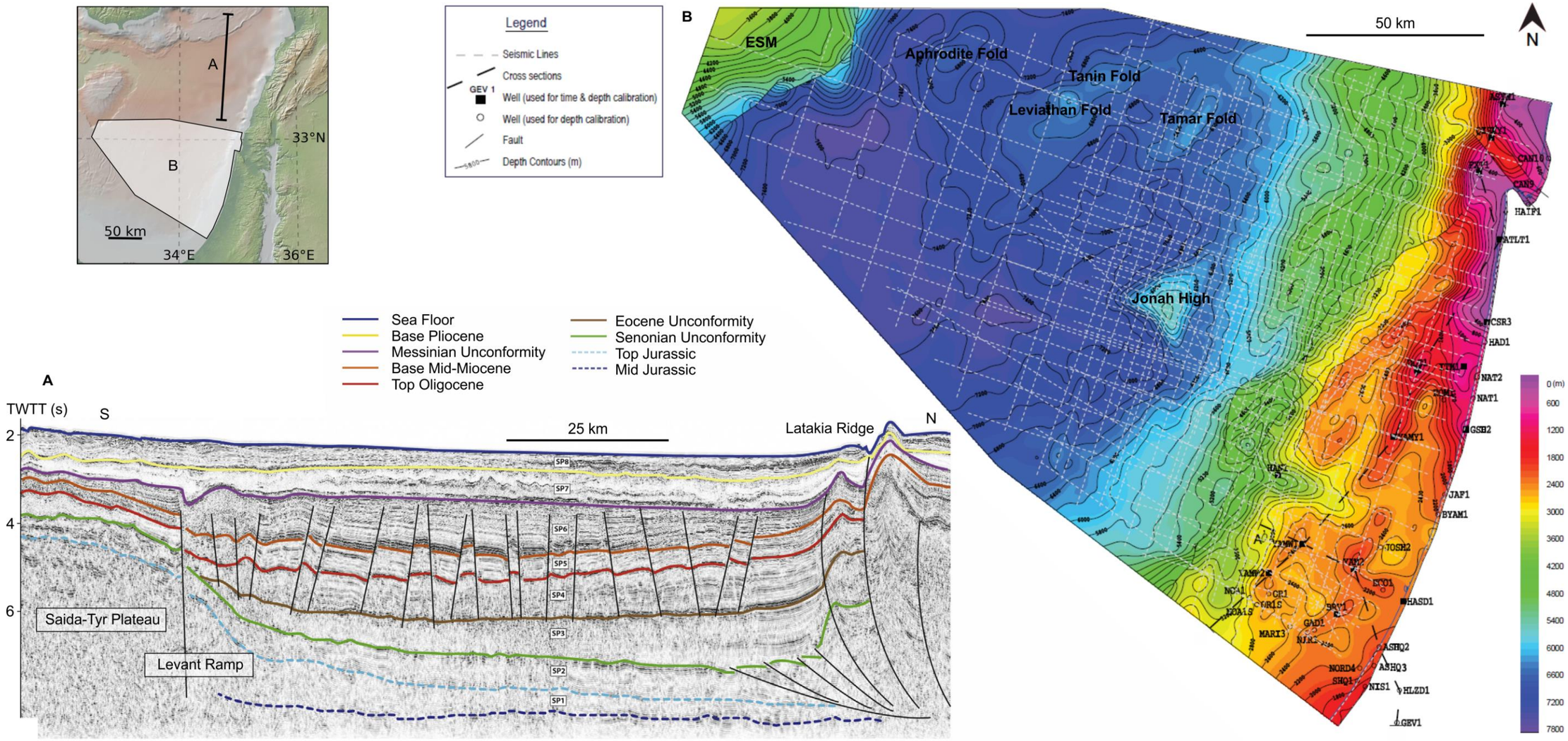

Figure 2.6-A) S-N striking interpreted seismic line across the Northern Levantine Basin and Levant Ramp adapted from Hawie (2013); B) Base Oligocene (equivalent to Eocene Unconformity on the seismic line) surface map adapted from Gardosh et al. (2008b) with some features labelled. The global relief (Ryan et al., 2009) vertical scale on the minimap is shown on Figure 1.1 and the supplementary figure.

2.3.5 Levant Continental Margin

The Levant continental margin lies between the Levantine Basin and LSZ. It forms a component part of the Tethys rift margin which extends from northern Sinai to the Syrian Coast (Figure 1.1). The margin has minimal rift faults visible and has undergone some inversion offshore Lebanon (Figure 2.7; Ghalayini et al., 2016), and significant folding associated with the Syrian Arc offshore Israel (Figure 2.6B; Figure 2.5; Gardosh et al., 2008b).

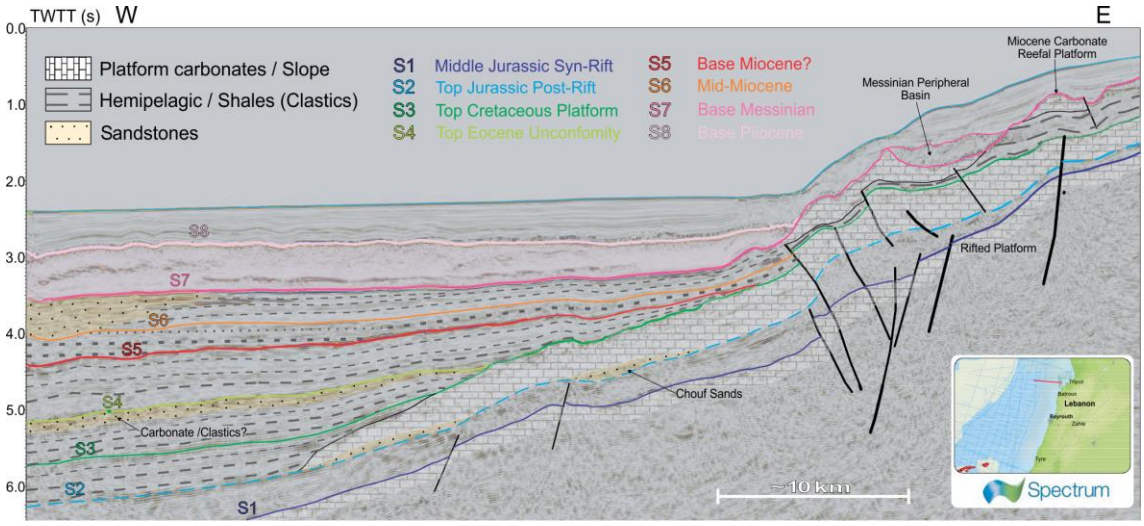

Figure 2.7-W-E striking seismic line showing the Levant margin offshore Lebanon (adapted from Nader et al., 2016).

Several canyons have formed along the margin; in the Plio-Quaternary offshore Syria (Tahchi et al., 2010), in the early Cretaceous offshore Lebanon (Hawie et al., 2013), and throughout the Cenozoic offshore Israel (Druckman et al., 1995; Gardosh et al., 2008b; Garfunkel et al., 1979; Katz et al., 2015; Lugli et al., 2013). Recent gravity collapses have also formed along the margin (Garfunkel et al., 1979; Tahchi et al., 2010). The largest of these superficial margin features is the Palmahim disturbance, a Palaeogene canyon re-eroded during the Messinian and subsequently the site of mass wasting, the decollement surface for which is an embayment of evaporites deposited in the Messinian canyon (Garfunkel et al., 1979; Katz et al., 2015).

2.3.6 Eratosthenes and Hecataeus Continental Fragments

The Eratosthenes Seamount is a bathymetric high ~100 km south of Cyprus (Figure 2.8). Although originally interpreted as a volcanic seamount, analysis of refraction lines and magnetic data suggest it is underlain by a heavily intruded continental crust (Ben-Avraham et al., 2002, 1976; Garfunkel and Derin, 1984; Kempler, 1998; Rybakov et al., 2011; Welford et al., 2015; Zverev and Ilinsky, 2005, 2000). OPD wells drilled on the structure showed it is capped by a drowned carbonate platform (Robertson, 1998b). Some studies use the term Eratosthenes Continental Block to describe the feature (Hawie et al., 2013; Montadert et al., 2014; Skiple et al., 2011), but this term implies exclusion of the carbonate platform that overlies the basement high, and makes an unproven assertion about the composition of the basement high. Consequently, this study uses the name Eratosthenes Seamount (abbreviated to ESM) to describe the intruded continental block (or volcanic edifice) and carbonate platform that make up the bathymetric high.

This matches the terminology of other authors who also consider the feature to be non-volcanic (Loncke et al., 2006; Reiche and Hübscher, 2015; Robertson et al., 1998; Schattner, 2010; Welford et al., 2015). It also matches the definition of the International Hydrographic Organization (IHO) that defines a seamount without any volcanic connotations:

"A distinct generally equidimensional elevation greater than 1000 m above the surrounding relief as measured from the deepest isobath that surrounds most of the feature" (IHO, 2013).

Although various publications have focused on aspects of the periphery, post-MSC sediments, and deep structure of the ESM (Erbek and Dolmaz, 2014; Galindo-Zaldívar et al., 2001; Klimke and Ehrhardt, 2014; Loncke et al., 2006; Spezzaferri and Tamburini, 2007; Welford et al., 2015; Zverev and Ilinsky, 2005), the only publications known to this author to have explored Mesozoic and Cenozoic stratigraphy of the features are the suite of papers on the results of the ODP survey, summarised in Robertson (1998c), and Montadert et al. (2014). Figure 2.24 and Figure 2.8 illustrate the results of these studies respectively.

The Hecataeus Rise lies <50 km SE of Cyprus and is a less pronounced bathymetric high (Figure 2.8; Reiche and Hübscher, 2015). Seismic refraction and gravity modelling suggests that it may also be underlain by continental crust (Welford et al., 2015). This feature and the Eratosthenes seamount are understood to be partially underthrusted into the relic subduction zone (Robertson, 1998b; Welford et al., 2015).

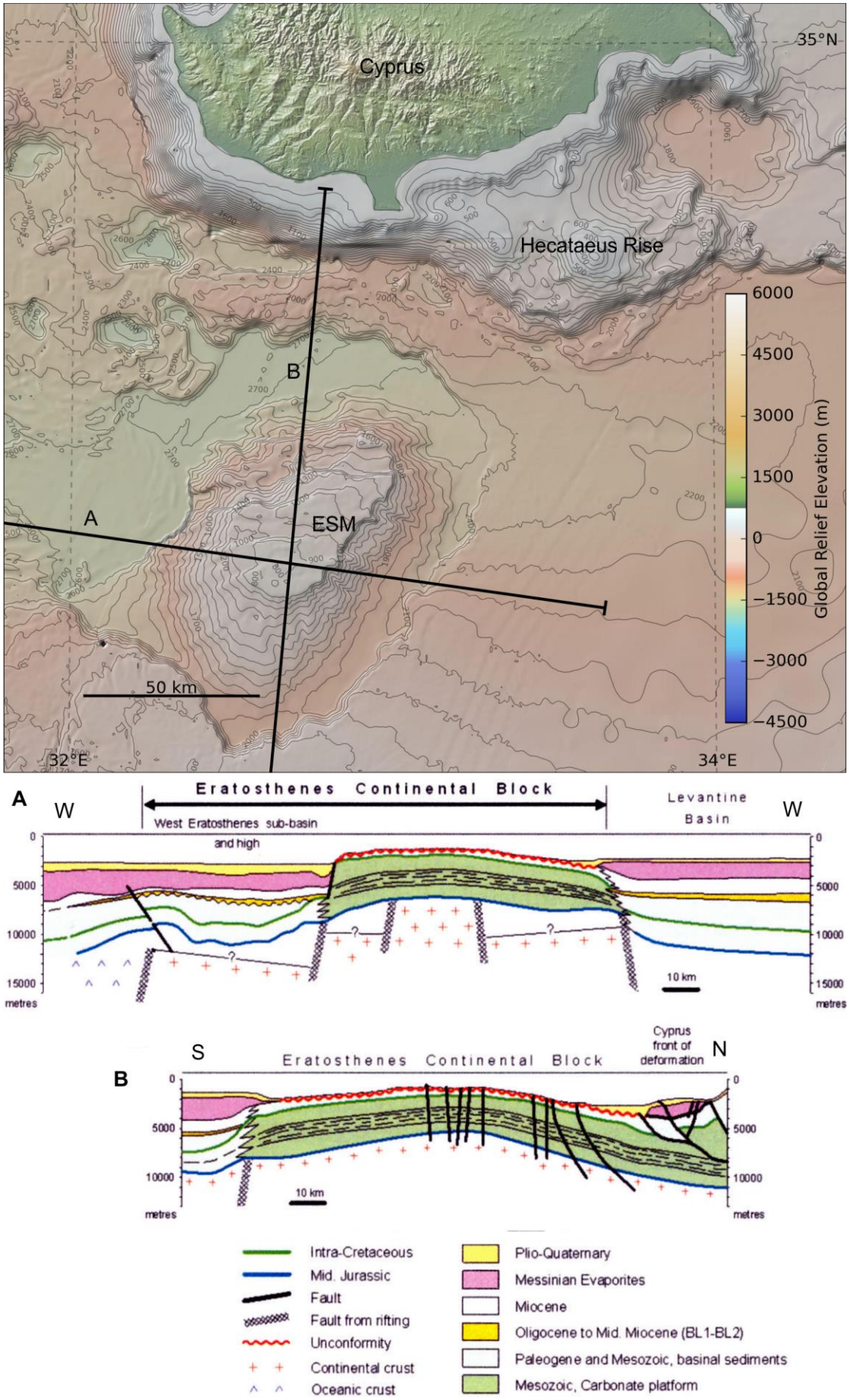

Figure 2.8-Bathymetry of the ESM and Hecataeus rise, and sketch cross sections over the ESM (adapted from Montadert et al., 2014).

2.3.7 Nile Cone

The Nile Cone is the name given to the accumulated sediments deposited by the River Nile into the Mediterranean basin since the Miocene (Said, 1981). It is c. 500 km in diameter (Figure 1.1) and the sediments are up to 3.5 km thick (Gaullier et al., 2000). The sediments consist mainly of deltaic and marine clastics which are occasionally offset by syn- and post-depositional faulting (Figure 2.9). The Nile cone is a prolific hydrocarbon province; the main play being deltaic sandstones charged by biogenic gas. Because of exploration activity, the stratigraphy of this offshore area is far better known than that of other parts of the offshore EMR (Figure 2.9). Two major fault trends exist off the Nile Delta shoreline, the NE-SW striking Rosetta fault and the NW-SE striking Temsah fault trends (see supplementary figure; Aal et al., 2001). The underlying Mesozoic basin architecture continues the linear shelf break trend of the north Sinai and Western Desert continental margins (Tassy et al., 2015).

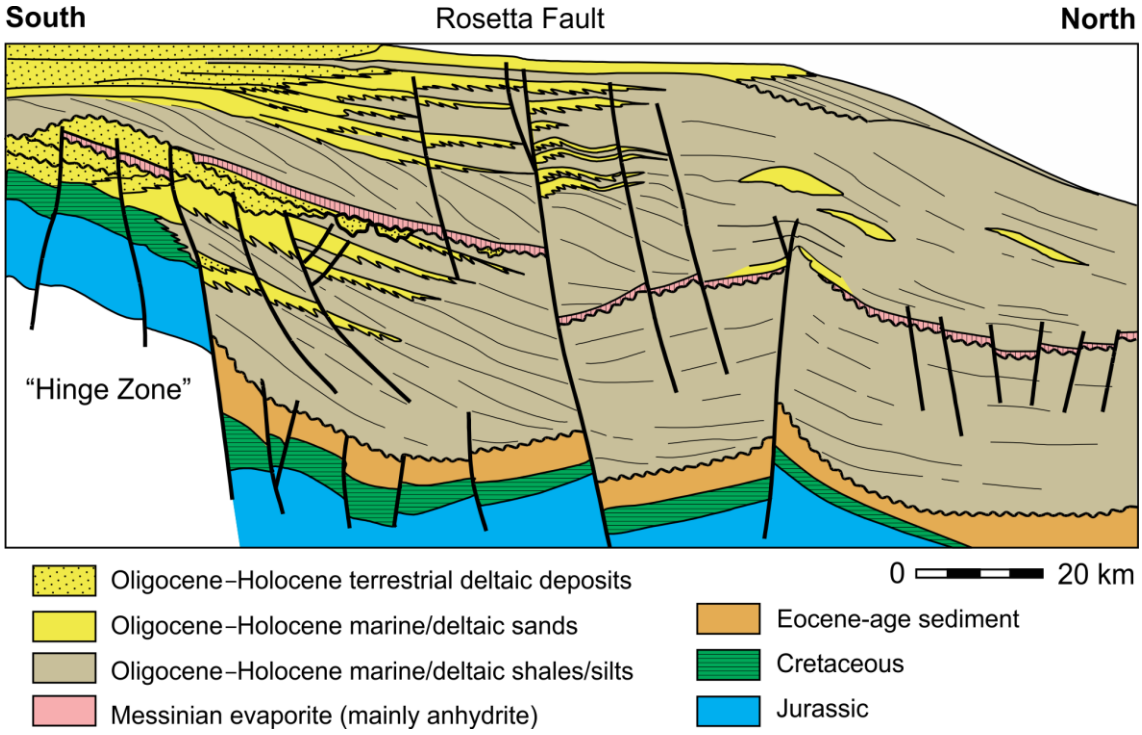

Figure 2.9-Type-example N-S striking cross section of the Nile cone (modified from Samuel et al., 2003).

2.3.8 Herodotus Basin

The Herodotus Basin is a deep oceanic basin capped by Plio-Quaternary sediments deformed by complex salt tectonics (Allen et al., 2016; Camera et al., 2010; this study; Loncke et al., 2006; Montadert et al., 2014; Skiple et al., 2012). It extends from the Nile Cone, ESM and western limb of the Cyprus Arc to the Hellenic Arc and African margin. Please refer to Section 2.5.4 for the background on the presence of the salt. The area has seen little in the way of exploratory drilling and is therefore poorly defined chronostratigraphically. However, it is understood to be underlain by the last remnants of Early Mesozoic Neotethys oceanic crust (Figure 2.1; also see Section 4.5). Active subduction of this crust is occurring at its northern margin (Rotstein and Kafka, 1982), although some authors draw a deformation/subduction front through the centre of the basin

(Avigad et al., 2016; Camera et al., 2010; Inati et al., 2016). Two spurs of the Mesozoic ESM carbonate platform extend under the eastern edge of the Herodotus Basin (Montadert et al., 2014).

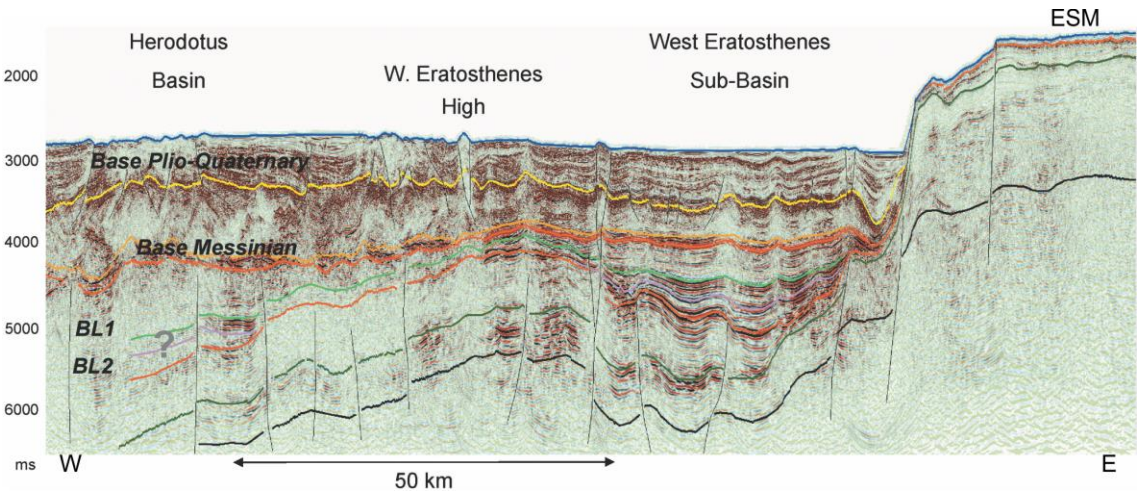

Figure 2.10-E-W striking seismic line across the Herodotus basin, adapted from Montadert et al. (2014).

2.3.9 Cyprus

Cyprus is an island c. 150 km in diameter in the easternmost Mediterranean Sea. It is composed of four geological terrains (Figure 2.12); 1) the structurally complex Kyrenia Terrane composed of Permian to Recent sedimentary and limited metamorphic and igneous rocks, 2) the Middle Triassic to Upper Cretaceous Mamonia Complex of igneous, metamorphic and sedimentary lithology, 3) the Upper Cretaceous Troodos Ophiolites, and 4) the Upper Cretaceous to Pleistocene autochthonous sedimentary rocks (Robertson and Xenophontos, 1997). It is located adjacent to the southern convergent margin of the Anatolian Plate and has been subject to ongoing uplift since the Miocene resulting in its progressive emergence (Figure 2.12; Robertson and Xenophontos, 1997). Underthrusting and serpentinite diapirism related uplift has also inverted the island, with progressively older rocks now exposed topographically higher (Figure 2.12; Figure 2.12; Robertson and Xenophontos, 1997).

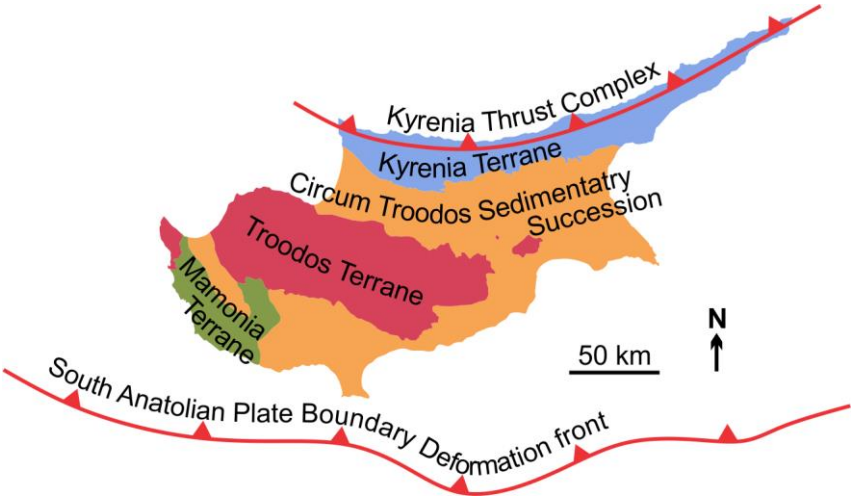

Figure 2.11-The different geological terrains of Cyprus (adapted from Constantinou, 1995) and location of the adjacent plate boundary deformation front.

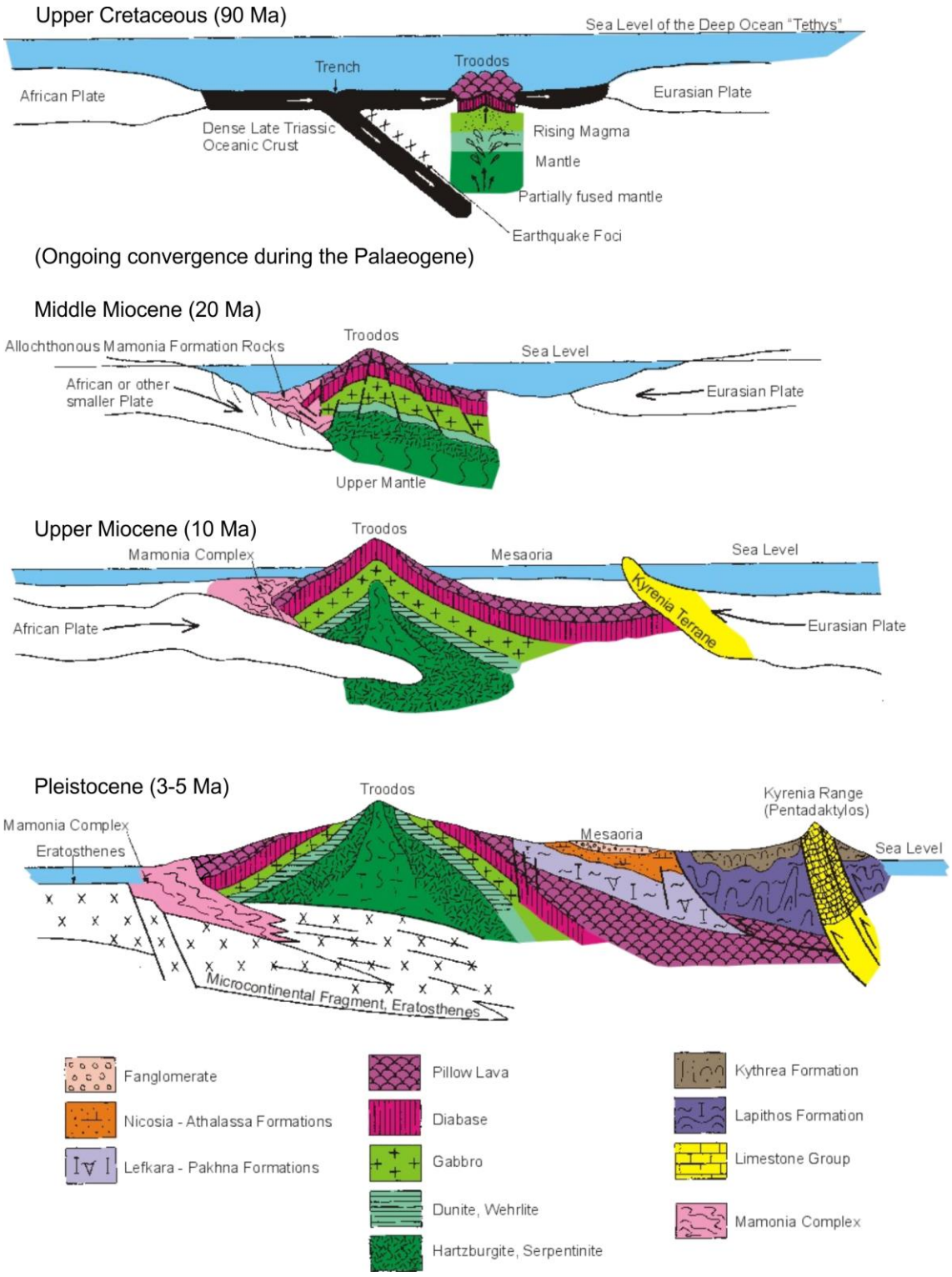

Figure 2.12- Schematic presentation of the genesis of the Troodos Ophiolite and the evolution of the Island of Cyprus, adapted from a figure prepared the Geological Survey Department of the Republic of Cyprus (Unknown, 2005).

2.3.10 Cyprus Arc

The Cyprus Arc is an arcuate zone of topographical and bathymetric highs underlain by convergent structures along the southern margin of the Anatolian Plate (Ben-Avraham et al., 1995; Bowman, 2011; Hall et al., 2005b; Reiche et al., 2015; Sage and Letouzey, 1990; Vidal et al., 2000a; Woodside et al., 2002) that includes the island of Cyprus (Section 2.3.9). A series of

bathymetric ridges and the southern margin of Cyprus represent the leading edge of the Cyprus Arc deformation and the southern margin of the Anatolian Plate. The seaward extensions of the Kyrenia Range thrust system in northernmost Cyprus represents the northern margin of the Cyprus Arc (Section 2.5). Much of the nomenclature associated with the Cyprus Arc is inconsistent in published literature. Resolution of this issue is included in the investigation of the Cyprus Arc in Chapter 5. To the east the Arc joins the Bitlis Suture, and to the west it joins the Hellenic Arc at the Anaximander Mountains.

Although originally formed through subduction of Tethyan oceanic lithosphere, the Cyprus Arc is understood to be undergoing incipient continent-continent collision (Bowman, 2011). Collision and docking of continental blocks (Section 2.3.4) in the subduction zone has brought about this transition (Robertson, 1998b; Welford et al., 2015). The Cyprus Arcs arcuate shape means that the components of convergent and transform deformation varies along the strike of the feature (Vidal et al., 2000a). The Cyprus Arc and associated deformation is introduced in more detail and investigated in Chapter 5.

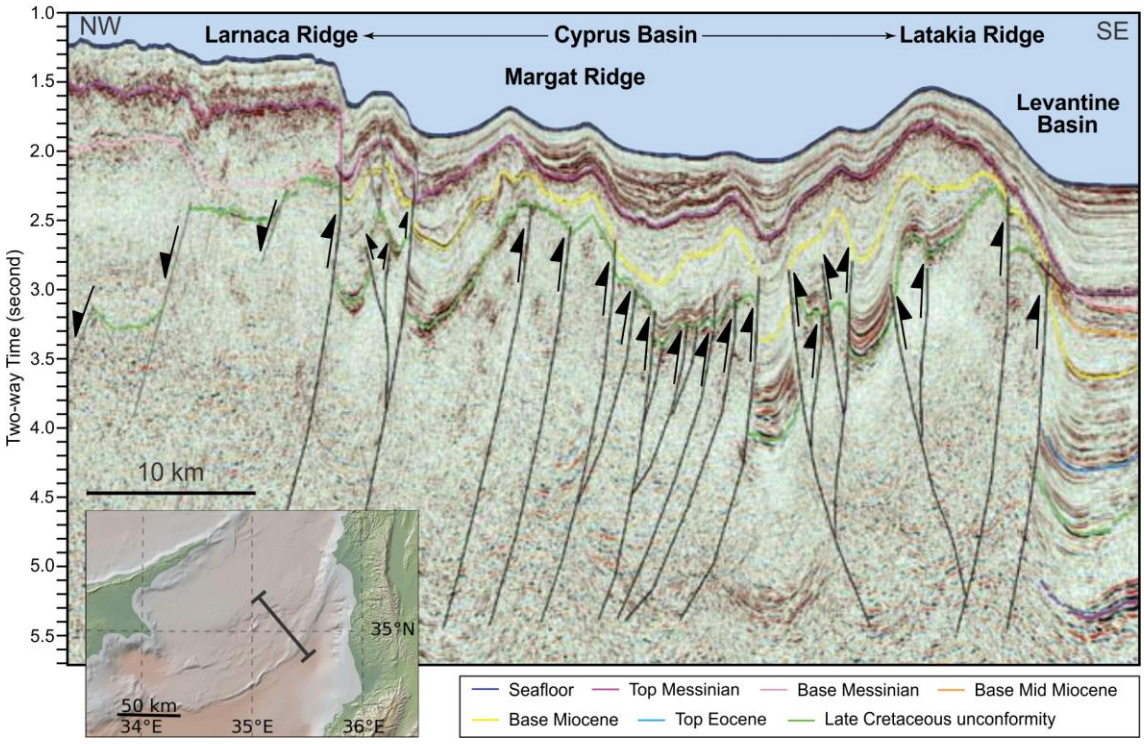

Figure 2.13-Seismic Line across the Cyprus Arc east of Cyprus adapted from Bowman (2011). The global relief (Ryan et al., 2009) vertical scale on the minimap is shown on Figure 1.1 and the supplementary figure.

An alternative to the section of plate boundary south of Cyprus was suggested by Papazachos & Papaioannou (1999) based on focal mechanisms and comparison with the Hellenic Arc. Their alternative runs further south than that drawn on Figure 2.11 and includes a NS transform fault south of the western edge of Cyprus. However this doesn't match data in later studies of the area (Reiche et al., 2015; Reiche and Hübscher, 2015; Welford et al., 2015).

2.3.11 Peripheral Features

The Hellenic Arc is an active subduction zone formed by the southward motion of the Aegean Plate over the Herodotus Basin oceanic crust (Figure 1.1). If forms the island arc of Southern Greece.

The Bitlis Suture is the tectonic boundary between the Arabian and Eurasian Plates (Figure 1.1) and represents the collision stage of the Wilson Cycle (Wilson, 1966) following the closure of the Neo-Tethys Ocean.

The African passive continental margin adjacent to the EMR runs along the Libyan and northern Egyptian coastline, connecting the African continental craton with the oceanic crust of the Herodotus Basin (Figure 2.1; Figure 2.2). Further east the passive continental margin is less abrupt as the continent ocean boundary trends NE from the Nile Delta, and the Nile Delta covers the edge of the crystalline basement (Figure 2.1; Figure 2.2).

The Red Sea and its northern and southern continuations, the Gulf of Suez and Gulf of Aden respectively, are underlain by thinned continental crust that formed by rifting of the Arabian Plate from the African Plate during the Tertiary.

2.4 Stratigraphic Configuration

The best understanding of the stratigraphy of the EMR integrates geophysical data (Figure 2.1), surface geological mapping (Figure 2.14), seismic reflection and seismic refraction data, and well data. Wells drilled in the onshore EMR have been combined to produce stratigraphic columns (Figure 2.15). Numerous wells have been drilled in the offshore EMR, the majority in the Nile Cone but many offshore Israel, some in the Iskenderun Basin and recently a few in the deep Levantine Basin. However, the vast majority, including all those in the deeper portions of the basins, are generally inaccessible to the wider scientific community. Some shallow academic boreholes have been drilled but on bathymetric highs. Consequently, the offshore stratigraphy is uncertain and a full chronostratigraphic description is not possible as part of this study. A speculative stratigraphic column offshore south Cyprus based on 2D seismic reflection data, regional knowledge and limited well control is the most complete published stratigraphic column of the offshore EMR that transects the data available to this study (Figure 2.15).

Many studies have been published in the EMR that utilise seismic reflection data (Table 1). Cross sections drawn from this data, at a scale that covers national and single geological features, were shown with the description of the pertinent feature in Section 2.3. No summarising EMR scale cross sections published in recent (i.e. last 10 years) peer-reviewed publications were uncovered during the investigation by this study. The older EMR cross sections (Garfunkel, 1998; Sage and Letouzey, 1990) contain elements that have been shown to be inaccurate by later publications, and so are not included here. Regional offshore cross sections based on the regional seismic data available to this study are shown later in Figure 3.14.

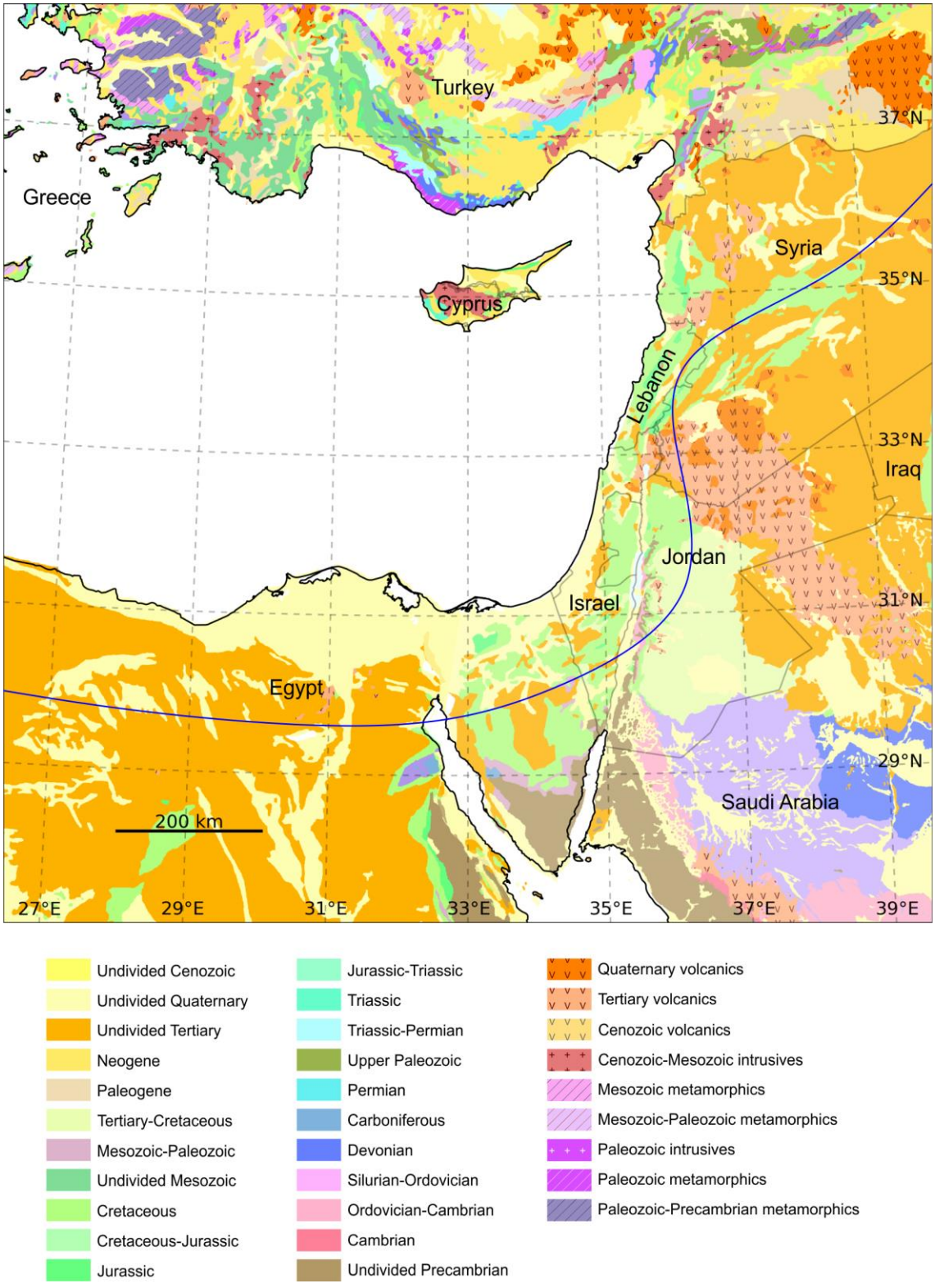

Figure 2.14-Geological map of the EMR (data courtesy of the U.S. Geological Survey). The blue line shows the approximate trace of the well correlation shown in Figure 2.15, no specific location for this well correlation was provided.

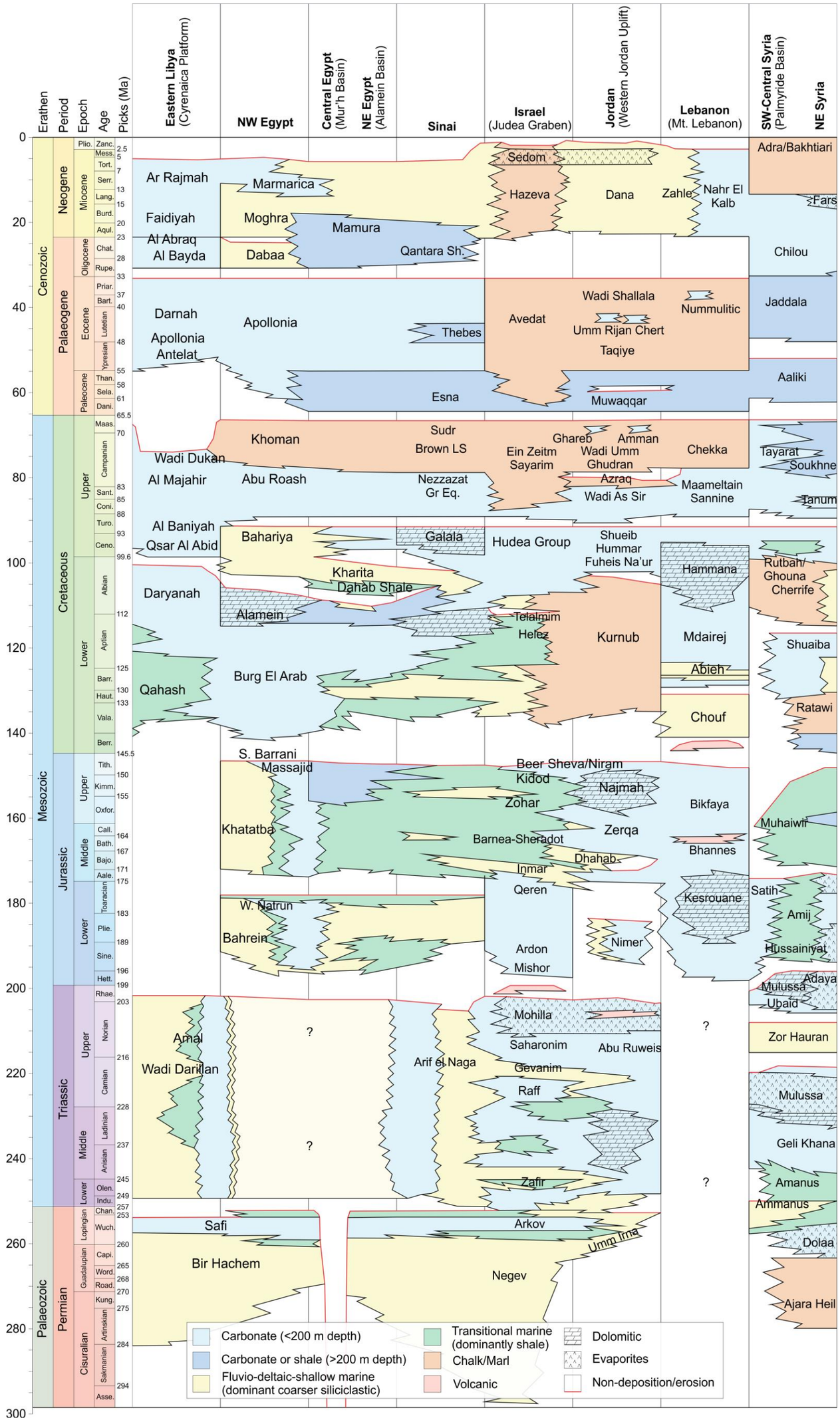

Figure 2.15-Comparitive stratigraphic columns across the onshore EMR, adapted from Kendall et al. (2014). The approximate trace of the correlation is shown in Figure 2.14.

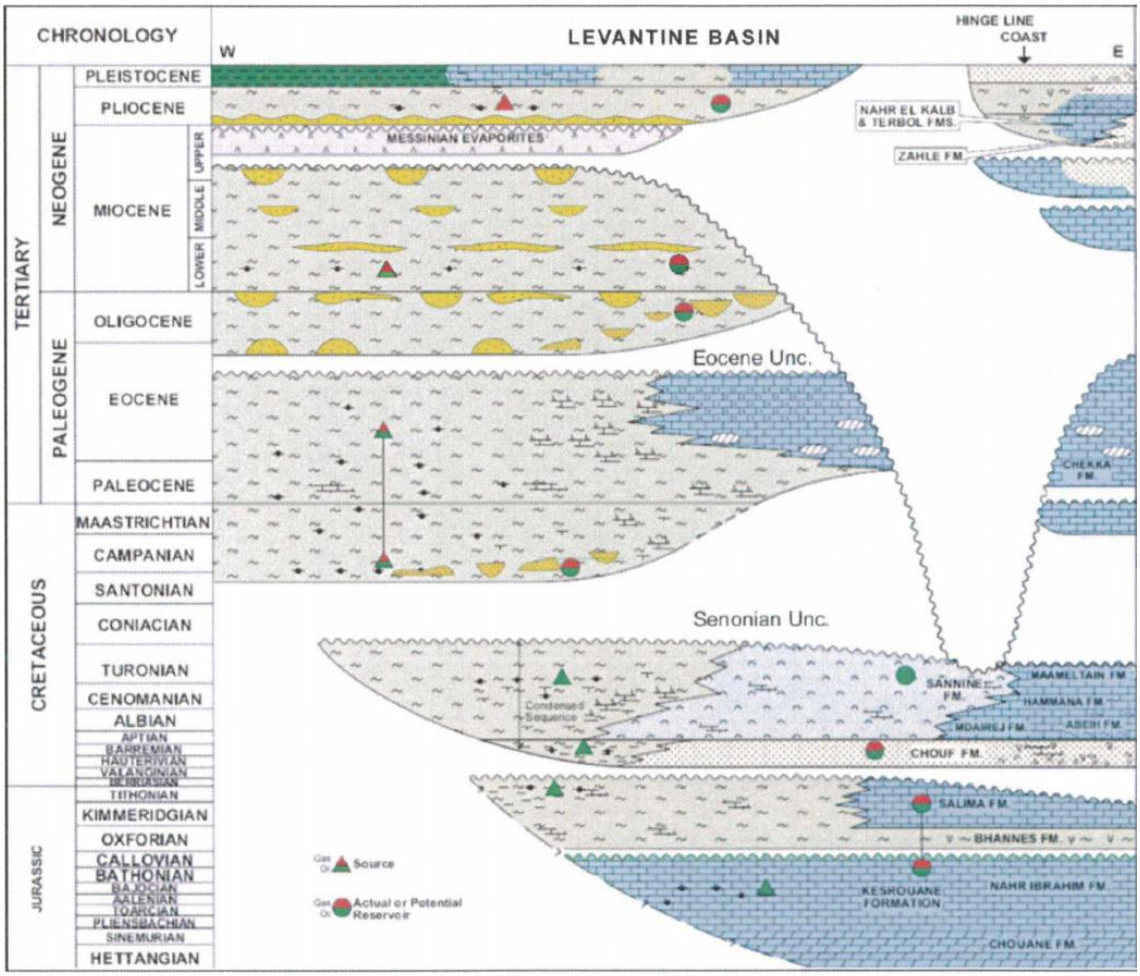

Figure 2.16-Stratigraphic column of the Northern Levantine Basin adapted from Skiple et al (2011). No specific location was given.

Table 1-List of studies including published interpretations of seismic reflection data in the EMR (non-exhaustive).

Seismic Coverage	Onshore	Offshore	
		2D data	3D (and 2D) Data
Israel	(Mechie et al., 2009)	(Ben-Avraham et al., 2006; Ben-Gai et al., 2005; Cartwright and Jackson, 2008; Druckman et al., 1995; Gardosh, 2013, 2009, Gardosh et al., 2011, 2010, 2008a; Gardosh and Druckman, 2006; Gradmann et al., 2005; Gvirtzman, 2010; Gvirtzman et al., 2008; Katz et al., 2015; Netzeband, 2006; Sagy et al., 2015; Schattner et al., 2006; Schattner and Ben-Avraham, 2007)	(Baudon and Cartwright, 2008; Bertoni and Cartwright, 2015, 2007, 2006, 2005; Cartwright et al., 2012; Clark and Cartwright, 2013; Feng et al., 2016; Feng and Reshef, 2016; Frey-Martínez et al., 2006; Frey-Martínez, 2005; Fuhrmann, 2010; Gvirtzman et al., 2013; Omeru and Cartwright, 2015; Zucker et al., 2017)
Egypt	(Moustafa, 2010; Sarhan et al., 2013)	(Aal et al., 2001, 2000; Camera et al., 2010; Loncke et al., 2006; Tari et al., 2012; Tassy et al., 2015; Yousef et al., 2010)	(Cross et al., 2009; Hanafy et al., 2016; Kirkham et al., 2017; Omeru and Cartwright, 2015; Samuel et al., 2003; Tari et al., 2012)
Lebanon	(Nader et al., 2016)	(Hawie et al., 2013; Nader et al., 2016; Reiche et al., 2014a)	(Ghalayini et al., 2014; Kosi et al., 2012; Lie and Trayfoot, 2009)
Syria and east of Cyprus	(Brew, 2001; Brew et al., 2001a, 2001b; Litak et al., 1998)	(Ben-Avraham et al., 1995, 1988; Bowman, 2011; Bridge et al., 2005; Calon et al., 2005a; Hall et al., 2005a, 2005b; Hübscher et al., 2009; Kempler, 1998; Kempler and Garfunkel, 1994; Maillard et al., 2011; Plummer et al., 2013; Tahchi et al., 2010; Vidal et al., 2000a)	
South of Cyprus	(Ben-Avraham et al., 2006; Calon et al., 2005a; Klimke and Ehrhardt, 2014; Mascle et al., 2000; Montadert et al., 2014; Reiche, 2015; Reiche et al., 2015, 2014b; Reiche and Hübscher, 2015; Robertson, 1998b; Schattner, 2010)		
West of Cyprus	(Aksu et al., 2009; Calon et al., 2005b; ten Veen et al., 2004; Woodside et al., 2002; Zitter et al., 2003)		
South of Turkey	(Aksu et al., 2014, 2005b; Albora et al., 2006; Hall et al., 2014; Sellier et al., 2013)		
Regional	(Allen et al., 2016; Ben-Avraham et al., 2002; Camera et al., 2010; Esestime et al., 2016; Gorini et al., 2015; Lofi et al., 2011; Netzeband et al., 2006b; Roberts et al., 2010; Roberts and Peace, 2007; Skiple et al., 2012)		

Widespread unconformities appear in the early Palaeocene, Oligocene and late Miocene in the onshore stratigraphy (Figure 2.15). These unconformities also form major boundaries offshore and are key horizons interpreted later in this study (see Chapter 3).

2.5 Tectonic Evolution

A large volume of literature exists contains information on the tectonic evolution of the EMR and various studies have summarised different aspects of the tectonic evolution of the EMR. For a focussed look at different areas the reader is referred to the paper referenced for each area on

Figure 2.17. Several plate scale tectonic reconstructions have been published that include the EMR, these are summarised in Table 2. A synthesis of our understanding of the tectonics of the EMR is summarised graphically in Figure 2.18, and outlined in the following sections.

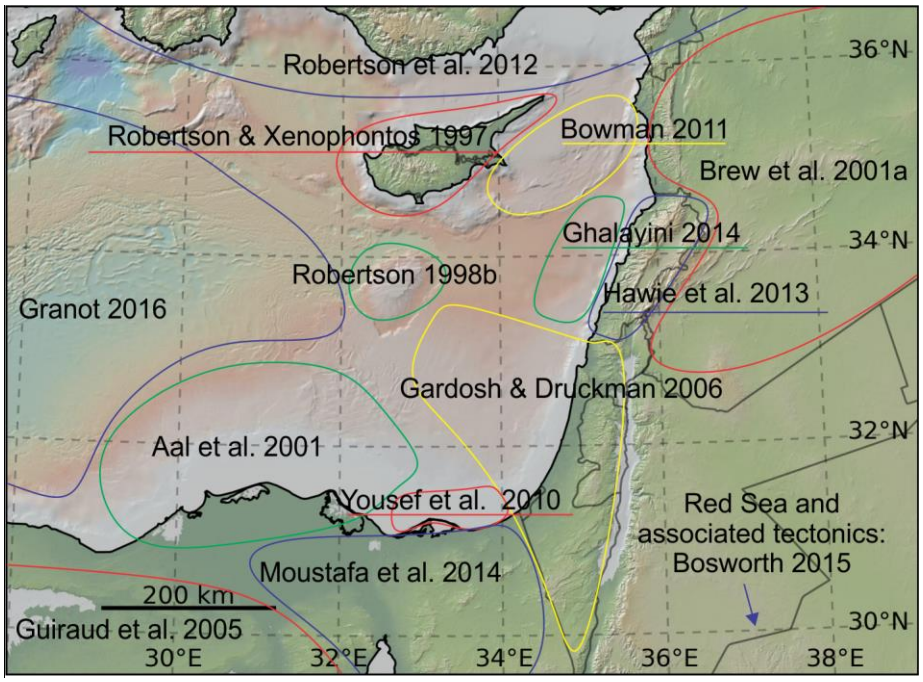

Figure 2.17-Map showing the different areas summarised in the cited studies (the reader is advised that these are not necessarily the most recent papers that provide a summary of the area, but the most suitable study for providing regional context). Offshore studies are generally (re)interpretations of a review of the data in the area, and onshore studies are generally collations of the conclusions of previous studies. The global relief (Ryan et al., 2009) vertical scale is shown on Figure 1.1 and the supplementary figure.

Table 2-List of plate reconstructions that include the EMR (listed in ascending age of publication).

Author(s)	Remit	Reconstruction output and notes
van Hinsbergen (2016)	Central Anatolia (Turkey)	Subset of a Mediterranean-wide GPlates (Williams et al., 2012) digital reconstruction model, likely to be released in 2017 (van Hinsbergen, personal communication October 2016).
Berra & Angiolini (2014)	Tethyan margins	10 global paleogeography and major depositional settings of the Tethys from the Cambrian. Integrates new data since Barrier & Vrielynck (2008).
Robertson et al. (2013)	Anatolia and periphery	6 palaeotectonic maps for late Permian to mid-Miocene. Focuses of accretion of Anatolian continental slivers.
Barrier & Vrielynck (2008)	Middle East	14 detailed tectono-sedimentary-palinspastic maps showing late Norian to Pliocene.
Guiraud et al. (2005)	Northern and central Africa	27 Phanerozoic palaeogeographical and palaeogeological maps. Considers tectonic forces at plate margins (so indirectly covers the EMR).
Stampfli and Borel (2002)	Global, Tethyan focus	21 Ordovician to Cretaceous tectono-palinspastic maps. Focuses on considering plate driving forces.

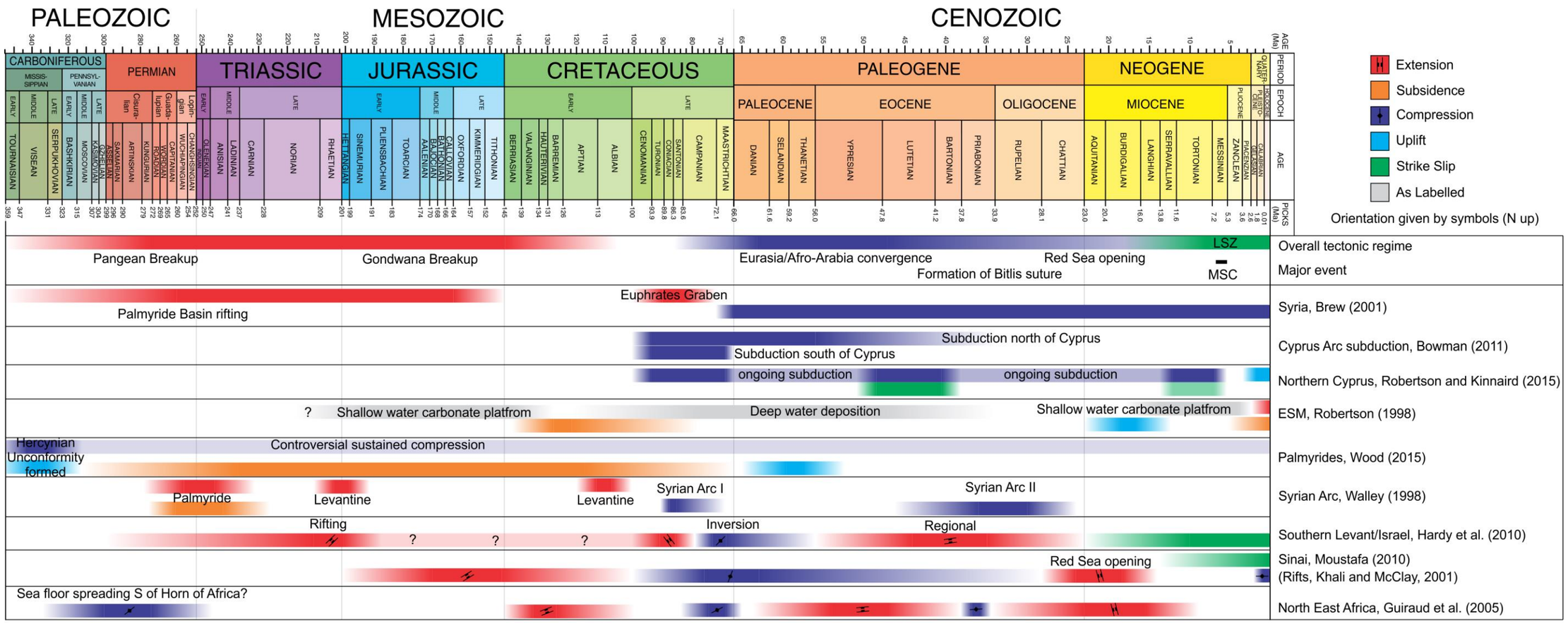

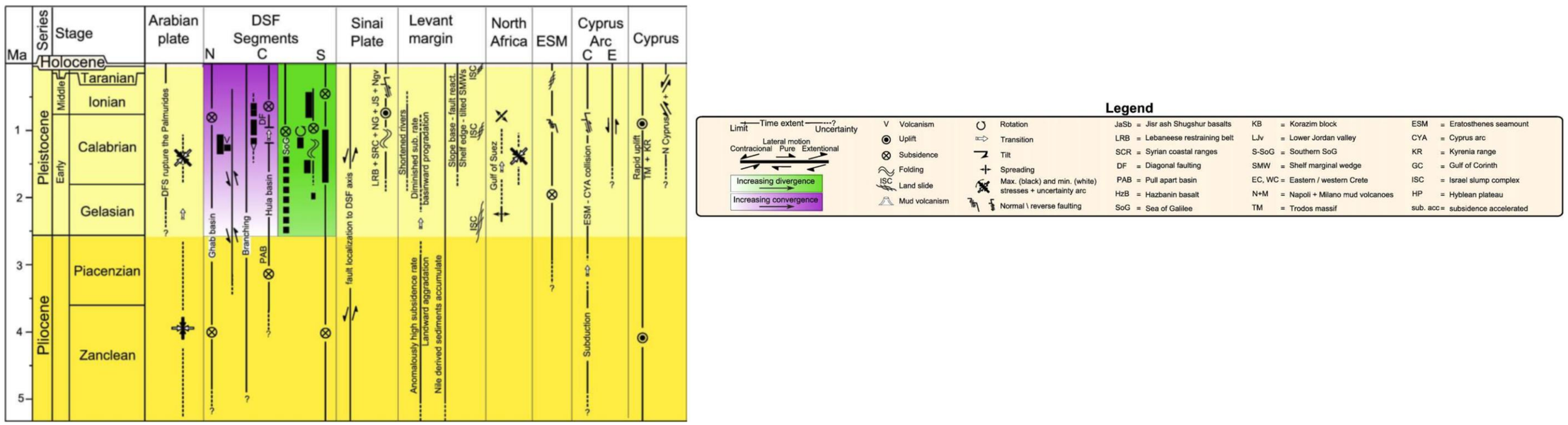

Figure 2.18-A synthesis of the different tectonic regimes in different sub areas of the EMR since the late Palaeozoic, and for the Plio-Pleistocene adapted from Schattner (2010).

The Mediterranean Sea is the last remnant of the Tethys oceanic domain that existed during the Palaeozoic and Mesozoic between the two supercontinents Gondwana and Laurasia (Van der Voo, 2005). Three oceans are understood to have opened and closed in this domain; the Proto-, Paleo- and Neo-Tethys oceans (Berra and Angiolini, 2014). The formation and destruction of the Neo-Tethys Ocean has defined the tectonic architecture of the EMR since it opened at the end of the Palaeozoic (Berra and Angiolini, 2014). The tectonic evolution of the EMR may be summarised in three phases; late Palaeozoic to early Mesozoic rifting (formation of the Neo-Tethys), Late Cretaceous to Palaeogene compression (subduction of the Neo-Tethys) and Middle Miocene to present strike slip (terminal subduction of the Neo-Tethys and continental collision; Figure 2.15). These three phases coincide with the rifting, subduction and collision and suturing phases of the Wilson cycle respectively (Wilson, 1966). These phases and temporally proximal smaller tectonic episodes are outlined in the subsequent sections.

2.5.1 Palaeozoic to Late Cretaceous Rift Phase

The supercontinent of Gondwana formed near the South Pole in the Cambrian; it included the landmasses which now form Antarctica, South America, Africa, Madagascar, Australia, the Arabian Peninsula and the Indian subcontinent (Meert and Van Der Voo, 1997). The Palaeo-Tethys Ocean existed at the northern margin of Gondwana until the formation of Pangea in the latest Palaeozoic (Figure 2.19). Whilst the Palaeo-Tethys existed the continental lithosphere that would eventually form the EMR was situated near the edge of Gondwana but separated from the Palaeo-Tethys by the continental lithosphere which now forms the Taurides (Figure 2.19).

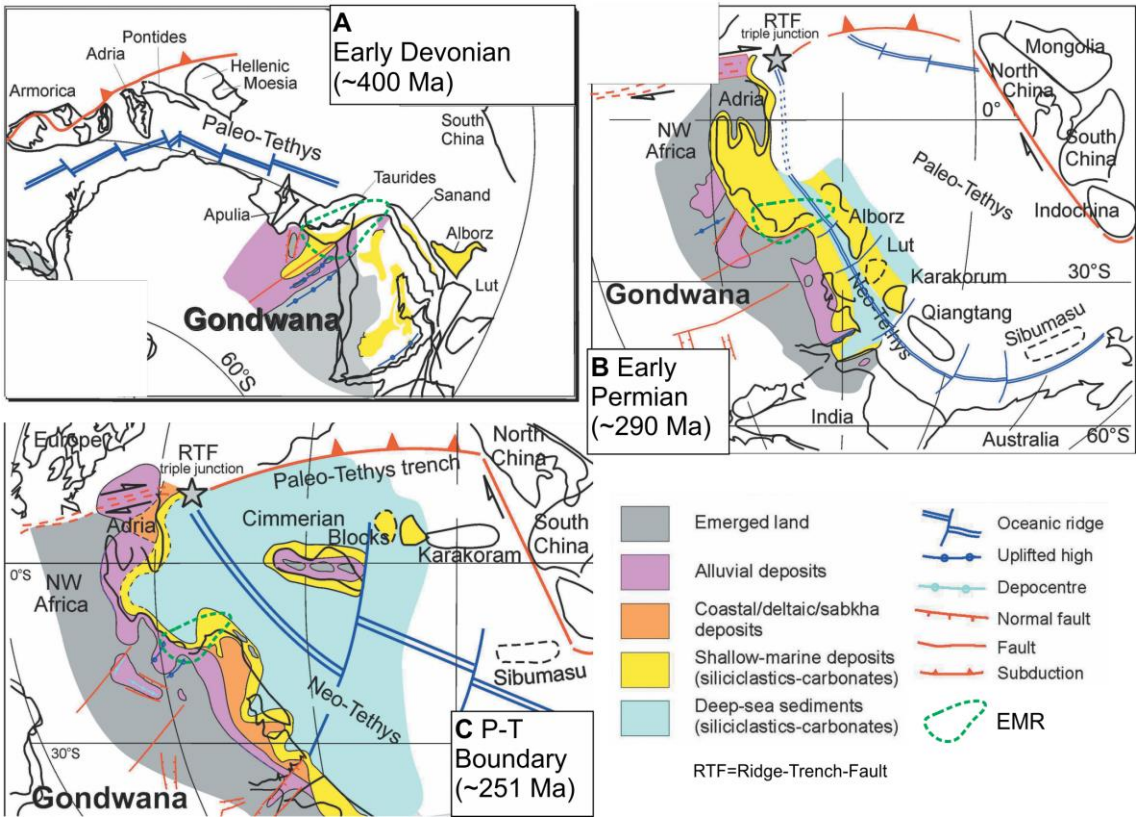

Figure 2.19-Tectonic evolution of major depositional settings in the southern margin of the Tethys at key intervals during the Palaeozoic (adapted from Berra and Angiolini, 2014).

Neo-Tethyan rifting in the Levant was accentuated in three phases over 120 Myrs; (1) late Palaeozoic (Carboniferous to Permian), (2) Middle to Late Triassic and (3) Early to Middle Jurassic (Gardosh et al., 2010; Garfunkel, 1998; Garfunkel and Derin, 1984; Robertson et al., 2012a). The rifting during these phases defined the current lithospheric architecture of the portions of the Arabian, Sinai and African Plates in the EMR by forming the continental margins and the corresponding oceanic and thinned continental lithosphere. Evidence of the rifting may be observed from extensional features onshore and geophysical methods offshore (Figure 2.20). A recent study of sea floor magnetic anomalies tentatively suggested the age of oceanic crust beneath the Herodotus Basin was 340±25 Ma (Granot, 2016), indicating full attenuation of the crust occurred during the first phase of rifting.

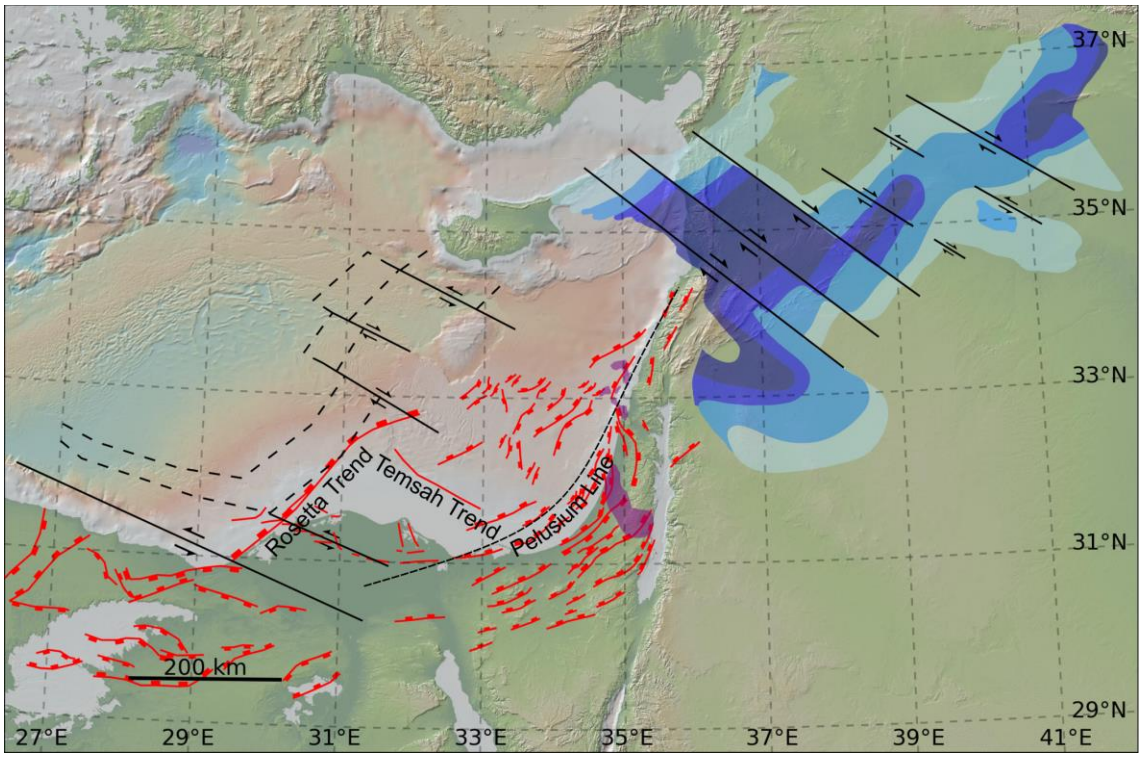

Figure 2.20-Figure showing the Tethyan rift features of the EMR (Anatolian Plate features are not shown); faults in red, magnetic anomalies (assumed volcanics) in purple. Faults are from seismic, gravity and field data (Aal et al., 2001, 2000; Bosworth et al., 1999; Gardosh et al., 2010; Sarhan et al., 2013). Black lines are the interpreted locations of transform faults and black dashed lines are interpreted to be the limits of transitional crust (Longacre et al., 2007). Blue colours indicate a rough isopach for Triassic rift sediments (Wood, 2015), with darker colours indicating thicker sediments. The Pelusium Line marks a transition to contrastingly attenuated continental crust to the NW (Section 2.3.3). The Rosetta and Temsah trend are basement trends beneath the Cyprus Arc (Aal et al., 2001). The global relief (Ryan et al., 2009) vertical scale is shown on Figure 1.1 and the supplementary figure.

A summary of the three rift phases follows:

(1) During the latest Palaeozoic the Taurides, along with many other continental fragments collectively termed the Cimmerian terranes, were rifted from the Gondwanan margin by the opening of the Neo-Tethys ocean (Robertson et al., 2012a; Şengör, 1979). These continental fragments then separated the Palaeo- and Neo-Tethys Oceans, the former of which had begun to be subducted beneath Eurasia at the northern oceanic margin. There is no evidence

for significant magmatic activity around the Levantine margin during this period (Gardosh et al., 2010). The Syrian Palmyra basin that underlies the Palmyride fold belt (Figure 1.1) has acted as a depocentre since the late Permian (Brew et al., 2001a) and Triassic (Chaimov et al., 1992). No fault set has been identified as basin defining rift faults in Syria (Brew et al., 2001a; Wood, 2015), instead the Mesozoic sediments thin out laterally. The absence of the expected rift faults is discussed further in Section 2.6.1.

(2) A second phase of extensional faulting occurred in the Middle to Late Triassic (Figure 2.21 A) following post-rift thermal subsidence (Gardosh et al., 2010). Minor magmatic activity is recorded by igneous rocks in well data in the Negev and Palmyride areas (Segev, 2005). The presence of Triassic deep-water sediments and extensive volcanism including mid-ocean-ridge type in northern Syria, SW Turkey and the Mamonia Complex of western Cyprus (Robertson, 2007, 1998a) but not in the Levantine margin area indicates that a deep Tethyan ocean did not extend as far as this region (Gardosh et al., 2010). This is consistent with the interpretation for thinned continental crust underlying the Levantine Basin (Section 2.2).

(3) The breakup of Gondwana in the Jurassic is contemporaneous with the final phase of Tethyan rifting recorded in the EMR (Figure 2.21 B & C). This phase of rifting is the locus of extension in the Levant and is marked by large-scale vertical motions and alkaline volcanism (Gardosh et al., 2010). In the Jurassic to Early Cretaceous a series of NE-SW trending extensional basins opened in Northern Sinai, and a pre-existing EW trending extensional fabric was extensionally reactivated (Moustafa et al., 2014). Extension and normal faulting also occurred in the Palmyride Basin during the Jurassic and Late Cretaceous (Best et al., 1993; Brew et al., 2001a; Chaimov et al., 1993; Litak et al., 1998). This final rift phase left the EMR on the edge of the African continental plate (Figure 2.21 B & C).

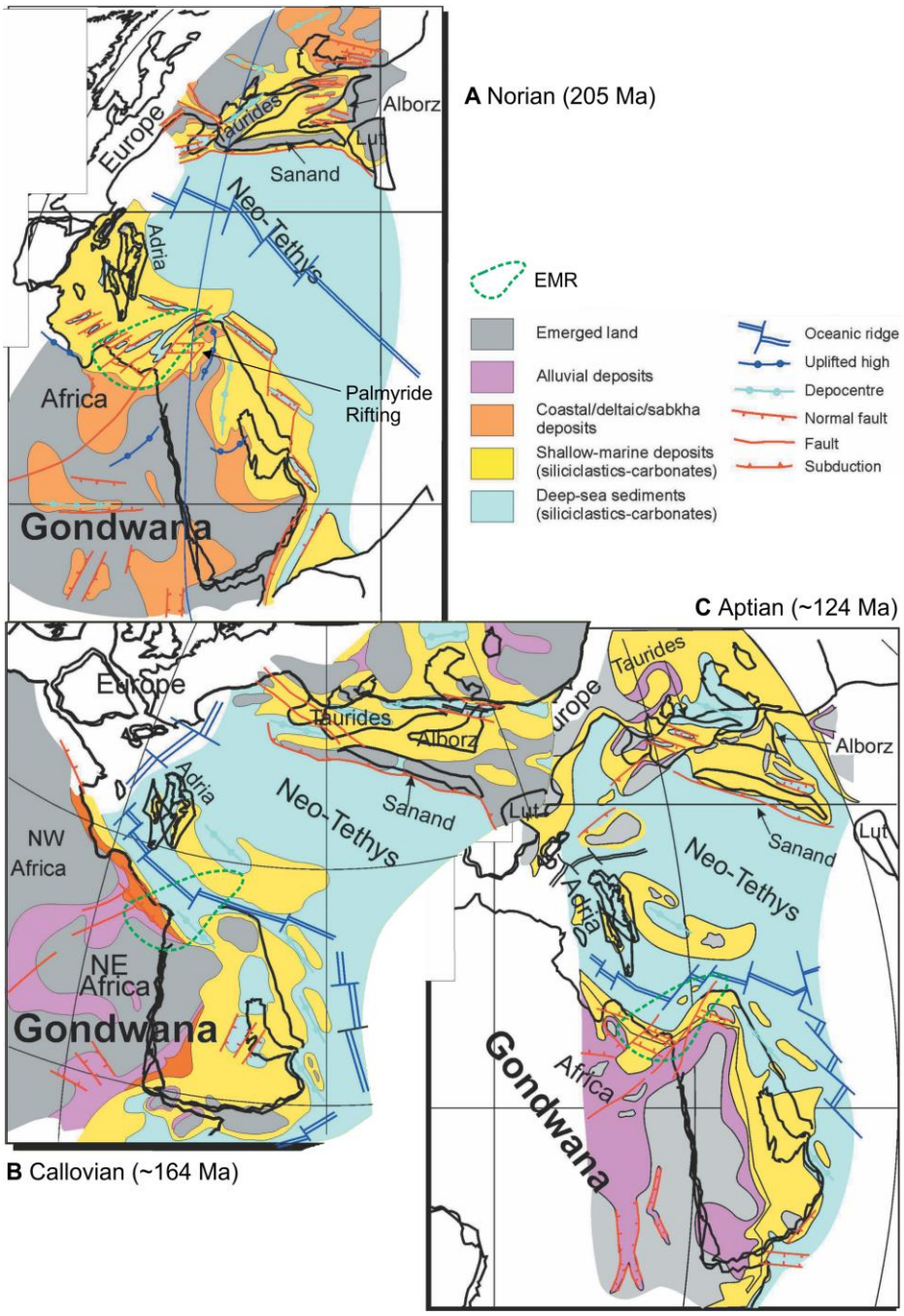

Figure 2.21-Palaeogeography of the EMR during the (A) Norian (205 Ma), (B) Callovian (~164 Ma) and (C) Aptian (~120 Ma), adapted from Berra & Angiolini (2014).

Detailed evidence of the architecture of rifts described in the previous paragraphs is absent in published literature. Consequently, there are many uncertainties regarding their evolution. For the final rift phase three controversies in the published literature may be highlighted. The extension direction of this final rift (discussed in Section 2.6.1), the timing of sea floor spreading following the rifting (discussed in 2.6.3), and the genesis of the Palmyride Basin (basin shown in Figure 2.21A, discussed in Section 2.6.1).

Rift volcanics are commonly associated with rifting (e.g. White and McKenzie, 1989). The most extensive volcanics of the EMR exist in onshore Israel (Gardosh et al., 2010), although Early Jurassic tholeiitic basalts are recorded along onshore Lebanon and Syria indicating volcanism extended along the whole Levant margin (Brew et al., 2001a) Figure 2.20). A magnetic anomaly

located on the narrow horst called the Jonah High (Folkman and Ben-Gai, 2004) may be associated with extrusive volcanic body of early Mesozoic age (Gardosh et al., 2008b), and the ESM overlies a positive magnetic anomaly that has been associated with a deep igneous body (Ben-Menahem et al., 1976; Garfunkel and Derin, 1984). Some authors have interpreted the ESM to be an Early Mesozoic volcano edifice based on seismic refraction profiles (Zverev and Ilinsky, 2005 via Gardosh et al. 2008), however the current consensus lies with an intruded continental fragment (Welford et al., 2015). In either case its formation is associated with Tethyan rifting.

The ESM continental fragment and other horst block fragments underlying the Levantine basin, such as the Jonah High (Sagy et al., 2015), would have rifted from the Gondwanan landmass during the Tethyan rift phases (Netzeband et al., 2006a). During the Jurassic and Cretaceous these highs and the surrounding continental margins were capped by carbonate platforms (Robertson, 1998b; Sagy et al., 2015; Tassy et al., 2015).

Several features in the EMR can be attributed to have formed subsequently to, but in association with, Tethyan rift features. The Mamonia Complex of west Cyprus (Section 2.3.9) and rocks of the Kyrenia Range of northern Cyprus (Section 2.3.9) formed along the rifted continental margins of the Tethys that developed during these Late Palaeozoic to Jurassic rift phases (Robertson and Xenophontos, 1997). Under the Nile Cone the NW-SE Temsah and NE-SW Rosetta fault trends delta (Figure 2.20) are believed to be inherited features that formed along basement faults (Aal et al., 2000).

The oceans encroached upon the continental lithosphere of the EMR during this rift period as evidenced by the deposition of mixed shallow marine sediments. Deposition of evaporitic and playa facies during the Late Triassic points to an arid climate during this period (Berra and Angiolini, 2014).

Some studies purport to trace deep faults in the EMR using only gravity and magnetic data (Eppelbaum, 2011; Eppelbaum and Katz, 2015; Granot, 2016; Saleh, 2013; Selim et al., 2016; Selim, 2013), but almost without exception these faults do not correlate even to a small degree with what is interpreted from any and all other data sources in other publications, and from the data available to this study. Consequently, these interpretations are disregarded here.

2.5.2 Late Cretaceous to Miocene Compressive Phase

Isochrons in the Atlantic Ocean indicate that the African and Eurasian Plates began to converge between 120-83 Ma (Rosenbaum et al., 2002). This convergence and the associated plate stress reconfiguration may be inferred from compressional features across the EMR, including thrusts, folds and emplaced ophiolites (Figure 2.22). Complex microplate reconfigurations were occurring at the northern margin of the Neo-Tethys at this time (Figure 2.23; Robertson et al., 2013), the precise movements of which are actively debated with several competing models (see refs. within Berra and Angiolini, 2014). It is suggested that, in addition to the general regional stress field generated by the convergence, local pulses of compressional stress also resulted from the terminal subduction and accretion of microplates at these northern Tethyan margins (Figure 2.23),

and it is likely that terminal subduction of some of these plates generated pulses of compressional stresses that formed these features.

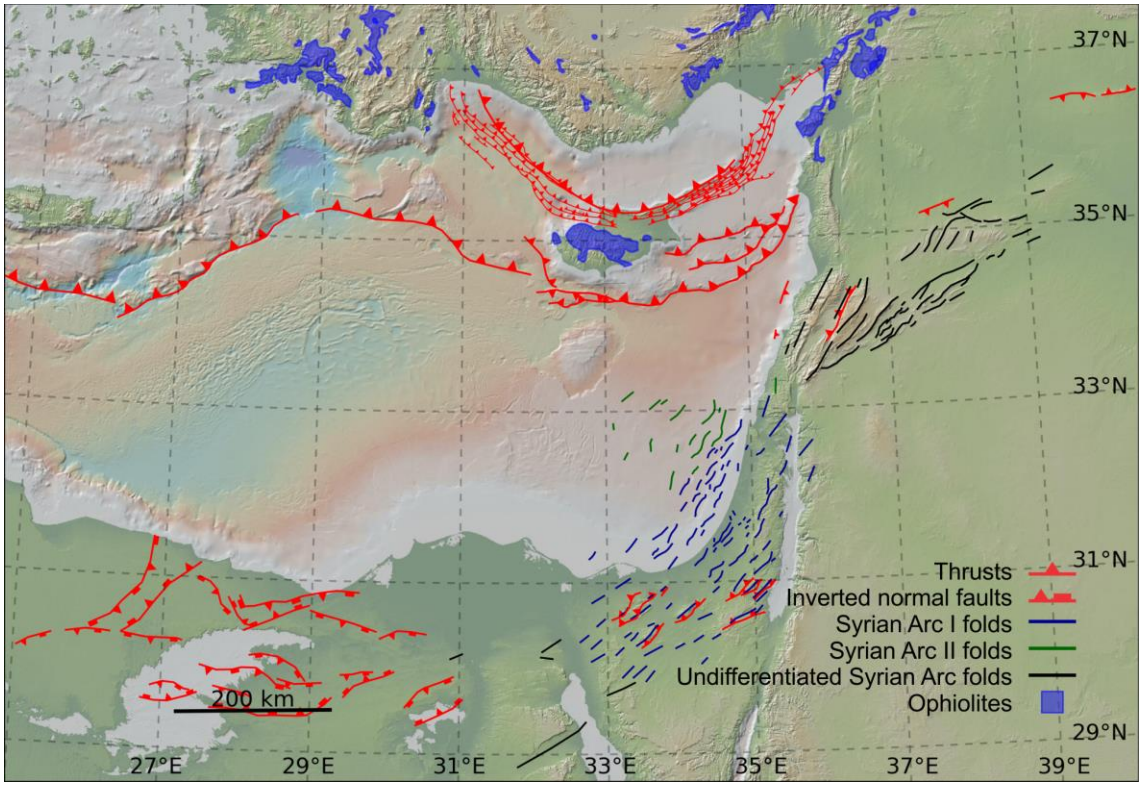

Figure 2.22-Cretaceous and Palaeogene compressive features of the EMR (please note many Anatolian Plate features are not shown). The Syrian Arc I and II folds are from Gardosh & Tannenbaumn (2014); undifferentiated Syrian Arc folds are from Walley (1998); the inverted faults of the Sinai Peninsula are from Moustafa et al. (2014); the African Plate faults from Bosworth et al. (1999); thrusts north of Cyprus are from Isler et al. (2005), Hall et al. (2005), and Hall et al. (2014); the ophiolite data is courtesy of the U.S. Geological Survey; the ages of other thrusts are from Barrier & Vrielynck (2008). The global relief (Ryan et al., 2009) vertical scale is shown on Figure 1.1 and the supplementary figure.

The first identified evidence of the Neo-Tethyan convergence in the EMR was the Mid Turonian emplacement of ophiolites along the eastern margin of the Arabian Plate (Ziegler, 2001). Convergence accommodation was partitioned on several subduction and suture zones in the Tethys realm as the small ocean basins located between the Tethyan microcontinents began to close (Robertson et al., 2013). Approximately one third of the ca. 1800 km convergence was accommodated on the southern margin of the Tauride microcontinent, forming what is now the Cyprus Arc (Garfunkel, 2004).

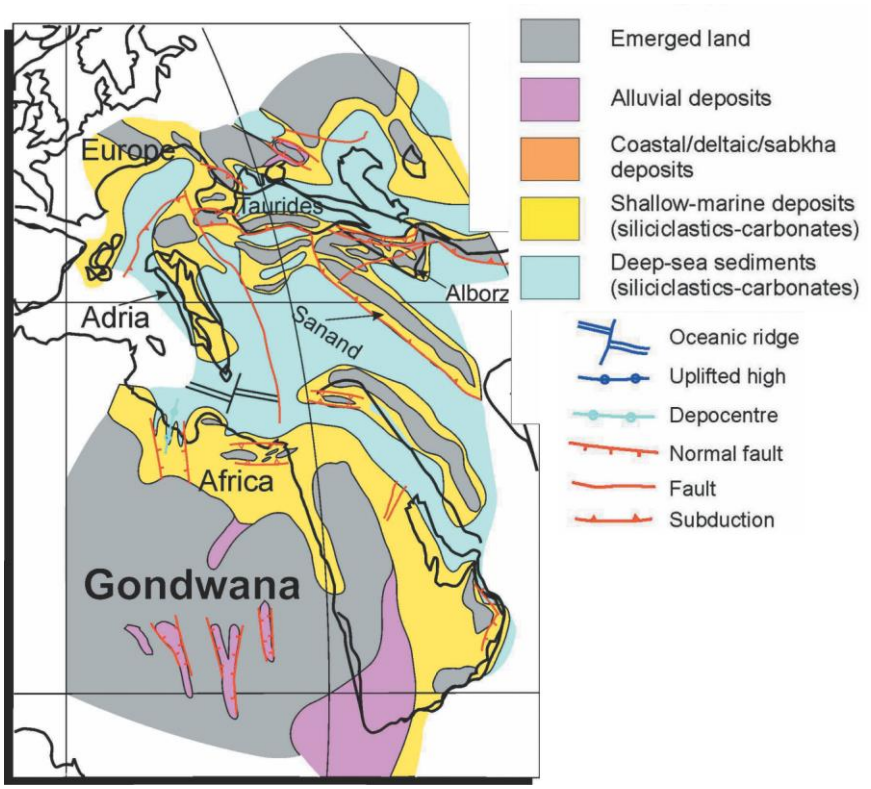

Figure 2.23-Plate reconstruction and paleogeography of the EMR during the Cretaceous-Palaeocene boundary (about 65.5 Ma; Berra and Angiolini, 2014).

The Cyprus Arc as a whole has a complex history involving multiple subduction zones and episodes of thrusting (Bowman, 2011; Calon et al., 2005a; Hall et al., 2005b; Robertson, 1998a; Robertson et al., 2014, 2004; Robertson and Kinnaird, 2015; Vidal et al., 2000a) with some variations in how it is understood (Section 2.6.6). The evolution of the arc is described in detail and explored further in Chapter 5, in this chapter a briefer description is integrated into this temporally sequential description.

Analysis of 2D seismic located offshore Syria (Bowman, 2011) and Lebanon (Hawie et al., 2013) suggests the Latakia Ridge compressional fold-thrust system at the southern edge of the Arc initially formed in the middle to Late Cretaceous. This matches interpretations of field data from onshore Cyprus (Figure 2.24), although whether its later evolution involves subduction or simply further thrusting is not consistently described in published literature, a controversy described in more detail in Section 2.6.6 and investigated in Chapter 5. The compressional fold-thrust system that uplifted the Kyrenia range onshore Northern Cyprus is better dated and is thought to have formed in three phases; Late Cretaceous, mid-Eocene and late Miocene (Figure 2.24).

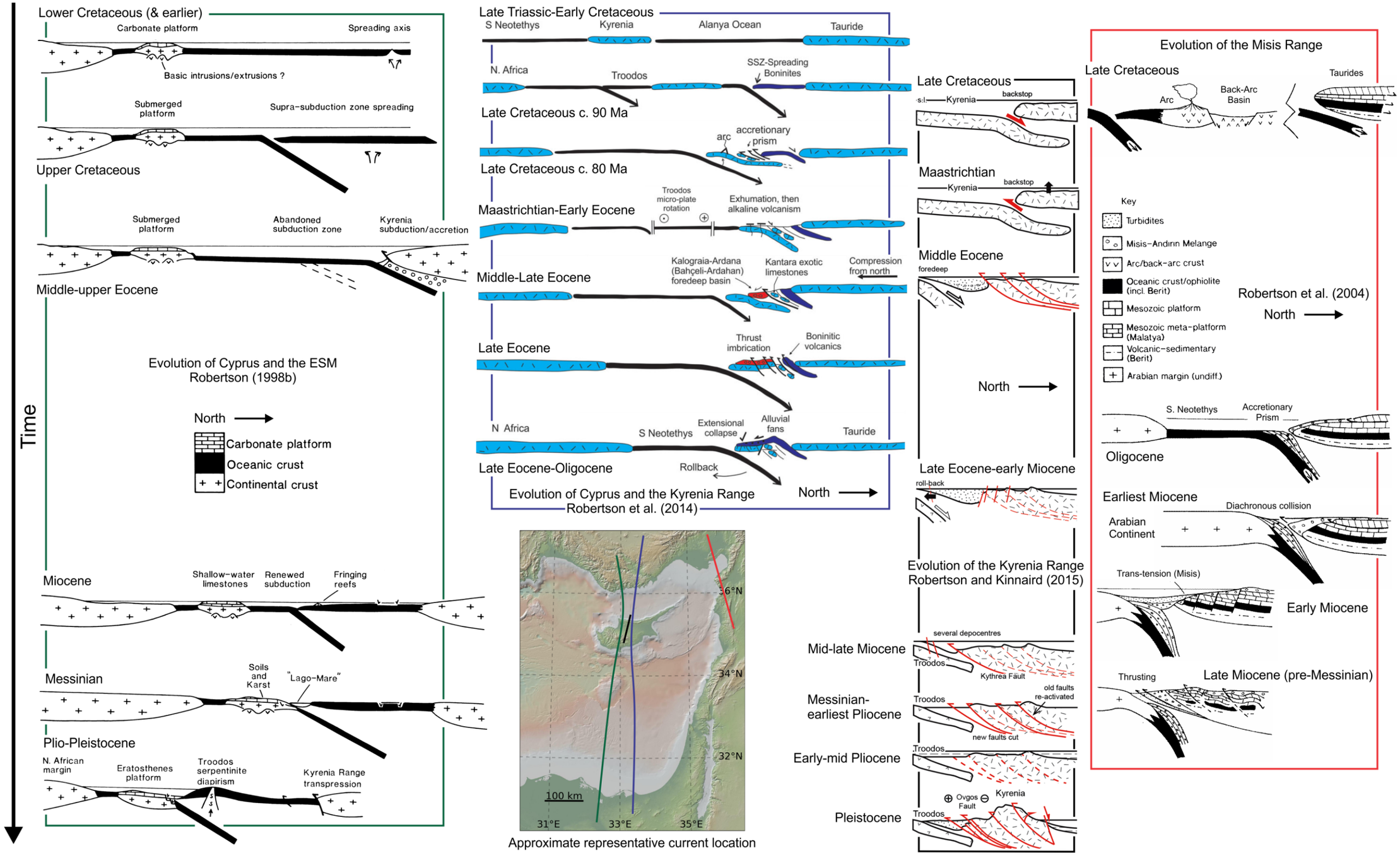

Figure 2.24-Comparison of sketch cross sections of the tectonic evolution of the Cyprus Arc adapted to be temporally sequential top to bottom; 1st column is an older restoration including our best understanding of the ESM; the 2nd column shows the evolution of Cyprus and an earlier portion of the Kyrenia Range evolution; the 3rd column shows a later potion of the Kyrenia Range evolution; and the 4th column shows the Misis Range in SE Turkey. The global relief (Ryan et al., 2009) vertical scale on the minimap is shown on Figure 1.1 and the supplementary figure.

Folds of the Syrian Arc (Section 2.3.3) may be observed in Egypt (Bosworth et al., 1999), Northern Sinai onshore (Moustafa, 2010) and offshore (Yousef et al., 2010), Israel onshore and offshore (Gardosh et al., 2008b), Lebanon onshore (Walley, 1998) and SW Syria (Brew et al., 2001a) as shown in Figure 2.22. Two episodes of folding have been identified, they are termed Syrian Arc I and II after Walley (1998).

Syrian Arc I occurred during the Late Cretaceous to Eocene contemporaneously with the initiation of convergence between the African and Eurasian Plates (Bosworth et al., 1999). Ghalayini et al. (2014) interpret Late Cretaceous or early Tertiary NNE-SSW striking thrust faults in 3D seismic data offshore Lebanon that may be part of the Syrian Arc I system. Syrian Arc II is poorly age constrained but initiated around the late Eocene in Lebanon and Israel and continued until the Miocene (Gardosh et al., 2008b; Walley, 1998). It is marked by unconformities in addition to folding (Ghalayini et al., 2016). Elsewhere, there is less differentiation between the phases; in Egypt (Bosworth et al., 1999) and Sinai (Moustafa, 2010) compression continued from Syrian Arc I intermittently and locally. The end of the formation of the Syrian Arc II is not constrained; Walley (1998) suggest this was in the late Oligocene, however Eyal (1996) suggests it may have continued into the Early Miocene or beyond. Irrespective of the end of the Syrian Arc II folds formation, Walley (1998) note the contemporaneous formation of the Bitlis Suture (Hempton, 1985) and link this event to the formation of the Syrian Arc II folds.

Many of the Syrian Arc I folds are associated with inversion of pre-existing extensional faults formed during the preceding rift phases (Gardosh et al., 2008b; Moustafa, 2010); consequently the orientation of some segments of the Syrian Arc reflect the former rifting axes (Walley, 1998). Some of the Syrian Arc I folds were then reactivated during the Syrian Arc II event (Gardosh et al., 2008b). Aspects of the Syrian Arc I and II events are investigated in greater detail in Sections 4.3 and 6.6.4 respectively.

During the Early Cretaceous, the ESM was a shallow water carbonate platform (Figure 2.24). From the Late Cretaceous the ESM progressively submerged until it reached bathyal depths (>1000 m) in the middle Eocene (Robertson, 1998b).

During the Late Cretaceous, the NE-SW Rosetta fault trend under the Nile cone activated with sinistral transpressional displacement (Aal et al., 2000). Around the same time Neo-Tethyan sea floor spreading formed the Troodos Ophiolite above an intra-oceanic subduction zone (McCulloch and Cameron, 1983; Mukasa and Ludden, 1987a; Robertson and Xenophontos, 1997, 1993). Palaeomagnetic data reveal this oceanic crust was then sinistrally rotated 90° and attached to the 30 to 75 million year old rocks of the Mamonia Complex (Clube et al., 1985). The plate rotation is suggested to have occurred due to diachronous collision of the north Tethys subduction zone with the irregularly shaped south Tethyan continental margin (Morris et al., 2015).

The continuing convergence of Africa and Eurasia resulted in the collision and eventual suturing of Arabia with Eurasia in the Middle Eocene to Oligocene (Allen et al., 2004; Beydoun, 1993; Boulton, 2009; Dewey et al., 1973; Frizon de Lamotte et al., 2011; Hüsing et al., 2009; Sengör and Yilmaz, 1981; Ziegler, 2001). The subduction of the intermediate oceanic lithosphere meant the microplates that had detached from the Northern Gondwanan/African margin during the

Palaeo- and Neo-Tethys eras had progressively collided with and been accreted onto the southern margin of the Eurasian Plate (Robertson et al., 2013; Stampfli and Borel, 2002). North of the EMR these accreted terrains form the Anatolian Sub-Plate (Figure 2.25). Closure of the last deep seaway is believed to have occurred during the Miocene, around 11 Ma (Hüsing et al., 2009).

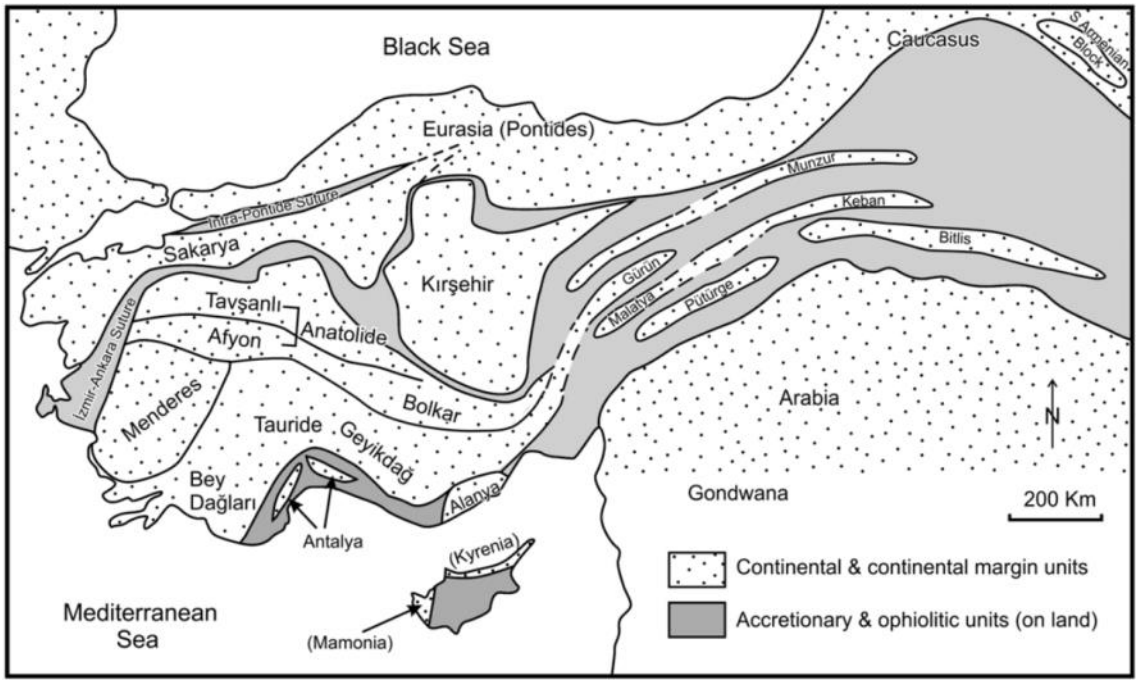

Figure 2.25-Cartoon depicting the accreted continental fragments of Anatolia (Robertson et al., 2013).

The Arabia-Eurasia collision caused uplift and emergence of the northern Arabian Plate (Bar et al., 2013), westward tectonic escape of Anatolia (e.g. Mart, 2013) and formed gentle NE-SW folds and angular unconformities in the Palmyrides and NW Syria (Ghalayini et al., 2014). In the late Eocene, the Kyrenia range of Northern Cyprus was thrust southwards against the Troodos Ophiolite to the south (Figure 2.24). This was related to the final closure of the portion of the Neo-Tethys ocean to the north of Cyprus (Robertson and Xenophontos, 1997).

During the Oligocene, an updoming phase prior to the rifting of the Red Sea uplifted and emerged much of the Arabian Plate (Ziegler, 2001). This caused a distinct change in the clastic/carbonate sedimentation ratio of the area (Druckman et al., 1995), and in the EMR uplift and emergence of the Levant margin resulted in a system of canyons along the Levant margin (Buchbinder and Zilberman, 1997; Druckman et al., 1995). The Arabia-Eurasia collision was contemporaneous with both the Oligocene to early Miocene rifting of Arabia from Africa, and the subsequent opening of the Red Sea (e.g. Mart, 2013). Mantle plume related uplift has been suggested to drive this rifting. However, later work favours slab pull of subducting Tethyan lithosphere as providing the principle driving force, with plume impingement providing the trigger (Bosworth, 2015). Whether formed by isostatic flexure or updoming, the formation of the Red Sea rift shoulders produced the current pathway of the Nile river system around 30 Ma, and is marked by a sharp change from carbonates to clastics under the Nile delta (Macgregor, 2012). Most of the sediments in the

Levantine and Herodotus basins have been sourced from the Nile since this time (Druckman et al., 1995; Hawie et al., 2013).

2.5.3 Miocene Strike-Slip Phase

In the late Oligocene, the Red Sea and Gulf of Suez Rifts formed, separating the Arabian and Sinai Plates from the Afro-Arabian Plate (Bosworth, 2015). Ongoing rifting in the Red Sea, but cessation of rifting in the Gulf of Suez (Bartov et al., 1980; Garfunkel, 1981; Le Pichon and Gaulier, 1988) allowed the sinistral Levant Shear Zone (LSZ) to form and propagate in the early-mid Miocene (Freund et al., 1970; Quennell, 1984), causing the Arabian Plate to move north faster than the African and Sinai Plates. This plate breakup is associated with a reconfiguration of plate stresses resulting from the collision of the Arabian promontory with Eurasia (Bosworth, 2015).

The LSZ may be partitioned into three segments, from south to north and youngest to oldest: the NS Dead Sea segment, the NNE-SSW central segment in Lebanon, and the NS Ghab Fault (Ghalayini et al., 2014; Mart and Vachtman, 2015) (Figure 2.26). The Dead Sea and Ghab fault segments are comprised of primarily strike-slip faults that include a series of pull-apart basins along their length. The Lebanese segment forms a restraining bend in-between, and has inverted the adjacent Palmyride Basin. Initial offsets on the Dead Sea segment are constrained as being after intrusion of dikes at 19 Ma, and before extrusion of basalt flows at 15.5-11.5 Ma (Eyal et al., 1981; Steinitz et al., 1978). Total movement on the LSZ may be summarised in two phases: (1) 60 km of mid-late Miocene sinistral slip on the Dead Sea segment and (2) latest Miocene-Pliocene sinistral slip partitioned into ~45 km along the Dead Sea segment and ~20-25 km along the Ghab Fault (Beydoun, 1999; Freund et al., 1970; Quennell, 1984, 1958; Searle et al., 2010). The discrepancy in displacement between the southern Dead Sea segment and the northern Ghab Fault may be due at least in part to shortening in the intermediate restraining bend of the central segment (Searle et al., 2010), and is discussed further in Section 2.6.8.

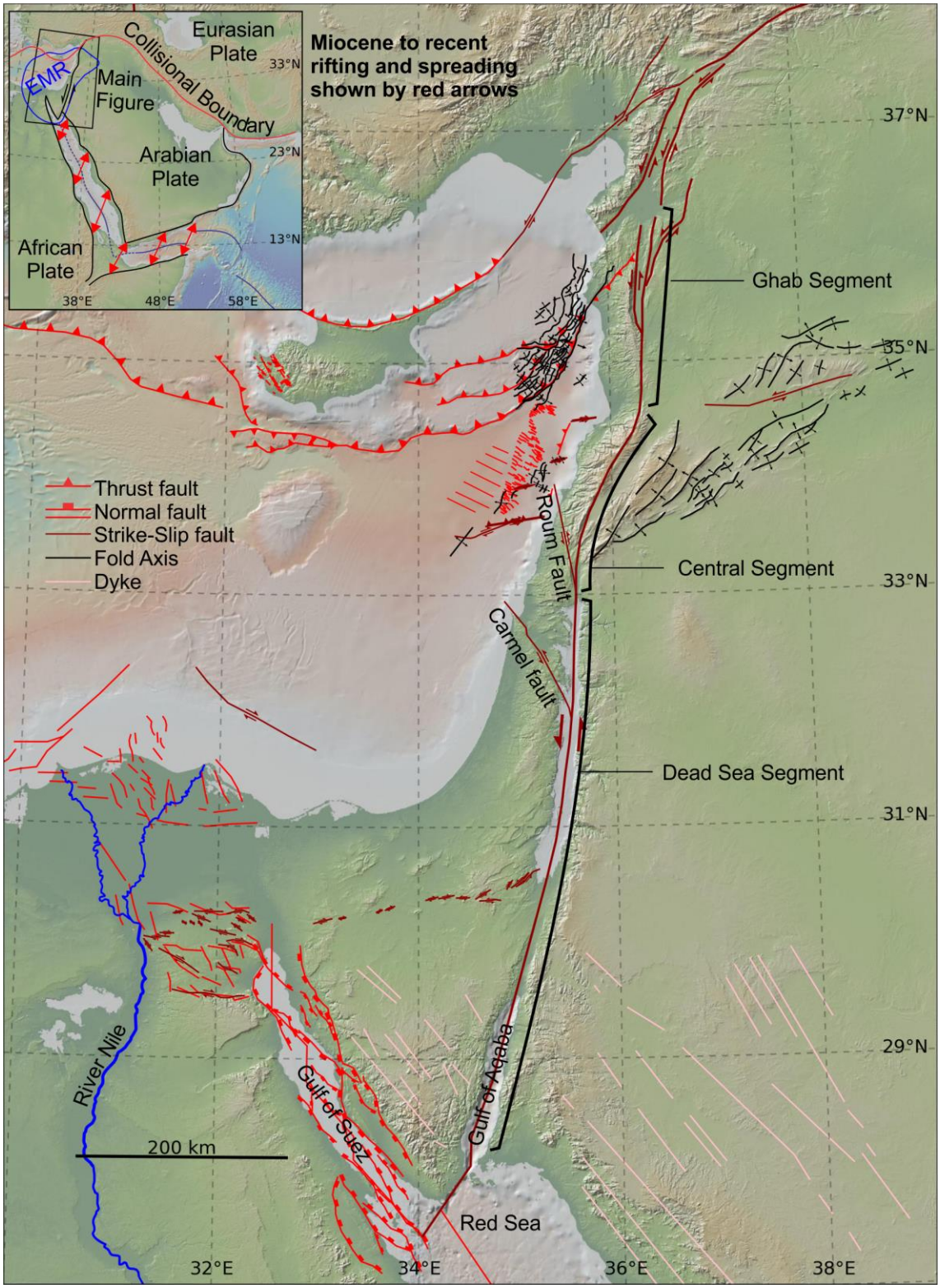

Figure 2.26-Map showing the Miocene structural features of the EMR (please note some Anatolian Plate features are not shown) documented in numerous sources (Bowman, 2011; Ghalayini et al., 2016, 2014; Kosi et al., 2012; Moustafa et al., 2014; Payne and Robertson, 1995; Searle et al., 2010; Tari et al., 2012). Inset plate boundaries are from Stern & Johnson (2010). The global relief (Ryan et al., 2009) vertical scale is shown on Figure 1.1 and the supplementary figure.

In the early Miocene, the ESM had been uplifted such that shallow marine carbonates were deposited on it (Robertson, 1998b). This was diachronous with Cyprus being uplifted above sea level (Robertson and Xenophontos, 1997). From the late Miocene to early Pliocene, Cyprus

underwent extension, this has been suggested to be related to roll-back of the subduction zone (Kinnaird and Robertson, 2012; Robertson and Xenophontos, 1997), although there are several controversies regarding the later evolution of the Cyprus subduction zone (Section 2.6.6).

In offshore Lebanese waters, thick-skinned ENE-WSW striking dextral strike-slip faults may be observed in 3D seismic (Ghalayini et al., 2014; Figure 2.26). They formed in the late Miocene and are currently active (Ghalayini et al., 2014). Contemporaneously, NNE trending anticlines that overly Late Cretaceous to early Tertiary structures formed offshore Lebanon (Ghalayini et al., 2014), although these are not currently active (Ghalayini et al., 2014).

2.5.4 Messinian Salinity Crisis

For ~650 kyr from ~5.97 Ma (Krijgsman et al., 1999; Manzi et al., 2013), the hydrodynamic equilibrium of the Mediterranean Sea was perturbed by a restriction of the seaway between Iberia and Africa (Hsü et al., 1973). The resulting freshwater deficit caused evaporites to be deposited throughout the Mediterranean (Figure 2.27). This event is commonly termed the Messinian Salinity Crisis (MSC). The MSC has been a source of much debate, and subjects such as onshore-offshore correlation, base level changes, depositional processes and impact on global climate continue to provoke much discussion (Gorini et al., 2015; Roveri et al., 2014).

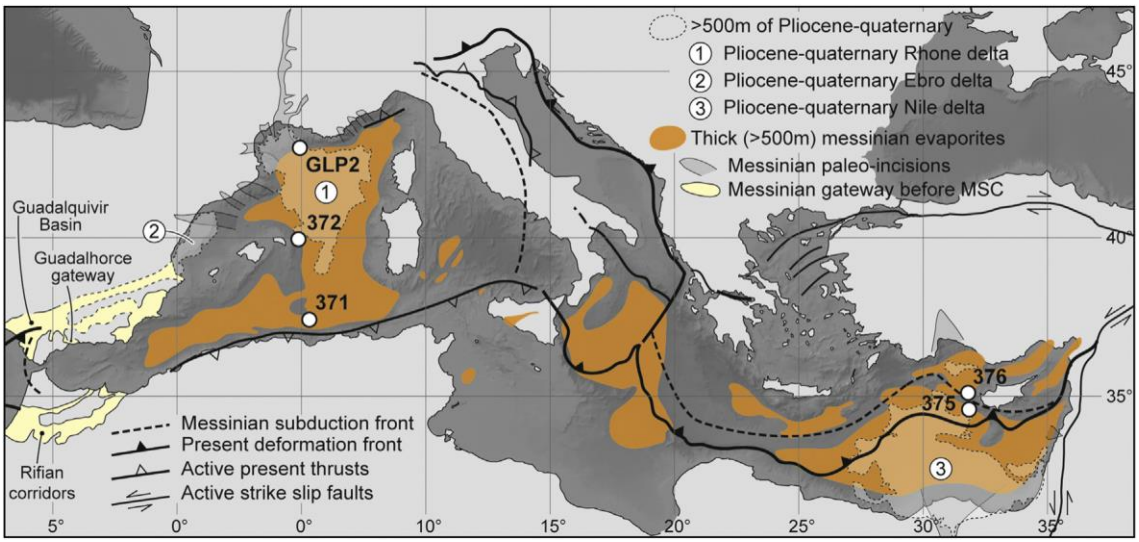

Figure 2.27-Map showing distribution of the MSC evaporites (Gorini et al., 2015).

In parts of the Levantine Basin, the MSC evaporite sequence is c. 2 km thick (Hsü et al., 1973; Ryan, 1978). Gorini et al. (2015) used seismic reflector characteristics across the east and west Mediterranean to subdivide the MSC sediments into two megasequences. The lower megasequence is a sequence of chaotic reflectors, interpreted to be clastic deposits that represent the basinward shift of depocentres during the MSC. The upper megasequence is a largely seismically transparent sequence that has recently been confirmed as massive halite by well data (Feng et al., 2016). In the EMR some linear internal reflectors may be observed with the massive halite sequence (Gorini et al., 2015). Drilling of these internal reflectors has revealed that they are primarily claystone (Feng et al., 2016). The MSC evaporites are an important component in understanding the deeper geology of the EMR due to their thickness and the effect on seismic

imaging of the evaporites (Feng and Reshef, 2016). Interpretation of the MSC sequence is shown in Section 3.7.

The draw-down of the Mediterranean Sea during the MSC generated widespread unconformities, especially in areas where thick evaporites were not deposited (see Figure 2.27 for locations) and locally both above and below the deposited evaporites. These MSC unconformities and evaporites may be observed onshore (Lugli et al., 2013; Manzi et al., 2014; Robertson and Xenophontos, 1997), in offshore well data (Gardosh et al., 2008b; Robertson, 1998b) and in seismic data (e.g. Bertoni and Cartwright, 2006; Ghalayini et al., 2014; Gorini et al., 2015; Gvirtzman et al., 2013; Hawie et al., 2013; Skiple et al., 2012). The timing, amplitude, and amount of variation of sea level fall during in the MSC is controversial, and evidence and arguments exist for most possible alternatives (Gorini et al., 2015; Roveri et al., 2014).

In the EMR, erosion at both the start (Lofi et al., 2011) and end (Bertoni and Cartwright, 2007) of the MSC is documented in seismic data. Claystone internal reflectors point to a return to marine conditions during the MSC (Feng et al., 2016). Cyprus is a key location in the EMR for field evidence regarding the MSC in the Eastern Mediterranean due to its subsequent uplift (Section 2.5.5). Shallow water sedimentation features and stromatolites in evaporite basins onshore Cyprus have been suggested as evidence for sea level draw-down at the start of the MSC (Orszag-Sperber et al., 2009). However, this is disputed by other authors on the basis of reinterpretation of the stromatolites as purely sedimentary features as opposed to biogenic (Manzi et al., 2014). Seismic data demonstrating erosion at the onset of the MSC in the deep portion of the Southern Levantine Basin is shown in Section 2.6.5.

The mobile properties of evaporites like halite are well documented (see refs. within Hudec and Jackson, 2007; Rowan et al., 2012). The MSC evaporites are no exception; the MSC evaporite sequence contains clay units that generate internal reflector sequences within the evaporite body on seismic data (Feng et al., 2016 and refs. within) and deformation of these internal reflectors has facilitated studies into the modes of deformation of the mobile MSC evaporites (Allen et al., 2016; Bertoni and Cartwright, 2007; Cartwright et al., 2012; Cartwright and Jackson, 2008; Netzeband et al., 2006b; Reiche et al., 2014a). Basinward tilting of the internal reflectors was interpreted in the past to indicate propagating clinoforms (Gradmann et al., 2005), but has since been linked to basin subsidence after the MSC (Allen et al., 2016; Bertoni and Cartwright, 2007; Cartwright et al., 2012; Cartwright and Jackson, 2008; Netzeband et al., 2006b). The deformation of the internal reflectors and the salt overburden unambiguously indicate a post MSC episode of salt motion, purported to have initiated around the late Pliocene or Pleistocene (Cartwright et al., 2012; Gvirtzman et al., 2013). In many locations, internal salt reflectors are truncated by the end MSC unconformity, indicating that sea level draw down occurred at the end of the MSC in addition to the start. Some authors observe that some of the deformed structures are truncated, indicating a deformation event during the MSC (Bertoni and Cartwright, 2007; Gvirtzman et al., 2013). This is contested by Allen et al. (2016). This controversy is investigated in Section 3.7.1.

The return of the sea-level in the Mediterranean to that of the Atlantic around 5.33 Ma occurred as a catastrophic reflooding termed the Zanclean Flood, the evidence for which may be observed in a 250 m by 200 km incision near the Gibraltar straits revealed by seismic and borehole data

(Garcia-Castellanos et al., 2009; Van Couvering et al., 2000). In line with previous work (see refs. within Roveri et al., 2014) the term 'MSC' used in this study includes the time interval during the return to global sea level but after evaporite deposition had ended.

2.5.5 Plio-Quaternary to Recent Neotectonic Activity

During the early Pliocene, continued convergence of the African and Tauride Plates underthrusted the ESM carbonate platform beneath the Cyprus Arc (Kinnaird and Robertson, 2012), accelerating the uplift of Cyprus (Main et al., 2015; Palamakumbura and Robertson, 2016a; Poole and Robertson, 1991; Robertson, 1998b; Robertson and Xenophontos, 1997) and also causing the ESM to subside to bathyal depths on approach (Robertson, 1998b). If the ESM represented the limit of the thinned continental lithosphere, then its arrival at the Cyprus Arc changed the tectonic regime of the subduction zone to continent-continent collision.

Schattner (2010) suggests that the collision of the Eratosthenes Seamount with the Cyprus Arc triggered a tectonic transition throughout the whole region in the Early to Mid-Pleistocene (see Figure 2.18B). The collision is understood to be the primary driver of the intense uplift of Cyprus (Garfunkel, 1998; Kempler, 1998; Robertson, 1998b; Robertson et al., 2012a) and be responsible for uplift as far afield as central Anatolia (Schildgen et al., 2012). However, some of the evidence of this link is based on the timing of the collision coinciding with the initiation of rapid changes in the tectonic evolution of features in the area. Whilst underthrusting of a large continental fragment in a relic subduction zone is certain to have had an effect, it is uncertain what this might be on much larger scale plate tectonics and some 'effects' may be due to coincidental timing with other ongoing events such as the collision of Arabia and Eurasia. Regardless of its widespread effect, the Cyprus Arc is important as it represents the transition from subduction to collision, a process that is difficult to recognise in older examples because of overprinting and erosion as the collision-related uplift begins. The area is therefore key in informing on the evolution of the area, and is investigated in Chapter 4.

As part of the plate stress configuration change in the early Pliocene, changes in deformation morphology at the Cyprus Arc show the stress regime of the Latakia Ridge system switched from compressional to a sinistral strike-slip (Bowman, 2011). This is associated with the westward (relative) tectonic escape of the Anatolian Plate rather than the ESM collision (Hall et al., 2005b; Le Pichon and Kreemer, 2010; Reilinger et al., 2006; Sengör and Yilmaz, 1981).

The fairly undisturbed near-MSC strata around the junction between Cyprus and the Hecataeus Rise suggests long term proximity between these two features (Reiche and Hübscher, 2015). This contrasts with the sediments between the ESM and Cyprus, and suggests that the Hecataeus and ESM continental fragments are not in their post-rift configuration. Continued subsidence of the ESM occurred in the late Pliocene to early Quaternary, coeval with strong surface uplift of southern Cyprus (Robertson, 1998b). Normal faulting across the ESM is understood to be part of the breakup/subduction process (Robertson, 1998b). Recent interpretation of seismic data in the area has demonstrated that the plate boundary south of Cyprus is further north than previously speculated (Kinnaird and Robertson, 2012; Reiche and Hübscher, 2015).

The Plio-Quaternary supra-salt sediments in the EMR show widespread deformation in the form of extensional faults up slope, thrusts, strike-slip faults and innumerable small folds (Clark and Cartwright, 2013; Garfunkel et al., 1979; Gradmann et al., 2005; Gvirtzman et al., 2015, 2013; Katz et al., 2015; Kurkin et al., 2013; Loncke et al., 2006; Reiche et al., 2015; Sellier et al., 2013). This is understood to be a consequence of salt-related detachment and halokinesis. This includes rafting of the supra-salt sediments on the MSC salt, with translation being driven by gravity, either directly where a slope exits, or from far-field via transmission through the translating sediment body (Gvirtzman et al., 2015). The translation is primarily expressed at the high and low limits of the salt body by extensional and compressional structures respectively. The sediments of the Nile cone are of large enough volume that they are causing quantifiable subsidence in the area (Tibor et al. 1992). This sediment deposit is the primary driver of this translation as it provides both the slope gradient and the differential sediment loading that result in far-field forces (Loncke et al., 2006). Simulation of this extension-translation-compression relationship is attempted in Chapter 7. Recent slumps disassociated with evaporites may also be observed on bathymetry and seismic data covering the marine slopes of the EMR (Katz et al., 2015; Omeru and Cartwright, 2015; Tahchi et al., 2010).

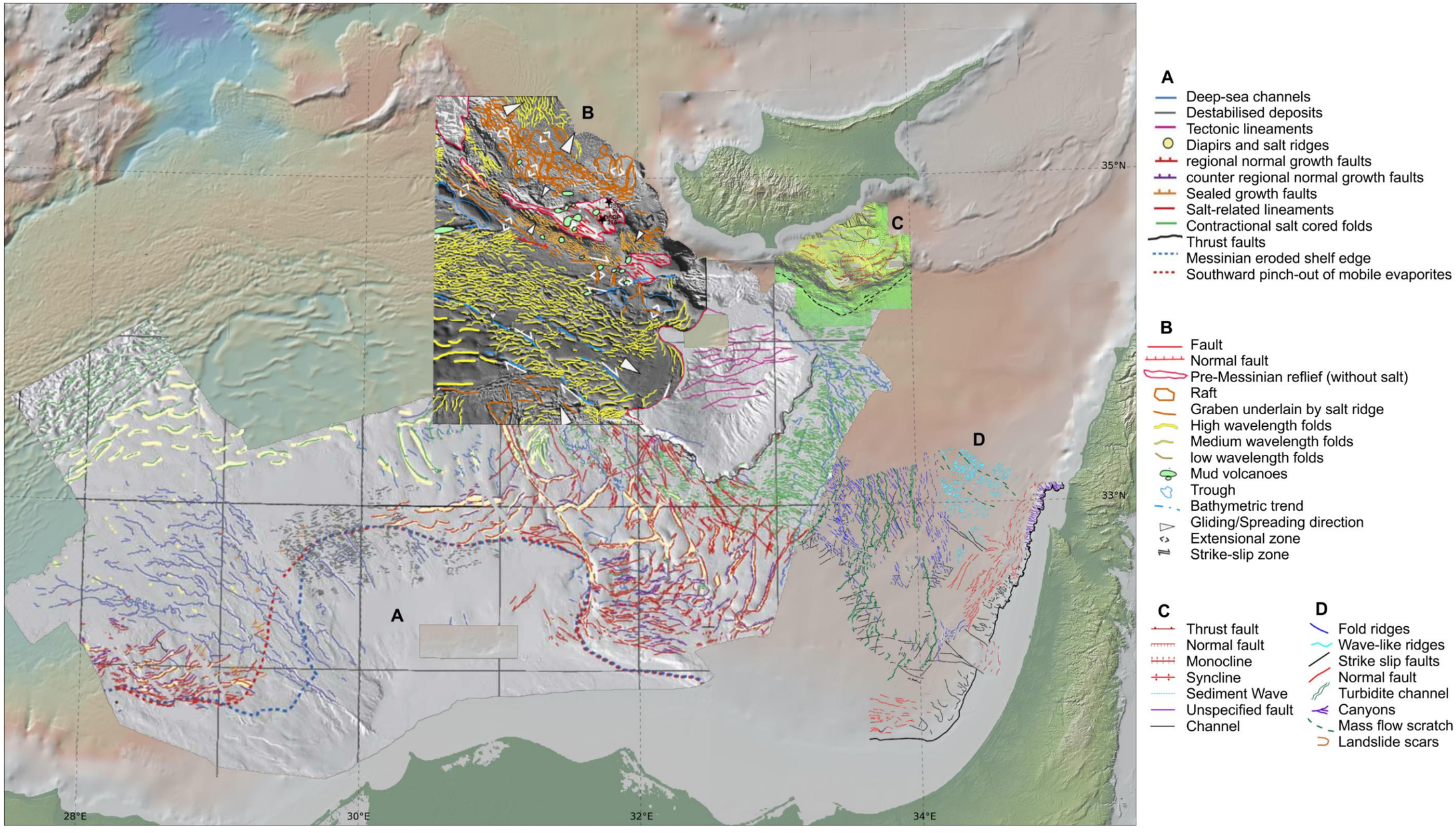

Figure 2.28-Compilation of documented deformation of the Plio-Pleistocene sediments visible at the seafloor (D: Gvirtzman et al., 2015; A: Loncke et al., 2006; C: Reiche and Hübscher, 2015; B: Sellier et al., 2013). The global relief (Ryan et al., 2009) vertical scale is shown on Figure 1.1 and the supplementary figure.

In the EMR, and elsewhere where there is underlying salt, this thin-skinned deformation of the post-MSC sediments has often been attributed to thick-skinned tectonic processes (e.g. Aal et al., 2001; Bowman, 2011; Kempler, 1998; Mascle et al., 2000). By mapping out the limits of the evaporite body it is possible to resolve between the two; this is undertaken in Section 3.7.

The ESM is surrounded on three sides by a depression defined by an external escarpment. In the past this was interpreted to be to have formed by normal faulting (Gardosh et al., 2008b; Kempler, 1998), strike-slip faulting (Aal et al., 2000), gravity sliding of supra-evaporite sediments causing thrusting (Loncke et al., 2006), dissolution of underlying evaporites (Major et al., 1998), and kinematic evacuation of underlying evaporites (Montadert et al., 2014). It is now believed that the surrounding seafloor was uplifted above ESM-directed salt advance (Reiche et al., 2015). This advance of salt is proposed to be gravity driven to the south and east of the ESM (Gaullier et al., 2000; Loncke et al., 2006; Mascle et al., 2006, 2001), and driven by continued subduction pushing the evaporites to the north (Reiche et al., 2015). Halokinesis of MSC evaporites and the ESM peripheral depression are looked at in more detail in Chapter 7.

The Levant continental margin contains a series of submarine canyons that have formed since the MSC (Katz et al., 2015; Tahchi et al., 2010; Section 2.3.5). Submarine channels in the Levantine Basin are also understood to be affected by underlying salt tectonics (Zucker et al., 2017).

2.6 Summary of Controversies

Many controversies pertaining to the tectonic evolution of the portion of the Tethys Ocean to the NW of the EMR produce a large amount of debate (Frizon de Lamotte et al., 2011); this area is outside the remit of this study so they are not discussed here. Where controversies exist in our understanding of the EMR a more detailed outline of the pertinent literature is presented below.

2.6.1 Palmyride Basin Genesis

In Libya faults bounding Mesozoic basins may be observed (Wood, 2011). In Syria however, no direct evidence exists for basin bounding faults around Mesozoic sediments of the Palmyride trough despite the basin being commonly illustrated as being fault bounded (e.g. Berra and Angiolini, 2014); instead the sediments appear to thin out laterally on seismic data (Wood, 2011). Wood (2015) suggests that the Mesozoic sediments are filling the depression formed by the erosion of a pre-existing geanticline (Figure 2.29), indicated by subcrop of early Mesozoic rocks onto a Hercynian age unconformity. The geanticline is suggested to be the NE continuation of the Awaynat-Bahariyah Arch of Egypt (Guiraud and Bosworth, 1999; Wood, 2015).

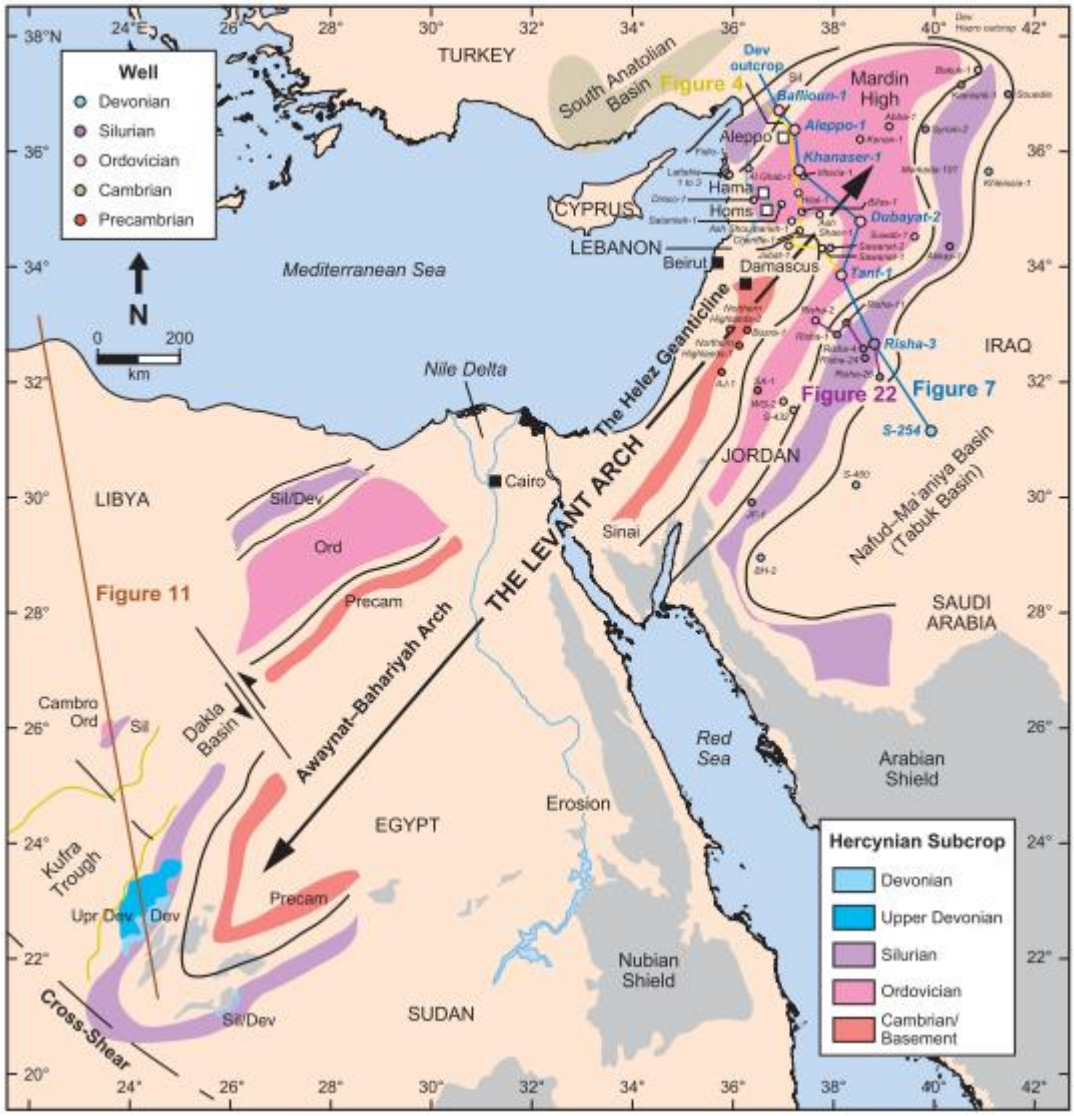

Figure 2.29-Outline of the Levant Arch geanticline hypothesis proposed by Wood (2015). Please refer to Wood (2015) to view the annotated 'Figure 7' and Figure '22'.

Another possibility is that the rift faults beneath the Palmyride basin exist at a depth below current seismic imaging techniques. In the Weald Basin in southern England early seismic only resolved lateral thinning of sediments, it was only with advances in seismic imaging that the deeper rift faults underlying the sediments where resolved (Butler and Pullan, 1990).

2.6.2 Direction of Rifting in the Eastern Mediterranean

The direction of the Latest Palaeozoic to Jurassic rifting that formed the Neo-Tethyan ocean remains equivocal in the EMR. Variations between the end members of NNE and WNW have been suggested (directions relative to current orientation of Africa; Figure 2.30). Based on refraction analysis of the continental margins and comparison with margins of known genesis elsewhere, Schattner and Ben-Avraham (2007) propose a two phase alternative; NNE-SSW extension in the Permian, and Triassic-Early Jurassic NW-SE extension. The uncertainty for this has arisen from the deep burial of the relevant features. This is explored in Section 4.6.

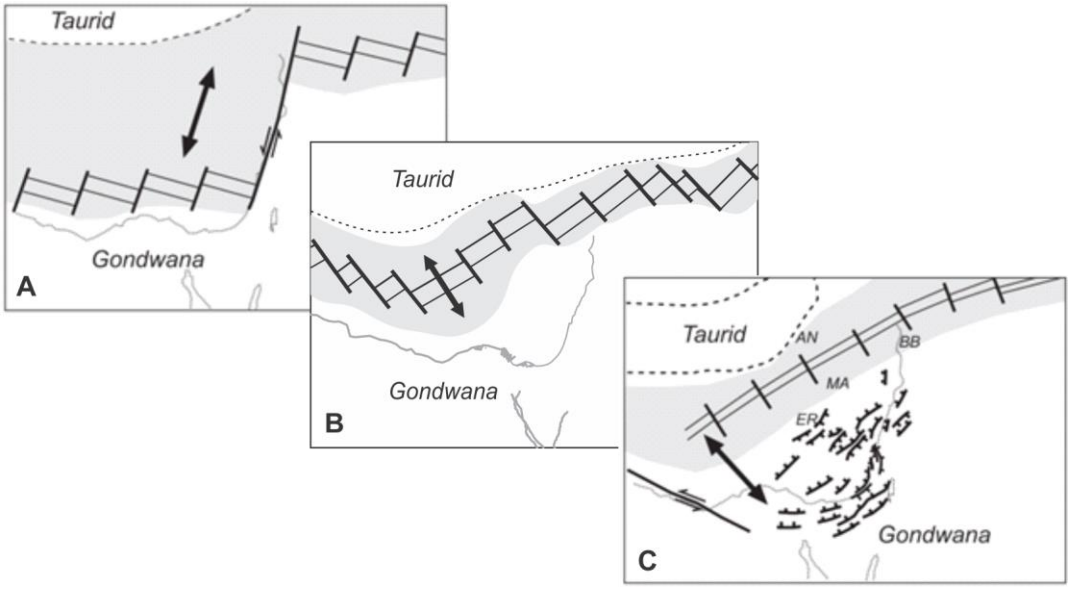

Figure 2.30-Different hypothesises for the direction of Neo-Tethys rifting in the EMR (adapted from Gardosh et al., 2010). A (Dewey et al., 1973; Robertson et al., 2012a; Stampfli and Borel, 2002), B (Barrier and Vrielynck, 2008; Montadert et al., 2014), C (Cowie and Kusznir, 2012b; Gardosh et al., 2010; Longacre et al., 2007).

2.6.3 Timing of Eastern Mediterranean Spreading

The size of the EMR means that there are local timing discrepancies for most regional tectonic events (Figure 2.18). However, the depth of the oceanic crust means that there is a large discrepancy for the onset of sea floor spreading in the Neo-Tethys. The presence of marine basin sediments of Permian age in the Palmyrides, Southern Tunisia, Sicily and Eastern Crete (Frizon de Lamotte et al., 2011) suggest that an earlier phase of late Palaeozoic rifting took place (Stampfli et al., 2001, 1991; Stampfli and Borel, 2004). However, it has not been established if these sediments were deposited in a rifting setting, or that spreading would have been temporally proximal to their deposition (Frizon de Lamotte et al., 2011). Garfunkel (1998) and Robertson (2006) constrain rifting along the Levant margin and around the ESM to the Late Triassic–Jurassic based on onshore data from the Egyptian Western Desert and subsurface data from Israel. This is used in some recent collationary palaeogeographic maps (Barrier and Vrielynck, 2008) although earlier reconstructions prefer the Cretaceous (Dercourt et al., 1993; Ricou, 1994). A recent investigation into magnetic anomalies in the Herodotus Basin concluding on the basis of magnetic anomaly skewness and the geomagnetic chron signature, that the underlying oceanic crust formed around 340 ± 25 Ma (Granot, 2016).

2.6.4 South Cyprus Continent-Ocean Boundary (COB)

As discussed in Section 2.2, the limits of the oceanic crust south of Cyprus are uncertain. The location of this boundary also marks a possible edge of the Sinai Plate (Section 2.6.4), and is pertinent to the direction of rifting in the Levantine Basin (Section 2.6.1). A NW-SE trend of the COB is consistently drawn by different authors, but there is several hundred kilometres of variation in where the boundary is drawn, although some discrepancy has likely resulted from the use of lower resolution data sets (Figure 2.31). This is investigated further in Section 4.5.

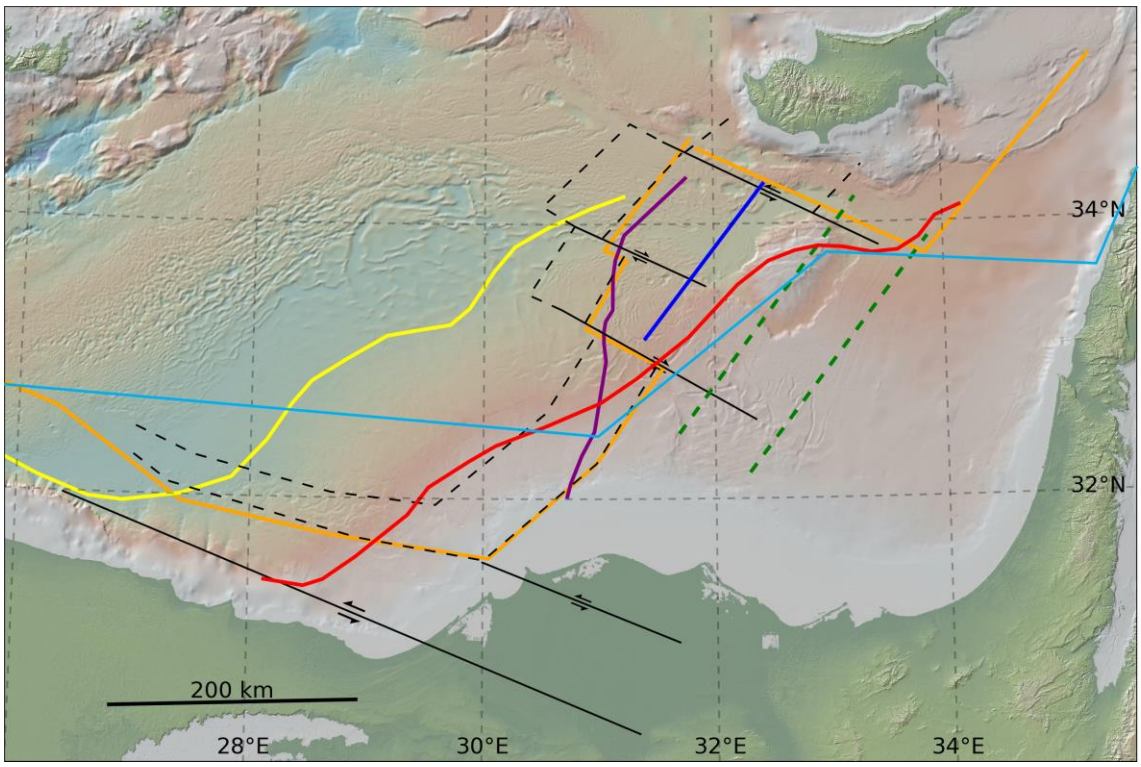

Figure 2.31-Different continent-ocean crustal boundaries south of Cyprus, indicated by the different colours; orange (Longacre et al., 2007) black (Bevan, 2012 after Longacre et al., 2007), red (Harrison et al., 2012), dark blue (Montadert et al., 2010), green (Cowie and Kusznir, 2012a), purple (Granot, 2016), yellow (Avigad et al., 2016) and light blue (Stampfli and Borel, 2002). Dashed lines indicate the interpreted limits of transitional crust. The global relief (Ryan et al., 2009) vertical scale is shown on Figure 1.1 and the supplementary figure.

2.6.5 Delineation of the Sinai Plate

Seismicity in the Gulf of Suez, in conjunction with its morphology, led earlier workers to suggest that the Sinai Peninsula could be a tectonic plate at least partially separated from the African Plate (see refs. within Badawy and Horvath, 1999; Ben-Menahem et al., 1976; McKenzie, 1970; Salamon et al., 1996). Mascle at al. (2000) extended the interpreted western boundary of the Sinai Plate to run from the Gulf of Suez to the west side of the ESM based on interpretation on shallow seismic and bathymetry data over the Nile cone. Further seismotectonic work (Salamon et al., 2003) and GPS data (Mahmoud et al., 2005) concurred with this hypothesis. However, later studies (Loncke et al., 2006; Skiple et al., 2012) of bathymetry and seismic data reveal that the lineations picked out by Mascle at al. (2000) were formed by thin-skinned salt tectonics. Despite this many publications continue to use the boundary of Mascle at al. (2000), or variations thereof (Mahmoud et al., 2005; Nocquet, 2012; Reilinger et al., 2006; Wdowinski et al., 2006).

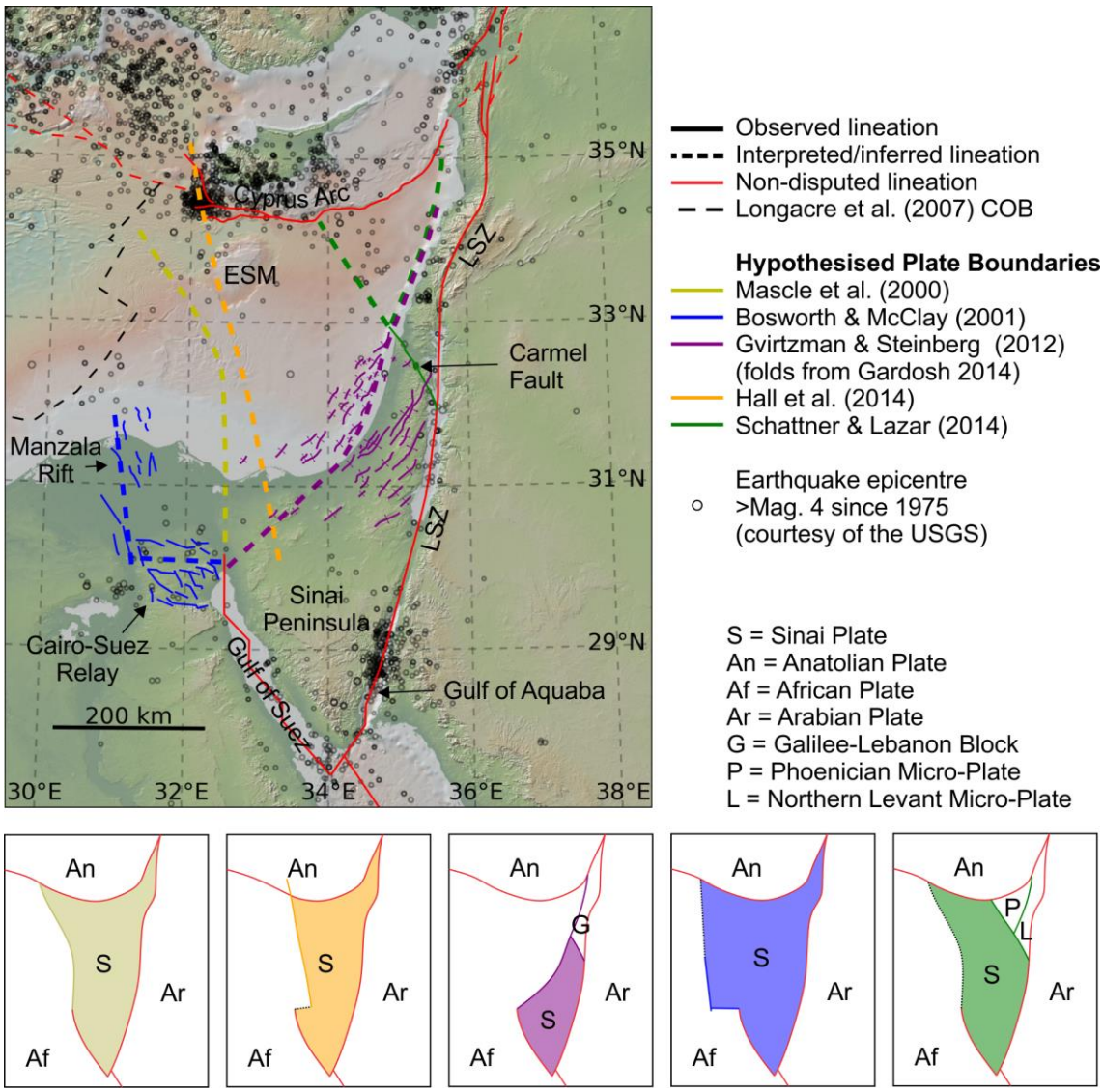

Figure 2.32-Map showing the hypothesised boundaries of the Sinai Plate. The global relief (Ryan et al., 2009) vertical scale is shown on Figure 1.1 and the supplementary figure.

Despite little active deformation, the morphology and continuous seismic activity of the Gulf of Suez attests to a plate boundary there (Badawy and Horvath, 1999; Le Beon et al., 2008; Salamon et al., 1996), however the Gulf of Suez rift faults of the tip out north of the waterway (Bosworth and McClay, 2001; Moustafa et al., 2014). This requires a transform feature perpendicular to the end of the rift. Two alternative plate boundaries have been postulated that suggest transform motion at this location. Bosworth & McClay (2001) postulate that the rift extension is transferred from the termination of the Gulf of Suez to the early Miocene Manzala rift via a set of faults termed the Cairo-Suez relay, and Gvirtzman & Steinberg (2012) suggest that the north Sinai continental margin was a transform boundary during the opening of the Gulf of Suez.

Schattner & Lazar (2014) postulate two additional microplates in the triangle formed by the LSZ and Cyprus Arc. They suggest that the Carmel fault was part of an offshore continuation of the LSZ along which differential movement occurred, separating the microplates.

The NW limit of the Sinai Plate, the continent-ocean boundary, is also controversial and was discussed in Section 2.6.4. The delineation of the Sinai Plate is investigated in Chapter 4.

2.6.6 Cyprus Arc Subduction

The Cyprus Arc is commonly described and/or discussed as an active subduction zone (e.g. Kempler, 1998; Kinnaird and Robertson, 2012; Mart and Ryan, 2002; Montadert et al., 2014; Morris et al., 2015; Palamakumbura and Robertson, 2016b; Reiche et al., 2014b; Vidal et al., 2000a). Tomographic imaging of the arc suggests there is an underlying downgoing slab (Faccenna et al., 2006, Fig. 3B), and normal faulting onshore Cyprus has been linked to subduction roll back, contributing to some studies interpreting that subduction restarted, albeit in a more minor form, at the southern edge of Cyprus in the Miocene (Kempler, 1998; Morris et al., 2015; Robertson, 1998b). However, based on seismic reflection (Bowman, 2011; Klimke and Ehrhardt, 2014; Robertson, 1998b), refraction and gravity modelling (Welford et al., 2015), plate motions inferred from earthquake focal mechanisms and comparison with the Hellenic arc (Papazachos and Papaioannou, 1999), and the absence of a volcanic arc (Harrison et al., 2012) it is also widely accepted that subduction has ceased due to docking of continental blocks in the subduction zone, although the suggested timing varies across the full range of the Cenozoic. The nomenclature and data are therefore at odds.

There is also a large amount of uncertainty as to the current relative plate motions across the Cyprus Arc (Ben-Avraham et al., 1995; Bowman, 2011; Hall et al., 2005b; Harrison et al., 2004; Vidal et al., 2000a). Wdowinski et al. (2006) determine from seismic activity that the Cyprus Arc is convergent and transform on its western and eastern flanks respectively (Figure 2.33). However Woodside et al. (2002) interpret the current motion across the Florence Rise to be primarily transform as opposed to convergent. The relatively minor amount relative plate motion across the feature, and the complex plate motions around the Arc, have likely lead to this uncertainty (Figure 2.1B).

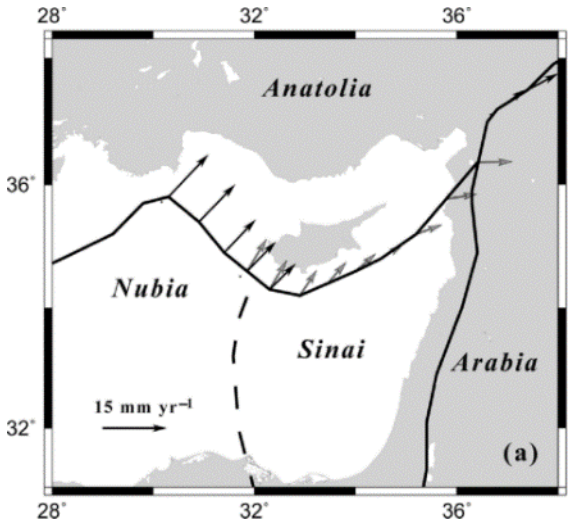

Figure 2.33-Relative plate motions along the Cyprus Arc, as indicated by length and direction of the arrows (Wdowinski et al., 2006). The global relief (Ryan et al., 2009) vertical scale is shown on Figure 1.1 and the supplementary figure.

This feature is investigated further in Chapter 5.

2.6.7 Anomalous Extension

In the Northern Levant Basin >400 late Miocene normal faults, termed the 'Piano Key Faults' (PKFs), have been documented (see supplementary figure; Kosi et al., 2012). The faults strike WNW-ESE and throws over 200 m are widespread. The ongoing broadly NS convergence of the African and Sinai Plates with Eurasia at this time mean these extensional faults exist spatially and at an orientation where compressional features might be expected. The PKFs are layer bound, strain is partitioned above by Messinian evaporites and below by a mobile horizon, presumed to be shale, in which the faults detach (Kosi et al., 2012). They are transected by perpendicular contemporaneous folds. Suggestions for their genesis have included unloading of water burden during the MSC, down slope extension and polygonal faulting orientated by perpendicular compression, but none of these explanations are consistently compatible with what may be observed in seismic data (this study; Ghalayini et al., 2016, 2014; Kosi et al., 2012; Reiche et al., 2014a). These faults are investigated in Chapter 6.

2.6.8 Missing Levant Shear Zone Displacement

Field evidence (Beydoun, 1999) suggests c. 107 km of sinistral displacement has occurred on the LSZ south of the Palmyrides (Searle et al., 2010). More uncertain is the amount of displacement north of the Palmyrides, with estimates ranging between ~20 km in Syria (Searle et al., 2010) and ~65 km in Southern Turkey (Westaway, 2004a). Up to 20 km of compression may be accommodated in the Palmyrides (Chaimov et al., 1990); the remaining 'missing' shortening remains controversial. Some authors have suggested the missing displacement might be accommodated offshore (Brew et al., 2001a; Butler et al., 1998; Carton et al., 2009; Chaimov et al., 1990; Elias et al., 2007; Rukieh et al., 2005; Schattner et al., 2006), however 3D seismic offshore Lebanon indicates this is not the case (Ghalayini et al., 2014). It has been suggested that the Jhar Fault in the Palmyrides may represent the eastern continuation of a fault near Saida west of the LSZ (Ghalayini, 2017). If this is the case then this would mean there has been c. 100 km of offset at the Palmyride restraining bend, necessitating a greater offset on the LSZ further to the north.

2.6.9 Timing of Messinian Evaporite Deformation

Much of the Plio-Quaternary deformation in the Levantine Basin, Nile Cone and Herodotus Basin is understood to be due to motion of the underlying evaporites (Section 2.5.5). This episode of halokinesis is undisputed, but whilst some authors observe another episode of halokinetic deformation due to gravity tectonics during the MSC, on the basis of truncated internal reflectors at the top of the evaporite body (Bertoni and Cartwright, 2007; Gvirtzman et al., 2013; Hodgson, 2012), others argue against this (Allen et al., 2016). This is investigated in Section 3.7.1.

2.6.10 Timing of Messinian Erosion

Contrasting interpretations have been made for (Orszag-Sperber et al., 2009) and against (Manzi et al., 2014) sea level draw down at the onset of the MSC. Seismic data demonstrating erosion

at the onset of the MSC in the deep portion of the Southern Levantine Basin is shown and discussed in Section 3.6.5.

Chapter 3 Seismic Interpretation

3.1 Seismic Metadata

This study uses seismic data as the principal source of information to investigate tectonics via stratigraphic sequence interpretation. A map of the six seismic surveys available to this study is given in Figure 3.1, along with the well data used to date reflectors in the seismic. The details of the well data is shown in Section 3.3. The key to the different surveys in Figure 3.1 is valid for all other subsequent figures in this study that include the seismic lines. The details of the surveys are shown in Table 3.

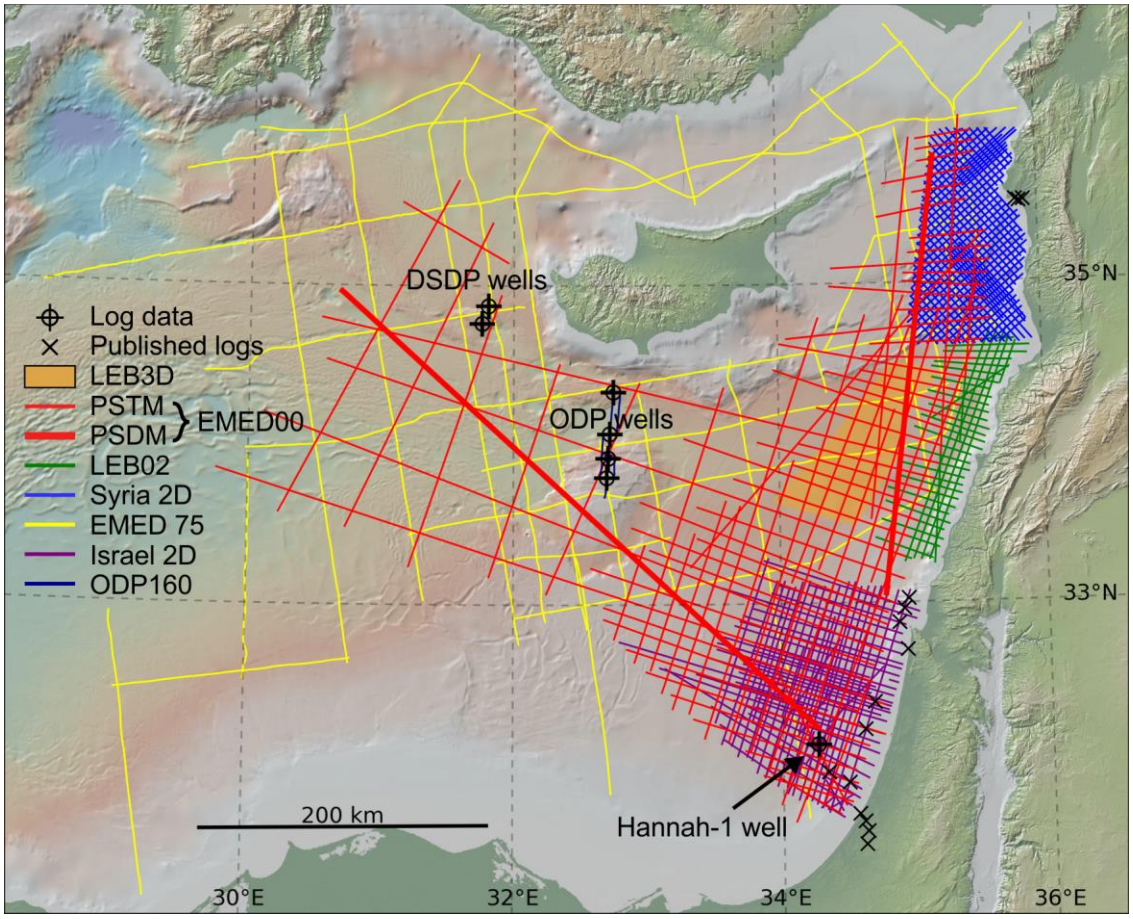

Figure 3.1-Map showing the location of seismic and well data available to this study. Survey details (including supplier) are given in Table 3, well details are given in Table 5. The global relief (Ryan et al., 2009) vertical scale is shown on Figure 1.1 and the supplementary figure.

Table 3-Details of the seismic data available to this study. PSTM is Post Stack Time Migrated and PSDM is Post Stack Depth Migrated.

Survey	Owner	Type	Extent	Vintage and details	Penetration
LEB3D	Spectrum ASA	3D PSTM	5358 km^2	2012-13	9.5 s TWTT
EMED00		2D PSTM	12304 km	2000, reprocessed 2011-12	12 s TWTT
		2D PSDM	753 km	Lines 027 and 047	16 km
LEB02		2D PSTM	2006 km	2002, reprocessed 2012	9 s TWTT
Syria 2D		2D PSTM	4988 km	2005, reprocessed 2011	8.9 s TWTT
EMED75		2D PSTM	7834 km	1975, reprocessed 1999	6-8 s TWTT
Israel 2D	TGS	2D PSTM	6831 km	2001	9 s TWTT
ODP160	Public Domain	2D Single Channel	199 km	1995	2.5-3.5 s TWTT

The seismic data available to this study provides coverage of the Levant Margin from Israel to offshore Syria with seismic line spacing ranging from ~2 to ~8 km (Figure 3.1). This allows for the confident interpretation of detailed geometries of the basin scale features. Seismic line coverage of the western portion of the Levantine Basin is less dense, with average line spacing around 10 km. This still permits delineation of basin scale features (Figure 3.1). West of Cyprus and over the ESM and Herodotus basin the average line spacing of c. 25 km resolves geological trends but not feature geometries (Figure 3.1). 2D lines of 1975 vintage that extend into the Nile Cone and offshore Turkey were available to this study (Figure 3.1). The vintage of their acquisition and processing techniques mean they rarely confidently resolve reflectors below the MSC salt. Their primary use in this study was to assess potential extensions of features identified elsewhere in the study. The LEB3D data set permitted detailed interpretations of a section of the Northern Levantine Basin (Figure 3.1). The limited coverage, penetration and imaging clarity of the ODP160 survey meant it served only to aid well correlation (Figure 3.1).

All but two of the seismic lines available to this study were time migrated as opposed to depth migrated (Table 3). Data in time provide a more abstract representation of the geometries of subsurface features than data in depth, exacerbated by reasons discussed in Section 3.2.5. This provides challenges in interpretation. Data in depth generally provide a closer approximation to the truth, however the assumptions made in the conversion or migration of data into the depth domain can lead to issues as discussed in Section 3.2.3.

This study favours a hot-grey-cold colour table (Figure 3.2A) for depicting seismic data, as opposed to the black-grey-white colour tables (Figure 3.2B) used by some workers. By including different wavelengths of light as well as intensity, the hot-grey-cold colour table fundamentally spreads out the information in the seismic trace across a more varied range (Figure 3.2C). This results in greater perceived contrast between two signals of matching polarity but contrasting amplitude (Figure 3.2C), but in some cases reduced perceived contrast between the depictions of two signals of equal amplitudes but opposite polarities (Figure 3.2C). There are many debatable subtleties, but in practise this (subjectively and debatably) means that the character of a given seismic package may be more distinct from the character of other seismic packages, especially where the seismic data contains reflectors of varying amplitude (Figure 3.2D). Conversely, the

more limited perceived contrast between matching polarities depicted by the black-grey-white colour table can aid detection of laterally polarity switching reflector offsets that may represent fault offsets (again subjectively and debatably) as the eye is drawn to amplitude switching rather than reductions or increases (Figure 3.2D). The limited well data in the EMR means that correlation of seismic packages is key to interpretations of the area, thus the favoured hot-grey-cold colour table for the figures in this document. An exception to this is the ODP160 survey, which contains very little amplitude variation between reflectors and consequently is depicted in the black-grey-white colour table.

Limited well data and multiple seismic surveys including some without processing reports mean absolute amplitudes were of limited application in this study. Consequently, absolute amplitudes are not shown on the figures in this study. Additionally, the regional remit of this study means that most key observations of the seismic data are at package scale as opposed to reflector scale; limiting any additional insights from reflector amplitude.

The images of seismic data in this study are shown in Society of Exploration Geophysicists (SEG) reverse polarity: negative amplitude reflectors (the ‘cold’ end of the colour table) represent a positive increase in impedance and vice versa. This is to conform with the convention set by most the seismic data available to this study.

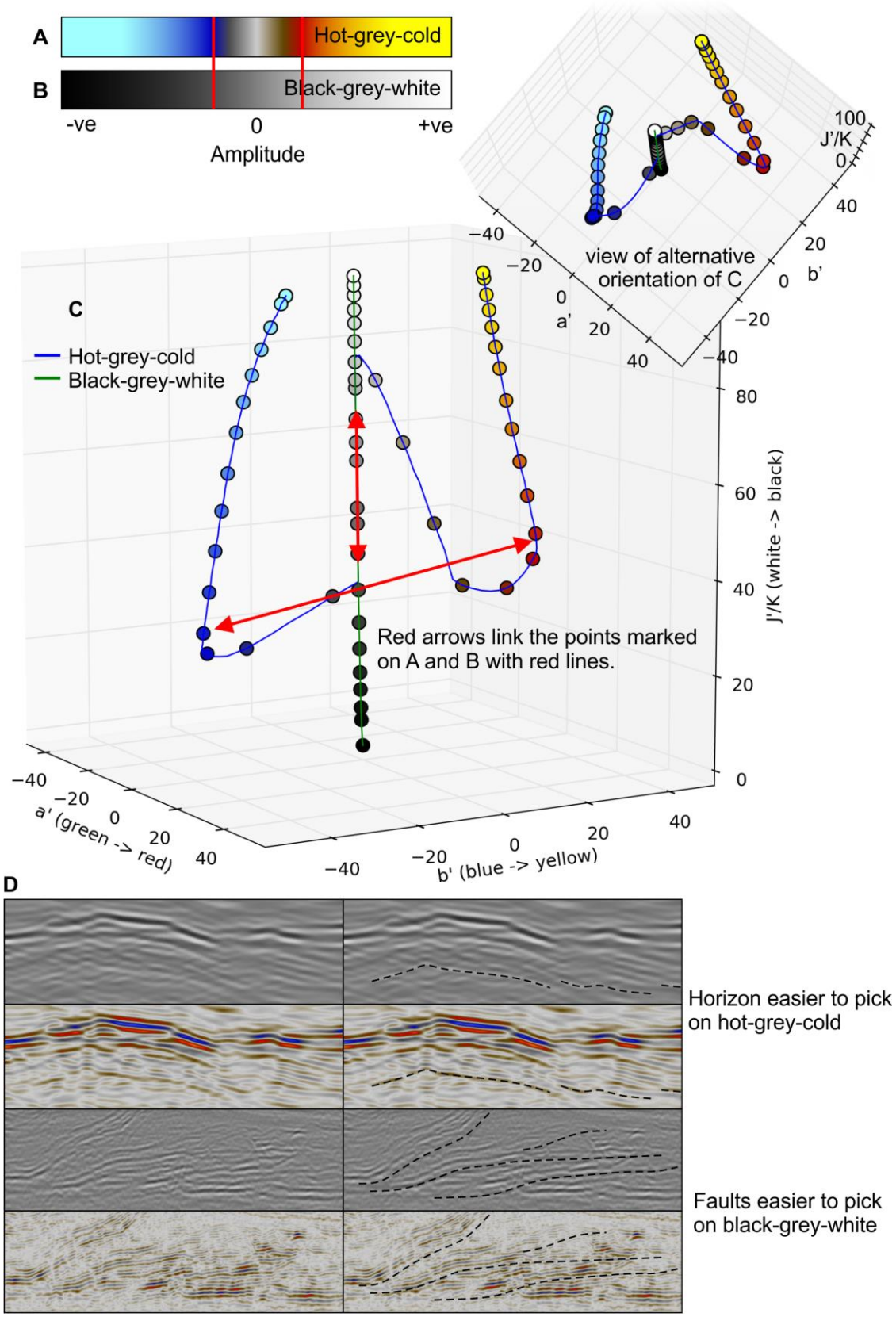

Figure 3.2-Comparison of A) hot-grey-cold and B) black-grey-white colour tables, by C) plotting of these colour tables in CAM02UCS colour space (Li et al., 2012), meaning that the Euclidian distance between plotted points is linearly proportional to human perception between the two colours represented by the points, and D) seismic lines demonstrating these differences.

Discounting conference presentations and hydrocarbon orientated magazine articles (Esestime et al., 2016; Hodgson, 2014, 2013, 2012; Hodgson and Karyna, 2015; Roberts et al., 2010), the only peer reviewed articles published on the seismic surveys available to this study are:

- Reiche et al. (2014) and Reiche (2015), who looked at four lines of the EMED00 survey in the Northern Levantine Basin.
- Peace et al. (2012) and who looked at the EMED00, LEB02 and EMED75 surveys but published no surfaces and limited interpretations.
- Roberts and Peace (2007) who explored the hydrocarbon prospectivity of the EMED00, LEB02 and EMED75 surveys.
- Bowman (2011) who looked at the Syria 2D survey and focused on prospectivity.
- Sagy et al. (2015), Gardosh and Druckman (2006) and Gardosh et al. (2010) who looked at the Israel 2D dataset.

Consequently, with the exception of the Israel 2D survey, these data sets are relatively poorly documented in published scientific literature. However, there is some crossover between the areas covered by these surveys and surveys available to other studies, especially in the Levantine Basin (Table 1).

3.2 Evaluation of Seismic Data

Before the seismic data is presented, it is important to consider different issues that must be considered when interpreting the data. These issues are discussed in the following sub-sections.

3.2.1 Survey Processing

The different seismic surveys available to this study have undergone different processing routines (e.g. Table 4). As reprocessing of seismic data is beyond the scope of this study, and some of the processing reports for the surveys were unavailable, a full break-down and comparison of the processing undertaken for each survey is also beyond the scope of this regional scale geological study.

Table 4-Details of the processing undergone by the EMED00, EMED75 and LEB02 surveys.

EMED00 2011 reprocessing parameters applied
1. Reformat (SEGD to Internal Format)
2. Source De-signature to minimum phase
3. Resample to 4ms
4. 4Hz (18db/Oct) Low Cut Filter
5. Amplitude Recovery (removable T Squared Correction)
6. NOISERM – applied to common channels, 25 trace filter, 7.5 Threshold
7. FK Noise Modelling +/-8ms per trace modelled in FK domain and subtracted from data in XT domain, shot ordered.
8. SRME - model subtracted in offset mode – 1st iteration 101trace 800ms/ 2nd iteration 101 trace 1200ms windows
9. Trace Reduction (Spatial ant-alias filter followed by re-sampling in the x-domain, simulating 25m group interval)
10. Velocity Analysis 2km Intervals
11. High Resolution Radon – -500 to 3000ms moveout, offset 7238 with 550ms cut

12. TVF
13. PSTM Velocity Analysis (1km intervals)
14. PSTM
15. Amplitude Recovery (T Squared V correction)
16. High Resolution Radon – -500 to 3000ms moveout, offset 7238 with 250ms cut
17. VELTUNE – Fourth order velocity tuning
18. NMO Correction
19. Residual Gain
20. Outer Trace Mute (Space Varied)
21. Stack (72 Fold)
22. Static correction for Source and Streamer Depth (+11ms)
23. Zero Phase conversion
24. Coherency Enhancement
25. Eigenvector noise attenuation (time & space variant application)
26. Targeted residual multiple attenuation
27. Time and space varied bandpass filtering
28. Robust AGC – Expanding window from 750ms at 700ms below water bottom to 3000ms at 9 seconds

EMED75 2000 reprocessing parameters applied

1. Reformat (SEGC)
2. Spherical divergence VTT inelastic attenuation (2db per second (1000 – 7000 ms)
3. FK filter +/- 16 ms/trace (Wrap around AGC)
4. FX filter in offset domain (9 point filter with time variant addback)
5. Common midpoint gather (24 fold)
6. Velocity analysis (2km intervals)
7. Radon demultiple
8. Shot interpolation in offset domain
9. DMO (FK algorithm)
10. Deconvolution (Wiener-Levinson least squares, Operator-200ms, gap -24ms, design window (wb+100ms) - (record length - 100ms) , Application window 0 - record length
11. NMO moveout correction
12. Outer trace mute
13. AGC (500ms)
14. Inner trace mute
15. Stack (48 fold)
16. Gun and cable statics (+21ms)
17. Deconvolution (Wiener-Levinson least squares, Operator-184ms, gap -24ms, Design window (wb+100ms) - (record length - 100ms), Application window 0 - record length)
18. FX migration (Stacking velocities smoothed and scaled by 90%)
19. Space + time variant filters
20. Scaling (500ms overlapping gates)

LEB02 2012 reprocessing parameters applied

1. Reformat (SEGD to Internal Format)
2. Source De-signature to zero phase
3. Resample to 4ms
4. 4Hz (18db/Oct) Low Cut Filter
5. Amplitude Recovery (removable T Squared Correction)
6. Swell Noise Attenuation – 2 passes in shot domain
7. FK Noise Modelling +/-8ms per trace modelled in FK domain & subtracted from data in XT domain, shot ordered.
8. SRME - model subtracted in offset mode – 2 iterations of multiple model prior to subtraction

9. Trace Reduction (Spatial ant-alias filter followed by re-sampling in the x-domain, simulating 25m group interval)
10. Velocity Analysis 2km Intervals
11. High Resolution Radon – -200 to 2600ms move-out, reference offset 6000 with 400ms cut
12. Diffracted Noise Attenuation
13. TVF
14. PSTM Velocity Analysis (1km intervals)
15. PSTM
16. Amplitude Recovery (T Squared V correction)
17. High Resolution Radon – +/- 3000ms move-out, reference offset 5000 with a time variant move-out cut
18. VELTUNE – Fourth order velocity tuning
19. NMO Correction
20. Outer Trace Mute (Space Varied)
21. Stack (120 Fold)
22. Static correction for Source and Streamer Depth (+11ms)
23. Coherency Enhancement
24. Eigenvector noise attenuation (time & space variant application)
25. Time and space varied bandpass filtering
26. Robust AGC – Expanding window from 500ms down to top salt increasing to 1000ms at data end.

However, where aspects of the processing sequence affect what may be interpreted an awareness of this is beneficial. Consequently, one aspect of the processing of the EMED00 survey requires mention, especially as it is the primary regional survey. Comparison of EMED00 data to data of another survey best demonstrates this issue (Figure 3.3).

The processing method of the EMED00 survey accentuates reflector continuity, to an apparently greater extent compared to similar processing steps used by the other surveys available to this study. This was noted as some reflectors appear to be synthetically continuous at low vertical exaggerations. In some areas, this results in less chaotic reflectors that are more readily resolved (e.g. Figure 3.3C and D), and nearly ubiquitously it results in reflectors that lend themselves more readily to autotracking. However, by using processing that laterally joins up reflectors in this way some signals are lost, especially where the true reflector signal truncates laterally. This may be observed most readily at non-continuous steeply dipping features (Figure 3.3A), and where reflectors are faulted (Figure 3.3B and E). The structural focus of this study means that this fault resolution issue is particularly problematic, as it introduces artificial events that can mask the true location of faults.

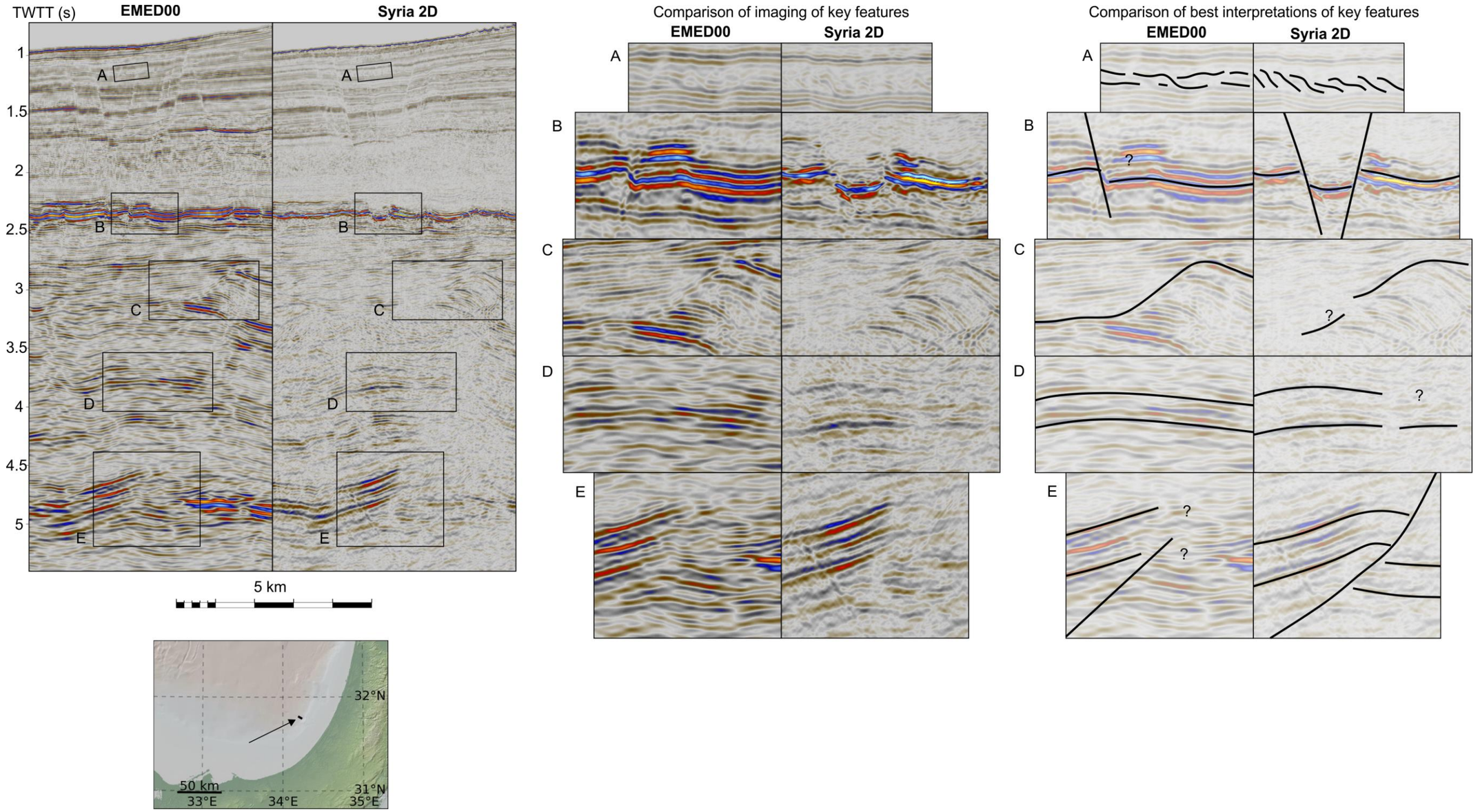

Figure 3.3-Comparison of reflectors resolved by lines of the EMED00 and Syria 2D surveys at the same location, highlighting differences in imaging caused by variations in processing sequences. The global relief (Ryan et al., 2009) vertical scale on the minimap is shown on Figure 1.1 and the supplementary figure.

3.2.2 Multiples

The EMED00, LEB02 and LEB3D surveys are well processed and multiples are suppressed. In contrast, the ODP160 survey contains many multiples, although its sole application in this study to link well-ties (see Figure 3.10), and its limited coverage of <0.5% of the data available to this study (Table 3) means these are not discussed here.

The Syria and Israel 2D surveys both contain multiples that affect several lines. In both surveys these appear to be generated by a combination of the sea floor and MSC unconformities. The multiples only appear where a seismically resolvable evaporite sequence is absent, which indicates the multiples are due to the high impedance contrast at the MSC unconformity. For the Israel 2D survey the multiple appears below the MSC unconformity, at twice the TWTT of the sea floor, indicating that the seismic wavepath of the multiple included an extra sea surface to sea floor leg (Figure 3.4A). For the Syria 2D survey the multiple also appears below the MSC unconformity, but at an offset equal to the TWTT between the seafloor and MSC unconformities, indicating that the seismic wavepath of the multiple included a leg between these surfaces (Figure 3.4B). Some reflectors on the Syria 2D survey that are consistently offset from the base MSC unconformity could be interpreted as a multiple, however careful interpretation to locations where the reflectors diverge reveal this is not the case (Section 5.4).

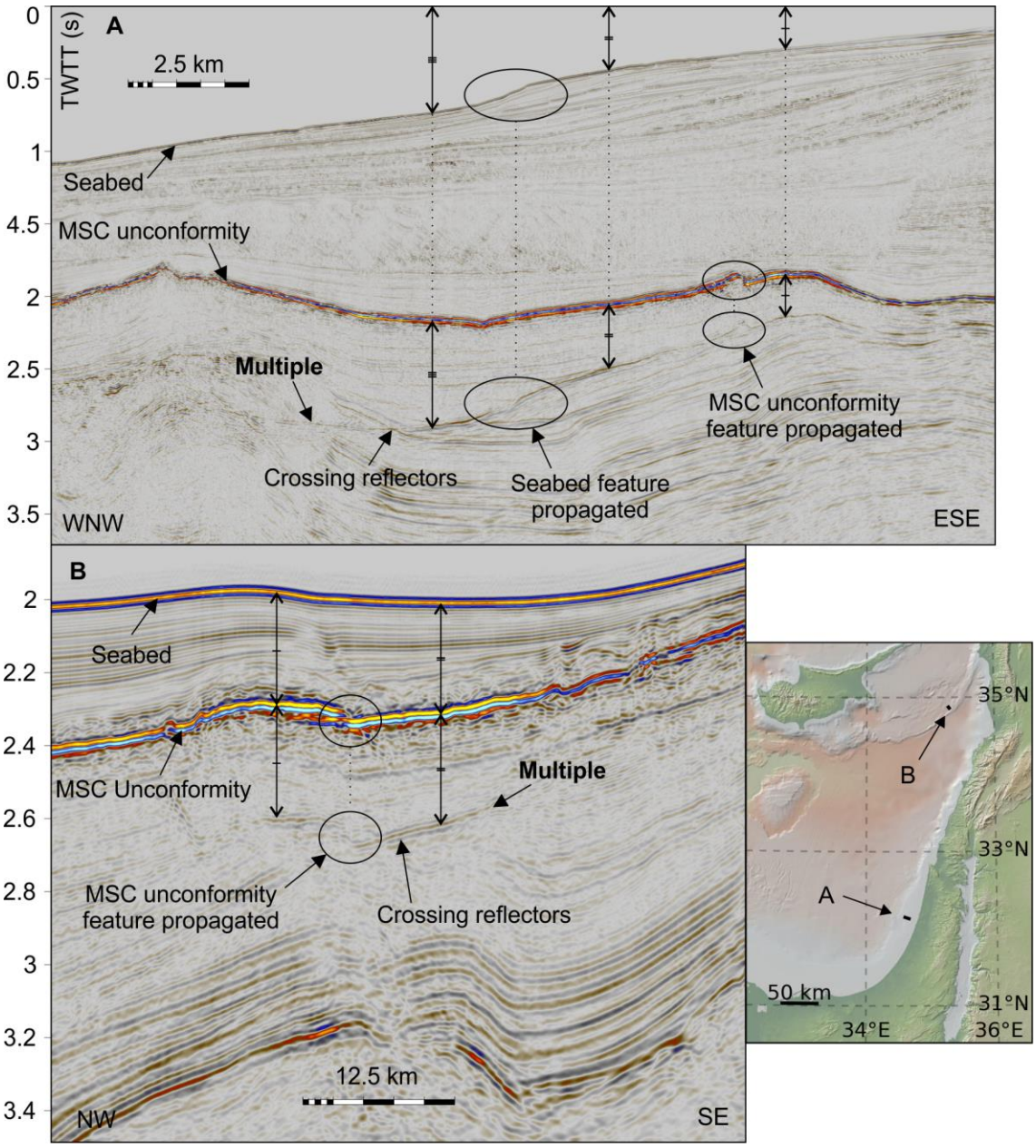

Figure 3.4-Seismic lines highlighting multiples and the features used to define them in the A) Israel 2D survey and B) Syria 2D survey. The global relief (Ryan et al., 2009) vertical scale on the minimap is shown on Figure 1.1 and the supplementary figure.

3.2.3 Misties

Misties (based on the depth of the seabed reflector) between lines of the EMED75 and ODP160 surveys and others (including those of the same survey) are common (Figure 3.5). The EMED75 reprocessing reports reveal that navigation data were digitised from an old map, and observers' logs were of poor quality and sometimes indecipherable. As noted in the reprocessing report these geometric inaccuracies likely resulted in the misties. As misties on the other surveys available to this study are uncommon and relatively minor (Figure 3.5) the other surveys were taken as the preferred horizon elevation. Unless otherwise discussed the misties have not detracted from the interpretations made here, as picking of confident reflectors such as the seafloor allowed the misties to be corrected by vertically shifting the seismic lines.

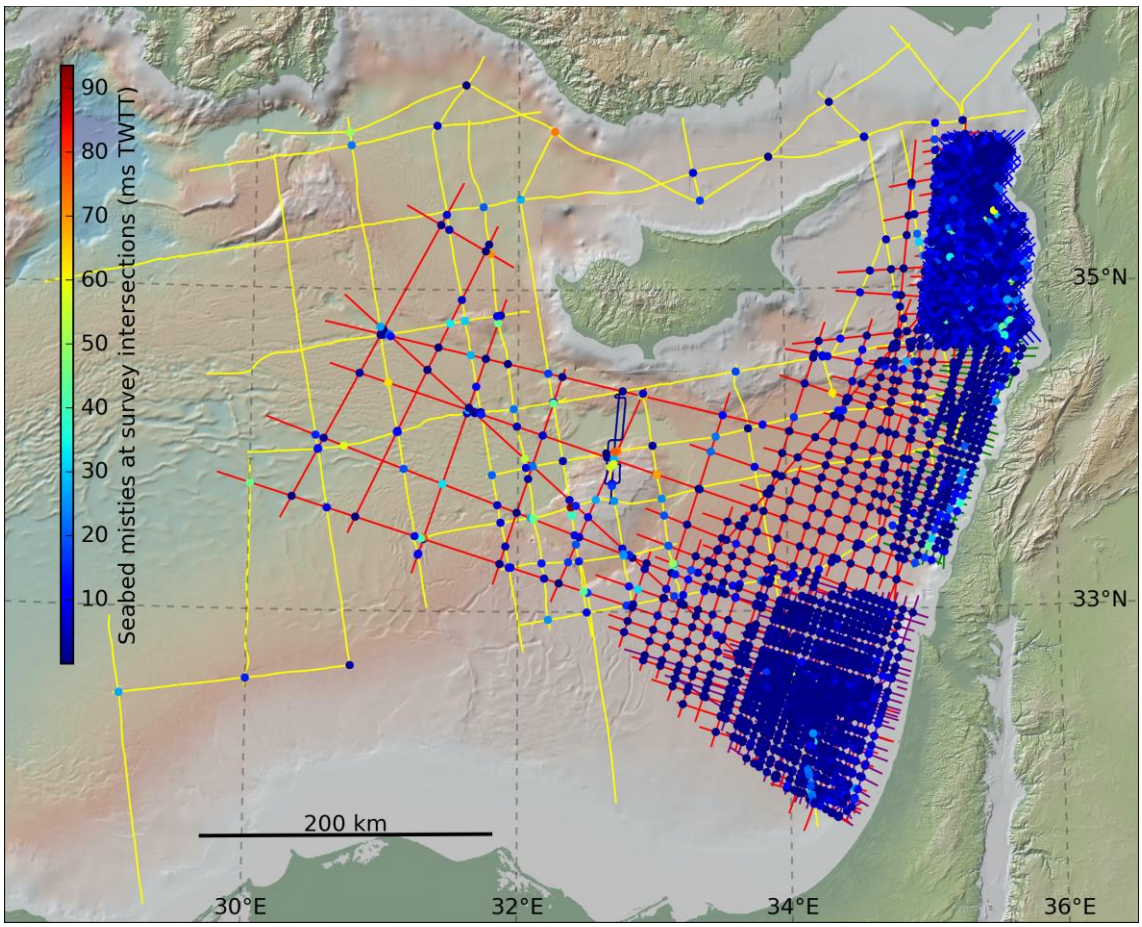

Figure 3.5-Map showing the misties in the surveys available to this study. The global relief (Ryan et al., 2009) vertical scale is shown on Figure 1.1 and the supplementary figure.

Large areas of the EMR have undergone extensive convergent deformation (Section 2.5.2). In the Cyprus Arc this has produced features with steeply dipping reflectors. Where a perpendicular intersection between 2D seismic lines occurs at steeply dipping reflectors misties are common; an example is shown in Figure 3.6. Confidence in the interpretations continued between lines via these mistied reflectors is then reduced. This is particularly prevalent in the Syria and EMED75 surveys between Cyprus and Syria, especially in deeper reflectors that have experienced more deformation. However, loop-tying allowed most this lost confidence to be restored.

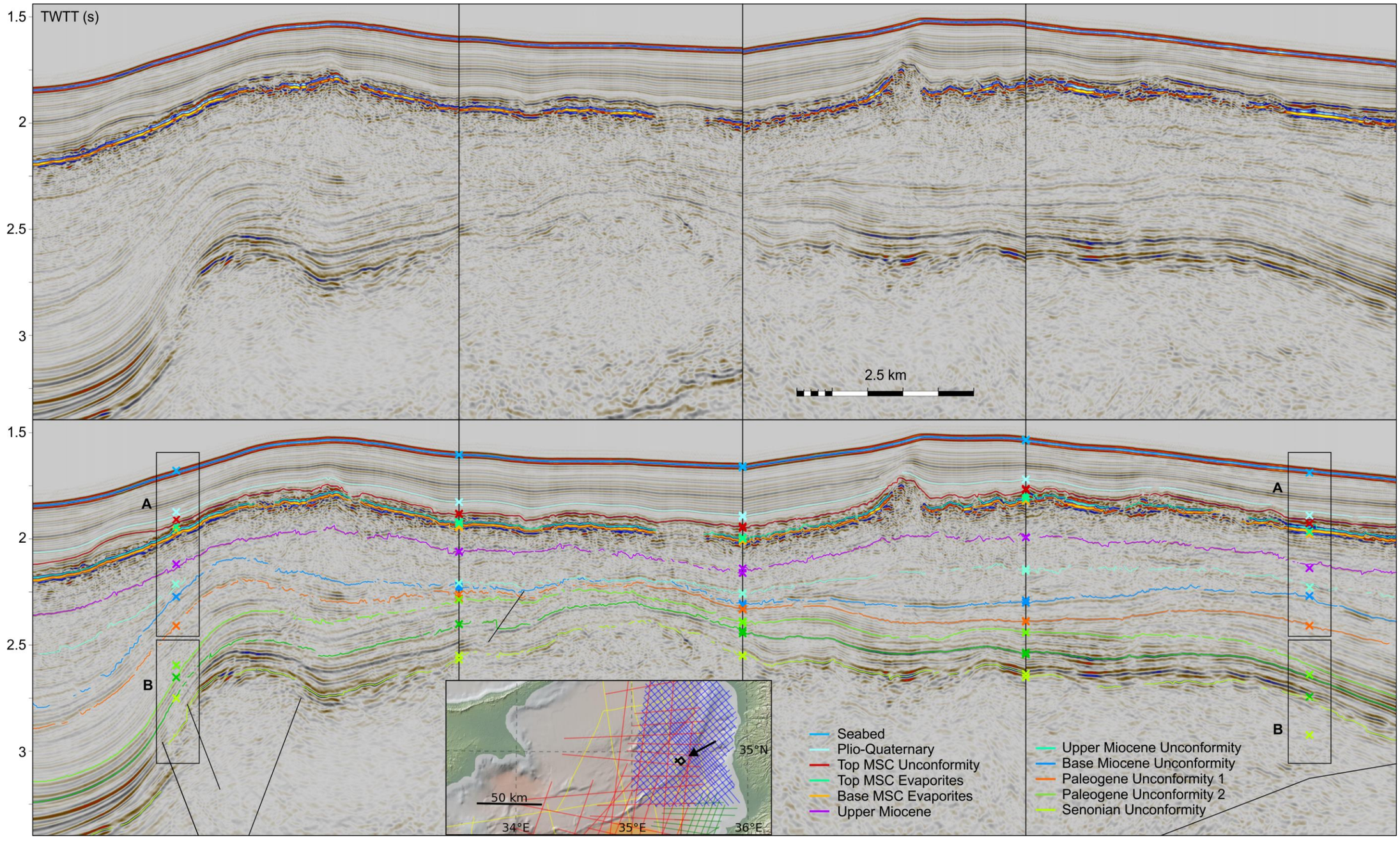

Figure 3.6-Looped composite seismic line showing a location in the Cyprus Arc where steeply dipping stratigraphy results in misties of only deeper reflectors (B as opposed to A).

3.2.4 Depth Migration

The two PSDM lines available to this study would have required manual construction of a velocity model to produce. Where the stratigraphy is planar the results are geological realistic, however in some areas of the Cyprus Arc convergent deformation has resulted in complex stratigraphy. The time consuming iterative process of constructing a velocity model means that only larger velocity variations are commonly accounted for. Consequently, an inaccuracy in the velocity model has produced synthetic trends in the PSDM data.

On PSDM line EMED00-047 a small velocity model error may be observed. Comparison with the equivalent PSTM line reveals that the base of the evaporites has been incorrectly picked in one location at the Larnaca Ridge, causing a series of reflectors representing sub-MSC horizons to be artificially stretched, as they were likely migrated with a velocity equivalent to that of massive halite (Figure 3.7). Coherent linear reflectors and no overlying halokinesis suggest the sequence is clastics as opposed to evaporites (Figure 3.7).

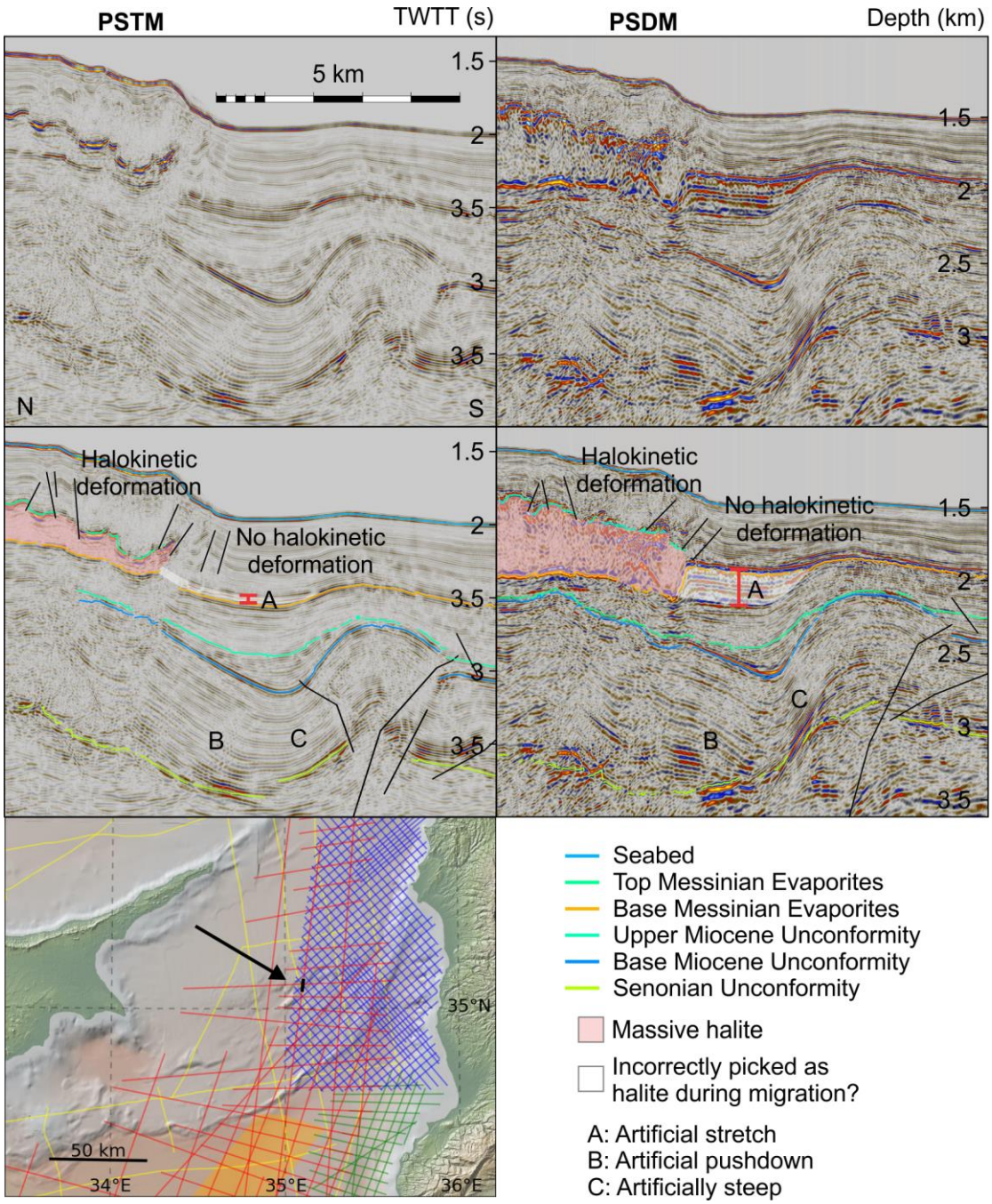

Figure 3.7-Demonstration of a possible depth migration error in a PSDM line at the Eastern Cyprus Arc. The global relief (Ryan et al., 2009) vertical scale on the minimap is shown on Figure 1.1 and the supplementary figure.

3.2.5 Effect of Evaporites

Evaporites have some geological properties that affect seismic imaging of geological sequences containing evaporites. Pertinent to this study are the incompressible and mobility of halite. Following common usage, this study uses the term salt to describe rock intervals primarily composed of halite (Hudec and Jackson, 2007).

The incompressibility means they have a high seismic velocity at the surface that does not change at depth. This contrasts with other sediments that become more compact with increasing depth, resulting in increased seismic velocities at depth. The velocity of the evaporites contrasts with

shallow sediments and the corresponding large impedance contrast absorbs a significant portion of seismic energy. Advances in imaging techniques over the last ~20 years means that clear sub-salt images may now be achieved, albeit with reduced energy. As this returned seismic energy is reduced typical seismic processing artificially increases the amplitude to compensate for the corresponding reflector amplitude. This amplitude increase also amplifies any noise, reducing the clarity of the seismic image. As salt is incompressible the high impedance reflectors that typify shallow evaporites are reduced or even absent at depths where the velocity of surrounding compressed sediments matches that of the evaporites.

The mobility of salt means that halite rich bodies and overlying sediments are often heavily deformed, and the resulting non-linear seismic wavepaths further restrict imaging of underlying reflectors.

These properties can cause two major issues when interpreting evaporitic stratigraphic sequences. The first is a reduction in the imaging clarity of sub-salt sediments. On seismic of older vintage sub-salt coherent reflectors can be almost entirely absent. The second major issue can occur in areas with laterally contrasting thicknesses of evaporites. The high seismic velocity of evaporites can mean a reflector underneath an evaporite body will occur at a reduced TWTT relative to the same reflector at the same depth that is not underneath an evaporite body. This effect is called seismic ‘pull-up’, or ‘push-down’ for the opposite. Examples of this phenomenon with a present and absent evaporite body, and an evaporite body of varying thickness are shown on Figure 3.8 A and B respectively. Non-consideration, or insufficient consideration, of this effect has resulted in several published erroneous interpretations in the EMR, including ‘highs’ around the ESM (Figure 3.8A; Esestime et al., 2016) and at the Latakia Ridge (Section 3.6.1).

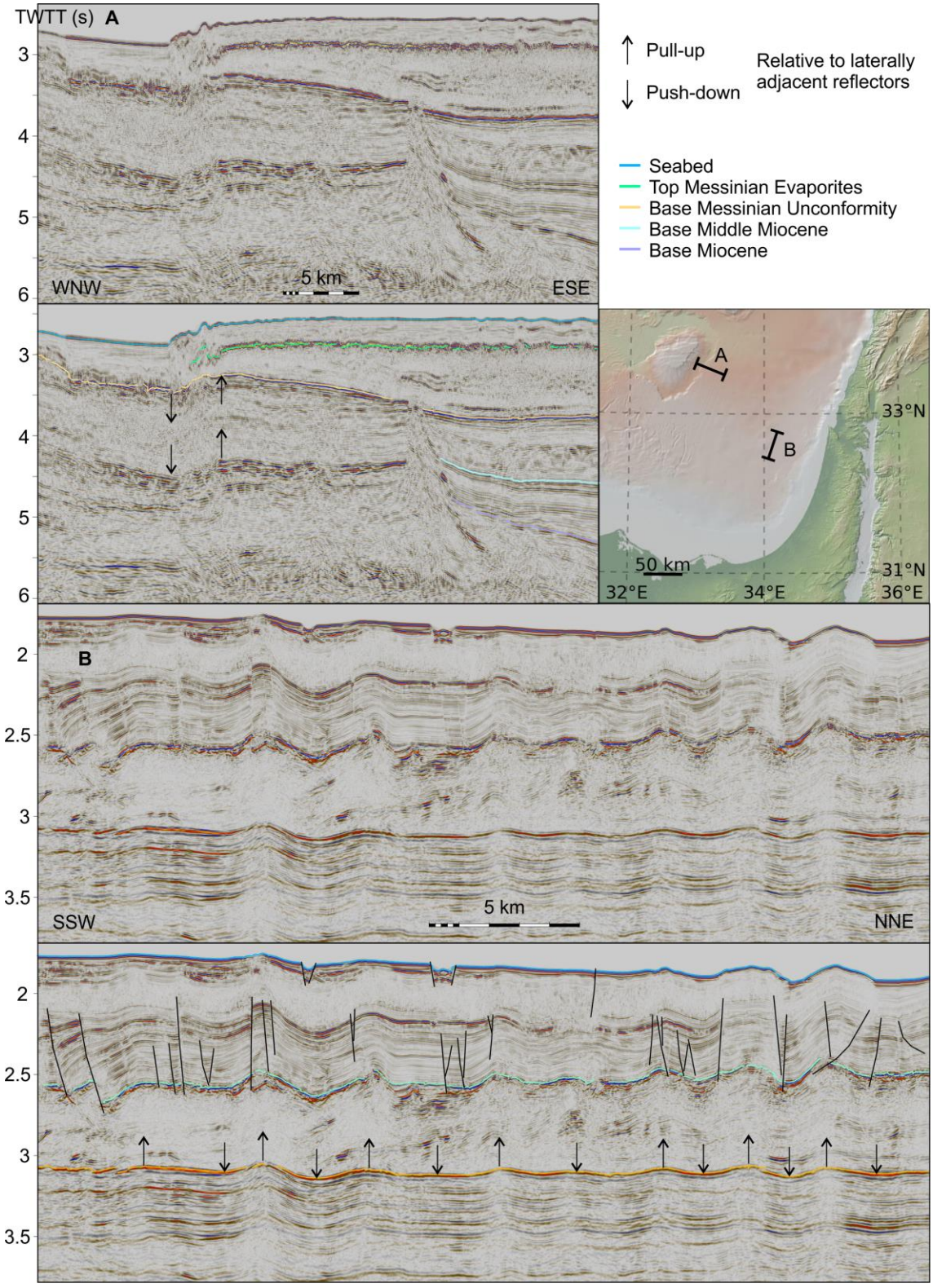

Figure 3.8-Example of seismic pull up A) where the evaporite sequence is present and absent and B) where the thickness of the evaporites varies. The global relief (Ryan et al., 2009) vertical scale on the minimap is shown on Figure 1.1 and the supplementary figure.

3.3 Well Data

Hannah-1 is the only well in the interior of the EMR basins that pierces the sediments below the Senonian unconformity horizon, albeit on the basin flank (Figure 3.9). The Tamar-1 well

demonstrated that horizons that had been interpreted as Senonian-Eocene (Gardosh and Druckman, 2006; Roberts and Peace, 2007) or Cretaceous (Peck, 2008) were in fact Miocene (Steinberg et al., 2011). In conjunction these two wells then demonstrated that a reflector that had previously been considered a Late Jurassic unconformity could be confidently interpreted as a Late Cretaceous in age (Bowman, 2011). The tying of the Hannah-1 well to the sediments of the Levant Basin is shown in Figure 3.9 (also see Figure 3.14). This is the only well available to this study that permits confident dating of sediments in the Levantine Basin. Consequently, all the horizon ages used in this study, apart from those on the ESM, time back to this well. The horizon ages used by this study concur with horizons dated by another study with access to more well data (Gardosh et al., 2008b).

Publically available borehole data from the Ocean Drilling Program (ODP) and Deep Sea Drilling Program (DSDP) are available in the region but are comparatively shallow. Those in the EMR have mostly been drilled on bathymetric highs (Figure 3.10; Figure 3.11) and consequently they either do not pierce sediments older than the Neogene, or reflectors pertaining to older sediments cannot be confidently traced off the relevant bathymetric high. ODP well 967 pierced Cretaceous sediments, and although logs that could constrain seismic velocity are absent, this permitted dating of reflector packages, if not specific reflectors, at the ESM. Crucially this elevated the Senonian Unconformity pick much shallower than it might have been had it been traced from the Levantine Basin, as it demonstrates significant paleo-relief of the ESM carbonate platform (see Figure 3.14B).

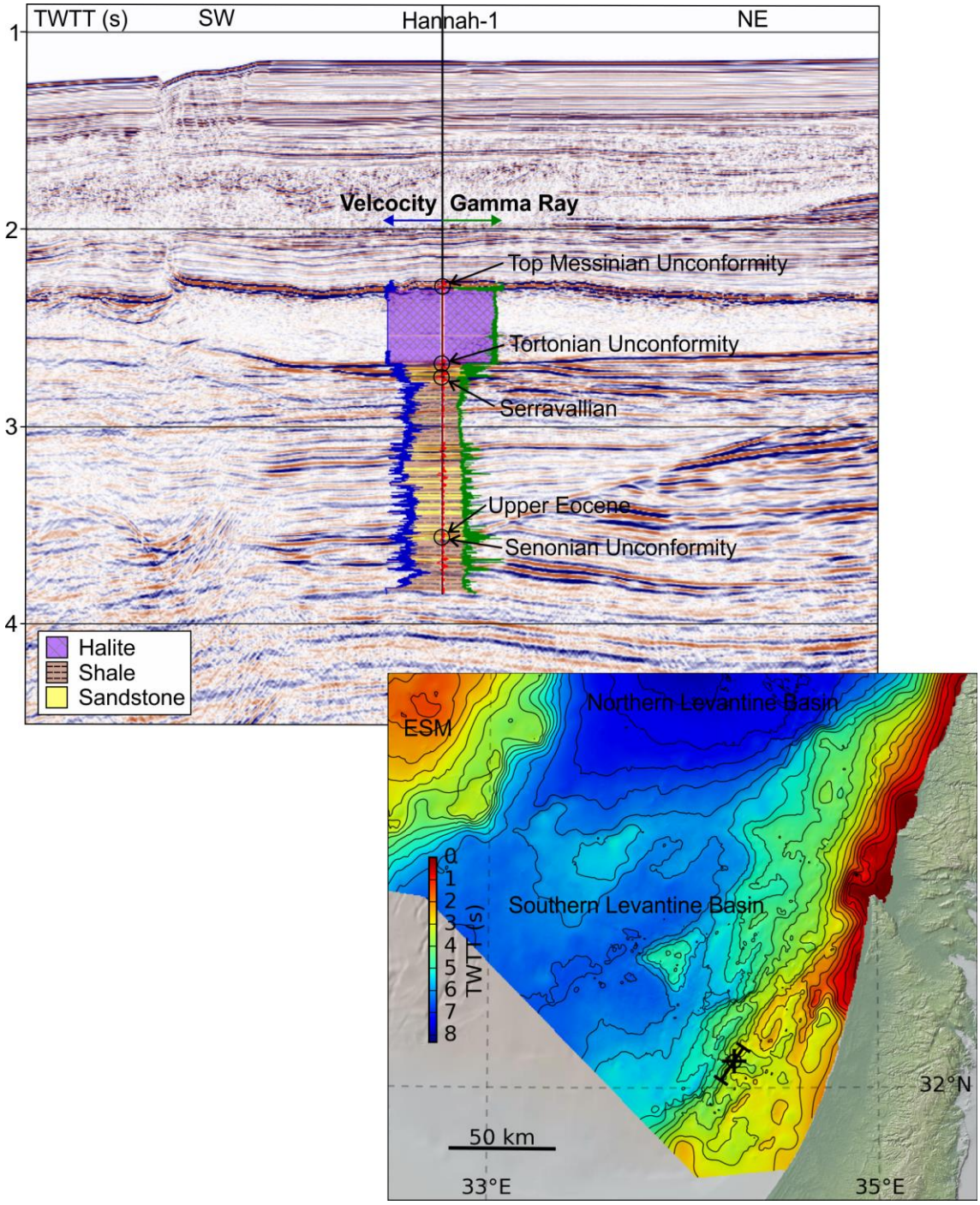

Figure 3.9-Logs and crossing seismic line of the Hannah-1 well offshore Israel, and map showing the location of the well in relation to the flank of the basin as defined by the Senonian Unconformity horizon. Well tops are from Gardosh et al. 2008b. See Figure 3.14 for correlation of Hannah-1 with the deep basin. The global relief (Ryan et al., 2009) vertical scale on the minimap is shown on Figure 1.1 and the supplementary figure.

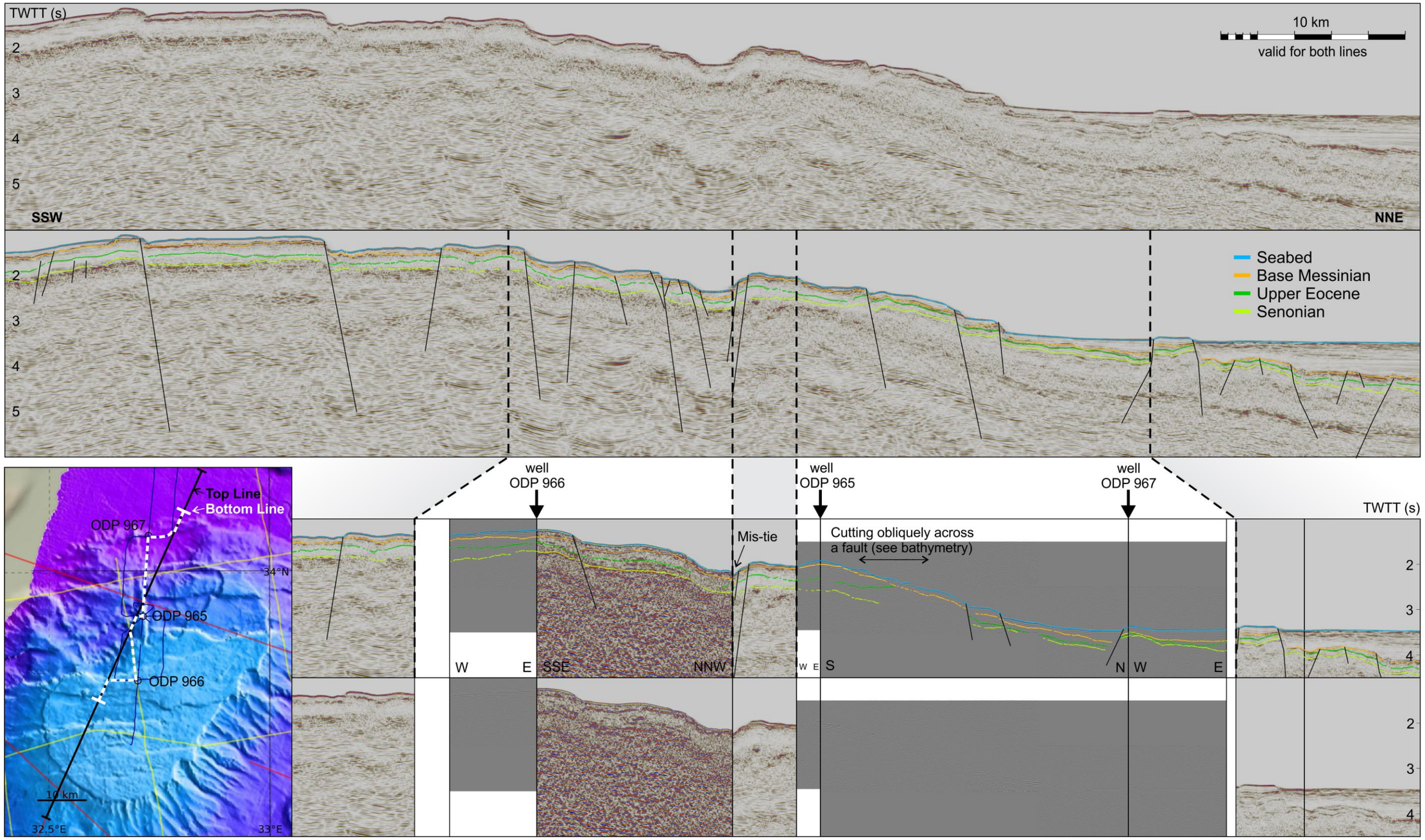

Figure 3.10-SSW-NNE striking seismic line near to the ODP wells at the ESM resolving clear reflectors to depth, and composite line including 90's vintage ODP seismic data correlating the proximal ODP wells to the SSW-NNE line. The blue bathymetry inset is from Ehrhardt et al. (2011).

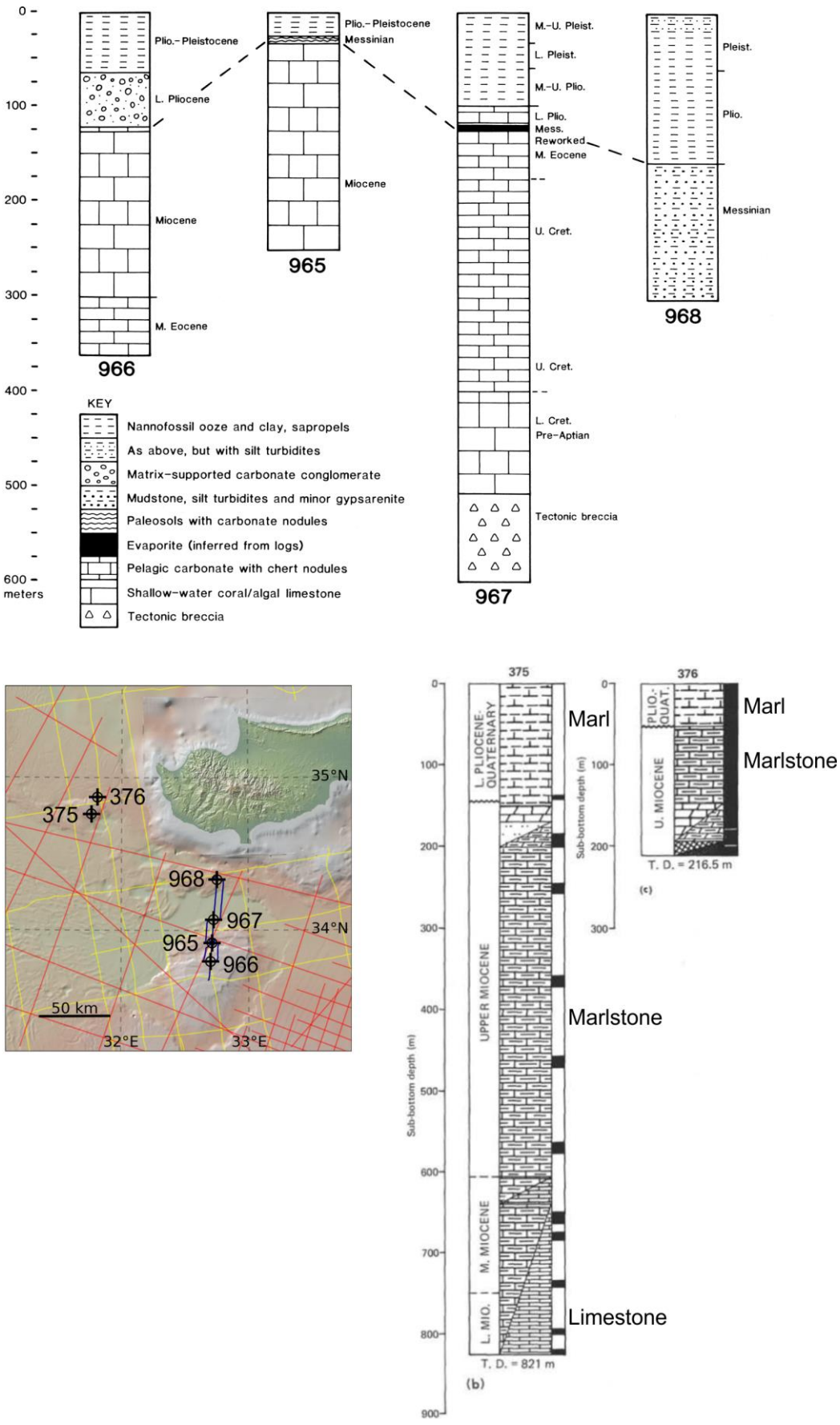

Figure 3.11-ODP (965-968) and DSDP (375, 376) lithological logs (Robertson, 1998c; Shipboard Scientific Party, 1978). The global relief (Ryan et al., 2009) vertical scale on the minimap is shown on Figure 1.1 and the supplementary figure.

Some offshore Israel well tops and images of well logs have been published (Table 5). These wells are drilled on the Southern Levantine basin margins and lack constraints in time. Wells that pierce sediments down to Miocene in age exist above gas fields (Figure 1.1) in the centre of the basin but are not available to this study (Gardosh, 2013). Thus, the lack of alternatives meant that horizons had to be traced up to 350 km from the Hannah-1 well to other areas of the EMR.

Table 5-Details of well log data documented in publication figures in the EMR. Note that none of the wells listed here penetrate the deep sediments in the basin.

Well	**Depth (m)**	**Source**	**Location** (see Figure 3.1)	**Content**
Latakia 2	3939	Bowman (2011)	onshore Syria (no survey intersects with data available to this study)	Lithological logs
Latakia 1	4237			
Fidio 1	4112			
Yam West 1	5250	Gardosh et al. (2008b)	offshore Israel (intersecting Israel 2D data).	Formation well tops, GR, acoustic and/or resistivity without scales
Yam-2	5370			
Ashqelon-2	4076			
Talme Yafe-4	4204			
Helez Deep-1A	6093			
Gevim-1	4620			
Yam Yafo-1	5787			
Delta-1A	4423			
Asher Atlit Deep-1	6531			
Foxtrot-1	2153			
Qishon Yam-1	1800			
Asher Yam-1	2020			
Terbol-1	2676	Hawie et al. (2013)	onshore Lebanon (no survey intersects with data available to this study)	Lithological logs
Adloun-1	2080			

3.4 Seismic Stratigraphy

The main horizons picked in this study are consistent with those picked in published works that had access to well data offshore Israel (Gardosh et al., 2008b; Gvirtzman and Steinberg, 2012; Steinberg et al., 2011), and publications that extend these horizons to the Northern Levantine Basin (Hawie et al., 2013), offshore Syria (Bowman, 2011) and Herodotus Basin (Skiple et al., 2012). These references also contain detailed written descriptions of the character of selected seismic facies in the relevant area.

The regional coverage of the seismic data available to this study means that some (and others sometimes locally) of the interpreted surfaces delineate between reflector sequences as opposed to specific reflectors. In conjunction with the lack of well data, this means the terminology used for the interpreted horizons would be more accurately prefixed with ‘near’ or ‘intra’. Even the more confidently resolved reflectors are subject to this; for example field data onshore Cyprus reveal that the base of the MSC is not marked by the onset of evaporite deposition, but exists in a gypsum-free clastic carbonate unit (Manzi et al., 2014). However, given the regional scope of the

study and the imprecise timing constraint of the tectonic events investigated these prefixes are not used.

Figure 3.12 shows surfaces of key seismic horizons across the EMR and the isochore maps in time that have been generated for the interval between these surfaces. The key horizons are those that may be traced across the majority of the seismic available to this study. The wide range of tectonic regimes that are covered by this study means that the character of a given seismic interval changes. Consequently, examples of typical seismic sequences are shown in the pertinent area of each surface shown in Figure 3.12A. The depth of each of the well logs corresponds to typical penetration depths.

Where halokinesis of the MSC salt has mobilised the overlying sediments it degrades the continuity and amplitude of reflectors on the seismic image below (Section 3.2.5). Where significant supra-salt mobilisation has occurred, such as in zones of diapirism or at the upslope extensional domain of the supra-salt horizons (see section 2.5.5 for details of these domains) the underlying seismic image can be degraded to the point where reflectors cannot be traced. This is the cause of much of the uncertainty in the age of the reflectors where they have been traced from the interior of the basin. Consequently, not all the horizons could be traced over all the data, as shown in Figure 3.12. Note that many of the interpretations become more speculative around the terrestrial margins and west of the ESM.

Table 6-Table showing approximate confidence values for the horizons and areas shown in Figure 3.12A. confidence values are given out of 10, with 10 being the highest. The number(s) before the dash indicates confidence in the picked wavelet, the number(s) after the dash indicates confidence in the picked interval. A slash indicates bimodal average confidence values, typically where diapirism is present. No numbers indicates the horizon was not picked in that location.

	Top MSC Unconformity	Base MSC Evaporites	Base Middle Miocene	Base Miocene	Upper Eocene Unconformity	Senonian Unconformity
S. Levantine Basin	5-9	8-9	4-7	6-8	4-5	4-8
N. Levantine Basin	6-9	8-9	4-7	6-8	4-5	4-8
Israeli Margin	7-10	-	7-8	-	5-6	6-8
Saida Tyr Plateau	6-9	7-9	3-6	6-8	3-4	5-7
ESM	6-8	-	-	-	5-6	3-6
Tartus Basin	6-9	7-9	2-4	5-6	2-4	5-7
Latakia Basin	6-8	6-8	-	-	-	2-3
Herodotus Basin	4/2-8/2	3/1-6/2	-	-	-	1-2
Antalya Basin	5-8	5-7	-	-	-	2-3

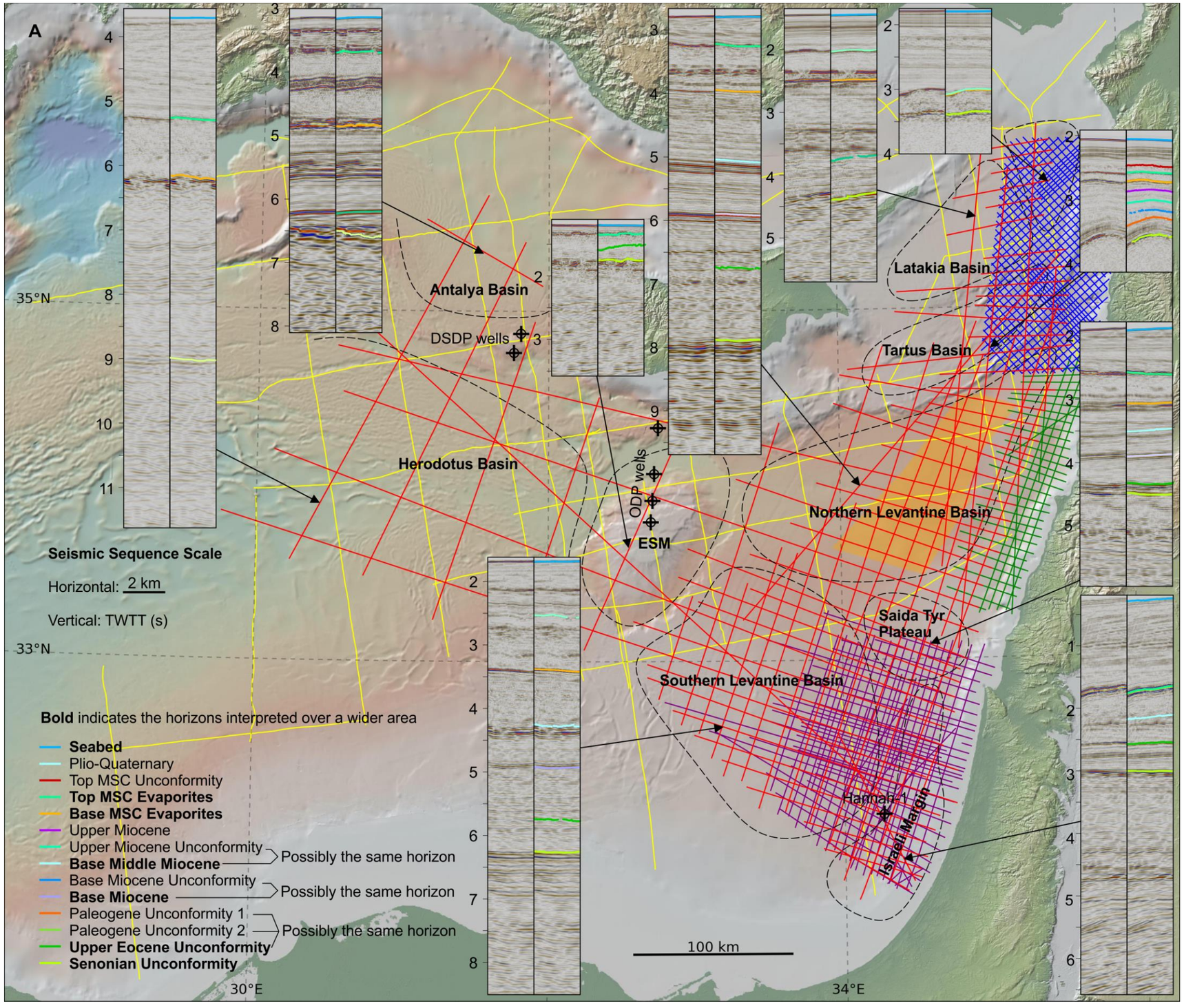

Figure 3.12-A) Map showing example seismic sequences in the EMR; B-M) maps of the surfaces in time of key seismic horizons in the EMR, and isochore maps in time of the intervals between these horizons. The global relief (Ryan et al., 2009) vertical is shown on Figure 1.1 and the supplementary figure.

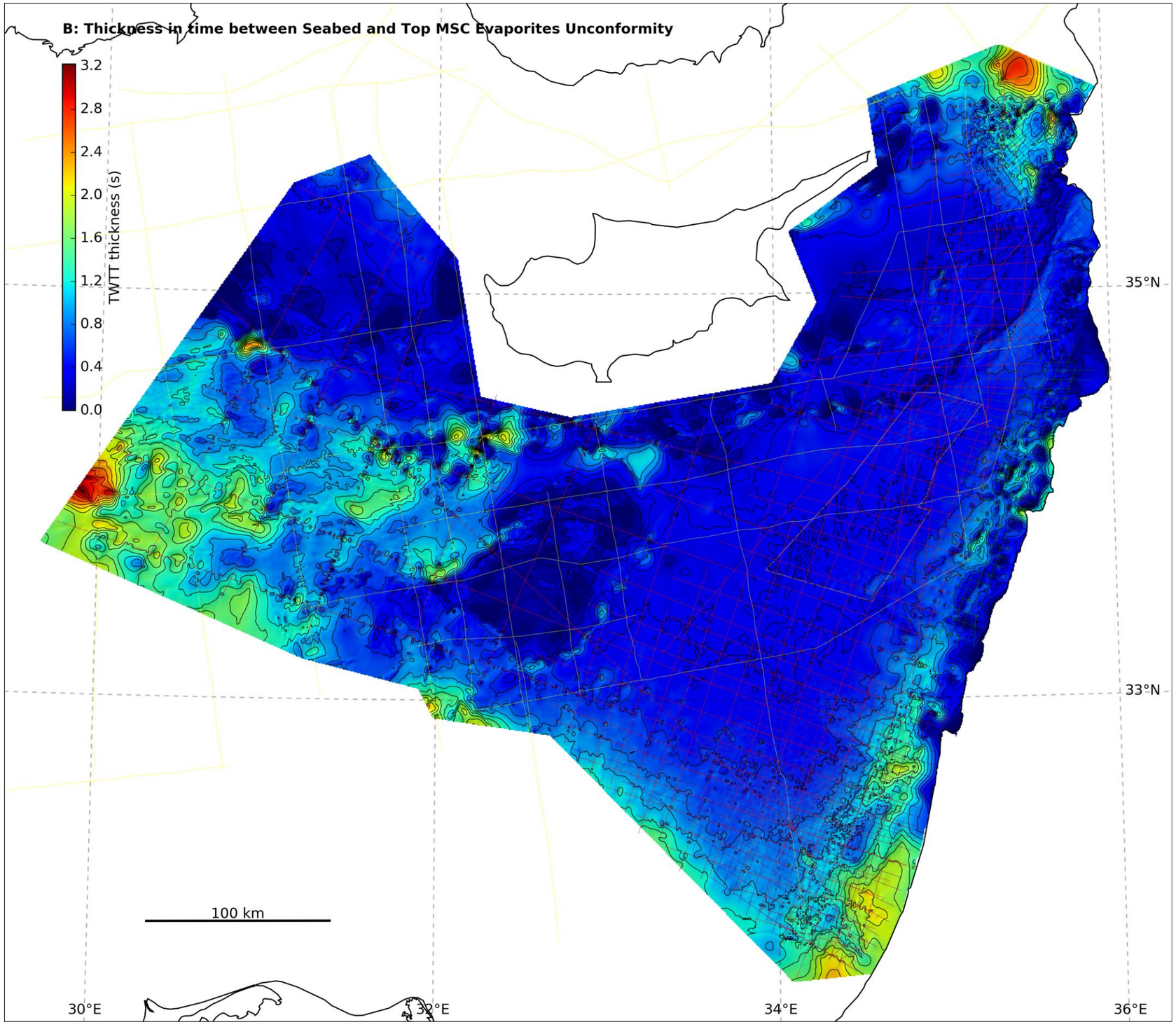
B: Thickness in time between Seabed and Top MSC Evaporites Unconformity
TWTT thickness (s)
3.2
2.8
2.4
2.0
1.6
1.2
0.8
0.4
0.0
35°N
33°N
100 km
30°E
32°E
34°E
36°E

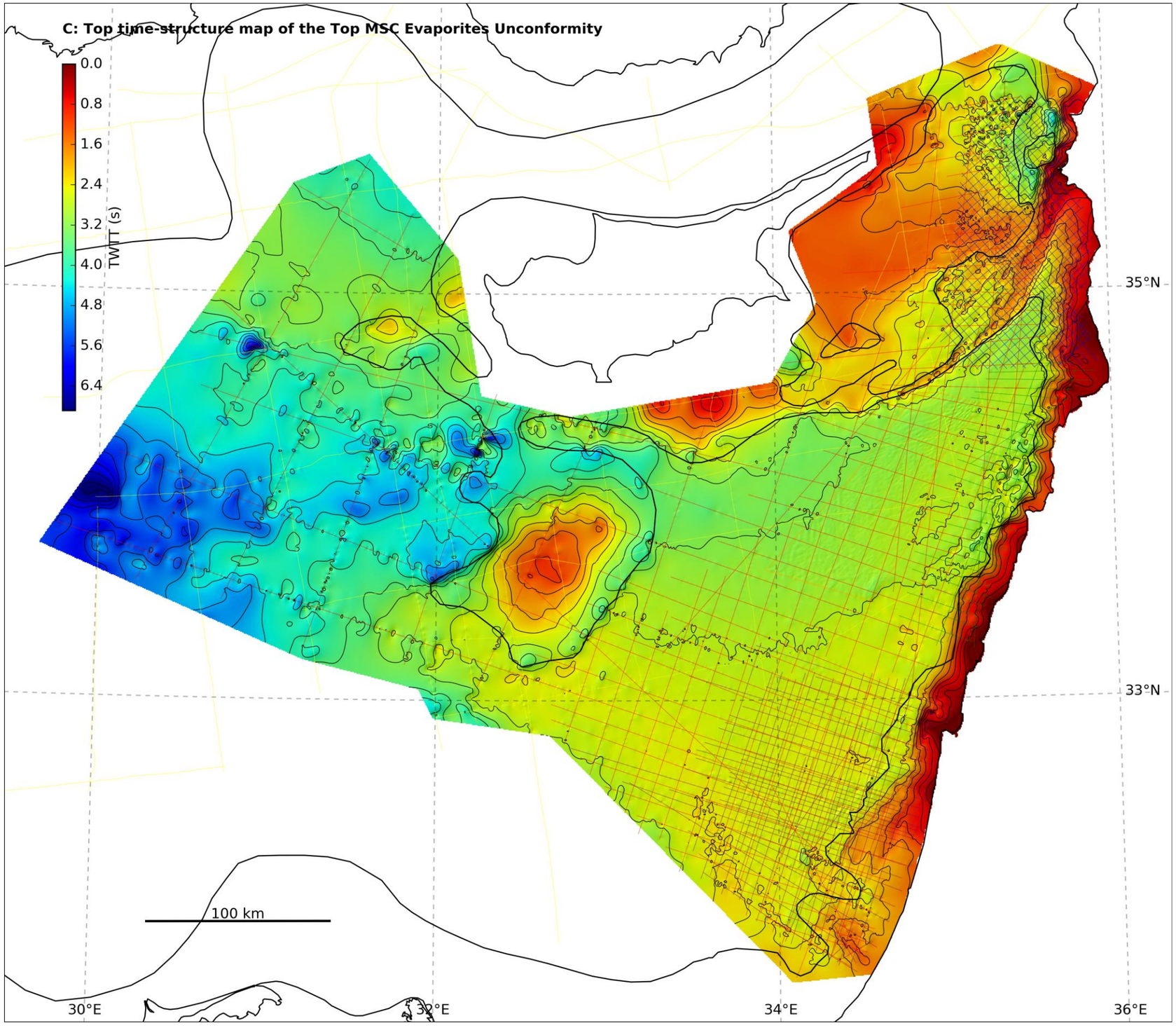
C: Top time-structure map of the Top MSC Evaporites Unconformity
0.0
0.8
1.6
2.4
3.2
4.0
4.8
5.6
6.4
TWTT (s)
35°N
33°N
100 km
30°E
32°E
34°E
36°E

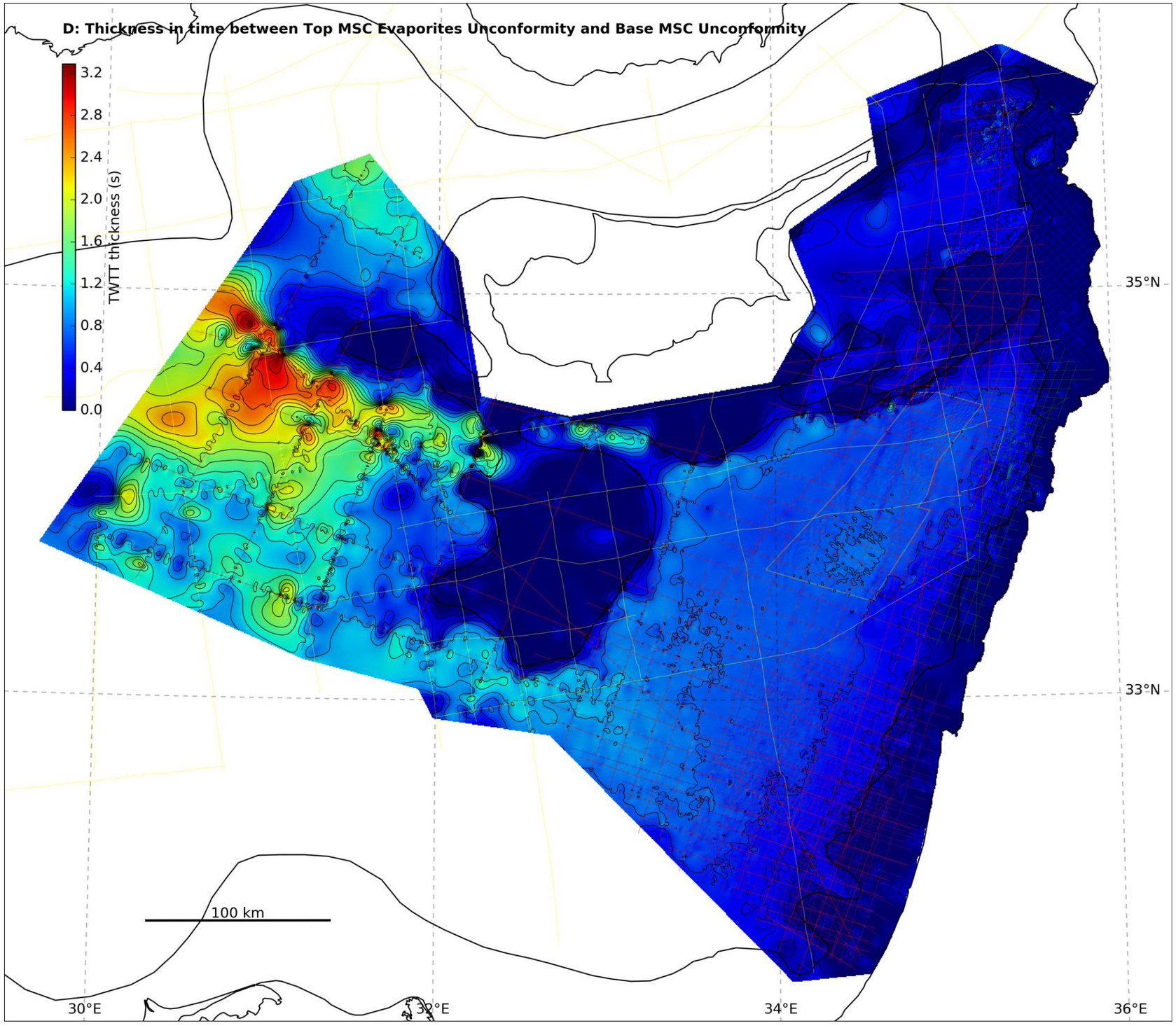
D: Thickness in time between Top MSC Evaporites Unconformity and Base MSC Unconformity
TWTT thickness (s)
3.2
2.8
2.4
2.0
1.6
1.2
0.8
0.4
0.0
35°N
33°N
100 km
30°E
32°E
34°E
36°E

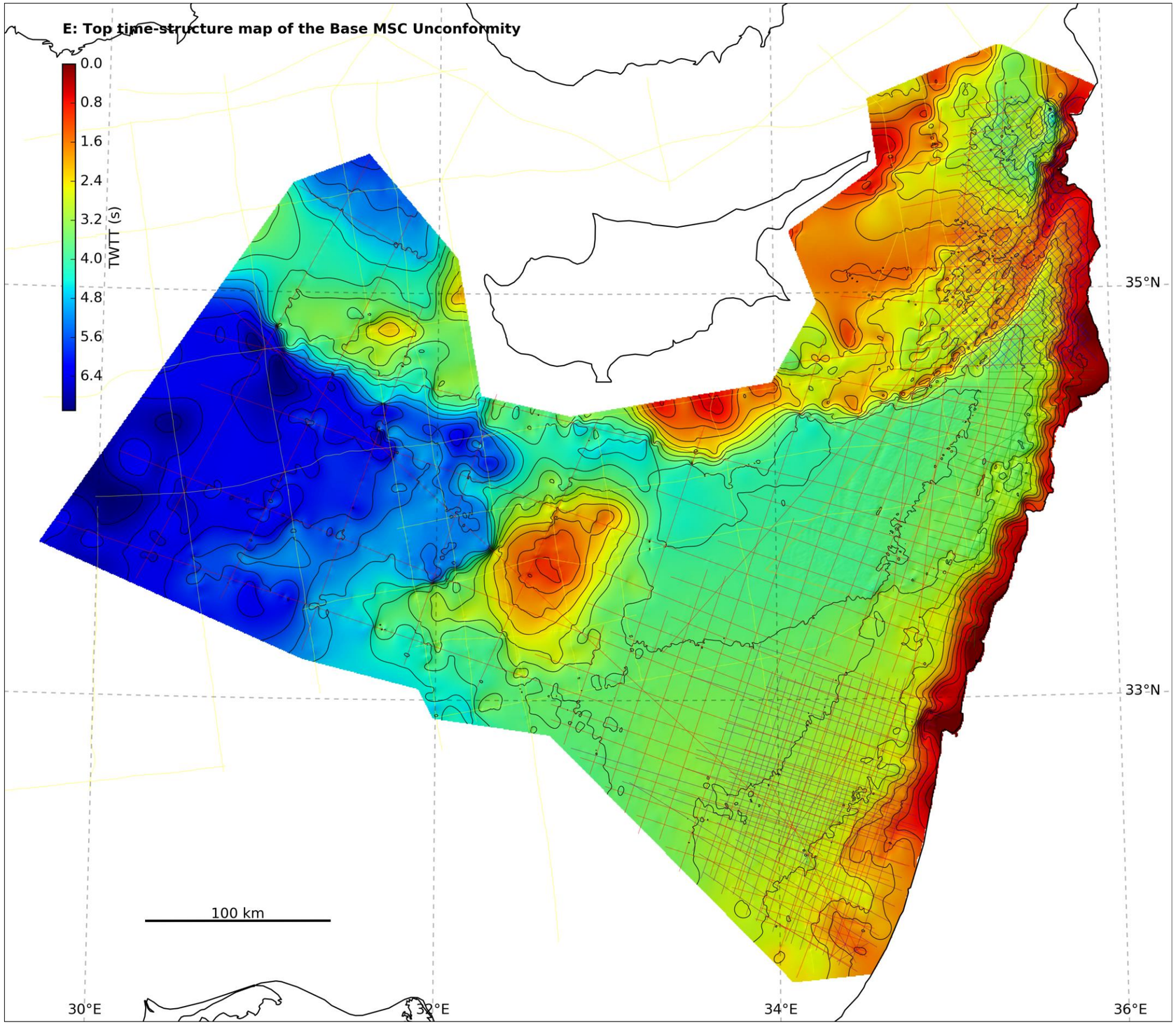
E: Top time-structure map of the Base MSC Unconformity
0.0
0.8
1.6
2.4
3.2
4.0
4.8
5.6
6.4
TWTT (s)
35°N
33°N
100 km
30°E
32°E
34°E
36°E

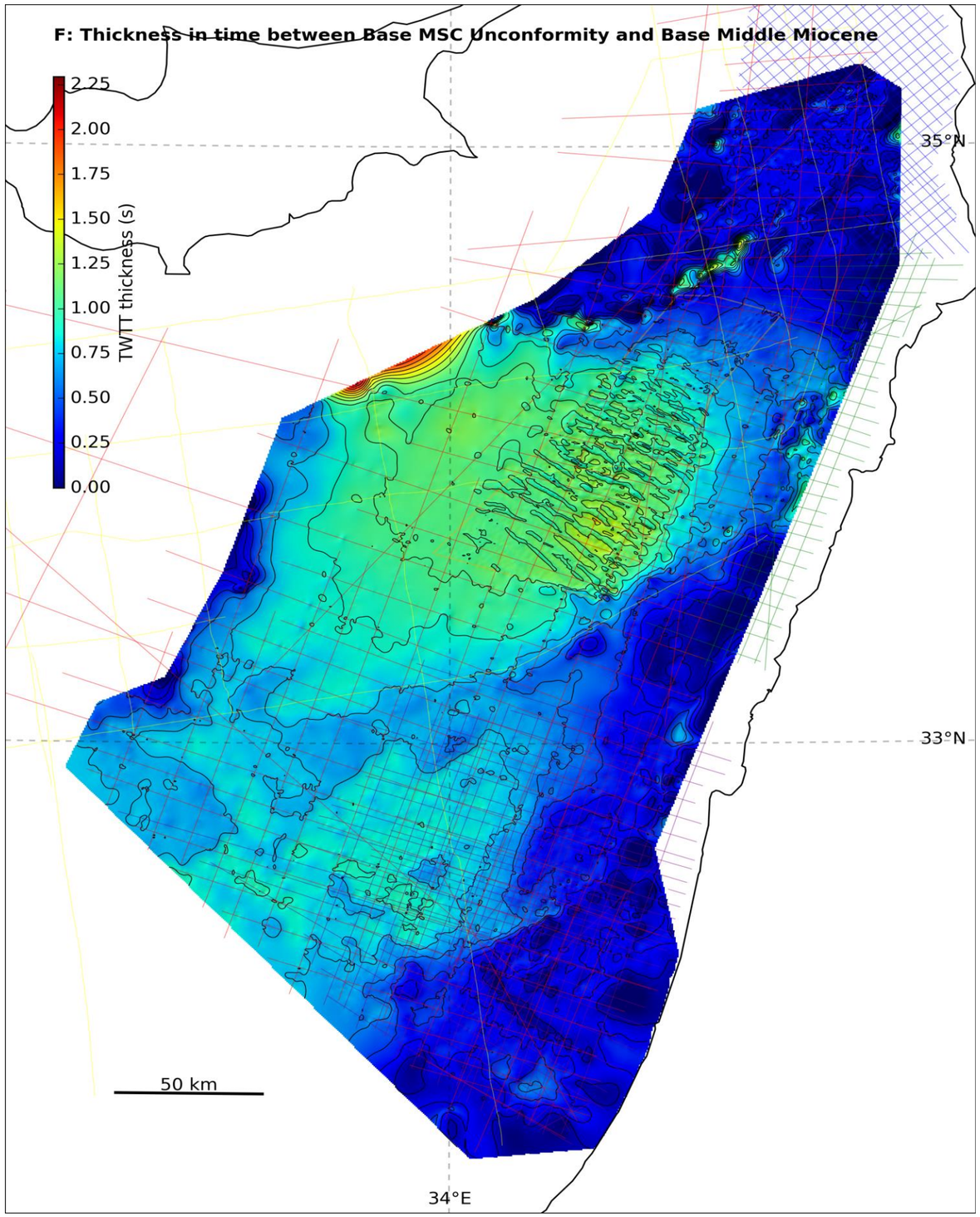
F: Thickness in time between Base MSC Unconformity and Base Middle Miocene
TWTT thickness (s)
2.25
2.00
1.75
1.50
1.25
1.00
0.75
0.50
0.25
0.00
35°N
33°N
34°E
50 km

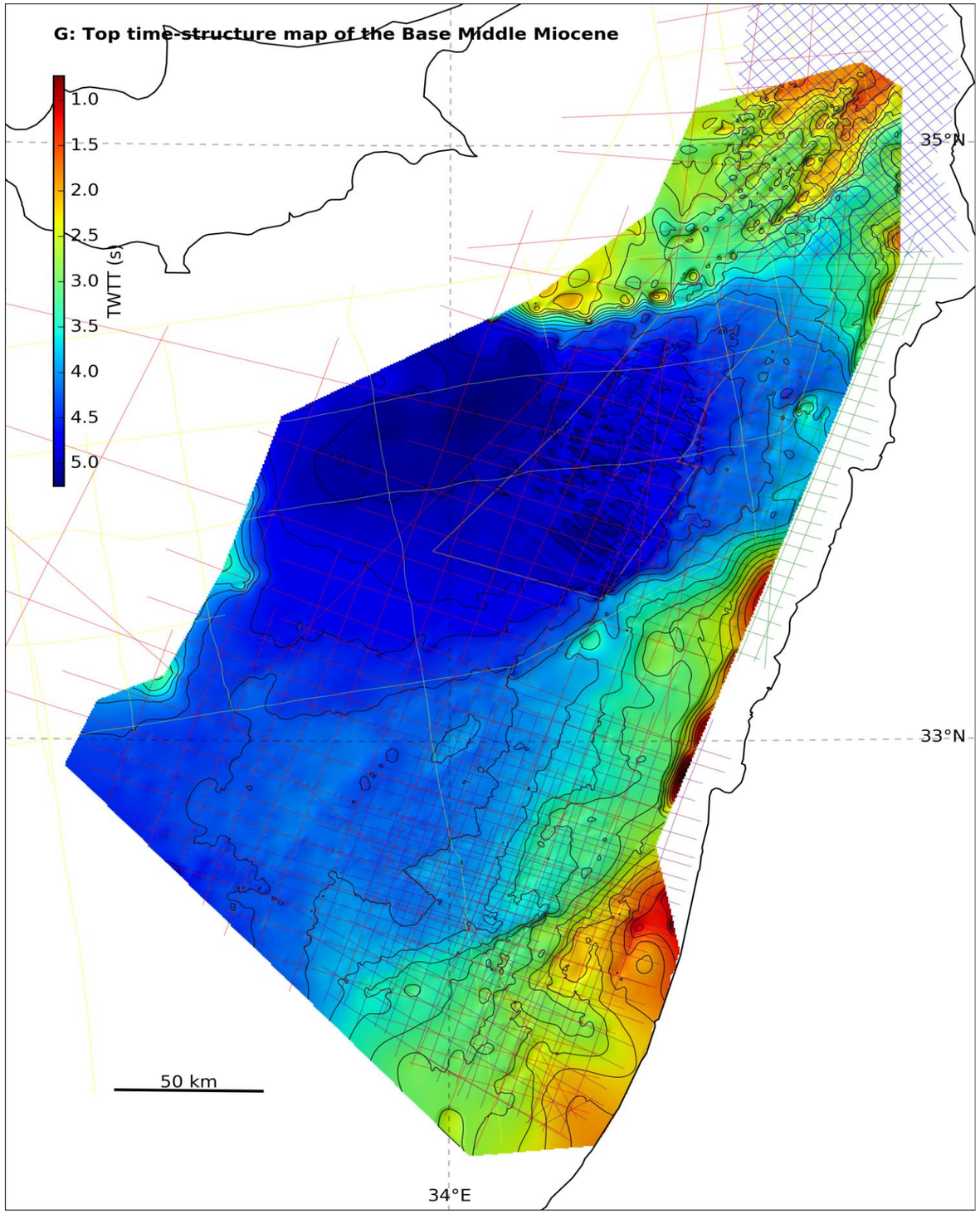
G: Top time-structure map of the Base Middle Miocene
TWTT (s)
1.0
1.5
2.0
2.5
3.0
3.5
4.0
4.5
5.0
35°N
33°N
34°E
50 km

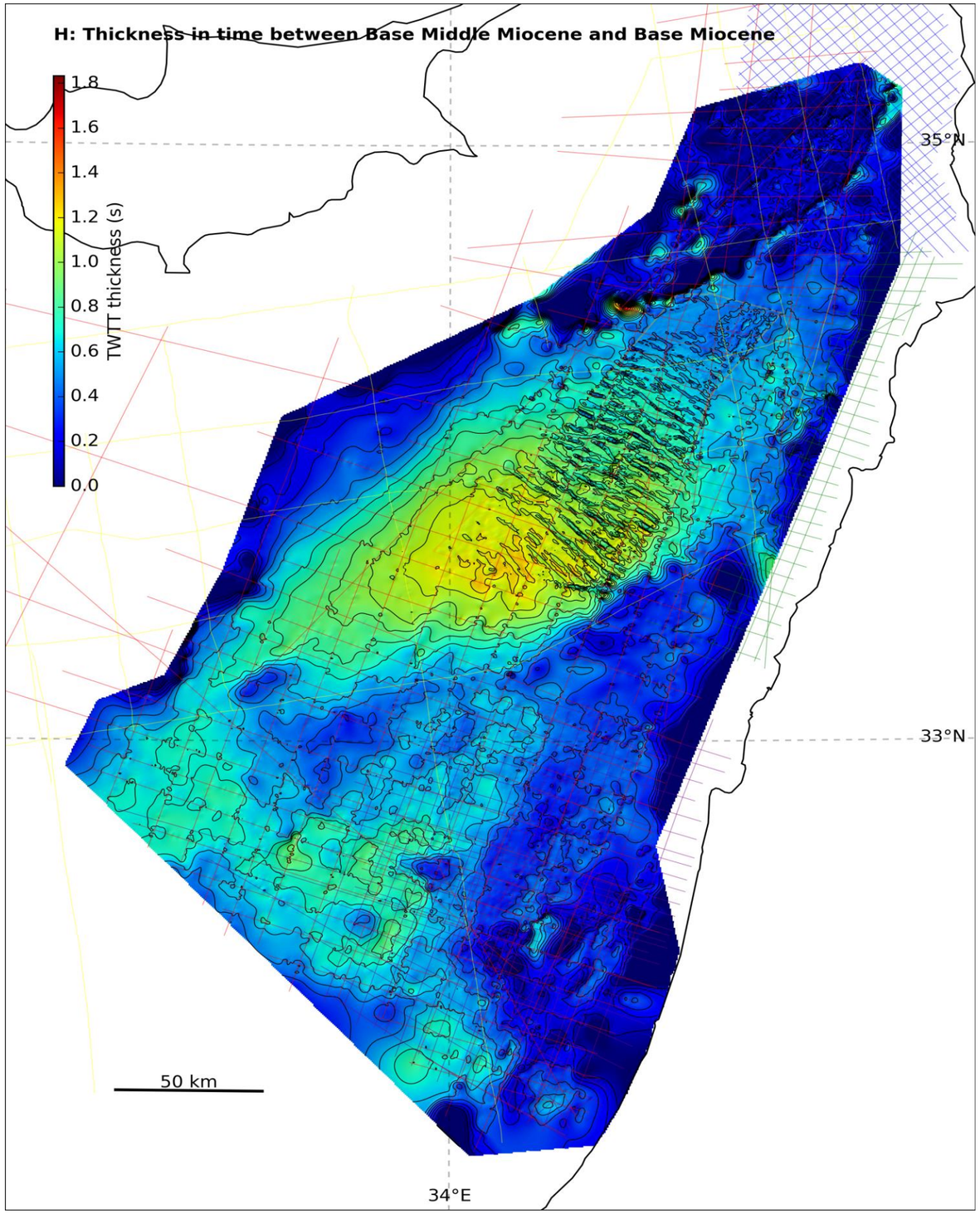
H: Thickness in time between Base Middle Miocene and Base Miocene
TWTT thickness (s)
1.8
1.6
1.4
1.2
1.0
0.8
0.6
0.4
0.2
0.0
35°N
33°N
34°E
50 km

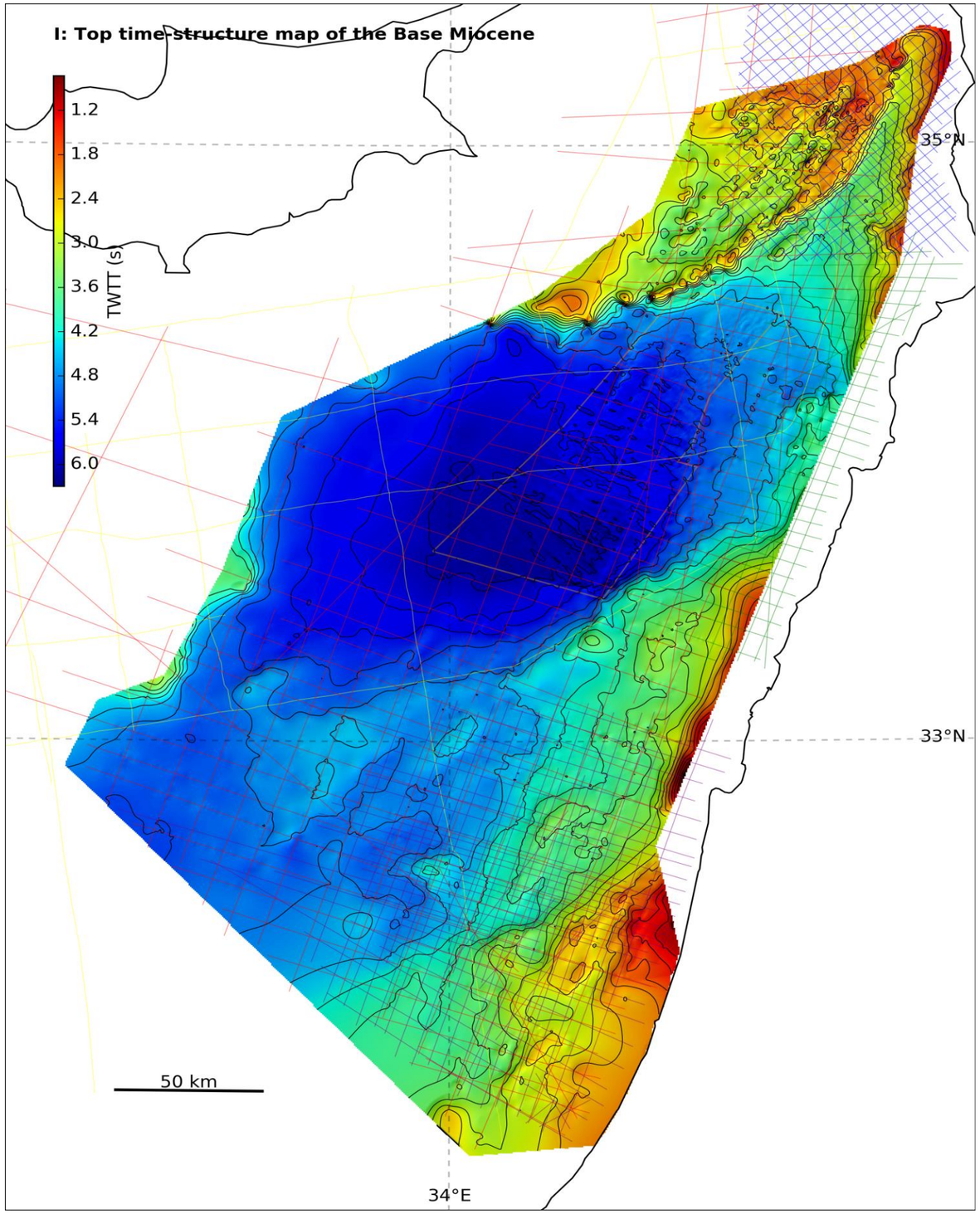
I: Top time-structure map of the Base Miocene
TWTT (s)
1.2
1.8
2.4
3.0
3.6
4.2
4.8
5.4
6.0
35°N
33°N
34°E
50 km

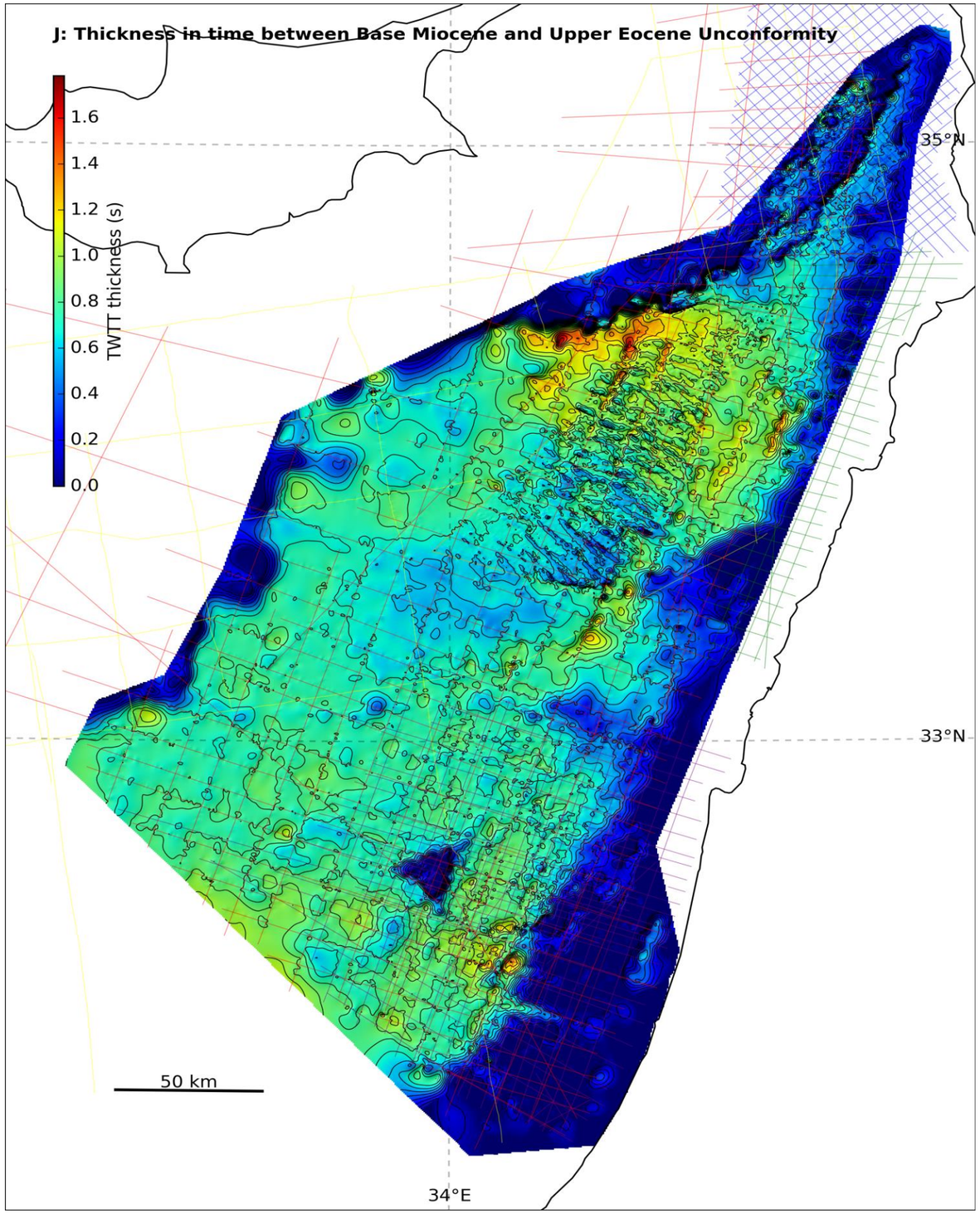
J: Thickness in time between Base Miocene and Upper Eocene Unconformity
TWTT thickness (s)
1.6
1.4
1.2
1.0
0.8
0.6
0.4
0.2
0.0
35°N
33°N
34°E
50 km

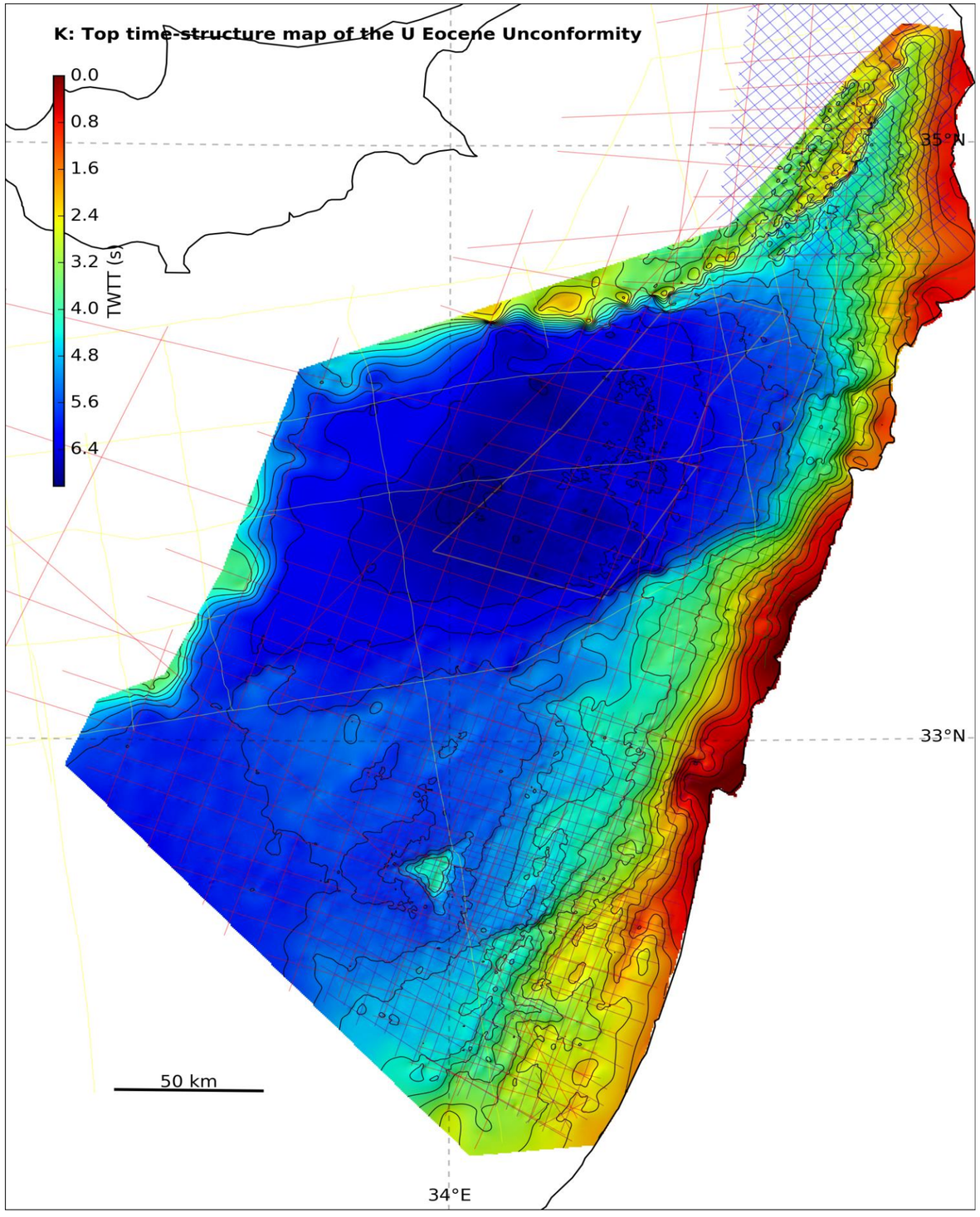
K: Top time-structure map of the U Eocene Unconformity
0.0
0.8
1.6
2.4
3.2
4.0
4.8
5.6
6.4
TWTT (s
35°N
33°N
50 km
34°E

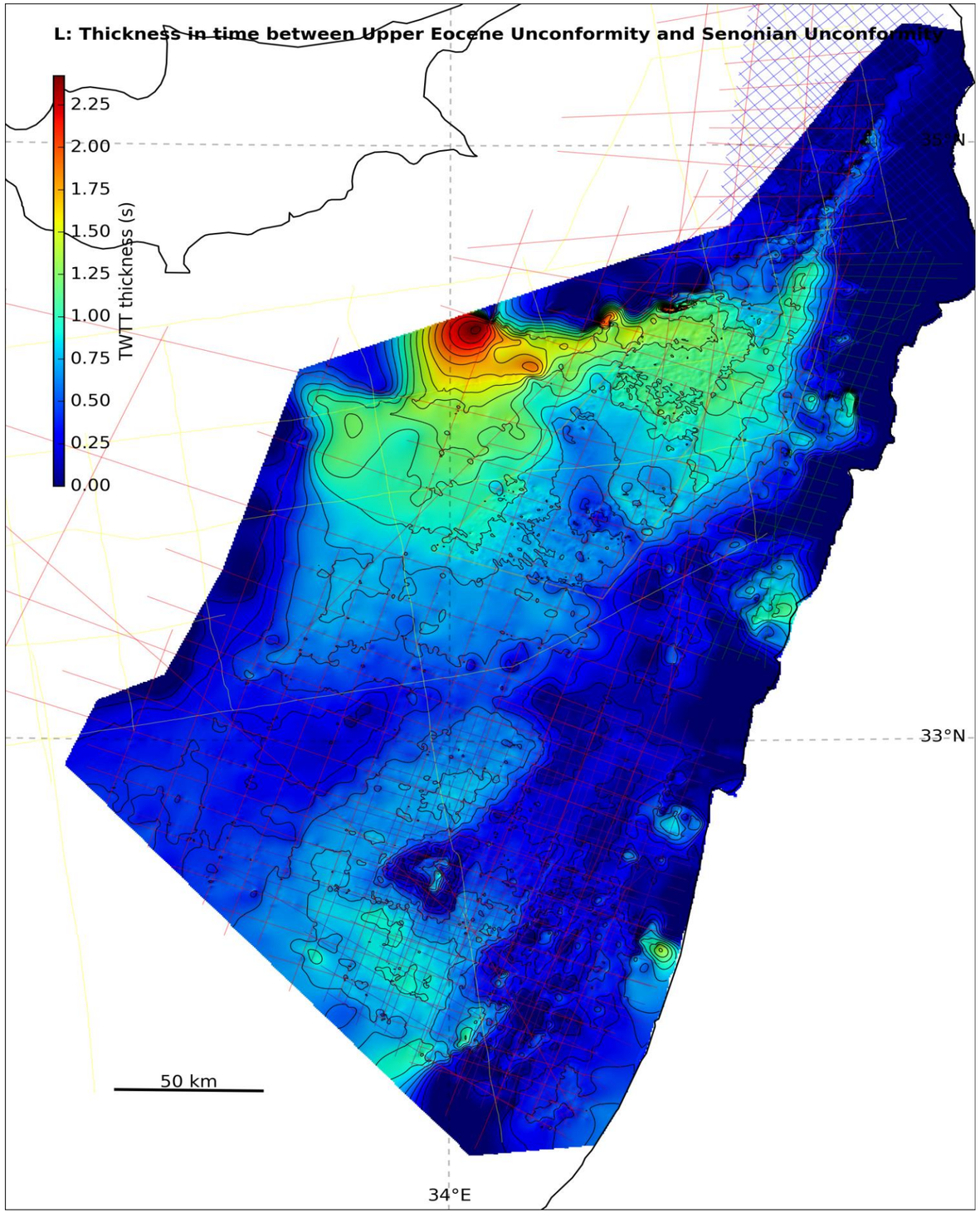
L: Thickness in time between Upper Eocene Unconformity and Senonian Unconformity
TWTT thickness (s)
2.25
2.00
1.75
1.50
1.25
1.00
0.75
0.50
0.25
0.00
35°N
33°N
34°E
50 km

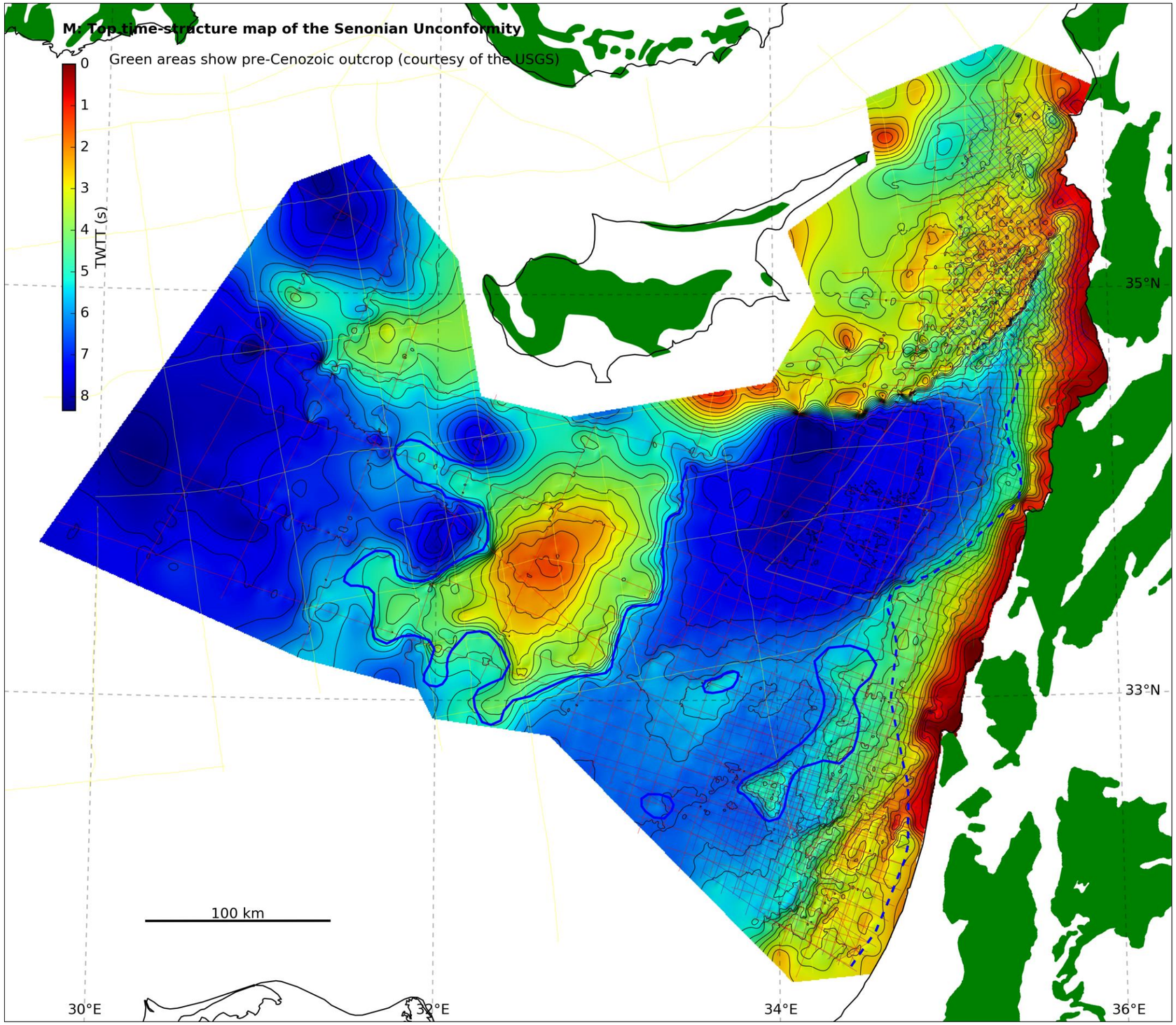
M: Top time-structure map of the Senonian Unconformity
Green areas show pre-Cenozoic outcrop (courtesy of the USGS)
TWTT (s)
0
1
2
3
4
5
6
7
8
35°N
33°N
100 km
30°E
32°E
34°E
36°E

Figure 3.13 shows the speculative chrono-stratigraphic column of the offshore EMR based on:

- Horizon surface interpretations
- Well logs
- Seismic character
- Published speculative stratigraphic columns of the Northern Levant Basin (Skiple et al. 2011 and Ghalayini 2014)
- Regional knowledge of the areas tectonic history.

Many of these constraints are discussed or described later in this document; a brief description of the constraints for each location numbered on Figure 3.13 is listed with any pertinent references in Table 7.

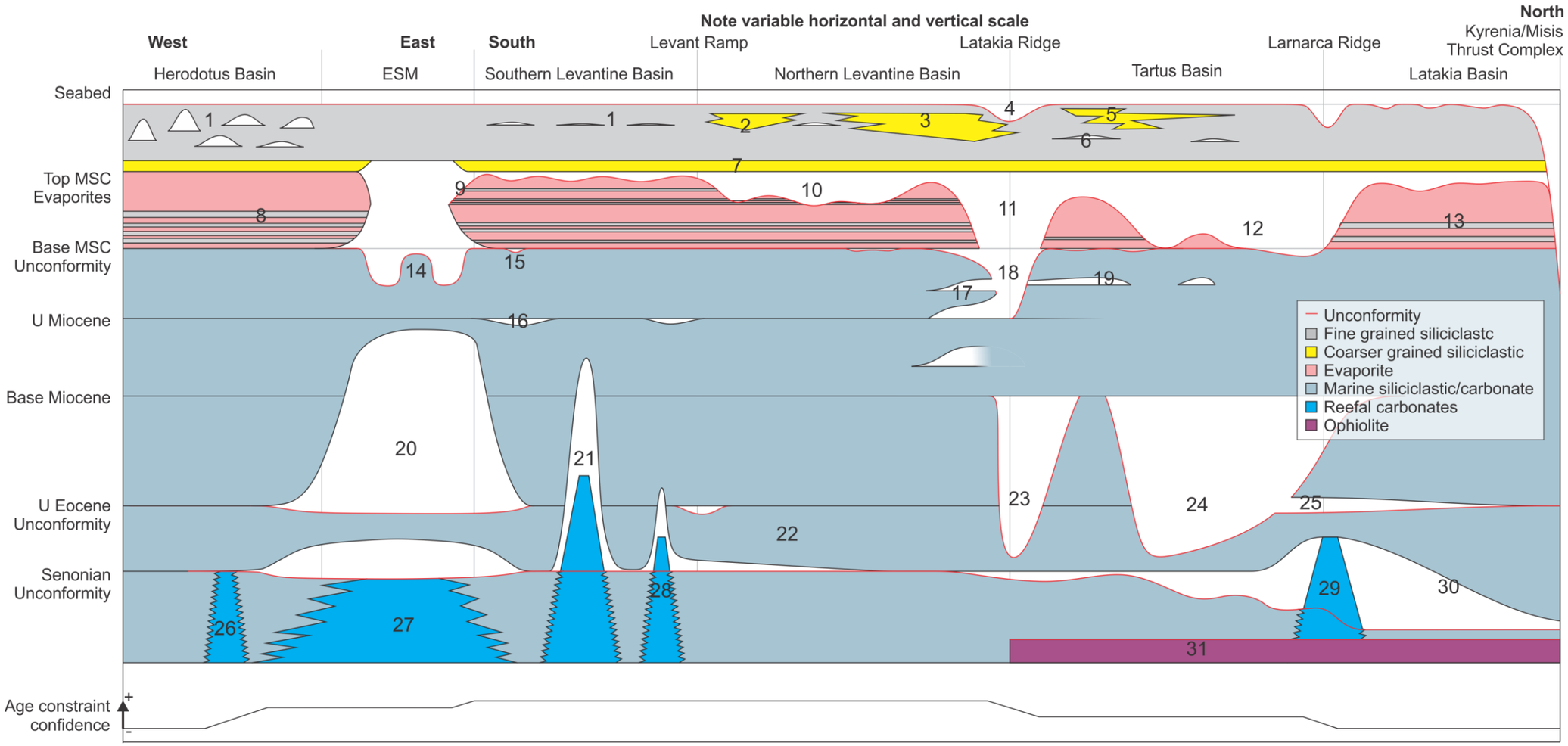

Figure 3.13-Chrono-stratigraphic diagram of the offshore EMR, broadly following the trends of the regional lines (Figure 3.14), indicating the relationships between the intervals between the different seismic picks. The numbers refer to the entry in Table 7, detailing a brief description and source for the area of the figure. Note that the ages of features not aligned to a named temporal boundary are speculative.

Table 7-List of references constraining the numbered points on Figure 3.13.

#	Description	Example Ref.
1	MSC evaporite salt tectonic related onlap and non-deposition	Section 3.7.3
2	Channel sands in the Levantine Basin	Section 3.6.3
3	Erosional debris from the Latakia Ridge?	Section 3.6.3
4	Active erosion at the Latakia Ridge	Figure 5.27
5	Syncline sands in the Tartus Basin	Figure 5.18
6	Onlap against Cyprus Arc folds in the Plio-Quaternary sequence	Figure 5.18
7	Post MSC transitional sediments	Section 3.7.2
8	Lower MSC megasequence clastics	Section 3.7.1
9	MSC evaporite onlap at the ESM	Section 7.1.2
10	Erosion of the top of the MSC sequence	Section 3.7.1
11	Non MSC evaporite deposition at the Latakia Ridge	Figure 3.14A
12	Non MSC evaporite deposition at the Larnaca Ridge	Figure 3.14A
13	Lower MSC megasequence clastics	Section 3.7.1
14	ESM platform erosion during the MSC	Section 3.6.6
15	Channel erosion at the start of the MSC	Section 3.6.5
16	Onlap onto Syrian Arc II structures	Figure 3.14
17	Progressive onlap onto the Latakia Ridge	Figure 5.13A
18	Erosion at the Latakia Ridge	Figure 5.27
19	Onlap onto folds of the Cyprus Arc	Figure 5.19
20	Non-deposition during carbonate platform submergence	Section 3.6.6
21	Jonah High carbonate platform	Figure 3.14B
22	Erosion and onlap at the Levant Ramp	Section 3.6.4
23	Erosion at the Latakia Ridge	Figure 5.19
24	Significant erosion of the Cyprus Arc	Figure 5.19
25	Angular unconformity in the Latakia Basin	Section 5.5.3
26	Satellite carbonate highs around the ESM	Section 3.6.6
27	ESM carbonate platform	Section 3.6.6
28	Deeply buried carbonate platforms in the Southern Levantine Basin.	Figure 4.13
29	Buried carbonate cap on the Larnaca Ridge	Section 5.5.3
30	Palaeoslope onlap in the Latakia Basin	Figure 5.23
31	Ophiolitic basement beneath Cyprus Arc	Section 5.6.7

There are innumerable faults and folds in the post-MSC sediments, especially in the Levantine and Herodotus Basins. Due to the large number of these faults and the time constraints of this study, these faults were only interpreted where pertinent to a specific element of this study, such as the recent deformation in the Cyprus Arc (Chapter 5) and the modes of deformation around the ESM (Chapter 7).

3.5 Regional Lines

Figure 3.14 shows regional seismic lines across the study area, selected to demonstrate typical examples of the lateral stratigraphic relationships between features. Descriptions of the labelled features are given in Section 3.6. A crossing of the Hannah-1 well is included in Figure 3.14 to

demonstrate how horizons may be correlated from this age constraint, the only good constraint for the vast majority of the seismic data available to this study.

The correlation of horizon ages from Hannah-1 to the Northern Levantine Basin is an important component of this study. The consistency of the seismic character of the Cenozoic sequence between the Southern Levantine Basin to the Northern Levantine Basin is therefore an important aspect of these regional lines that should be noted, as it results in a high confidence in the ages picked for reflectors in the Northern Levantine Basin. The consistent and characteristic seismic character of the MSC sequence should also be noted.

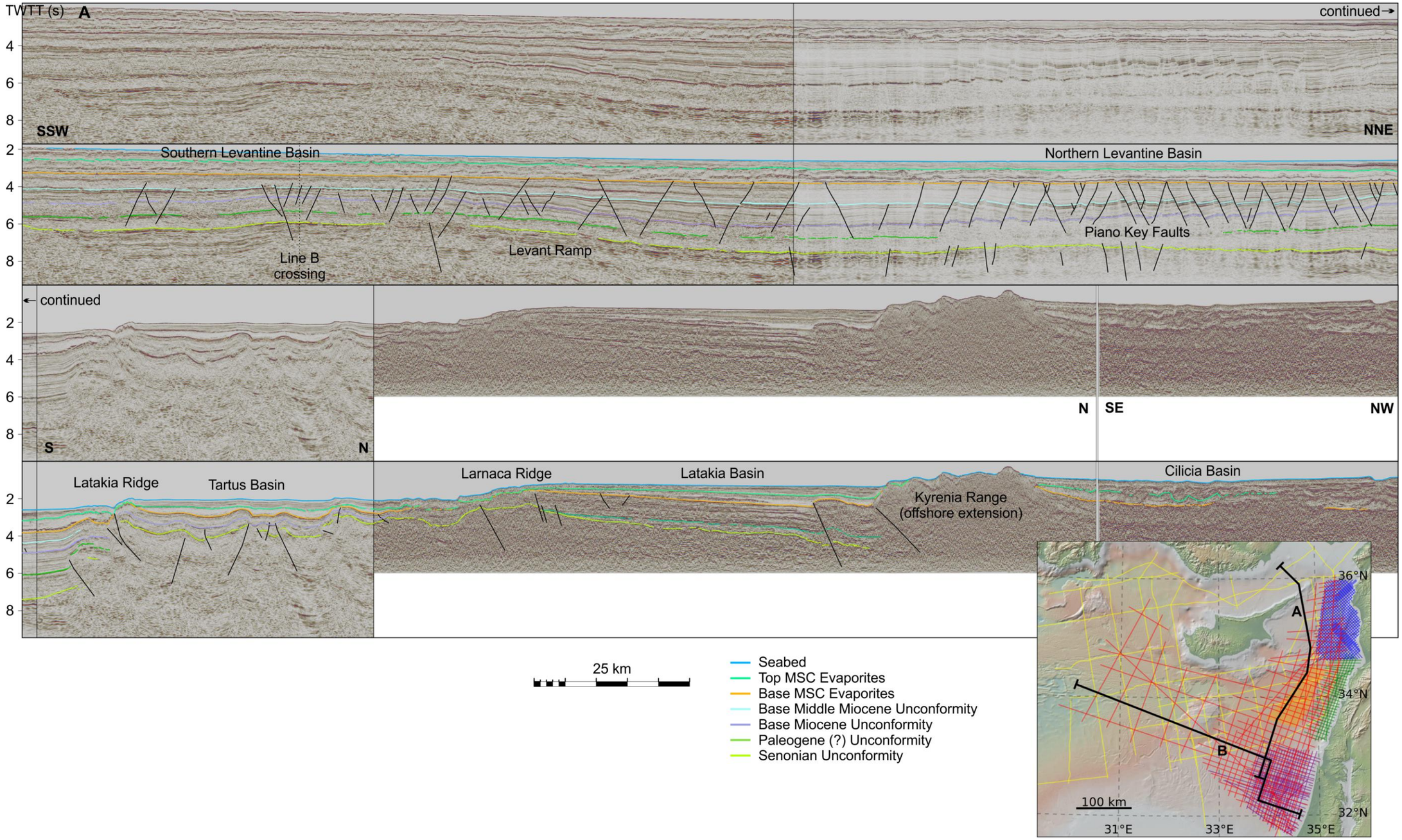

Figure 3.14-Regional seismic lines of the EMR; A) a NS line showing the Cilicia Basin, Cyprus Arc and Basins, the Levantine Basin; B) an EW line of the Herodotus Basin through to Southern Levantine Basin showing features including the Syrian Arc, Tamar, Leviathan and Aphrodite gas fields and southern flank of the ESM (the dashed black line is discussed in Section 4.5). The Hannah-1 well on line A was the primary dating constraint used on the horizons. The global relief (Ryan et al., 2009) vertical scale on the minimap is shown on Figure 1.1 and the supplementary figure.

TWTT (s) **B**

continued →

WNW ESE

Herodotus Basin

Eratosthenes Seamount (flank)

25 km

← continued

WNW ESE

NNE SSW

WNW ESE

Line A crossing

Southern Levantine Basin

Hannah-1 Well

Palmahim disturbance

Aphrodite Field

Leviathan Field

Tamar Field

Jonah High

Syrian Arc Folds

Spectrum seismic line EMED00-029 permits the tracing of seismic horizons from the Levantine Basin north across part of the Latakia ridge thrust system where the thrusting is distributed such that the overlying reflectors are not significantly offset (Figure 3.15). For the seismic data available to this study this is not unique for the shallow horizons, however it is the only line that permits confident tracing of the Senonian Unconformity across the Latakia Ridge. This is key as no wells have been drilled offshore Syria, and without this line the Senonian horizon on the Anatolian Plate side of the Latakia Ridge could instead be interpreted as Upper Eocene. There are wells in the Cilicia Basin offshore southern Turkey but they are not sufficiently proximal to the seismic data available to this study to provide correlation. In the Levantine Basin, the depth of clear imaging, the line density and the largely undeformed Cenozoic sediments of the basin mean this horizon correlation has high confidence unless otherwise discussed.

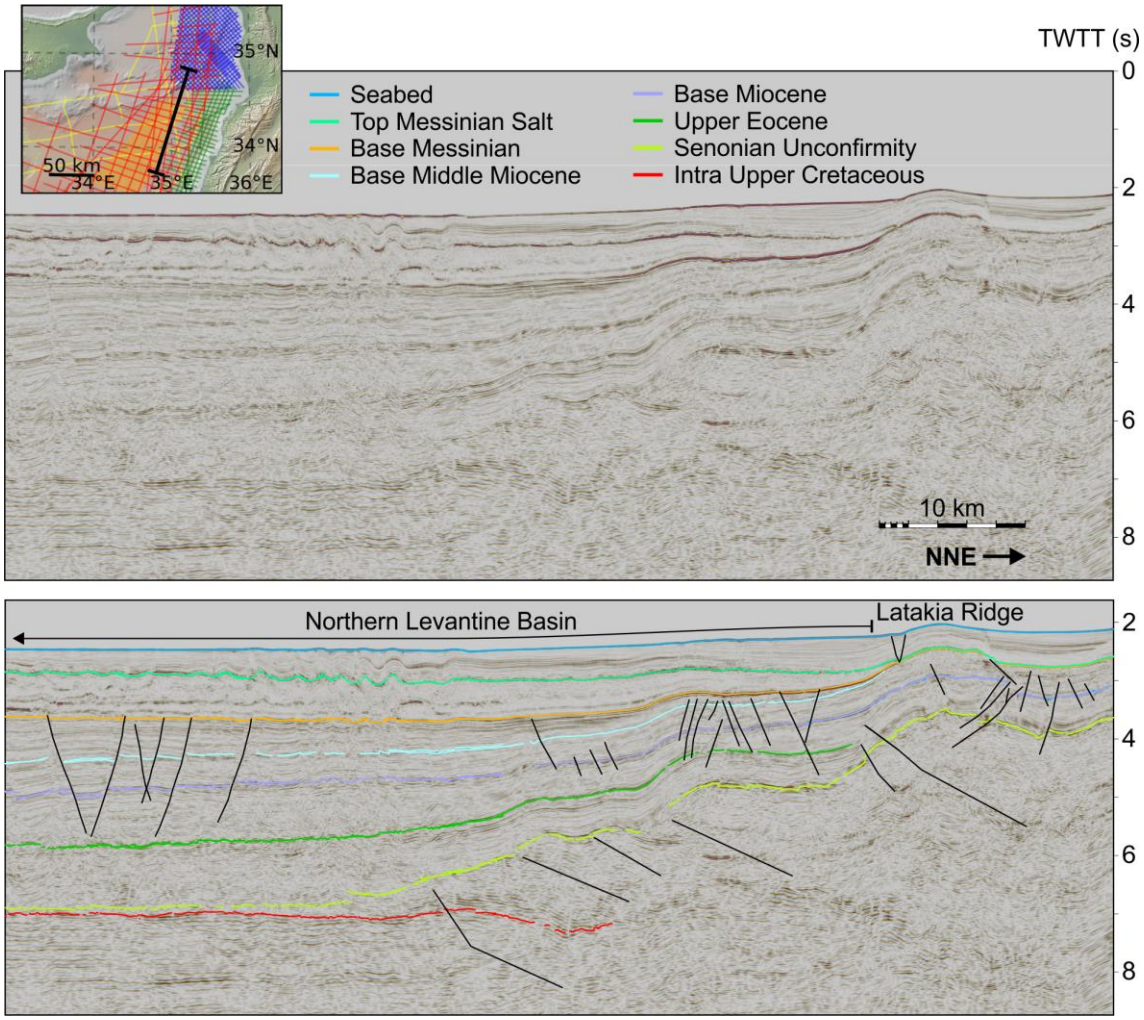

Figure 3.15-Seismic line EMED00-029 showing the tracing of horizons from the Levantine Basin across the Latakia Ridge. The global relief (Ryan et al., 2009) vertical scale on the minimap is shown on Figure 1.1 and the supplementary figure.

3.6 Area Interpretations

The regional coverage of the seismic data available to this study means that a variety of geological terrains and deformation episodes are imaged. This demands that much of the description of the seismic interpretation carried out for this study are divided spatially. Some aspects of some of the

areas are described in detail in later pertinent chapters. Consequently, these aspects are only briefly described here, with reference to their detailed description. A map of each described area is shown in Figure 3.16.

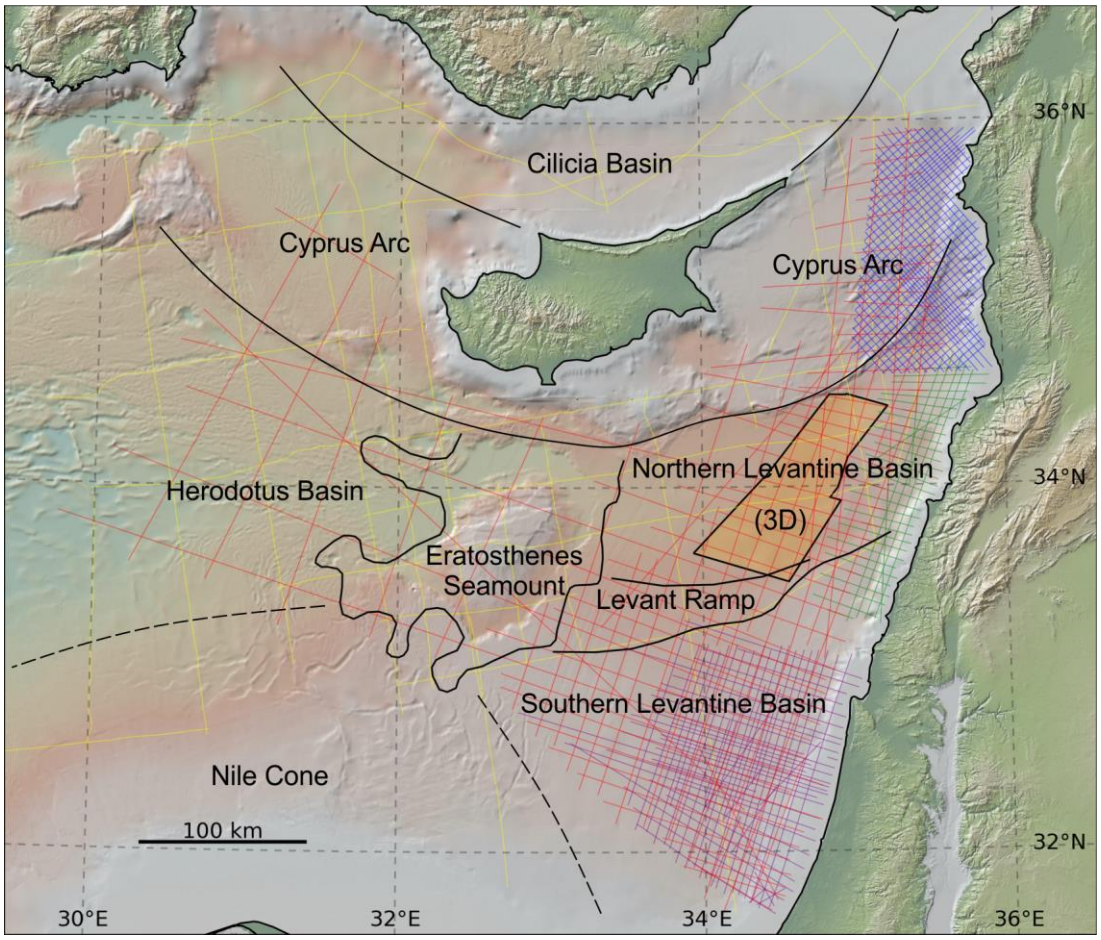

Figure 3.16-Map showing the different offshore areas described in this Section. Note that the outline of the ESM is the underlying drowned carbonate platform (see Section 3.6.6). The global relief (Ryan et al., 2009) vertical scale is shown on Figure 1.1 and the supplementary figure.

Few seismic lines, and only that of 1975 vintage, were available to this study over the Cilicia Basin and Nile Cone (Figure 3.14A). Studies of the Nile Cone (Section 2.3.7) allow it to be integrated in some aspects of this investigation. Few published studies investigate the deeper geology of the Cilicia Basin, and those that do use only shallow seismic data. Consequently, the Cilicia Basin is poorly understood geologically although evidence has been published suggesting it is a back-arc basin that formed in the Plio-Quaternary (Mart and Ryan, 2002), and a foredeep basin that formed in the Miocene (Aksu et al., 2005a). The data available to this study do not directly inform on this issue, however the investigation into the Cyprus Arc concurs with the back-arc hypothesis, albeit at an earlier time (see Section 5.8.5).

Some features are resolvable in the seismic data available to this study, but have previously been described and discussed in published literature. If no new insights were made by this study, no description of the feature is given in this section. These features include:

- Plio-Quaternary mass wasting and canyon features along the Levant Margin (Section 2.5.5).

- Sand intrusions offshore Israel (Fuhrmann, 2010).
- The structure of the Lebanese terrestrial margin (Ghalayini et al., 2014; Nader et al., 2016).
- The distribution of Mesozoic faults in the Southern Levantine Basin (Section 2.5.1).
- Much of the Plio-Quaternary deformation associated with underlying salt tectonics (Section 2.5.5).
- Interpretations of Syrian Arc folds offshore Israel (Gardosh et al., 2011, 2008b).

The Senonian Unconformity is a ubiquitous horizon that may be traced across the whole of the EMR, although in places it merges with a series of strong reflectors and choosing which of these represents the Senonian Unconformity presents some difficulty. To generate a reflector that transcends other stratigraphic and tectonic boundaries across an area the size of the EMR requires a substantial event. Onshore Syria a widespread Late Cretaceous unconformity is linked to the collision of the Arabian Promontory with a subduction zone (Brew et al., 2001a). The same event likely formed the offshore Senonian Unconformity. The Senonian Unconformity is useful as it is the oldest widely picked reflector, and thus can be used to define the show architecture of the EMR.

Unconformities concomitant with the MSC are also nearly ubiquitous across the EMR, and are discussed in Section 3.7.

3.6.1 Cyprus Arc

Chapter 5 investigates the structural evolution of the Cyprus Arc area in detail. Here, a broad description of features in the area is given.

The Cyprus Arc is an expression of the boundary between the Eurasian (locally the Anatolian) and Afro-Arabian (and Sinai in the EMR) Plates (Figure 2.1). The arcuate shape of the feature and the varying plate motions mean that there are varying degrees of convergent and transform motion along its length (Figure 2.33; Vidal et al. 2000). As a result, many of the faults that delineate the feature facilitate recent motion that might be better classified as strike-slip as opposed to thrust. However, the subjectivity and difficulty in resolving which mode of displacement is dominant means that in this introductory section all the faults are referred to as thrusts.

To the west of Cyprus, the southern limit of the Cyprus Arc is visible on the seismic data as a basement high that pierces the sea floor as the Florence Rise and Anaximander Seamounts, and the northern limit as a series of thrusts in the pre-MSC sediments with no bathymetric expression (see Section 5.7). To the east of Cyprus, the better coverage of the seismic data available to this study permits more detailed mapping. Here the Cyprus Arc is delimited at its southern edge by the thrusts of the Latakia and Tartus Ridges (Figure 3.14A; supplementary figure). Generally, these ridges have one main thrust verging southwards and reaching to the sea floor, with intermittent deeper leading thrusts (Figure 3.14A; Figure 3.15). The thrust planes in the ridge become less clear to the NE as the mode of deformation becomes more transform dominated. The back of the ridge is often extended perpendicular to the strike of the ridge by parallel striking antithetic thrusts (Figure 3.15; also see Figure 5.8A). In many places the Latakia Ridge represents

the most southward manifestation of the Cyprus Arc by the Levantine Basin. In part of the eastern Latakia Ridge however, an accretionary wedge may be observed beneath the Senonian Unconformity (Figure 3.14A; Figure 3.15).

To the north of these ridges is a network of mini-basins and thrust and ridge systems, not all of which reach the sea floor (Figure 3.14A). To the east of Cyprus this area is termed the Tartus Basin and joins with the Latakia Basin to the north around the Larnaca Ridge, a bathymetric high that runs NE-SW to the east of Cyprus (supplementary figure).

The Latakia basin is delimited by the Kyrenia range thrusts to the north, the Syrian continental margin to the east and Cyprus island to the west. The Plio-Pleistocene sediments thicken from west to east, with localised increases in thickness off the Syrian coast (Figure 3.17; Figure 3.12). Although these can appear to be half grabens in cross section (Figure 3.17) the surrounding tectonic configuration and deformation indicates these are pull apart basins formed by transtension on the eastern limb of the Cyprus Arc (see Section 5.8.2). In the north and east of the Latakia Basin there is a 500 ms TWTT MSC salt interval with widespread diapirism affecting the overlying sediments (Figure 3.17)?

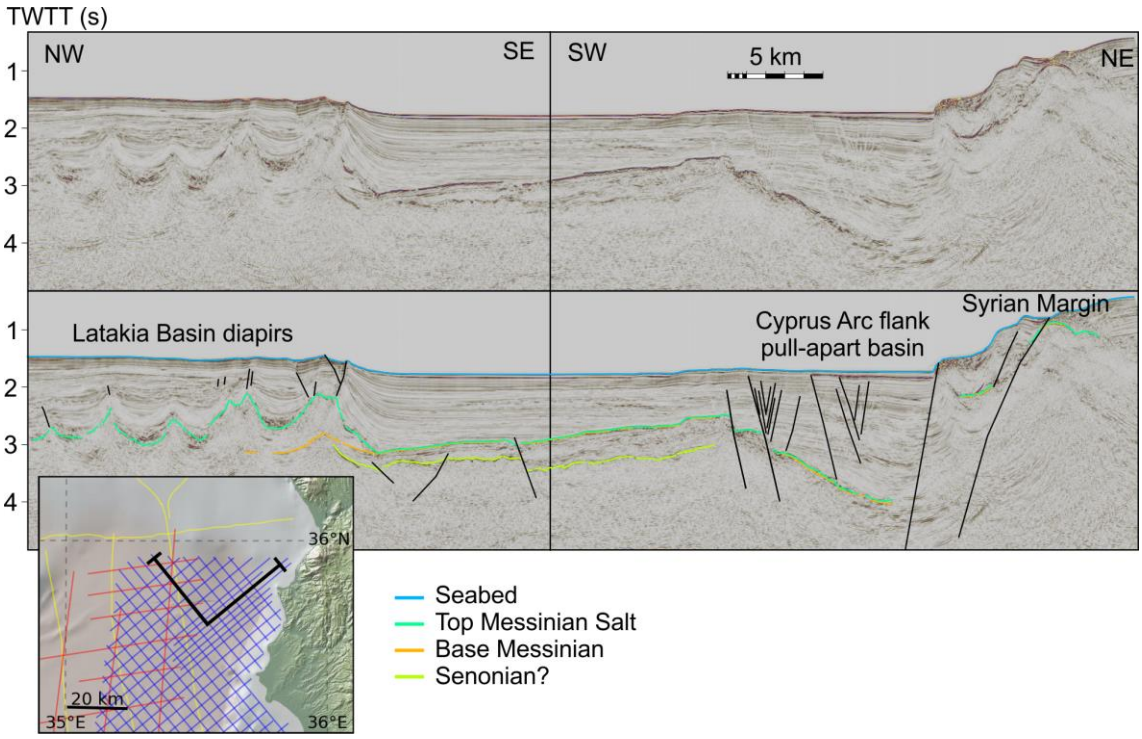

Figure 3.17-Composite seismic line showing the diapirs, pull-apart half graben and elevated seismically transparent crystalline basement in the NE of the Latakia Basin. The global relief (Ryan et al., 2009) vertical scale on the minimap is shown on Figure 1.1 and the supplementary figure.

The age constraints of the sub-MSC sediments in the Latakia Basin are uncertain as the reflectors have been traced over the Latakia and Tartus Ridges (Figure 3.15). Based on these interpreted reflectors the sequence of pre-MSC Cenozoic sediments is approximately half as thick as the Levantine Basin (Figure 3.14A). The pre-MSC reflectors are largely unfolded in the Latakia Basin but are normally faulted along the basins southern edge (Figure 3.14A). These faults have the greatest displacement in the SE portion of the basin and appear to be orientated broadly NE-SW based on correlation between 2D lines (see Section 6.2.2).

Cyprus Island is the most striking example of the collisional uplift at the Cyprus Arc. The onshore geology of Cyprus is comparatively well studied, and the focus on the offshore seismic data available to this study means that study of onshore Cyprus is only undertaken in this study by comparison of features with offshore Cyprus.

As with much of the EMR, a thick interval of MSC salt exists in much of the Cyprus Arc (Figure 3.14). Where the salt body terminates, the underlying sediments appear artificially deformed due to the velocity contrast of the salt causing seismic pull up of the underlying sediments (Figure 3.18, Section 3.2.5). The limit of the salt body may have been interpreted by Bowman (2011) as a thrust, this interpreted thrust is oblique to the trend of the other thrusts of the Cyprus Arc and matches the limits of the salt body. There is a small thrust in the Plio-Pleistocene sediments around the south and east edges of the salt body that may be interpreted to have been generated by rafting of the supra-salt sediments (Figure 3.18), as has been suggested in a more distributed fashion further SE along the edge of this salt body (Hübscher et al., 2009). However, other thrusts of this size are not marked on the interpretations of Bowman (2011).

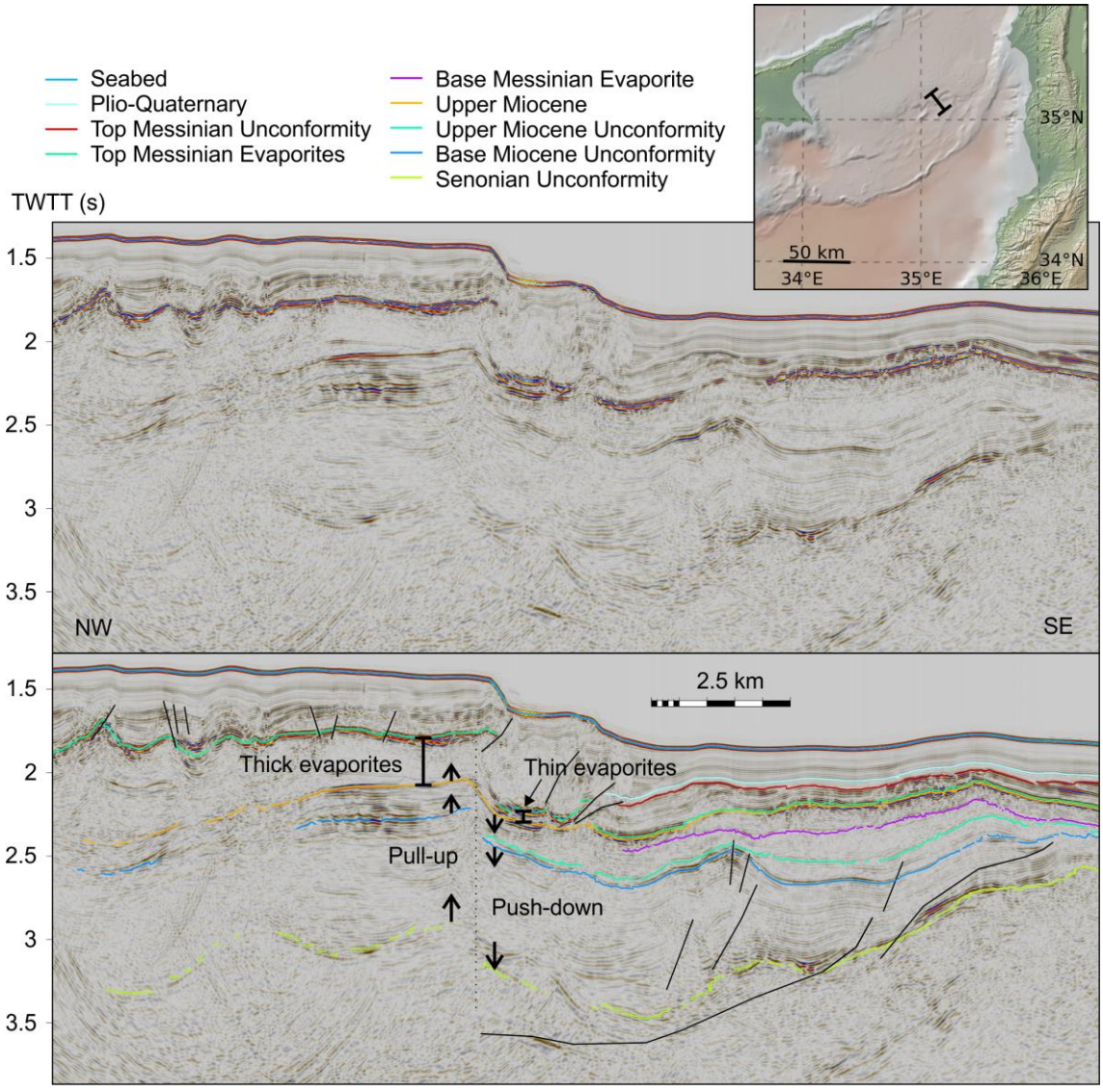

Figure 3.18-Velocity pull-up due to contrasting overlying evaporite thicknesses at the southern limit of the Latakia Basin, previously interpreted as thrust faulting. Note most reflectors are constrained

by perpendicular lines. The global relief (Ryan et al., 2009) vertical scale on the minimap is shown on Figure 1.1 and the supplementary figure.

3.6.2 Northern Levantine Basin (2D Data)

The Northern Levantine Basin is delimited to the north by the thrusts of the Latakia ridge, to the east by the continental margin of the Arabian Plate, to the south by the Levant ramp, and to the west by the ESM (Figure 3.16). It contains a thick (up to 5 s TWTT) succession of Cenozoic sediments. The pre-MSC sediments contain a swarm of normal faults termed the Piano Key Faults (PKFs; Figure 3.14, Figure 3.12), which are looked at in more detail in Chapter 6. The normal faults detach in a seismically transparent horizon interpreted to be shale (Kosi et al., 2012). Perpendicular to the PKFs are a set of folds, the orientations of which match a set of structures with geometries suggesting inverted normal fault folds at the eastern margin of the basin (also explored in Chapter 6). The Senonian Unconformity represents the deepest consistently traceable reflector; this surface defines the geometry of the basin. It is offset by a series of normal faults that are clearly resolved on PSDM data available to this study, and explored in Section 6.6.8.

A 'finger' of the Northern Levant basin extends from the NE corner of the main body of the Northern Levant basin immediately south of, and perpendicular to, the Tartus Ridge (Figure 3.12J, L). The seismic expression of the sediment sequence in this spur remains the same as in the main body of the Levantine Basin, but the sediments shallow NE-ward (see Figure 6.2). Bowman (2011) interprets this Levantine Basin 'finger' as a foreland basin that formed due to lithospheric loading from the thrusts of the ridge. This matches the narrow geometry of the basin formed by the finger, but does not match the wider southward extent of the Northern Levantine Basin. This indicates that flexural subsidence of a foreland basin cannot solely explain the Northern Levantine Basin. The subsidence is explored further in Section 3.6.4. The late Miocene normal faults in this area (see Figure 6.2) are likely linked to the PKFs, explored in Section 6.2.1.

Some low-throw normal faults may be observed along the Lebanese margin. However, the offsets of these faults do not generate the elevation change that defines the margin (Figure 2.7). Instead the elevation change arises from the slope of these offset horizons. This demonstrates these normal faults are not the rift faults that formed the margin, and that the rift faults and break up unconformity must be deeper than the seismic resolves. This rift depth, due in a large part to the age of the rift, means that this continental margin appears dissimilar in comparison to 'classical' rifted margins as the rift faults are not well imaged (e.g. Pindell et al., 2014).

A single isolated diapir may be observed in the west of the Northern Levantine Basin on the seismic data available to this study (Figure 3.19). The diapir features steeply dipping flaps in the Miocene sediments with an intermediate weld, and a possible collapsed crest. The ages of the diapir flaps suggest that the diapir formed in the MSC due to mobilisation of Oligocene age sediment. Degradation of reflector clarity beneath the diapir poses a challenging interpretation, as tracing of the more obvious reflectors results in interpretations which have inconsistent package thicknesses (Figure 3.19B), or reflector cross-cutting (Figure 3.19C). Close inspection of the seismic data permits interpretation of a series of parallel, equal length and vertically stacked reflectors beneath each flank of the diapir (Figure 3.19A). Their geometric consistency indicates

they are artificial signals, and disregarding these reflectors permits an interpretation of the feature that is geologically realistic (Figure 3.19A). The substrate that has mobilised to form the diapir in this interpretation is of the equivalent interval as the mobile shale in which the PKFs detach. This diapir is discussed further, in the context of an evacuation pathway for the mobile substrate, in Section 6.2.3.

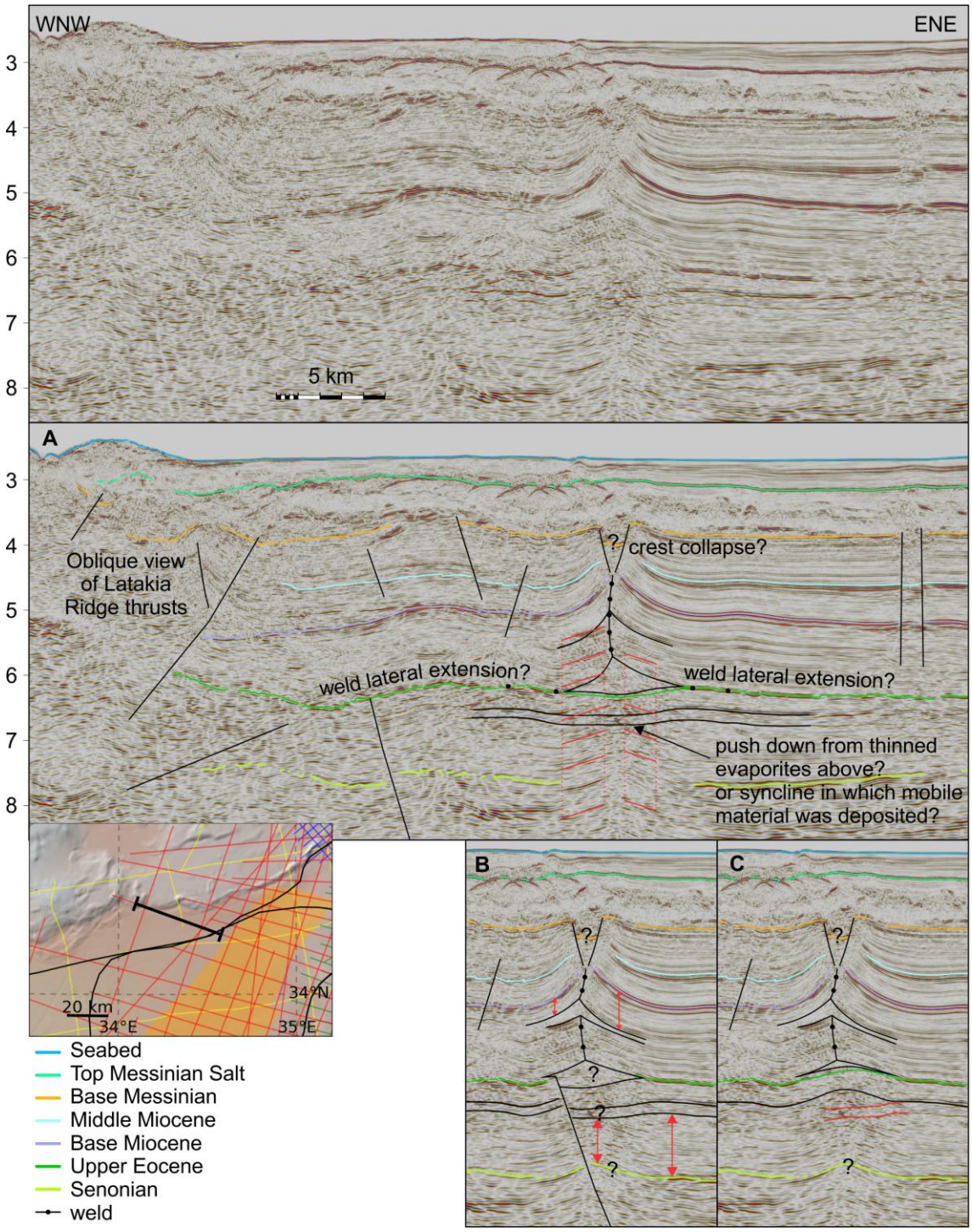

Figure 3.19-WNW-ESE striking seismic line showing the location of a diapir in the Oligo-Miocene sediments in the west of the Northern Levantine Basin, with alternative interpretations. Red lines illustrate aspects discussed in the text. The global relief (Ryan et al., 2009) vertical scale on the minimap is shown on Figure 1.1 and the supplementary figure.

East of this diapir, a block of the same sediment sequence has been negatively offset between a pair of faults which are vertical, in stark contrast to the rest of the Miocene normal faults in the basin (Figure 3.19A). With the limited information available, the favoured interpretation of this study for these features block collapse into the mobile horizon in which the Piano Key Faults detach, possibly due to evacuation of the mobile substrate up the diapir. A strike slip interpretation might be preferred for the vertically offset block, however the steep angle of the diapir flaps is infeasible for a purely strike-slip genesis, and the simplest solution is that it represents a single mobile horizon explanation, as opposed to this in conjunction with strike-slip. Compression associated with the proximal Cyprus Arc convergence may have affected either the formation of the diapir, or a structure that the diapirism then exploited.

Two areas of diapirism, as opposed to single isolated occurrences, are present in the Northern Levantine Basin, one c. 50 km offshore Lebanon and another adjacent to the Lebanese continental margin. The diapirism is discussed in Section 3.7.3. Margin collapse of the post-MSC sediments due to evacuation of underlying MSC evaporites is common along the Levant margin of the northern Levantine Basin. This is explored in Chapter 7.

The sediments of the Levantine basin onlap onto the ESM. This relationship is looked at in more detail in the ESM Section (3.6.6).

3.6.3 Northern Levantine Basin (3D Data)

The LEB3D survey covers the central portion of the Northern Levantine Basin (Figure 3.16; Figure 3.20). The benefits of 3D data and the younger vintage of the survey mean that several extra features can be resolved in comparison to the 2D data.

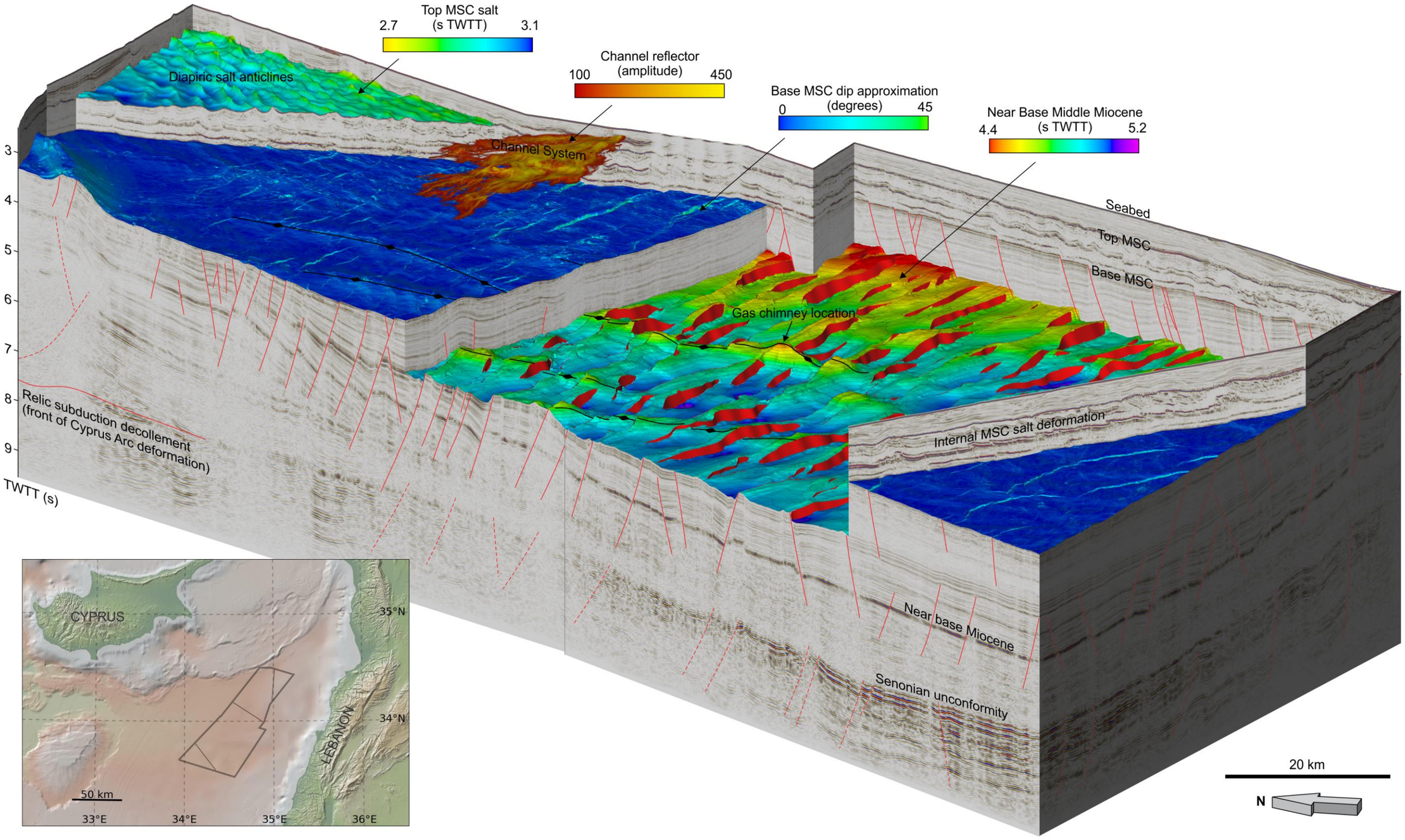

Figure 3.20-Block diagram highlighting features of the LEB3D seismic survey discussed in the text. The global relief (Ryan et al., 2009) vertical scale on the minimap is shown on Figure 1.1 and the supplementary figure.

Internal reflectors of the MSC interval are clearly imaged in the LEB3D seismic (Figure 3.20). Mapping of these internal reflectors reveals innumerable folds, thrusts and significant truncation of the younger reflectors by the Top MSC unconformity. The deformation has been the focus of several studies and there is some controversy as to its timing (Section 2.6.9). The timing is investigated further in light of the LEB3D data in Section 3.7.1. More general aspects of this halokinesis, and structures associated with it, are investigated in detail in Chapter 7.

The late Miocene PKFs are well imaged in 3D and are underlain by sub-parallel Senonian age normal faults, although these are imaged less clearly (Figure 3.20). These deeper faults were interpreted but not discussed by Reiche et al. (2014a, fig. 2a). They are explored in Section 6.6.8.

Some of the folds that are perpendicular to the PKFs have dipping-limb thrusts (Figure 3.20). All these features are investigated in detail in Chapter 6. Some of the folds also have summits which contain a section of chaotic reflectors (Figure 3.21A and B). This block of chaotic reflectors may be traced non-linearly though the MSC sequence up to a column in the post-MSC sequence that is topped by a small depression on the sea floor (Figure 3.21D, E and F). In close proximity are areas where reflectors undergo a significant and laterally sudden increase in amplitude at the summits of convex-up structures (Figure 3.21A and E). Thus, these chaotic sequences may be interpreted as gas chimneys, the depression as a pock-marks from gas escape, and the high amplitudes as trapped hydrocarbons.

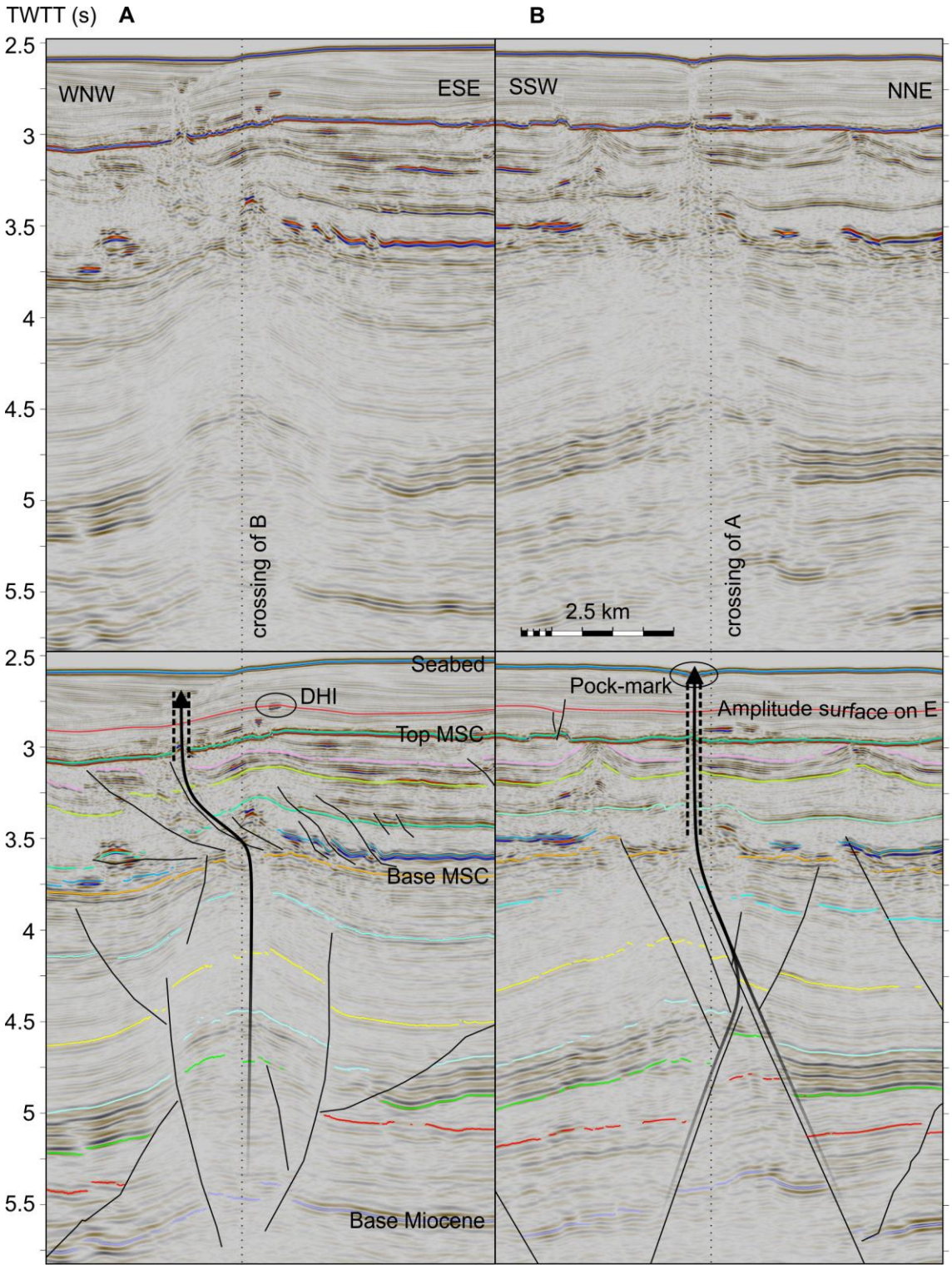
TWTT (s)
A
B
2.5
3
3.5
4
4.5
5
5.5
WNW
ESE
SSW
NNE
crossing of B
crossing of A
2.5 km
Seabed
DHI
Top MSC
Base MSC
Base Miocene
Pock-mark
Amplitude surface on E

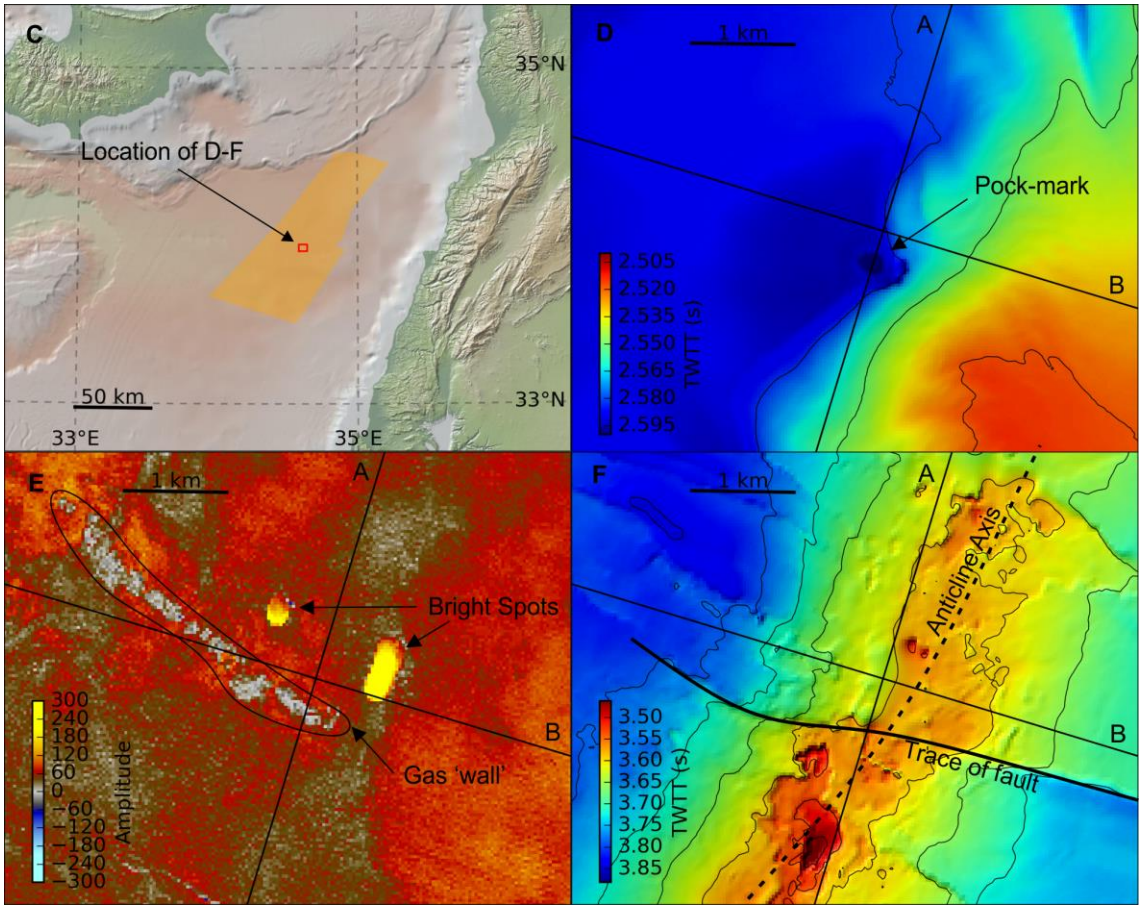

Figure 3.21-A) E-W striking seismic line illustrating a possible hydrocarbon migration path up the anticline axis, through the MSC evaporites via a thrust plane and gas chimney evidence, and a brightening reflector (DHI) in a Plio-Quaternary anticline; B) N-S striking seismic line showing a possible hydrocarbon migration path up a fault plane, and a seismic chimney between the top of the fault and a pock-mark on the sea floor; C) Map showing the location of D-F, the global relief (Ryan et al., 2009) vertical scale is shown on Figure 1.1 and the supplementary figure; D) Seabed surface in time showing a pock-mark on the sea floor; E) Amplitude map of the Plio-Quaternary reflector marked on A and B, showing bright spots and a line of gas chimneys; F) TWTT surface of the Base MSC unconformity illustrating the intersection between an anticline and fault.

The morphology of a series of bright reflectors in the Plio-Pleistocene sediments of the LEB3D seismic are consistent with a channel complex c. 15 km in diameter and deep sea fan complex >30 km is diameter (Figure 3.22; Figure 3.20). Their bright character is consistent with a sand rich interval (in contrast to the muddy surrounding sediments). A likely explanation for a channel complex is a reconfiguration in river pathways resulting from the LSZ restraining bend uplifting the Palmyrides. Additional study would be required to explore these features further.

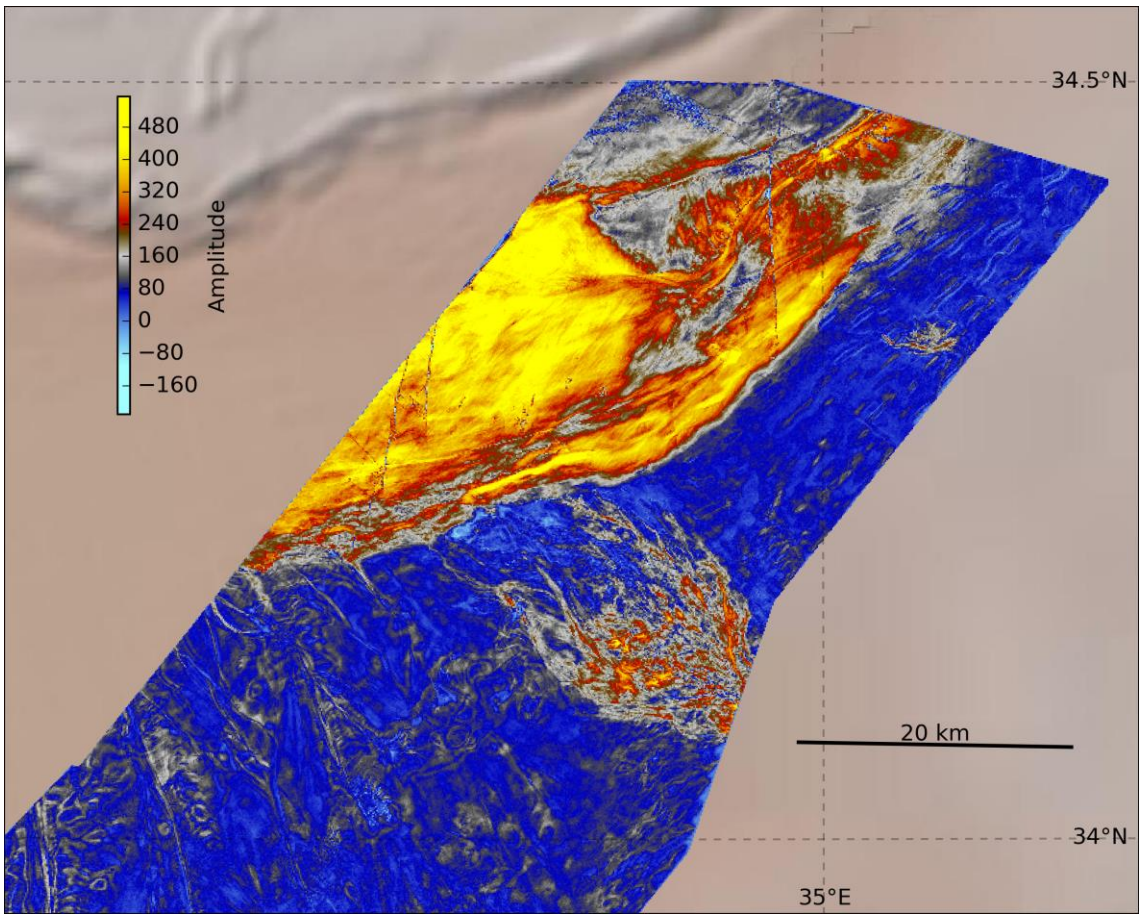

Figure 3.22-Amplitude map showing a channel complex (SE) and deep sea fan complex (NW) that appears in the post-MSC sediments of the LEB3D volume. The global relief (Ryan et al., 2009) vertical scale is shown on Figure 1.1 and the supplementary figure.

In the NE of the LEB3D data set the Northern Levantine Basin diapirism is well resolved. This is explored in Section 3.7.3.

3.6.4 Levant Ramp

The 'Levant Ramp', after Hodgson (2012), is a monoclinal feature which separates the Northern and Southern Levantine Basins (Figure 3.16, Figure 3.23). Fault offsets indicate the feature formed shortly after the Senonian Unconformity (Figure 3.23). Overlying sediments are progressively draped on top (Figure 3.23). This horizon changes elevation by c. 2 s TWTT across the Levant Ramp, and transitions from a low slope angle (2 s over c. 50 km) at its western edge at the ESM (Figure 3.23A) to a faulted slope at its eastern edge at the Levant margin (Figure 3.23D). The high side of this faulted slope is the Saida-Tyr Plateau, a >1000 km² area of relatively elevated acoustic basement adjacent to the Israel-Lebanon border (Figure 3.23D; Ghalayini et al., 2014).

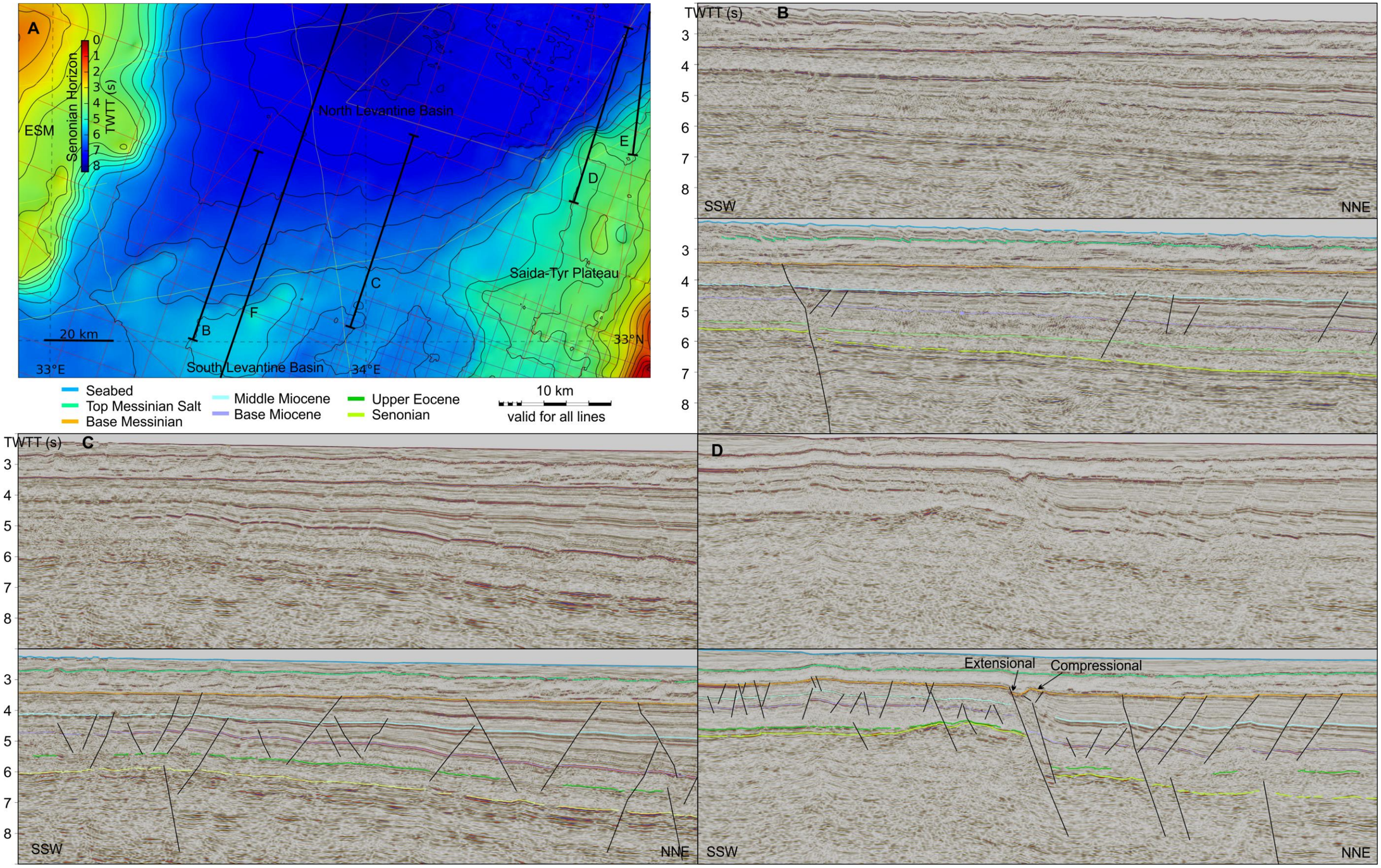

Figure 3.23-A) Map of the Senonian Unconformity over the Levant Ramp, the global relief (Ryan et al., 2009) vertical scale is shown on Figure 1.1 and the supplementary figure.; B-D) PSTM seismic lines perpendicular to the western, central and eastern portions of the Levant Ramp respectively; E) PSDM line over the easternmost Levant Ramp with highlighted syn-kinematic package discussed in the text; F) Laterally compressed PSTM seismic line from the Levant Ramp to the Cyprus Arc.

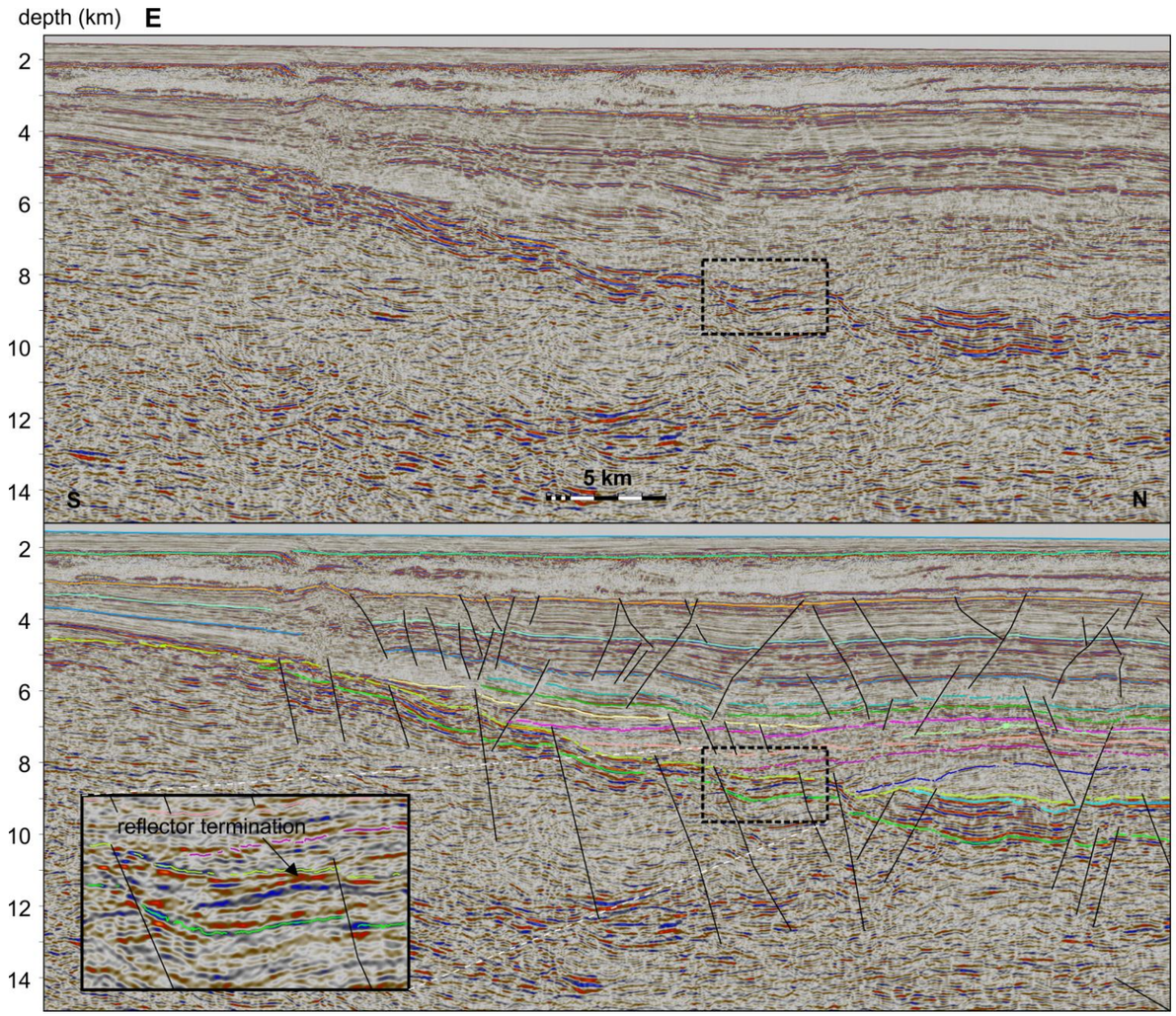
depth (km)
E
2
4
6
8
10
12
14
S
5 km
N
reflector termination

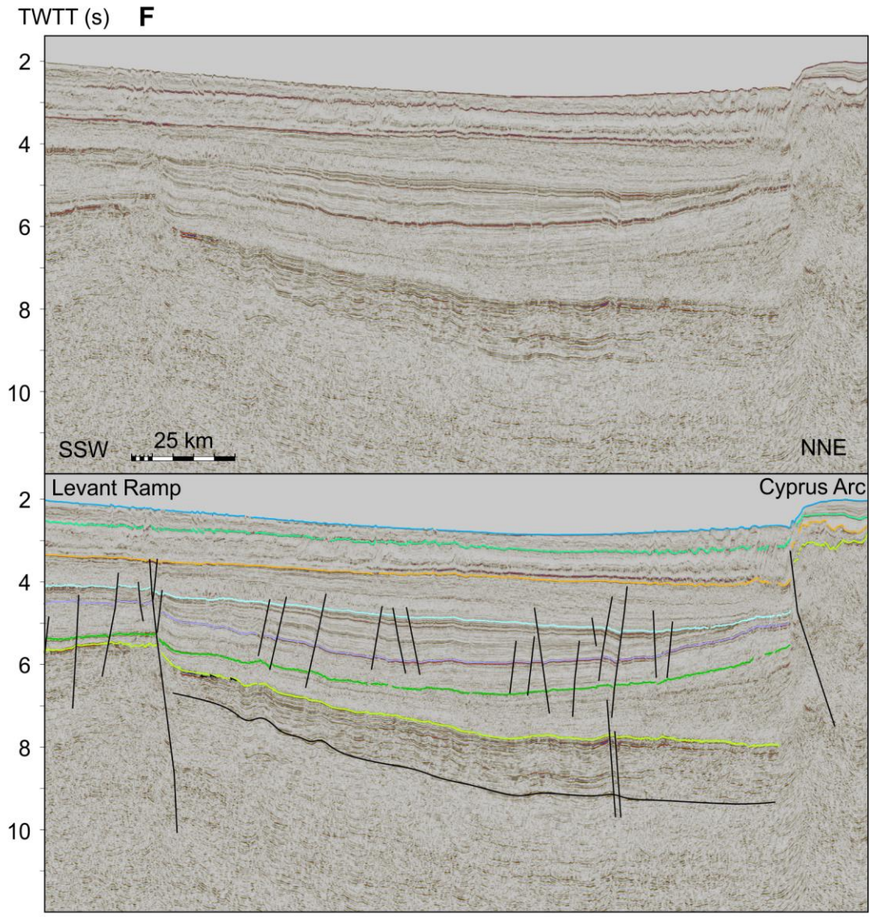
TWTT (s)
F
2
4
6
8
10
SSW
25 km
NNE
Levant Ramp
Cyprus Arc

The Miocene sediments thin southward over the ramp without any onlap that may be interpreted with confidence (Figure 3.23). This indicates a progressive increase in the elevation difference between the Northern and Southern Levantine Basins occurred during this period. Differential isostatic subsidence could provide this mechanism, but would require a pre-existing contrasting sediment load. The sediments between the Senonian and Upper Eocene Reflectors are poorly imaged on PSTM data, and few coherent reflectors are resolved (Figure 3.23B-C). On the PSDM line, these lower Palaeogene sediments are more clearly resolved, and may be observed to onlap onto the Senonian Unconformity horizon (Figure 3.23E). This indicates that significant subsidence of the Northern Levantine Basin relative to the Southern Levantine Basin occurred during the formation of the Senonian Unconformity. Northward thickening of the sub-Senonian reflector sequence from the Levant Ramp indicates that some subsidence of the Northern Levantine Basin occurred prior to the Senonian (Figure 3.23F). Underthrusting at the Cyprus Arc subduction zone to the north, the subsidence of the oceanic crust that the subduction zone has consumed, and the faulting at the Levant Ramp are possible mechanisms behind the Levant Ramp subsidence.

The fault that appears to facilitate much of the offset in the eastern portion of the Levant Ramp ('Main Levant Ramp Fault') is interpreted as a strike slip fault by Ghalayini et al. (2014). Recent deformation including both compressional and extensional features (Figure 3.23D) concurs that it has undergone recent strike slip motion, however the offsets of the Senonian horizon relative to the Miocene ones demonstrates that this was a pre-existing feature (Figure 3.23D). The offsets of the deeper horizons along the feature are compatible with a pre-existing normal fault downthrowing the Northern Levantine Basin. This is backed up by the eastern continuation of the Main Levant Ramp Fault being imaged as a series of pre-Senonian faults with normal offsets on the PSDM line (Figure 3.23E).

The PSDM line also reveals what is either a syn-kinematic package above one of the normal fault blocks (Figure 3.23E), indicating that either some of the faults were active around the Senonian, or significant Senonian erosion of the fault blocks. Given that these faults are in a deep part of the basin, and would have lowered their elevation further when they formed, the former might be considered more likely than large amounts of erosion.

On the basis of the observations in the preceding pair of paragraphs it may be concluded that the Levant Ramp monocline initially formed during the Cretaceous. This occurred by a combination of normal faulting mainly in its eastern portion and subduction related subsidence causing northward tilting. Once an initial basin had formed preferential sediment deposition and the resulting isostatic compensation enhanced the feature. The question remains as to why the Levant Ramp initially formed where it did, and not further to the north or south. The trend of the Palmyride Basin appears to match that of the Levant Ramp. It is possible that the Palaeozoic Rifting that initially formed the Palmyride Basin (Section 2.3.2) extended further west beneath what is now the Levant Ramp, and was reactivated as faulting in the Cretaceous. Further rifting of the Palmyrides in the Late Cretaceous (Section 2.3.2) matches this hypothesis. The relative northward motion of the Palmyrides due to offsets on the LSZ (Section 2.3.1) suggests that the Levant Ramp may have been aligned with the northern edge of the Palmyrides. However, this would result in an opposing relationship of hangingwall and footwall sides of the fault trends. It

may therefore be possible that there was a pre-existing basement trend at that orientation, that was reactivated as the Palmyrides as the Levant Ramp. Further study could test this hypothesis.

The crustal type of the Northern Levantine Basin is not definitely established, so another possibility is that the Levant Ramp represents the boundary between oceanic crust to the north and (thinned) continental crust to the south. This issue is discussed further in Section 4.6.

3.6.5 Southern Levantine Basin

This basin is defined at its northern margin by the Levant ramp, at its western margin by the ESM, at its eastern margin by the Levantine margins and to the southeast by the Nile Cone (Figure 3.16). The sediment fill is equivalent to the Northern Levant basin, but with a thinner Senonian to MSC sequence; the main reflectors may be directly traced between the two basins without significant changes in the character of the packages (Figure 3.23). There are several high points in these basement reflectors present in the basin that pierce through the overlying Cenozoic sediments (Figure 3.12M). These are thought to be consistent with carbonate platforms on horsts bounded by grabens (Gardosh et al., 2008b; Sagy et al., 2015). Carbonate platforms also exist along the basin margin (Section 2.3.5; Figure 2.5), and form the Saida-Tyr Plateau (Ghalayini et al., 2014).

There are numerous anticlinal structures in the Southern Levantine Basin containing gas fields (Section 2.6). In the interior of the basin these are normal fault inversion and differential compaction anticlines (Figure 3.14B). The well data from these gas fields remains inaccessible to the wider scientific community so lithologies may only be constrained by seismic character and more inboard well data. On the Levant margin inverted basin rift normal faults form the well-imaged offshore portion of the Syrian Arc. The sediments of the Levant basin onlap onto the ESM. This relationship is discussed in more detail in the ESM section (3.6.6).

In the Southern Levantine Basin, reflector terminations indicate a channel eroded the underlying sediments at the start of the MSC (Bertoni and Cartwright, 2006; Lofi et al., 2011). The seismic data available to this study permit the tracing of this channel deeper into the basin than previous studies (Figure 3.24). Note that the high seismic velocity of the evaporite sequence reduces the relief of the channel when viewed in time (Figure 3.24). It appears the channel cuts around the southern limit of the ESM carbonate platform, likely with flow heading towards the deeper Herodotus Basin, but low reflector clarity on the older vintage seismic data in the area means that an alternative route over a promontory of the carbonate platform cannot be discounted. Some of the lows in the Base MSC Unconformity surface, such as that at the end of the speculated channel route marked on Figure 3.24, are due to push-down from thickened post-MSC sediments. When picking the channel care was taken to take potential push-down into account, so that the interpreted channel lows are not underneath lows in the top of the salt body (Figure 3.24).

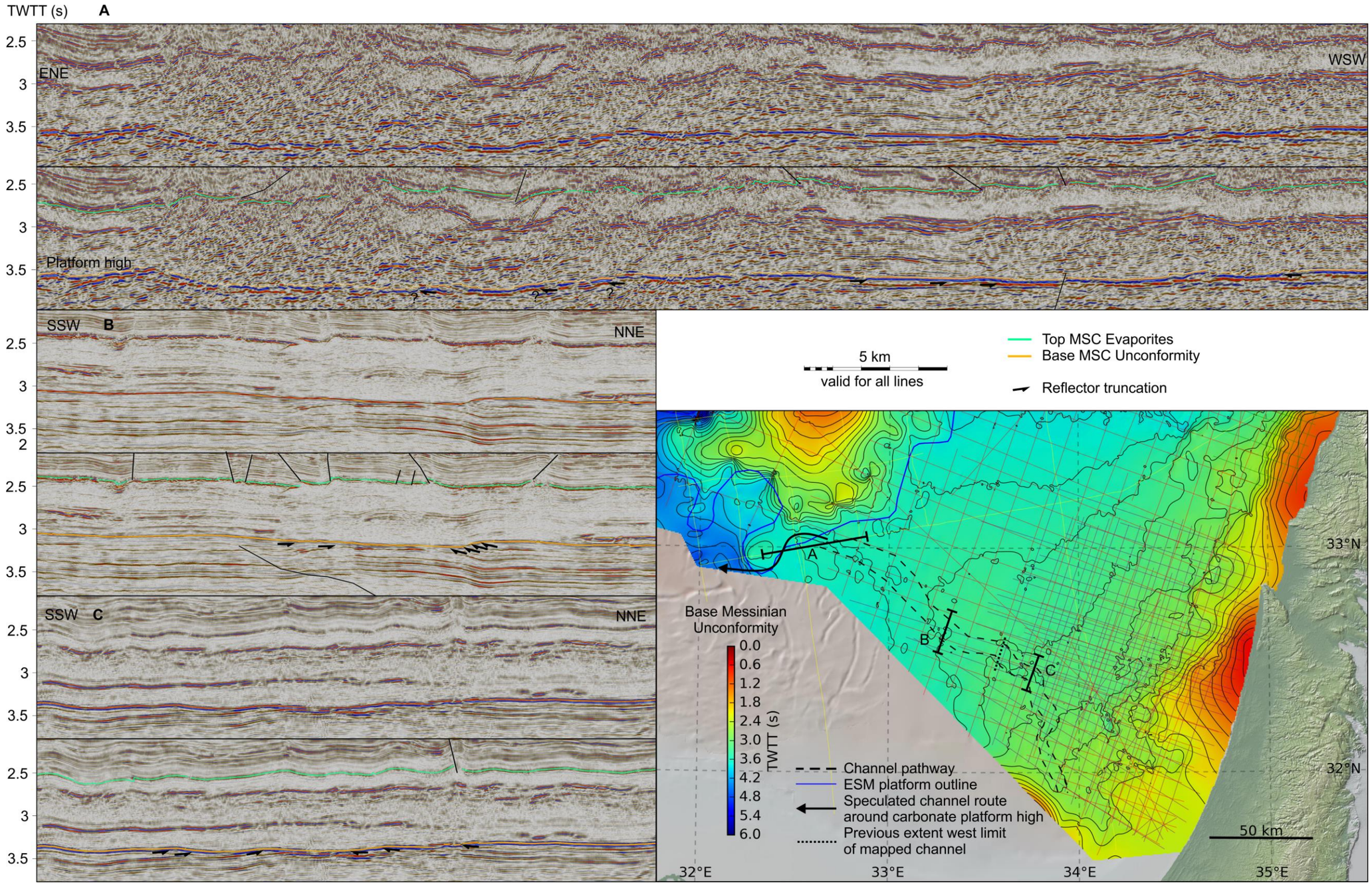

Figure 3.24-Seismic lines and map of the Base MSC Unconformity showing the location of a channel eroding into the sediments beneath the Base MSC Unconformity. The global relief (Ryan et al., 2009) vertical scale on the map is shown on Figure 1.1 and the supplementary figure.

Sequences of coherent reflectors are present in the seismic data offshore Israel below the Senonian Unconformity horizon, but these are often not present on the seismic data available to this study elsewhere in the EMR. Detailed interpretations of these Mesozoic reflectors have been undertaken by Gardosh et al. (2008) and the resulting maps published. To avoid duplication of work, and given the reflectors non-regional extent and the regional remit of this study, regional interpretations of these deeper reflectors was not undertaken. For some aspects of this study it was pertinent to make local interpretations of these reflectors which are shown and described in the relevant figures (e.g. Figure 4.13).

3.6.6 Eratosthenes Seamount

The ESM exists between the Levantine and Herodotus Basins (Figure 3.26; Figure 3.16). ODP well 967 reveals shallow (<250 m) Cretaceous carbonates on the northern flank of the feature (Figure 3.11; Figure 3.26). This means the Senonian unconformity is very shallow over the seamount relative to the adjacent Herodotus and Levantine Basins, and may be used to show the geometry of the ESM relative to the surrounding basins (Figure 3.26B). This Mesozoic high also results in a seismic sequence that contrasts to most the EMR (Figure 3.12A). The Pre-MSC Cenozoic sediments of the Levantine and Herodotus basins and Nile Cone onlap onto the Cretaceous carbonate platform flanks of the ESM (Figure 3.14).

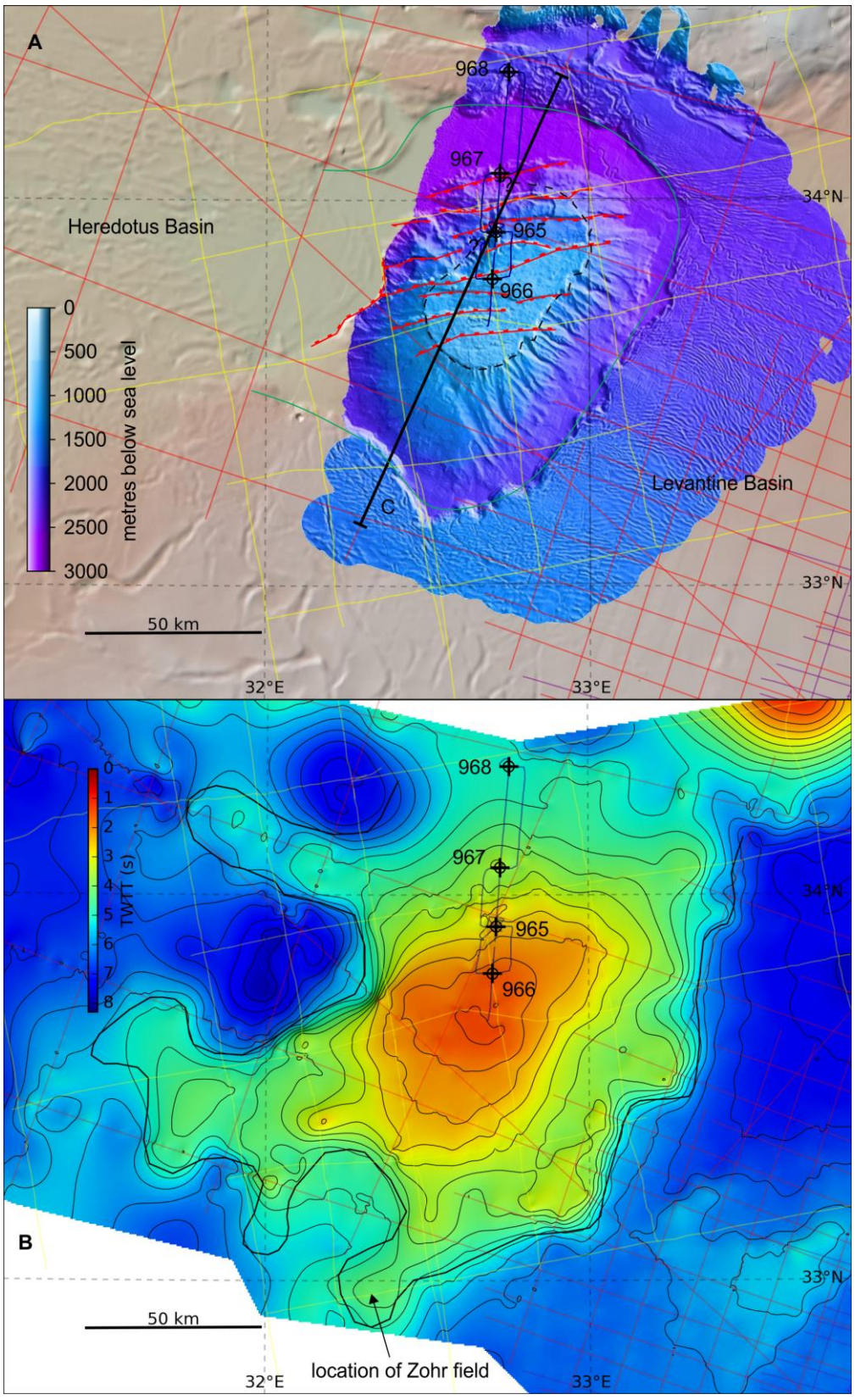

Figure 3.25-A) Bathymetry map of the ESM with inset (Ehrhardt et al., 2011) showing the normal faults, summit escarpment, and moat, outlined in red black and green respectively, the global relief (Ryan et al., 2009) vertical scale is shown on Figure 1.1 and the supplementary figure. B) Senonian Unconformity surface demonstrating the limit of the Mesozoic carbonate platform (outlined). Where spacing of the seismic data available to this study is large, portions of the platform outline are drawn from other sources with access to other seismic data (Kassinis, 2011; Klimke and Ehrhardt, 2014; Tassy et al., 2015). ODP borehole data is marked with the borehole number on both A and B. C marks the location of Figure 3.26.

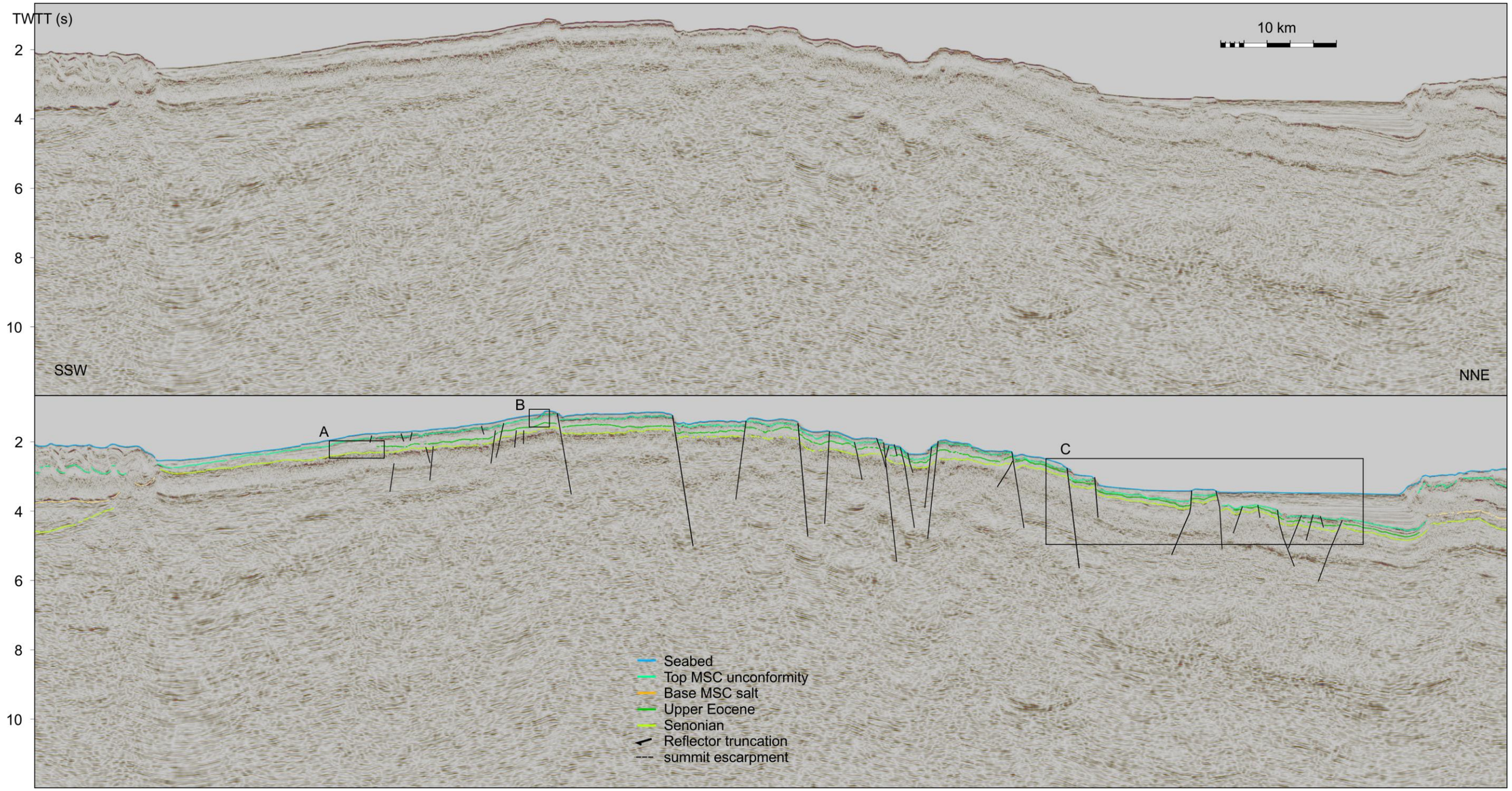

Figure 3.26-SSW-NNE striking seismic line across the ESM demonstrating the faulted reflectors and deeper uncertain reflectors. The location of the line is shown on Figure 3.25. A, B and C refer to the insets shown on Figure 3.27. Please refer to Figure 3.10 for well ties.

The summit of the ESM and its northern flank is bisected by a series of normal faults (Figure 3.25; Figure 3.26). These are associated with the breakup of the seamount as it is underthrust beneath Cyprus (Robertson, 1998b). Some authors have interpreted normal faults around the edge of the ESM carbonate platform (Montadert et al., 2014; Tassy et al., 2015). Except for an exceptionally abrupt lateral termination of the carbonate platform on the west side of the ESM (Figure 3.25A), that appears to join with the escarpment of one of the ESM summit faults, no normal faults, other than very slight offsets likely associated with differential compaction, were observed around the buried ESM carbonate platform on the data available to this study. Mutually inclusive possible explanations of this western fault include flexural forces from differential subsidence, a break-up fault orientated by a pre-existing feature, or differential compaction.

The ODP wells reached a maximum depth of 600 m in Cretaceous carbonates and consequently the ages of the underlying reflectors are unknown. Only the top c. 200 ms TWTT of reflectors are clearly resolved at the ESM on the seismic data available to this study, however trends in deeper reflectors may be picked out (Figure 3.26; Figure 3.14). These trends, both shallow and deep, are generally sea-floor parallel (Figure 3.14), and cut by faults that offset the seabed (Figure 3.25A; Figure 3.26). Most of these faults have normal offsets although there are some faults with apparent reverse offsets (Montadert et al., 2014; also Figure 2.25B). These may be linked to a component of transverse motion affecting the Cyprus Arc (see Section 5.8.2).

A plateau at the ESM summit is defined by a c. 200 m high external escarpment that is offset by the recent normal faults (Figure 3.26A), and a ‘moat’ around the bathymetric high of the ESM is defined by an up to c. 400 m high external escarpment (Figure 3.25A; Figure 3.26). The summit escarpment is explored later in this sub-section and the moat is explored in Chapter 7.

The character of the pre-MSC reflectors undergo significant variation right across the ESM, including sub-parallel, chaotic and sigmoidal reflectors (Figure 3.14; Figure 3.26; also see Figure 3.27). This can be interpreted as varied carbonate platform features, including karstification, patch reefs and lagoonal areas. Adjacent to the Nile cone and Levantine basin the massive MSC evaporite interval encroaches onto the ESM carbonate platform (Figure 3.14; Figure 3.26).

The seismic data available to this study images the sediments of the ESM more clearly than the seismic lines illustrated in other published studies of the feature (Klimke and Ehrhardt, 2014; Montadert et al., 2014; Robertson, 1998c). Consequently, several features previously undiscussed in published literature are resolved, including:

- Sigmoidal and other curvilinear reflectors within the Cenozoic sequence (e.g. Figure 3.27C).
- Significant erosion, marked by reflector truncations, on the northern ESM flank (Figure 3.27D).
- Reflector truncations beneath the ESM summit escarpment (Figure 3.27C, E).
- The geometries and relationships of some of the deeper reflectors (see Figure 3.29).

These new observations can be used to further our understanding of the formation of the ESM, and are discussed in the remainder of this subsection.

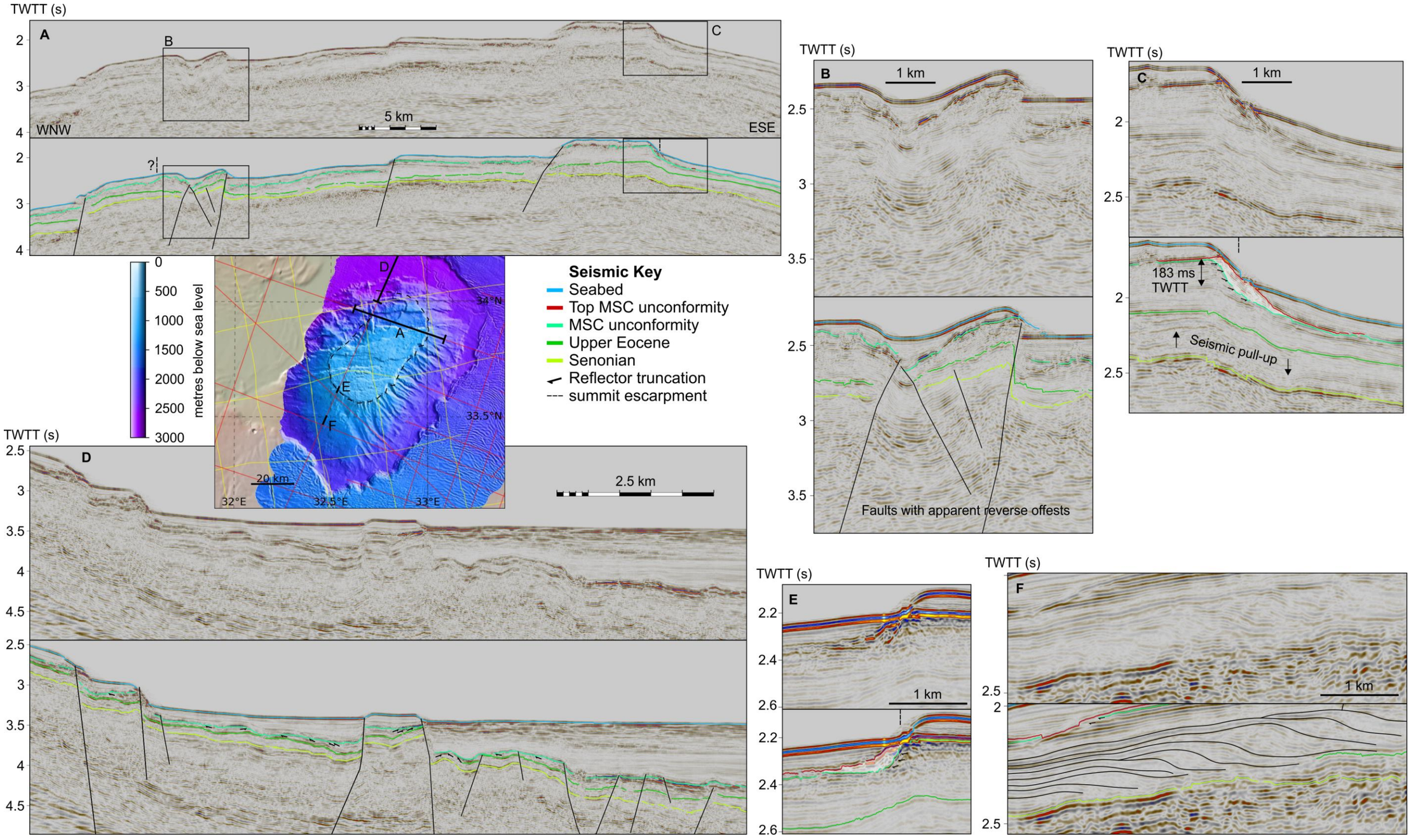

Figure 3.27-Seismic lines across the ESM including insets highlighting features discussed in the text. The location of D, E and F is shown on the larger scale line on Figure 3.26 as well as the mini map shown here. Bathymetry inset is from Ehrhardt et al. (2011). The global relief (Ryan et al., 2009) vertical scale on the minimap is shown on Figure 1.1 and the supplementary figure.

One understanding of the ESM is that its summit escarpment represents the limits of a shallow marine carbonate platform that has been intermittently aggrading since the Mesozoic (Figure 3.28). This implies that the flanks of the ESM represent extended talus slopes of this late Miocene carbonate platform. Several lines of evidence indicate that this is not the case:

- Recent drilling of a satellite carbonate platform at the southern edge of the ESM platform (Figure 3.25B) revealed the shallow marine carbonates were Miocene in age (Bertello et al., 2016). This means that in the Miocene this satellite platform and the ESM summit were both in the photic zone.
- Reflector packages may be interpreted from beneath the summit plateau all the way down the flanks of the ESM without significant changes in character (Figure 3.26; Figure 3.27A). This contrasts with the changes in seismic facies that are common in the transition from a shallow to deeper water carbonate setting (Eberli et al., 2004). Although not definitive on its own, this indicates that the flanks of the seamount were likely sub-planar when formed.
- Sigmoidal foresets may be observed to prograde up the flanks of the ESM in the Oligo-Miocene interval (Figure 3.27F). As the sigmoidal foresets prograde up, as opposed to down, the flanks of the ESM then at the time they formed the ESM flank slope must have been either absent or reversed. These features could be interpreted as imbricate thrusts that are formed gravitationally, however the top limbs of the sigmoids consistently aggrade as opposed to truncating and/or converging (Figure 3.27F). For imbricates to image with the observed consistent aggradation would require implausibly consistent periodic thrust movement, demonstrating the sigmoids are depositional.
- Where the MSC unconformity is undulose is in stark contrast with the underlying planar reflector morphology, both on and off the summit plateau (Figure 3.27). The amount of erosion by the MSC unconformity does not appear to vary much away from the ESM summit platform, with the exception of the northern flank (Figure 3.27D). This suggests no major topographical relief during the MSC.

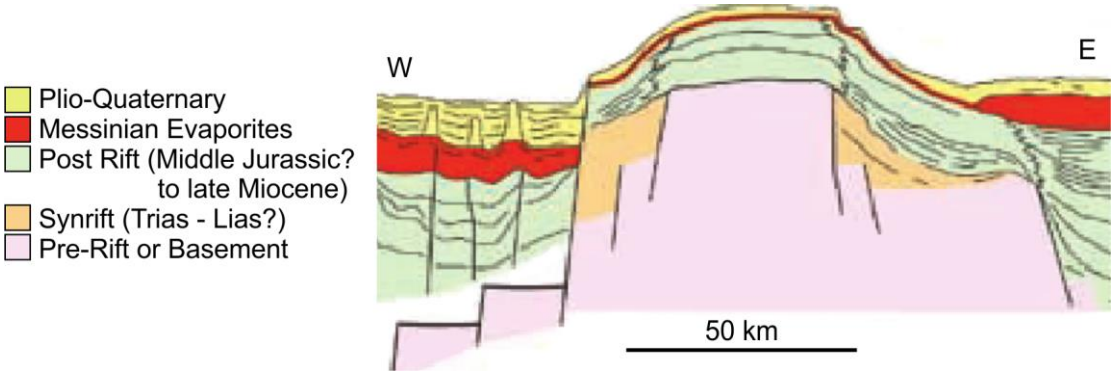

Figure 3.28-Sketch of the ESM showing aggradational reef facies at the summit of the plateau, adapted from Montadert et al. (2010).

The alternative explanation is that the flanks of the ESM were part of the plateau of the late Miocene carbonate platform, which was then subject to post-MSC subsidence resulting in the current convex upwards morphology of the feature (Figure 3.26; Figure 3.27). This means that

the ESM summit escarpment is another feature superimposed on this Miocene carbonate platform, and suggests that the northern flank of the ESM also represents a subsided Miocene shallow water carbonate platform.

This last implication is at odds with what was observed in ODP well 967 since no Miocene carbonates were recorded and instead middle Eocene pelagic carbonates are unconformably overlain by MSC sediments (Figure 3.11). The horst block that this well was drilled into is imaged on a 2011 vintage seismic line ~5 km along strike from the drill site (Figure 3.10). This seismic data reveals significant erosion of the Oligo-Miocene sediments by the MSC unconformities (Figure 3.27D). It is unclear at this location if this erosion occurred at the start or end of the MSC, or a combination of both, however it may mean that a mid-Miocene shallow water carbonate platform existed at this location before it was eroded during the MSC.

Close inspection of the escarpment encircling the ESM summit reveals a matching escarpment at the Base MSC unconformity reflector. Post-MSC reflectors terminate against the MSC unconformity escarpment (Figure 3.27C, E). Two possible explanations exist for this feature; either erosion of the flanks of the seamount at the end of the MSC (erosion scenario), or the flank of a carbonate platform that formed at the summit of the ESM during the MSC (reef scenario). As the current bathymetric escarpment is a mould of the underlying MSC escarpment, 'escarpment' in the following paragraphs refers to the MSC escarpment. Both explanations require significant post-MSC deformation of the ESM summit as the plateau escarpment is not currently at a consistent elevation (Figure 3.27A). This would be consistent with the ESM summit breakup due to underthrusting at the Cyprus Arc (Robertson, 1998b).

The shallow marine carbonates drilled at the ESM could not be reliably be dated to a specific portion of the Miocene (Robertson, 1998b), so they could either be mid- or early-Miocene carbonates in the erosion scenario, or MSC carbonates in the reef scenario. A section of lower Pliocene carbonate platform was drilled at ODP site 967, demonstrating that shallow marine carbonates were deposited around the MSC (Figure 3.11). Robertson (1998b) interpreted an Early Pliocene talus and debris flow sequence at well 966 as evidence of MSC erosion, which correlates to an unconformity in seismic data (Figure 3.27D; see Section 3.7.1). These observations from well data are compatible with both the reef scenario (MSC reef build up followed by a draw down event with lower Pliocene reef building during restoration to global sea level), and the erosion scenario (pre-MSC Miocene reef build up followed by erosive draw down events in the MSC with lower Pliocene reef building during restoration to global sea level). The following paragraphs evaluates these explanations in light of observations from seismic data.

At the base of the summit escarpment there are packages of reflectors that are unconformable at the base and onlapped onto above (Figure 3.27C, E). In the erosion scenario, this could be erosion debris from the platform summit, and in the reef scenario this could be reef talus from the summit reef, or lowstand carbonate build-ups. Thus, this is inconclusive.

Three arguments exist that suggest the escarpment is erosional:

- The common morphology of carbonate platforms, both those that exist today and that have been documented in seismic data, is for reef facies at the perimeter of the carbonate

platform and lagoonal facies in the interior, a model that has been interpreted at the ESM summit in the past (Robertson, 1998b). Lagoonal and reefal facies produce seismic reflectors that are contrastingly planar and chaotic respectively (Eberli et al., 2004). The reflectors that may be observed at the ESM summit escarpment are fairly sub-planar on the seismic data available to this study (Figure 3.27D, F). There are narrow sections where they are more chaotic immediately adjacent to the peak of the escarpment, but there are also significant changes in overburden above, perhaps indicating imaging changes resulting from contrasting raypath mediums. This is non-diagnostic, but the narrow (c. 100 m) width of the chaotic sections adjacent to the ESM summit escarpment indicates that they may be due to imaging issues from overburden heterogeneities introduced by the bathymetric escarpment.

- If the ESM summit plateau escarpment is the edge of a carbonate platform, then the lack of any significant progradational or retrogradational reef systems demands that there was a steady balance between the relative increase in sea level and carbonate growth in order to form a very narrow aggradational reef, the only form compatible with what may be observed on seismic data (relatively minor low stand deposits notwithstanding).
- Erosional features at the Base MSC unconformity in the Levantine Basin indicate (see Section 3.7.1) significant sea level draw down at the start of the MSC. If a carbonate platform had formed during the MSC at the summit of the ESM, then an underlying erosional unconformity might be expected. Given the elevation of the ESM, and the karstification that would take place, such an unconformity might be expected to produce a significant seismic signal. No such reflector is observed at the ESM summit (Figure 3.27).

Primarily because of this last argument, this study favours the explanation that the ESM summit escarpment is an erosional escarpment, formed during the MSC. However, a MSC summit reef has not been entirely discounted.

If the ESM summit escarpment is erosional, two mutually inclusive explanations could exist for the morphology of the escarpment; a cap of more resistant rock resulting in a bluff that retreated as erosion progressed, or a wave cut cliff during a sustained lower sea level during the MSC.

Sediment deposition in the adjacent Levantine Basin, Nile Cone, and Herodotus Basins, and the underthrusting of the northern limit of the ESM platform under Cyprus provide mechanisms that can explain subsidence around the ESM. That a large amount of differential subsidence has occurred since the MSC is perhaps not surprising, as significant isostatic compensation might be expected after deposition of >2 km of overburden. A discussion on the absolution amounts of subsidence is undertaken in Section 7.3.2. What is less obvious is why the ESM summit remained as relatively elevated as it is when surrounded by subsiding basins and underthrusting to the north, as flexural forces might be expected to cause it undergo a less contrasting amount of subsidence. However, if there is a large enough component of Airy isostatic compensation then this is not infeasible (Watts, 2011). Additionally, as the continental fragment or intrusion complex that forms the core of the ESM has been in place significantly longer than the surrounding basin sediments, it will be close to isostatic equilibrium, and so will be contrastingly buoyant in

comparison to the surrounding basins and their sediment load. However, the narrow (compared to typical flexural isostatic compensation distances) size of the ESM and amplitude of proximal subsidence suggests there may be more factors at play. Further study could inform on this.

Inspection of the deep seismic data reveals steeply dipping reflectors in the core of the ESM (Figure 3.29). These dipping reflectors defy explanation if the ESM is simply a carbonate platform on top of a rifted continental block, as stepped reflectors representing the faulted top of the crystalline basement might be expected instead. Syn-rift wedges might produce dipping reflectors, but for a syn rift surface to be imaged but not the top crystalline basement seems unlikely. The lateral continuity of the dipping reflectors observed also doesn't fit with a faulted syn-rift sequence.

An alternative explanation that fits these observations, and has been suggested for the ESM before, is that it is underlain by a volcanic edifice rooted in the attenuated continental crust of the EMR (Zverev and Ilinsky, 2005, 2000, via Gardosh et al., 2010). This hypothesis is based on interpretation of the magnetic anomaly beneath the ESM as an igneous body, as opposed to associating it with an underlying crustal block. Gridding of the top of the steeply dipping reflectors reveals a surface that appears to correlate with a magnetic anomaly beneath the ESM (Figure 3.29). It was not possible to confidently trace these reflectors beneath locations where MSC evaporites were present, due to a combination of the reflector degradation below where the salt body tips out and possible seismic pull-up. Thus, the limits of the salt body define the limits of the gridded surface (Figure 3.29).

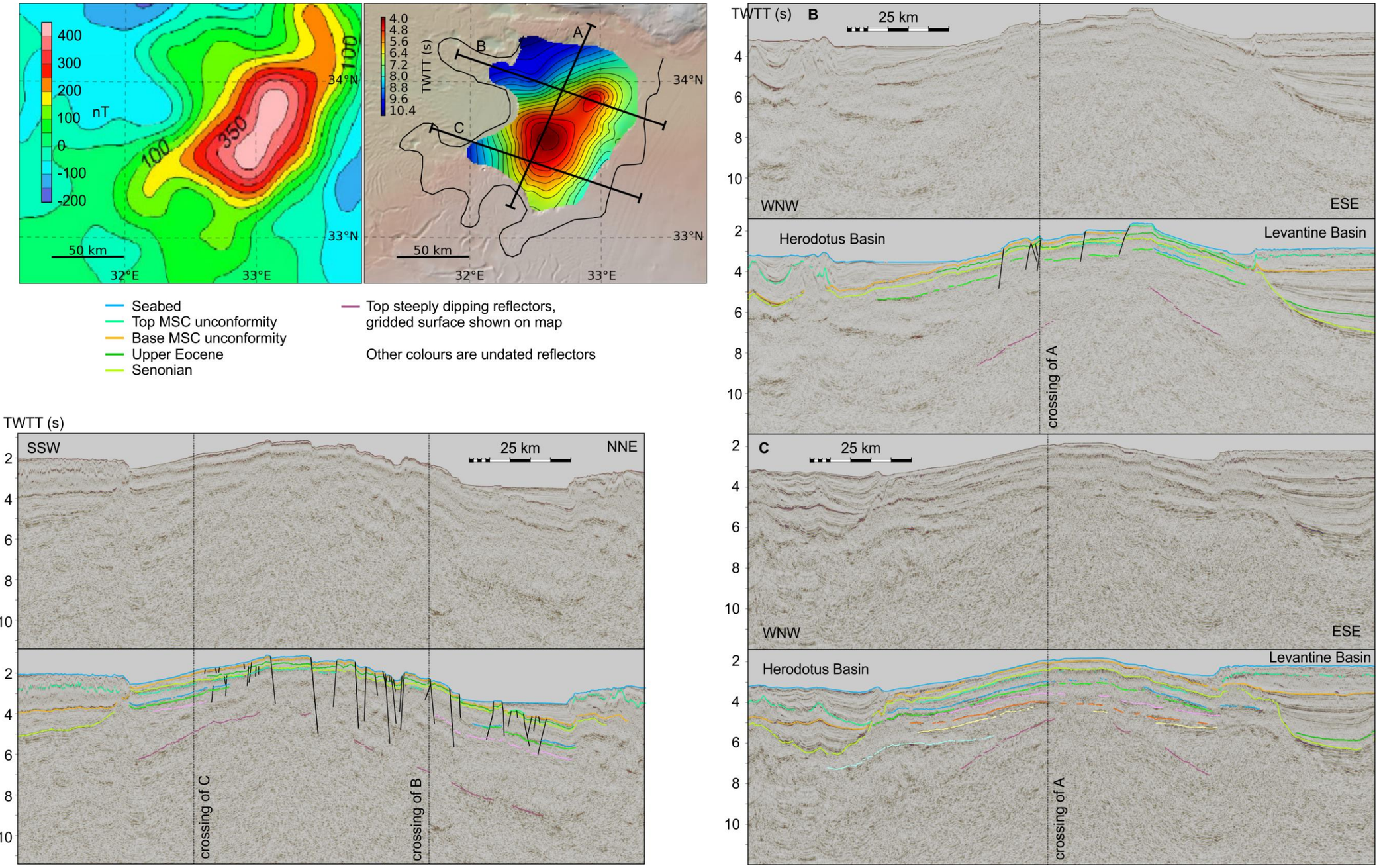

Figure 3.29-Low pass filter magnetic anomaly map adapted from Erbek and Dolmaz (2014), surface showing the gridded surface of interpretations of the top of dipping reflectors at the ESM, and seismic lines showing the deep reflectors of the ESM. The curved black line on the bottom map shows the approximate limit of the Cretaceous carbonate platform. The global relief (Ryan et al., 2009) vertical scale on the minimap is shown on Figure 1.1 and the supplementary figure.

A possible modern analogue of the ESM prior to its subsidence to pelagic depths is the SE extent of the Bahama Platform. This complex of shallow water carbonate platforms is located on the west Atlantic margin, and is in the initial stages of colliding with the Puerto Rico Subduction Zone. Some of those platforms closest to the subduction zone, such as the Silver Bank and Navidad Bank, are undergoing subsidence at their subduction-proximal sides. The Bahama Banks have been subsiding under the weight of the build-up of shallow water carbonates, such that 5-10 km of predominantly shallow water carbonates has built up since the Late Jurassic (Carew and Mylroie, 1997).

3.6.7 Herodotus Basin

The portion of the Herodotus Basin imaged by the seismic data available to this study is bound to the east by the ESM, to the north by the Cyprus Arc and elsewhere by the data limits (Figure 3.16; Figure 3.30). It contains a very thick (up to 2 s TWTT) Plio-Pleistocene sequence that is highly distorted by salt tectonics of the underlying MSC salt. Diapirism, sheets, welds and mini basins may all be identified (Figure 3.14). The salt tectonics mean that the underlying horizons are very poorly imaged, but a deepening trend to the west may be observed as the underlying crust transitions to being oceanic as opposed to continental (Figure 3.14). In some locations diapirism as caused the MSC evaporite body to thicken to over 2 s TWTT thick (> 5 km). Section 3.7.1 contains further discussion on the MSC evaporites.

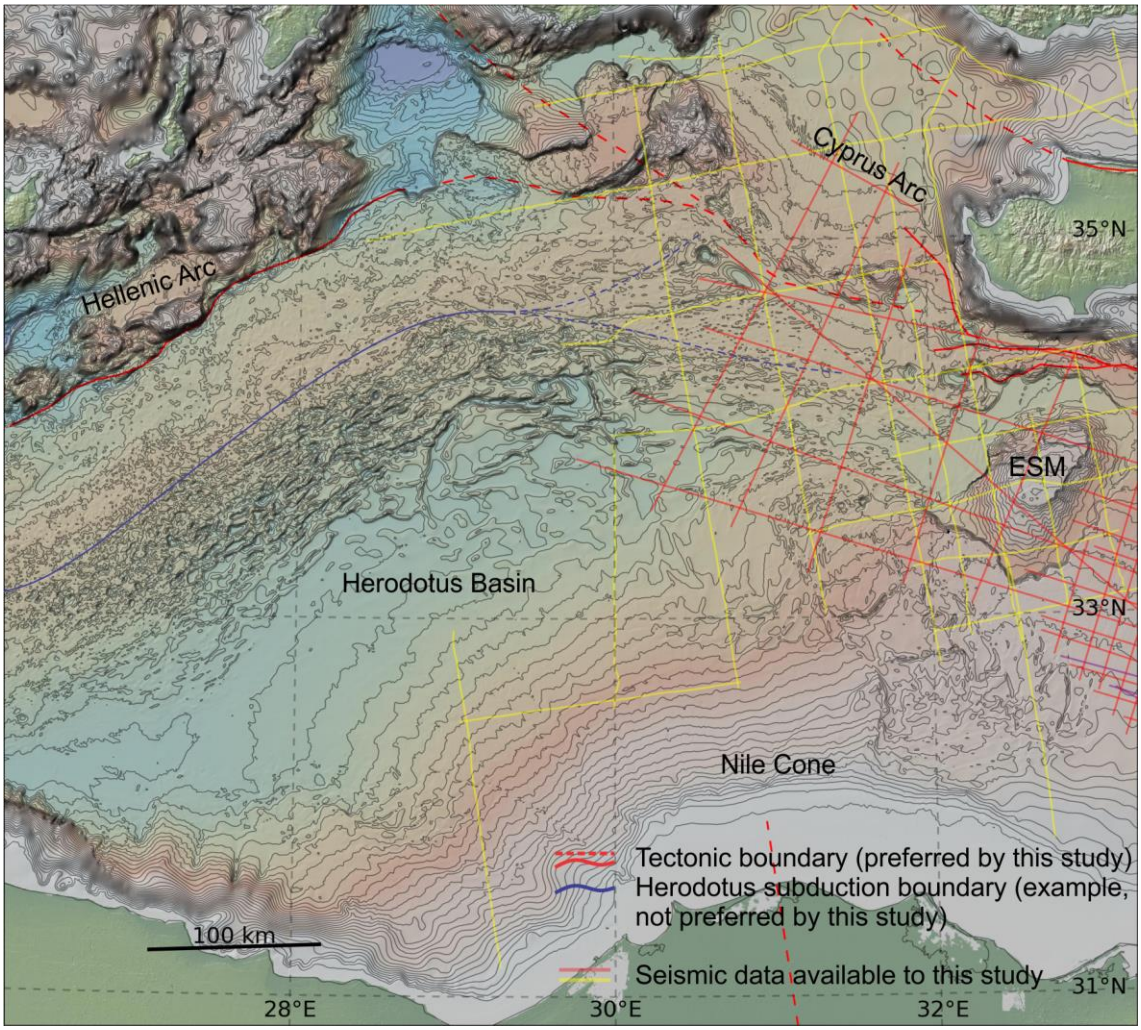

Figure 3.30-Map showing bathymetry (GEBCO) of the Herodotus Basin and surrounding areas, and seismic data and boundaries discussed in the text. The global relief (Ryan et al., 2009) vertical scale is shown on Figure 1.1 and the supplementary figure.

Some authors draw a subduction front, or front of deformation related to the Hellenic subduction zone to the north, through the southern portion of the Herodotus Basin in the EMR (Figure 3.30 (Allen et al., 2016; Avigad et al., 2016; Gorini et al., 2015; Hawie et al., 2013; Mascle et al., 2000; Westaway, 2004b). The seismic lines available to this study do not image this location, but it appears to correspond to a trend in the folds observable in bathymetric data in the area (Figure 3.30). Folds with an equivalent bathymetric expression, and that appear to be part of the same zone of deformation, are imaged on the seismic data available to this study (Figure 3.30). The seismic data shows that these folds are thin skinned deformation, related to either diapirism of the underlying MSC salt, or folds from basin directed gravity forces (e.g. Figure 3.14B). Consequently, this study favours a more northerly subduction or subduction related deformation front. This concurs with much of the information published in literature.

Deformation of the MSC sequence causes challenges with tracing of underlying reflectors, due to degraded imaging clarity. However, a general dip of the pre-Messinian sequence westward towards the deep basin may be observed (Figure 3.14B).

On some of the seismic data available to this study, some speculative offset reflector packages could be explained by faulting consistent with a COB (see Figure 4.10). On all the broadly EW seismic lines west of the ESM there are places where pre-MSC reflector packages appear to suddenly deepen westward, which would be consistent with the rift faults that formed the COB. This is discussed further in Section 4.5.

3.7 The Messinian Salinity Crisis

Evaporites deposited during the MSC (Section 2.5.4) exist across the EMR but are not ubiquitous (Figure 3.31). The sequence associated with the MSC is regionally variable, but has four components that may be traced across the EMR (Figure 3.13). They are briefly described (and numbered) here before a description of each component is given in the following sections. The oldest seismic reflector associated with the MSC is the Base MSC unconformity (1). The MSC evaporite body itself (2) contains sequences of different seismic packages which are again regionally variable. Capping and in some cases truncating the top of the MSC evaporites is the Top MSC Unconformity (3). Where MSC evaporites are absent the Top MSC Unconformity erodes or is indistinguishable from the Base MSC unconformity. Overlying this there is a sequence of reflectors that are higher amplitude and more variable in contrast to those overlying (4). This sequence is likely clastics and/or evaporites that mark the return of the basin to non-evaporitic marine deposition. The thickness of this sequence is regionally variable and sometimes its upper limit is ambiguous.

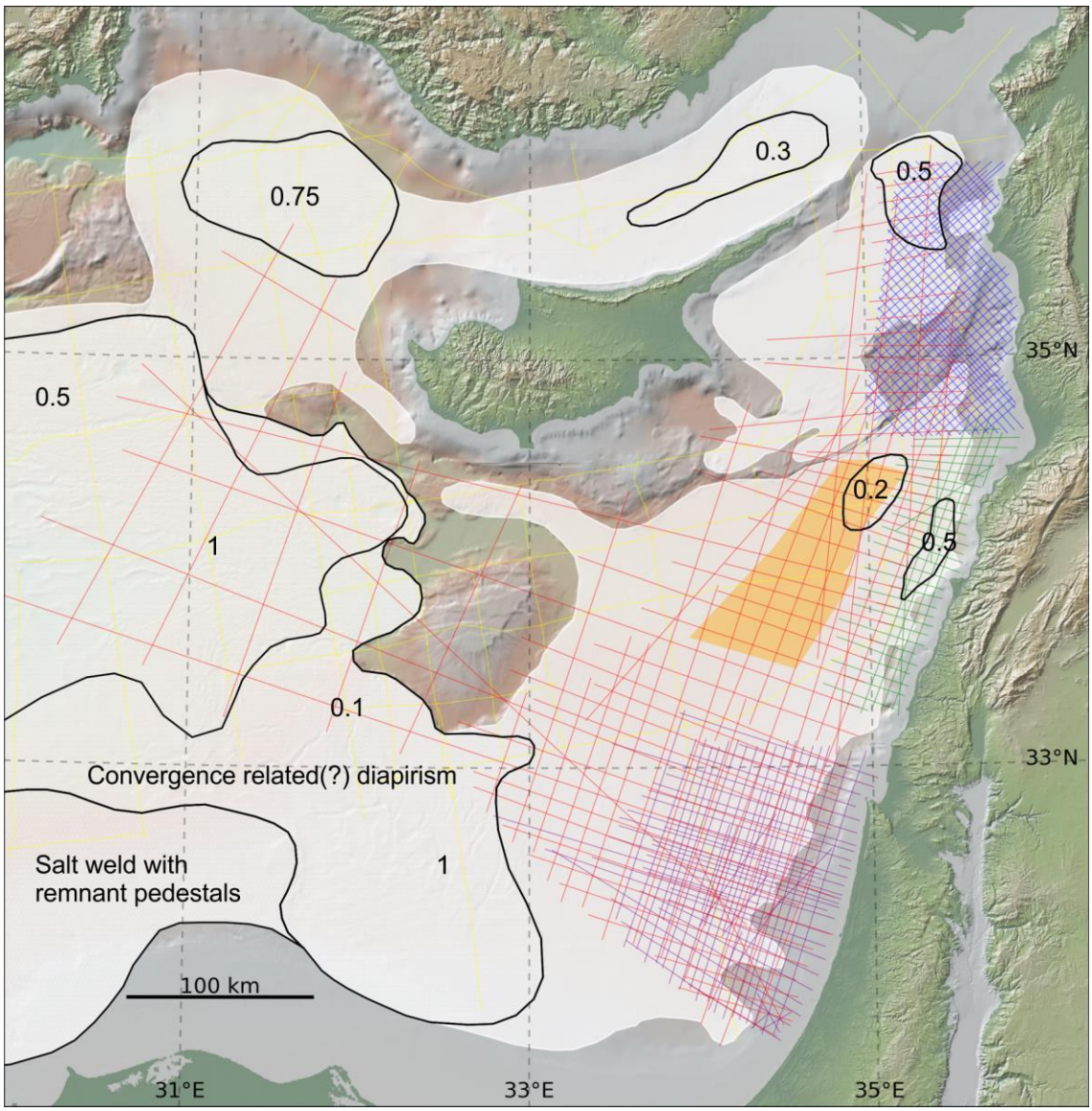

Figure 3.31-Map showing the location of massive MSC salt in white, based on the seismic data available to this study, with the areas of halokinetic diapirism (or 'pillowing' where it is smaller) outlined in black. Here the term 'diapirism' refers to the general vertical perturbation of the top of the salt body by salt-tectonic processes, including diapirs, salt anticlines, pillowing, salt rollers etc. The numbers refer to typical differential offsets, in seconds TWTT, between the peak of diapirs and the base of salt-withdrawal minibasins, for the underlying area. Additional constraints on the outline of the salt have been incorporated around the Nile Cone (Loncke et al., 2006), ESM (Kassinis, 2011), Cilicia Basin (Walsh-Kennedy et al., 2014), Latakia Basin (Calon et al., 2005a) and Tartus and Cyprus Basins (Lofi et al., 2011). Minor evaporite basins, such as those documented onshore Cyprus (Robertson et al., 1995) and on the Hecataeus Rise (Reiche and Hübscher, 2015) are omitted. The global relief (Ryan et al., 2009) vertical scale is shown on Figure 1.1 and the supplementary figure.

3.7.1 Evaporite Deposition Interval

Where it underlies MSC evaporites, the Base MSC reflector represents a strong negative impedance, as might be expected from the transition between evaporites and siliciclastic lithologies. Where the evaporites are absent it is hard to distinguish this reflector from the Top MSC Unconformity, and in many areas it has likely been eroded by it. The MSC evaporite sequence itself is highly locally variable. It is composed of massive seismically transparent evaporites, documented as halite, interbedded with reflective claystone (Feng et al., 2016). As

documented by Gorini et al. (2015), the MSC evaporite interval may be divided into two megasequences; the more clastic rich lower megasequence and the more seismically transparent upper megasequence.

In much of the EMR, the lower MSC megasequence contains a consistent sequence of internal reflectors (e.g. Figure 3.32A-D). In the Herodotus Basin, the top of this sequence forms a consistent intra salt reflector that can easily be mistaken for the base of the evaporites due to the exceptionally thick evaporite body (Figure 3.32). Only with regional scale interpretations, which allow the Base MSC Unconformity to be traced from the Levantine Basin where its location is well constrained, can the true thickness of the MSC evaporite sequence be confidently resolved. This reveals that the thickness of the MSC evaporites in parts of the Herodotus Basin exceeds 4 s TWTT (Figure 3.32; Montadert et al., 2014). This is significantly more than previous interpretations for this location compiled in Lofi et al. (2011), where it is likely the intra-evaporite clastics were interpreted as the base of the MSC evaporites.

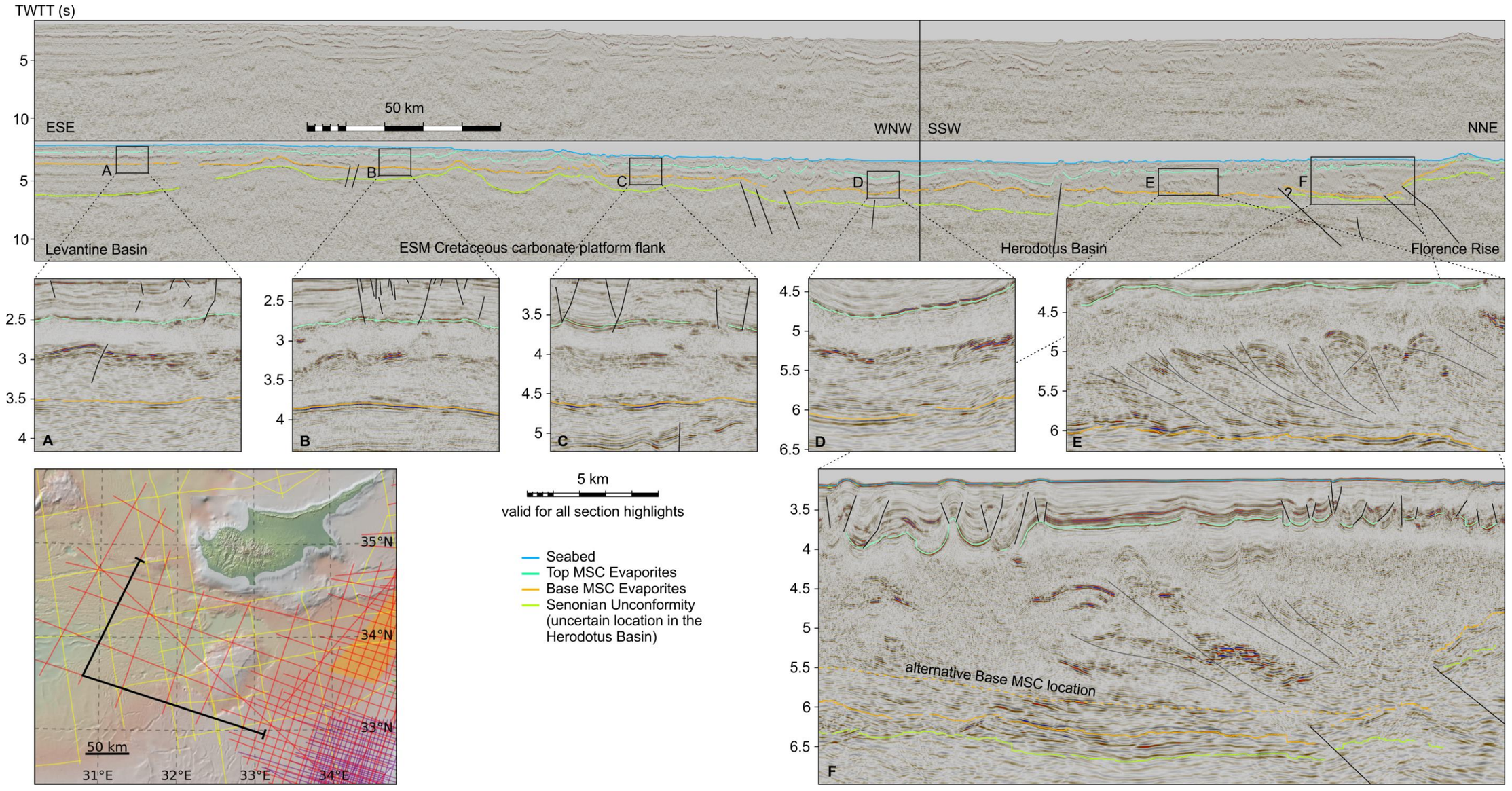

Figure 3.32-Regional composite seismic line with highlights illustrating the tracing of the MSC Evaporite sequence from the Levantine Basin (A) to the Herodotus Basin adjacent to the Cyprus Arc (F). The global relief (Ryan et al., 2009) vertical scale on the minimap is shown on Figure 1.1 and the supplementary figure.

Assuming an instantaneous velocity of 4.2 km/s for the evaporites, a lower-bound for the value from well data elsewhere in the EMR (Feng et al., 2016) and used in later depth conversions (see Section 6.4.1), indicates the evaporite sequence adjacent to the Cyprus Arc in the Herodotus Basin exceeds 4 km (also consistent with the PSDM data available to this study). This thickness was likely enhanced by a combination of basin directed flow and shortening accommodation at the Cyprus Arc (see Chapter 7). This is corroborated by significant internal deformation of the interval reflectors where it is thickened. In the Herodotus Basin the precise location of the Base of the MSC Evaporites at wavelet resolution is still uncertain, due in part to the seismic imaging difficulties associated with mobile evaporites (Section 3.2.5). In much of the Herodotus Basin very little sub-salt imaging is achieved beneath the large scale MSC diapirism (Figure 3.32). Figure 3.32D and E are rare examples of locations in the Herodotus Basin where post-MSC diapirism is absent, so the underlying packages are more clearly resolved. These examples and other equivalents mean the presence of an evaporite thickness >4 km may be assumed with confidence. This also matches with an interpretation of a MSC evaporite interval c. 4 s TWTT thick in the Herodotus Basin west of the Nile Cone, outside the EMR (Lofi et al., 2011). An evaporite thickness of 4 km equates to a deposition rate of ~6 mm/yr for the c. 650 kyr duration of the MSC (Krijgsman et al., 1999; Manzi et al., 2013) although this does not consider any thickening from salt flow (see Chapter 7).

Over the southern portion of the Cyprus Arc, the MSC evaporites are largely free of internal reflectors (see Tartus Basin on Figure 3.14A and figs. of seismic in Chapter 5). This may be because they represent only the upper megasequence, however both megasequences appear in the Latakia Basin to the north and Levantine Basin to the south (Figure 3.14A). This suggests that the palaeo-bathymetric highs of the Larnaca ridge to the north, and Latakia and Tartus Ridges to the south, partitioned the intermediate minibasins from the sources of clastic sediments that form the internal reflectors.

Erosion by the Base MSC Unconformity beneath the MSC evaporites may be observed in several locations:

- At the peak of anticlines, thrusts and (relatively) uplifted fault blocks offshore Lebanon (Ghalayini et al., 2016, 2014).
- Around thrusts of the Latakia Ridge (see Figure 5.13A).
- A channel in the south Levantine Basin (Figure 3.24).

Submarine erosion could explain the erosion at the Latakia Ridge and the channel. However, much of the erosion documented by Ghalayini et al. (2014, 2016) offshore Lebanon defy a submarine explation. This is because the erosion only occurs in locations where there would have been palaeo-relief highs, and some of the erosion has occurred at features with very shallow slopes to the highs.

There is some controversy as to the timing of deformation of the MSC evaporites in the Levantine Basin. Truncation by the top MSC unconformity of reflectors within the MSC evaporite sequence has led some authors to suggest there was an intra-MSC deformation event, whilst others suggest the truncations are strain-induced (Section 2.6.9). The following paragraphs explore this.

The 3D seismic data available to this study clearly images internal deformation of the MSC interval. Interpretation of some of these internal reflectors reveals innumerable folds that are asymmetric, non-cylindrical, horizontally inclined and commonly isoclinal (Figure 3.33). Generally, the larger the folds the more open they are, with parasitic folds appearing on the larger folds (Figure 3.33A). There may be some fault displacement along many of the fold axes, and many of the smaller features marked as folds here could be interpreted as faults instead of folds (Figure 3.33A). However, the smallest folds that may be interpreted as such because of a seismically resolved short limb between the displaced long limbs, are small enough that the short limb is on the limits of seismic resolution (Figure 3.33A). The largest features that could alternatively be interpreted as faults instead of folds are small enough that if they are folds then the small limb is below seismic resolution (Figure 3.33A). As the larger folds will have formed from equivalent smaller folds, and in conjunction with the previous points, it may be concluded that the overwhelming majority of the observed features have primarily accommodated shortening through ductile folding, as opposed to brittle faulting. This is corroborated by three points:

1) The low mechanical strength of the materials involved: evaporites and clays.
2) As the overturned limbs of the inclined tight to isoclinal folds are steeply dipping, this reduces their seismic expression and consequently the short limb is often poorly imaged, and may therefore sometimes be un-resolved on seismic data. This could make folds appear as faults.
3) The apparent proportional relationship between accommodation of displacement on the folds, and angle between the limbs of the folds, suggests that as the larger folds have grown from smaller ones then the smallest examples should have isoclinal to parallel limbs, which would reduce their seismic expression. This could contribute to folds appearing as faults.

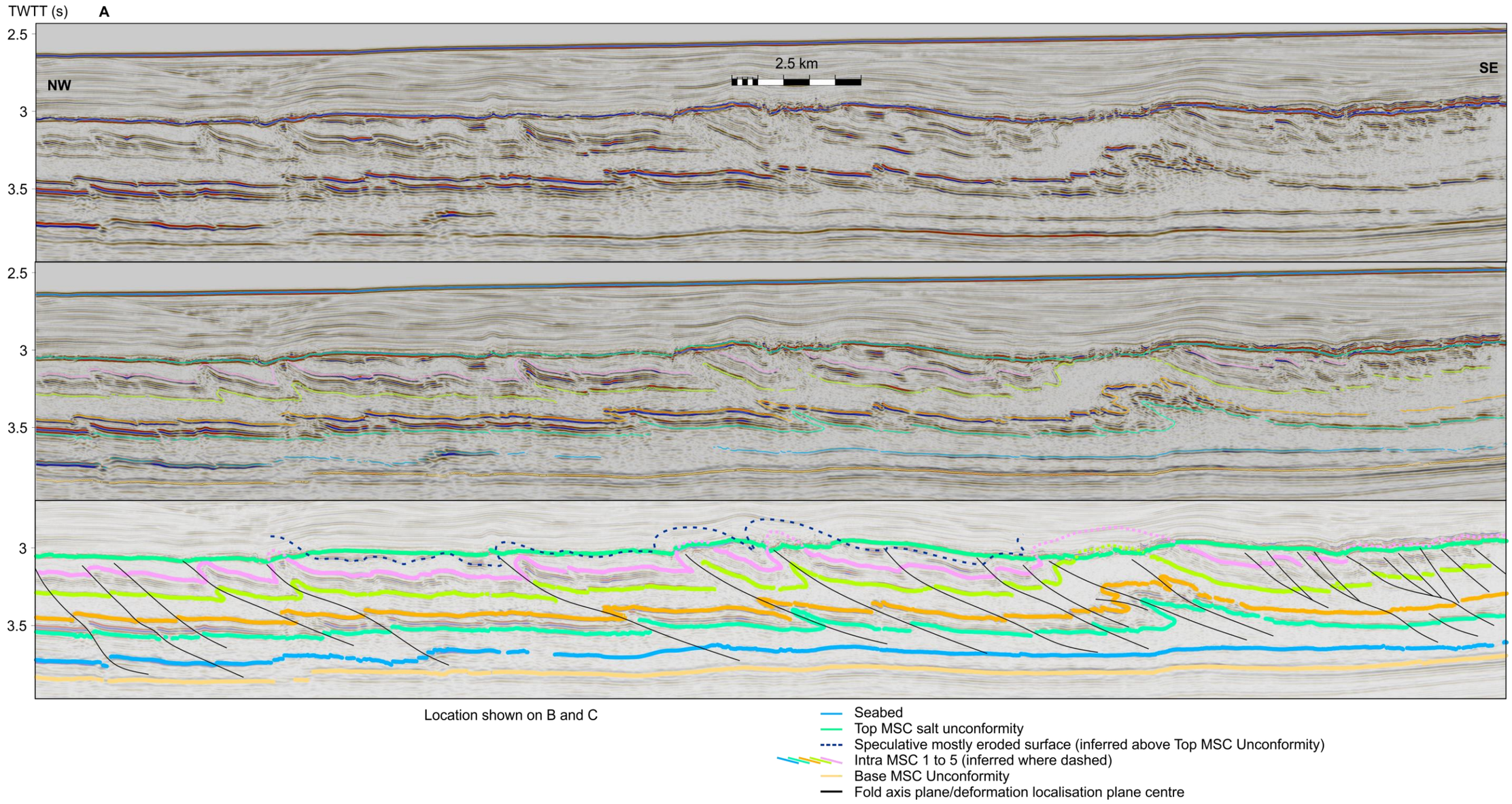

Figure 3.33-A) Seismic line showing folded and thrusted reflectors internal to the MSC interval and truncation of upper internal reflectors by the Top MSC unconformity. Some inferred horizons, had they not been eroded, are marked. B-F) 3D interpretations of some of the internal MSC reflectors. This are shown as interpretations as opposed to surfaces to illustrate where they are absent. The global relief (Ryan et al., 2009) vertical scale on the minimap is shown on Figure 1.1 and the supplementary figure.

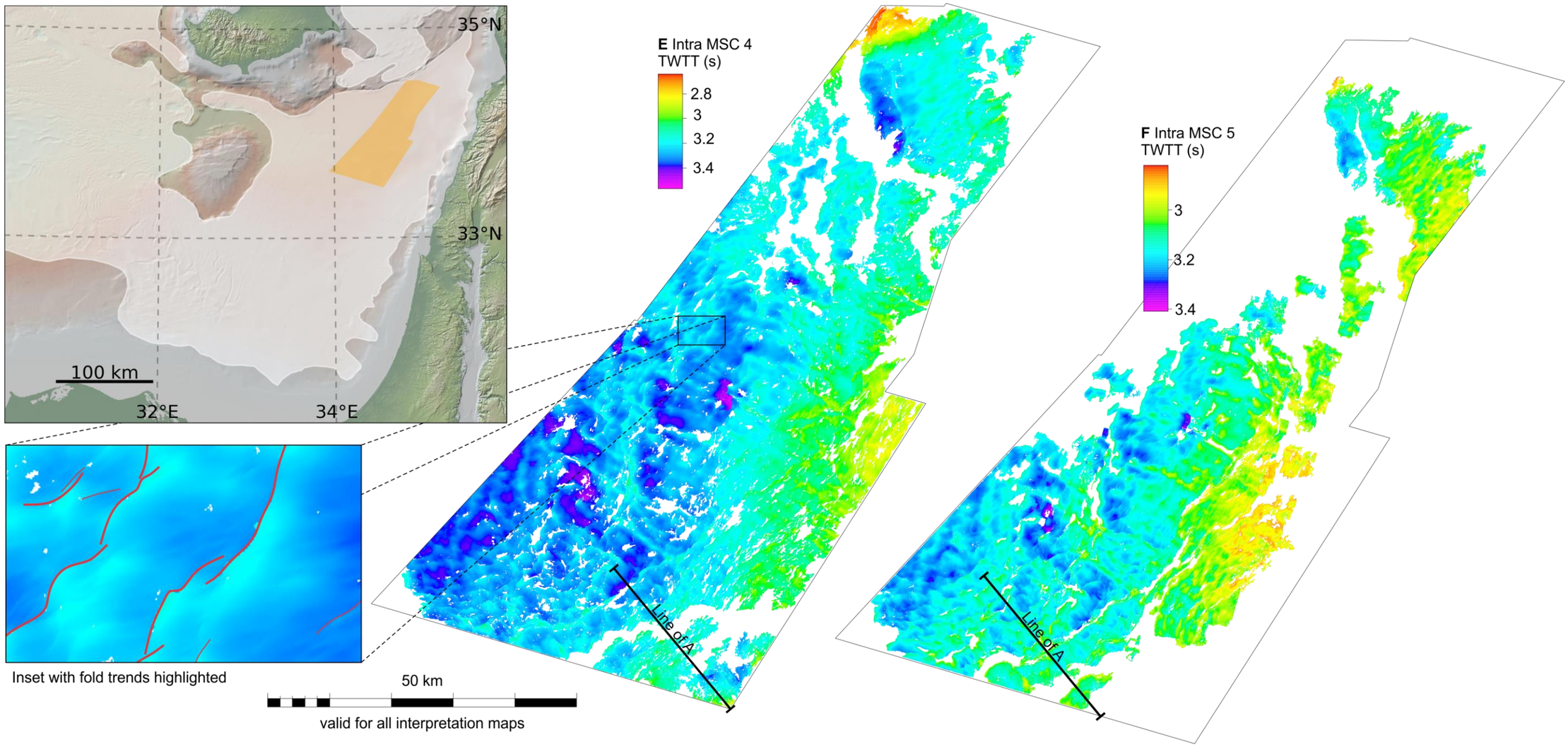
35°N
33°N
100 km
32°E
34°E
E Intra MSC 4
TWTT (s)
2.8
3
3.2
3.4
F Intra MSC 5
TWTT (s)
3
3.2
3.4
Line of A
Line of A
Inset with fold trends highlighted
50 km
valid for all interpretation maps

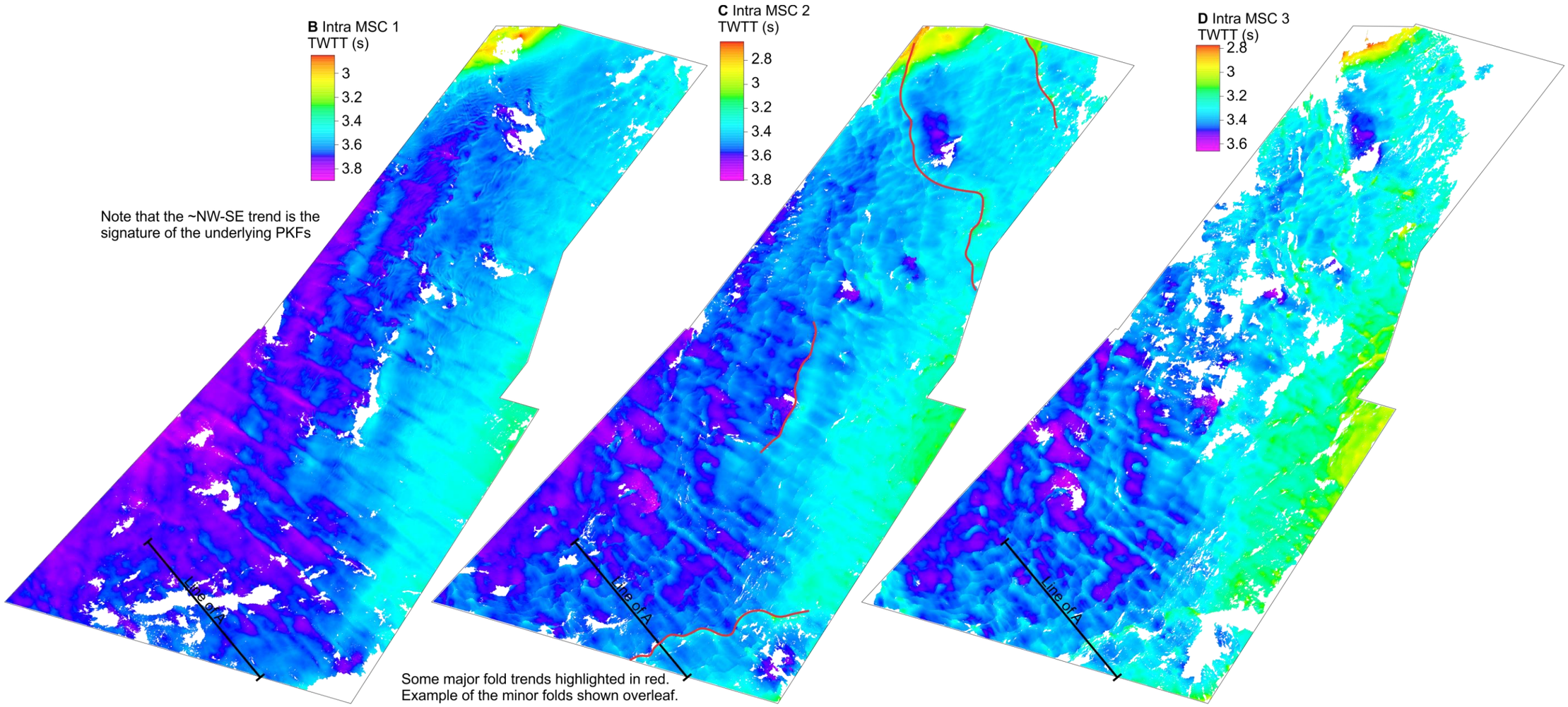
B Intra MSC 1
TWTT (s)
3
3.2
3.4
3.6
3.8
C Intra MSC 2
TWTT (s)
2.8
3
3.2
3.4
3.6
3.8
D Intra MSC 3
TWTT (s)
2.8
3
3.2
3.4
3.6
Note that the ~NW-SE trend is the signature of the underlying PKFs
Line of A
Line of A
Line of A
Some major fold trends highlighted in red.
Example of the minor folds shown overleaf.

In many locations, but especially where elevated by folding, the internal reflectors are truncated by the Top MSC surface (Figure 3.33A, E, F). This occurs right across the dataset, as demonstrated by the absence of some of the interpreted horizons for large areas of the dataset (Figure 3.33E, F). In some locations >200 ms TWTT of un-deformed (at that point) MSC sequence appears above the most elevated intra-MSC horizon shown in Figure 3.33, demonstrating significant erosion has taken place above the MSC sequence.

Because of the points outlined in this subsection, it may be confidently concluded that an episode of halokinetic deformation occurred during the MSC. This rejects the contrary assertion of Allen at al. (2016) and concurs with the earlier conclusions of Bertoni and Cartwright (2007) and Gvirtzman et al. (2013). The sequence of internal reflectors is subparallel where not folded, indicating that deposition of the sequence took place in stable conditions, before the halokinetic episode at the end of the MSC. The deformation indicates this halokinesis was likely downslope translation.

The MSC interval has also been subject to post MSC gliding and spreading. This is described and investigated in Chapter 7.

3.7.2 Post-Evaporite Deposition Interval

Erosional truncation of the top of the evaporite sequence (see previous section) demonstrates significant sea-level drawn down at the end of the MSC evaporite sequence. In much of the EMR, the unconformity at the top of the MSC evaporite sequence is overlain by an interval with several properties that distinguishes it from the rest of the post-MSC evaporite sequence (Figure 3.34). This interval is generally higher in amplitude, but with less laterally continuous amplitudes and reflectors, and in some locations it is unconformable with the overlying sediments (Figure 3.34). It thins to below seismic resolution in much of the deep basin, but reaches >200 ms TWTT thickness where significant end-of-MSC topography existed, such as the Levant Margin and the Cyprus Arc (Figure 3.34). These characteristics indicates that it is likely to be a clastic rich interval deposited during a sea level draw down event that saw depocentres shifting basinward. Locations where unconformities can be resolved at both the top of the evaporites, and top of the clastic rich interval attest to erosive events, possibly with complete desiccation of the Mediterranean Sea in the Levantine Basin, at both the initiation and end of this end-MSC draw down event (Figure 3.34C).

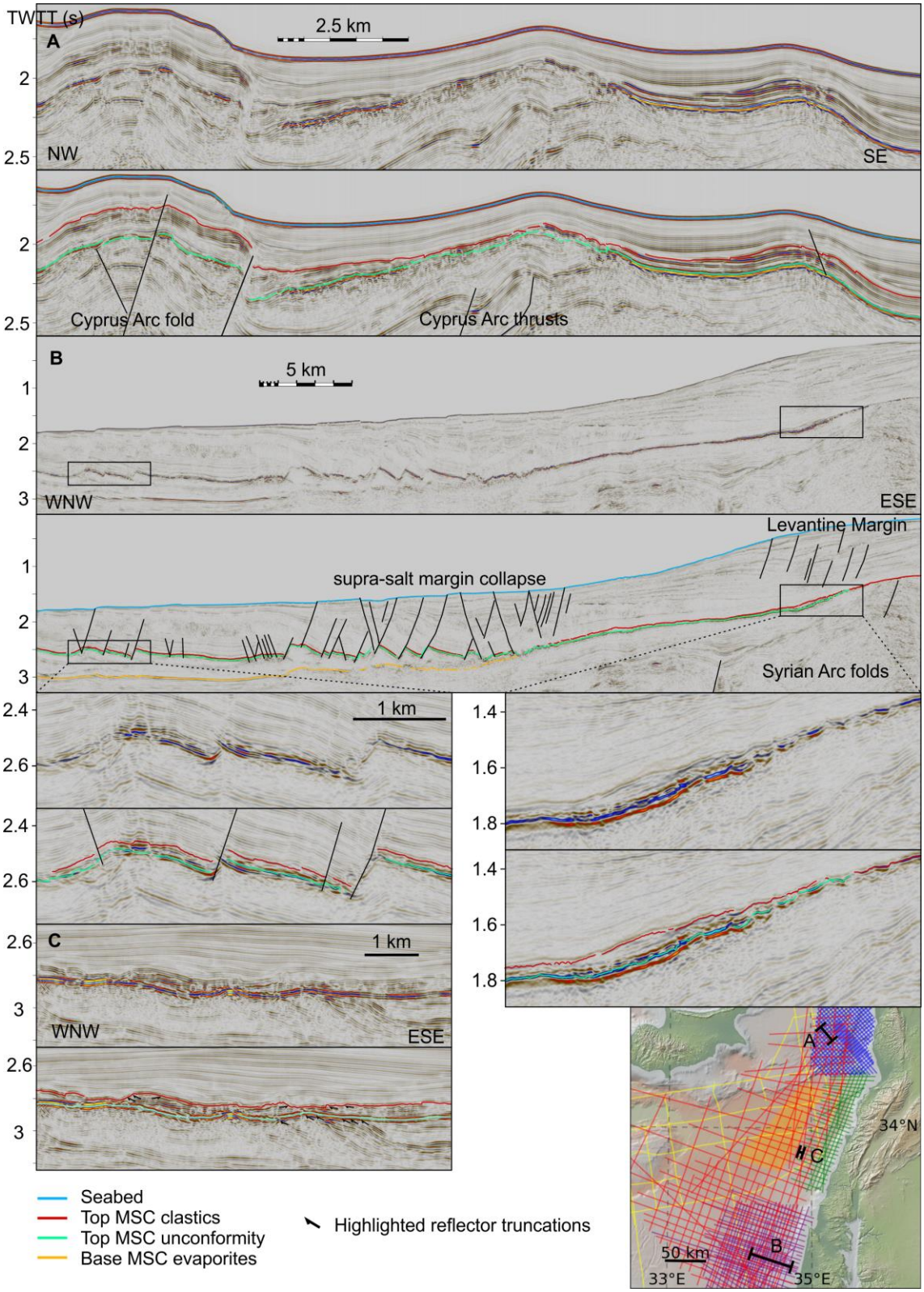

Figure 3.34-Seismic lines demonstrating the clastic interval deposited at the end of the MSC. The global relief (Ryan et al., 2009) vertical scale on the minimap is shown on Figure 1.1 and the supplementary figure.

Combined with the erosion at the start of the MSC (Section 3.7.1), this demonstrates drawdown of the sea level at both the start and end of the MSC. Claystone horizons, an absence of further unconformities within the MSC evaporites, and parallel (pre-halokinesis) intra salt reflectors demonstrates that the basin returned to a sub-marine state between these drawdown events.

3.7.3 Thinned Skinned Salt Tectonics

The basin-wide occurrence of mobile MSC evaporites (Figure 3.12) has resulted in widespread salt tectonics that has deformed the overlying sediments (Figure 2.28). This process has caused much of the deformation observable on the bathymetry across much of the EMR (Section 2.5.5). Because this salt deformation is thin-skinned caution is required when interpreting thick-skinned tectonic features from bathymetry. This pitfall has caused authors to make interpretations that seismic later shows to be incorrect in several places in the EMR, including the ESM moat (see Section 7.1.1), the Larnaca Ridge (Section 3.6.1), Nile cone translation (see Section 4.2), and Herodotus Basin seafloor buckling (Section 3.6.7).

An additional complication of the evaporite deformation is the tendency for halokinesis to localise above features that perturb the base of the salt body (Reiche et al., 2014a). More convoluted raypaths results in reduced clarity in the seismic images of the structures perturbing the base of the salt. This introduces interpretation challenges when investigating the EMR, and in many cases the perturbing features are key structures in this investigation (see Section 4.5, Chapter 5 and Section 6.2).

Another issue with the localisation of stresses associated with the MSC evaporite sequence is its potential ability to mask underlying deformation. This is most clearly seen in the Antalya Basin, where the MSC evaporite sequence covers significant deformation that has uplifted the base of evaporite sequence since the MSC (Figure 3.35).

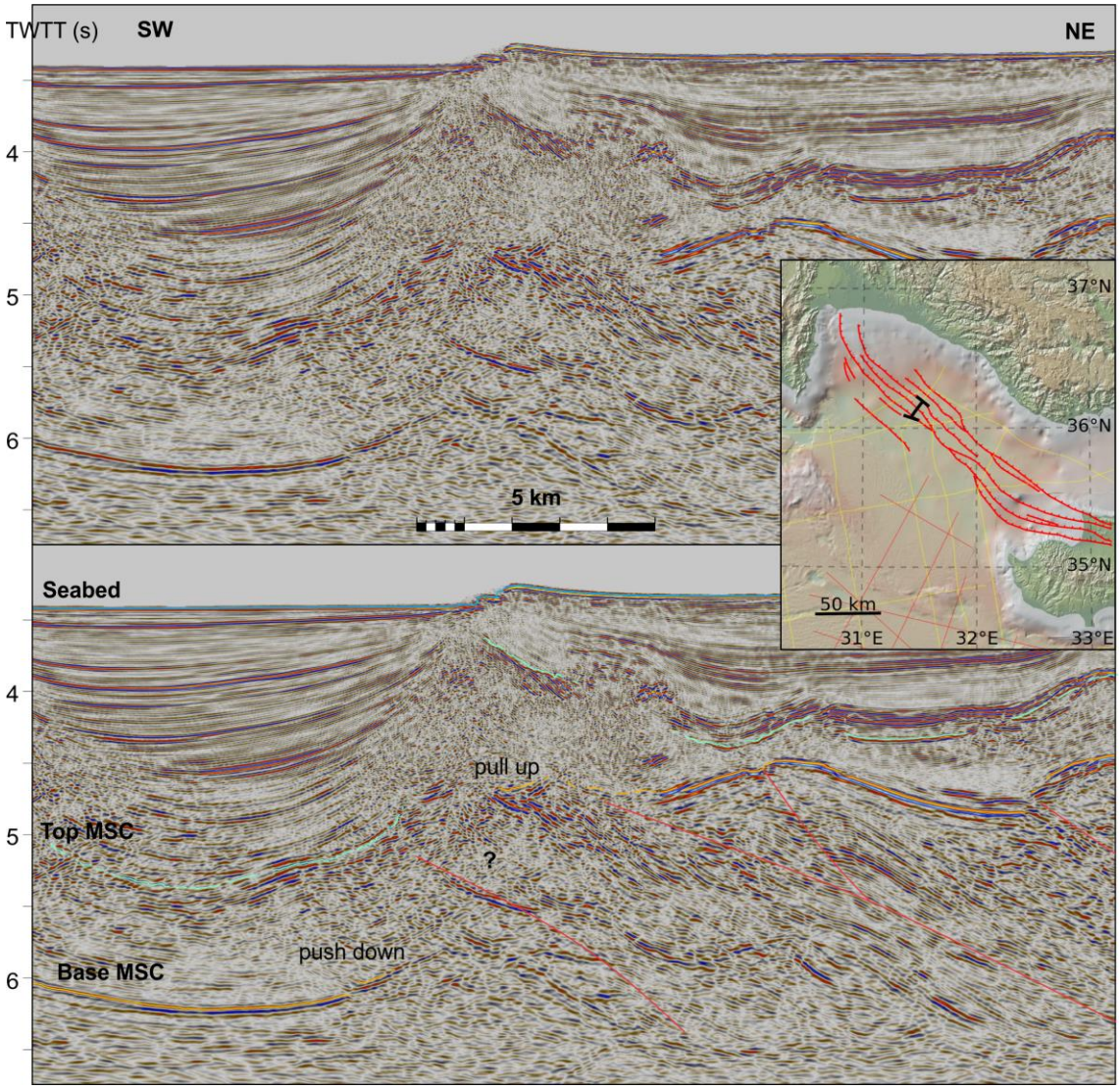

Figure 3.35-Seismic line showing how strain partitioning by the MSC evaporites has resulted in a relatively small bathymetric expression of a relatively large amount of sub-MSC deformation. Note that as the seismic line is in time seismic pull up from thickened salt and push down from thickened sediment has enhanced the apparent elevation change in the Base MSC horizon (Section 3.2.5). The global relief (Ryan et al., 2009) vertical scale on the minimap is shown on Figure 1.1 and the supplementary figure.

3.7.4 Distribution of Diapirism

Here the term 'diapirism' refers to the general vertical perturbation of the top of the salt body by halokinetic processes, including diapirs, salt anticlines, pillowing, salt rollers etc. Across the EMR some areas have been subject to diapiric halokinesis, whilst other areas have very minor deformation of supra-salt sediments (Figure 3.31). The proclivity towards diapirism in the deeper portions of the basins is perhaps intuitive, as the deep basin setting is conducive to deposition of thick salt and thick overburden. The more extreme geostatic pressures from these thicker sediments then results in diapirism. However, there are also thicknesses of salt and overburden that seem to produce diapirism in some areas but not others (Figure 3.36).

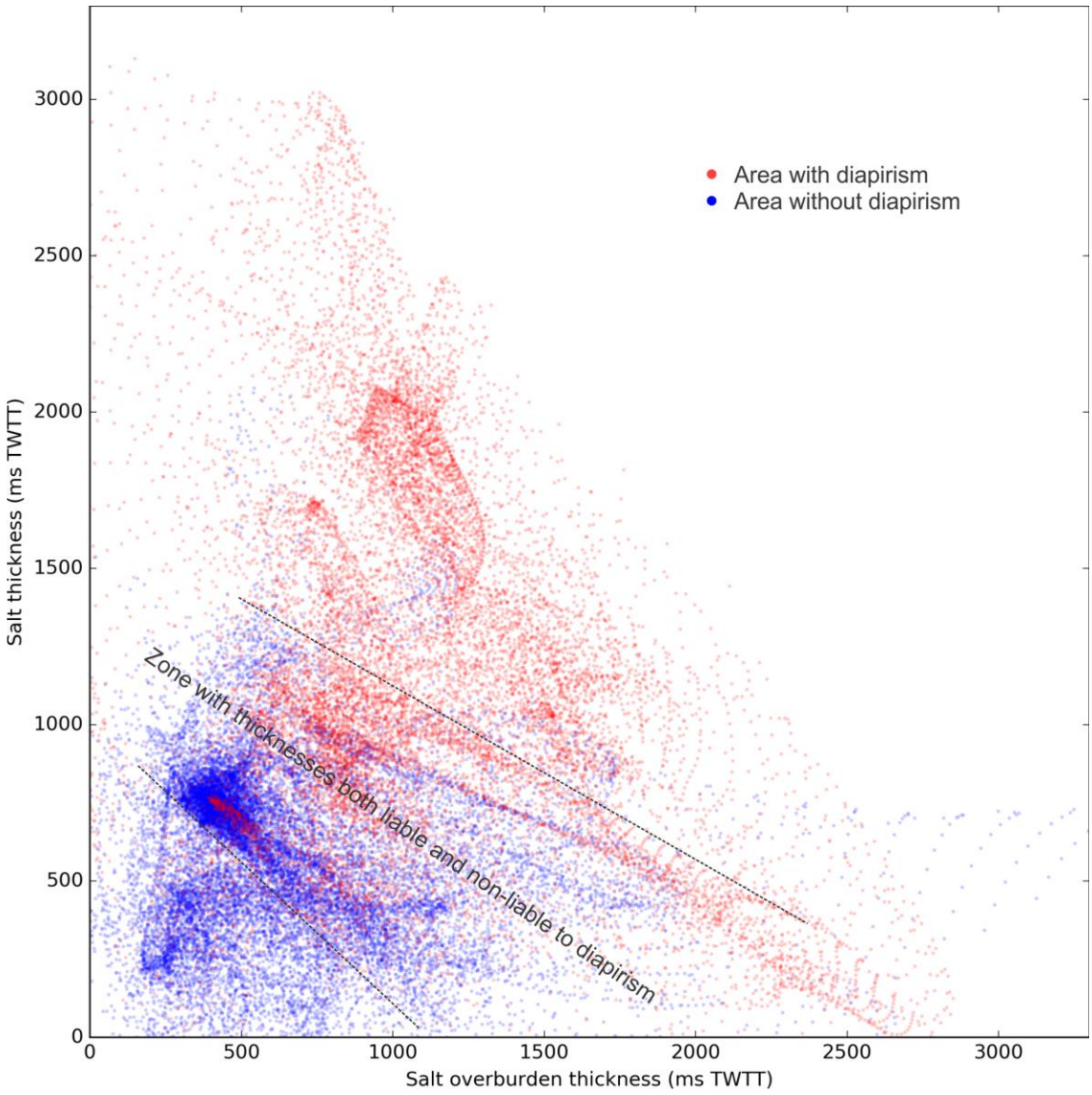

Figure 3.36-Graph showing the thickness of MSC salt plotted against the thickness of the overburden at the same location (note thicknesses are in TWTT). The wide spread of the points in diapiric areas can be attributed to the diapirs themselves and intermediate minibasins.

The main example of this may be observed offshore Lebanon. Here the salt body is consistently thick relative to its margin proximity (Figure 3.37A), and the overburden is 0.6-0.8 s TWTT thick (Figure 3.37B), but diapirism only occurs in two areas (Figure 3.31; Figure 3.37A). The near-shore diapirism could be attributed to the thicker overburden from the proximity to sediment supply, but an explanation for the area of salt pillowing to the west is less obvious. A possible explanation for this variance becomes apparent if one considers the relationship between these two areas of diapirism.

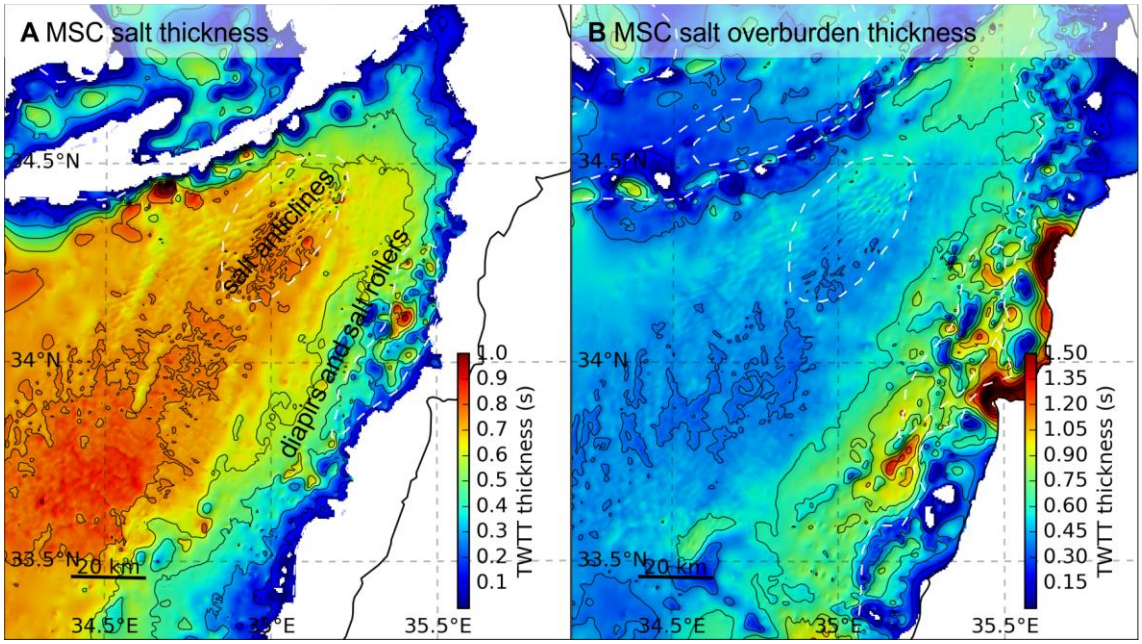

Figure 3.37-Maps showing thickness of the MSC salt body (A) and its overburden (B) offshore Lebanon, with areas of diapirism and salt body outline highlighted by the white dashed lines.

The near-shore diapirism variably forms diapirism with normally faulted crests (Figure 3.38B). Additionally, there are widespread salt rollers along the whole of the Levant Margin. The salt anticlines that almost exclusively form the more basinward diapirs offshore Lebanon strike perpendicularly to the direction of the near-shore diapirism (Figure 3.38A). It may therefore be concluded that translation of the supra-salt sediment has occurred in this location, forming extensional diapirism upslope and contractional diapirism downslope. Once morphological variations in the salt body had formed due to these processes, the diapiric processes would have likely exploited or exacerbated them.

The localisation of this deformation is likely linked to the morphology of the base of the salt body. Inversion structures in the Base MSC unconformity, associated with compression along the margin (Section 6.3), produce relief which may be hypothesised to focus halokinesis (Figure 3.38). This could then lead to diapirism, which could have exacerbated extensional faulting along the Levant margin, enhancing basin-directed supra-salt sediment translation. Note that the oblique normal fault marked on Figure 3.38 is atypical for this deformation.

The suggested direction of this down-slope translation is consistent with previous studies of supra-salt translation related deformation in the Southern Levantine Basin (Figure 2.28; Gvirtzman et al., 2015).

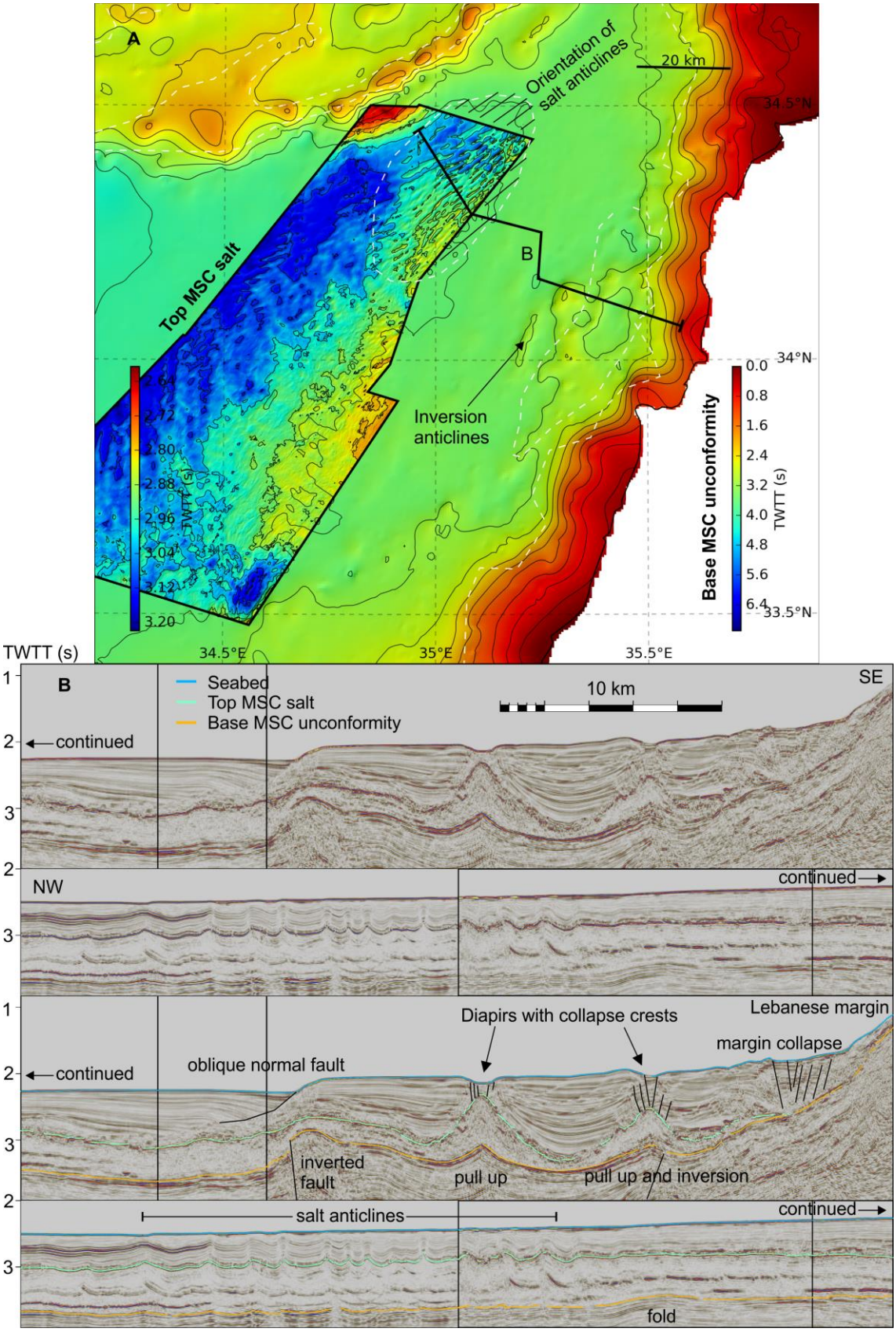

Figure 3.38-A) Map of the top and base of the MSC evaporite body, and B) seismic line across the Lebanese diapirism, with features discussed in the text annotated.

Chapter 4 The Sinai-Levantine Crustal Promontory

4.1 Introduction

The Sinai Plate as described in the literature is a sub-plate at the NE corner of the African Plate (Figure 4.1; Section 2.2; Badawy and Horvath, 1999; Ben-Menahem et al., 1976; Bosworth and McClay, 2001; Gvirtzman and Steinberg, 2012; Le Beon et al., 2008; Mahmoud et al., 2005; Mascle et al., 2000; Nocquet, 2012; Reilinger et al., 2006; Salamon et al., 2003; Schattner and Lazar, 2014; Wdowinski et al., 2006). Its SE limits are the most clearly defined since they effectively bound the two sides of the Sinai Peninsula, where the Gulfs of Suez and Aqaba form a clear crustal scale rift to the west and strike-slip transcurrent fault to the east respectively (Figure 4.1). Divergence of the Sinai Sub-Plate (and the then adjoined Arabian Plate) from the African Plate occurred in the late Oligocene to late-middle Miocene with the rifting of the Gulf of Suez (Bosworth and McClay, 2001). This rifting ceased before spreading had initiated in the Gulf of Suez. Thus, as the Sinai Plate continental crust is still contiguous with the African plate continental crust, albeit via a section of thinned faulted crust, there is an argument that considering the Sinai Plate as a separate entity to the African Plate is erroneous. Instead, it may be argued that it would be better considered a component part of the African Plate. This is corroborated by the fact that contiguous continental crust separated by a failed rift is not considered a plate boundary in other locations, such as in the North Sea (Ziegler, 1978).

However, this poses (or exposes) a problem with how to define a tectonic plate. Some widely accepted plates do not have a contrasting change in crustal type along any of their boundaries, such as the Juan de Fuca and Nazca Plates. Requiring a change in crustal type would also mean that during rifting the separating ‘plates’ should be considered a single plate. Oceanic spreading on at least one portion of the plate boundary might then provide an alternative defining attribute, however this would mean Plates such as the Anatolian and Aegean lose their definition as tectonic plates. Currently active movement, or a trend in seismicity, is a convenient definition for neotectonics, but does not lend itself to studies of past tectonics. There are other possible alternative definitions, including minimum plate size and minimum rate or absolute amount of convergence or divergence.

Ultimately however, the internal deformation within plates and scaling concept of what may be readily considered a single tectonic entity means this is a semantic issue. As is the case with the Sinai Plate, it is convenient and lends clarity to have a label for the concept of a crustal scale unit that can be considered to move as a single entity relative to another crustal scale unit. Consequently, the Sinai Plate is referred to as such in this study. It should be noted however, that the ‘Sinai Plate’ could also be correctly considered a partially rifted crustal promontory of the African Plate. This is in line with some earlier work (Badawy and Horvath, 1999; Ben-Menahem et al., 1976).

Separation of the Sinai Plate from the Arabian Plate occurred in the Miocene with the formation of the LSZ (Freund et al., 1970; Quennell, 1984). The Gulf of Suez and LSZ limits of the Sinai Plate are undisputed, as they are unambiguously defined geophysically and topographically

(Figure 2.1), and demonstrate continuous seismic activity without widespread new deformation (Le Beon et al., 2008). In contrast, definition of the other limits of the Sinai Plate are controversial (Figure 4.1). By review of literature, critical analysis of the hypothesised boundaries within their wider tectonic environment, and interpretation of seismic data this chapter aims to resolve some of these controversies. Different hypothesised limits are shown in Figure 4.1 and are described later in this Section, before their appraisal is carried out in subsequent Sections. The discussion encompasses the crustal type around the subject Sinai Plate limits. More clear resolution of the plate boundaries beneath the EMR aids the later investigation of deformation in the overlying stratigraphy.

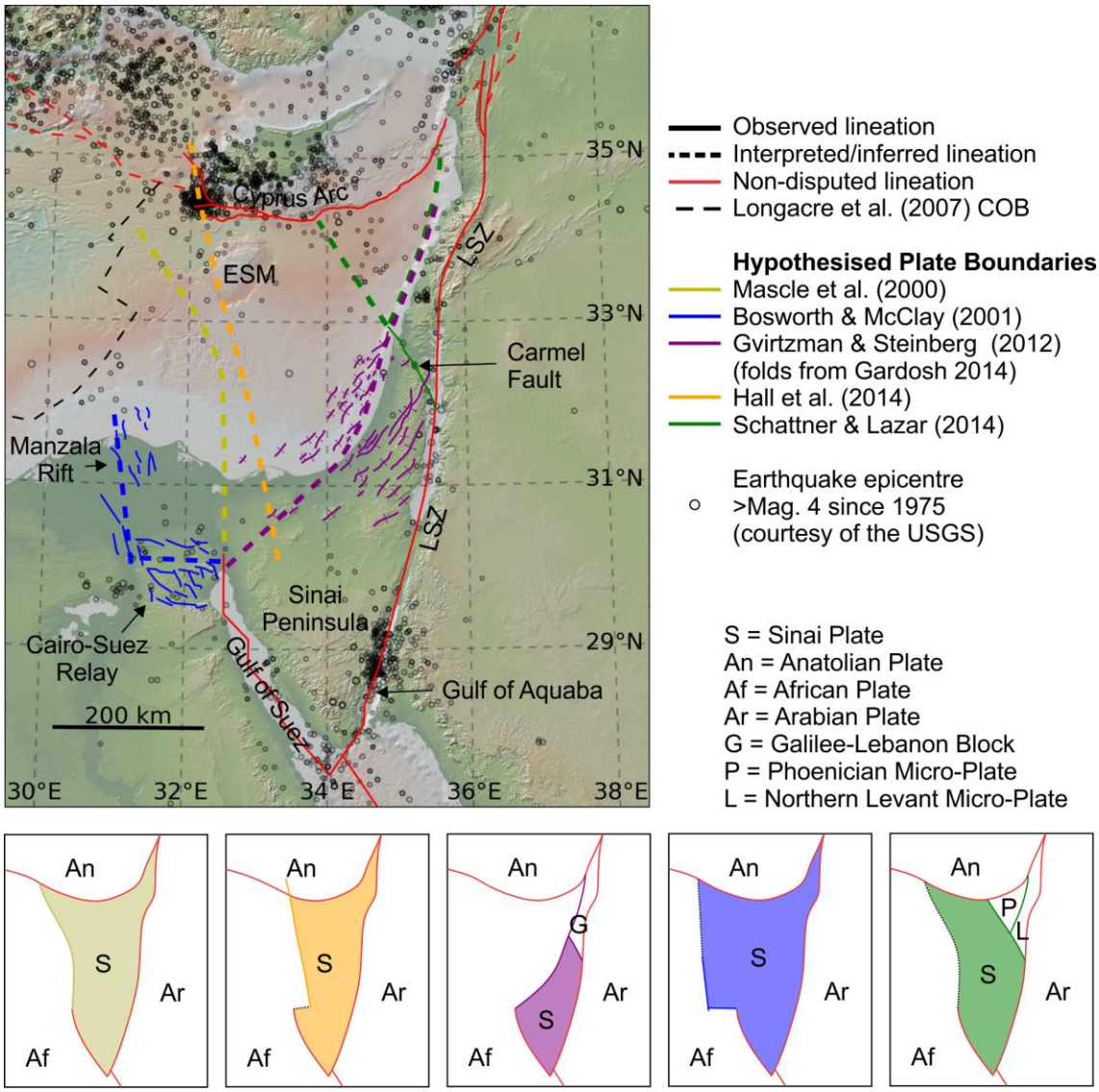

Figure 4.1-Map showing the hypothesised boundaries of the Sinai Plate, discussed in the text. The global relief (Ryan et al., 2009) vertical scale on the main map is shown on Figure 1.1 and the supplementary figure.

The LSZ and its southern marine extension, the Gulf of Aqaba, form the western edge of the Arabian Plate (Figure 4.1). It is unanimously accepted this is also the eastern edge of the Sinai Plate (Figure 4.1). The southern limit of at least part of the Cyprus Arc is also widely accepted as forming the northern edge of the Sinai Plate (Figure 4.1).

The most uncertain limit of the Sinai Plate is its western edge north of the Gulf of Suez, as there is no clear topographic or geophysical break extending from the end of the Gulf (Bosworth and McClay, 2001; Steckler and Brink, 1986). Steckler and Brink (1986) suggest that heterogeneous lithosphere strength contributed to the northward termination of the Gulf of Suez faults. When the Sinai Plate was delineated by Mascle et al. (2000) its western edge was drawn as the northward continuation of the trend of the Gulf of Suez until it joined with the Cyprus Arc boundary NW of the ESM. This interpretation, or slight variations thereof, is the limits of the Sinai Plate most commonly drawn in published literature (Eppelbaum and Katz, 2015; Mahmoud et al., 2005; Nocquet, 2012; Reilinger et al., 2006; Wdowinski et al., 2006). An extreme variation of this is that by Hall et al. (2014), who draw a linear join between the plate boundary at the gulf of Suez and the seismogenically underlain bathymetric escarpment west of Cyprus (Figure 4.1). This escarpment has been previously interpreted as part of the Cyprus Arc plate boundary on the basis of seismological data (Papazachos and Papaioannou, 1999). By making this linear join the plate boundary of Hall et al. (2014) transects the western edge of the ESM.

Two Sinai Plate boundaries have been postulated that reactivate structures that are part of the Syrian Arc deformation belt (Section 2.3.3). Gvirtzman and Steinberg (2012) suggest that Syrian Arc folds of north Sinai accommodated transform boundary during the opening of the Gulf of Suez, and that the northward continuation of this is the continental margin of the Levant (Figure 4.1). Bosworth & McClay (2001) postulate that the rift extension is transferred from the termination of the Gulf of Suez to the early Miocene Manzala rift via a set of faults termed the Cairo-Suez relay (Figure 4.1), which were previously reactivated as part of the Syrian Arc.

Almost all the hypothesised Sinai Plate limits draw its boundaries as extending north to the join between the LSZ and southern limit of the Cyprus Arc. However, Gvirtzman and Steinberg (2012) limit the Sinai Plate by Syrian Arc Folds of northern Sinai and the Carmel Fault, and Schattner & Lazar (2014) contend that the Carmel Fault is a plate boundary triple junction, with the Sinai Plate to the south of the Carmel Fault boundary and further microplates to the north (Figure 4.1).

4.2 Initial Assessment of Hypotheses

The west Sinai Plate margin, as interpreted by Mascle et al. (2000), was largely based on bathymetry and supra-salt seismic reflectors. However, the lineation that was picked out has since been shown to be thin-skinned and is attributed to gravity spreading of the supra-salt sediments due to differential loading of the Nile cone (Loncke et al., 2006; Skiple et al., 2012). The seismic data available to this study concurs with this thin-skinned interpretation (Figure 3.14B; Chapter 3). No deformation is observed on the ESM that could correspond to its transection by a plate boundary (Chapter 3), as drawn by Hall et al. (2014). It is probable that plate boundaries that are drawn as transecting the ESM, or follow trends that do not align with the Gulf of Suez, are intended as approximate illustrations.

No rift faults are observed in the relevant onshore or offshore portions of Egypt and the Nile Cone that could represent a continuation of the Gulf of Suez rift directly northward (Bosworth et al., 2005; Moustafa and Khalil, 1995; Moustafa et al., 2014; Steckler et al., 1998; Steckler and Brink,

1986; The Egyptian Geological Survey, 1981). This observation is discordant with the plate boundary of Mascle at al. (2000). Thus, many of the Sinai Plate boundaries drawn in the literature are demonstrably inaccurate. Although the Gulf of Suez is a north-tapering rift, at its northern limit there is still >30 km of separation between the rift flanks. Even allowing for significant ductile plate deformation, to circumvent a space problem accommodation of the rift offsets observable in the Gulf of Suez requires a transform feature perpendicular to the end of the rift. This may be on faults to the west of the Gulf of Suez, called the Cairo-Suez relay, as hypothesised by Bosworth & McClay (2001), or to the east of the Gulf of Suez on folds of the Syrian Arc in northern Sinai as hypothesised by Gvirtzman & Steinberg (2012). These possibilities are discussed in Sections 4.3 and 4.4 respectively.

Schattner & Lazar (2014) interpret a pair of microplates between the Cyprus Arc and LSZ (Figure 4.1) on the basis of gravity, magnetic, GPS and stress modelling data. They suggest that they have formed since the Pliocene when subduction cessation at the Cyprus Arc meant the accommodation of differential plate motion shifted to reactivation of the Levant margin. However, 3D seismic data from the Northern Levantine Basin reveals no deformation trend that demonstrates these plate boundaries (Figure 4.2). The Carmel fault has also been postulated to provide a pathway for displacement on the LSZ, but this was rejected by a study reviewing pertinent 3D seismic data not available to this study (Ghalayini et al., 2014). This backs up the argument that this Sinai Plate boundary may be discounted.

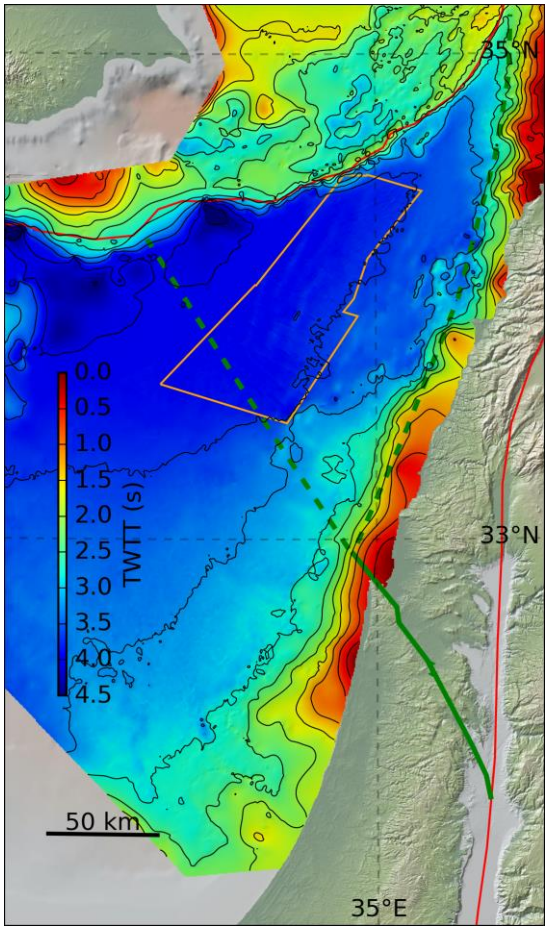

Figure 4.2-Sinai Plate boundary hypothesised by Schattner & Lazar (2014; green lines) overlaid on the Base MSC Unconformity TWTT surface interpreted by this study. The LEB3D survey is outlined

in orange to highlight the lack of a deformation trend that follows the hypothesised Sinai Plate boundary. The global relief (Ryan et al., 2009) vertical scale is shown on Figure 1.1 and the supplementary figure.

4.3 Syrian Arc Folds Transform Motion

Gvirtzman & Steinberg (2012) suggest that the ~10 km of displacement at the Gulf of Suez may be accommodated by transform reactivation of the folds of the Syrian Arc (Figure 4.3). They interpret a component of strike-slip motion in folds observable in seismic data offshore Israel, an interpretation mirrored in a later study by Marlow (2014). The published interpretations of Gvirtzman & Steinberg (2012) do not illustrate any features that are definitively strike-slip, such as deformation systems with contemporaneous, proximal and opposing σ1 and σ3. Therefore the features they interpret may be explained more simply by convergent motion, as was interpreted by earlier studies of the same data (Gardosh et al., 2011, 2008a, 2008b). The interpretations made by this study, on the same seismic data, do not find any evidence of deformation best explained by transform motion as opposed to convergent (Section 3.6.5).

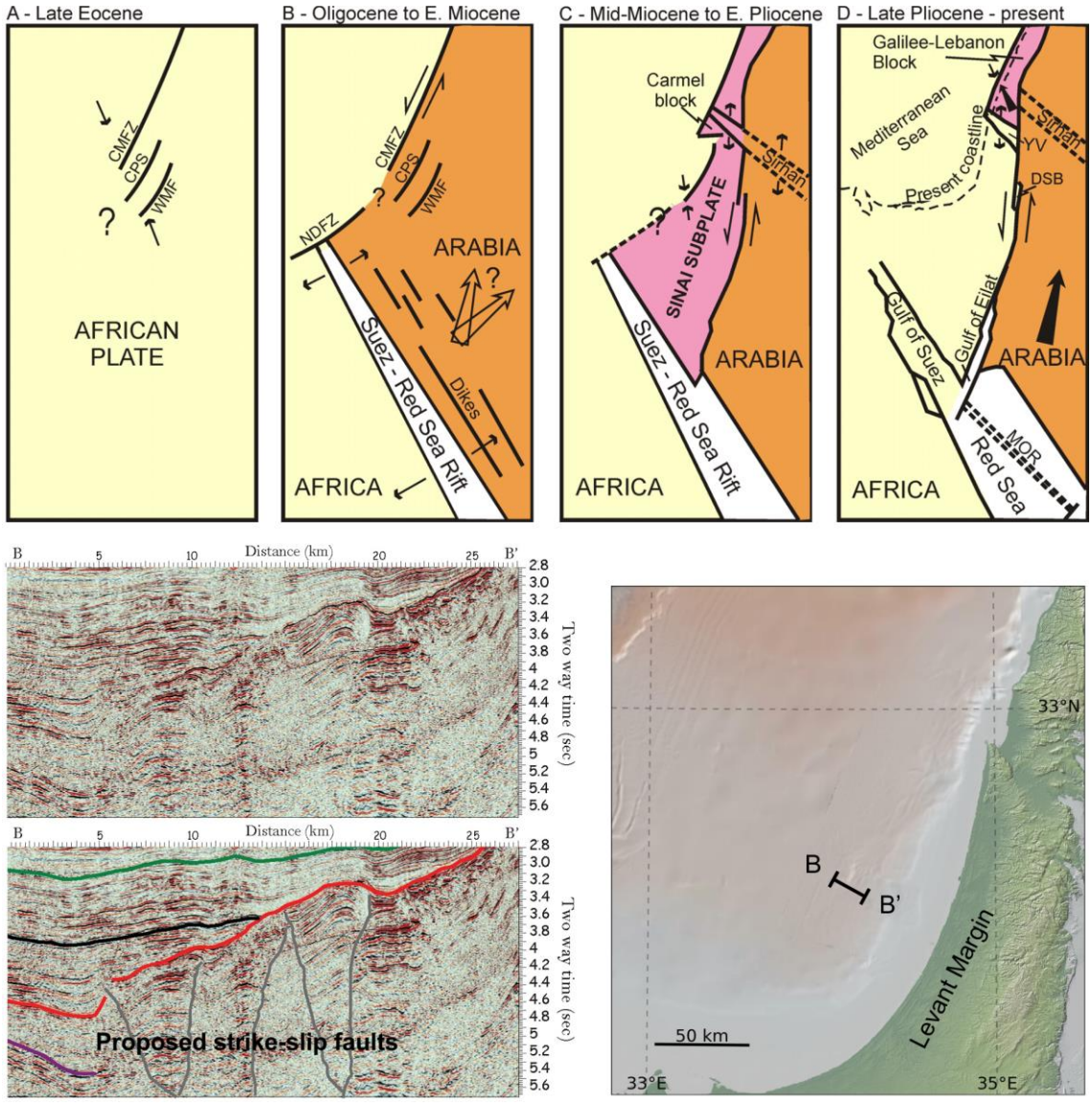

Figure 4.3-Formation of the Sinai sub-Plate boundaries via inland jump of the Arabian northwest Plate boundary (Gvirtzman and Steinberg, 2012). Colours indicate separately deforming plates.

CMFZ-Continental margin fault Zone; CPS-Coastal plain step; WMF-west (Judea) mountain front; NDFZ-Nile Delta Flexure Zone. The global relief (Ryan et al., 2009) vertical scale on the minimap is shown on Figure 1.1 and the supplementary figure.

On the Sinai Plate, the Sinai Hinge Belt (and Themed Fault) is documented as being dextrally and not sinistrally reactivated during the rifting of the Gulf of Suez (Figure 4.4). If the hypothesis of Gvirtzman & Steinberg (2012) had occurred this would require the stress fields on these two proximal features to be in opposition during the Miocene.

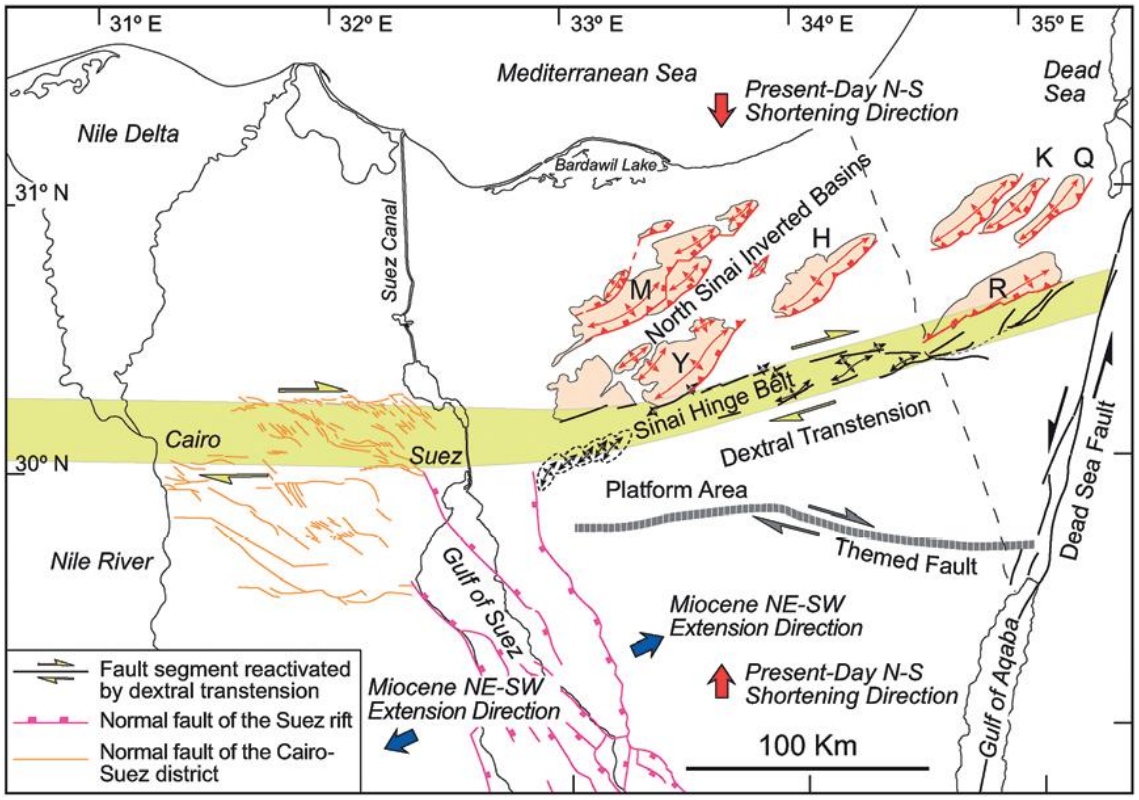

Figure 4.4-Map showing deformation in north Sinai since the Early Miocene (Moustafa et al., 2014).

If the Syrian-Arc folds were reactivated with transform motion and the continental margin of the Levant is the northern continuation of this, then strike-slip deformation might be expected along the Levant margin. Although small scale strike-slip faults exist there are no large scale strike slip faults observed in the seismic data available to this study (Figure 4.5), or documented in 3D data available to other studies (Ghalayini et al., 2016, 2014). The small-scale strike-slip faults are likely associated with the formation of the LSZ (see Chapter 6). Additionally, the formation of the LSZ adjacent to the Levant continental margin effectively precludes the possibility of a transform fault at the Levant margin, as if this was the case then later transform strain would likely localise there.

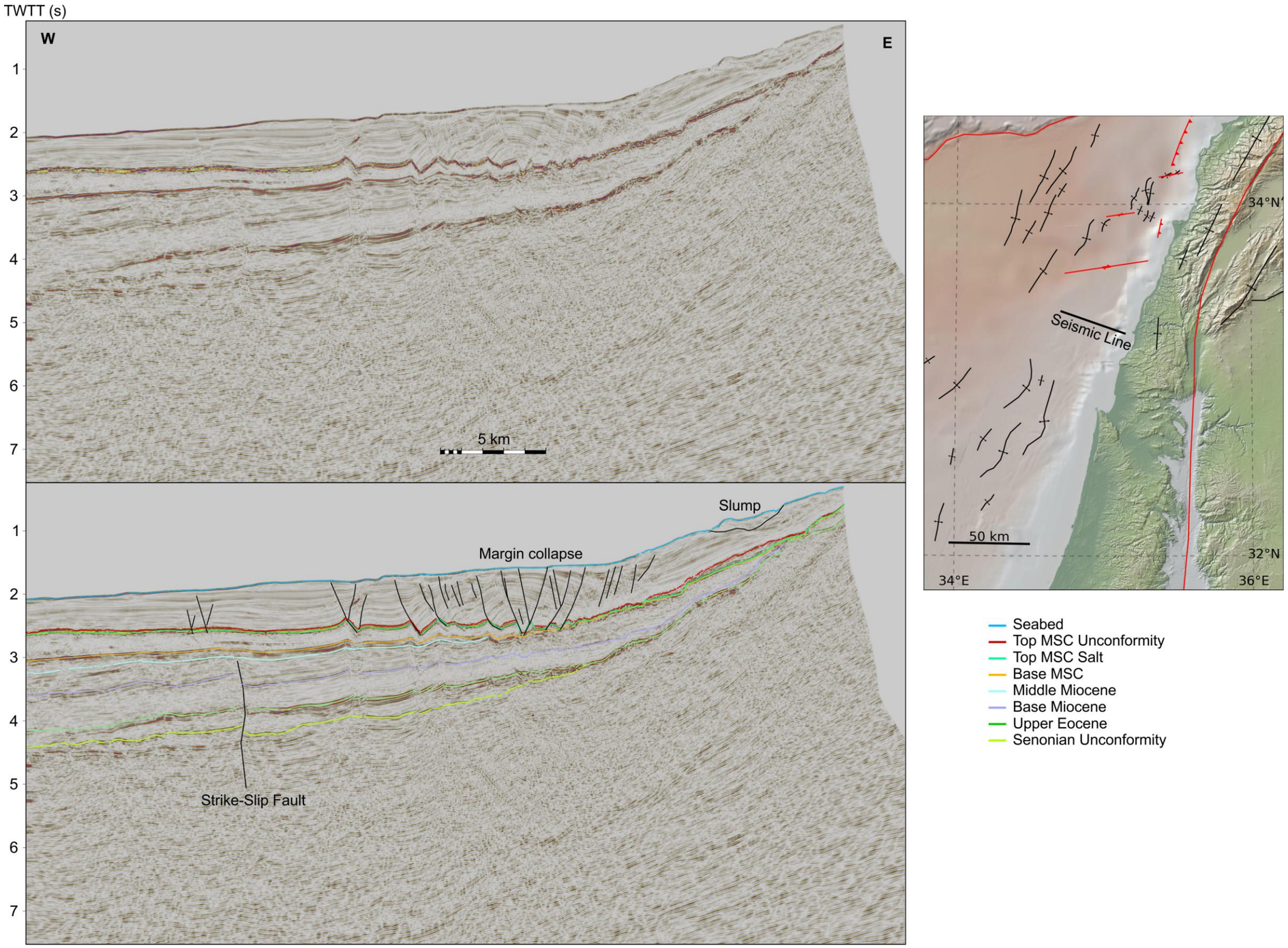

Figure 4.5-Seismic line of the Levant Margin. Features on the map are after this study and Ghalayini at al. (2013; 2014). The global relief (Ryan et al., 2009) vertical scale on the minimap is shown on Figure 1.1 and the supplementary figure.

The challenges involved in definitively interpreting transform as opposed to compressional deformation mean that a component of strike-slip motion on the Syrian Arc cannot be discounted. However, the seismic data available to this study can be interpreted to suggest that the component of transform motion is the secondary mode of deformation at most. This means that although a component of the Gulf of Suez rift offset may have been accommodated on structures to the east of the Rift, evidence suggests they did not provide the primary pathway.

4.4 Cairo-Suez Relay Motion

Bosworth & McClay (2001) suggest that faults north and west of the northern limit of the Gulf of Suez provided accommodation for the offsets observable in the Gulf of Suez. They suggest that the Cairo-Suez faults provided a relay between the Gulf of Suez Rift and what they term the Manzala Rift, a set of NS striking normal faults under the Nile Delta (Figure 4.6). Sarhan et al. (2013) corroborate the Manzala Rift interpretation by showing examples of seismic lines with faults compatible with the location of the Manzala Rift. Although Sarhan et al. (2013) interpret the age of the normal faults as late Miocene, they concur with the link to the opening of the Gulf of Suez. The Cairo-Suez Relay, the westward portion of the Sinai Hinge Belt, has documented Miocene age dextral offsets (Moustafa et al., 2014; Figure 4.4). This is compatible with a link between the Gulf of Suez rift and faults under the Nile Delta. Additionally, the little seismicity in the area appears to better support a relic crustal boundary extending west, as opposed to east, from the end of the Gulf of Suez (Figure 4.6).

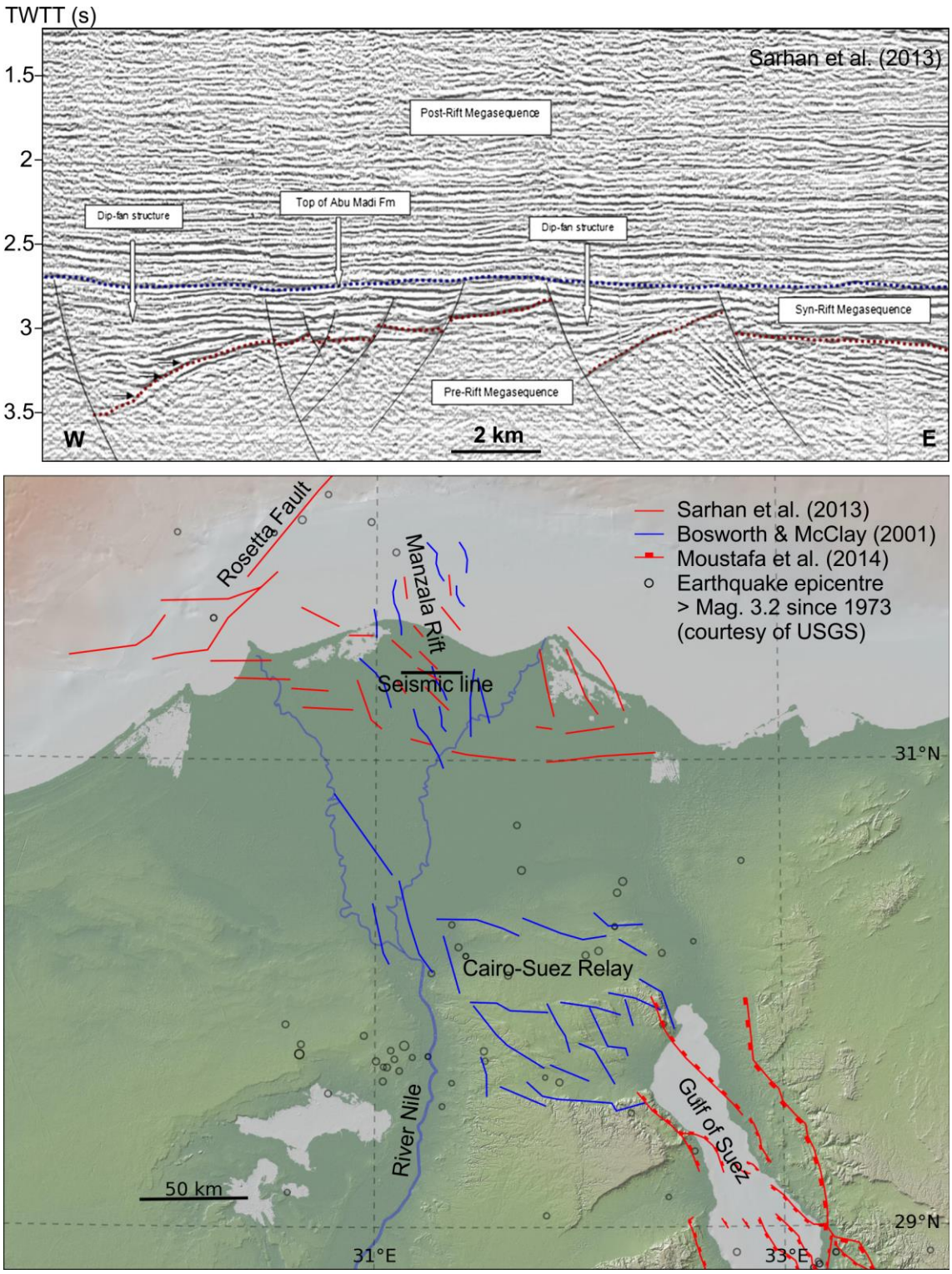

Figure 4.6-Documented faults forming the possible limits of the Sinai Plate between the Gulf of Suez and Nile Delta. The global relief (Ryan et al., 2009) vertical scale on the map is shown on Figure 1.1 and the supplementary figure.

4.5 West Sinai Plate Continent Ocean Boundary

The figures of Bosworth and McClay (2001) do not extend north of their faults drawn on Figure 4.6, and they do not comment on any northward continuation (or otherwise) of the Manzala Rift. Their hypothesis therefore leaves open the question of what accommodates the differential offsets, and western Sinai Plate boundary, further north. The location of the COB north of the Nile

delta appears geometrically concordant with the Manzala Rift (Figure 4.7). This COB might therefore be considered a likely location for the western limit of the Sinai Plate, because although the rifting that formed the COB preceded the formation of the Gulf of Suez, the COB would have formed by crustal scale faulting, and is therefore likely to preferentially accommodate further crustal scale deformation. Additionally, the transition from relatively strong oceanic crust to weak attenuated continental crust forms a mechanical boundary that may have influenced the Sinai Plate boundary (Granot, 2016).

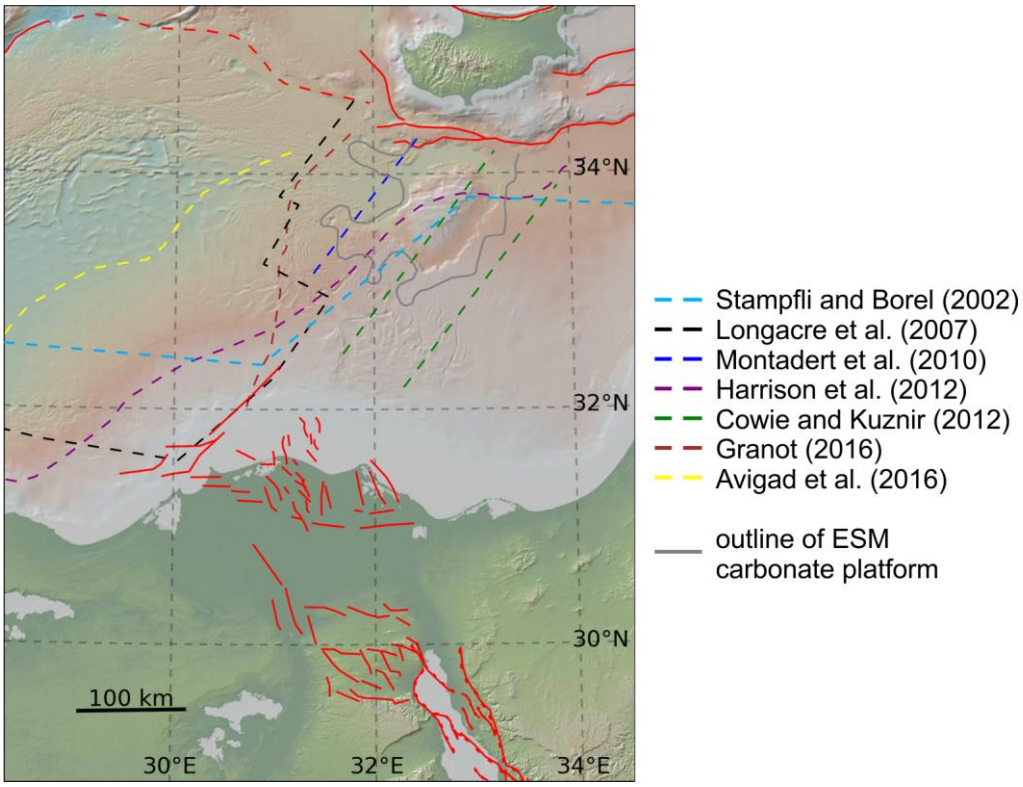

Figure 4.7-Map illustrating how the faults of the Manzala Rift and associated faults (Bosworth and McClay, 2001; Moustafa et al., 2014; Sarhan et al., 2013) are concordant with the interpreted locations of the COB. The global relief (Ryan et al., 2009) vertical is shown on Figure 1.1 and the supplementary figure.

Before further discussion on the possible reactivation of this COB during the separation of the Sinai Plate from the African Plate, it is pertinent to discuss the location of this COB. Several alternatives have been interpreted (Figure 4.7), based on gravity inversion (Cowie and Kusznir, 2012a), seismic data (Aal et al., 2001; Montadert et al., 2010), gravity gradient and ship-borne magnetic data (Granot, 2016), dynamic plate boundaries and restored synthetic oceanic isochrons (Stampfli and Borel, 2002), and integration and iterative modelling of proprietary gravity, magnetic, deep seismic reflection and ocean bottom seismograph crustal refraction seismic data (Longacre et al., 2007). Longacre et al. (2007) interpret an embayment in the COB east of the ESM (Figure 2.31), possibly with the understanding of active subduction at the Cyprus Arc (an idea widely accepted in published literature but argued against in Chapter 5) which demands the downgoing plate must be oceanic crust. Bevan (2012), a colleague of the authors of Longacre et al. (2007) updates this figure in to exclude this embayment, and on the basis of the discussion in Section 4.6 this study does the same.

The seismic data of the ESM and the underlying carbonate platform available to this study (Figure 4.7) reveal no features that might represent a COB (Section 3.6.6). Modern carbonate platforms are understood to extend over COBs (Pindell and Kennan, 2001), and the ESM carbonate platform post-dates the COB so this might appear inconclusive. However, the ESM itself is understood to be underlain by a fragment of continental crust (Section 2.3.4) and the deep seismic over the feature reveals an underlying basement high (Figure 3.29), not a feature indicative of a COB. Thus the COBs that transect the ESM are discredited; this is corroborated by the evidence shown later in this section. The remaining speculative COBs follow the same trend but are parallelly offset (Figure 4.7). As they are broadly parallel all of these COBs have the same concurring association with a perpendicular rifting direction (Section 2.6.1, also see Section 4.6). To resolve if the COB likely lies more outboard or inboard (to NW or SE respectively) five points are subsequently discussed:

- Where the uplift of Cyprus has occurred.
- Trends on gravity data.
- Trends on magnetic data.
- Interpretations of the seismic data available to this study (Figure 4.10).
- Mapped fault trends.

The uplift of Cyprus is associated with underthrusting of non-oceanic crustal material at the relic subduction zone beneath Cyprus. The lateral limits of this uplift may therefore be used to infer the lateral limits of the underthrusted non-oceanic crust. West of Cyprus island the water deepens to c. 2200 m in 20 km (Ryan et al., 2009), suggesting that underthrusted buoyant material, continental crust, may not extent much further west than the island. This matches the location of the western proposed COBs (Figure 4.7). Additionally, a cluster of earthquakes exists to the west of Cyprus (Figure 4.1), and may be linked to the mechanical boundary of the COB (Granot, 2016).

This matches the trend observable on maps of both the vertical gravity gradient (Figure 2.1B; also Figure 4.9 and Figure 4.12) and residual gravity (Figure 4.8). These trends suggest that the COB joins the Cyprus Arc 40-50 km to the west of Cyprus Island coastline.

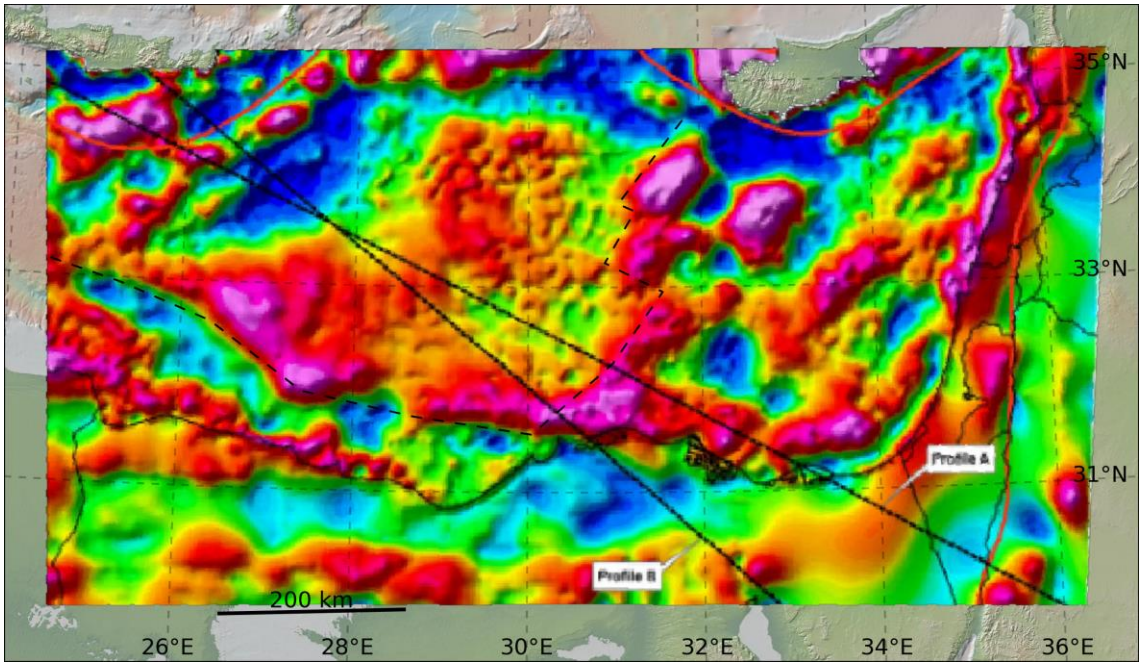

Figure 4.8-High pass (200 km) gravity data adapted from Longacre et al. (2007); the dashed line represents their interpreted COB location, the profile lines refer to crustal profiles in this paper. No scale was provided for the gravity data. The global relief (Ryan et al., 2009) vertical scale is shown on Figure 1.1 and the supplementary figure.

A recent study of shipborne magnetic data (Granot, 2016) reveals a linear high in the total field anomalies that parallels the gravity high noted by Longacre et al. (2007; Figure 4.9). Granot (2016) observe that it follows an equivalent trend in an alternative form of gravity data (high pass Bouguer, Figure 4.8 vs. vertical gravity gradient, Figure 4.9).

The sediments deposited since the late Miocene in the Herodotus Basin constitute a thick (c. 6 km) sequence, including MSC evaporites. The thickness of the sediments, and the effect of the evaporites, by both prevalent halokinetic structures and seismic energy absorption (Section 3.2.5), reduces seismic imaging clarity and confidence in any interpreted faults in the area. However, some features that could potentially be a rift plate boundary with some reactivated deformation are present on the seismic data available to this study (Figure 4.10), although this interpretation cannot be made with confidence due to low reflector clarity, possible secondary multiples, and an absence of well data. The equivalent reflector sequence on the PSDM data available to this study starts from 10 km depth and deepens basinward before being truncated by the base of the seismic (Figure 4.10). This is consistent with the 13 to 17 km rough oceanic crust depth estimate of Granot (2016).

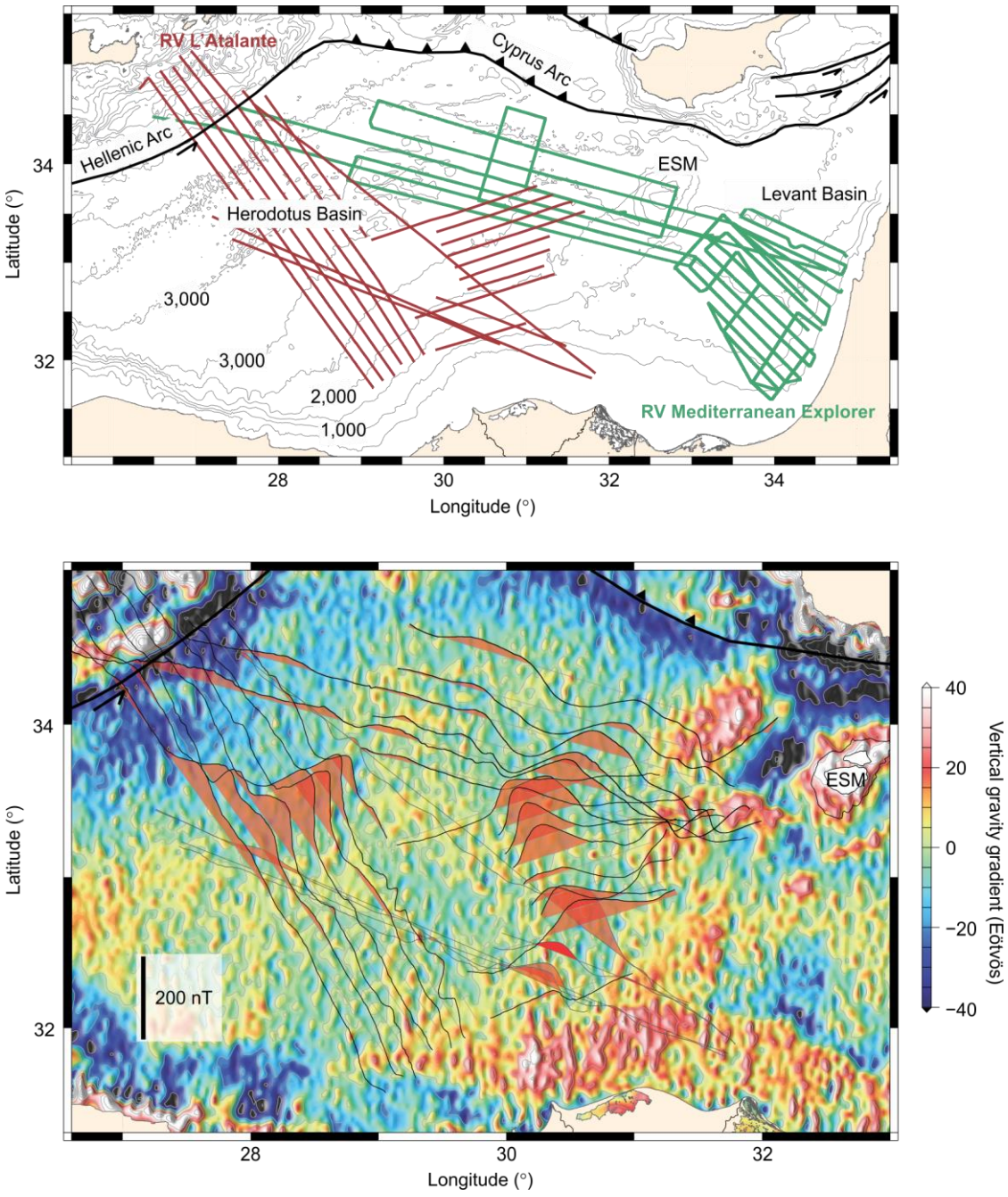

Figure 4.9-Total-field magnetic anomalies in the Herodotus Basin, adapted from Granot (2016). The green and brown lines show the tracks of ships collecting magnetic data. Total-field magnetic anomalies superimposed on a vertical gravity gradient map derived from satellite altimetry. The magnetic anomalies are plotted along tracks. Red shading indicates positive anomalies.

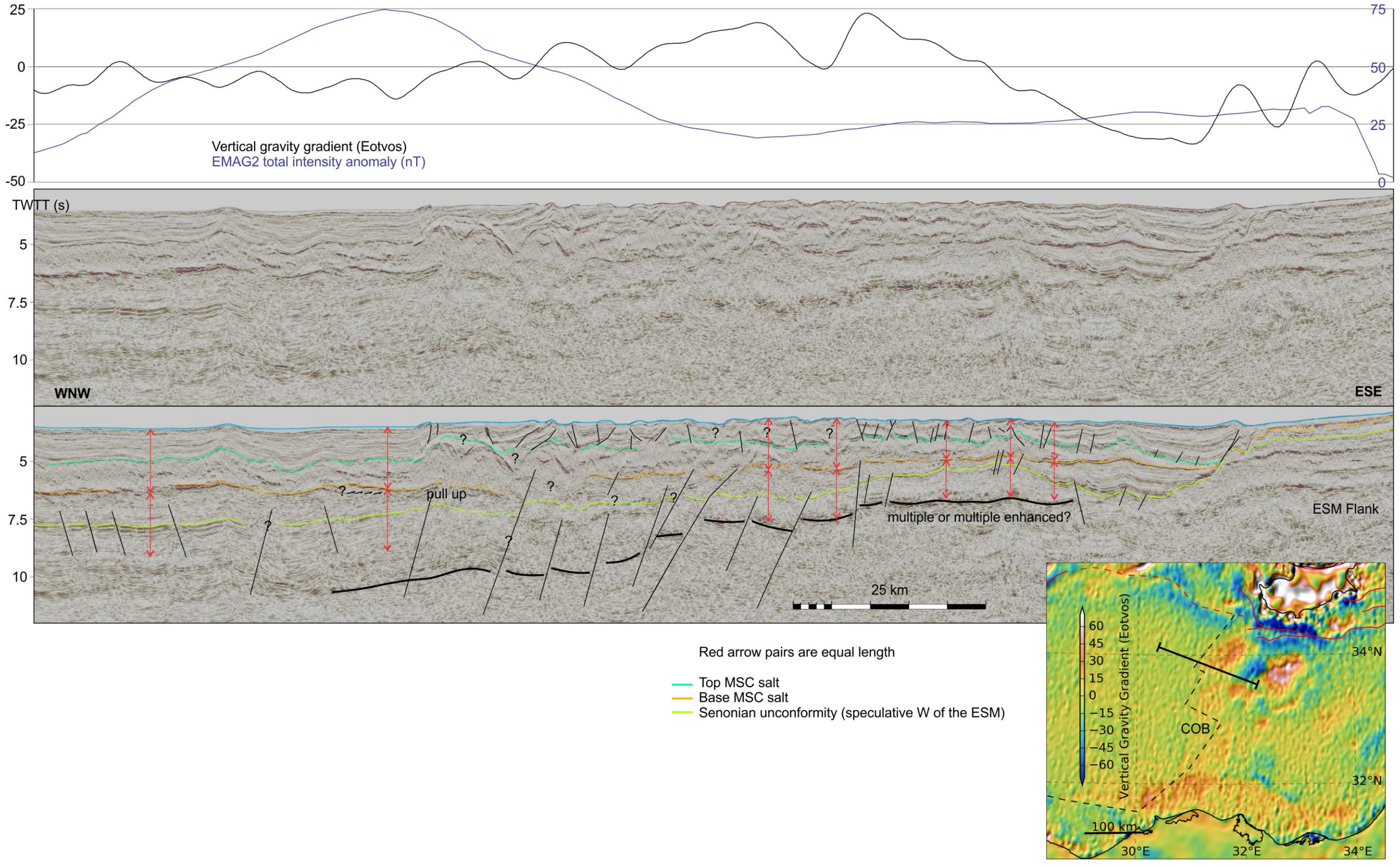

Figure 4.10-Seismic line across the location hypothesised by Longacre et al. (2007; dashed line on the minimap) to be a COB west of the ESM, and a speculative interpretation of a faulted margin shown by the bold black line. The red arrows demonstrate the coincidence of part of the interpreted margin reflector with where a multiple might be expected.

Thus far, all the evidence matches with the COB drawn by Longacre et al. (2007), as might be expected where they use the same data. As a result of this, with the minor modification that a portion of the COB follows the faults of the Temsah trend (Figure 4.11), this study favours this interpreted COB. Based on this COB, it is now possible to discuss potential deformation that may have occurred along it during the opening of the Gulf of Suez. Multiple estimates of the Euler pole for Red Sea Rift motion have been made, include polyphase motion, however all result in space problems so further work is required to better resolve this (Garfunkel, 2014). Broadly matching the orientation of transform faults in the Gulf of Aqaba and Red Sea results in an Euler Pole that resolves to primarily transform, as opposed to extensional, deformation at the hypothesised COB (Figure 4.11). This accords with the transform motion along the LSZ as a continuation of the same plate motion. As has been discussed previously, strike-slip deformation often has a reduced seismic expression in comparison to compressional or extensional deformation, reducing how easily it may be resolved. This plate motion vector also implies a large degree of transform motion at the Manzala Rift. Further investigation of seismic data over the Nile Delta and Cone could aid resolution of this issue.

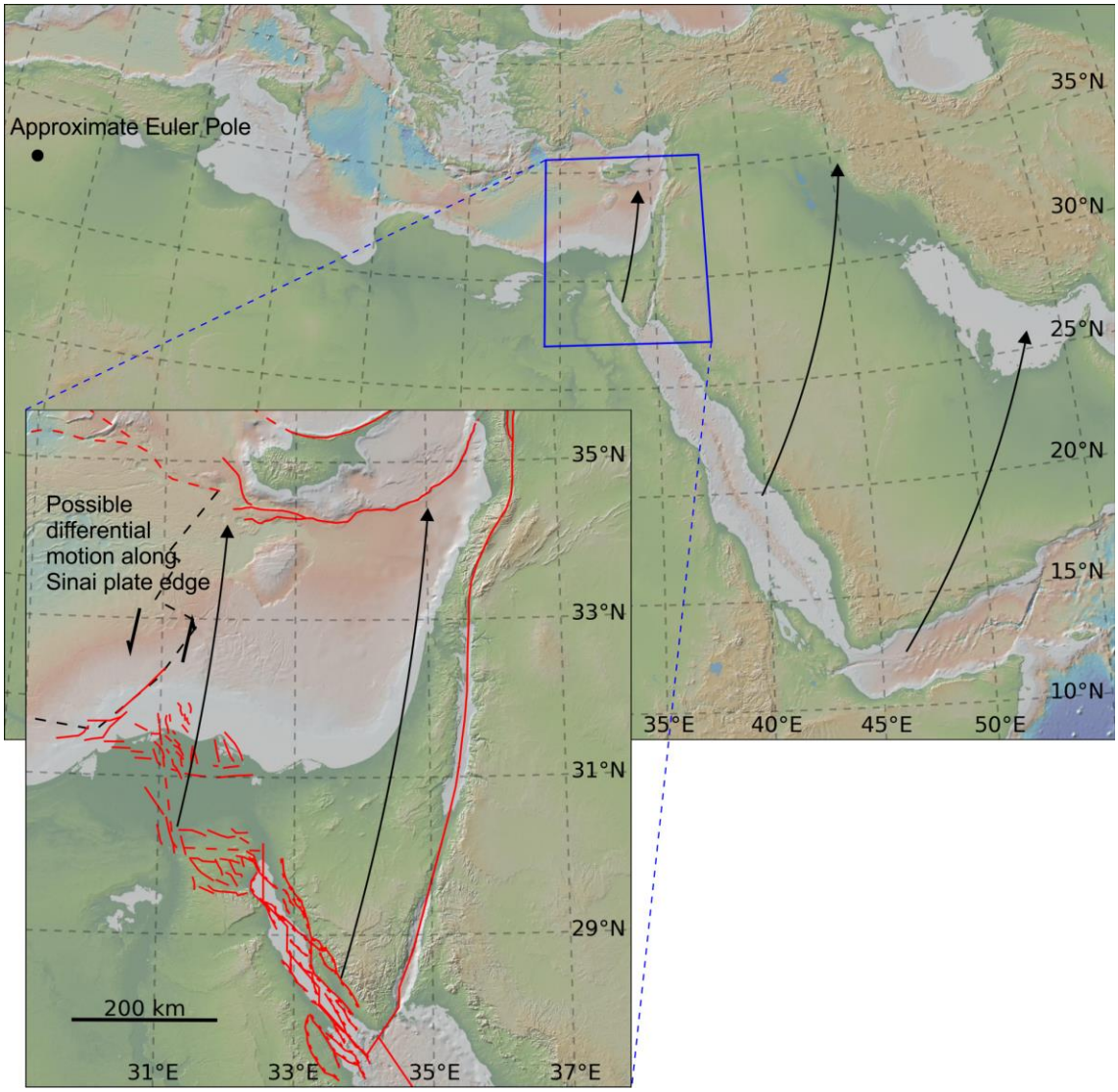

Figure 4.11-Maps showing how an approximate Euler Pole for the Red Sea Rift motion could correspond to transform motion at the western edge of the Sinai Plate. The arrows represent this

plate motion (relative to the African Plate) and faults at the western edge of the Sinai Plate are marked (Bosworth and McClay, 2001; Moustafa et al., 2014; Sarhan et al., 2013). The global relief (Ryan et al., 2009) vertical scale is shown on Figure 1.1 and the supplementary figure.

4.6 Direction of Tethyan Rifting

The direction of Tethyan rifting and spreading is uncertain in the EMR (Section 2.6.2), but several lines of enquiry can inform on this. The end members of the possible spreading direction, WNW-ESE and NNE-SSE, require the presence of a transformal continental margin (Figure 2.30), on either the north Egyptian continental margin or the Levant margin. The subsequent formation of the LSZ (Freund et al., 1970; Garfunkel, 1981) largely precludes another parallel transform in close proximity, indicating interpretations that the Levant margin is a transform fault are unlikely to be valid. The trends in the gravity and magnetic data (Figure 4.8; Figure 4.9), the inferred COB location (Figure 4.7), the orientation of documented Tethyan rift faults (Gardosh et al., 2008b), and the interpretation of the Egyptian continental margin as an oblique transform margin, due to its linearity and an absence of stepped rifts (Frizon de Lamotte et al., 2011; Tassy et al., 2015), suggest that the extension that formed the large scale crustal architecture of the region (Figure 2.2) was broadly NW-SE (relative to current place orientation; Figure 4.12).

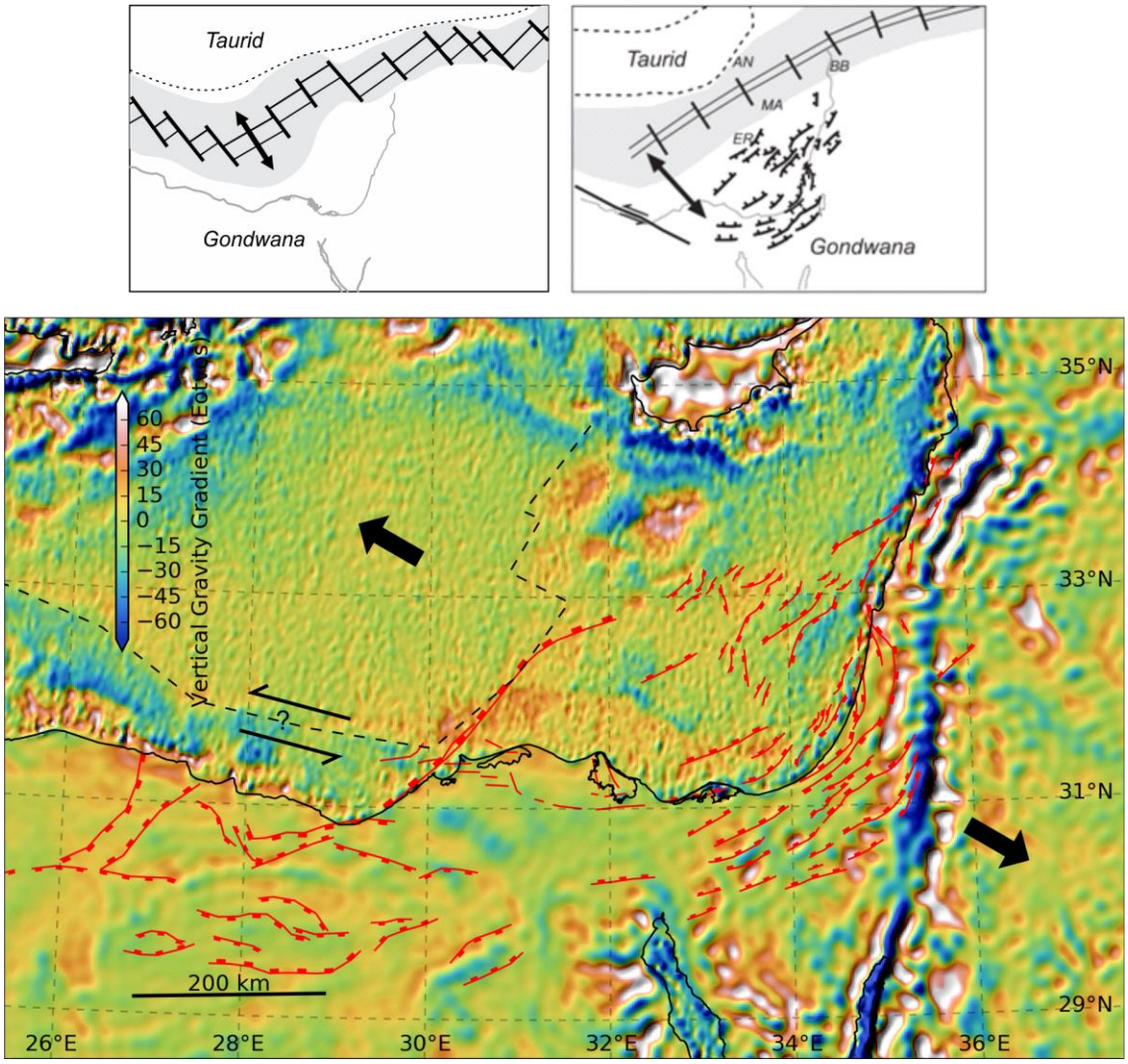

Figure 4.12-Sketch maps (adapted from Figure 2.30) comparing hypothesised spreading directions with rift and spreading related features in the EMR (Aal et al., 2001; Bosworth et al., 1999; Gardosh et al., 2010; Sarhan et al., 2013) overlaid on gravity data (Sandwell et al., 2014, 2013; Sandwell and Smith, 2009).

These observations do not preclude phased multi-directional rifting, but on the basis of an explanation which matches all the features observed and Occam's Razor (Encyclopædia Britannica, 2010; Gauch, 2003), a NW-SE direction of rifting is favoured by this study. This contrasts with some earlier high profile reconstructions (Stampfli and Borel, 2002) but is in line with many more recent studies (Barrier and Vrielynck, 2008; Cowie and Kusznir, 2012b; Gardosh et al., 2010; Longacre et al., 2007; Montadert et al., 2014). The scale of the spreading and its occurrence on the spherical Earth means some lateral variation is likely (i.e. for the same geometric reasons that plates move about Euler Poles), which appears to match with the evidence (Figure 4.12). Further study of the Egyptian Mediterranean margin may clarify this.

4.7 Distribution of Crustal Domains

The reflector sequence of the rocks currently docked in the Cyprus Arc subduction zone beneath the accretionary wedge may be traced without any large changes in thickness or sharp changes in character >200 km to the Southern Levantine Basin (Figure 4.13). This indicates that these

sediments in the Southern Levantine Basin, which are believed to be Jurassic in age, are representative of those currently docked in the subduction zone. This is controversial, as the Southern Levantine Basin Jurassic sediments are widely accepted as being underlain by thinned continental crust (Section 2.2). Gardosh et al. (2008b) note:

"The basement layer in the central part of the [Southern Levantine] basin does not show any characteristics of oceanic crust such as described in other passive continental margins (Klitgord et al., 1988) or in the central part of the Mediterranean Sea (Avedik et al., 1995; Finetti, 1985)."

This would imply that that thinned continental crust can enter a subduction zone without significant deformation of the accretionary wedge. Three alternatives exist:

- Part of the Sinai Plate, the Northern Levantine Basin, is underlain by oceanic crust. The COB interpretation of Longacre et al. (2007) included an embayment of oceanic crust in this area (Figure 2.31).
- There is a COB in the crustal rocks underlying the Levant Ramp. Although the basement is not well imaged the lack of any change in seismic character or thickness in the overlying rocks does not fit with the contrast in palaeodepth that might be expected if this was the case (Figure 4.13).
- The interpretations of attenuated continental crust on the Southern Levantine Basin are incorrect, and the whole Levantine Basin is underlain by oceanic crust. Given the seismic refraction data, gravity data and presence of continental fragments and carbonate reefs such as the ESM, this appears unlikely (see remainder of this Section).

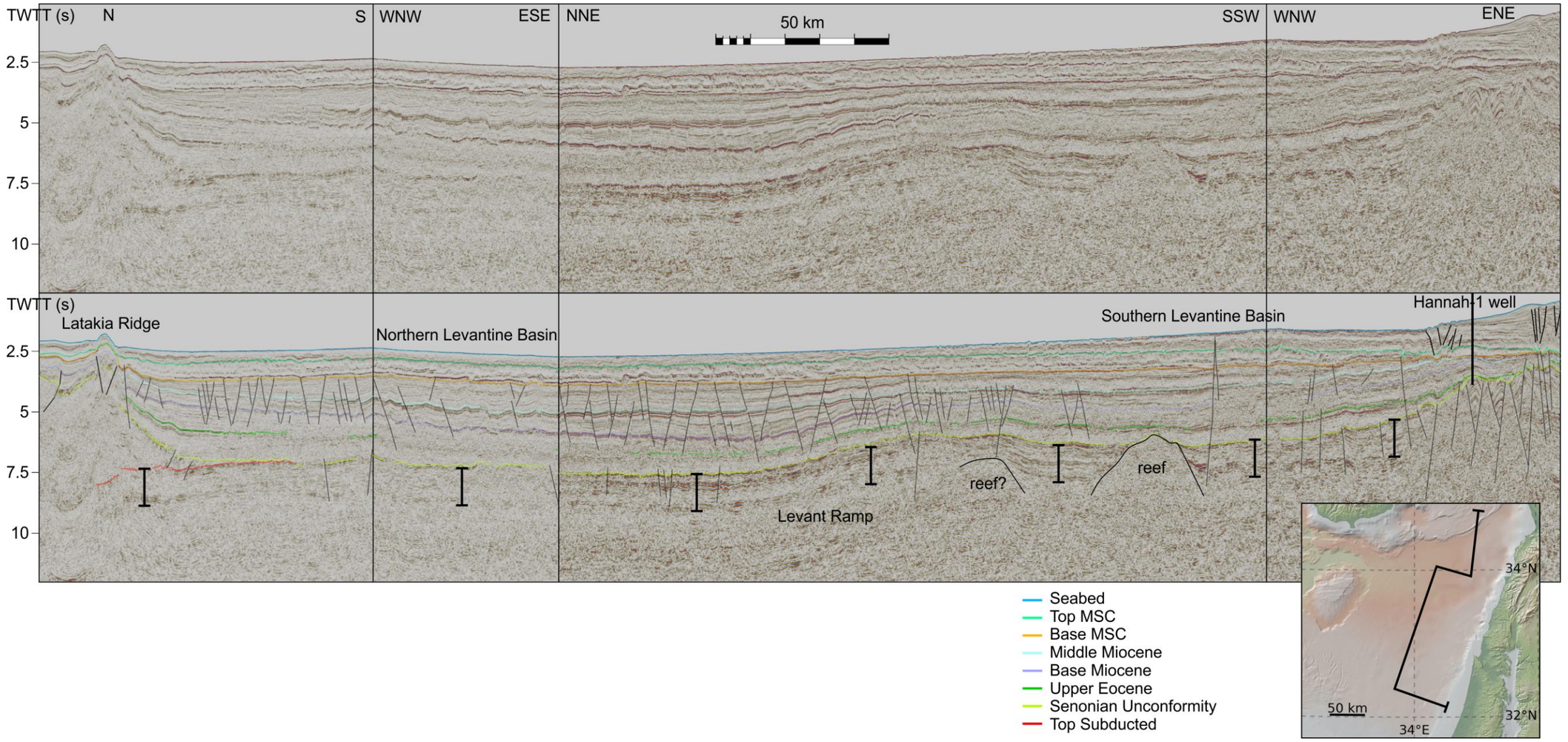

Figure 4.13-Composite seismic line from the subduction front to the Hannah-1 well illustrating the seismic character of the seismic package underneath the Senonian Unconformity. The global relief (Ryan et al., 2009) vertical scale on the minimap is shown on Figure 1.1 and the supplementary figure.

To investigate this further, it is necessary to revisit the evidence that led to the conclusion of thinned continental crust beneath the Levantine Basin. There are several lines of evidence for type of basement crust in the Northern Levantine Basin, both direct and indirect from different data types; magnetic, gravity, earthquake, seismic refraction and seismic reflection.

Inversion of satellite gravity data suggests that 15-20 km of thinned crust (including the sediment overburden) exist beneath the Levantine Basin (Figure 4.14). PSDM data (Figure 3.23E), a later larger scale estimate of crustal thickness (Bilim et al., 2016), and crustal modelling based on gravity and heat glow data (Inati et al., 2016) are compatible with this conclusion. It should be noted that the break-up age used in the earlier gravity inversion is 115 Myrs younger than a recent study of magnetic anomalies in the area (Granot, 2016).

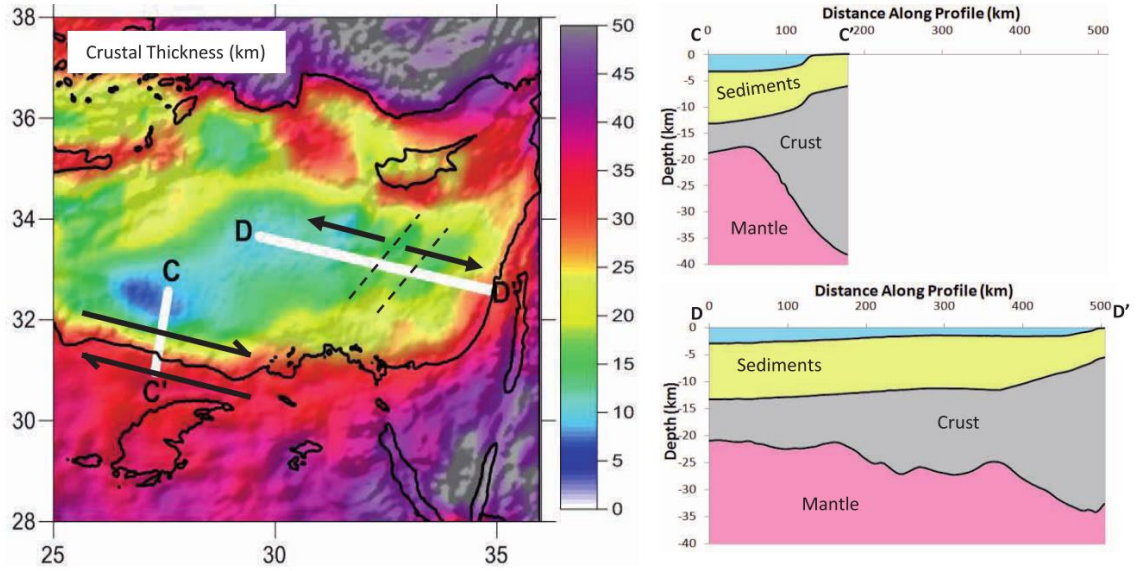

Figure 4.14-Map of the Levantine Basin, showing predicted crustal thickness determined from gravity inversion using a late Triassic (225 Ma) break-up age. Arrows indicate rift and transform margin kinematics. Dashed lines indicate NE-SW strike of rifting on the Levant margin. Cross-sections C–C′ and D–D′ show crustal structure cross-section through the transform margin and the rift margin, respectively. From Cowie and Kusznir (2012).

There are no obvious linear seafloor magnetic anomalies in the Levantine Basin (Longacre et al., 2007). Analysis of recent ship-borne magnetic data has revealed linear magnetic trends in the Herodotus Basin (Figure 4.9), but none are documented in the Southern Levantine Basin (Granot, 2016). The pertinent survey did not traverse the Northern Levantine Basin (Figure 4.9), the more likely of the Levantine Basins to be underlain by oceanic crust, although the relatively small size of the basin relative to the wavelength of the magnetic signal would likely preclude their observation if there was underlying oceanic crust (Figure 4.9). Thus this is inconclusive.

Using earthquake seismic data Papazachos and Papaioannou (1999) interpret the presence of a Benioff zone below the western Antalya Basin but do not observe this Benioff zone to extend any further east. A Benioff zone is an indicator of active subduction and requires oceanic crust. The lack of seismic indicators of subduction under the rest of the Cyprus Arc could be evidence for continental crust in the Levantine Basin. However, if subduction had ceased for another reason (see Chapter 5) this would also diminish seismicity. Thus this is also inconclusive.

The only seismic refraction line that transects the Northern Levantine Basin is line 2 from Welford et al. (2015), but this is in close proximity to the ESM (Figure 4.15). The ESM is not representative of the stratigraphy in the Levantine Basin (Chapter 3), and Welford et al. (2015) does not expand on the interpretation of Netzeband et al. (2006a) of highly thinned continental crust in the Levantine Basin. Thus, no direct interpretations of the crustal structure of the Northern Levantine basin have been drawn from refraction lines.

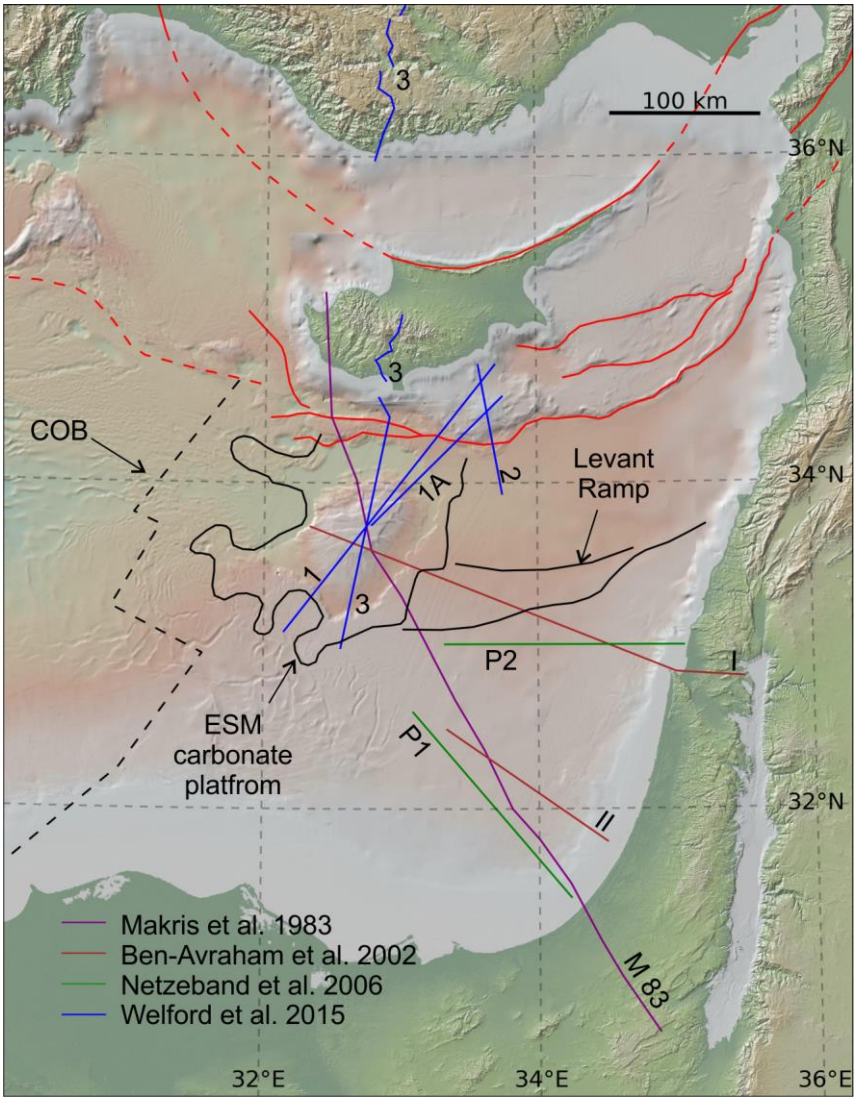

Figure 4.15-Map showing the location of refraction lines in the EMR. The line numbers are those used in the referenced papers. The global relief (Ryan et al., 2009) vertical scale is shown on Figure 1.1 and the supplementary figure.

Refraction lines of the Southern Levantine Basin do permit direct interpretations of thinned continental crust in this area (Ben-Avraham et al., 2002; Makris et al., 1983; Netzeband et al., 2006a). If the Southern Levantine Basin basement can be confidently interpreted as the same as the Northern Levantine Basin, this could be a strong indicator of its crustal type.

The Levant Ramp likely represents a change in underlying crustal properties (Section 3.6.4). Therefore, interpretations of the crustal type of the Southern Levantine Basin may not be representative of those of the Northern Levantine Basin. Syn-kinematic sediment packages indicate that the Levant Ramp normal faults formed in the Cretaceous (Figure 3.23E). Therefore,

extension at the Levant Ramp post-dates the Triassic rifting that would form a COB. However, this does not preclude the Levant Ramp forming a COB as the faulting may have exploited pre-existing underlying rift faults that would exist if there were an underlying COB.

The seismic character of the subducted interval can inform on its composition. Both oceanic crust and crystalline continental crust consistently appear on seismic images without coherent internal reflectors (Butler et al., 2016; Pindell et al., 2014). It may be observed that the subducted crust has numerous internal reflectors (Figure 4.13). These could be interpreted to be multiples but there is enough internal variation and no reflectors at consistent TWTT intervals that they can be confidently interpreted as a true reflector. This interpretation is compounded by tracing of the reflectors from where they are under the subduction zone over the Levant ramp to the Southern Levantine Basin. Here features interpreted to be reefs may be clearly observed to segment the reflector packages (Figure 4.13).

This means the top of the subducted interval is sedimentary, permitting the conclusion that an interval of non-crystalline basement rocks where at least partially subducted without significant deformation. This reflector package does not change significantly in thickness or character between the Northern and Southern Levantine Basins (Figure 4.13), strongly suggesting that the palaeo-relief of the underlying rocks was sub-planar. It is highly unlikely that this would have been the case had there been an underling rift-formed COB, as one might expect the oceanic crust side of a COB to be resolveably lower than the crust side. This then leaves two possibilities, either subsequent sedimentation resulted in infill of the oceanic side of the COB such that no paleo-relief remained, or the Northern Levantine Basin is underlain by the same crust type as the Southern Levantine Basin. For infill, as opposed to drape, sedimentation to occur without producing its own depocentre derived paleo-relief is infeasible.

Therefore, evidence suggests that thinned continental crust has entered the relic subduction zone at the southern edge of the Cyprus Arc, without deforming the overlying sediments such that their subduction-related geometries, such as the accretionary wedge, may still be clearly resolved. It may be confidently concluded that sedimentary rocks were at least partially underthrusted without being resolveably deformed following the last stages of subduction. Despite this lack of deformation, the recent uplift of Cyprus (Section 2.3.9) and the Cyprus Arc (see Section 5.6) indicates that material more buoyant that oceanic crust is being underthrusted at the Cyprus Arc.

4.8 Conclusion

The information available to this study, including publically available literature, provides evidence against all the plate boundaries hypothesised for the western edge of Sinai Plate apart from that by Bosworth and McClay (2001). They postulate that an EW trending relay between the limit of the Suez rift and a NS trending rift under the Nile Delta accommodate the offsets that may be observed at the northern end of the Gulf of Suez. Only publically available data is available to this study in these onshore areas, limiting critical evaluation, but it is compatible with all offshore data available to this study and documented evidence in published literature. The northward offshore continuation of the NS trending rift is buried under thick sediments and so is not well resolved,

but likely joins with a COB that follows the same trend (Figure 4.16). The direction of the motion of the Sinai Plate during the rifting of the Gulf of Suez means that this COB would have accommodated motion that was primarily transform during this period. The magnitude of this motion is small enough that it may even have been distributed such that there is little evidence of deformation to be observed. Without the clear crustal break at the Gulf of Suez it is unlikely that the Sinai Plate could be defined as a separate tectonic entity to the African Plate.

On the basis of these points, this study uses the COB of Longacre et al. (2007) shown in Figure 4.16. The lithosphere of the Sinai Plate is concluded to be thinned continental offshore and continental onshore (Figure 4.16). The northern limit of this thinned continental crust is postulated to be docked in the relic subduction zone at the southern edge of the Cyprus Arc, and to have brought about the transition from subduction to collision there. The contrasting average elevation between the Island of Cyprus and the areas of the Cyprus Arc to the east and west could be attributed to the type of the underthrusted crust, with thicker and less dense crust causing more uplift. Thus, the oceanic crust downgoing at west of Cyprus has resulted in little bathymetric relief and water c. 2500 m deep, hyper extended continental crust underthrusted east of Cyprus has resulted in some bathymetric relief and water c. 900-1500 m deep, and the carbonate capped continental block of the ESM underthrusted at the central portion of the Cyprus Arc has uplifted Cyprus to become an Island with a topographical peak at 1952 m (Figure 4.16; Ryan et al., 2009). The Cyprus Arc is investigated in the following chapter.

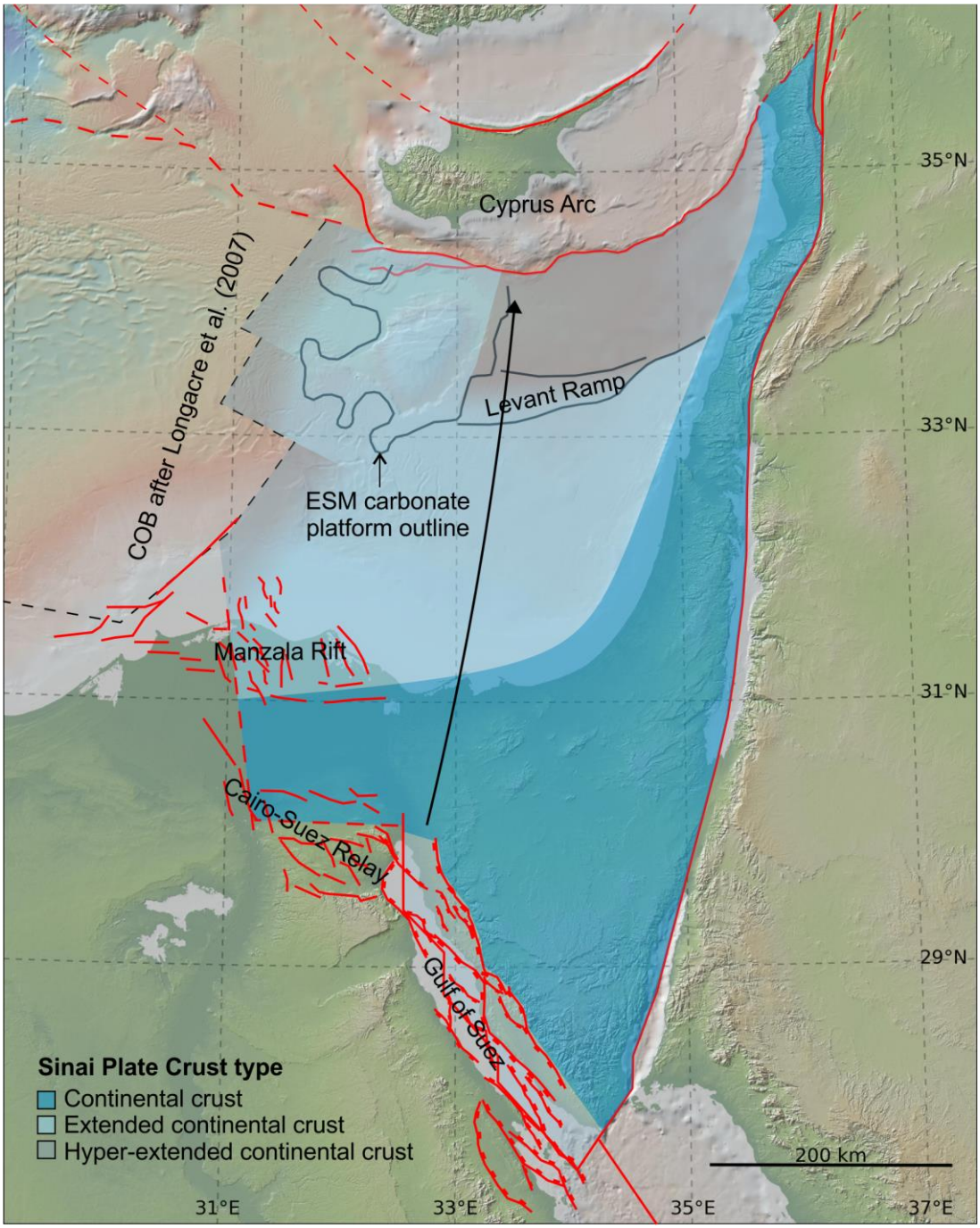

Figure 4.16-Map showing the outline of the Sinai Plate as concluded by this study. The arrow indicates the Sinai Plate motion vector during the rifting of the Gulf of Suez, relative to the African Plate. Note faults on the western edge of the Sinai Plate are marked to a smaller scale than elsewhere on the map as these have been a key focus for the investigation into the western 'plate' boundary. The global relief (Ryan et al., 2009) vertical scale is shown on Figure 1.1 and the supplementary figure.

The crustal type distribution shown in Figure 4.16, and the associated tectonic evolution is incorporated with the other conclusions of this study in the reconstructions shown in Figure 8.1. To reiterate the discussion in Section 4.1, although the 'Sinai Plate' can be correctly considered a partially rifted crustal promontory of the African Plate, 'Sinai Plate' remains the convenient label used here.

Chapter 5 Cypriot Subduction and Collision

5.1 Introduction

The Cyprus Arc is an arcuate zone of convergent deformation, the southern margin of which defines part of the Anatolian Plate margin (Figure 1.1; Section 2.3.10). It is part of a larger geological feature that represents the convergent boundary between the African and Eurasian Plates. To the west of the Cyprus Arc this convergent boundary is actively subducting the oceanic crust of the Herodotus Basin beneath the Hellenic Arc, and to the east of the Cyprus Arc it forms the Bitlis continental suture (Figure 1.1; Figure 5.1). The broad structure of the offshore Cyprus Arc subduction/collision zone has been examined on a wider scale since acquisition of the first seismic lines in the area and many of the larger details remain unchanged from these early investigations (Figure 5.1). However, there are large uncertainties as to the timing, nature and evolution of the relative motions of the tectonic plates on either side of the feature (Section 2.6.6). Studies indicate that the area is experiencing incipient continent-continent collision between the Anatolian Plate and African (Sinai) Plate (Harrison et al., 2004; Jolivet and Faccenna, 2000; Kempler and Garfunkel, 1994; Kinnaird and Robertson, 2012; Robertson, 1998a, 1998b; Vidal et al., 2000a). The transition from oceanic-continent collision to continent-continent collision means that incipient continent-continent collision is marine and comparatively short lived, and thus not well studied (e.g. Bry et al., 2004; Kinnaird and Robertson, 2012; Ten Veen and Kleinspehn, 2003). The subduction/collision zone around Cyprus represents an opportunity to study this further.

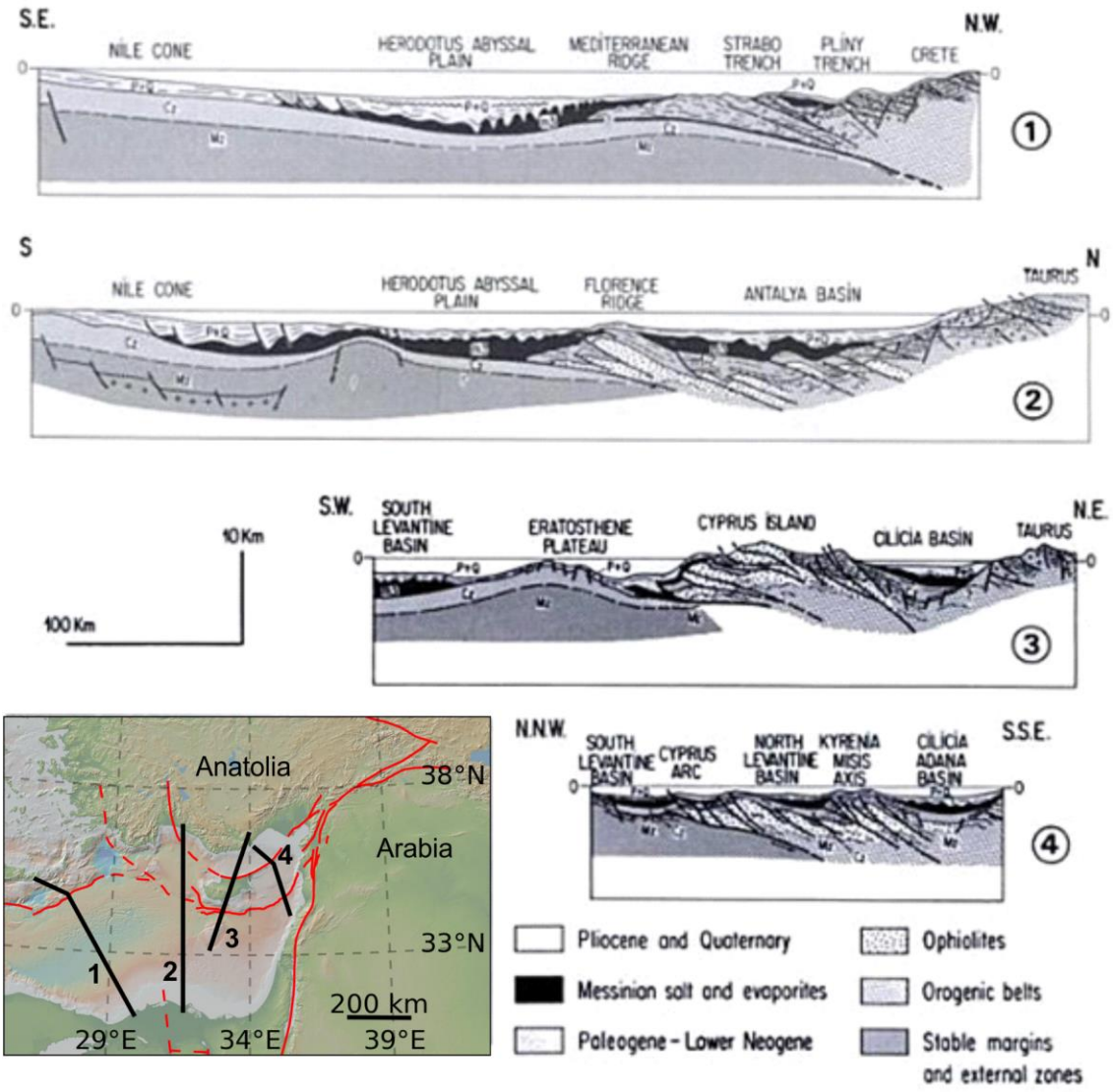

Figure 5.1-Regional structure of the Afro-Arabian-Eurasian Plate boundary in the EMR (now partially outdated, see Figure 5.22) from Sage & Letouzey (1990). The global relief (Ryan et al., 2009) vertical scale on the minimap is shown on Figure 1.1 and the supplementary figure.

Before discussion of the transition between subduction and continental collision at the Cyprus Arc, it is pertinent to define the difference between the two. In this study, subduction refers to the underthrusting of oceanic crust beneath another plate. As soon as continental crust, including attenuated continental crust, is underthrust at what was previously a subduction zone then this is termed continental collision. Continental lithosphere can be deeply underthrust into the mantle, but studies indicate only the lower crust is 'subducted'; the upper crust is accreted onto the overriding plate generating uplift (Capitanio et al., 2010; Gupta et al., 2016; Li et al., 2008; Replumaz et al., 2010; Seno and Rehman, 2011; Xu et al., 2015). The type example for this is the 'subduction' of Indian lithosphere, and the resulting uplift formed the Himalayas. The precise geological configuration involved is still debated, however processes associated with continental collision precede this subduction of continental lithosphere (Li et al., 2008; Replumaz et al., 2010; Seno and Rehman, 2011; Xu et al., 2015). Crucially, the contrastingly lower density imparted by some component of continental crust means that there will be some additional component of uplift

in the overriding plate during attempted subduction or collision of continental lithosphere, relative to the preceding subduction of oceanic lithosphere.

Many of the bathymetric features around Cyprus have been named, but there is some inconsistency in the nomenclature used. Figure 5.2 shows the terms used by this study after appraisal and consideration of consistency, time of first use, location of namesake, and ambiguity of the terms. Details of the inconsistencies are shown in Table 8. Note that some of the terms preferred by this study (and others) are assigned to alternate locations by other studies.

A key nomenclature issue is the use of the term ‘Cyprus Arc’. ‘Arc’, in the geological sense, refers to an arcuate feature or series of features often associated with tectonic convergence (Allaby, 2008). Some authors refer to the southernmost convergent deformation front around Cyprus as the ‘Cyprus Arc’ (Table 8), however as the global relief high associated with this arcuate area of convergent deformation extends to the northern edge of Cyprus (see Section 5.2), this study uses the term ‘Cyprus Arc’ to describe the whole arcuate global relief high. This is consistent with other published studies (Ben-Avraham et al., 2006; Bridge et al., 2005; Hall et al., 2005a, 2005b; Maillard et al., 2011). To the west it joins with the Hellenic Arc at the Anaximander Mountains and Isparta Triangle (ten Veen et al., 2004; Zitter et al., 2003), and to the east it merges with the LSZ and Bitlis Sutures (Robertson et al., 2004).

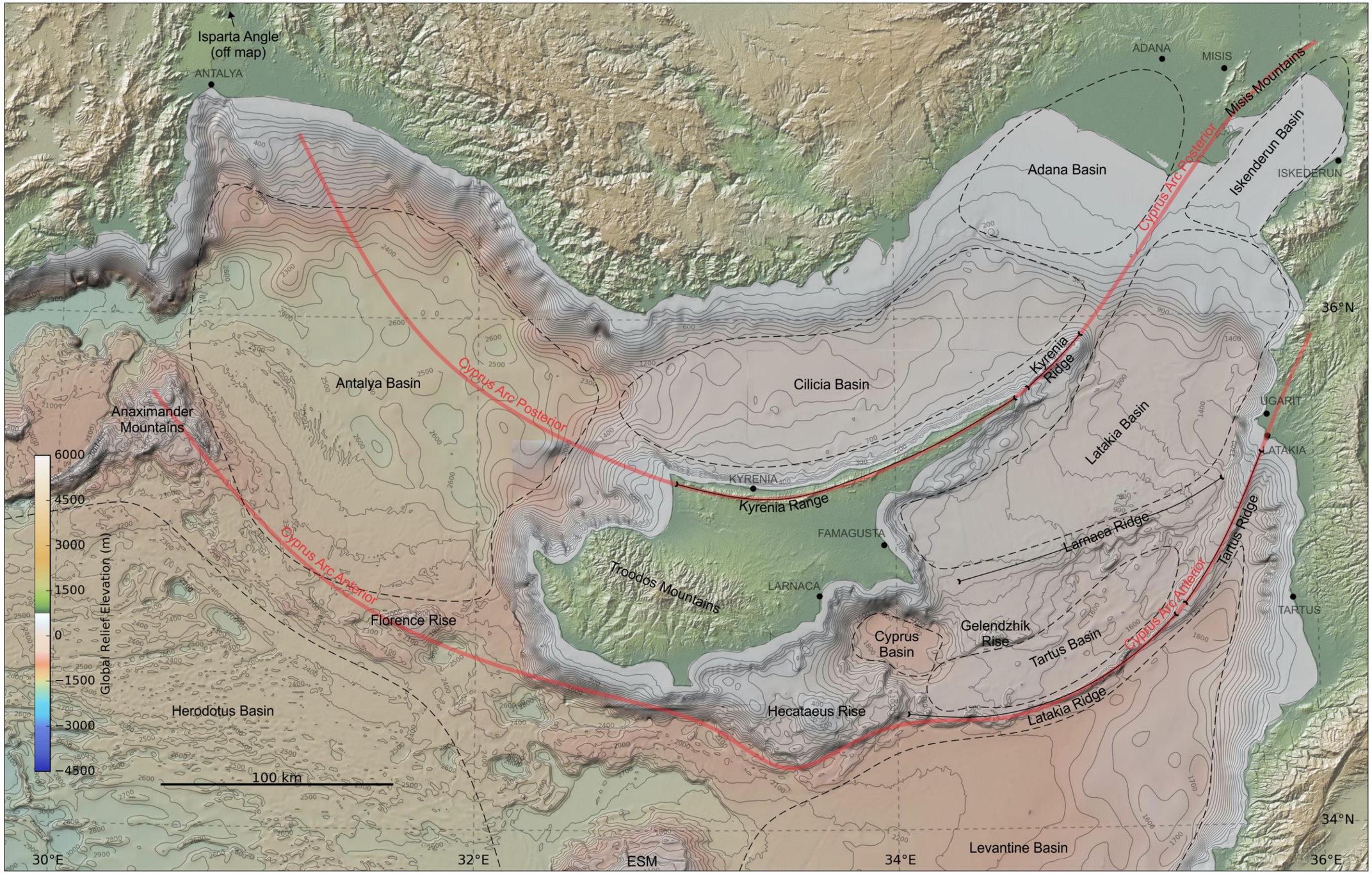

Figure 5.2-Map showing the nomenclature used by this study for global relief features around Cyprus overlaid on bathymetric contours at 100m intervals (GEBCO). See Table 8 for the source of the bathymetric names. The dotted locations are namesakes of items in Table 8.

Table 8-Source (not necessarily original) and alternatives for the nomenclature used for bathymetric features around Cyprus.

Name used by this study as on Figure 5.2:	This name is after:	Alternative name(s):	Alternative name(s) after:
Latakia Ridge	(Ben-Avraham et al., 1995)	Cyprus Arc	(Kempler and Garfunkel, 1994; Reiche, 2015; Tahchi et al., 2010)
Latakia Basin (Latakia Trough)	(Kempler and Garfunkel, 1994)	Famagusta-Latakia Basin	(Tahchi et al., 2010)
		Larnaca-Latakia Basin	(Maillard et al., 2011)
		Larnaca Basin	(Ben-Avraham et al., 2006; Lofi et al., 2011)
Larnaca Ridge (Larnaka Ridge)	(Ben-Avraham et al., 1995)	Gelendzhik Rise	(Tahchi et al., 2010)
		Ugarit Complex (?)	(Tahchi et al., 2010)
		Larnaca-Latakia Culmination	(Maillard et al., 2011)
Tartus Basin	(Lofi et al., 2011; Maillard et al., 2011)	Cyprus Basin	(Bowman, 2011; Plummer et al., 2013)
		Latakia Basin	(Ben-Avraham et al., 2006)
Tartus Ridge (Tartous Ridge)	(Hall et al., 2005a, 2005b)	Latakia Ridge	(Maillard et al., 2011; Tahchi et al., 2010)
Kyrenia Ridge (Karpas Ridge)	(Öztürk and Rovere, 2015; Vidal et al., 2000b)	Misis Ridge	(Robertson, 1998a)
Gelendzhik Rise	(Hall et al., 2005b)	Margat Ridge (for the eastern extension of the structural high under the Tartus basin)	(Bowman, 2011)
Cyprus Basin (Cyprean Basin)		(Vidal et al., 2000a)	
Hecataeus Rise (Hecataeus Ridge, Seamount, Plateau)		(Ben-Avraham et al., 1995; Öztürk and Rovere, 2015)	
Adana Basin		(Kempler and Garfunkel, 1994)	
Iskenderun Basin			
Cilicia Basin			
Florence Rise		(Hsü et al., 1973)	
Antalya Basin			
Anaximander Mountains		(Zitter et al., 2003)	

5.2 Tectonic Evolution Summary

Prior to its closure, the Neo-Tethys contained numerous continental blocks separated by multiple seaways (Barrier and Vrielynck, 2008; Berra and Angiolini, 2014; Robertson et al., 2012a). Consequently, the Late Cretaceous convergence of the African and Eurasian Plates generated subduction in multiple places at multiple times (Figure 2.24; Barrier and Vrielynck, 2008; Berra and Angiolini, 2014; Robertson et al., 2012a). There is a large amount of uncertainty as to the geometry and temporal and spatial continuity of these subduction zones, and consequently

different restorations draw the subduction zones in different places. This study discusses only those crustal units adjacent to the Cyprus Arc. However, the following tectonic evolution is consistent with the geology of crustal units not mentioned in this text (see refs. within Barrier and Vrielynck, 2008; Berra and Angiolini, 2014; and Robertson et al., 2012a).

An understanding of the large-scale tectonic evolution of the Cyprus Arc is summarised in Figure 5.3 and discussed subsequently. This understanding does not consider the continental crust underlying the Levant Basin (Section 4.8), however it represents the most up to date published evolution of the Cyprus Arc subduction zones. Both these details and the crustal configuration from Section 4.8 are incorporated into the conclusions of this chapter (see Figure 5.35).

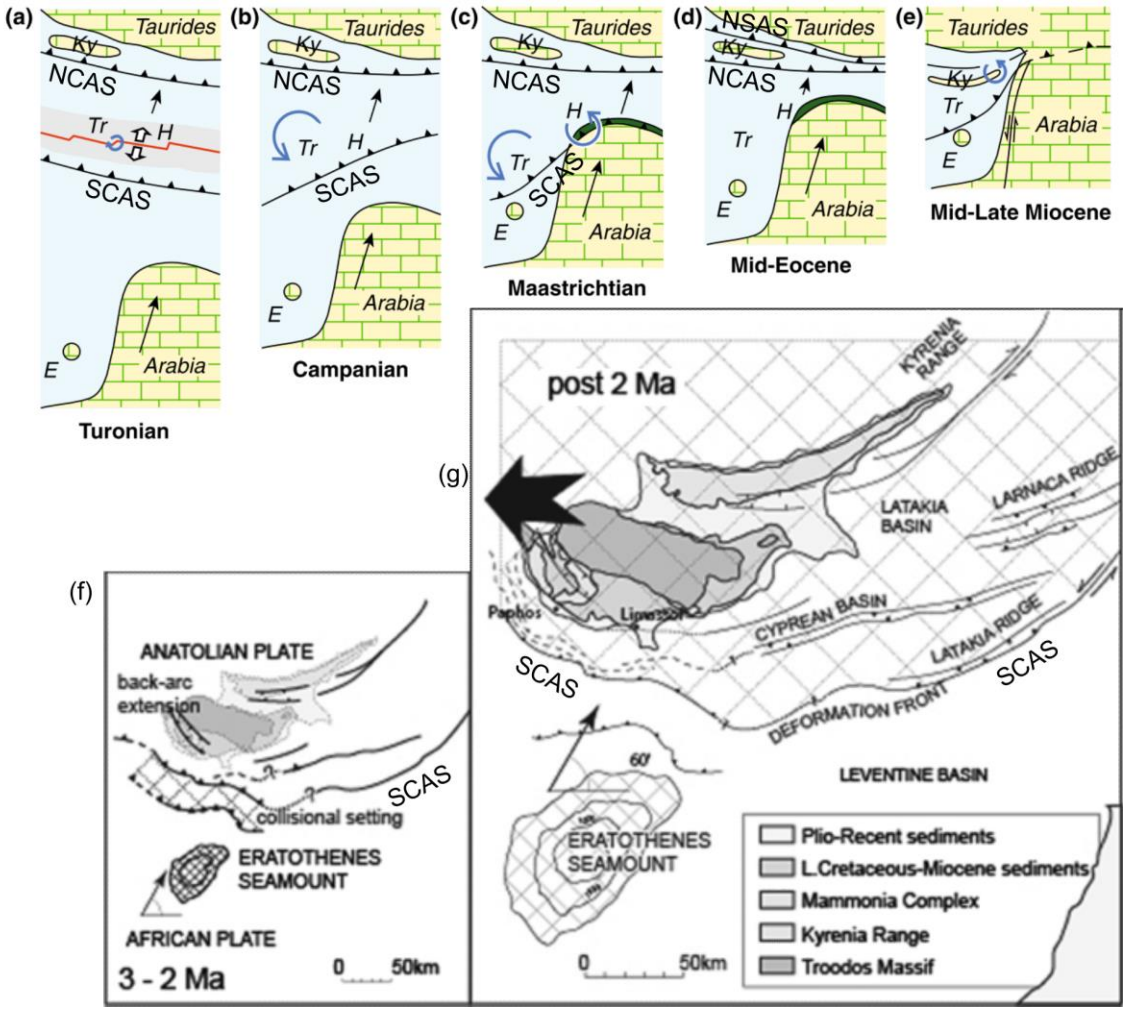

Figure 5.3-Current understanding of the tectonic evolution of the subduction/convergent zones around Cyprus (adapted from: Kinnaird and Robertson, 2012; Morris et al., 2015). Blue circular arrows indicate inferred senses of tectonic rotation, black arrows indicate regional convergence direction, blue is oceanic crust, yellow is continental crust, and green is ophiolite. Ky: Kyrenia Range, Tr: Troodos, H: Hatay, E: Eratosthenes Seamount, Northern Cyprus Arc Subduction Zone: NCAS, Southern Cyprus Arc Subduction Zone: SCAS.

In the Late Cretaceous at least two subduction zones had formed between the Arabian and Tauride Continental blocks, here termed the Northern and Southern Cyprus Arc Subduction Zones (NCAS, SCAS; Figure 5.3). The SCAS corresponds to the current southern edge of the Cyprus Arc. The formation of the Troodos Ophiolite at a spreading ridge above a north-dipping subduction zone around 90 Ma provides a upper minimum constraint on the age of the formation

of SCAS (McCulloch and Cameron, 1983; Mukasa and Ludden, 1987a; Robertson and Xenophontos, 1997, 1993). The NCAS is inconsistently drawn in the literature, with some papers favouring a subduction front to the north of the Kyrenia Range (Robertson et al., 2013; Robertson and Kinnaird, 2015) and/or to the south (Morris et al., 2015; Robertson et al., 2012b). Five documented lines of evidence exist for the NCAS:

1. The Campanian–Early Maastrichtian (?) arc-type volcanism in the Kyrenia Range demonstrates proximity to a subduction zone (Baroz, 1979; Robertson et al., 2012a). The SCAS provided melt to the spreading ridge that formed the Troodos in the Turonian (Figure 5.3). It could have supplied the melt for the arc volcanism in the Kyrenia Range, however the spreading preceded the Kyrenia range volcanics. As this spreading ridge was to the south of the Kyrenia Range rocks, and would have moved them further away during spreading, the supply of melt would have had to have been divided, or it may have been too far north to receive melt from SCAS. Thus another subduction zone may be inferred. A counter argument to this is that typical volcanic Arcs are generally 100-200 km from their associated subduction zone (Stern, 2010), and the Kyrenia range is currently c. 100 km for the SCAS. Therefore it is conceivable that melt supply from the SCAS to both the spreading ridge and arc volcanism is possible, as may be observed elsewhere (e.g. Dhuime et al., 2007). However, the Troodos is currently c. 50 km from the SCAS, indicating closer ranged melt supply and/or subsequent shortening.
2. The Troodos ophiolite has been shown to have undergone ~90° of rotation between the Turonian and Eocene (Clube et al., 1985) Figure 5.3). The rocks of the Kyrenia Range show minor and ~30° rotation in the east and easternmost portions respectively (Morris et al., 2015). Because of their current adjacency (Figure 5.2), this disconnected history of the Kyrenia Range and Troodos ophiolite requires an intermediate microplate boundary during at least the early rotations (Morris et al., 2015). A subduction zone would provide this boundary.
3. The Misis thrust complex is the continuation of the Kyrenia Range thrust complex onshore SE Turkey (this study; Kelling et al., 1987; Kempler and Garfunkel, 1994; Robertson et al., 2004; Vidal et al., 2000a). Subduction is documented to have occurred here up until continental collision occurred in the Oligocene (Robertson et al., 2004). As the thrust complex extends to Northern Cyprus it follows that other associated features, like subductions zones, would follow the same trend.
4. By the Maastrichtian the continuing destruction of oceanic crust at the eastern end of the SCAS had juxtaposed it to the continental crust at the north of the Arabian Plate (Inwood et al., 2009). This led to obduction of the Hatay ophiolite, and the subsequent termination of subduction across the whole of the SCAS (Morris et al., 2015). The convergence of the African and Eurasian Plate was still ongoing however, so shortening had to be accommodated elsewhere (Berra and Angiolini, 2014; Garfunkel, 2004; Robertson et al., 2013; Ziegler, 2001). Another subduction zone active during this period could accommodate this shortening.
5. GPS data from Cyprus shows that it is moving north-eastward relative to the Anatolian Plate (McClusky et al., 2000). This indicates a tectonic boundary between the two locations

(Wdowinski et al., 2006). However, the rate of relative movement is relatively small (c. <5 mm/yr) so it is possible that this could be accommodated by distributed deformation. Additionally, the Anatolian and Aegean Plates are together rotating about an Euler pole to the south (McClusky et al., 2000), and the relative moment may be a result of Cyprus being closer to the pole or rotation.

A subduction zone that existed to the south of the Kyrenia range in the Palaeogene fits these five lines of evidence and is compatible with interpretations of seismic data shown later in this study. A convergent tectonic boundary is drawn in this location (Figure 5.3) by Morris et al. (2015), who suggest this boundary has been overridden and concealed by later phases of thrusting that have emplaced the Kyrenia Range above it. The main period of thrusting that formed the Kyrenia Range was during the Eocene, although episodes of more minor thrusting occurred subsequently (Robertson and Kinnaird, 2015).

By the Miocene Arabia and Eurasia had sutured, the Red Sea had opened and the LSZ had formed (Figure 5.3, Section 2.5). Many studies suggest subduction restarted south of Cyprus around this time (e.g. Kinnaird and Robertson, 2012; Morris et al., 2015; Robertson, 1998c; Robertson et al., 2012a), although some authors argue that the lack of volcanic arc and Benioff Zone indicates otherwise (Harrison et al., 2012, 2004). Seismic data over the eastern Cyprus Arc also indicates that subduction did not restart (Bowman, 2011; Plummer et al., 2013). Restarted subduction is used to explain both the uplift and emergence of Cyprus from underthrusting at the subduction zone, as evidenced by shallow marine carbonates and unconformities (Follows et al., 1996), and Neogene normal faulting via subduction roll-back in several locations in Cyprus (Robertson and Kinnaird, 2015; see refs. within Robertson and Xenophontos, 1997). Seismological evidence of a subducted slab has also been interpreted offshore western Cyprus (Papazachos and Papaioannou, 1999). New explanations are required to explain these observations if subduction had not restarted.

The post-MSC history of the offshore Cyprus Arc is significantly better documented than the pre-MSC history as the MSC salt and unconformity hinder imaging of underlying reflectors on seismic data (Hall et al., 2005b; Işler et al., 2005; Vidal et al., 2000a).

In the Plio-Pleistocene the ESM continental fragment was underthrust in the (relic) subduction zone (Kempler, 1998; Payne and Robertson, 1995; Poole and Robertson, 1991; Robertson, 1998b). Around this time Cyprus, along with Anatolia, underwent westward tectonic escape from the Arabia-Eurasia collision (Kinnaird and Robertson, 2012).

Plummer et al. (2013) used seismic data over the southern edge of the Cyprus Arc east of Cyprus to produce the reconstructed cross sections shown on Figure 5.4. A written description of the depicted evolution is included adjacent to the pertinent reconstruction.

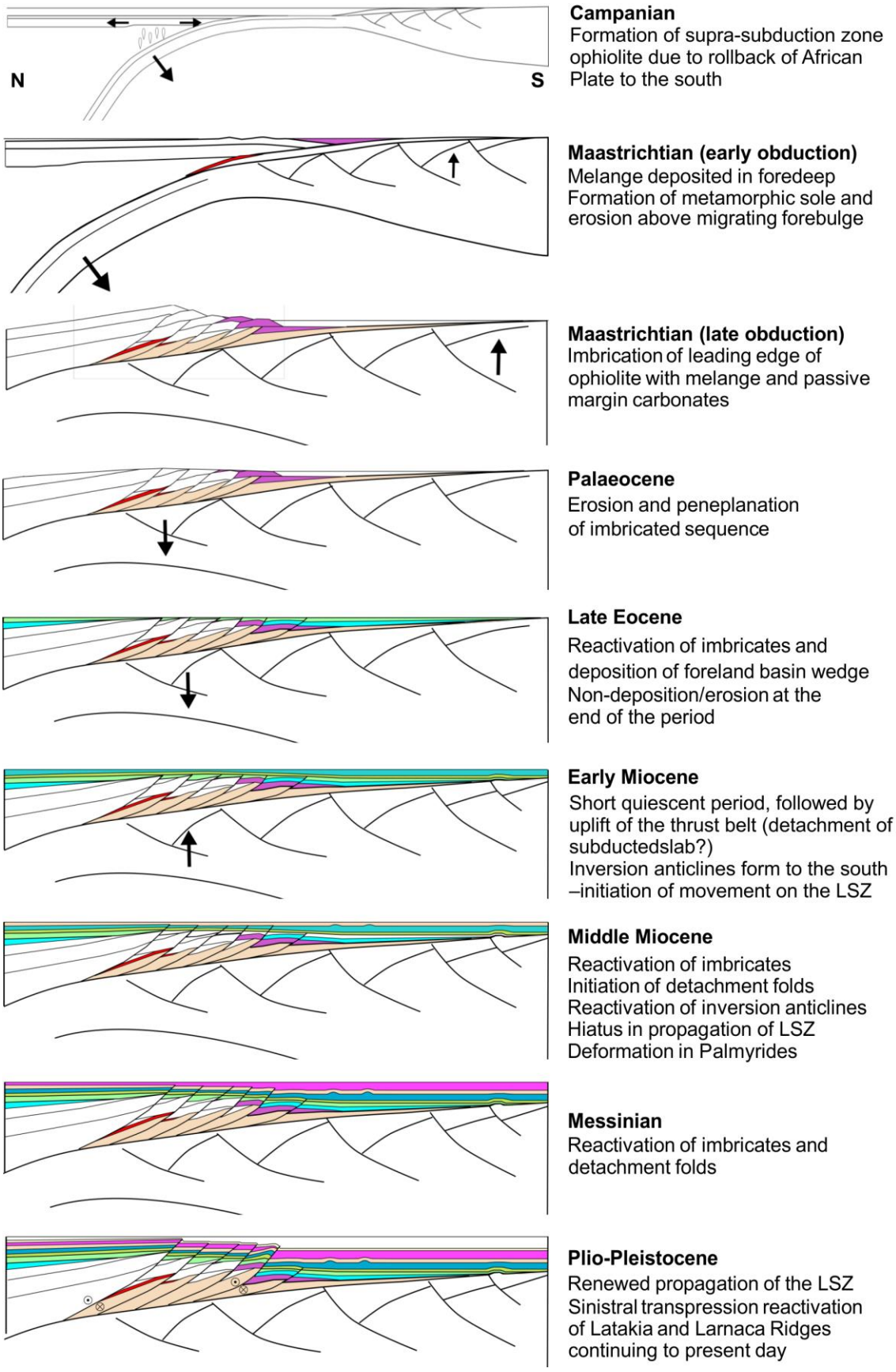

Figure 5.4-Reconstructed cross sections over the southern edge of the Cyprus Arc east of Cyprus adapted from Plummer et al (2013). No specific location, scale or key is given. Arrows indicate relative crustal movement.

Much study has been undertaken regarding the Plio-Quaternary uplift of Cyprus (Main et al., 2015; McCallum and Robertson, 1995; Palamakumbura et al., 2016; Palamakumbura and Robertson, 2016a, 2016b; Poole et al., 1990; Poole and Robertson, 1991; Robertson, 1977; Schattner, 2010; Schirmer et al., 2010). In the seismic data over the Cyprus Arc available to this study, features providing age constraints do not sub-divide the Plio-Quaternary. Consequently, this study does not investigate the Plio-Quaternary uplift.

A key factor in the uncertainty in the evolution of the Cyprus Arc is a lack of deep well data, and consequently only studies based on onshore data can give accurate time constraints for the Pre-MSC tectonic evolution of the area. For this reason, and the shallow penetration depth of many of the seismic reflection data sets, the above understanding of the tectonic evolution of the Cyprus Arc is based primarily on onshore data. A description of published studies of offshore data follows. To permit later critical analysis, discussions of the conclusions of these studies is integrated into the later sections of this Chapter.

5.3 Published Offshore Data

Some published studies investigate data spanning the whole of the offshore Cyprus Arc; including seismic reflection (Sage and Letouzey, 1990), gravity (Ergün et al., 2005) and earthquake seismic data (Papazachos and Papaioannou, 1999; Wdowinski et al., 2006). However, the focus of most studies that investigate that tectonics of the Cyprus Arc only cover portions of the Cyprus Arc.

The majority of the published studies of the Cyprus Arc east of Cyprus have seismic reflection data sets (Table 1), however gravity (Ben-Avraham et al., 1995), magnetic (Ben-Avraham et al., 1995) and bathymetry (Hübscher et al., 2009) data have also been used. Most the seismic surveys available to these studies do not clearly resolve horizons below the MSC salt.

Numerous studies have been published on the tectonic implications of the geology of the onshore portion of the Cyprus Arc, the island of Cyprus (refs. within Morris et al., 2015; Robertson and Xenophontos, 1997). Several publications have studied data between Cyprus and the ESM; this includes seismic reflection (Klimke and Ehrhardt, 2014; Reiche et al., 2015; Reiche and Hübscher, 2015), refraction (Welford et al., 2015), bathymetric (Ehrhardt et al., 2011) and gravity data (Welford et al., 2015). Additionally the ESM, a key feature in the Neo-tectonic evolution of the Cyprus Arc (Kempler, 1998), has been subject to shallow ODP drilling as well as geophysical investigation (Robertson, 1998b).

The Cyprus Arc west of Cyprus has more limited published studies based on academic seismic data and bathymetry (Işler et al., 2005; Sage and Letouzey, 1990; Sellier et al., 2013; Woodside et al., 2002), and the Florence Rise was subject to shallow ODP drilling (Shipboard Scientific Party, 1978). The Anaximander Mountains at the western extremity of the Cyprus Arc have been subject to other geophysical investigations (Aksu et al., 2009; ten Veen et al., 2004; Zitter et al., 2003).

This chapter aims to evaluate and expand upon the hypothesised evolution of the Cyprus Arc by integrating offshore seismic data with the published understanding summarised in Figure 5.3. It is demonstrated later in this chapter that the lack of deformation of sediments on the (previously)

downgoing plate at the southern edge of the Cyprus Arc, and a well imaged unconformity corresponding to the cessation of subduction, unequivocally shows that subduction had ceased in the SE Cyprus Arc by the Cenozoic (Section 5.8.1). The data set available to this study images structures significantly deeper than the surveys available to other published studies of the area with the exception of Bowman (2011). He used the 2D data set offshore Syria that is used in this chapter to conduct a regional investigation of hydrocarbon prospectivity. However, Bowman (2011) did not attempt any kinematic restorations and did not comment on any implications for our understanding of incipient continent-continent collision. Thus, this study represents the first detailed discussion of the pre-Neogene evolution of the Eastern Cyprus Arc based on seismic data. Outside the area of the Syria 2D survey, the interpretations deeper than the MSC interval and the insights these interpretations provide are largely unprecedented (apart from some widely spaced speculative pre-MSC interpretations, see Bridge et al., 2005; Calon et al., 2005a; Hall et al., 2005a, 2005b; Hübscher et al., 2009; Maillard et al., 2011; Vidal et al., 2000a), especially with the line spacing available (Figure 3.1). Consequently, the pre-MSC structure of the Cyprus Arc shown in Section 5.5, the structure of the collision front south of Cyprus shown in Figure 5.27, and the area shown west of Cyprus shown in Section 5.7.2 are original.

5.4 Data and Interpretation

Identifying the data available to this study that covers the Cyprus Arc requires defining the limits of the Cyprus Arc. The Kyrenia Range has a bathymetric continuation to the east of Cyprus (Figure 5.5). The thrusts underlying this bathymetric ridge link to the Misis Mountains of SE Turkey so the system is termed the Misis-Kyrenia thrust complex (Hall et al., 2005a). The Kyrenia Range, Misis-Kyrenia thrust complex and Misis Mountains are the most northerly representation of the Cyprus Arc East of Cyprus visible on global relief. The Latakia and Tartus ridges represent the most southerly (Figure 5.5). To the west of Cyprus, the global relief expression of the southern edge of the Cyprus Arc is the Florence Rise and Anaximander Mountains (Figure 5.5). No offshore continuation of the Kyrenia Range is observable west of Cyprus on bathymetry (Ryan et al., 2009). Based on these global relief limits four of the data sets available to this study image the Cyprus Arc; the EMED00 and EMED75 surveys provide regional cover of the Arc to the west and east of Cyprus, the LEB3D survey provides 3D coverage of a section of sediments at the southern edge of the Arc on its eastern limb, and the Syria 2D data set provides a c. 4 km grid of lines over a section of the Arc adjacent to the LEB3D survey (Figure 5.5). The significantly better seismic coverage means the portion of the Cyprus Arc east of Cyprus is the focus of this investigation, and is subsequently referred to as the ‘Eastern Cyprus Arc’ (Figure 5.5). The west and central portions of the Arc are referred to correspondingly (Figure 5.5). The horizons picked in the Levantine Basin (Chapter 3) were used to provide constraints on the age of features in the Eastern Cyprus Arc. The sparse seismic lines to the west of Cyprus and the lack of age constraint (Chapter 3) meant that quantitative restoration of this portion of the Arc could not be achieved with confidence. This limits the extent of the investigation in the Western Cyprus Arc, although comparison with the conclusions based on the Eastern Cyprus Arc is made in Section 5.7.

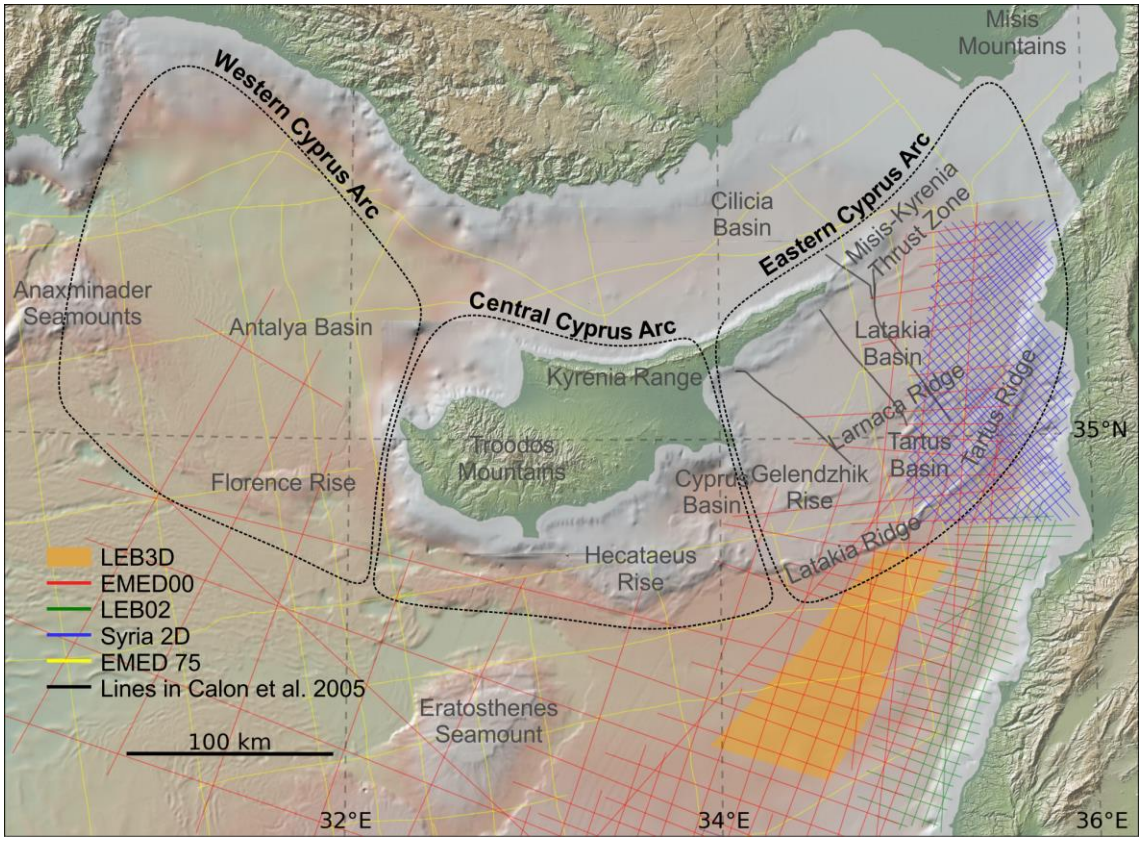

Figure 5.5-Map showing the location of the seismic lines used to investigate the Cyprus Arc, and the limits and location of the Eastern Cyprus Arc. The global relief (Ryan et al., 2009) vertical scale is shown on Figure 1.1 and the supplementary figure.

All the available seismic lines were interpreted as extensively as the data permitted confident correlation of horizons. The shallow depth and distinctive character of the seismic horizons associated with MSC meant they could be traced with confidence across the vast majority of the data. Between the seabed and MSC horizons a distinct kinematic package boundary was picked, termed the Plio-Quaternary horizon (Figure 5.6) which is discussed in Section 5.6.

Despite its depth, the Senonian unconformity could also be traced across the majority of the data, as seismic line EMED00-029 permitted correlation across the Latakia Ridge (Figure 3.15) and its distinctive character (Figure 3.14A; Figure 3.13A) allowed it to be picked with confidence north of the Latakia and Tartus Ridges. It should be reiterated that this pick represents the unconformable base of a sediment sequence; no ground-truthed constraint exists for the ages of the sediments under the pick on the Anatolian Plate, and structures observable in the seismic show these underlying sediments will vary in age (Figure 5.11 to Figure 5.16).

Four horizons between the Senonian Unconformity and MSC horizons were also picked across the southern half of the Eastern Cyprus Arc (Figure 5.6). These horizons are often unconformable in widespread but discontinuous locations (e.g. Figure 5.6). The folding of the sediments across the Latakia Ridge and other more northerly deformation fronts means many reflectors merge or tip out due to syn-deformation deposition (Figure 5.6). This meant that the age of these horizons is uncertain. One of the unconformities may be correlated with the Base Miocene pick in the Levantine Basin (Figure 3.15), and consequently is referred to as the Base Miocene Unconformity. The overlying and underlying horizons are referred to as the Upper Miocene and

Palaeogene (1 & 2) unconformities respectively and may include the regional Oligocene unconformity. As these horizons are defined by their depositional boundary characteristics they were used in the kinematic restoration attempted later in this chapter (Section 5.6).

The Upper Miocene Horizon is resolved as a weak reflector with stochastic breaks, and parallels the MSC reflectors (a property that is key to aspects of both this chapter and Chapter 6) to a degree that could suggest it is a multiple (Figure 5.6). This possibility is most apparent where undulations in the MSC reflectors appear to be mirrored in the Upper Miocene Horizon (Figure 5.6C). However, on a few key lines it may be resolved that this reflector diverges from the MSC reflectors without changing character (e.g. Figure 5.6D), and may therefore be resolved as a true reflector. It

Top structure maps, isochore maps in time and the faults in the area are shown in Figure 5.7. These interpretations reveal highly complex and varied deformation. To permit more concise description and discussion of the Eastern Cyprus Arc the areas were divided into the zones shown on Figure 5.7 and discussed in Section 5.5.

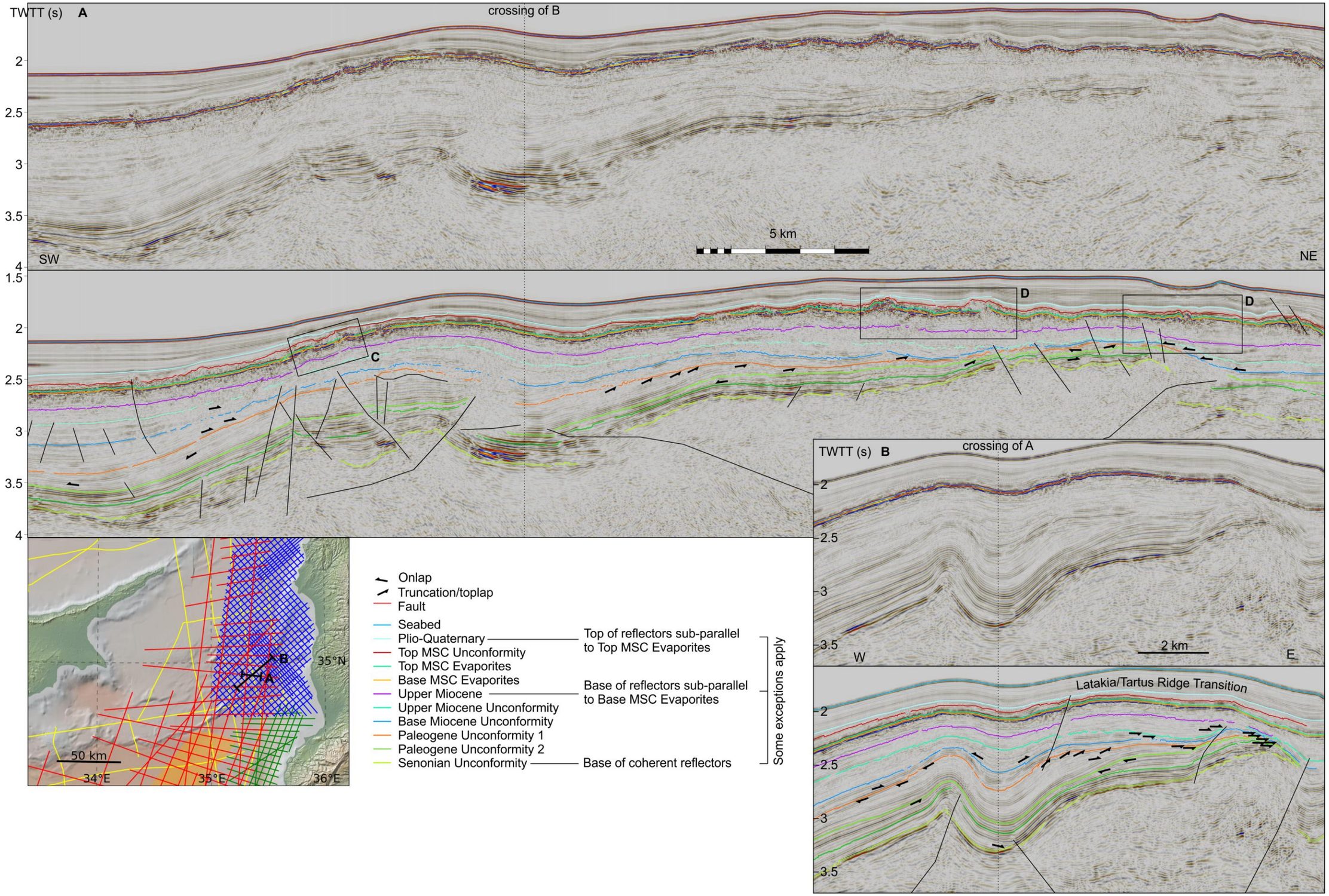

Figure 5.6-Seismic lines demonstrating the stratigraphic relationships and typical characteristics of the main reflectors picked over the Eastern Cyprus Arc. The labelled boxes highlight features discussed in the text. The global relief (Ryan et al., 2009) vertical scale on the minimap is shown on Figure 1.1 and the supplementary figure.

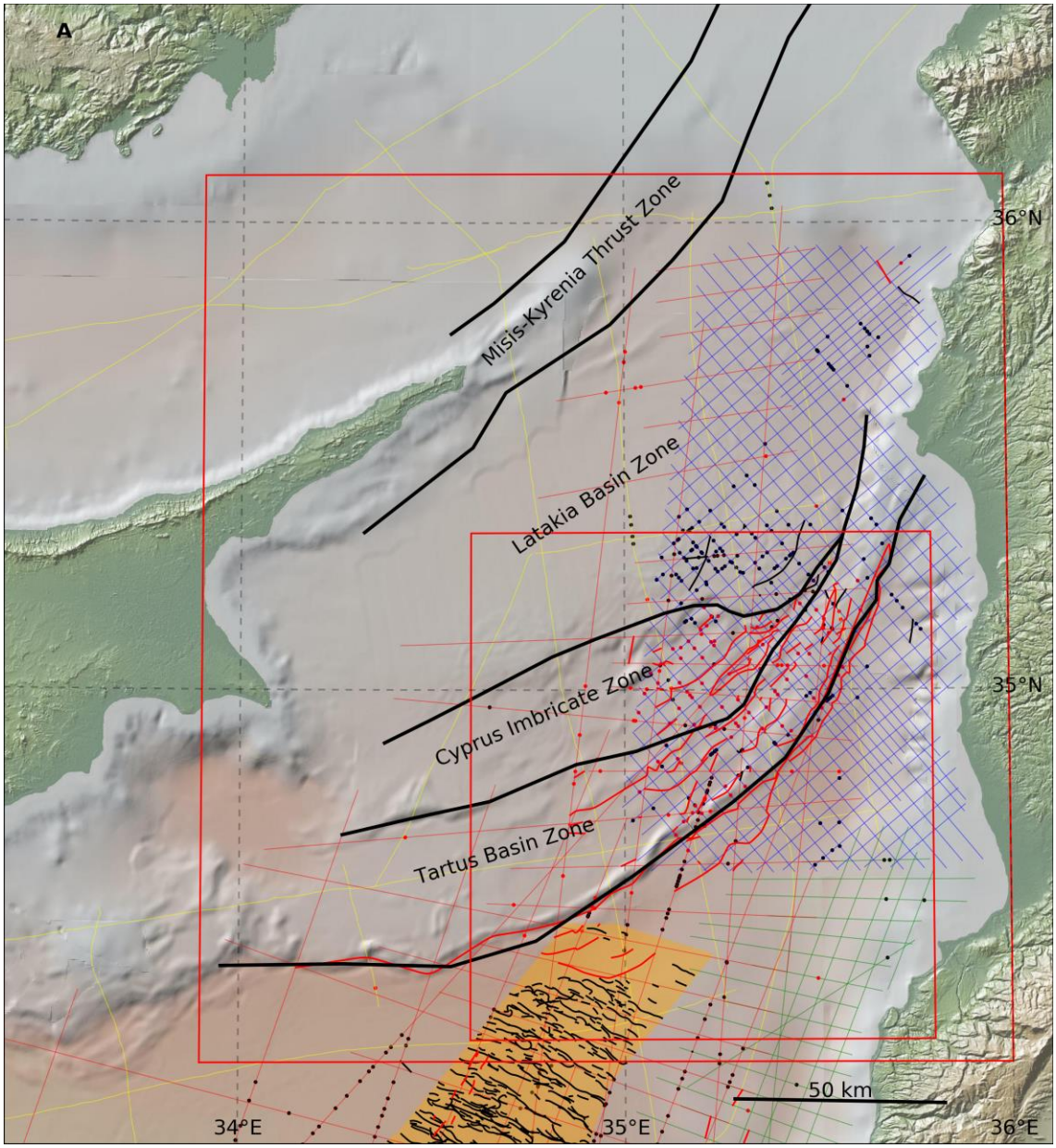

Figure 5.7-A) Faults picked in the Eastern Cyprus Arc and the locations of subfigures, B-I; B-I) Top Structure and isochore maps in time of the horizons labelled on each subfigure. Thick black lines indicate the limits of the structural zones described in Section 5.5, and dashed white lines indicate the limits of the MSC evaporite body. The global relief (Ryan et al., 2009) vertical scale on the maps is shown on Figure 1.1 and the supplementary figure.

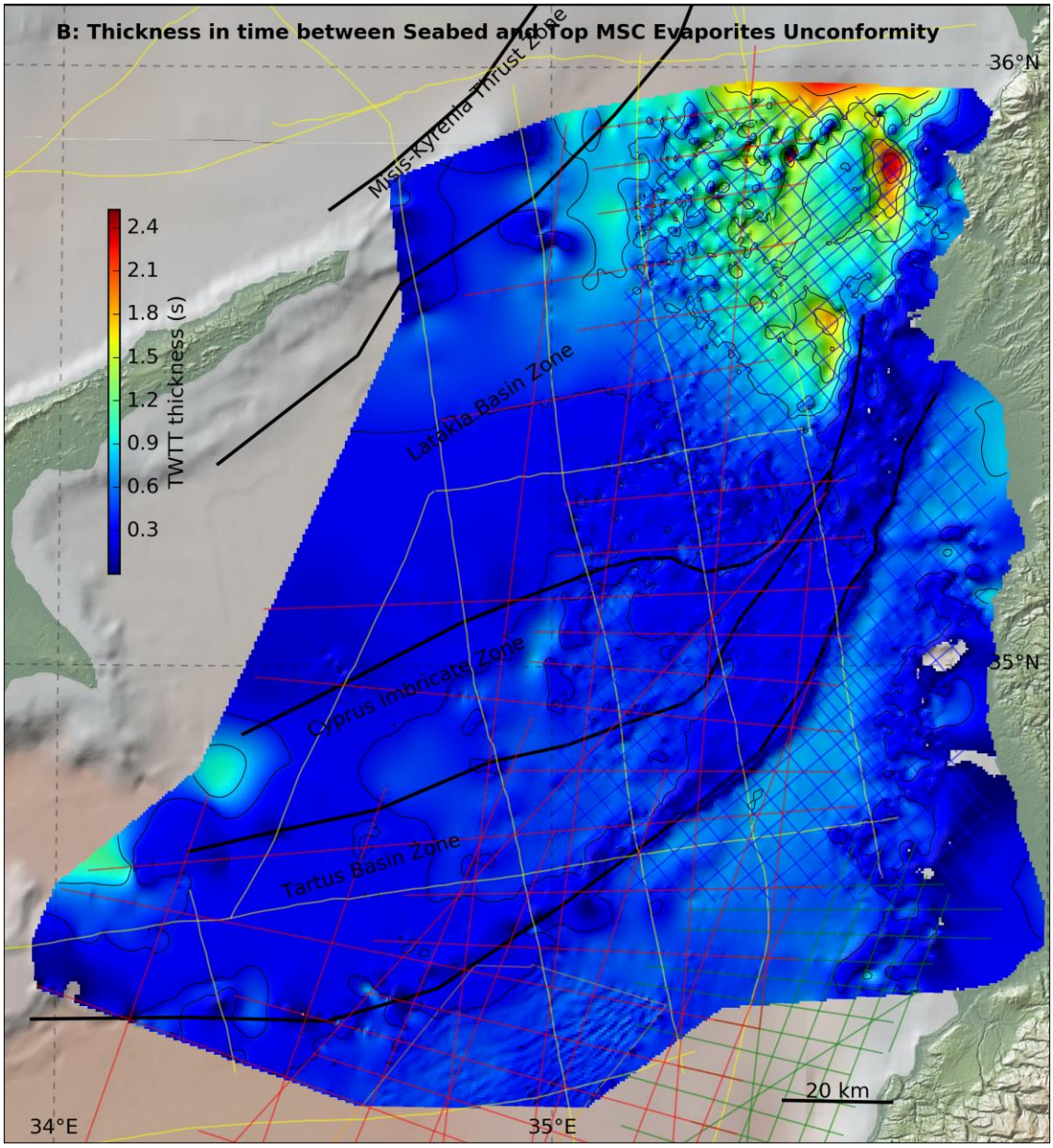
B: Thickness in time between Seabed and Top MSC Evaporites Unconformity
36°N
35°N
34°E
35°E
20 km
Misis-Kyrenia Thrust Zone
Latakia Basin Zone
Cyprus Imbricate Zone
Tartus Basin Zone
TWTT thickness (s)
2.4
2.1
1.8
1.5
1.2
0.9
0.6
0.3

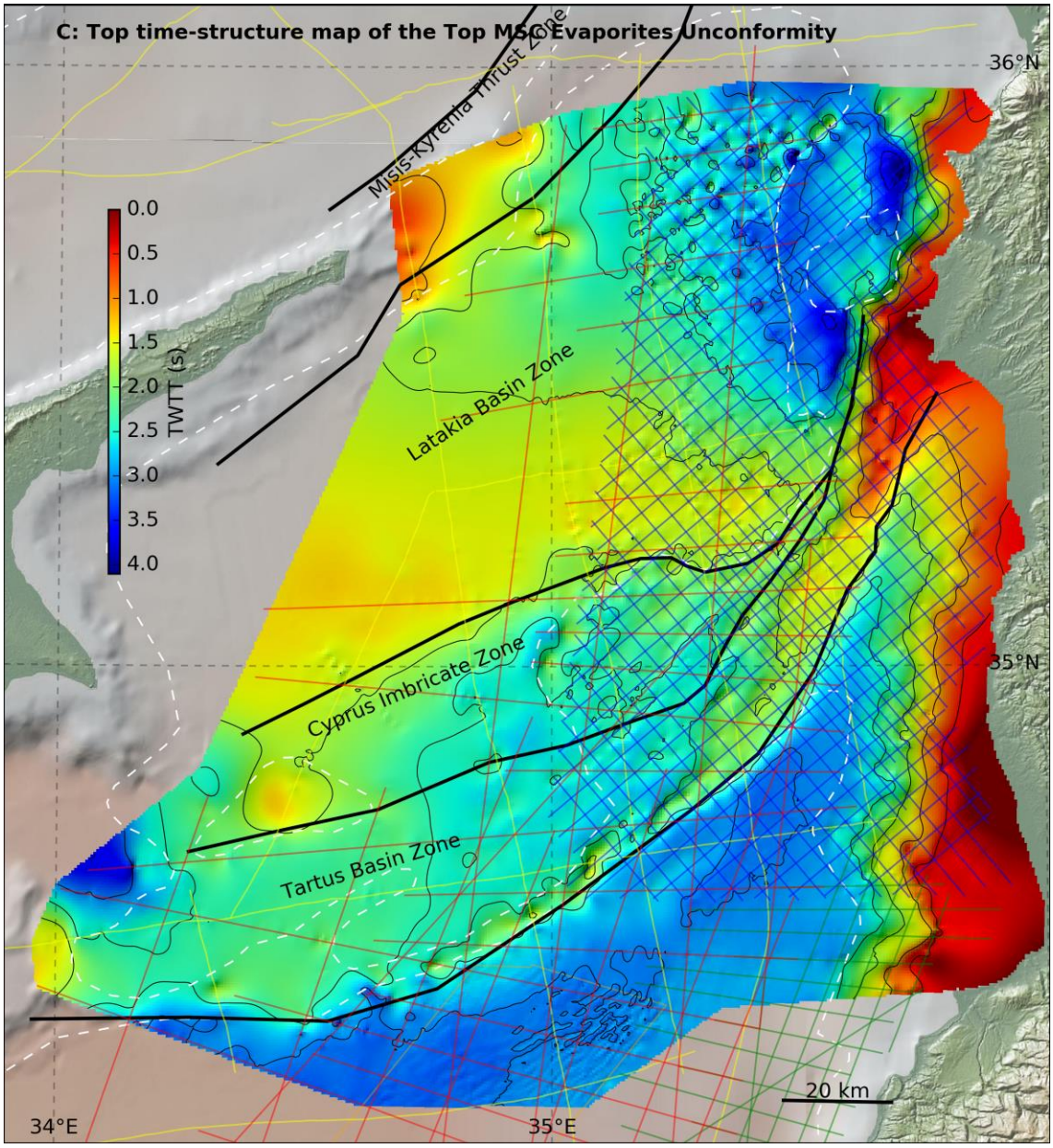
C: Top time-structure map of the Top MSC Evaporites Unconformity
36°N
35°N
34°E
35°E
20 km
Misis-Kyrenia Thrust Zone
Latakia Basin Zone
Cyprus Imbricate Zone
Tartus Basin Zone
TWTT (s)
0.0
0.5
1.0
1.5
2.0
2.5
3.0
3.5
4.0

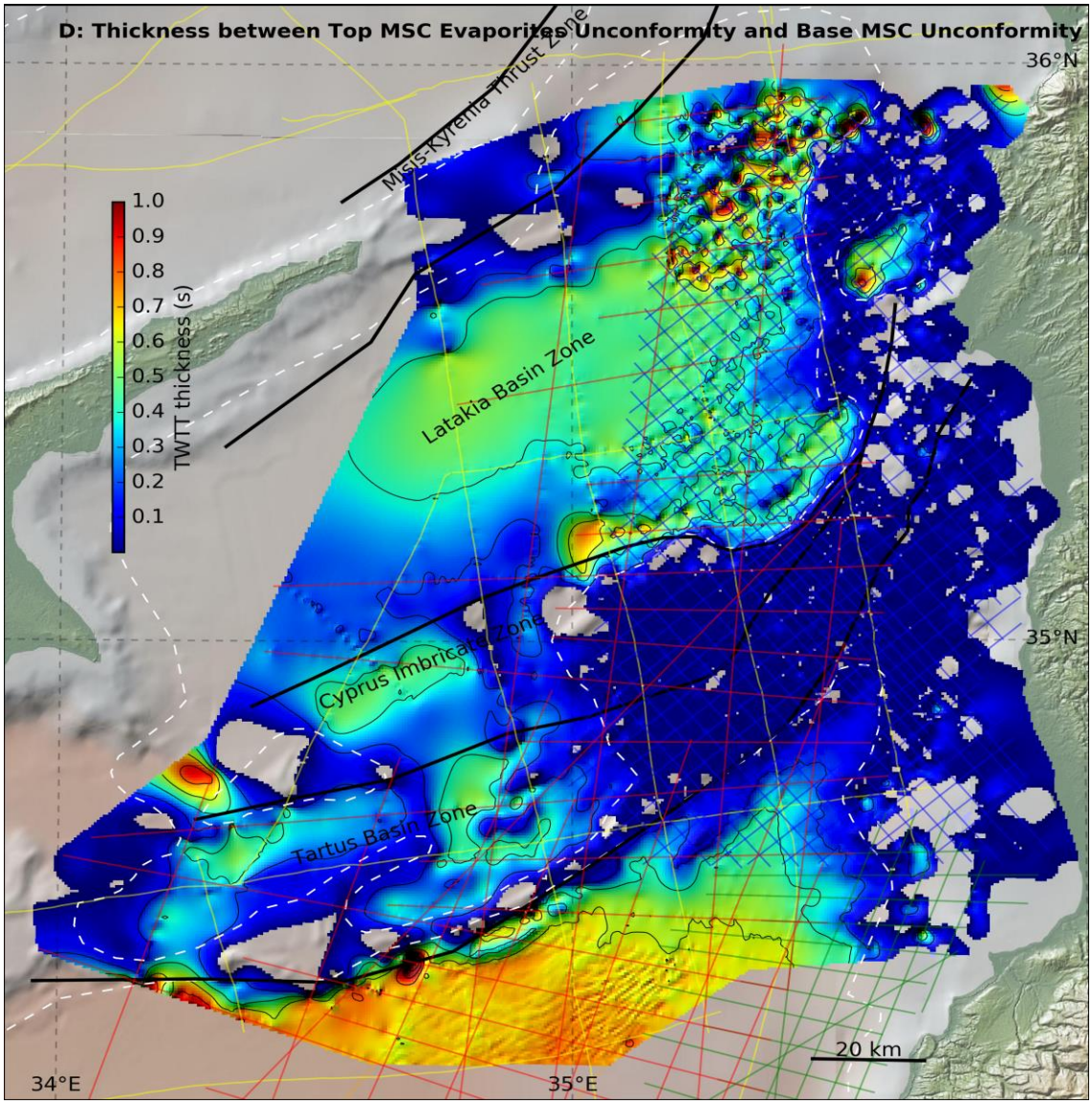
D: Thickness between Top MSC Evaporites Unconformity and Base MSC Unconformity
36°N
35°N
34°E
35°E
20 km
Misis-Kyrenia Thrust Zone
Latakia Basin Zone
Cyprus Imbricate Zone
Tartus Basin Zone
TWTT thickness (s)
1.0
0.9
0.8
0.7
0.6
0.5
0.4
0.3
0.2
0.1

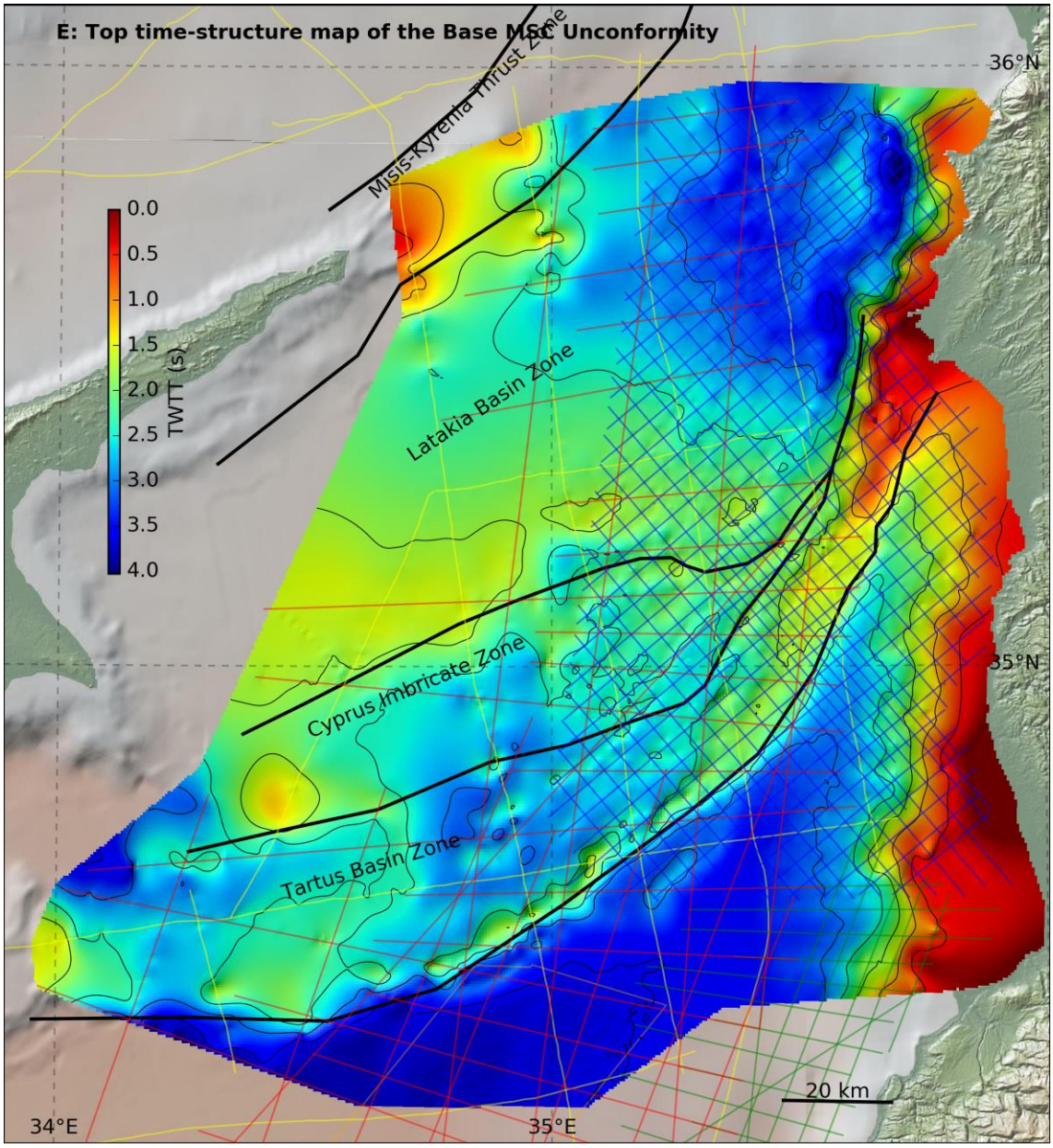
E: Top time-structure map of the Base MSC Unconformity
36°N
35°N
34°E
35°E
20 km
TWTT (s)
0.0
0.5
1.0
1.5
2.0
2.5
3.0
3.5
4.0
Misis-Kyrenia Thrust Zone
Latakia Basin Zone
Cyprus Imbricate Zone
Tartus Basin Zone

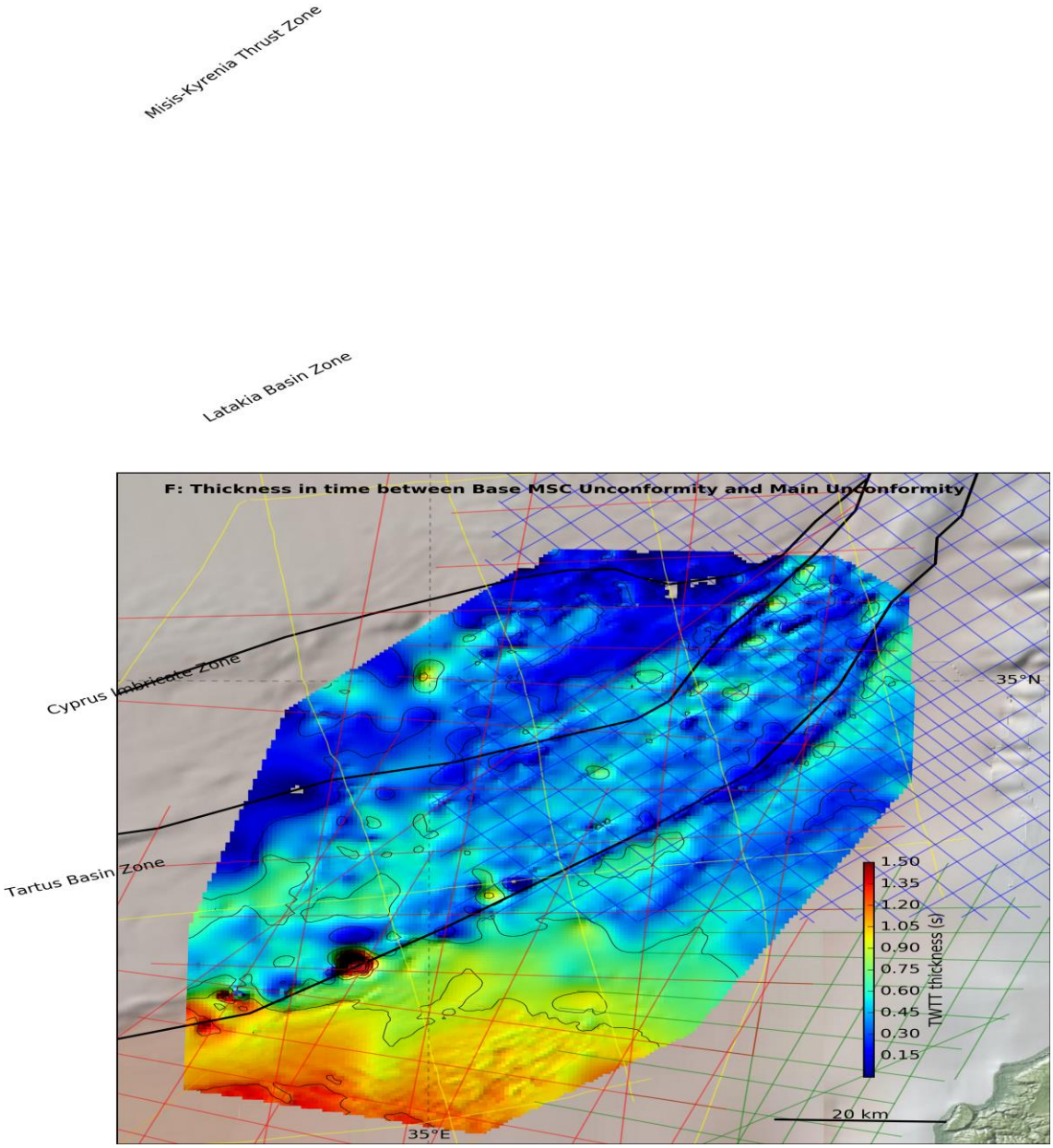
Misis-Kyrenia Thrust Zone
Latakia Basin Zone
F: Thickness in time between Base MSC Unconformity and Main Unconformity
Cyprus Lobriedte Zone
Tartus Basin Zone
35°N
35°E
1.50
1.35
1.20
1.05
0.90
0.75
0.60
0.45
0.30
0.15
TWTT thickness (s)
20 km

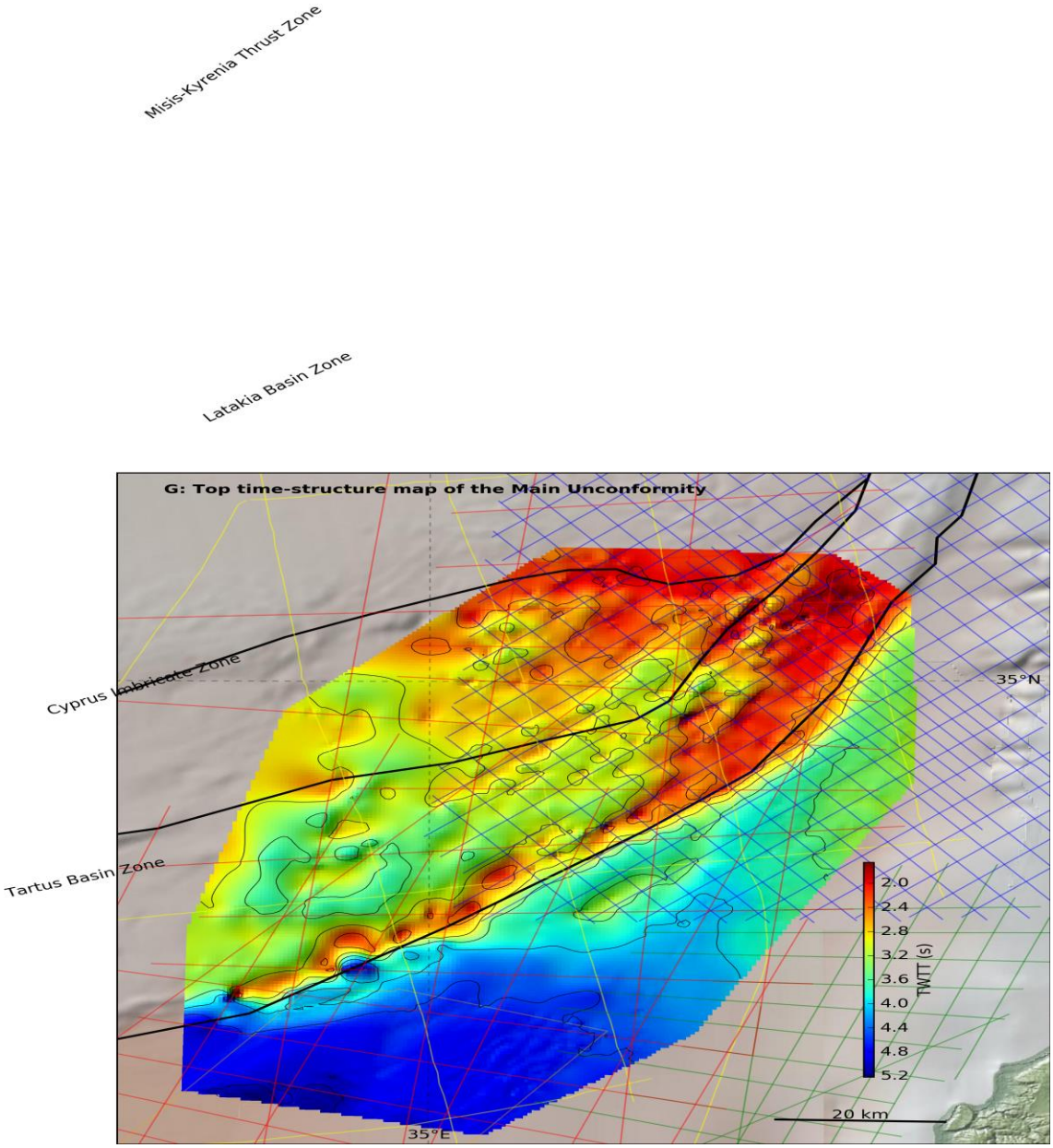
Misis-Kyrenia Thrust Zone
Latakia Basin Zone
G: Top time-structure map of the Main Unconformity
Cyprus Lobriedte Zone
Tartus Basin Zone
35°N
35°E
2.0
2.4
2.8
3.2
3.6
4.0
4.4
4.8
5.2
TWTT (s)
20 km

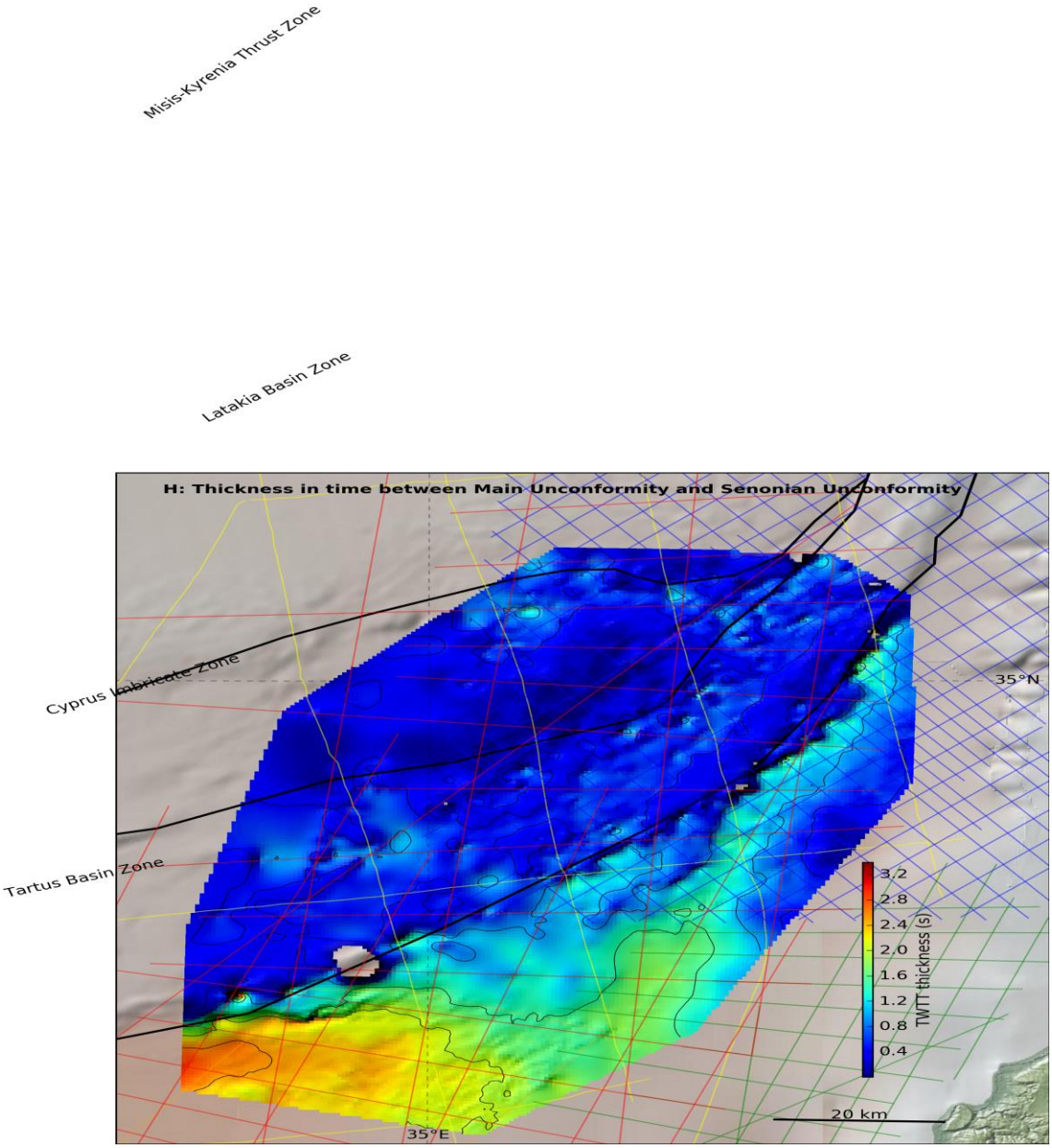
Misis-Kyrenia Thrust Zone
Latakia Basin Zone
H: Thickness in time between Main Unconformity and Senonian Unconformity
Cyprus Lobriedte Zone
Tartus Basin Zone
35°N
35°E
3.2
2.8
2.4
2.0
1.6
1.2
0.8
0.4
TWTT thickness (s)
20 km

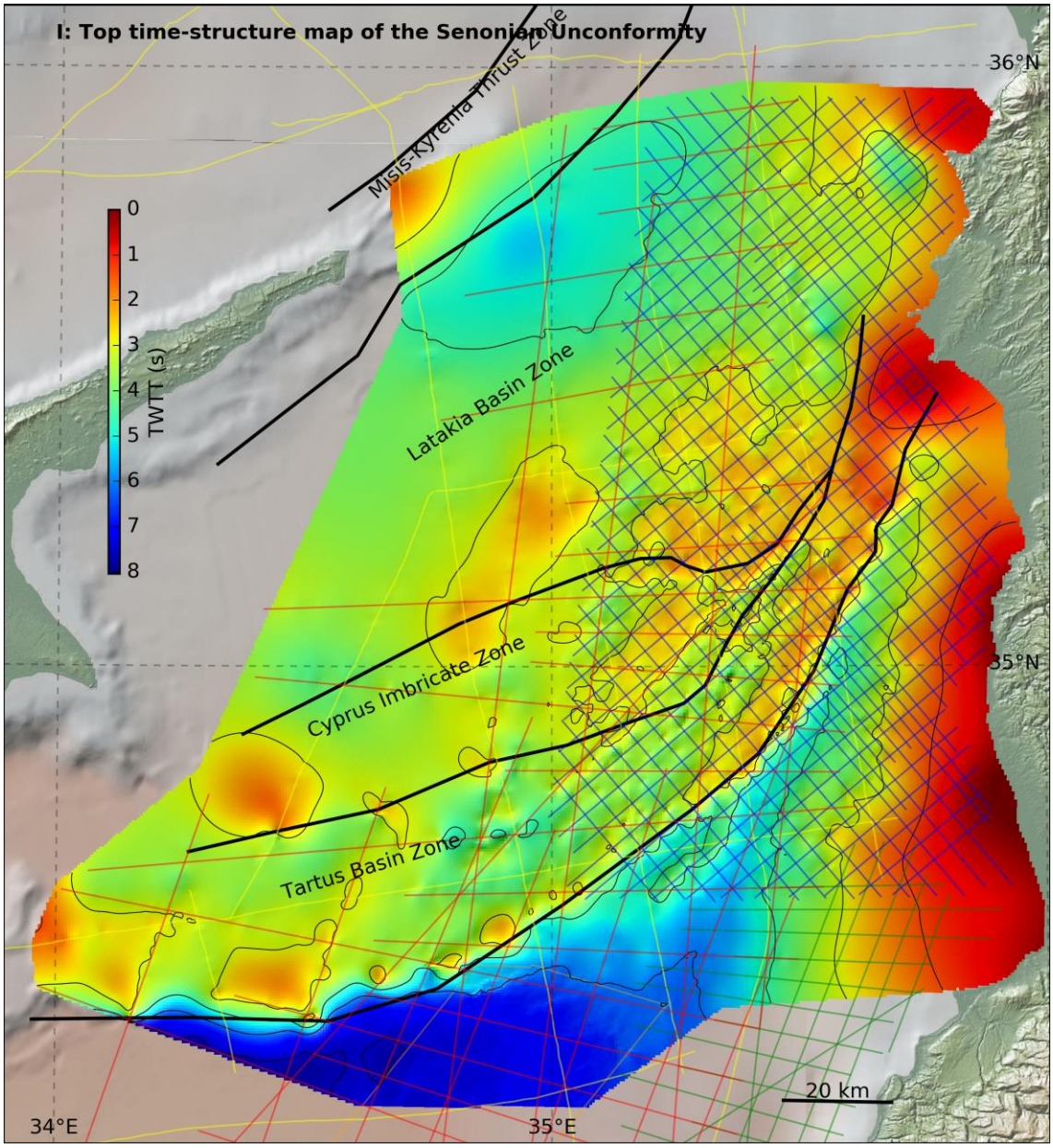
I: Top time-structure map of the Senonian Unconformity
36°N
35°N
34°E
35°E
Misis-Kyrenia Thrust Zone
Latakia Basin Zone
Cyprus Imbricate Zone
Tartus Basin Zone
TWTT (s)
0
1
2
3
4
5
6
7
8
20 km

5.5 Structural Zones

The complex series of structures and minibasins demand consistent nomenclature in order to be coherently described. Some zonal naming has been suggested by previous authors (Bowman, 2011; Maillard et al., 2011), however these previous versions variably do not consider deep structure, arc-wide structural trends (i.e. local zones instead), and previous nomenclature. Consequently, here an alternative zonal naming system is used, based on and accounting for pervasive trends over the whole Eastern Cyprus Arc, in the full sediment sequence down to the ophiolitic basement, and linking with onshore geology. The four structural zones are the:

1. Tartus Basin Zone
2. Cyprus Imbricate Zone
3. Latakia Basin Zone
4. Misis-Kyrenia Thrust Complex

These four zones are shown in cross section and lateral extent, in the area covered by the data available to this study, in Figure 5.8. A description of what defines each zone follows. Some comparable zoning with different names have been described by Kempler (1994 via Robertson, 1998a), but some key differences in the limits of the zones (due to newer, deeper seismic data) means the terms above have been used.

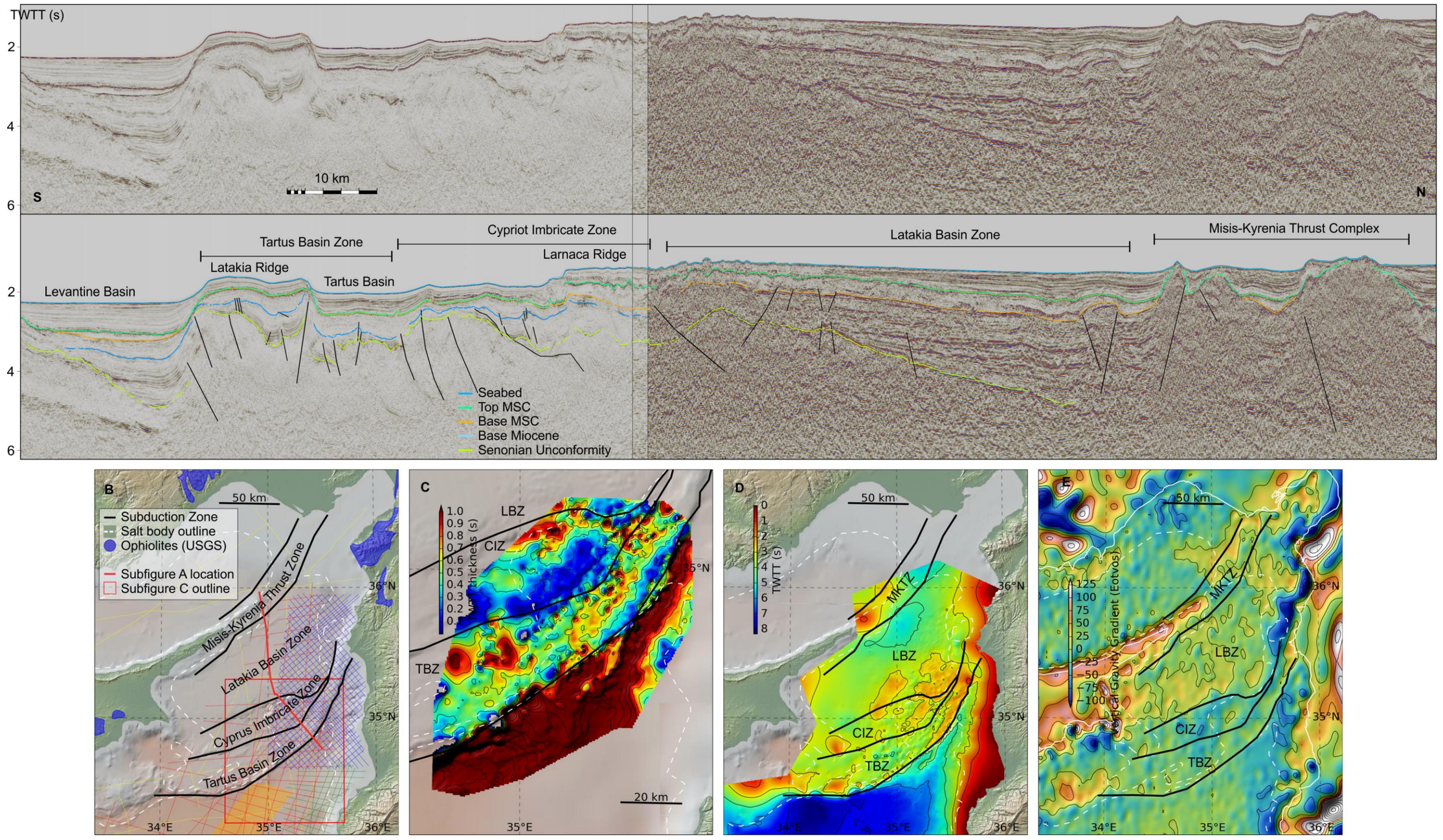

Figure 5.8-A) S-N striking regional seismic section across Cyprus Arc with deformation zones marked. Zones of deformation are marked on maps of: B) Global relief and seismic coverage; C) Isochore in time of Palaeogene sediments; D) Senonian Unconformity surface in time; E) Gravity anomalies (Sandwell et al., 2014, 2013; Sandwell and Smith, 2009). MKTZ: Misis-Kyrenia Thrust Zone, LBZ: Latakia Basin Zone, CIZ: Cyprus Imbricate Zone, TBZ: Tartus Basin Zone. The global relief (Ryan et al., 2009) vertical scale on the minimaps is shown on Figure 1.1 and the supplementary figure.

5.5.1 Tartus Basin Zone

The Tartus Basin Zone is delimited at its southern limit by, and includes, the Latakia and Tartus Ridges (Figure 5.8). Numerous seismic lines covering the Tartus basin are shown in Section 5.6. The thinner Tertiary sediment sequence, widespread thrust faults and elevated bathymetry that forms these ridges is in contrast with the Northern Levantine Basin and defines the subduction/collision plate boundary (Figure 5.8). The western limit of the Tartus Basin Zone is the Hecataeus rise, as the pre-Senonian basement is significantly elevated here relatively to surrounding areas (Figure 5.9). Offshore Syria, the Latakia Ridge bathymetric feature widens to over 10 km where an antithetic thrust at the north of the ridge uplifts a wider section of the seafloor. In the east of the Eastern Cyprus Arc the Tartus Basin Zone narrows until the widened Latakia ridge constitutes the whole zone. The eastern limit of the zone is therefore where the Latakia Ridge merges with the relief of the Syrian continual shelf. By this limit, the zone has changed significantly from its central portion; individual structures and horizons are rarely resolvable on the seismic. This is likely to be due to the large component of transform motion on the feature at this location which is discussed in more detail in Section 5.8.2.

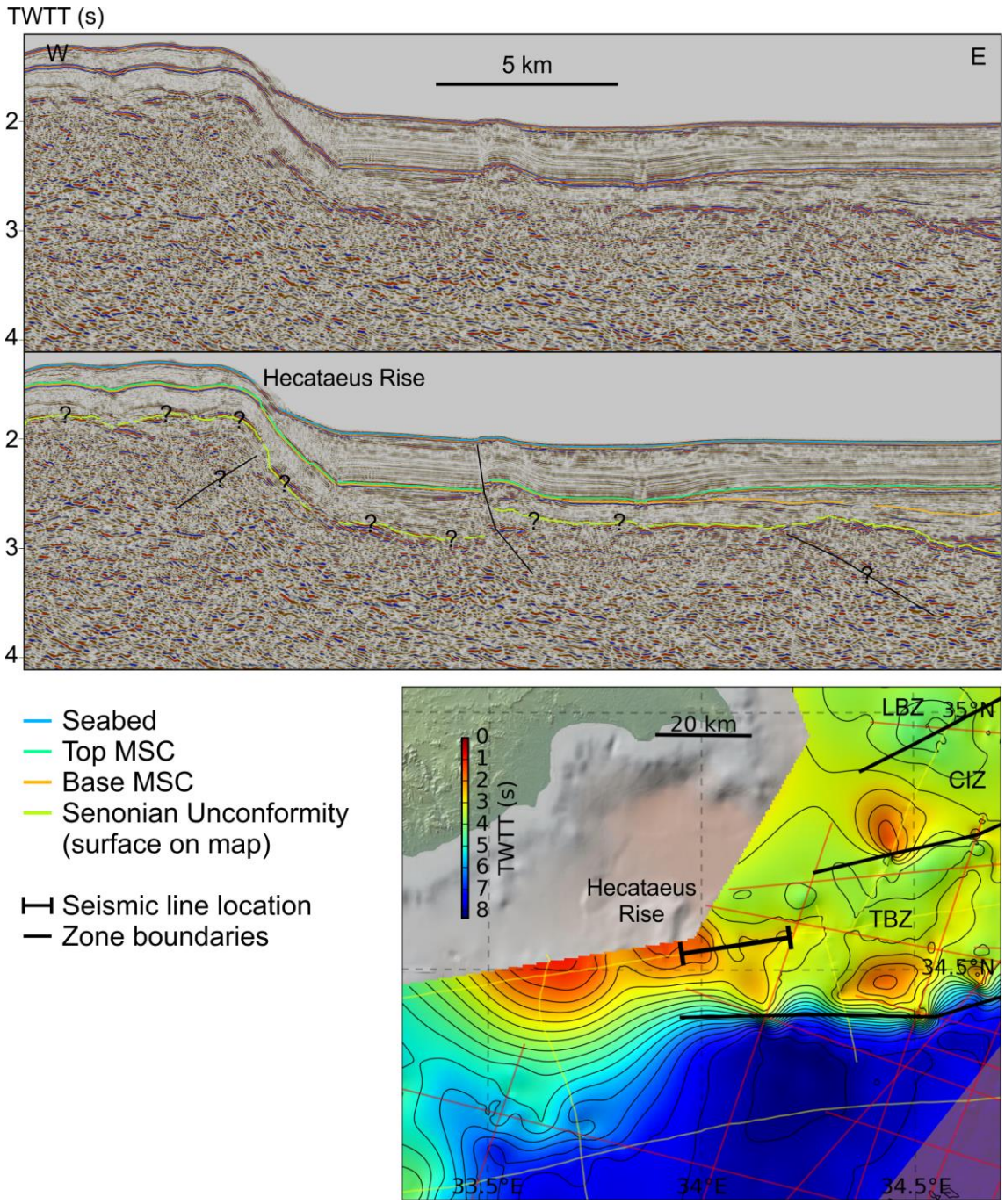

Figure 5.9-Seismic Line showing the western limit of the Tartus Basin Zone. LBZ: Latakia Basin Zone, CIZ: Cyprus Imbricate Zone, TBZ: Tartus Basin Zone. The global relief (Ryan et al., 2009) vertical scale on the minimap is shown on Figure 1.1 and the supplementary figure.

5.5.2 Cyprus Imbricate Zone

Moving northwards from the Tartus Basin Zone, the transition to the Cyprus Imbricate Zone is marked by an elevation in basement (termed the Margat Ridge by Bowman, 2011). The thrusts that generate this elevation only perturb the bathymetry at the Gelendzhik high (Figure 5.2), but the transition to elevated basement may be most clearly seen in plan view on the isochore map of Senonian to base Miocene sediments (Figure 5.8C). Imbricate stacks are not imaged throughout the Cyprus Imbricate Zone. However, stacked thrusts are clearly imaged on some lines (Figure 5.10) and thrusts with large (>200 ms TWTT) throws are widespread. Uplift of the pre-Senonian basement (Figure 5.8D) implies further thrusting where none is imaged seismically and also increases residual gravity data (Figure 5.8E). The eastern limit of the zone is the section of the Tartus Ridge that merges with the Syrian continental shelf.

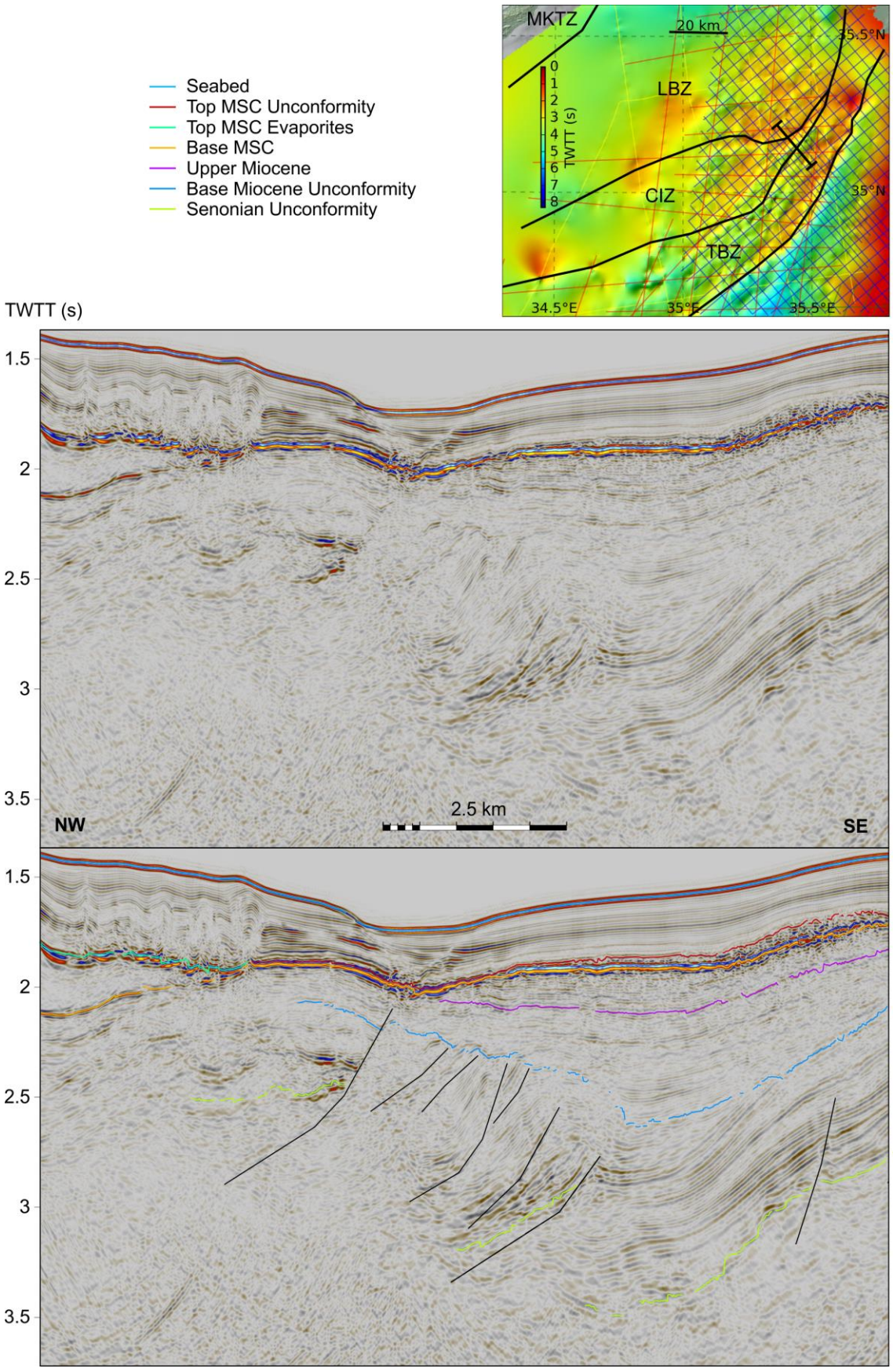

Figure 5.10-Seismic line showing imbricate stack within the Cyprus Imbricate Zone. The surface on the mini-map is the Senonian Unconformity. MKTZ: Misis-Kyrenia Thrust Zone, LBZ: Latakia Basin Zone, CIZ: Cyprus Imbricate Zone, TBZ: Tartus Basin Zone.

5.5.3 Latakia Basin (Zone)

Progressing northward the next zone is the Latakia Basin. In previous studies this basin has been delimited at its southern edge by the Larnaca ridge (Bowman, 2011; Calon et al., 2005a; Hall et al., 2005b), however inspection of seismic data reveals that in places this bathymetric feature coincides with the edge of the underlying MSC salt body (Figure 5.11). This forms a prominent bathymetric slope because the salt, and the overlying supra-salt sediments, have been gravitationally mobilised such that downslope at the edge of the salt body they are thickened (Hübscher et al., 2009; Maillard et al., 2011). Thus this ridge is a thin-skinned feature (Figure 5.7, Figure 5.8). Consequently, this study defines the southern limit of the Latakia Basin as edge of the peak of the basement high uplifted by the faults of the Cyprus Imbricate Zone. In much of the Eastern Cyprus Arc this coincides with the edge of the evaporite body. Consequently, the term 'Larnaca Ridge' is still used by this study, but in the broader sense to include the ridge of uplift that has uplifted the evaporites, the gravitational mobilisation of which has formed the bathymetric feature.

Thrust faulting is not observed in the majority of the Latakia Basin, instead the thick sequence of Tertiary sediments onlap the Larnaca Ridge and is largely undisturbed apart from a northward dip (Figure 5.11). This concurs with observations by Calon et al (2005a) who interpret this feature as a foredeep ramp. In the SE portion of this zone there are numerous previously undocumented normal faults (Figure 5.11). These faults offset the sediments at the base of the MSC evaporites and appear to strike broadly NE-SW. They are discussed further in Section 6.2.2.

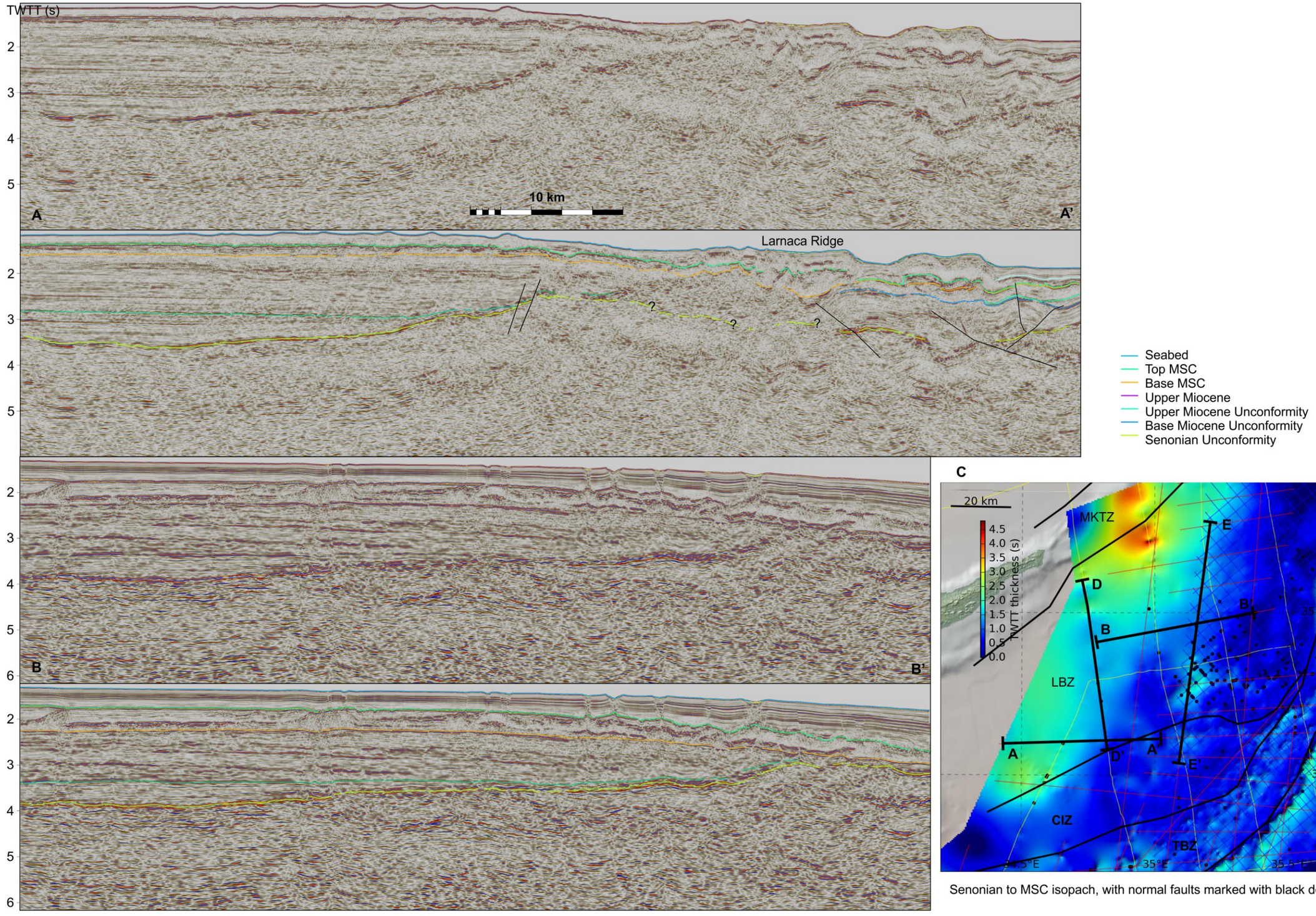

Figure 5.11-Seismic Lines and map showing the Latakia Basin sediments and late Miocene normal faulting. MKTZ: Misis-Kyrenia Thrust Zone, LBZ: Latakia Basin Zone, CIZ: Cyprus Imbricate Zone, TBZ: Tartus Basin Zone. The global relief (Ryan et al., 2009) vertical scale on the minimap is shown on Figure 1.1 and the supplementary figure.

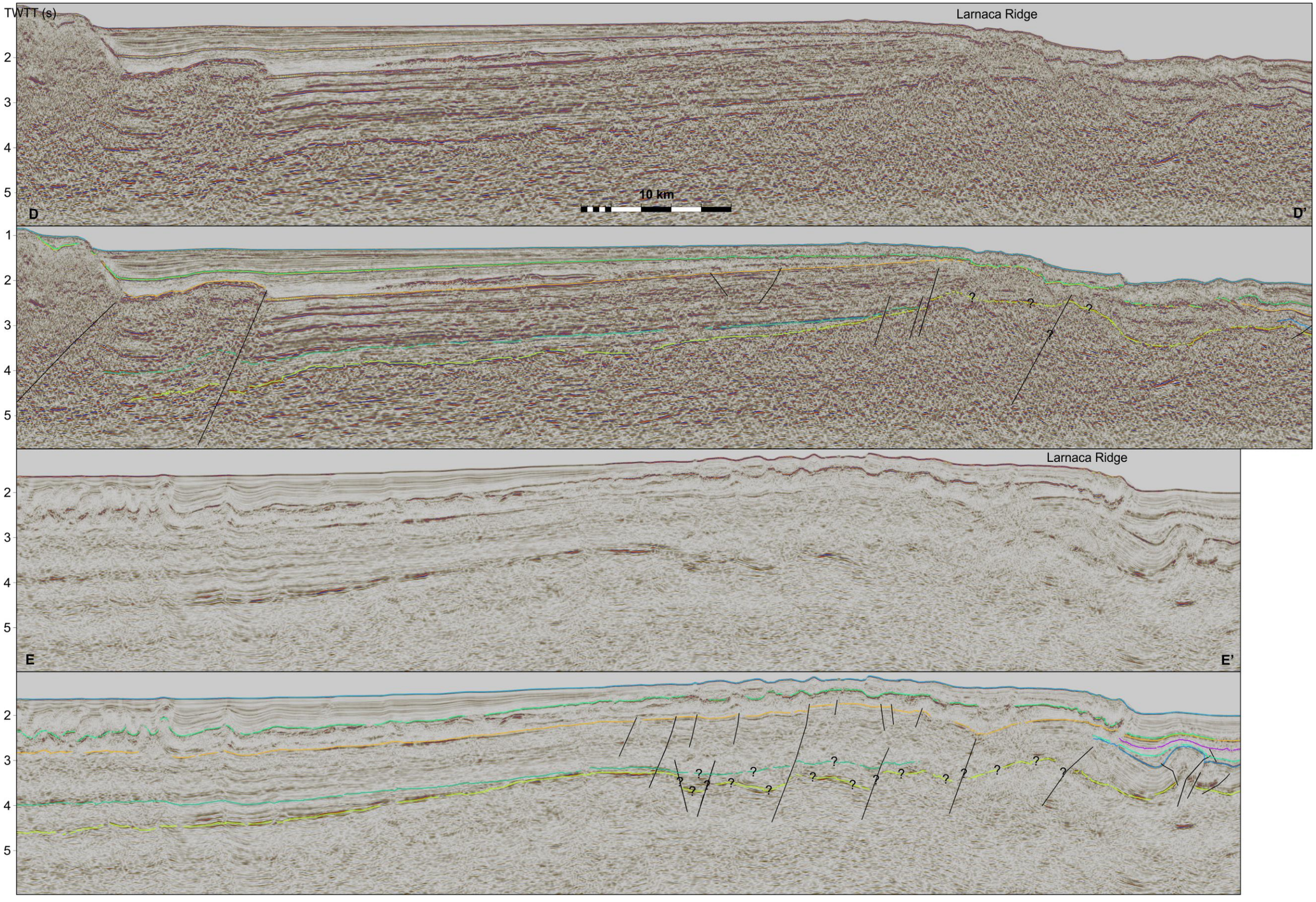
TWTT (s)
Larnaca Ridge
10 km
D
D'
1
2
3
4
5
?
Larnaca Ridge
E
E'

Beneath much of the Larnaca Ridge, the underlying pre-MSC reflectors become much more chaotic in comparison with the adjacent Latakia Basin and Cyprus Imbricate zones (Figure 5.11). This occurs in other locations in the EMR due to overlying salt tectonics, however in other areas of the Latakia Basin there are comparably more continuous seismic reflectors beneath comparably more salt tectonics, demonstrating this is not the case here (Figure 5.11E). The restoration carried out later in this chapter indicates that this area has been a Palaeo-high for much of the Cenozoic (see Section 5.6.8). Therefore, the speculative explanation for these more chaotic reflectors preferred by this study is that there is a carbonate platform distorting reflector imaging, distortion that may have been further exacerbated by karstic erosion during exposed uplift of the area.

5.5.4 Misis-Kyrenia Thrust Complex (Zone)

The most northward of the Eastern Cyprus Arc zones is the Misis-Kyrenia thrust complex. This feature is the intermediate section of the compressional feature that forms the Kyrenia Range in northern Cyprus (Robertson and Kinnaird, 2015) and the Misis Range of southern Turkey (Robertson et al., 2004). The bathymetric expression of the Misis-Kyrenia thrust complex tips out <40 km east of Cyprus. The thrust complex is imaged on four lines of 1975 vintage at the limits of the data set available to this study (Figure 5.12), including one without any bathymetric expression (Figure 5.12C). The vintage of the data that images them results in uncertain delineation of structures and highly uncertain age constraints. However, acoustic basement highs strongly contrast with sediments in the surrounding basins, and individual thrusted packages are clearly imaged (Figure 5.12C). This concurs with interpretations from previous studies (Calon et al., 2005a; Hall et al., 2005a).

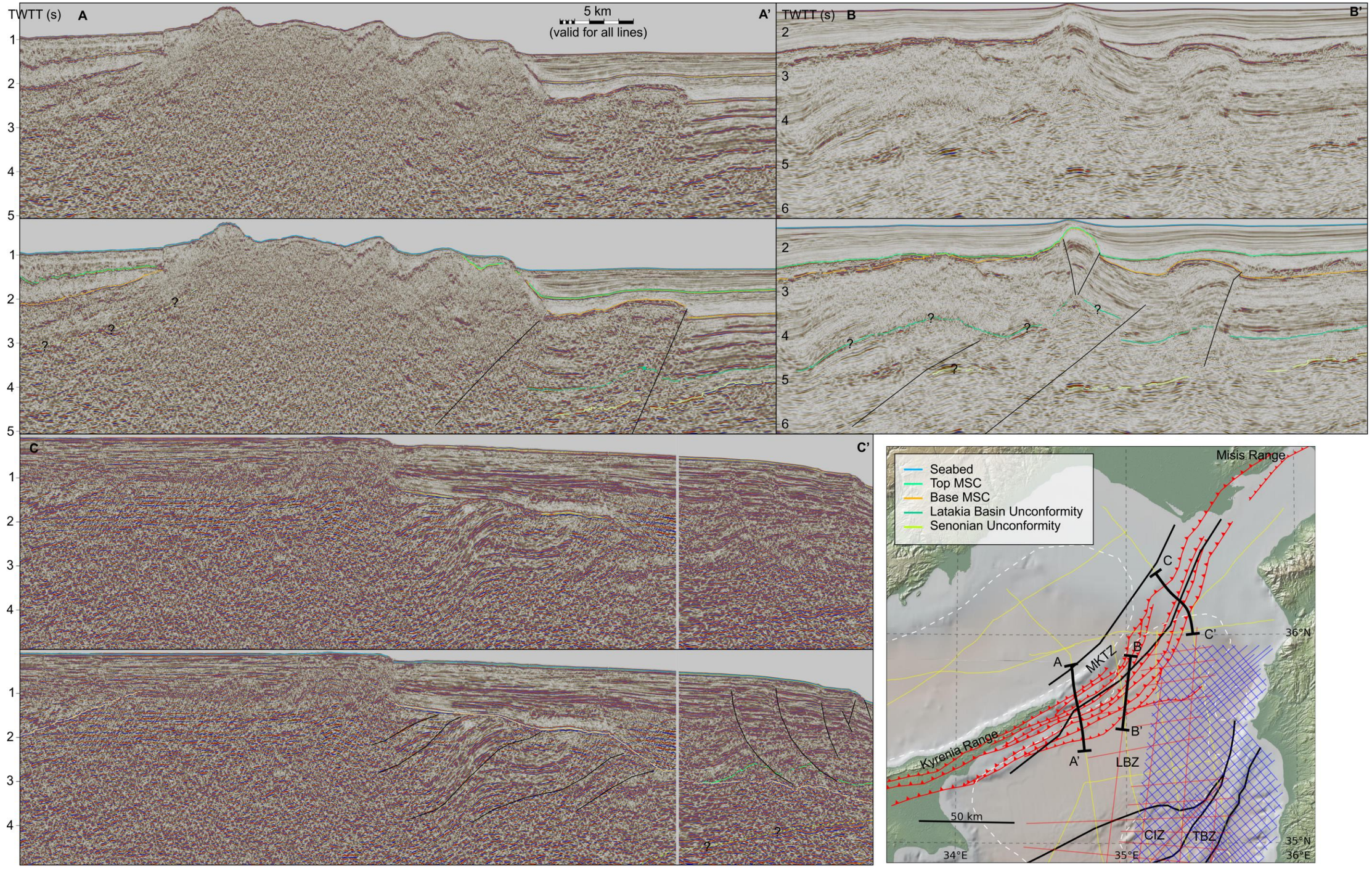

Figure 5.12-Figure showing the offshore continuation of the Kyrenia thrust zone. The thrusts marked on the map are from Hall et al. (2005a). MKTZ: Misis-Kyrenia Thrust Zone, LBZ: Latakia Basin Zone, CIZ: Cyprus Imbricate Zone, TBZ: Tartus Basin Zone. The global relief (Ryan et al., 2009) vertical scale on the minimap is shown on Figure 1.1 and the supplementary figure.

5.5.5 Arc-Anterior Deformation

Although referred to as the deformation front in this paper (for clarity and brevity), there are some expressions of the convergence across the Cyprus Arc that are south of the deformation front observable on bathymetry. The first is a 'spur' (as in lateral projection) of the Latakia Ridge that extends south beneath the MSC horizons of the Levantine Basin from the centre of the ridge (Figure 5.13A, C). The blind thrust fault of the spur folds the Cenozoic sediments above it (Figure 5.13A). The second is the normal faults that offset the summit plateau of the ESM (Figure 5.13B, C). These have previously been interpreted as having formed from flexural forces generated by docking of the ESM in the subduction zone (Ehrhardt et al., 2011; Robertson, 1998b). Their bathymetric relief and lack of syn-kinematic sediments indicate that they have formed very recently, and their localisation indicates they are linked to the ESM. An alternative would be that far-field forces related to the westward tectonic escape of Anatolia are reactivating other linear features on the ESM as faults, however the seismic and bathymetry data across the feature do not reveal any such features (Figure 5.13B, C), and the age of the ESM (Section 2.3.4) means pre-existing features might be expected to have reactivated earlier. Consequently, this study concurs with the previous interpretation, with the amendment that it underthrusting and not active subduction that is causing the flexure of the ESM crust. This amendment is based on evidence presented later in this chapter that indicates no currently active subduction (see Section 5.8.1).

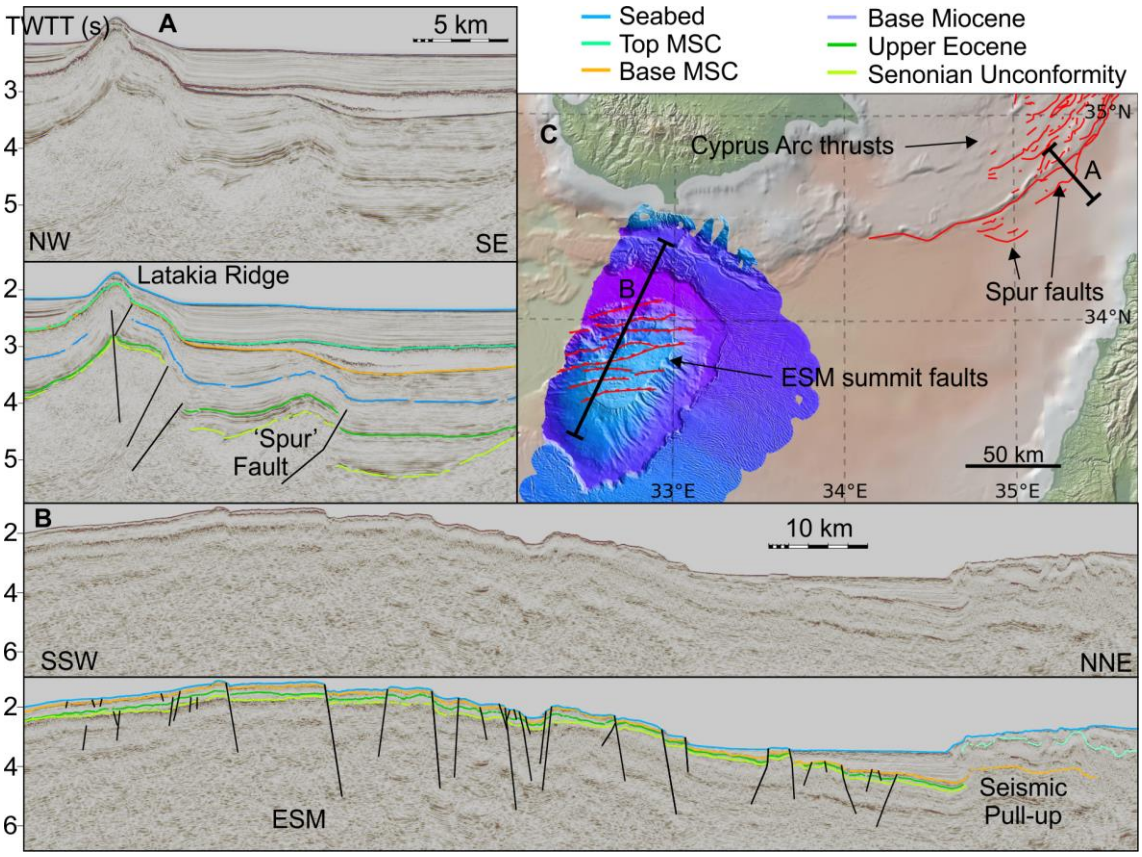

Figure 5.13-A) NW-SE striking seismic line showing a spur of the Latakia Ridge, B) SSW-NNE striking seismic line showing the normal faults on the ESM and C) map showing the location of A and B, faults of the Eastern Cyprus Arc interpreted on seismic data, faults of the ESM visible on bathymetry, and bathymetry showing folding adjacent to the Cyprus Arc (Ehrhardt et al., 2011; Ryan et al., 2009),

the global relief (Ryan et al., 2009) vertical scale is shown on Figure 1.1 and the supplementary figure..

Folding of the seafloor is observable on bathymetric maps and in some seismic data to the south of the whole Arc (Ehrhardt et al., 2011; Loncke et al., 2006; Reiche and Hübscher, 2015; Sellier et al., 2013) Figure 5.13C). In the Eastern and Central Cyprus Arc most this folding can only be clearly distinguished on high resolution multibeam bathymetry and may be linked to convergence across the Arc (underlying salt may also be an influence, see Chapter 7). South of the Western Cyprus Arc and further west in the Herodotus Basin larger (~1-5 km) scale folding may be observed on lower resolution bathymetry. This folding has caused some authors to draw the boundary of the African Plate with the Aegean and Cyprus Arcs, or the deformation front associated with that plate boundary, at the southern limit of these large scale but seismic data indicates these are thin-skinned feature related to halokinesis (Section 2.3.8).

5.6 Eastern Cyprus Arc Deformation Evolution

Deformation at the Eastern Cyprus Arc has varied in style and magnitude through time, and at each time the different structural zones have experienced different styles of deformation in varying magnitudes. To aid, constrain and verify deformation kinematic restoration may be attempted. Plummer et al. (2013) have produced sketch reconstructions (Figure 5.4), however more confident inferences may be made by carrying out a kinematic restoration that is spatially consistent. To do this for the Cyprus Arc cross sections in depth were required, so that the kinematic restorations remain spatially consistent during translation of a component of the vertical dimension to horizontal, and vice versa. Two options were available to this study to achieve this; use of a PSDM line or depth conversion of one or more PDTM lines. There are pros and cons to both options, discussed in the following section.

5.6.1 Line Selection for Kinematic Restoration

Only one PSDM line that crosses the Cyprus Arc is available to this study (Figure 5.14). This line is oblique to the trend of the Arc, restricting observation of dip-section feature geometries, but crosses the Arc in the centre of the Eastern Cyprus Arc. By crossing here as opposed to the east of the Eastern Cyprus Arc features imaged by the line were formed where the strike of the Arc is more representative of the rest of the Arc (Figure 5.14, Figure 5.2). In contrast, depth converting PSTM lines would mean several sections could be restored, and their location unrestricted. However, the only dip-section lines are in the eastern portion of the Eastern Cyprus Arc, where the strike of the Arc is less representative of the majority of the rest of the Arc. Published dip lines by Calon et al. (2005a) are available but they do not image the deeper reflectors required for restoration of the older stratigraphy.

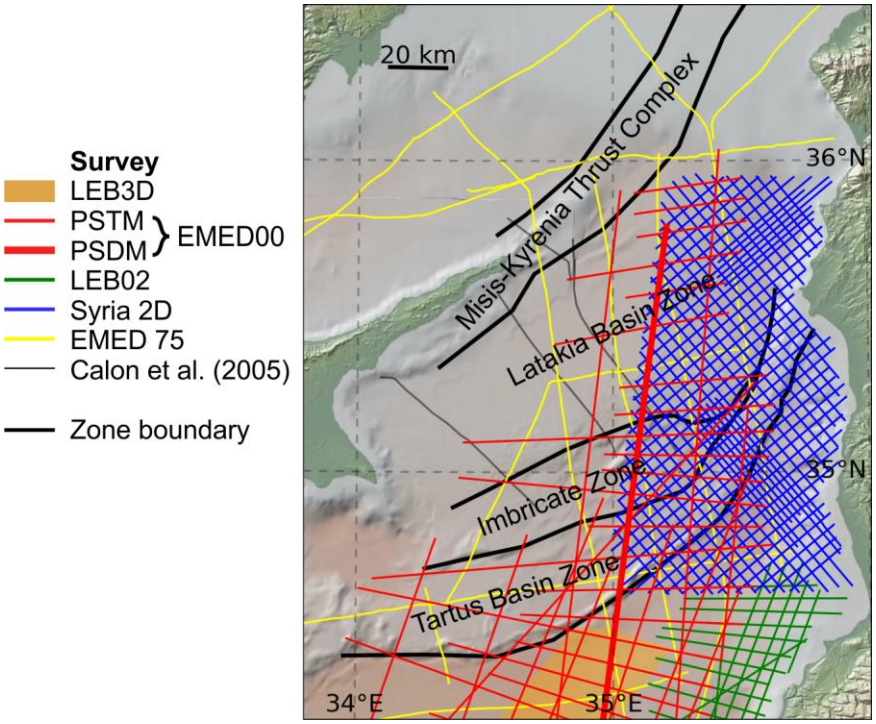

Figure 5.14-Seismic lines across the different zones of the Cyprus Arc. The bold red line shows the location of the PSDM line. The global relief (Ryan et al., 2009) vertical scale is shown on Figure 1.1 and the supplementary figure.

The PSDM line does not cover the Misis-Kyrenia Thrust complex zone (Figure 5.14), but no PSTM seismic lines available to this study image this feature well enough to confidently give constraints on the ages of different reflectors in the thrust-complex sequence, other than to indicate it is largely pre-MSC, so accurate kinematic restoration is not achievable via either depth conversion option. Consequently, this feature is omitted from the kinematic restoration and included in later conceptual diagrams on the basis of correlating low confidence horizons with onshore data.

Depth conversion of the PSTM seismic lines and volume requires velocity data of the imaged geology. The lack of any seismic velocity data over the Eastern Cyprus Arc, including lithological data and stacking velocities, meant that this depth conversion would be very speculative. The depth migration of the PSDM line was completed using stacking velocities .

Based on the discussion in the preceding paragraphs the PSDM line was selected for restoration. The depth migration errors noted on the PSDM line (Section 3.2.3) are taken into account during the restoration; the artificial pull-up is removed on the section used for kinematic restoration. The coherency of some reflectors on the line is better on the PSTM than the PSDM, and vice versa (Figure 5.15). The two versions of the line were interpreted jointly to improve the confidence in the final interpretation.

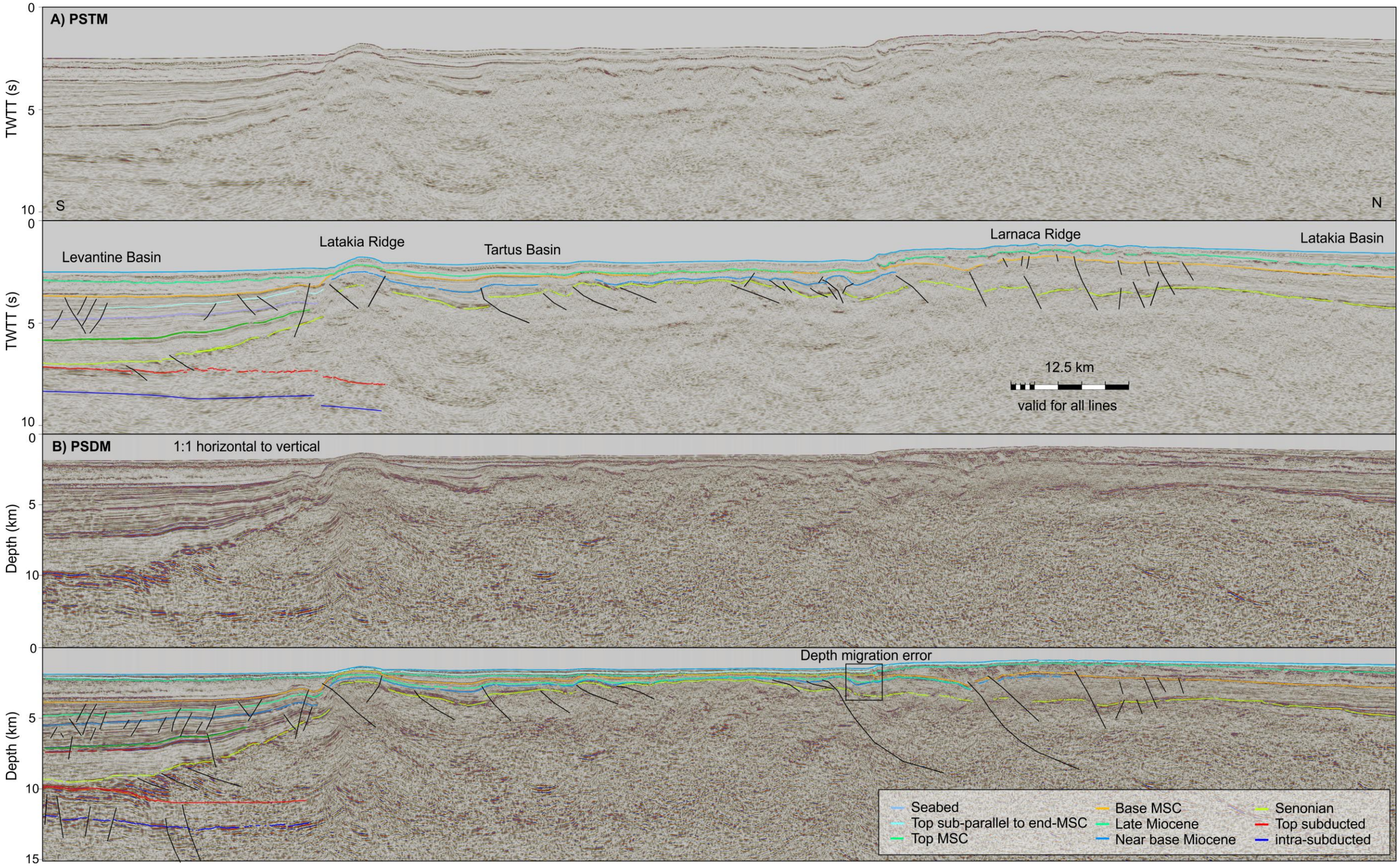

Figure 5.15-Interpreted and uninterpreted images of the (A) PSTM and (B) PSDM seismic lines, and (C) simplified cross section used in restorations. The PSDM error is discussed in Section 3.2.3. Location of the section is shown on Figure 5.14.

Numerous minor faults (i.e. < c. 30 m throws) are present on the interpreted cross section (Figure 5.15B). As the focus of this restoration is the large-scale changes pertinent to the wider Arc these small-scale features where omitted from the restoration. The restoration was accomplished using Midland Valley Move™ and CorelDRAW® software.

To attempt to understand the evolution of deformation across the Eastern Cyprus Arc, the interpreted horizons were selected to divide the sediment up into kinematic packages (see Section 5.4). These kinematic packages are defined by the truncation of reflectors in each package; planar (no truncations), erosive (base of package truncates underlying reflectors), onlapping (base of package truncates against underling package) and syn-kinematic (reflectors thin until truncation within package) and are shown in Table 9. These different packages contain information regarding the kinematic environment in which they were deposited, this is discussed during description of the deformation stages.

Table 9-Description of the different kinematic packages defined in the Eastern Cyprus Arc.

Package Age	Description
Plio-Quaternary	Syn-compression reflectors, erosive boundary with onlaps.
End MSC	Non-kinematic, and the end of the MSC occurred during this period. Consequently the reflectors are sub-parallel with the top of the salt.
Intra-MSC	Pulse of compression; pre- and post- compression kinematic packages in the salt sequences but no syn-kinematic packages that can be interpreted with confidence.
Late Miocene	Compression hiatus with normal faulting demonstrating extension. Onlapping present. The start of the MSC occurred during this period.
Miocene-Senonian	Many erosion surfaces and changes in compression rate, but syn-compression throughout.
Cretaceous	Active subduction, widespread unconformities and thrusting.

Although the stages of this restoration are discussed sequentially down through stratigraphy, some of the aspects to this restoration are reliant on observations of deeper stratigraphy. To avoid repetition, many of the references in the following sections are to sections and figures which follow the reference itself. For the same reasons, the restoration stages themselves are drawn together in Figure 5.21 on page 222.

5.6.2 Plio-Quaternary

In the Tartus Basin and Imbricate Zones the Plio-Quaternary sediments have many reflector truncations and thicker sediment sequences beneath current bathymetric depressions (Figure 5.16). This demonstrates the presence of several localised sequence boundaries within the package caused by folding of the underlying sediments during sediment deposition. The folds are fault-bend-folds above deeper blind thrust faults that are accommodating shortening across the section. In some areas of the Latakia and Tartus Ridges some thrusts offset reflectors in the Plio-Quaternary at the sea floor. The sudden transition from parallel reflectors to reflector thinning and terminations indicates the folding initiated over a short interval, assuming no drastic changes in sedimentation rate.

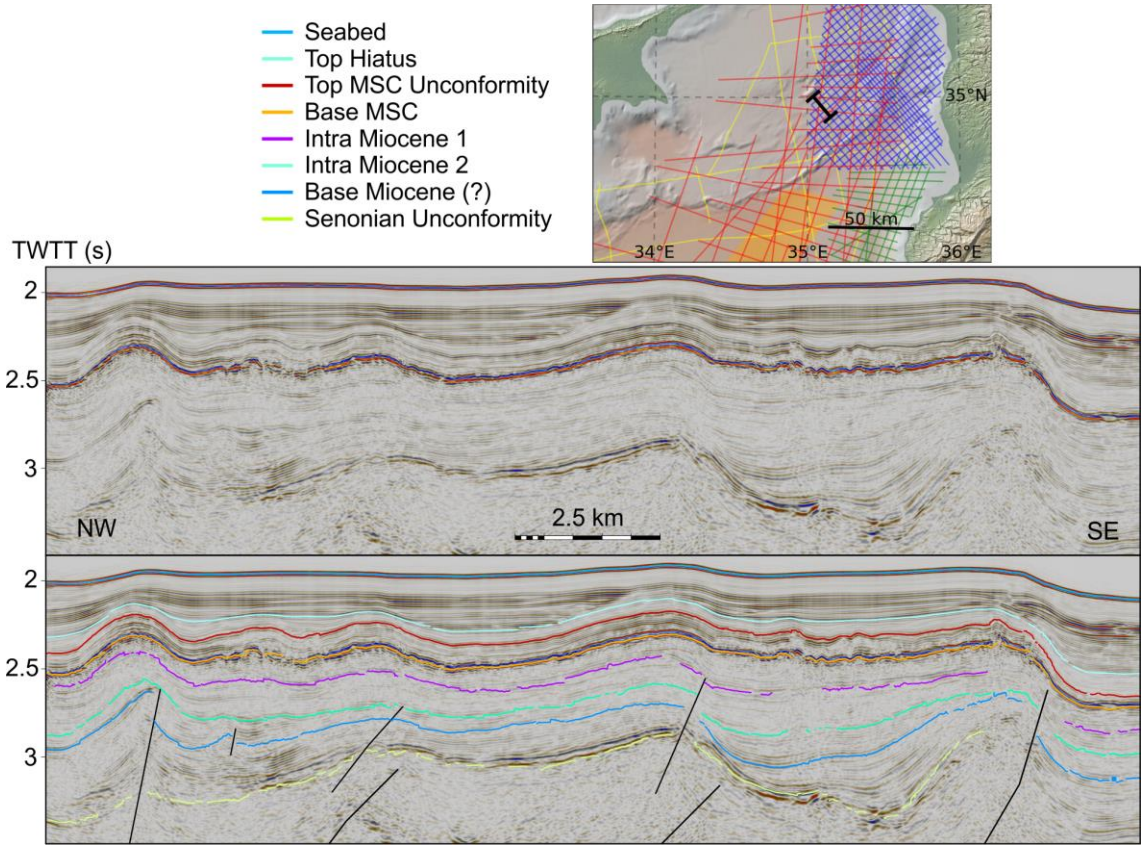

Figure 5.16-NW-SE striking seismic section showing deformation of post-MSC sediments. The global relief (Ryan et al., 2009) vertical scale on the minimap is shown on Figure 1.1 and the supplementary figure.

There are several observations that indicate the evaporite body which underlies the Latakia Basin Zone and part of the Imbricate Zone has been uplifted:

- This part of the evaporite body is shallower than the evaporites in the Tartus Basin Zone and remainder of the Imbricate Zone (Figure 5.17A-B). Thick evaporite sequences are typically deposited in bathymetric lows, as demonstrated elsewhere in the EMR (Chapter 3).
- This part of the evaporite body is convex up, despite being typically deposited sub-planar (Figure 5.17A).
- The leading edge of the evaporite body coincides with the edge of a gravity high (Figure 5.17B-C). Gravity highs are associated with elevated higher density rocks that the surroundings, basement uplift would achieve this. An alternative is that the gravity high is due to another process/feature that results in a bathymetric low, but given that the salt body is convex up in this area the former is more favourable.

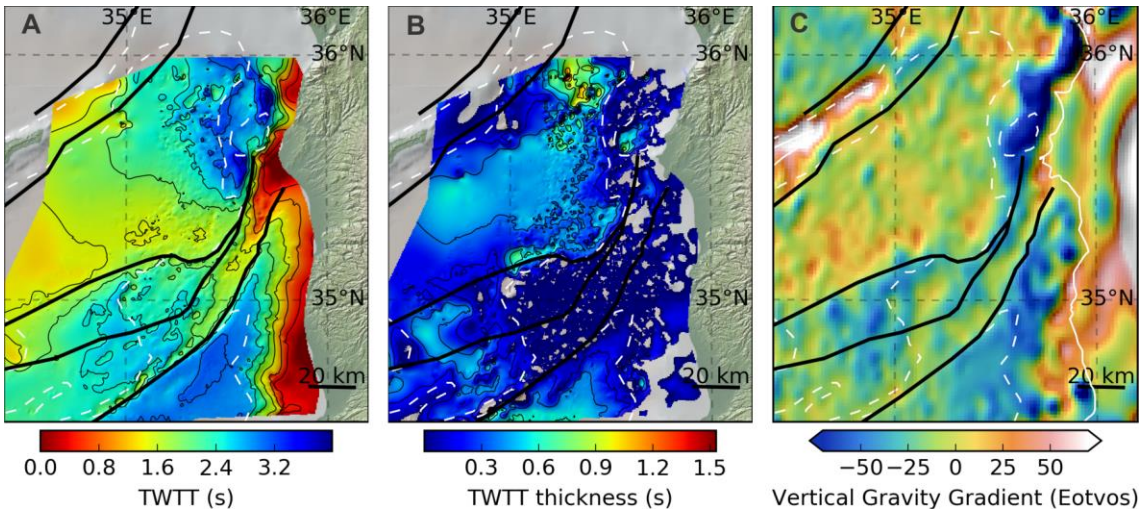

Figure 5.17-Grid data illustrating post-MSC uplift: A) TWTT top structure map of the top of the evaporite body or top MSC unconformity; B) evaporite thickness in TWTT, C) vertical gravity gradient (Sandwell et al., 2014, 2013; Sandwell and Smith, 2009). The thick black lines are the structural zone boundaries (Section 5.5), and the dashed white lines are the outlines of the MSC evaporite bodies. The global relief (Ryan et al., 2009) vertical scale on the maps is shown on Figure 1.1 and the supplementary figure.

Later discussion shows there was a non-compressional period following the MSC (see Section 5.6.3), which means the top of the end-MSC parallel reflectors is contemporaneous with the initiation of the compression that has uplifted the evaporites. It could be argued that this uplift could have occurred during the Intra-MSC compressional phase (see Section 5.6.4) but as the thickness of the uplifted evaporites is comparable to that of the evaporites which were not uplifted (see SW corner vs. centre of Figure 5.17B; Figure 3.14A) this seems unlikely. This is because if the evaporite uplift had occurred during the Intra-MSC compressional phase the uplifted evaporites would have ended on a high, where further evaporites would be non-preferentially deposited.

No fault offsets indicating thrusting may be observed beneath the uplifted evaporites. However, there are a series of Miocene age normal faults (Section 3.6.1). Partial inversion of these normal faults, and/or others that are listric at sub-seismic depths, could explain uplift of the evaporites. However, development of the normal faults appears to have ceased during the MSC (Figure 5.11; Figure 5.15B) and no evidence for inversion is observed. Alternative methods of uplift may be deeper thrusting not observed on the seismic data, or serpentinite diapirism as is the case for the Troodos Mountains in Cyprus (Section 2.3.9). This serpentinite diapirism forms the bulls-eye uplift of the Troodos (see Figure 5.26), which contrasts with the more linearly orientated uplift observed at the Latakia Basin (Figure 5.17). This suggests that deep blind thrusts may be the most likely explanation. Whatever the mechanism, that this uplift occurred during westward tectonic escape of Anatolia and the Cyprus Arc, and not during the intra-MSC or earlier compression, indicates that the stress configuration of these events is different; the later stresses must have been such that it was conducive to inversion of the Latakia Basin.

Based on these observations and constraints the Eastern Cyprus Arc Section may be restored as shown in Figure 5.21B. Further palaeo-bathymetric constraints for Figure 5.21B were derived from underlying stratigraphy and are discussed in Section 5.6.3.

The shallow depth of the sediments displaying the Plio-Quaternary tectonic deformation (and lack of overlying evaporites) means they are clearly imaged on seismic data, and consequently this deformation stage is well described in previous studies of the area (Calon et al., 2005a, 2005b, Hall et al., 2005a, 2005b; Maillard et al., 2011). They conclude, and this study concurs with, that this deformation episode initiated in the early-middle Pliocene and remains active today (Hall et al., 2005a, 2005b).

Halokinesis of the MSC salt has occurred in the Eastern Cyprus Arc, as shown by extensional and compressional structures upslope and downslope respectively at the Larnaca Ridge (Hübscher et al., 2009; Maillard et al., 2011) and diapirism in the NE Eastern Cyprus Arc (Bowman, 2011; Figure 3.17; Figure 3.31). Whilst this salt tectonics is thin-skinned, the uplift that resulted in the salt being gravitationally mobilised at the Larnaca Ridge is a consequence of the Cyprus Arc deformation (Maillard et al., 2011), and so may be considered to be part of the tectonic deformation.

Faulting across the Larnaca Ridge means the continuation of the base of the Plio-Quaternary kinematic package over the Larnaca Ridge is uncertain (Hübscher et al., 2009; Maillard et al., 2011). The faulting is a consequence of underlying halokinesis; bathymetric fault-scarps demonstrate this is ongoing (Hübscher et al., 2009; Maillard et al., 2011). The lack of constraint on the relative ages of overlying horizons means the overlying sediments do not inform on when this halokinesis initiated, other than generally Pliocene to Quaternary (Maillard et al., 2011). However, if one considers the uplift of the underlying evaporites then the initiation of the halokinesis must have been contemporaneous with or subsequent to the uplift.

5.6.3 End Messinian Salinity Crisis

Figure 5.21C shows the section restored to the top of the end-MSC parallel reflectors. The package of sediments between this reflector and the end-MSC reflector are of approximately constant thickness across the features that now form bathymetric relief (Figure 5.18). Therefore, it may be assumed that during deposition of this package the palaeo-bathymetry was sub-planar. As evaporites were deposited in depressions the gaps in the evaporites would have been bathymetric highs. For these reasons the end-MSC horizon and those parallel were restored to an arbitrary depth where underlying salt exists, and to slightly higher palaeo-bathymetry where underlying salt is absent. An arbitrary depth was used as non-speculative constraints are absent for the lithology, and therefore deposition depth, of the sediments in the offshore Cyprus Arc. The bathymetric highs were adjusted to be geometrically consistent with the adjacent portions of the geological section as no alternative constraints were available.

Parallel reflectors in the upper MSC interval indicate no deformation occurred during this time (Top Hiatus to Top MSC salt on Figure 5.18). Parallel reflectors in the pre-MSC package indicates no compressional deformation occurred during this time (Intra Miocene 1 or 2 to Base MSC Salt on Figure 5.18). This would indicate the deformation hiatus lasted from the late Miocene to shortly after the MSC. However, in some locations in the west of the Tartus Basin and Cyprus Imbricate Zones folding of the Base MSC Unconformity may be observed relative to the Top MSC Unconformity (Figure 5.18C', D). This demonstrates a pulse of compression occurred during the

MSC, described in the following section. The end of hiatus surface should not be confused with the vertically proximal top of the MSC clastic sequence (Figure 5.16).

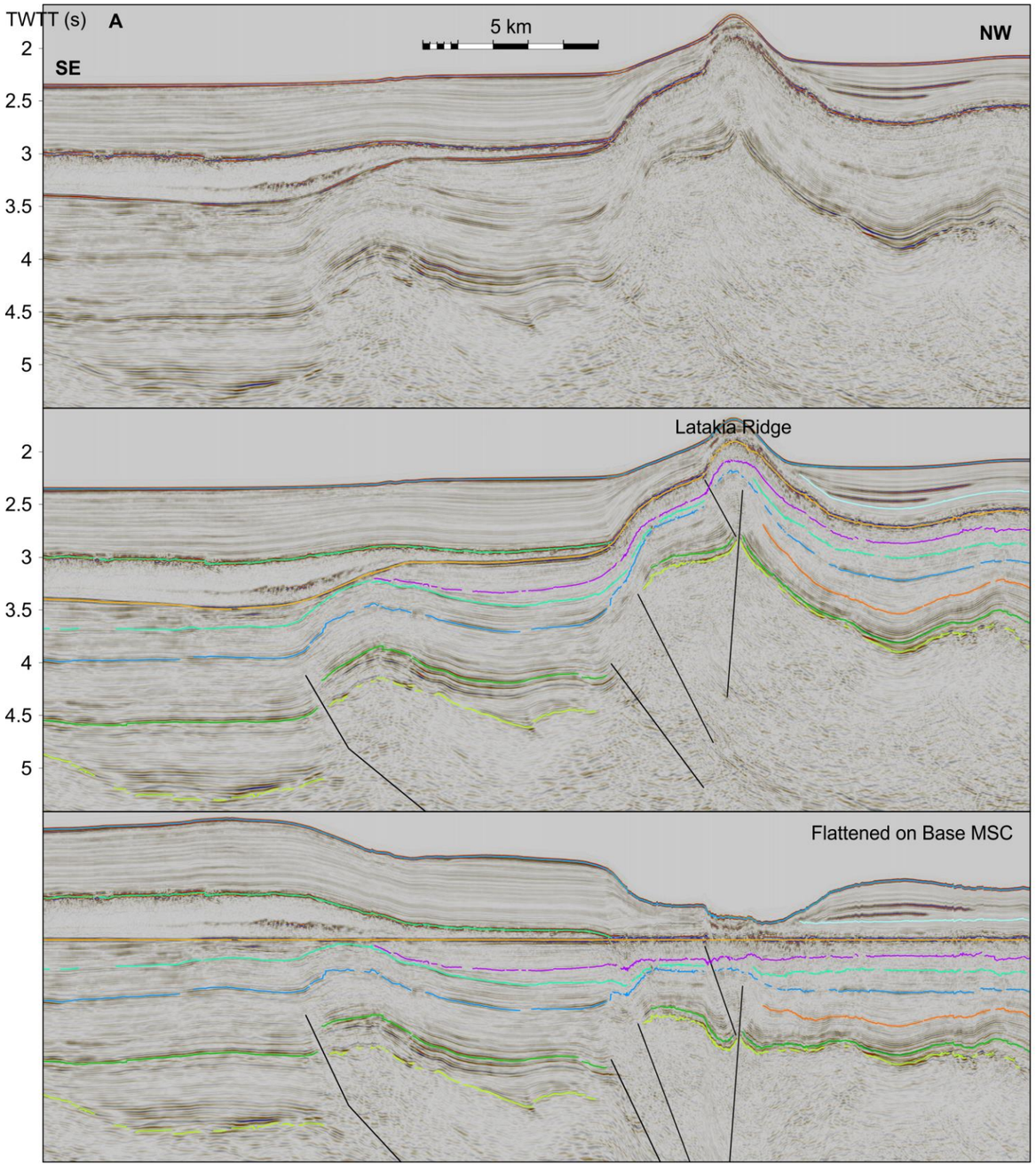

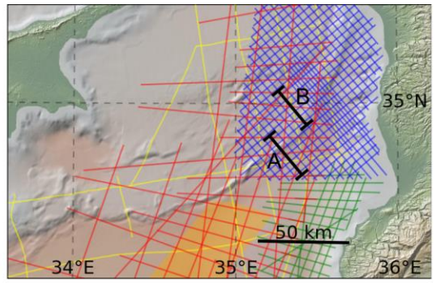

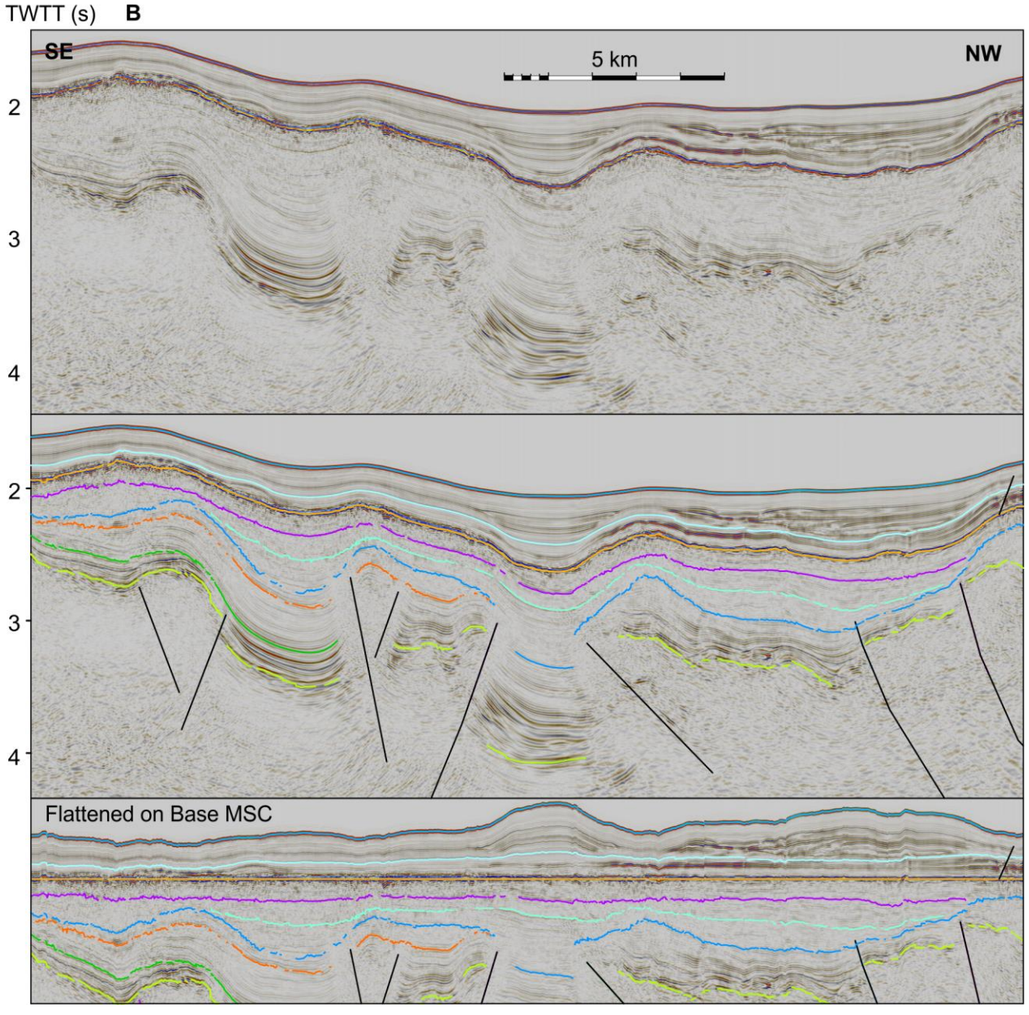

Figure 5.18-A), B) Seismic sections showing reflectors sub-parallel to the MSC unconformity reflectors; C), D) Seismic sections compressional deformation during the MSC. The global relief (Ryan et al., 2009) vertical scale on the minimaps is shown on Figure 1.1 and the supplementary figure.

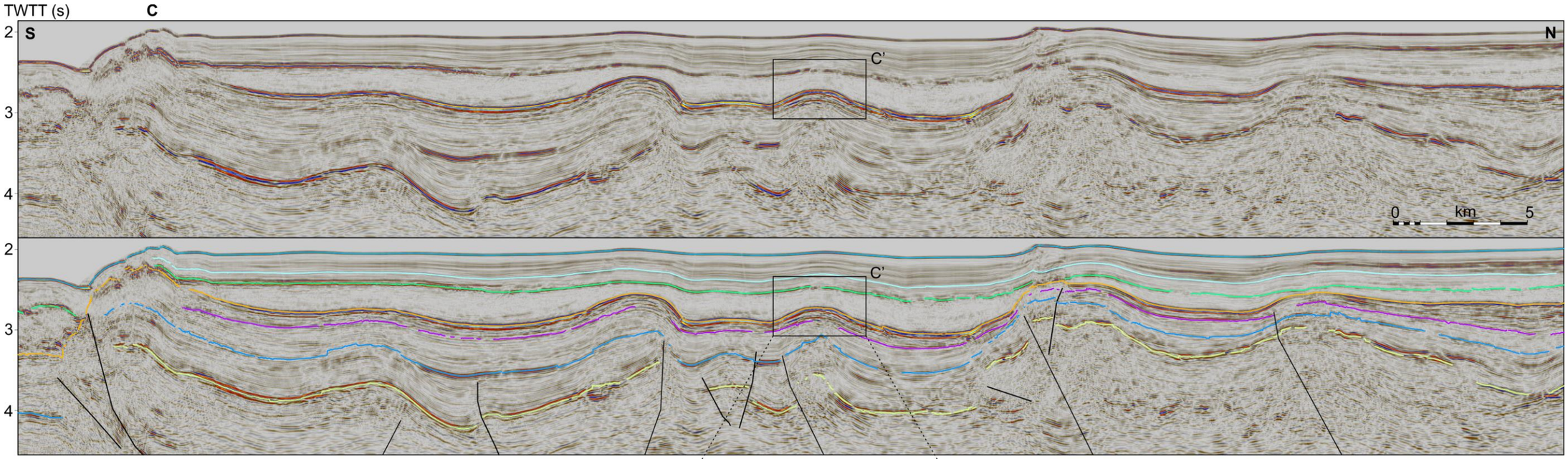
TWTT (s)
C
S
N
C'
2
3
4
0
km
5

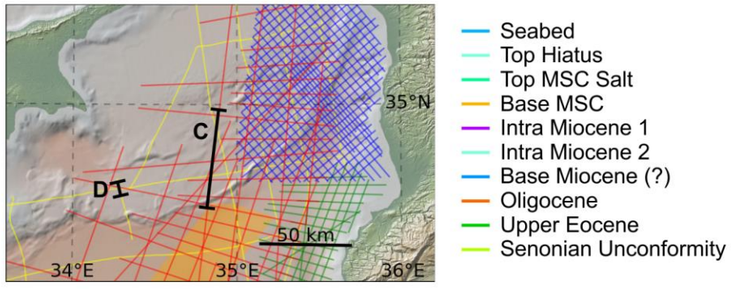
C
DI
35°N
50 km
34°E
35°E
36°E

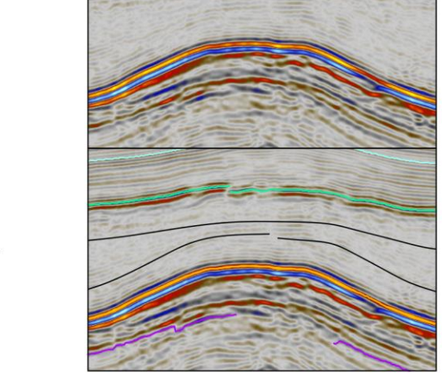
Seabed
Top Hiatus
Top MSC Salt
Base MSC
Intra Miocene 1
Intra Miocene 2
Base Miocene (?)
Oligocene
Upper Eocene
Senonian Unconformity

C'

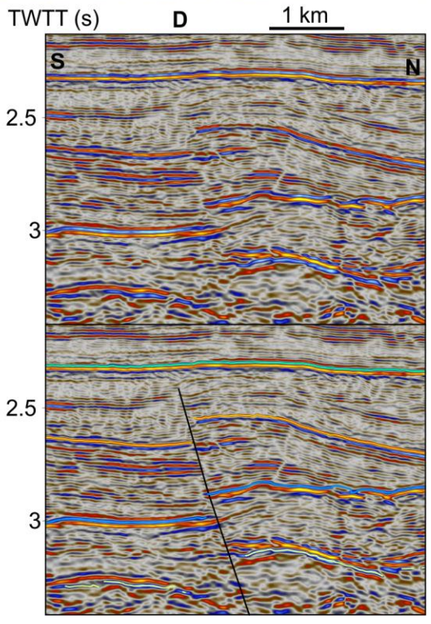
TWTT (s)
D
1 km
S
N
2.5
3
2.5
3

5.6.4 Intra-Messinian Salinity Crisis

Reflectors sub-parallel to the top of the MSC salt may be observed above the top of the salt, and reflectors sub-parallel to the bottom of the MSC salt may be observed below the bottom of the salt (Figure 5.18C, D). However, the top and bottom of the salt are not parallel; the base of the salt is more folded than the top (Figure 5.18C, D). Low amplitude reflectors within the top and bottom of the evaporite sequence are sub-parallel to the end and start MSC reflectors respectively (Figure 5.18C, D). These represent the pre-and post-kinematic depositional packages of the salt body relative to the compression pulse. This indicates a pulse of compression occurred during the MSC (Figure 5.18). The lack of a seismically resolvable syn-kinematic package indicates this was a short-lived event, especially considering the whole MSC lasted c. 650 ka (e.g. Roveri et al., 2014). An episode of shortening during the MSC has been interpreted in seismic in the Northern Levantine Basin (Reiche et al., 2014a). Maillard et al. (2011) infer that some Intra-MSC deformation continued in some localities until more widespread deformation occurred in the early-middle Pliocene, but this continuation of deformation is contrary to the reflectors sub-parallel to the top of the evaporite body.

Flattening the folds which display onlap relationships during the MSC permitted restoration of the Cyprus Arc section to the time of the start of the intra-MSC compression period (Figure 5.21D).

No massive halite is present beneath current bathymetric ridges and in near-shore areas (Figure 5.7). The lack of overlying salt-tectonic structures indicates this was due to non-deposition as opposed to subsequent evaporite evacuation. This non-deposition indicates that these areas were bathymetric highs during the whole of the MSC.

In the Levantine Basin, there are intra-salt body reflectors that are sub-parallel to the base MSC reflector (e.g. Figure 5.15). As the intra-salt reflectors were deposited sub-level, this indicates that the base of the salt was also planar. The current tilt of the base MSC reflector demonstrates that significant differential subsidence was occurring in the Levantine Basin during the MSC. A combination of isostatic subsidence due to the load of the MSC evaporites, and uplift during the pulse of MSC compression would explain this subsidence whilst conforming to the observations made by this study. To restore the Base MSC reflector it was restored to level where the overlying sub-parallel intra-MSC reflectors exist.

5.6.5 Late Miocene

During the late Miocene, there was a non-compressional period. This is evident from sub-parallel reflectors across compressional structures that were active before and after this time (e.g. Figure 5.18A, B). In the area of the Latakia Basin north of the Cyprus Imbricate Zone there are numerous previously undocumented normal faults that offset the Base MSC reflector (Figure 5.7). The age of these normal faults appears to correlate with extension in the northern Levantine Basin (Figure 2.26), a potential relationship that is explored in Chapter 6. The orientation of the normal faults in the Latakia Basin is not well constrained as few of them may be traced across multiple seismic lines with confidence, however the general trend appears to be NE-SW (Figure 5.7D). The age of initiation of the extension that formed these faults is not apparent from reflector offsets, however

if one assumes that extension on this scale (~200 m throws) is unlikely to be concurrent with thick skinned compressional structures < 5 km away then thrusting at the northern end of the imbricate zone suggests it initiated in the mid-Miocene. Because the late Miocene reflectors are sub-parallel to the MSC reflector to which the section was previously flattened, and the period was non-compressional, only restoration of the normal fault offsets was necessary to restore the section to this time point (Figure 5.21E).

In the Levantine Basin, there is widespread onlapping of the upper Miocene sediments onto an upper Miocene unconformity (e.g. Figure 5.15), showing that the Upper Miocene unconformity had some relief during subsequent sediment deposition. For this reason, the Upper Miocene unconformity was not restored level, but to half way to being level. This is a very rough approximation used in the absence of further constraints, but other constraints in later restorations means this approximation will not change the conclusions of the restorations.

5.6.6 Palaeogene

Reflector thinning may be observed in the Tartus Basin and Imbricate Zones beneath the mid-Miocene horizon package, indicating compression was active during sediment deposition. The interval between this lower Miocene syn-kinematic package and the Senonian unconformity contains multiple unconformities, thrust fault offsets and smaller syn-kinematic packages (Figure 5.19A). A faulted section of the Cretaceous-Eocene interval that repeated up to four times was encountered by a well at the faulted margin of the onshore portion of the Tartus Ridge, demonstrating major thrusting during this time (Bowman, 2011). There was widespread erosion at the Latakia Ridge towards the end of the Palaeogene (Figure 5.19B), and the resulting unconformity may be correlated to the Base Miocene reflector of the Levantine basin (Figure 3.15). The top of the syn-kinematic sediments may be traced further north to erosion in the imbricate basin zone (Figure 5.19). This would indicate that thrusting ceased earlier in the Tartus Basin Zone than in the Imbricate Zone. However, the lack of well constraint and the challenges of tracing reflectors across thrusts and diverging traces from unconformities means that this is a speculative.

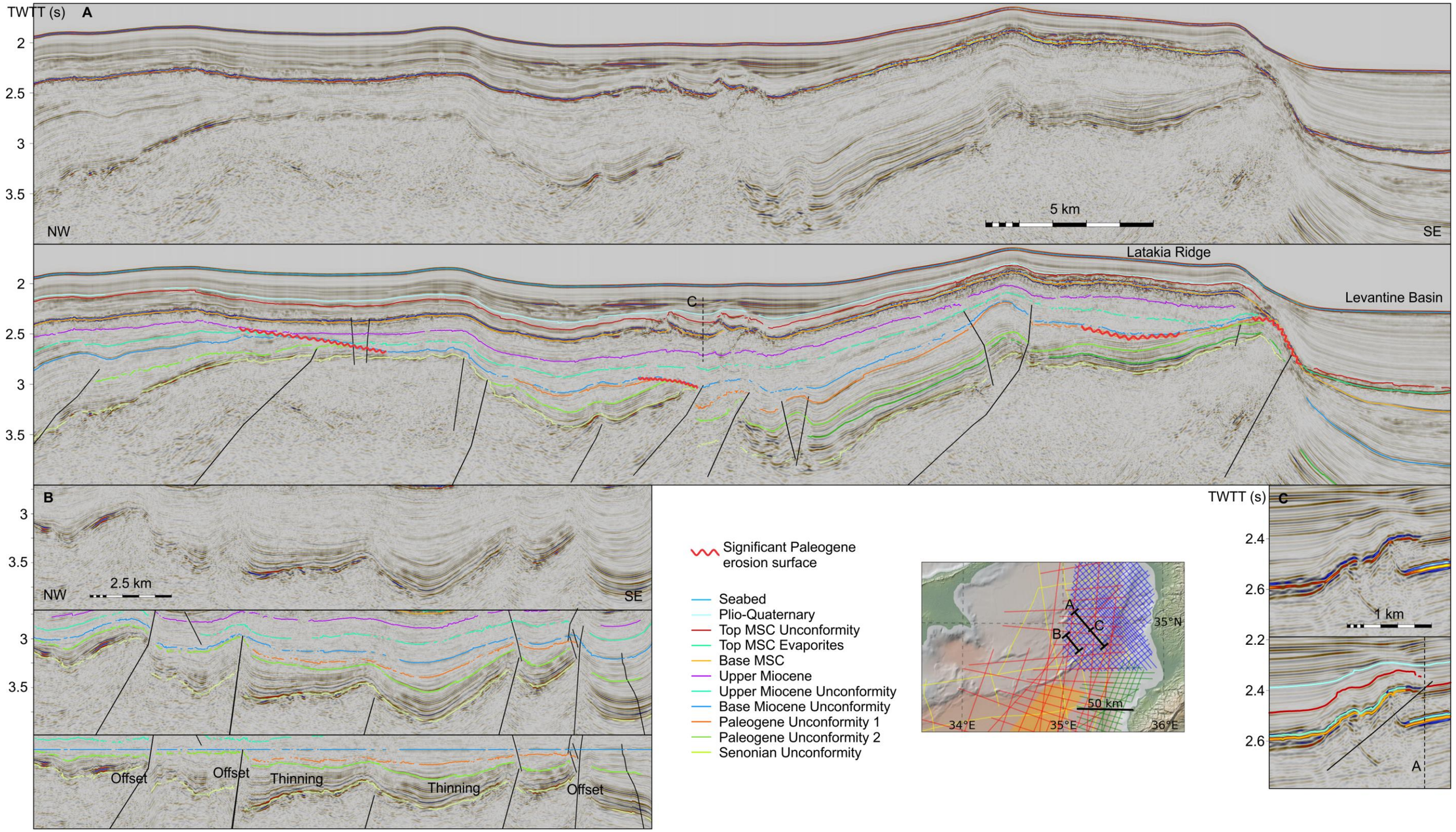

Figure 5.19-Seismic lines showing A) Eocene erosion of sediments uplifted by thrusts, B) thinning of reflectors and fault offsets beneath a flattened Base Miocene Horizon and C) a minor post-MSC thrust showing a thrust that is out of plane to both A and C. The global relief (Ryan et al., 2009) vertical scale on the minimap is shown on Figure 1.1 and the supplementary figure.

Reflector offsets at thrusts meant tracing of the deeper unconformities was limited to where they displayed reflector terminations that defined them as unconformities. This was adjacent to the junction of the Latakia and Tartus Ridges, indicating that this area was a high during this period as well as during the MSC. Because the unconformities are defined by overlying/underlying reflector terminations it is possible that the picked unconformity is diachronous. Care was taken to circumvent this issue by tracing around fault offsets where possible, however for the Palaeogene unconformities the number of thrusts made this possible in only local exceptions.

Across the Latakia Ridge, the Palaeogene sediments thin, although there some locations where the thinning is less pronounced (Figure 5.7H). This indicates the displacement on the ridge faults was initially distributed heterogeneously, before fault linkage during later compression smoothed the heterogeneities (Bowman, 2011).

In the Latakia Basin, the Palaeogene sediments are thick and sub-parallel with the start-MSC reflector (Figure 5.11). This demonstrates a period of structural quiescence in this area. In the early portion of this stratigraphic sequence an angular unconformity may be observed onto which the overlying sediments onlap (Figure 5.11). This indicates tilting of the underlying sediments occurred at the time of deposition of these horizons. However, it was not possible to trace the onlap horizon into an area where its age could be constrained.

Restoration of the Cyprus Arc cross section to the Base Miocene unconformity was achieved by restoring thrusts in the Latakia Basin Zone (Figure 5.21F-G). Because the Base Miocene unconformity is erosional the highs in this surface were left elevated (Figure 5.21G). As some fault offset occurred after the Base Miocene this leaves the palaeo-relief highs artificially high, but no further evidence was available to give additional constraint. As only a small amount of compressional fault motion occurred between the base Miocene and the MSC the errors this introduces to the size of the paleo-highs may be considered insignificant, especially when one considers the relative consequences of the lithological and temporal uncertainties of this restoration.

In the Levantine Basin, there is minimal onlap of Palaeogene sediments indicating that most the sediments were sub-level when deposited (Figure 5.15). The large change in sediment thickness from adjacent to the Cyprus Arc to the deeper Levantine Basin is instead achieved via sequence thinning. The resulting large change in reflector angle demonstrates that significant differential subsidence was occurring in the Levantine Basin. The onlap observable in the Palaeogene sediments of the Levantine Basin shows that there was some bathymetric relief and/or pulses in uplift. It is possible that isostatic subsidence due to the basin sediment load generated a constant slight gradient, and sudden increases in relief from compressional pulses formed the onlapping relationships. That there is not more widespread onlapping relationships, and instead sediment package thinning, justifies restoring the sediments to sub-level. This is likely to be artificially high, as to remain a depocentre the basin would have been a slight paleo-depression, but the errors this introduces may be considered insignificant in comparison to those introduced by the lithological and temporal uncertainties of this restoration.

In the Tartus Basin and Imbricate Zones restoration of the Palaeogene sediments of the cross section was achieved by removing fault offsets that cut the horizon (Figure 2.21G-H). The onlapping relationships of overlying sediments reveal that the Senonian unconformity had significant relief; c. 3 km of elevation difference between the bottom of the subduction trench and the top of the accretionary ridge. This is considered geologically realistic and in line with relative relief observed in subduction zones active today.

5.6.7 Cretaceous

Confident age constraints on the initiation of subduction beneath the Cyprus Arc are absent, however plate models and regional evidence indicates it would have occurred in the Late Cretaceous (e.g. Barrier and Vrielynck, 2008; Robertson et al., 2012a). An upper limit for this is the formation of the Troodos Ophiolite c. 90 Ma as this occurred above a subduction zone (Mukasa and Ludden, 1987b; Robertson and Xenophontos, 1993). Pre-Senonian horizons that may be observed to dip beneath the Latakia Ridge on some seismic lines agree with an interpretation of active subduction during this period (Figure 5.20). That the Senonian Unconformity horizon represents the top of the acoustic basement in the majority of the Eastern Cyprus Arc also concurs with this interpretation, as oceanic crust typically forms acoustic basement (Butler et al., 2016). This suggests that the rocks under the Senonian Unconformity of the Eastern Cyprus Arc are the offshore continuation of the oceanic crust rocks observable onshore as the Troodos Ophiolite in Cyprus and the Hatay and Baër-Bassit ophiolites in SE Turkey (Figure 5.8B). This concurs with earlier studies based on seismic, gravity and magnetic data of the centre of the Eastern Cyprus Arc (Ben-Avraham et al., 1995; Woodside, 1977), and well data at its easternmost limit at the Iskenderun Basin (Aksu et al., 2005b; Albora et al., 2006).

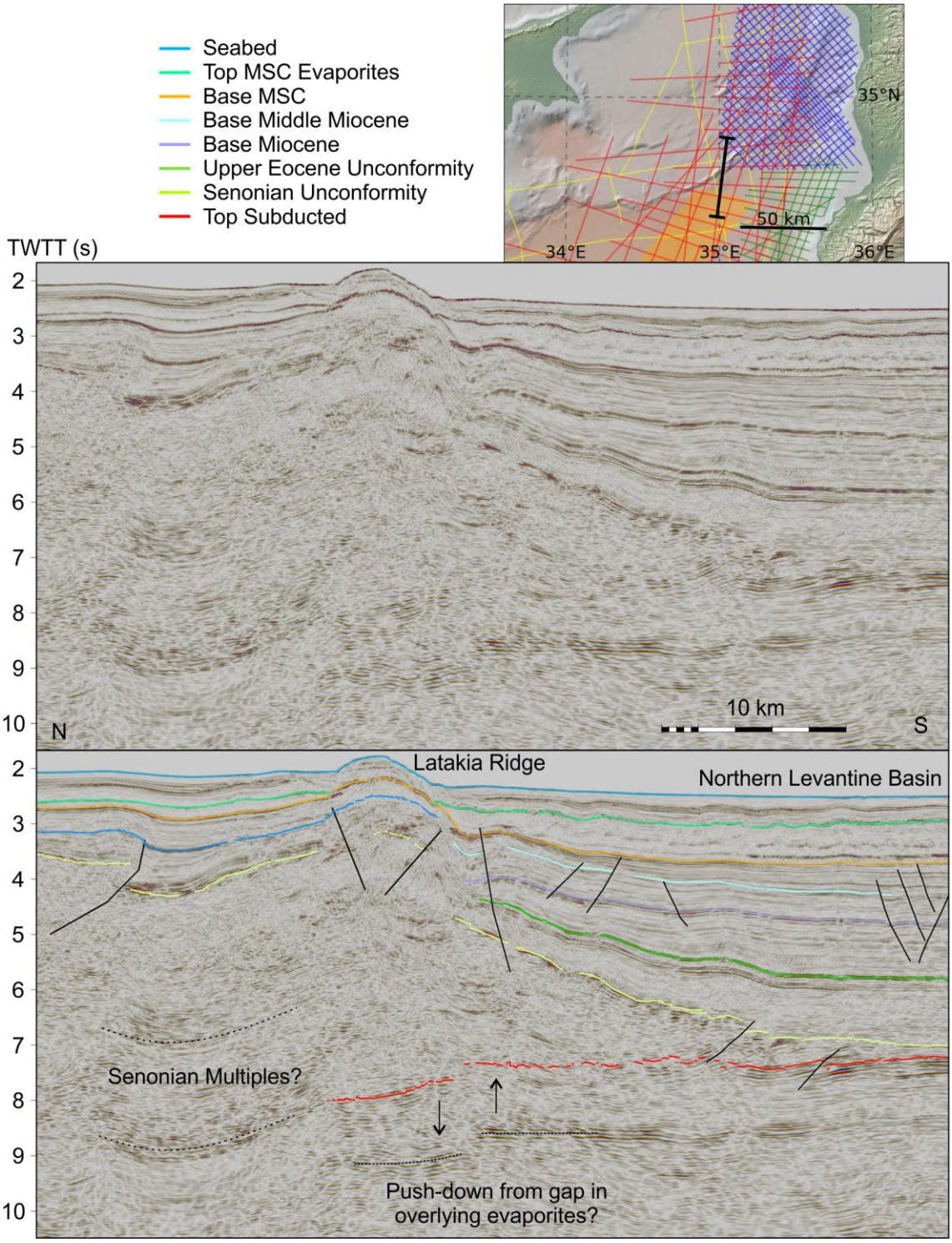

Figure 5.20-N-S striking seismic section showing interpretations of a subducted horizon. The global relief (Ryan et al., 2009) vertical scale on the minimap is shown on Figure 1.1 and the supplementary figure.

In the Latakia Basin the Cenozoic sediments onlap onto the Senonian unconformity (Figure 5.11). This demonstrates that the Senonian unconformity was a slope during this period.

5.6.8 Restoration Summary and Conclusions

This restoration, and more specifically the sediment at the northernmost edge of the Levantine Basin, demonstrates that subduction has not occurred at the southern limit of the Cyprus Arc

since the Senonian (Figure 5.21), concurring with previous studies (Bowman, 2011; Plummer et al., 2013). This means that the shape of the Cyprus Arc is inherited from this subduction. The footwall Senonian reflector is often in the seismic shadow of the hangingwall seismic reflector and consequently it is often poorly imaged, and in some cases possibly not imaged, around thrust faults. For this reason, it is infeasible to calculate a confident quantitative estimate of shortening across the Arc since the cessation of subduction. A summary of the evolution of the area follows.

At the cessation of subduction in the Senonian, the summit of the accretionary wedge was several kilometres higher than the subduction trench. A secondary wider high with an intermediate piggy lay behind the summit of the accretionary wedge. No fault offsets have been observed that are singularly attributable to subduction (i.e. not reactivated afterwards) but the form of the sub-Senonian reflectors make an accretionary wedge, implying significant subduction related thrusts. These implied thrusts are shown on Figure 5.21 as dotted lines.

The Latakia Basin was underlain by a south-dipping slope during the Senonian (Figure 5.21). This dip was likely due to the stacked thrusts of the subduction zone uplifting the stratigraphy to the south.

In the Palaeocene, an angular unconformity in the Latakia Basin marks a slight steepening of the basement slope. The age of this event is uncertain as the sediments of the secondary high are poorly imaged beneath deformed MSC salt, and so tracing of reflectors beneath them cannot be achieved with confidence. From the Senonian until this steepening event, and after the steepening event until the MSC, deformation is largely absent in much of the Latakia Basin resulting in regular undeformed sediment deposition. The exception is frontal thrusts of the offshore continuation of the Kyrenia Range in the north of the Latakia Basin. These thrusts are off the end of the section restored in Figure 5.21.

The Palaeogene marked a period of distributed thrusting throughout the Eastern Cyprus Arc. Thinning reflectors indicate steady compression across the Arc, and multiple unconformities indicate the thrusts were uplifting the accretionary summit. Localisation of thrust offsets occurred in two locations; the leading edge of the accretionary summit and the leading edge of the secondary summit. This suggests preferential reactivation of the decollements that initially formed these highs.

Compression tailed off during the Miocene after a pulse of compression that formed many of the blind thrust folds observable in the seismic. Unconformities formed throughout the Eastern Cyprus Arc subsequent to this thrusting. Confident tracing of these unconformities proved challenging, but the preferred interpretation in this study indicates that thrusting and unconformities formed first at the southern edge of the Arc, and stepped (or ‘broke’) further backwards after a brief interval. It is possible that there is a single unconformity horizon, but without additional timing or horizon constraints fully confident interpretation either way is unfeasible.

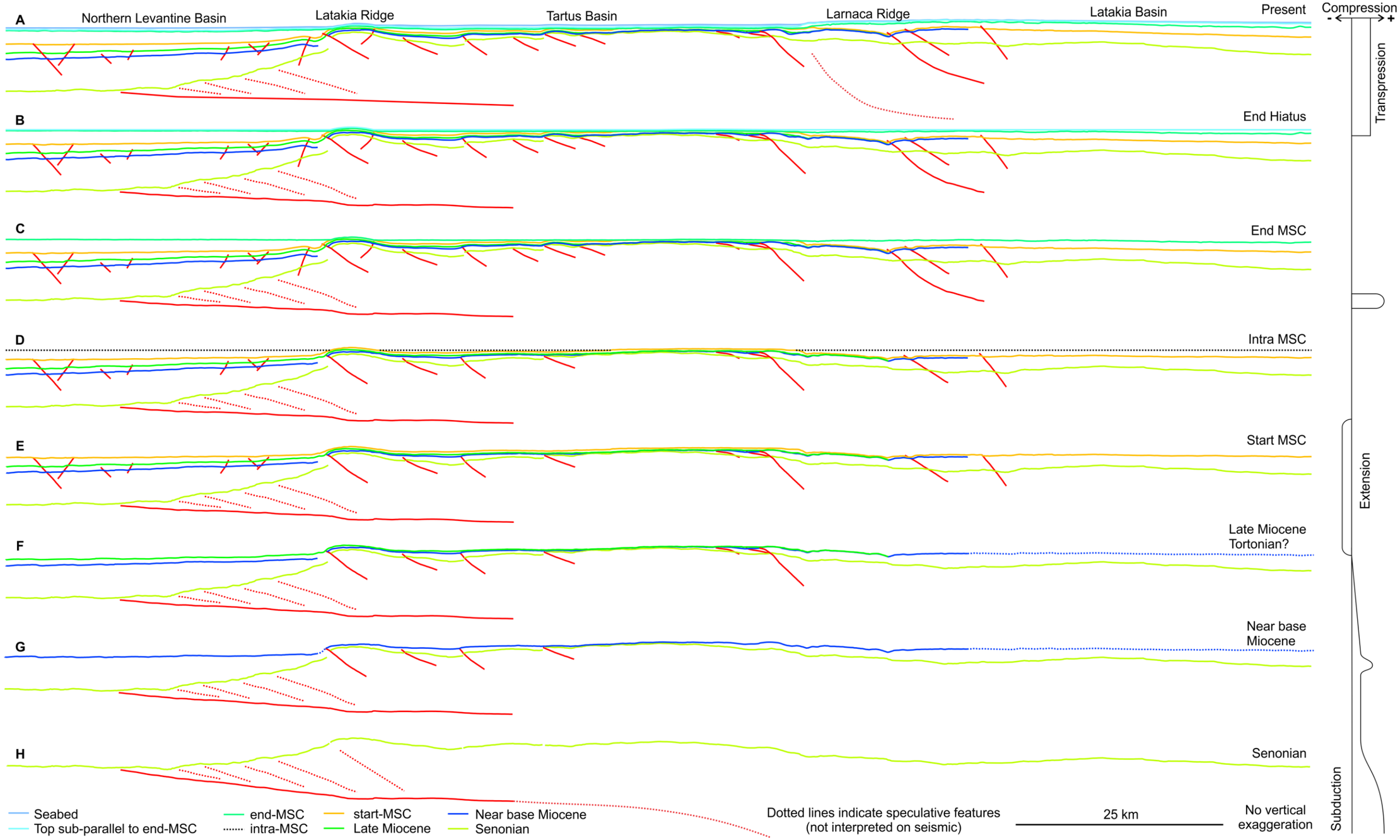

Figure 5.21-Restored cross sections across the Eastern Cyprus Arc. Faults are indicated in red, location shown in Figure 5.14.

There is a swarm of normal faults that offset the reflectors up to and including the Base MSC horizon. These normal faults are centred at the southern end of the Latakia Basin. Later study indicates they may be outer arc extension associated with uplift of the Eastern Cyprus Arc (see Section 6.2.2).

During the MSC, there was a short-lived pulse of compression that reactivated some of the thrusts. Afterwards, a period of tectonic quiescence is marked by reflectors sub-parallel to the top of the MSC. During this period, or shortly afterwards, the MSC evaporites were mobilised to form diapirs in the NE of the Eastern Cyprus Arc. Most this diapirism had ceased by the upper Plio-Quaternary.

In the lower post MSC sediments, assumed to be early Pliocene, a sudden change from sub-parallel to onlap, erosion and thinning in the deposited sediments marks the transition to transpression across the Eastern Cyprus Arc that is ongoing today. This transpression is compressionally reactivating many, but not all, pre-existing thrusts, and forming extensional faulting in the east of the Eastern Cyprus Arc. Inversion of the Latakia Basin has occurred, and is assumed to be on deep seated thrusts that formed the secondary high during subduction, which has elevated the MSC salt. This has resulted in gravity driven halokinesis.

All the constraints used to restore this section were based on relationships observable in the seismic data. This, coupled with the minimal change in geometry of the Senonian unconformity from the Senonian to the present (when considered at the section scale), means that the only information that may be gleaned from the restoration that is not observable from the raw seismic data is relatively minor. Instead, the section serves as a verification of these observations by geometrically comparing them to the other observations. It also generates an internally consistent visual representation of the tectonic evolution discussed in this chapter, constrained by observations and interpretations made during this study.

5.7 West and Central Cyprus Arc

As has been previously discussed, comparatively little seismic data over the West and Central portions of the Cyprus Arc was available to this study (Figure 5.19). Consequently, comparatively few original observations may be made in these areas. However, incorporating these observations, and those made in published literature, with those in the Eastern Cyprus Arc can still provide additional constraints to our understanding of the evolution of the West and Central Cyprus Arc.

5.7.1 Central Cyprus Arc

Only a few seismic lines transect the southern edge of the Arc in its central portion, however the island of Cyprus represents a part of the Central Cyprus Arc that has been elevated above sea level. Consequently, field studies of Cyprus can provide extensive information on lithology and age constraints of Cyprus Arc geology. Field investigations did not form a part of this study, so the onshore information discussed in the introduction to this chapter is from published literature.

The few seismic lines available to this study that transect the southern portion of the Cyprus Arc are widely spaced, and do not confidently resolve any reflectors below the MSC interval. Consequently, these lines are only used to verify or challenge conclusions from a previous study in the same area based on a different seismic survey (Reiche et al., 2015). These conclusions were:

- Neotectonic convergent structures indicate shortening is ongoing between Cyprus and the ESM at the present day.
- The northern flank of the ESM can be traced into an area previously thought to constitute the Anatolian Plate. Therefore, the southern boundary of the Anatolian Plate is located further north than previously considered, presumably near Cyprus.
- Convergent deformation indicates the convergence has been mainly orientated NS since the MSC.

Gravity, field and well data have been used by previous studies to produce some cross sections across the Central Cyprus Arc at outcrop and crustal scales, some of which are shown in Figure 5.22. These were integrated into the final model for the evolution of the area.

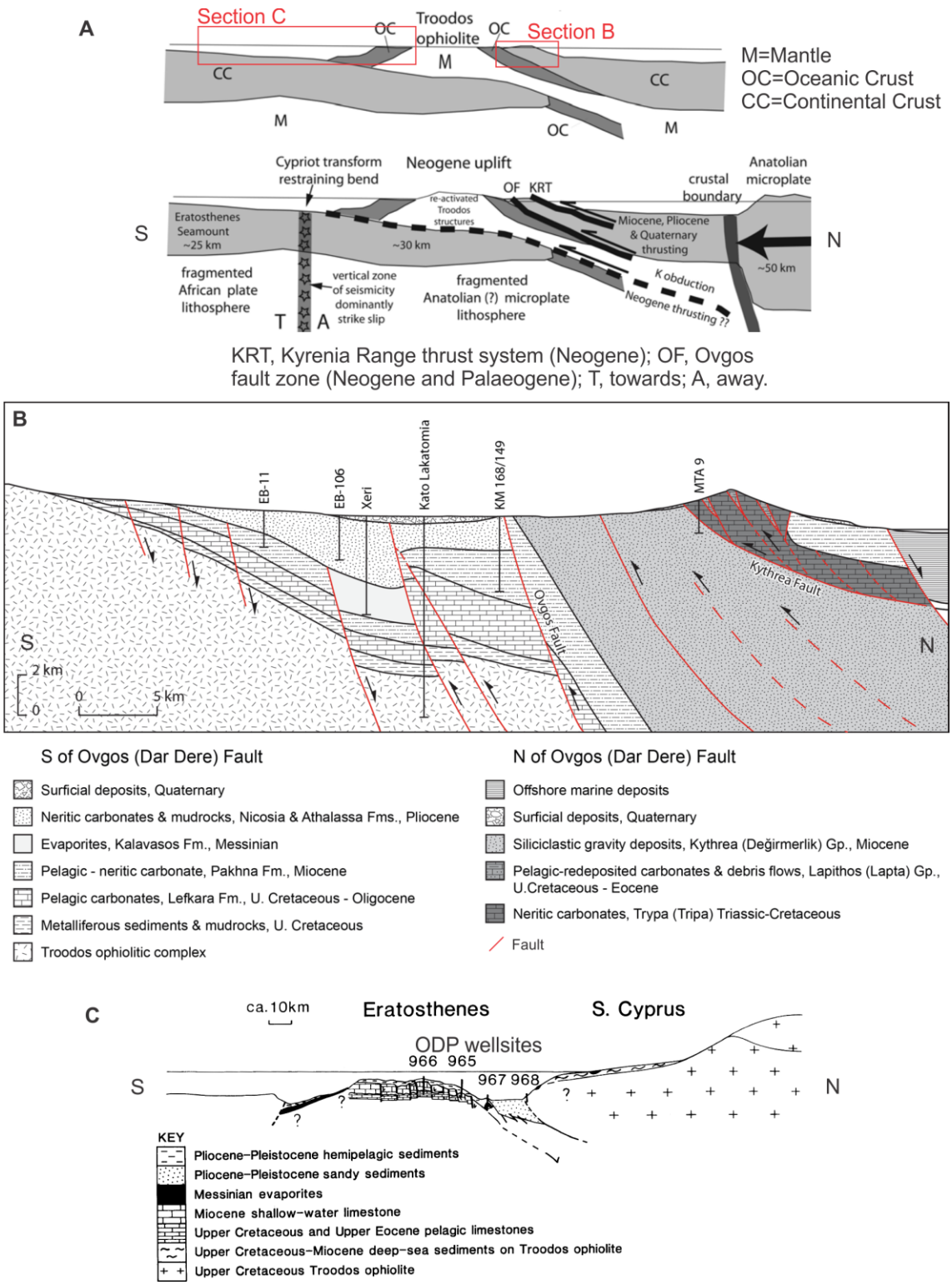

Figure 5.22-A) N-S striking crustal cross sections through Cyprus from Harrison et al. (2012); B) Regional NS cross section across the Kyrenia Range to the Troodos Mountains from Robertson & Kinnaird (2015); C) NS regional cross section from Cyprus across the ESM from Robertson (1998b).

5.7.2 Western Cyprus Arc Antalya Basin

The western section of the Cyprus Arc is formed by the Florence rise and southernmost portion of the Antalya Basin, and terminates at the Anaximander Seamounts and Isparta Angle. Imaging difficulties associated with evaporites (Section 3.2.5) mean that sub-evaporite reflectors are poorly imaged in this section of the Cyprus Arc (Fossen, 2010). Consequently, where salt cover

exists little may be resolved of the sub-salt geology, and where salt cover is absent there is no way of confidently constraining the age of any resolvable reflectors. Despite this some conclusions have been drawn by previous studies.

Woodside et al. (2002) conclude that the Cyprus Arc near the Florence Rise is a sutured subduction zone, and that current plate stress have formed it into a dextral wrench zone. They note that a large part of the neo-tectonic deformation observable on the seabed is likely to be thin skinned kinematics of sediment from the Herodotus Basin.

The Anaximander mountains have a complex Neogene tectonic history due to their location at the join between the Hellenic and Cyprus Arcs, but no direct observations have been made about the earlier evolution of this area (Aksu et al., 2009; ten Veen et al., 2004; Zitter et al., 2003). However, Zitter at al. (2003) note that "the connection between the Hellenic Arc and the Cyprus Arc does not occur in the Anaximander Mountains, but inland in southwest Turkey". This implies the deformation at the Anaximander Mountains is largely controlled by the same forces as the Western Cyprus Arc.

Although confident tracing of reflectors to the Antalya Basin is not possible some parallels may be drawn between the sediments of the Antalya and Latakia Basins on either side of Cyprus (Figure 5.23). Both basins contain:

- A thick (>3 s TWTT) sequence of north-dipping sub-planar sediments.
- A convex up (inverted) evaporite body.
- An angular unconformity near the base of these sediments.
- Chaotic reflectors where the basement is most elevated.

One main difference is that the sediments above the angular unconformity onlap/downlap to the north and south in the west and east of Cyprus respectively. This demonstrates a palaeoslope dip direction in the opposite direction. This could be related to underlying Late Cretaceous thrusting, however no evidence for thrusts underlying these sediments may be observed on the seismic data available to this study.

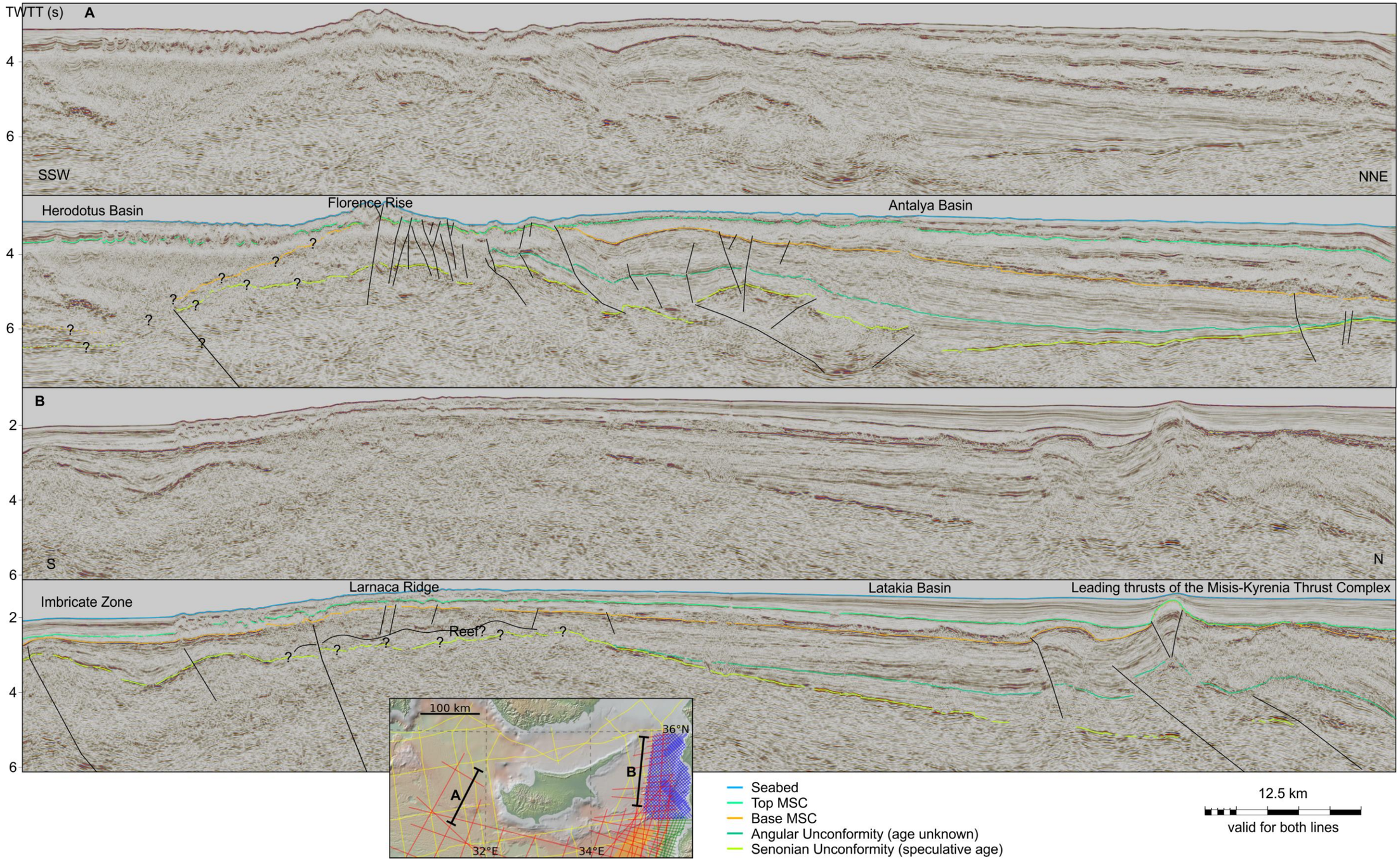

Figure 5.23-NS Seismic lines from the (A) west and (B) east of Cyprus showing the similarities discussed in the text. The global relief (Ryan et al., 2009) vertical scale on the minimap is shown on Figure 1.1 and the supplementary figure.

5.7.3 Kyrenia Range Western Marine Extension

The Kyrenia Range can be linked to the Misis Mountains via sub-sea thrust complexes documented in literature, observable in seismic data available to this study (Section 5.5.4) and part of the way in publically available bathymetry (e.g. Ryan et al., 2009). The western marine extension of the Kyrenia range has less certain constraints. Işler et al. (2005) and Hall et al. (2014) interpret pre-MSC thrusts, postulated to be Miocene, on seismic lines between Cyprus and Turkey, however the data image poorly beneath the MSC evaporites and consequently some of the interpreted thrusts are uncertain. The thrusting appears in a ~50 km wide zone across the Antalya Basin, and links the Kyrenia Range with the eastern limb of the Isparta Angle in SW Turkey (Figure 5.24). The Isparta Angle is a north-pointing triangular shaped tectonic province that has a complex and still debated tectonic history (Hall et al., 2014), but this history is considered compatible with the northerly subduction zone (Morris et al., 2015; Robertson et al., 2012a).

The global relief compilation used to generate the hillshade relief maps in the figures of this study (Ryan et al., 2009) contains an unsmoothed join between two surveys to the west of Cyprus. At the boundary between the two surveys the inboard bathymetry is shallower than that outboard, creating an artificial linear escarpment on the bathymetry (Figure 5.24) that does not appear on GEBCO bathymetry grids (Figure 5.2). Taking this into account there are no trends on the bathymetry maps available to this study that permit tracing of the western marine extension of the Kyrenia Range, in contrast to the eastern marine extension of the Kyrenia Range.

The seismic data available to this study image some pre-MSC thrusts (Figure 5.24) which corroborate with those interpreted by Işler et al. (2005) and Hall et al. (2014). However, the poor imaging clarity and sparse seismic coverage limits what additional constraint on deformation style or timing may be drawn. For example, some deformation may be observed at the seabed above one of the large scale thrusts on Figure 5.24. However, the limited reflector clarity means it is uncertain if this deformation is related to movement on the underlying thrust, or deformation related to halokinesis focused above the underlying thrust.

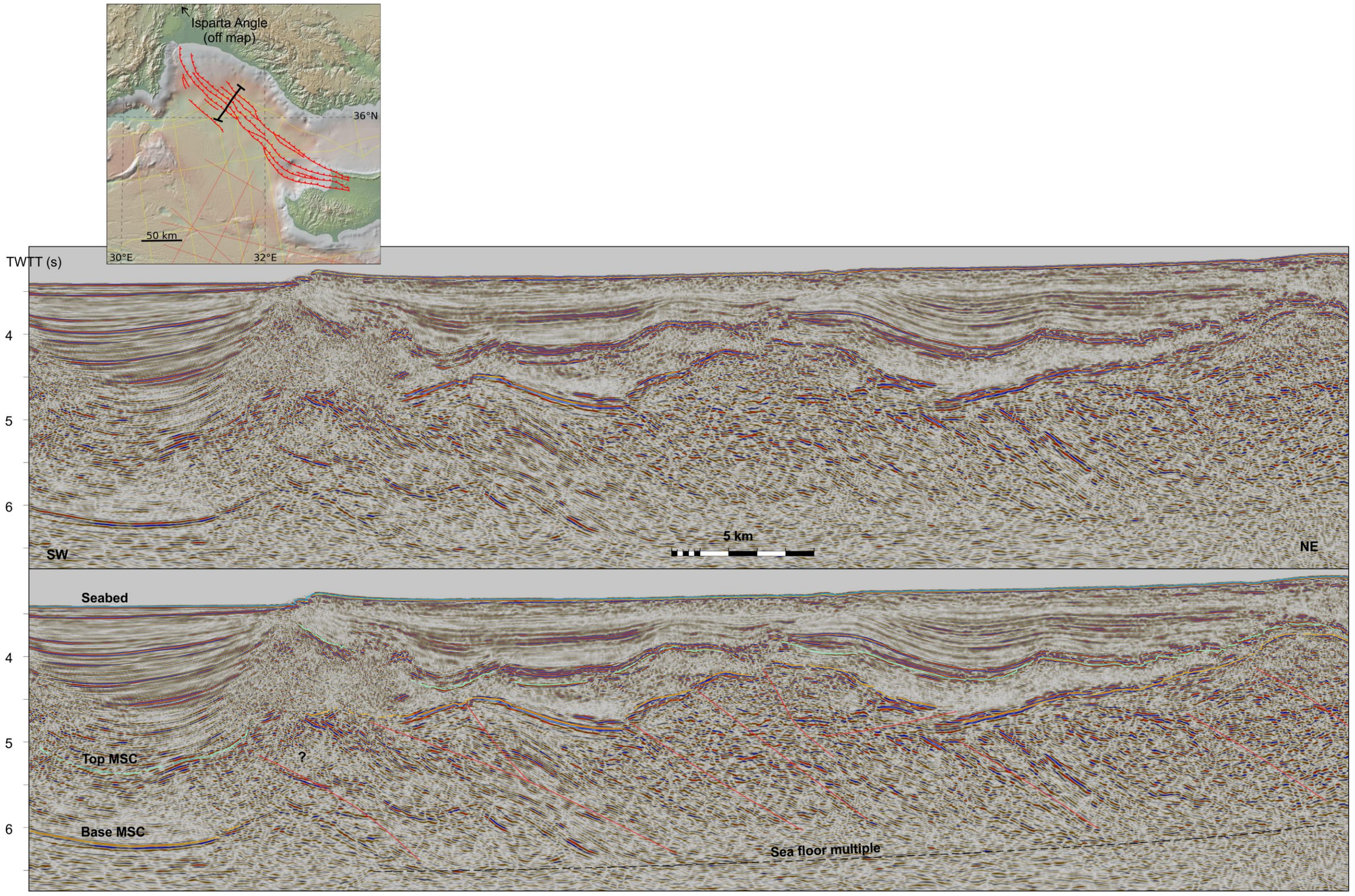

Figure 5.24-Map showing the thrusts of the western marine extension of the Kyrenia Range, from Işler et al. (2005) and Hall et al. (2014), and SW-NE striking seismic line across the western marine extension of the Kyrenia Range, as shown by dipping reflector sequences and offsets in the overlying horizons. The morphology of the Base MSC reflector has controlled the speculated positions of the thrusts (red lines). The global relief (Ryan et al., 2009) vertical scale on the minimap is shown on Figure 1.1 and the supplementary figure.

5.7.4 Onshore-Offshore Relationships

Many of the geological features observable on seismic data located offshore Cyprus appear to parallel features documented onshore Cyprus (this study; Ben-Avraham et al., 1995; Hall et al., 2005a), as might be expected along strike of an arcuate feature. Thus, lithological and temporal constraints from onshore Cyprus can be speculatively extended offshore. Reciprocally, observations of deep structural features offshore can be speculated to be analogous to that underlying onshore Cyprus. By this method it may be confidently assumed that the Misis-Kyrenia Thrust Complex shares a parallel history to the Kyrenia Range, and the Mesaoria Basin shares a parallel history with the Latakia Basin. Their respective cross sections also share many similarities, as might be expected as the two areas are along strike equivalents (Figure 5.25A, D, E). A key example of this is the post MSC-uplift observable in the seismic data (Section 5.6.8), and from onshore Cyprus (Main et al., 2015 and refs. within; Palamakumbura and Robertson, 2016b). The average elevation contrast, one emerged and the other submerged, can be attributed to variations in the crust type being underthrusted at the southern edge of the Cyprus Arc (Section 4.8).

Further south, the onshore-offshore parallels are more speculative:

- The Polis Graben could be equivalent to the normal faulting in the SE Latakia Basin (Figure 5.25F).
- Convergent deformation south of the Troodos, such as the Yerasa fold and thrust belt, could be equivalent to the leading edge of the imbricate zone (Figure 5.25F, A).
- Basin areas south of the Troodos, such as the Pissouri and Limassol Basins, could be the equivalent of the Tartus Basin (Figure 5.25F, A).
- The Akrotiri Peninsula could be analogous to the Gelendzhik Rise or Latakia Ridge (Figure 5.25A-C).

Given the large-scale similarities between the onshore and offshore it is likely that many of the finer details are also analogous, and can inform on each other. Contrasting features between the two areas may also give insights. Additionally, the NE continuation of the basins and structural trends to onshore Turkey and Syria (Kempler and Garfunkel, 1994) may also provide the same reciprocal information. Further study is required to explore these potential relationships and investigate what new insights may be forthcoming.

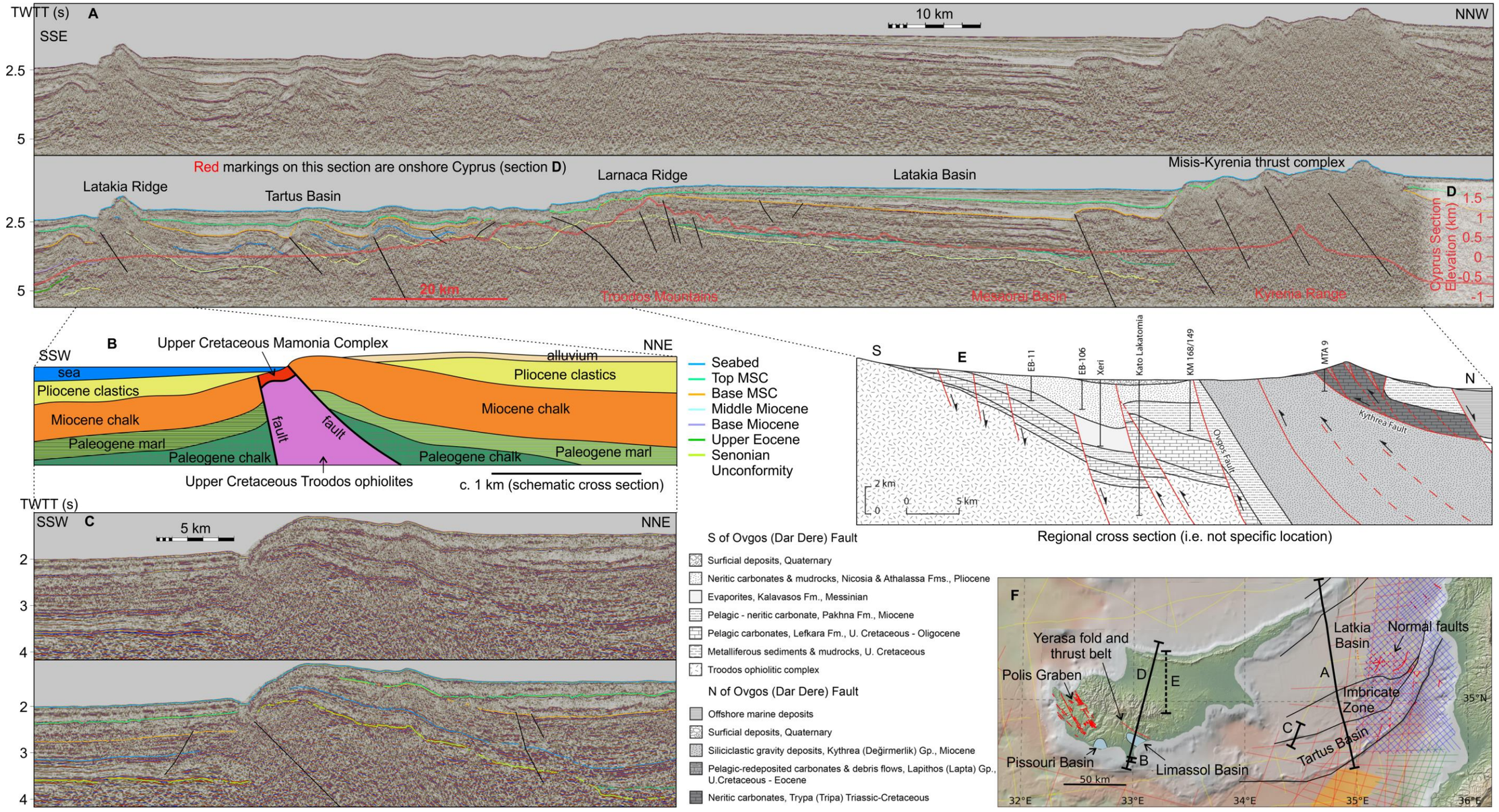

Figure 5.25-Comparison of some of the similarities between onshore and offshore Cyprus, including A) a NS seismic line of the offshore Arc overlaid by an onshore topographic profile with annotations in red; B) a schematic cross section of the Akrotiri Peninsula (adapted from Bear and Morel, 1960; updated after Robertson, 2000) compared to the Latakia Ridge and C) Gelendzhik Rise; D) the topography of Cyprus (Ryan et al., 2009) overlain on the offshore cross section; E) a schematic NS cross section of northern Cyprus (adapted from Robertson and Kinnaird, 2015) compared to the offshore equivalent; F) A map showing the locations of the other cross sections and normal faults on (Payne and Robertson, 1995) and offshore Cyprus. The global relief (Ryan et al., 2009) vertical scale on the minimap is shown on Figure 1.1 and the supplementary figure.

One key aspect of the uplift observable beneath the Larnaca Ridge is that it is asymmetrical (Figure 5.25A; i.e. with more basement uplift to one side of the highest basement), which indicates thrust driven uplift. The constraints provided by the contrasting sediment thickness to the north and south of the ridge indicate this was the case prior to the MSC, and the uplifted salt body to the north, without one being present south of the ridge, indicates that this has continued to be the case after the MSC (Figure 5.25A). The 'bulls eye' pattern of progressively deeper ophiolites inwards at the centre of the Troodos is symmetrical in both lateral dimensions (Figure 5.26), and the serpentinite diapirism used to explain this feature is also used to explain why the most extreme uplift affecting Cyprus is not immediately adjacent to the deformation front (Robertson 2016, pers. comm.). Field data provides a relatively superficial view of geological structures in comparison to seismic data, and as the onshore Cyprus geology is largely understood from field data this means resolving between symmetric and asymmetric uplift is more challenging. Exclusive of the deep ophiolite bullseye, the remainder of the Troodos ophiolite outcrop is much more elongate (Figure 5.26). Combined with the presence of the deeper ophiolites of the Yerasa fold and thrust belt, and isolated outcrops of deeper ophiolites (Figure 5.26), this suggests that thrusting may provide a better explanation for the rest of the Troodos uplift.

Another argument for thrust related Troodos uplift is the presence of numerous mapped WNE-ESE faults, including the Yerasa fold and thrust belt, at the southern edge of the ophiolite outcrop but not at the northern edge of the ophiolite outcrop (Figure 5.26). Although some of these are marked as normal faults on the geological map, many thrusts could be interpreted as normal without information on the dip of the fault plane, and above large-scale thrusts normal faults can also form as a function of outer arc extension and gravity collapse (see Figure 5.27; Fossen, 2010). Thus, this observed asymmetric presence of faults could infer underlying south-verging thrusting. The extra uplift that Cyprus has experienced relative to the western and eastern Cyprus Arc could simply be explained by the different crust type colliding at the southern edge of the Arc (Section 4.8). One final piece of speculative evidence is that the thickened crust beneath Cyprus indicated by tomography could be thrust related thickening (see Figure 5.29).

Serpentinite diapirism remains the preferred mechanism for the uplift at the centre of the Troodos because of the observed symmetrical uplift around the centre of the Troodos precluding most other explanations, and serpentinite forming the deepest exposed ophiolites. Other, albeit unlikely, possibilities include laterally in-extensive fault bend or fault propagation folds associated with a large scale blind thrust. Symmetrical serpentinite diapirism superimposed on asymmetrical thrust related uplift is feasible. It was previously suggested that serpentinisation occurred during the Miocene prior to uplift of the Troodos (Robertson and Xenophontos, 1997). As subduction is now shown to have been inactive since the Cretaceous, and subduction remains the most likely vector by which water reaches the mantle to form serpentinite, it is possible that the serpentinisation occurred earlier during the Cretaceous, and it was only with later thrust related uplift that the Troodos became denuded.

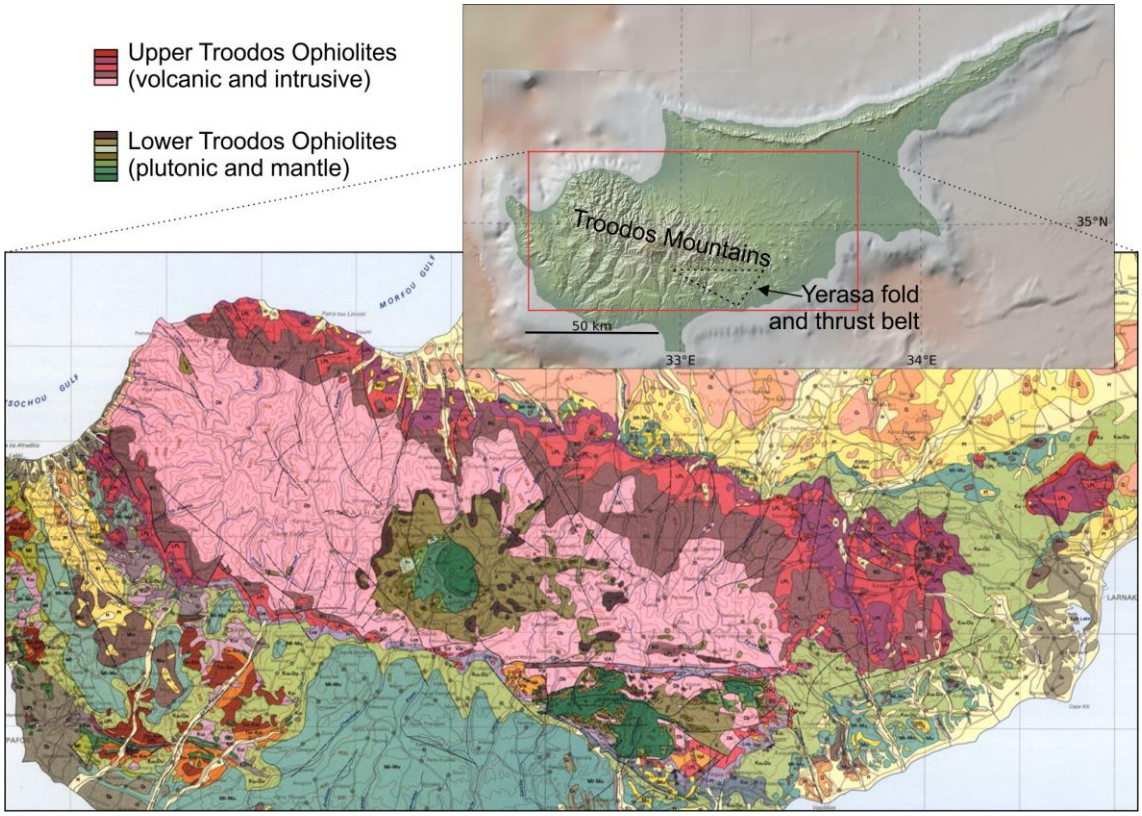

Figure 5.26-Part of a Geological map of Cyprus (Constantinou, 1995) illustrating the form of the Troodos Ophiolites. The global relief (Ryan et al., 2009) vertical scale on the minimap is shown on Figure 1.1 and the supplementary figure.

Applying Occam's Razor (Encyclopædia Britannica, 2010; Gauch, 2003) on the basis of what may be observed in seismic data offshore suggests that thrusting, as opposed to serpentinite diapirism, may provide a better explanation for why the uplift that has exhumed the Troodos Mountains is focused >50 km behind the deformation front. However, further work must be undertaken onshore Cyprus to critically assess this alternative hypothesis, with an affirmative result, before it can be asserted to have displaced serpentinite diapirism as the best explanation for the uplift of the whole Troodos. The domal uplift of the deeper ophiolite bullseye remains best explained by serpentinite diapirism.

5.8 Discussion

The previous sections in this chapter show observations based on interpretation of seismic data. Before discussion of the implications of these observations it is important to consider some of the limitations of this method of investigating tectonics, and the effect of these limitations on any conclusions drawn from the investigation.

Most the seismic data available to this study that covers the Cyprus Arc is at the eastern end of the Cyprus Arc (Figure 5.5). This means much of the observed deformation is associated with a section of the Arc with a contrasting strike to most the Arc. Thus, many of the observations of smaller scale details may only be assumed to be relevant to this locality. Observations pertinent to large scales, such as the Senonian cessation of subduction, still have confident implications

for the whole Arc because alternatives would generate space problems without significant (and unobserved) deformation.

The use of reflectors with uncertain ages introduces uncertainties on ages given to different events recognised in the evolution of the Cyprus Arc. However, these uncertainties do not affect confidence in the qualitative relative ages of the events.

Changes in sedimentation including bulk rate, sediment type and transportation mechanism can cause seismic package thinning and reflector terminations (Hart, 2011). In this study, seismic package thinning and reflector terminations have been used to infer changes in deformation (Section 5.6). It is conceivable that extreme changes in sedimentation rate could cause some of the reflector changes documented by this study during a constant stress regime. For example, the hiatuses in compression that are temporally proximal to the MSC (Section 5.6.3) could be due to a large increase in sedimentation rate. However, given the absence of any mechanism or other evidence for a drastic sedimentation increase, and in the presence of other tectonic evidence supporting changes in the stress regime, drastic changes in sedimentation rate may be considered implausible-MSC evaporite deposition notwithstanding. In the example above the normal faulting and intra-MSC compression (Section 5.5.4) provide evidence of stress regime changes in addition to the change in kinematic reflector packages.

As the Cyprus Arc has experienced compression locations exist where horizons have been thrusted above themselves. Software and surface-display limitations mean that picking of both the upper and lower horizons is not feasible; therefore, the upper horizon was picked by default. This means that horizon surfaces and isopachs locally do not inform on the lower horizon.

5.8.1 Cessation of Subduction on the Whole Arc?

A key observation of the investigation into the Eastern Cyprus Arc is that subduction ceased at its southern edge in the Senonian and has not been active since (Section 5.6.8), as this is in contrast to some publications that suggest subduction ceased in the Senonian but restarted, albeit in a more minor form, in the Miocene (Figure 5.3; Section 2.6.6). The seismic data available to this study over the West and Central Cyprus Arc does not image the downgoing stratigraphy beneath the southern edge of the Arc (Figure 5.27C-J). This means the observations of the relic downgoing plate in the Eastern Cyprus Arc cannot be made in the Central and Western portions of the Arc. This raises the possibility that subduction only remained inactive in the Eastern Cyprus Arc. An initial observation backs this up; the Senonian unconformity may be observed to shallow adjacent to the bathymetric ridge in the portion of the Arc proximal to the line used for restoration (Figure 5.27A, B). This contrasts with elsewhere on the Arc (Figure 5.27C-J). To address the query of whole Arc subduction cessation, the following assessments of bathymetric, GPS, seismological, tectonic, seismic refraction and seismic reflection data were made.

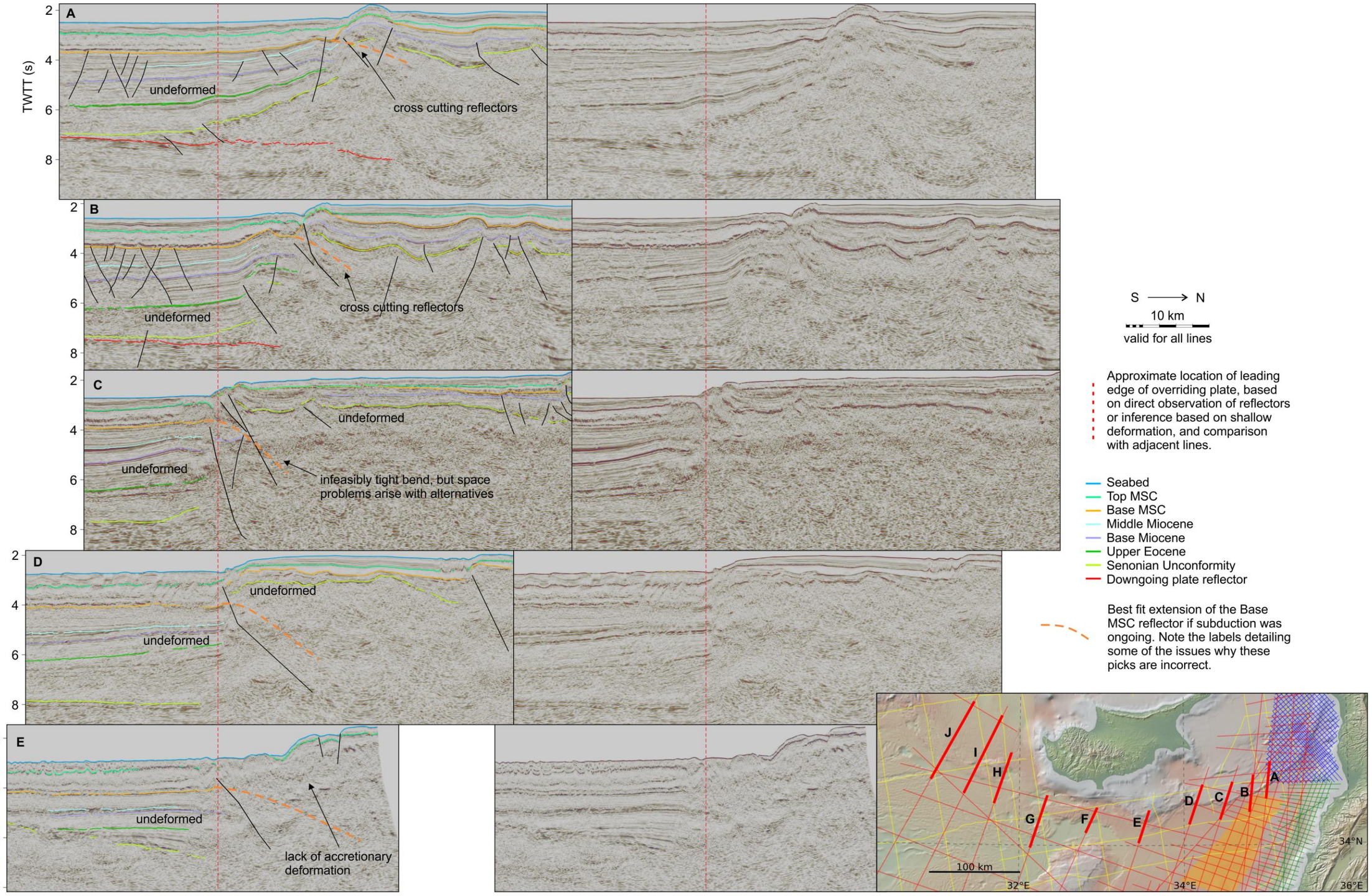

Figure 5.27-Seismic lines across the southern edge of the Cyprus Arc comparing the likely location of the edge of the overriding plate. The global relief (Ryan et al., 2009) vertical scale on the minimap is shown on Figure 1.1 and the supplementary figure.

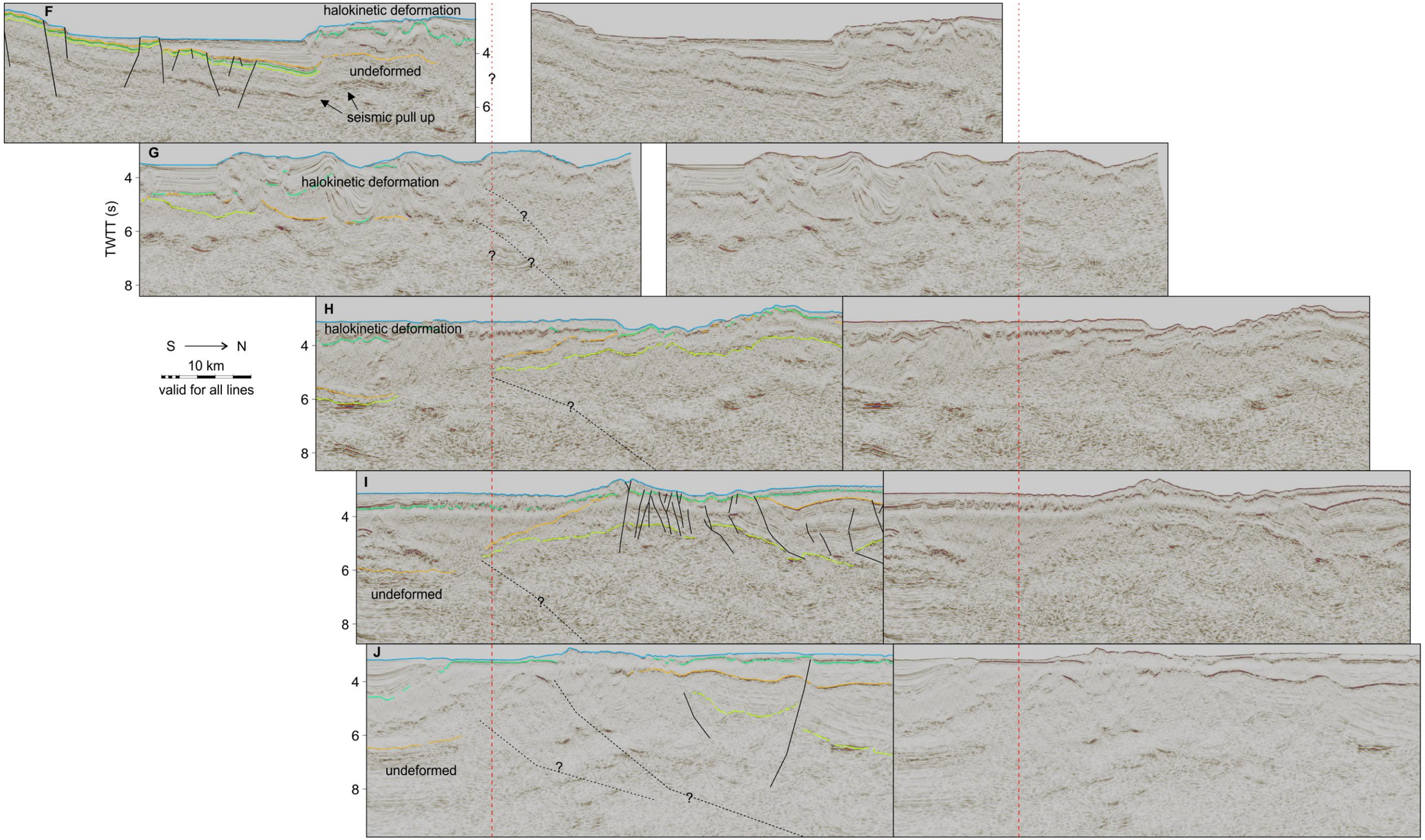
F
halokinetic deformation
undeformed
seismic pull up
4
?
6
G
halokinetic deformation
TWTT (s)
4
6
8
H
halokinetic deformation
4
6
8
S → N
10 km
valid for all lines
I
4
6
8
undeformed
J
4
6
8
undeformed

If subduction were active today, then rugose relief and deep trenches might be expected on the bathymetry. This may be observed on the adjacent Hellenic Arc where subduction is well documented (Figure 5.28). In contrast, ridges as opposed to trenches define the southern edge of the Cyprus Arc, and the deeper side of the feature has significantly more planar bathymetry than the Hellenic Arc (Figure 5.27; Figure 5.28). In places either side of the Florence Rise, the 'ridge' defining the Arc here is marked by c. 200 m of elevation change (Figure 5.28), significantly less than might be expected at an active subduction margin. Additionally, apart from between Cyprus and the ESM the post-MSC sediments do not thicken adjacent to ridge at the southern edge of the Arc (Figure 5.27), as might be expected if a trench had been present during this interval. These bathymetric observations do not support active subduction at the Cyprus Arc.

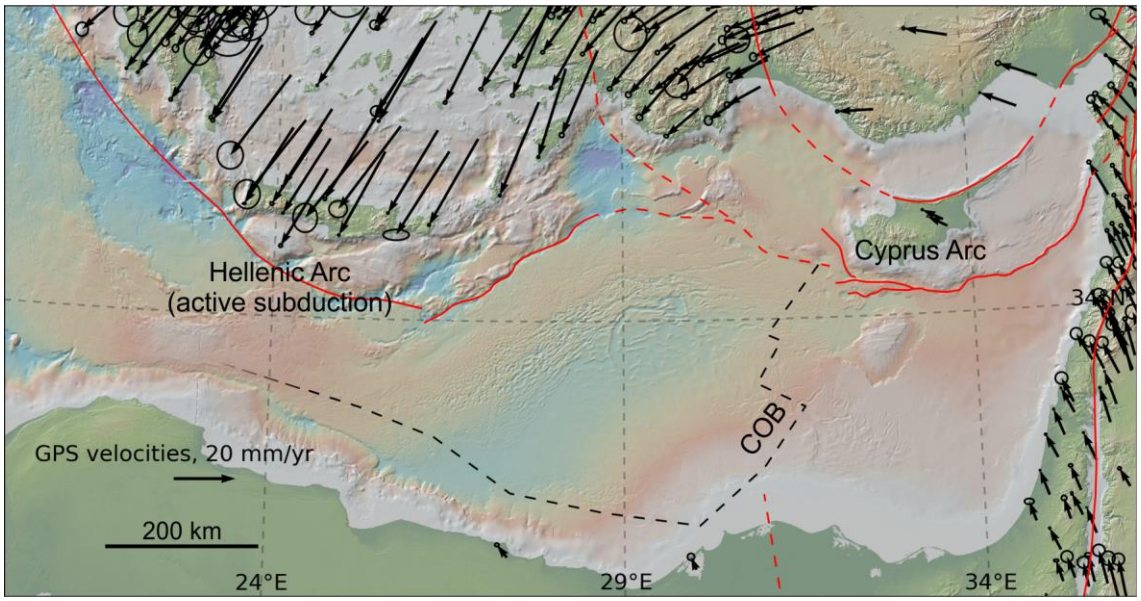

Figure 5.28-Comparison of the global relief between the Cyprus Arc and Hellenic Arc. The GPS velocities are a compilation of GPS data from Nocquet (2012) and are relative to the Eurasia Plate. The COB is from Longacre (2007). Dashed lines indicate more uncertain exact locations. The global relief (Ryan et al., 2009) vertical scale is shown on Figure 1.1 and the supplementary figure.

Unambiguous GPS evidence of convergence may be observed at the Hellenic Arc (~35 mm/yr), in contrast to the less clear GPS convergence evidence at the Cyprus Arc (~5 mm/yr; Figure 5.28; Nocquet 2012). This could just mean that the convergence rate of subduction is low, but convergence rates this low is more simply explained by other plate deformation. Thus, the GPS data are inconclusive, but on balance do not support whole arc subduction.

Wdowinski et al. (2006) used a combination of seismological and GPS data to infer subduction on the western Cyprus Arc, and transform motion on the central and eastern Cyprus Arc. The GPS data they use, and seismotectonic work, is in disagreement with other, including more recent, compilations of GPS data that suggest NNW-SSE convergence across the Arc (Nocquet, 2012; Reilinger et al., 2006). This suggests that the focal mechanisms recorded in the area during the last few decades may not be representative of the plate motions as recorded by GPS data over the last couple of decades. A possible explanation for this is that the Cyprus Arc existed as a broadly NS convergence feature up until the westward tectonic escape of Anatolia initiated in the Pliocene (Boulton and Robertson, 2008; Bowman, 2011). Consequently, structures capable

of accommodating broadly NS relative motion are well established and therefore relative motion parallel to the established convergence direction may be accommodated along pre-existing structures. This contrasts with the accommodation of relative motion orientated more normal to the established convergence direction, which would require the re-configuration of structures including the propagation of new fault surfaces. The formation of these fault surfaces is likely to be more seismogenic than movement along pre-existing fault surfaces. Consequently, this may generate a bias in seismological data that enhances the component of relative motion oblique to an established convergent direction. This is however speculative, and if it is not the case then it casts some doubt on the interpretations of strike-slip features at the Florence Rise (Woodside et al., 2002). Papazachos and Papaioannou (1999) use seismological data to infer a convergent margin, but not subduction, across the Cyprus Arc.

A study of tomographic data interprets the presence of a subducted slab beneath the Cyprus Arc (Figure 5.29; Berk Biryol et al. 2011). They suggest that the tearing of this slab is consistent with and consequent of restricted subduction at the Cyprus Arc relative the Aegean Arc, and that this is due to the attempted subduction of continental crust at the SCAS. They conclude that the sub-vertical geometry of the slab argues for stagnation of the subduction of the Cyprus slab, and hence, a terminal-stage of subduction and early stage of detachment. This concurs with studies of refraction data over the Cyprus Arc (Welford et al., 2015; Wortel et al., 2006).

The ESM continental fragment is widely considered to be jamming the SCAS (Ben-Avraham et al., 1988; Robertson, 1998b; Welford et al., 2015). The ESM summit faults are recent and related to underthrusting of the ESM continental fragment under Cyprus (Section 5.5.5). This means that subduction may have only recently ceased, potentially allowing depressions such as subduction trenches to be infilled. If this were the case, then A) the palaeotrenches would be depicted in the younger sediments on the seismic data and B) subduction-related deformation should be observable on seismic data in the sediments deposited since the initial subduction ceased. However, the seismic data show A) evidence of recent subsidence between the ESM and Cyprus but no evidence of recent palaeotrenches elsewhere on the Cyprus Arc and B) sub-planar post-initial-subduction sediments on either side of the Arc in most of the lines (Figure 5.27). As illustrated in Figure 5.30 it is conceivable that during restarted subduction sediments on either the downgoing or overriding plate of the subduction zone would remain unaffected by subduction related deformation, depending on the relative stratigraphic height of the subduction decollement. For sediments on both the overriding and ‘downgoing’ plates to remain largely undeformed is therefore an indication that subduction has not been active since those sediments were being deposited.

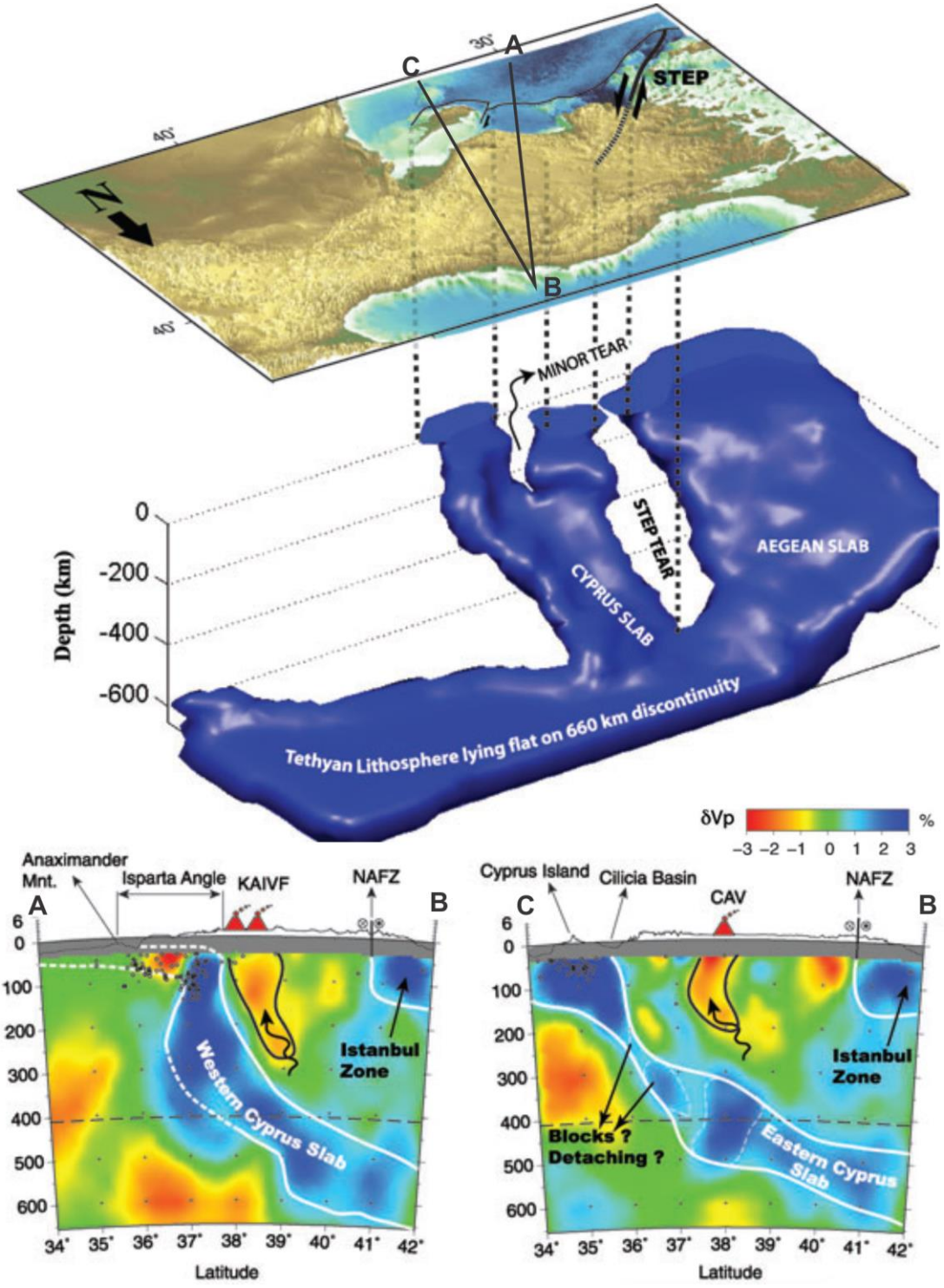

Figure 5.29-3D diagram of the resolved segmented geometry of the subducting African lithosphere beneath Anatolia (adapted from Berk Biryol et al., 2011). Dashed black lines shows the projected locations of the slab features on the surface.

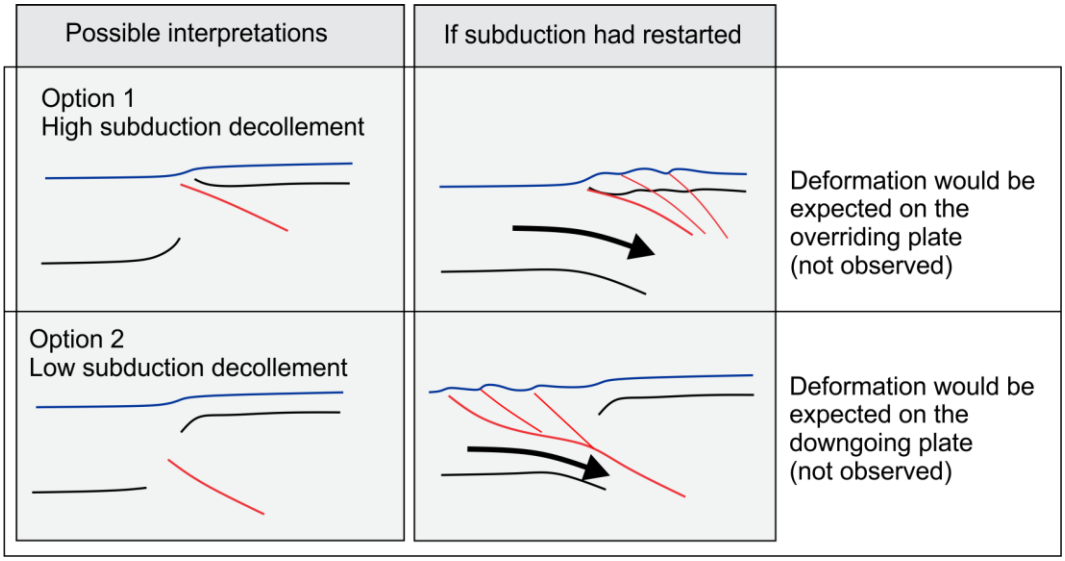

Figure 5.30-Sketch illustration of why different relative stratigraphic heights of the subduction decollement may be expected to produce deformation on the downgoing or overriding plate, in a scenario where subduction restarted.

If subduction had ceased on the Eastern Cyprus Arc but continued elsewhere on the Arc, then deformation such as transform faults might be expected to accommodate the differential movement. No such deformation is apparent that does not better suit explanation by suture tightening; no faults in the west of the Eastern Cyprus Arc have features that cannot be attributed to compression.

In the offshore Central Cyprus Arc, and to a lesser extent in the Western Cyprus Arc, salt tectonics in the post-MSC sediments obscures and distorts the imaging of underlying reflectors (Figure 5.27E-J). This thin-skinned deformation creates bathymetric deformation without any plate tectonic related deformation, and is likely responsible for interpretations of subduction related tectonics on shallow seismic lines. On lines where the seismic imaging is not too degraded by overlying salt, unformed pre-MSC reflectors may be resolved (Figure 5.27F-J). There is also some recent deformation where salt is absent on the Central and Western Cyprus Arc (Figure 5.27E, F, I) but it is extensional and on the ridge of the overriding plate. Therefore, it may be attributed to strike-slip deformation and not subduction. Exceptions to this are the normal faults of the ESM that have been linked to flexural forces from attempted subduction of the continental fragment beneath Cyprus (Section 5.5.5). No explanation for these faults is known to this study that would not require underthrusting of the ESM continental fragment under Cyprus.

In conclusion, based on the evidence outlined above, subduction in the strict sense of underthrusting and destruction of purely oceanic crust may be considered to have ceased in the Senonian across the whole southern edge of the Cyprus Arc, with the possible exception of the western limit of the Cyprus Arc where it joins with the currently active Hellenic Arc. Instead, the observations from various data sources may be better explained by convergence across the Arc leading to suture tightening and underthrusting of the relic slab which likely includes continental crust. Thus, the observation of cessation of subduction in the Senonian without subsequent restart may be considered valid for the East and Central Arc.

5.8.2 Eastern Cyprus Arc Current Deformation Regime

The eastern Cyprus Arc changes in strike from ~85° to ~25° at its east and west extremities respectively. This wide range of strikes results in inherent variation in the relative proportions of transverse and convergent movement across the Arc. This is the case irrespective of the precise relative plate motions across the Arc. Previous seismic based studies in the area have interpreted that there is currently a component of transform motion on the Eastern Cyprus Arc (Bowman, 2011; Hall et al., 2005b; Vidal et al., 2000a, 2000b) and studies of plate motions concur (Nocquet, 2012; Reilinger et al., 2006; Wdowinski et al., 2006). A large proportion of the Plio-Quaternary deformation described in the zones of the Eastern Cyprus Arc could be attributed to purely compressional stresses, however localisation of transpressional deformation on pre-existing thrusts could explain this.

In the eastern Tartus Basin Zone, convoluted deformation may be observed that defies interpretation of a non-stochastic local stress field (Figure 5.31A). Progressively eastward from this convoluted deformation faulting gets progressively less distinct, to the point that individual fault planes may only be speculatively distinguished in the easternmost portions of the Arc (Figure 5.31B). This implies that to the east the deformation becomes progressively more convoluted until coherent packages of reflectors become absent. Sediments deformed in an apparently stochastic stress field is indicative of strike-slip motion (Fossen, 2010). Given clear thrusting in the west of the Eastern Cyprus Arc these observations suggest that transformal compression becomes progressively more dominant west to east. This fits two other observations; (1) the widening of the thrust front that forms the Latakia ridge to the pop-up structure that forms the Tartus Ridge (Figure 5.31C). This widened portion of basement uplift produces a gravity high (Figure 5.31D2) and thins overlying sediments (Figure 5.31E2). (2) Thickened post-MSC sediments in eastern Latakia Basin with roll-over anticlines (Figure 5.31E1; Figure 3.17), interpreted as pull-apart basins (Bowman, 2011) that may be the offshore extension of the Hatay Graben to the NE (Boulton and Robertson, 2008; Bowman, 2011). These basins coincide with gravity lows (Figure 5.31D1), demonstrating that they are basement-involved structures. The absence of underlying MSC evaporites (Figure 3.17) indicates these basins did not exist during the MSC.

Based on the well imaged features in the seismic available to this study, it may be concluded that the Eastern Cyprus Arc is primarily compressional in its central portion, and in the eastern portion transitions from dominantly compressional through dominantly transpressional to transtensional at the easternmost extremity (see Figure 5.32).

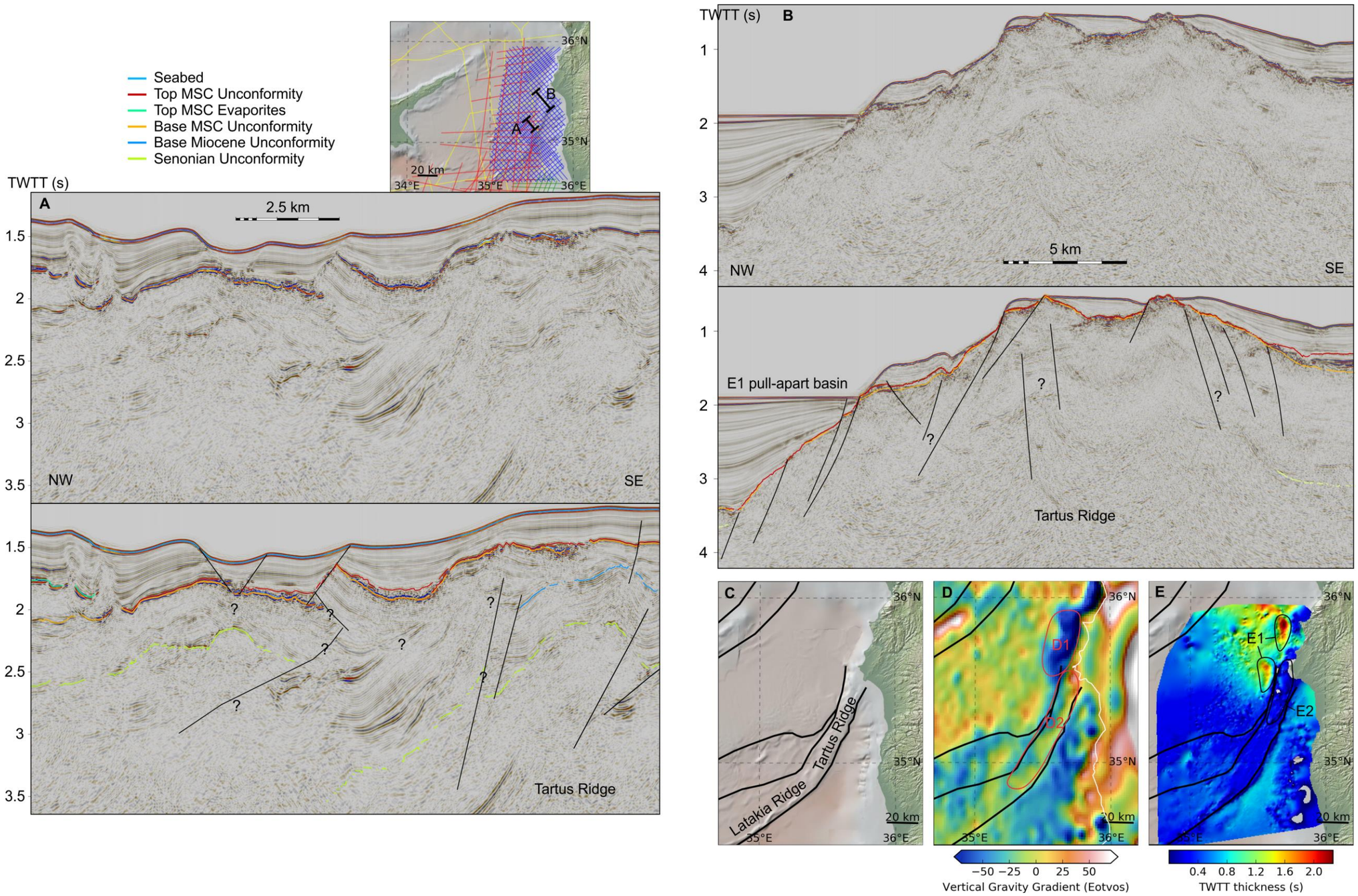

Figure 5.31-Seismic lines showing convoluted deformation at the Tartus Ridge (A, B) and maps showing evidence of strike slip deformation in the Eastern Cyprus Arc: C) bathymetry; D) gravity anomalies (Sandwell et al., 2014, 2013; Sandwell and Smith, 2009); E) post-MSC sediment thickness. Labelled areas are referred to in the text, the thick black lines are structural zone boundaries (Section 5.5) and the red lines on B) are structures with dominantly compressional displacement that may be traced across multiple seismic lines. The global relief (Ryan et al., 2009) vertical scale on the minimap is shown on Figure 1.1 and the supplementary figure.

5.8.3 Neotectonic Plate Movement

The orientation of the normal faults breaking up the summit of the ESM (Section 5.8.4) suggests a precise value for the orientation of neotectonic convergence across the Cyprus Arc: ~345° (Figure 5.32). This is in contrast with seismotectonic evidence that indicates a larger degree of transform motion across this portion of the Arc (Wdowinski et al., 2006), but concurs with Nocquet (2012), who suggests a convergence angle of c. 340° in the central Cyprus Arc based on a compilation of GPS data. The shape of the Arc is structurally inherited (Section 5.6.8) so although the shape doesn't inform on the Neotectonic plate motions, the deformation style of recent sediments in relation to the strike of the Arc does. The deformation observed backs up the ~345° convergence angle; progressively eastward in the Eastern Cyprus Arc deformation transitions from dominantly compressional through dominantly transpressional to dominantly transtensional close to the Syrian coastline (Section 5.8.2; Figure 5.32). Given the minimal change in strike of the Arc between transpressional and transtensional deformation this would appear to require non-uniform plate motion on either side of the Arc. However, if one considers that the Anatolian Plate is rotating about an Euler pole (Euler, 1776) located to the south of the Cyprus Arc at around 31° N 32° E (McClusky et al., 2000) then two alternatives may be posed.

As the portion of the Cyprus Arc along which the transpression-transtension change occurs is orientated sub-radially to the Anatolian Plate Euler pole, it follows that the relative motion of the Anatolian Plate will increase further from its Euler pole. As this motion is away from the Arc at this point (when considered in a fixed-Eurasia reference form as in Figure 4.17) this increase could transition the cross Cyprus Arc motions from net convergence to net divergence. This might explain the observed transpressional-transtensional change, but it would seem unlikely that such a marked difference in relative motions could occur in <100 km when the Euler Pole is >500 km away. Consequently, this may be considered a secondary factor in the transpressional-transtensional change.

The primary factor may be the geometry of the Cyprus Arc generating compressional structures where the Arc strikes ~EW, and extensional structures where it strikes ~NE-SW. At the transition between these two orientations, and at the end of the ~NE-SW segment, the ~NNW-SSE orientated compression forms structures that overprints most the transtensional features in those areas. Some transtensional features (apparent-normal faults offsets) may be observed to be active in the area suggested by this hypothesis (Figure 5.31A).

The ~345° convergence direction suggested by the ESM normal faults and Cyprus Arc deformation concurs with recent strike-slip features documented in the Florence Rise (Woodside et al., 2002). For two reasons care needs to be taken with interpretations of strike slip deformation on convergent boundaries.

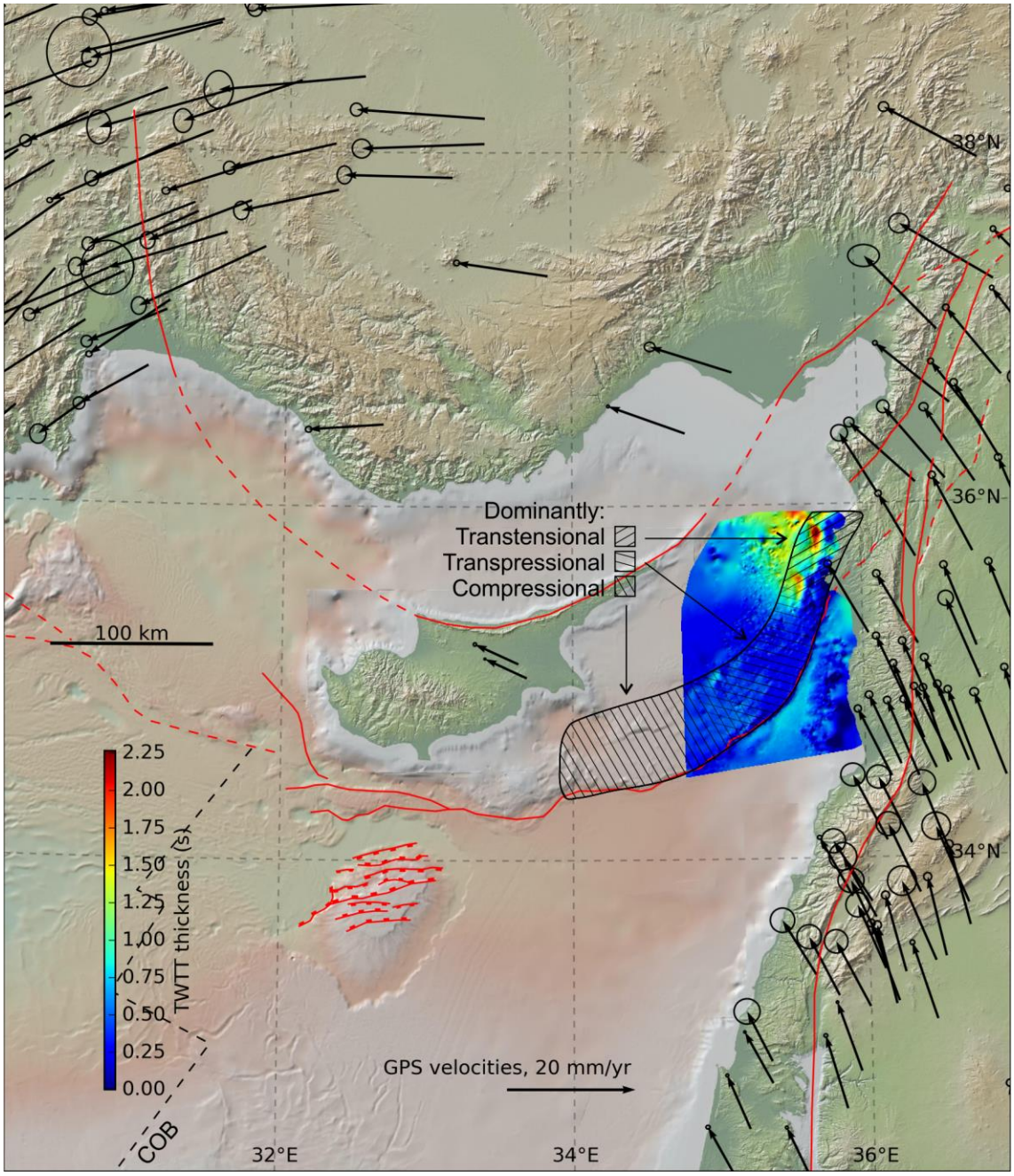

Figure 5.32-Constraints on the direction of convergence across the Cyprus Arc. GPS data are from Nocquet (2012) and relative to the Eurasian Plate, the ellipses are proportional to the error in the measurement. The surface is post-MSC sediment thickness, demonstrating the pull-apart basins in the transtensional zone at the eastern extremity of the Cyprus Arc, and the red lines over the surface are thrust/transpressional faults that may be observed in seismic data. The global relief (Ryan et al., 2009) vertical scale is shown on Figure 1.1 and the supplementary figure.

The first is that there are documented cases of subduction occurring at highly oblique angles to the subduction zone, where strain partitioning means dominantly compressional deformation is observable in the overriding plate (e.g. Nielsen et al., 2004). The second is that many structures, especially when in groups, can be interpreted to represent strike slip deformation (Harding, 1990) especially when pre-existing geological features add extra complexity to the structures. Purely strike slip structures can only be confidently interpreted as such from seismic data when the vertical section of the strike slip fault (stem of the flower structure) may also be observed (Harding, 1990).

Evidence suggests that the downgoing plate at the Florence rise is composed of oceanic crust (Section 4.7). This further supports the argument that oblique motion of the Herodotus Basin crust would not necessarily form strike-slip deformation at the Florence Rise, due to preferential strain accommodation at the relic subduction decollement (e.g. Nielsen et al., 2004) that has not transitioned to continental collision.

Strike slip at the western Cyprus Arc also opposes seismotectonic evidence which indicate that compression is singularly dominant in this area (Papazachos and Papaioannou, 1999; Wdowinski et al., 2006), however for the reasons discussed in Section 5.8.1 we do not favour this evidence.

5.8.4 Arc Curvature

The seismic data available to this study show no evidence for active destruction or accretion of material at the Eastern Cyprus Arc subduction front since the Senonian (Section 5.6.8). Subsequent deformation has involved spatially distributed thrusting, with localisation of shortening on reactivated thrusts of the relic subduction zone (Section 5.6.8). These thrusts reactivated to form the arcuate shape of the ridges that define the bathymetric expression of the Eastern Cyprus Arc, and thus the arcuate shape is inherited from the relic subduction zone. The seismic data indicate that the West and Central Cyprus Arc has also experienced no subduction at its southern edge since the latest Cretaceous (Section 5.8.1). It follows that the geometry of this southern edge of the Cyprus Arc has not changed since the cessation of subduction, so its curved shape is also structurally inherited.

The arcuate shape of the Cyprus Arc has likely arisen from, A) the naturally arcuate shape of intra-oceanic subduction zones and B) tectonic dragging. Both concepts are described below and discussed subsequently.

A) Many modern intra-oceanic subduction zones are arcuate (Hall et al., 1995; Mahadevan et al., 2010) Figure 5.28). Arcuate and linear subduction zones are understood to be characteristic of slab-pull and externally forced subduction zones respectively (Mahadevan et al., 2010). The arcuate shape arises from the combination of forces that exist during buckling of a portion of the surface of a sphere (Mahadevan et al., 2010).
B) Here, the term ‘tectonic dragging’ is used to described the large-scale differential offsets and rotation that result in the lateral bending of crustal scale trends, due to the proximal lateral motion of more mechanically resilient crust. Examples of this phenomenon are documented in SE Asia on either side of the Indian Plate where it has collided with Eurasia (Lawrence et al., 1981; Tapponnier et al., 1983), and on the Sinai Peninsula as the LSZ formed (Moustafa and Khalil, 1994). Tectonically dragged, curved geological trends observed in the exhumed accretionary wedge of Southern Pakistan form a scale-equivalent potential analogy for those in the Cyprus Arc (Lawrence et al., 1981). A geometric comparison showing similarities of form and scale is shown in Figure 5.33.

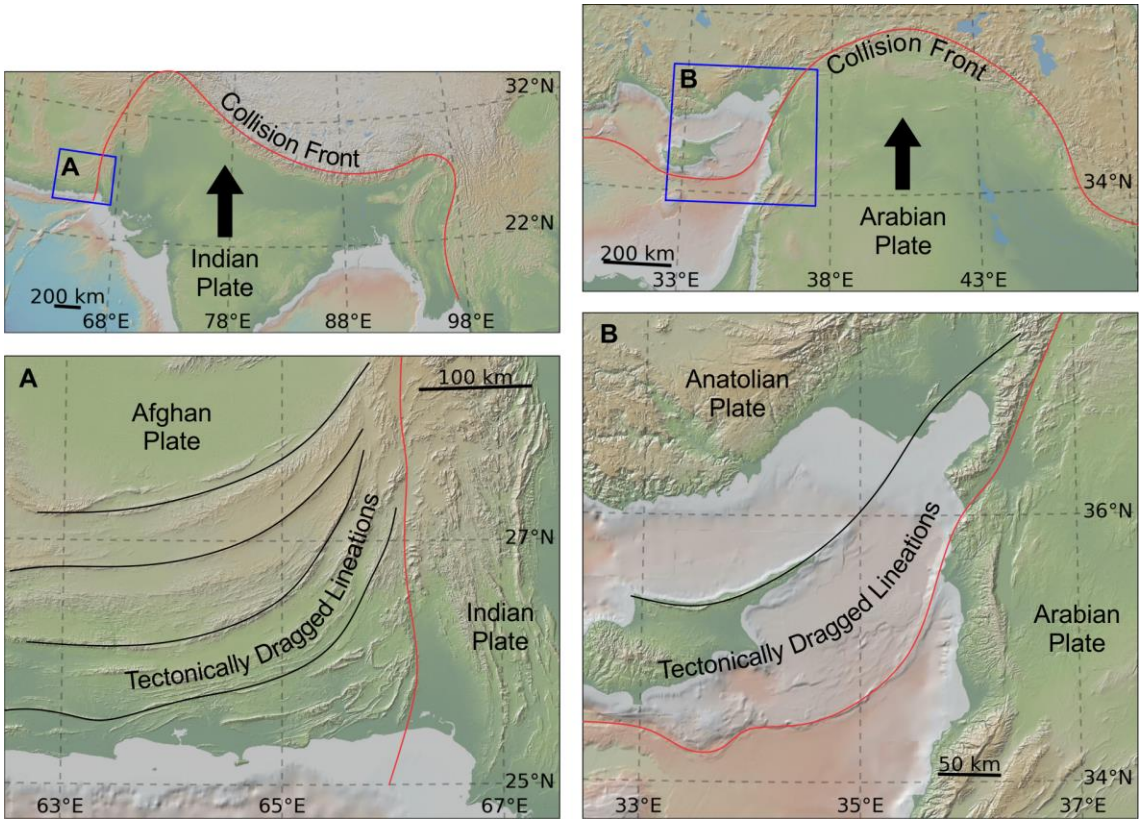

Figure 5.33-Maps illustrating how geological trends of the Afghan Plate appear to have been dragged by the neighbouring northward motion of the Indian Plate (A; e.g. Lawrence et al., 1981), and how this appears comparable with the Eastern Cyprus Arc (B). The global relief (Ryan et al., 2009) vertical scale on the maps is shown on Figure 1.1 and the supplementary figure.

If one side of the arc underwent significant tectonic dragging, one might expect a higher degree of curvature adjacent to the body doing the tectonic dragging which would result in an asymmetric arc. The symmetry of the east and west SCAS (Figure 5.2) therefore suggests that its arcuate shape is probably primarily the result of intra-oceanic subduction. The centre of the curvature is located to the west of the Arabian Promontory, suggesting the curvature formed during roll back of the SCAS after collision of the Arabian Promontory with the SCAS further to the east.

The current geometry of accreted continental fragments around the Arabian Promontory demonstrates that some tectonic indentation occurred, and with it some tectonic dragging (Figure 2.25). If tectonic dragging during the Cenozoic was responsible for the bend in the Latakia and Tartus Ridges, then deformation would be expected in Cenozoic Levantine Basin sediments adjacent to the Ridges. The absence of this deformation suggests that tectonic dragging of these SCAS ridges after the Senonian may be discounted. Thus, the tectonic dragging must have occurred during collision of the Arabian Promontory with the SCAS whilst subduction was still active. This would have perhaps aided, or aided setup of, the intra-oceanic subduction configuration which led to the arcuate shape of the SCAS.

The arcuate trend of the Latakia and Tartus Ridges at the relic SCAS matches that of the Kyrenia-Misis lineation at the relic NCAS. Thus, the same mechanism that curved the Latakia and Tartus Ridges might be expected to have also curved the Kyrenia Range, and one might expect this to be coeval. However, the cessation of subduction at the Misis Range, the north-eastern

continuation of the Kyrenia Range, probably occurred during the mid-late Miocene (Morris et al., 2015). Hence, subduction in the NCAS was still ongoing after the cessation of subduction and bending of the SCAS. The undeformed Cenozoic sediments of the Levantine Basin adjacent to the SCAS discussed in the previous paragraph means the Arabian Promontory must have extended >200 km north of the SCAS shortly after subduction had ceased there. It seems highly improbable that the NCAS would have formed a shape to match the SCAS prior to either their adjacency or comparable plate configurations, given this >200 km separation. This supports the conjecture that the arcuate shape of the NCAS formed after that of the SCAS.

Three possibilities exist to explain how the NCAS, and associated features such as the Kyrenia Range, gained arcuity to match that of the SCAS:

- The collision of the Arabian Promontory with the SCAS was followed by formation of the arcuate shape of the SCAS. This occurred due to intra-oceanic subduction on the shortened still active section of the SCAS to the west of Arabia. Therefore, it might be expected that collision of the Arabian Promontory with the NCAS would also be followed by formation of an arcuate shape of the NCAS west of the Arabian Promontory. The contemporaneous and then ongoing collision of the Arabian promontory with Eurasia meant there was likely to be at least partial tectonic dragging of the NCAS as the Arabian Promontory indented Eurasia. The sediments adjacent to the NCAS are not as well seismically imaged as those of the SCAS (Section 5.4), so Cenozoic and post-subduction tectonic dragging of this subduction zone cannot be discounted. However, this fails to explain the similarity in shape of the NCAS and SCAS.
- Morris et al. (2015) present palaeomagnetic data that indicate the eastern extremity of the Kyrenia Range, the Karpas Peninsula, was tectonically rotated anticlockwise by ~30° at some point since the Maastrichtian. Because Afro-Arabia has been converging with Anatolia and Eurasia since the Cretaceous (Section 2.5) it may be confidently assumed that regional stress patterns related to this convergence, as opposed to some other far field stress, provided the tectonic forces that formed the rotation. Morris et al. (2015) suggest that this rotation of the Kyrenia Range occurred in the mid–late Miocene, although they understood subduction on the SCAS to have reactivated at this time, albeit in a more minor form (Figure 5.3). With SCAS subduction ceased by the end Senonian, and the rotation of the Karpas Peninsula to have taken place sometime since the Maastrichtian, there remains a geologically brief 7 Myr in which this rotation could have occurred, if it were related to bending of the SCAS. It is conceivable that this rotation could have occurred after the cessation of SCAS subduction, and without deformation of Levantine basin sediments, if significant (c. 30 km) shortening was accommodated in the West and Central Cyprus Arc. Thrusts of significant heaves and of a compatible age are present in the imbricate zone of the Eastern Cyprus Arc (Section 5.5.2), however their location at the eastern end of the Cyprus Arc would oppose the observed anticlockwise rotation at the Kyrenia Range. It is unclear if the underthrusting of the ESM continental fragment under Cyprus (Section 2.3.10), or some other mechanism, could provide 30 km of shortening, but the lack of deformation in the west of the Latakia Basin indicate that this is a highly speculative explanation.

- The restoration in Section 5.6 revealed that at the cessation of subduction at the SCAS the overlying stratigraphy was thickened above the subduction zone and consequently it formed a palaeoslope dipping north in both the east and west of Cyprus (Sections 5.6.8, 5.7.2). Collision of the NCAS with this palaeoslope would have restricted subduction where the crust was elevated and thickened. Thus, ongoing subduction could have progressively deformed the NCAS to match the SCAS (Figure 5.34).

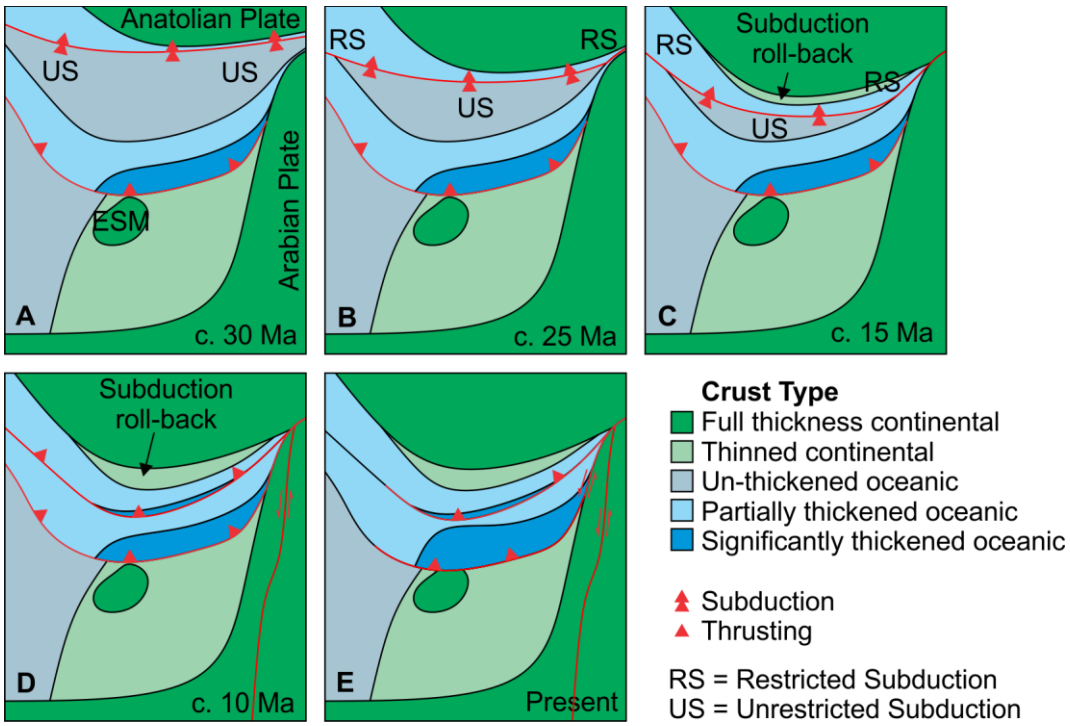

Figure 5.34-Sketch explanation of the how the thickened crust of an overriding plate of a relic subduction zone could cause restriction of subduction in another active subduction zone, such that the form of the active subduction zone evolves to match that of the relic subduction zone.

Considering all the arguments in this section, and in the context of the restoration demonstrated later in Section 5.9, a combination of similar tectonic configurations (first explanation) and relic-SCAS-guided NCAS subduction (last explanation) best fit the evidence in order to explain the matching arcuate shape of the northern and southern limits of the Cyprus Arc.

5.8.5 Additional Discrete Implications

North of the Kyrenia Range lies the Cilicia Basin. The evolution of this basin is largely unknown prior to the MSC. The NCAS curvature hypothesis detailed in Figure 5.34 concurs with the hypothesis that subduction rollback could have formed the basin. This is however speculative, and further work onshore Southern Turkey, or collection and interpretation of seismic data in the Cilicia Basin, could help inform on this issue.

The 90° anticlockwise rotation of the Troodos microplate has been related to rotation at a transform intersection with the ridge that formed the ophiolite (Morris et al., 2015) and rotation of the subduction zone during its collision with the Arabian Promontory (Inwood et al., 2009). This is a large amount of rotation to be explained by these mechanisms. A recent study interpreted the Hecataeus Rise to represent a collage of oceanic fragments that accreted in the adjacent

subduction zone (Welford et al., 2015). If this accreted body docked in the subduction zone after the Maastrichtian, then continued subduction/suture tightening could have bowed the plate boundary around it. This indentation could have introduced further minor rotations to the Troodos ophiolites, although this is highly speculative.

5.9 Regional Tectonic Congruity

The Bitlis Suture, Misis thrust complex, Central Cyprus Arc and Isparta Angle all share histories involving both Late Cretaceous subduction ceasing in the latest Cretaceous and middle Eocene continent-continent collision related (or unknown cause) compression (Brew et al., 2001a; Hall et al., 2014; Hempton, 1985; Morris et al., 2015; Poisson et al., 2003; Robertson et al., 2013, 2004). These same events may be observed in the Eastern Cyprus Arc, however in contrast to some earlier studies which hypothesise resumption of subduction where it had previously ceased, no resumption of subduction may be observed.

Integrating the observations made by this study with references collated from published literature permitted formulation of the reconstructions drawn in Figure 5.35. These reconstructions are spatially consistent, and use oceanic magnetic anomalies in the Atlantic and Indian Oceans to determine the locations of the Eurasian and African Plates (Gurnis et al., 2012; Seton et al., 2012). As the magnetic anomalies of the Atlantic and Indian Oceans are well resolved in satellite data, the reconstructed locations of the adjacent continental boundaries are confident at the scale of these figures. For the reconstructed southern Eurasian margin and northern African margin some inaccuracies will be introduced by internal plate deformation, however the need to be globally spatially consistent means the locations of these margins is reasonably confident at this scale. The indentation of the Eurasian Plate by the Arabian promontory means its pre-collision geometry is uncertain, however its current location gives a southern limit.

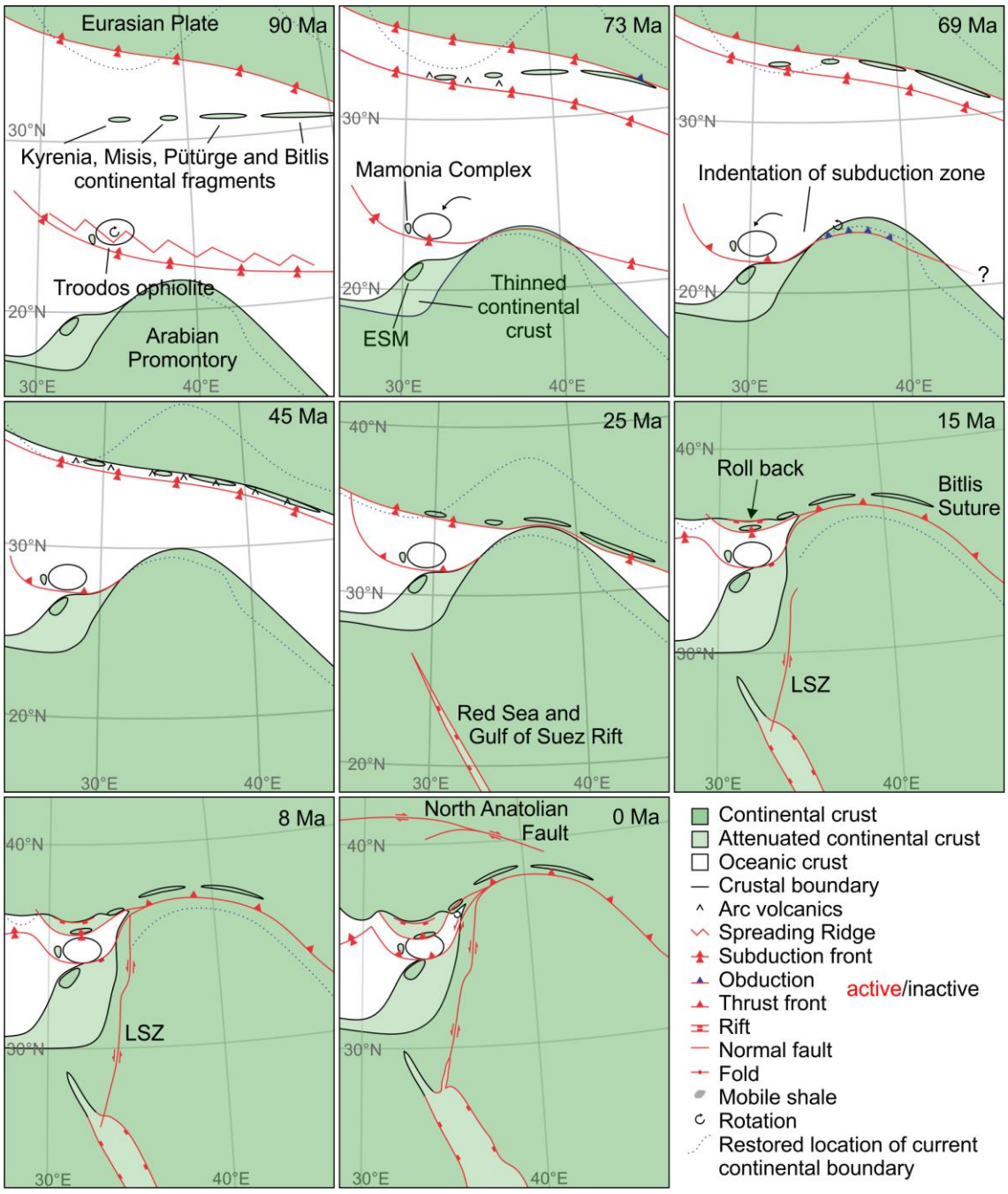

Figure 5.35-Palinspastic sketches of the Cyprus Arc after integration with the elements discussed in this chapter and information from published literature (see text for source and discussion). Some features on the Eurasian Plate are omitted for clarity (see Barrier and Vrielynck, 2008).

A single subduction zone active during the Cenozoic is in contrast to some earlier reconstructions (Morris et al., 2015; Robertson et al., 2012a). The rocks of the Kyrenia and Misis Ranges, and Pütürge and Bitlis continental fragments may be reconstructed as part of a single island chain. This means that they share a comparable tectonic history. The Kyrenia Range rocks cannot be north of the most northerly subduction drawn on Figure 5.35A and B as Late Cretaceous supra-subduction zone ophiolites fragments are documented in the Kyrenia Range (Robertson et al., 2014), so the Kyrenia Range rocks must have been on a downgoing plate at this time. The Kyrenia Range rocks cannot be immediately to the north of the most southerly subduction drawn at 90 and 73 Ma because the Troodos and Kyrenia Range have separate rotation histories (Morris et

al., 2015), and as the arcuity of the Kyrenia Range developed later (Section 5.8.4). Differences in timing of collision and ophiolite obduction at the different localities in the island arc (Robertson et al., 2012a) may be explained if the island arc was at an angle to the adjacent subduction zones. This is consistent with the lack of Late cretaceous volcanics in the Pütürge and Bitlis continental fragments, and the earlier obduction of ophiolites in the eastern localities. On this basis Eocene volcanics in the Kyrenia and Misis Ranges, previously attributed to palaeorotation of the Troodos microplate but acknowledged as possibly subduction related (Robertson et al., 2012b), may instead be considered part of the Eocene Arc-volcanics that affected the Pütürge and Bitlis continental fragments.

Around the latest Cretaceous the most northerly subduction zone collided with the Pütürge and Bitlis continental fragments, the most southerly subduction zone collided with the Arabian promontory, and an intermediate subduction zone generated volcanics in the Kyrenia and Misis Ranges. These events occurred across three different subduction zones. Timing constraints indicate all three subduction zones may have been active simultaneously, however the initiation of collision at the northern and southern subduction zones could have restricted subduction, demanding that shortening be accommodated at a new subduction zone. It makes mechanical sense for this to form adjacent to relatively more mechanically resilient crust, in this case south of the continental fragment lineation that included the Kyrenia range. It is possible that the intermediate subduction zone existed earlier, however as this would require three subduction zones to be fully active concurrently this scenario is unfavourable.

The reconstructions assume that significant indentation of the southern Eurasian continental margin occurred from collision with the Arabian promontory. This is backed up by earlier reconstructions (Table 2), palaeomagmatic rotational data (Morris et al., 2015), analogues (Lawrence et al., 1981; Tapponnier et al., 1983) and an Occam's Razor (Encyclopædia Britannica, 2010; Gauch, 2003) approach to lineation of subsequent deformed.

Effort has been made to keep the restorations here as simple as may adequately explain the discussed observations. Given the complexity of areas with multiple active subduction zones active today in a comparably sized area, such as may be found SE Asia and the SW Pacific (Hall, 2002; Schellart et al., 2006), it is possible that a more complex configuration existed in the EMR. However, without additional information to suggest otherwise, the simplest options may be argued to be the most likely (Encyclopædia Britannica, 2010; Gauch, 2003).

Continuation of the Cyprus Arc subduction zones west of Cyprus is in contrast to some earlier reconstructions (Barrier and Vrielynck, 2008; Berra and Angiolini, 2014) but favours others (Morris et al., 2015; Robertson et al., 2012a).

5.10 Conclusions

In summary the key conclusions of this chapter are:

- The last subduction at the southern edge of the Cyprus Arc was prior to the formation of the Senonian Unconformity horizon. It may be speculated that the collision and uplift associated with the cessation and uplift may have influenced the formation of the Senonian unconformity.

Subsequent convergence across the southern edge of the Cyprus Arc has been relatively minor (i.e. <50 km), and has been accommodated by underthrusting of the relic downgoing plate as evidenced by the uplift of Cyprus and deformation at the ESM, and by distributed thrusting in the overriding plate, demonstrated by thrusts in seismic data east of Cyprus (Section 5.6.8).

- The current geometry of the southern edge of the Arc is due to structural inheritance from the Cretaceous subduction. The form of the Cretaceous subduction zone was probably 'tectonically dragged' by the adjacent Arabian promontory (Section 5.8.4).
- Evidence suggests subduction was active at the northern edge of the Arc until the earliest Miocene. That the shape of this subduction zone matches that of the relic subduction zone to the south is likely due to laterally variable rates of subduction influenced by the thickened crust behind the relic subduction zone to the south (Section 5.8.4).
- Convergence has continued at both relic subduction zones since the cessation of subduction (Section 5.6.8). The currently active normal faults on the ESM seamount indicate that there is some convergence still occurring across the arc (Section 5.5.5). Minimal convergence has been accommodated on the southern subduction décollement since the cessation of subduction (Section 5.8.1). Instead shortening has occurred as distributed thrusting in the leading edge of the overriding plate (Section 5.8.1). This hiatus may have occurred because Eurasia-Afro-Arabia convergence was accommodated by the LSZ, leading to differential extension. This extension may be observed elsewhere in the EMR (Chapter 6).
- The cessation of subduction at the Cyprus Arc and the uplift of Cyprus infer the underthrusting of less dense continental crust as opposed to oceanic crust. This indicates that continental crust has entered what was previously a subduction zone. This concurs with the interpretation of thinned continental crust in the Northern Levantine Basin (Section 4.6). However, the question remains if this is true continent-continent collision, as the crust of the overriding plate is oceanic (Section 5.6.7).

The large variation in deformation style across the Cyprus Arc has likely contributed to the wide range of interpretations and hypothesis for the evolution of the Arc. Access to a seismic data set covering the whole of the offshore Arc permitted observation that the full range of deformation styles is concurrently valid, and only by considering these different deformation styles together have these conclusions been reached. The evolution of the Cyprus Arc as understood here is summarised and integrated with the other findings of this study in Section 8.6.

Chapter 6 The Piano Key Faults

6.1 Introduction

Previous analysis of seismic data in the Northern Levantine Basin offshore Lebanon has identified a dense network of late Miocene normal faults (Figure 6.1; Figure 3.14A) that have been termed the Piano Key Faults (PKFs) (Ghalayini et al., 2016, 2014; Hawie et al., 2013; Hodgson, 2013, 2012; Klimke and Ehrhardt, 2014; Kosi et al., 2012; Lie et al., 2013; Reiche, 2015; Reiche et al., 2014a). The documented faults number more than 400, have a consistent WNW-ESE strike, and throws over 200 m are widespread (Figure 6.1). The Cyprus Arc collision zone is 50-100 km to the north of the PKFs; this feature represents the boundary between the African and Eurasian plates which have been converging since the late Mesozoic (Chapter 4). Thus, these extensional faults exist spatially and at an orientation where compressional features might be expected.

The genesis of these faults is uncertain and a number of competing theories have been proposed (Ghalayini et al., 2016; Kosi et al., 2012; Reiche et al., 2014a). These are reviewed in Section 6.4.6 after the faults have been described, and a new numerical analysis of their geometries presented. This analysis generates evidence against the previously published hypotheses and other alternatives, except for regional tectonic forces associated with the LSZ. An additional aspect of the PKF story that has been overlooked in previously published literature are the contemporaneous perpendicular folds (Figure 6.1C). These are described in Section 6.3 and play a key role in the development of a new hypothesis for the formation of the PKFs (Section 6.6.1).

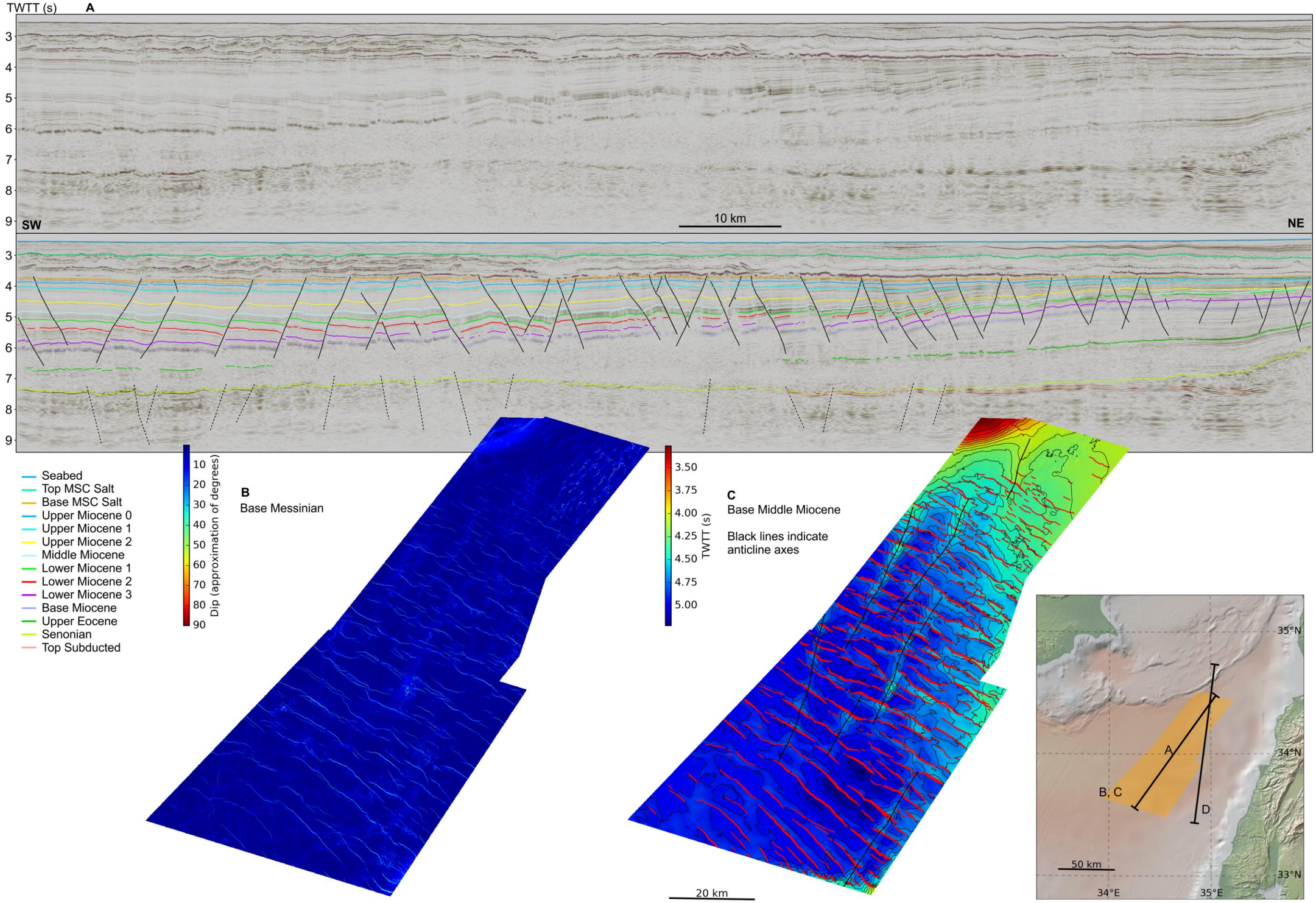

Figure 6.1-A) Seismic line along the dip direction of the PKFs; B) Dip estimate (linear TWTT-depth relationship) of the Base MSC surface; C) TWTT of the Base Middle Miocene surface with the PKFs filled in red; D) PSDM line crossing the PKFs. The global relief (Ryan et al., 2009) vertical scale on the minimap is shown on Figure 1.1 and the supplementary figure.

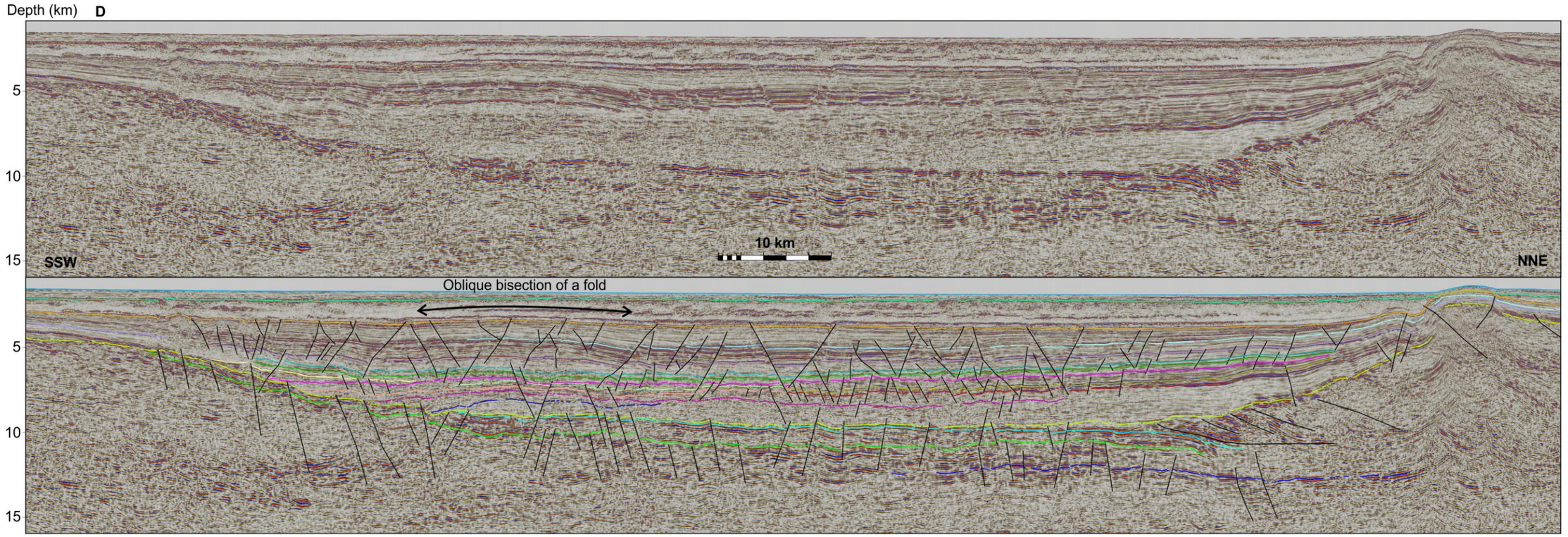
Depth (km)
D
5
10
15
SSW
10 km
NNE
Oblique bisection of a fold
5
10
15
Key horizon ages
(others are relative)
Seabed
Top MSC
Base MSC
Base Middle Miocene
Base Miocene
Upper Eocene
Senonian Unconformity

6.2 Distribution of Faults

The PKFs as documented in previous literature exist in an area of the Northern Levantine basin bounded to the east by the continental margin of Lebanon, to the NW by the Latakia Ridge and to the SE by the Levant Ramp (Figure 6.2; Ghalayini et al., 2016, 2014; Reiche et al., 2014a). To the west the fault throws diminish to sub-seismic resolution within the lateral limits of the sediments of the Levantine Basin, a limit likely controlled by the sediments in the basin (see Section 6.2.3). To properly place the PKFs in their regional context, and to permit consideration of the system that formed the PKFs at its full scale, the first stage of this investigation was to outline the limits of the PKF extensional system. The regional coverage of the seismic data available to this study facilitated this.

The LEB3D volume is a merge of two surveys, the more southerly of which was the dataset used by Kosi et al. (2012) and Hodgson (2013), although only partial maps of the PKFs were provided in both publications. Hawie et al. (2013), Klimke and Ehrhardt (2014) and Reiche (2015) each used a small number of 2D lines (not available to this study) in different locations in the Northern Levantine Basin that imaged some of the PKFs, but did not include any mapped faults. Reiche et al. (2014a) investigated the effect of the PKFs on deformation in the overlying evaporites on the basis of EMED00 seismic lines, but again do not provide any maps of the faults. Lie et al. (2013) and Ghalayini et al. (2016, 2014) used a large 3D volume that covers the area between the LEB3D volume and the Lebanese coastline, and included maps of the PKFs they picked. These mapped faults are drawn in Figure 6.2 as red lines. Thus the other marked faults are original interpretations.

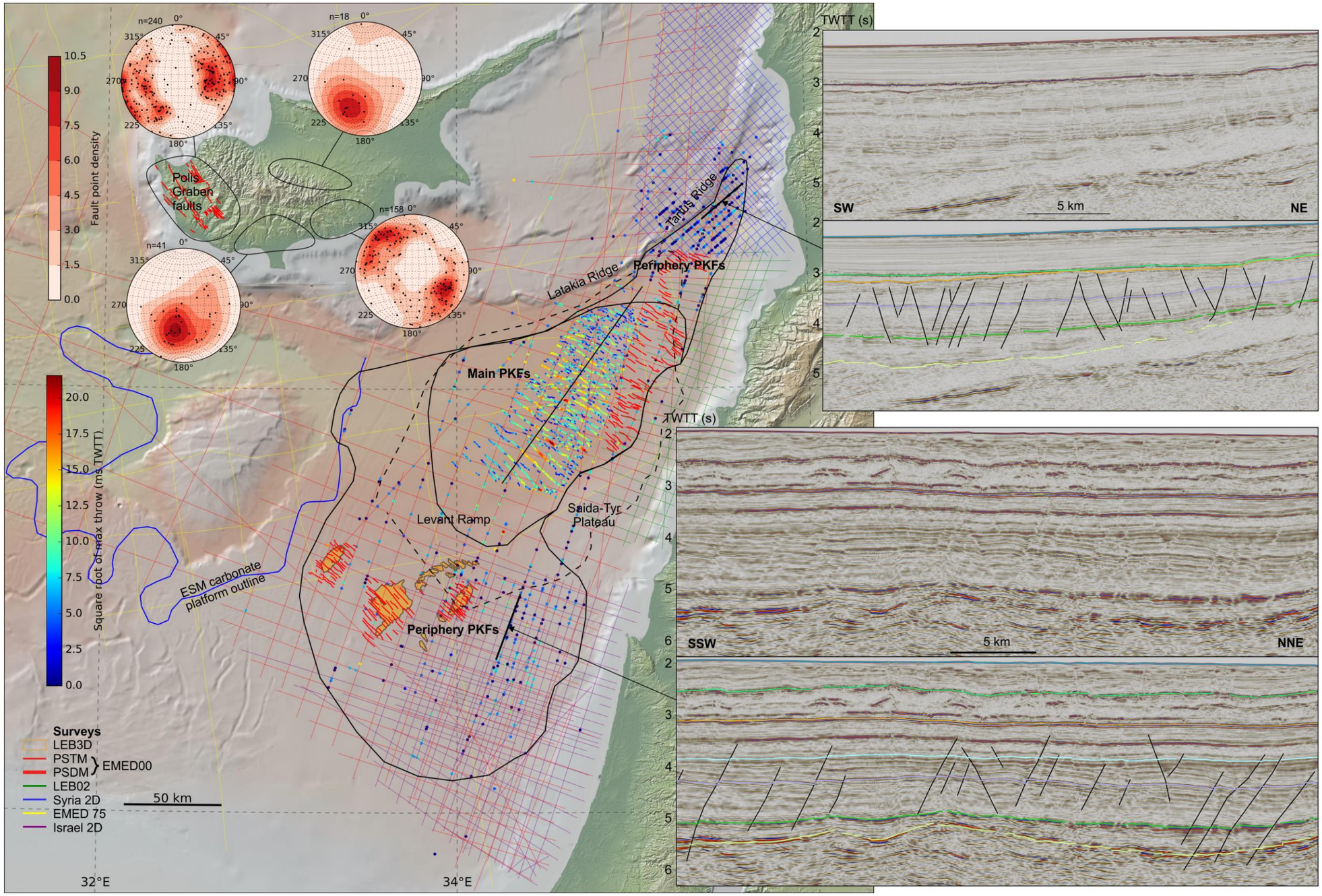

Figure 6.2-Outline of the different Miocene normal faults documented in published literature or observed by this study in the EMR. The two black rings outline the main and peripheral PKFs, discussed in Section 6.2.1. The dashed black line shows the area previous interpreted to be affected by PKF deformation (Ghalayini et al., 2016, 2014; Reiche et al., 2014a). The seismic line marked in the main PKFs is shown in Figure 6.1A. The colour of the marked PKFs is a proxy for throw to aid size comparison. The faults in red around the marked hydrocarbon fields are traced from surface images of the hydrocarbon fields (Christensen et al., 2013; Delek Drilling & Anver Oil, 2014) and those in red adjacent to the LEB3D volume and onshore Cyprus are published fault traces (Ghalayini et al., 2014; Payne and Robertson, 1995 respectively). The stereonets are based on the data from Kinnaird (2008) and correspond to normal faults cutting the Miocene and Palaeocene sediments in the circled areas. The global relief (Ryan et al., 2009) vertical scale on the map is shown on Figure 1.1 and the supplementary figure.

6.2.1 Levantine Basin

The Spectrum LEB3D seismic volume permitted delineation of the PKFs in the Northern Levantine Basin, and the Spectrum EMED00 regional 2D seismic lines allowed an assessment of the wider extent of the PKFs in the whole Levantine Basin and the relevant stratigraphic packages (Chapter 3). The Hannah-01 well offshore Israel is the closest available pertinent well data by which to constrain the stratigraphy and hence the timing of their formation (Figure 3.9). The ages of the horizons in this well may be traced by the Israel 2D and EMED00 2D lines to the LEB3D volume with high confidence (Figure 3.14). The designated ages of the reflectors picked by this study fits those in preceding studies (Ghalayini et al., 2014; Hawie et al., 2013; Reiche et al., 2014a).

Further Miocene age extensional faults with relatively minor offsets are revealed by inspection of the seismic data available to this study in the Southern Levant Basin and in the finger of the Levant Basin that extends parallel to the Tartus Ridge (Figure 6.2). The majority of the PKFs in the Southern Levantine Basin (south of the Levant Ramp) do not offset the Base MSC reflector, and many have absent or significantly reduced offsets in the upper Miocene interval (Figure 6.2), indicating the timing of their formation may be different from those in the Northern Levantine Basin. This timing is explored further in Section 6.6.2. This study refers to all of these Levantine Basin Miocene faults as the PKFs, and terms the larger and smaller throw swarms as the 'main' and 'periphery' PKFs respectively (Figure 6.2).

3D seismic imaging of the periphery PKFs is not available to this study, and the 2D data that images them cannot confidently derive their orientation. Published surface maps of hydrocarbon fields in the Southern Levantine Basin and dip surface maps of the NE Northern Levantine Basin reveal the strikes of portions of the peripheral PKFs is sub-parallel with those in the Northern Levantine Basin (Figure 6.2 & refs. in caption). Elsewhere the peripheral PKFs are significantly better imaged on NNE-SSW trending seismic lines than those perpendicular, indicating their strike is congruent with the surrounding PKFs. Additionally, published hydrocarbon field outlines with reservoir rocks in the Miocene interval show segmentation along the strike of the PKFs, inferring further sub-parallel faults (Figure 6.2).

6.2.2 Anatolian Plate

Late Miocene extensional faulting has been documented in field studies of onshore Cyprus (Kinnaird and Robertson, 2012; Payne and Robertson, 1995), and may be observed in seismic data north of the Tartus Ridge (Figure 6.2; Section 5.5.3). The intermediate plate boundary might be considered to compartmentalise them from the PKFs. This is discussed in Section 6.6.7 to permit focus on the new hypothesis for the formation of the PKFs, but concludes on the basis of published examples that the mechanical configuration of a relic subduction zone does not preclude transmission of extensional forces. Therefore, even though these locations are on a different tectonic plate to the PKFs, they are included in the consideration of compatible age extension in the region-a region that might be expected to be compressional as it is located adjacent to the convergent plate boundary.

The late Messinian extensional faulting onshore Cyprus has previously been attributed to subduction-roll back and back-arc extension (Kinnaird and Robertson, 2012; Payne and Robertson, 1995). However, if subduction ceased at the end of the Cretaceous (Chapter 4) these mechanisms are thrown into question. The Polis Graben faults onshore Cyprus appear to match the trend of the PKFs, and are of compatible age (Figure 6.2; Payne and Robertson, 1995). This suggests they may have formed via the same mechanism.

Conversely, the average orientation of other late Miocene normal faults onshore Cyprus does not follow the same trend, instead appearing to strike concentrically around the Troodos mountains (Figure 6.2). These mountains are understood to have been uplifted via serpentinite diapirism and underthrusting (Robertson, 1990 via Main et al., 2015) which was focused in the centre of the Troodos in the Pleistocene (Poole and Robertson, 1991; Robertson, 1977). Consequently, the flanking areas could have been subject to crestal collapse and convex up extension (Figure 6.3). The Cypriot normal faulting in Figure 6.2 is dated by the age of the sediments which are offset (Kinnaird and Robertson, 2012), which only provides a lower limit to the age of the normal faulting. These mechanisms are therefore alternative explanations for the Cypriot normal faulting, including faulting in the Cretaceous rocks of the Troodos mountains not included on Figure 6.2 (Kinnaird and Robertson, 2012). The Polis Graben is the only documented graben system of its (larger) scale on Cyprus, and the resulting topography is geometrically distinct from other areas of Cyprus (Ryan et al., 2009). This could be an indication that it formed via a different mechanism. Further study is required to evaluate the potential link between the faults onshore Cyprus and the PKFs.

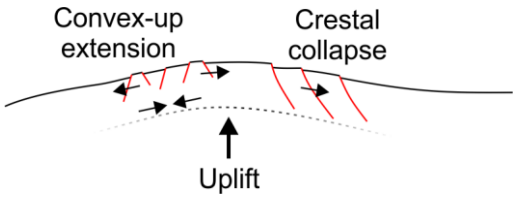

Figure 6.3-Sketch demonstrating two different possible mechanisms for normal faulting onshore Cyprus related to uplift of the Troodos mountains. Uplift may be related to serpentinite diapirism or thrusting (Section 5.7.4).

The seismic data available to this study offshore Syria reveals late Miocene extensional faulting north of the Tartus Ridge (Section 5.5.3). Tracing of larger offset faults demonstrates a NE-SW orientation-roughly perpendicular to the PKFs. The area has also been uplifted, possibly by underthrusting, in the Plio-Quaternary (Section 5.6.8) which suggests that the same extensional fault mechanisms as for the faults onshore Cyprus (Figure 6.3) might be responsible. However, these faults offset the Base- and pre-MSC reflectors (Figure 6.4), suggesting formation prior to the major post-MSC phase of uplift in the area. Alternatively, the mobility of the MSC salt can lead to stratigraphic partitioning of strain (Section 3.7.1). This could cause faults that formed after the MSC to form blindly within the pre-MSC sediments, with a separate or analogous mechanism accommodating the equivalent strain in the overlying sediments. The post-MSC sediments display layer bound extension, lending credence to this hypothesis (Figure 6.4). Crucially, the pre-MSC normal faults appear to be focussed beneath the convex up portion of the Base-MSC reflector (Figure 6.4).

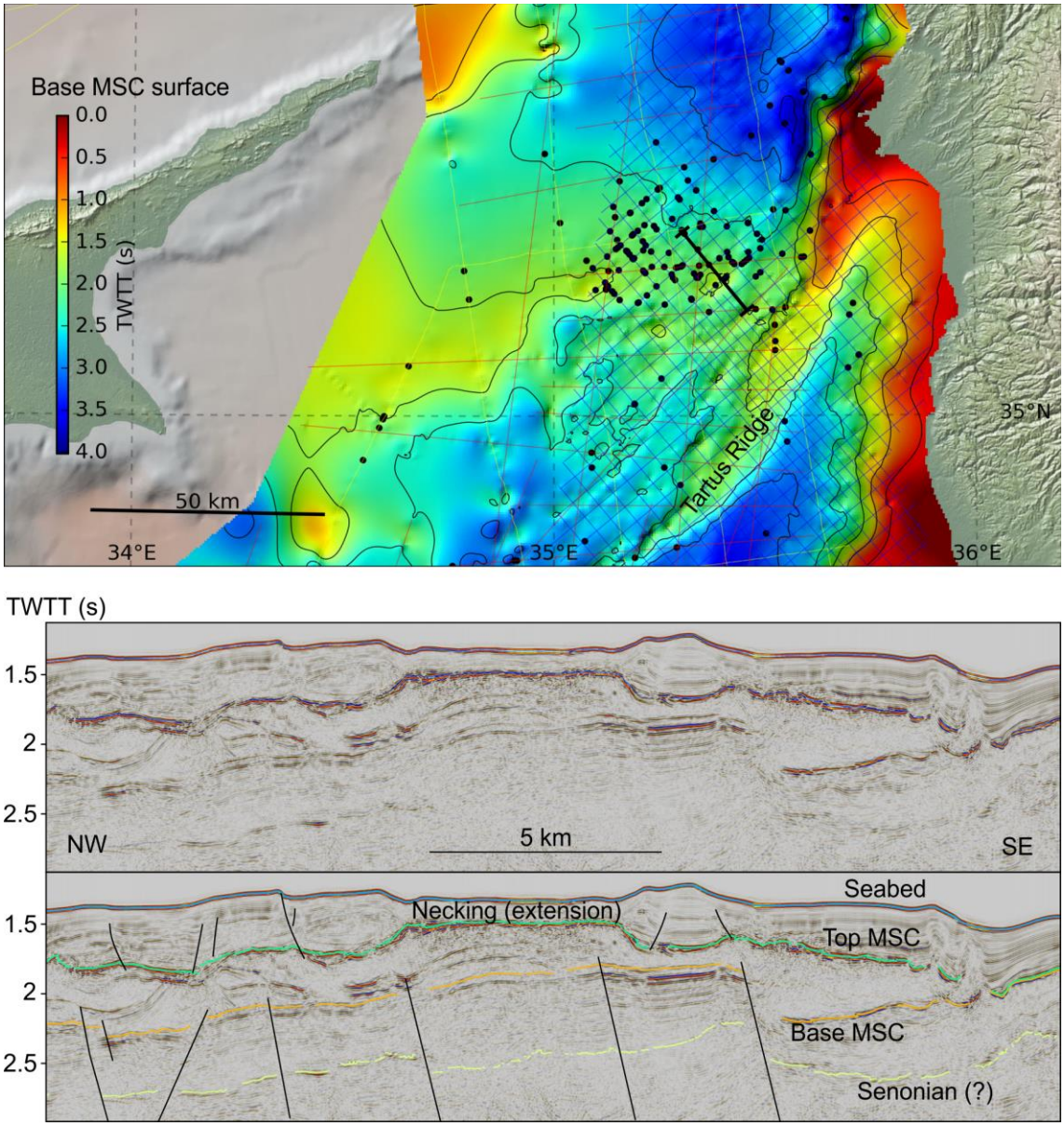

Figure 6.4-Base MSC surface with faults that cut it marked by black dots, and seismic line across the peak of the uplifted area demonstrating partitioned intervals of normal faulting and necking above the mobile MSC salt. The global relief (Ryan et al., 2009) vertical scale on the map is shown on Figure 1.1 and the supplementary figure.

6.2.3 Decollement Regulated Incidence?

Small fault offsets in the Base MSC reflector may be observed at the main PKFs (Figure 6.1A, B). Interaction between these faults and later halokinesis has been documented (Reiche et al., 2014a), but displacement on the faults ceased shortly after the initiation of the MSC (Figure 6.1A; Reiche et al., 2014a). Large fault offsets may be observed in the Base Miocene reflector of the main PKFs, but no confident offsets may be interpreted in the underlying Eocene reflector (Figure 6.1A). Thus it may be inferred that the faults detach in the intermediate interval (Ghalayini et al., 2016; Kosi et al., 2012), which is assumed to be Oligocene in age based on the ages of overlying and underlying reflectors. The fault surfaces do not appear to undergo any significant reduction in dip angle up to and inclusive of the Base Miocene reflector, the deepest confident reflector

showing offsets (Figure 6.1A), indicating the decollement interval may be interpreted as being mechanically mobile.

The mobile interval itself appears to be seismically transparent beneath the main PKFs, with reflectors appearing more strongly in the equivalent interval further from the main swarm. It is possible that this apparent transparency is due to reduced imaging clarity that results from the convoluted raypaths of the seismic energy through the sediments which have been faulted. This would contrast with where the PKFs are absent, and the low impedance reflectors are then imaged. Multiple sequences of layer bound faults may be speculatively interpreted within this interval below the PKFs on PSDM data (Figure 6.1A, D). This affirms that this interval is mobile, but that the transparency on the PSTM data is due to a reduction in imaging clarity due to convoluted raypaths, and not inherent seismic transparency that might be expected of a massive mobile shale unit. The mobile interval might therefore be packages of evaporites or mobile shales, but if it were evaporites high amplitude overlying and underling reflectors would be expected. The Base Miocene is a high amplitude reflector, but retains this characteristic outside the zone of the main PKFs (Figure 6.1A). Thus the decollement interval is interpreted by this study to be mobile shale, in agreement with previous work (Kosi et al., 2012).

The PKFs typically have dips c. 45° (Reiche et al., 2014a; this study) suggesting they have formed in incompetent sediments (Ghalayini et al., 2016), but despite this low angle there is very little block rotation (Figure 6.1A). To generate fault offsets without block rotation requires vertical fault block motion, which in turn requires motion on multiple faults simultaneously. This generates a space problem if there is not a mobile underling horizon, corroborating the interpretation of a mobile substrate. Analogies have been drawn between vertical block motion and the keys on a piano (Fossen, 2010), which is likely where the name ‘Piano Key Faults’ came from.

Ghalayini et al. (2016) interpret a positive correlation between the distribution of the PKFs and the thickness of the host sediments. Their data set is on the east side of the Northern Levantine Basin and here this correlation holds (Figure 6.5A). However, in the west of the Northern Levantine Basin this does not appear to be the case, as the area of the main PKFs does not match the area where the host sediments are thicker (Figure 6.5A, B). An alternative explanation for the distribution of the main PKFs is that it is regulated by the thickness and presence of the mobile interval in which the main PKFs detach. Possible controls on the occurrence of this interval are discussed subsequently.

The mobile horizon appears to be deepest under the western half of the main PKFs (Figure 6.5C), but thickest under the eastern half of the main PKFs (Figure 6.5D). Concavity of the palaeo-bathymetry and distality to a continental margin are properties that are conducive to the deposition of a thick fine-grained interval. A thick interval and fine-grain size are both favourable properties for mobility, and if the thickness of the decollement controls the occurrence of the PKFs it might therefore be assumed that offsets on the PKFs might be greater further from the continental margin. That the western half of the main PKFs is not underlain by the thickest mobile horizon might then be considered counter to this. This purports two possible explanations; partial evacuation of the mobile substrate underneath the faults of the western Northern Levantine Basin,

or an aspect of sediment provenance resulting in increased sediment deposition in the eastern Northern Levantine Basin.

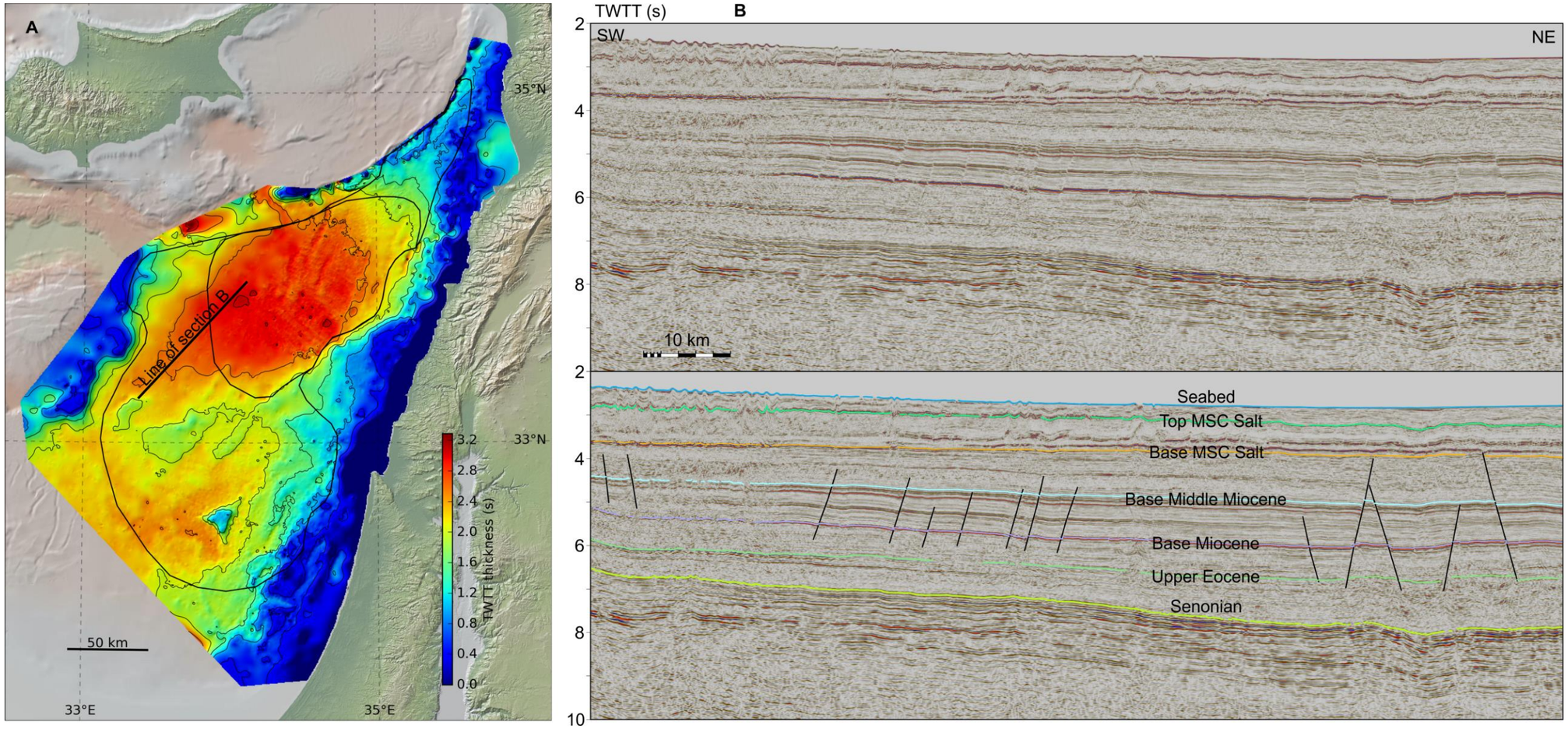

Figure 6.5- A) Upper Eocene to Base Salt Isochore, B) SW-NE striking seismic section of the western portion of the Northern Levantine Basin, C) Base Miocene surface, and D) Upper Eocene to Base Miocene Isochore with the main and peripheral PKFs outlined with the smaller and larger black lines respectively. The global relief (Ryan et al., 2009) vertical scale on the maps is shown on Figure 1.1 and the supplementary figure.

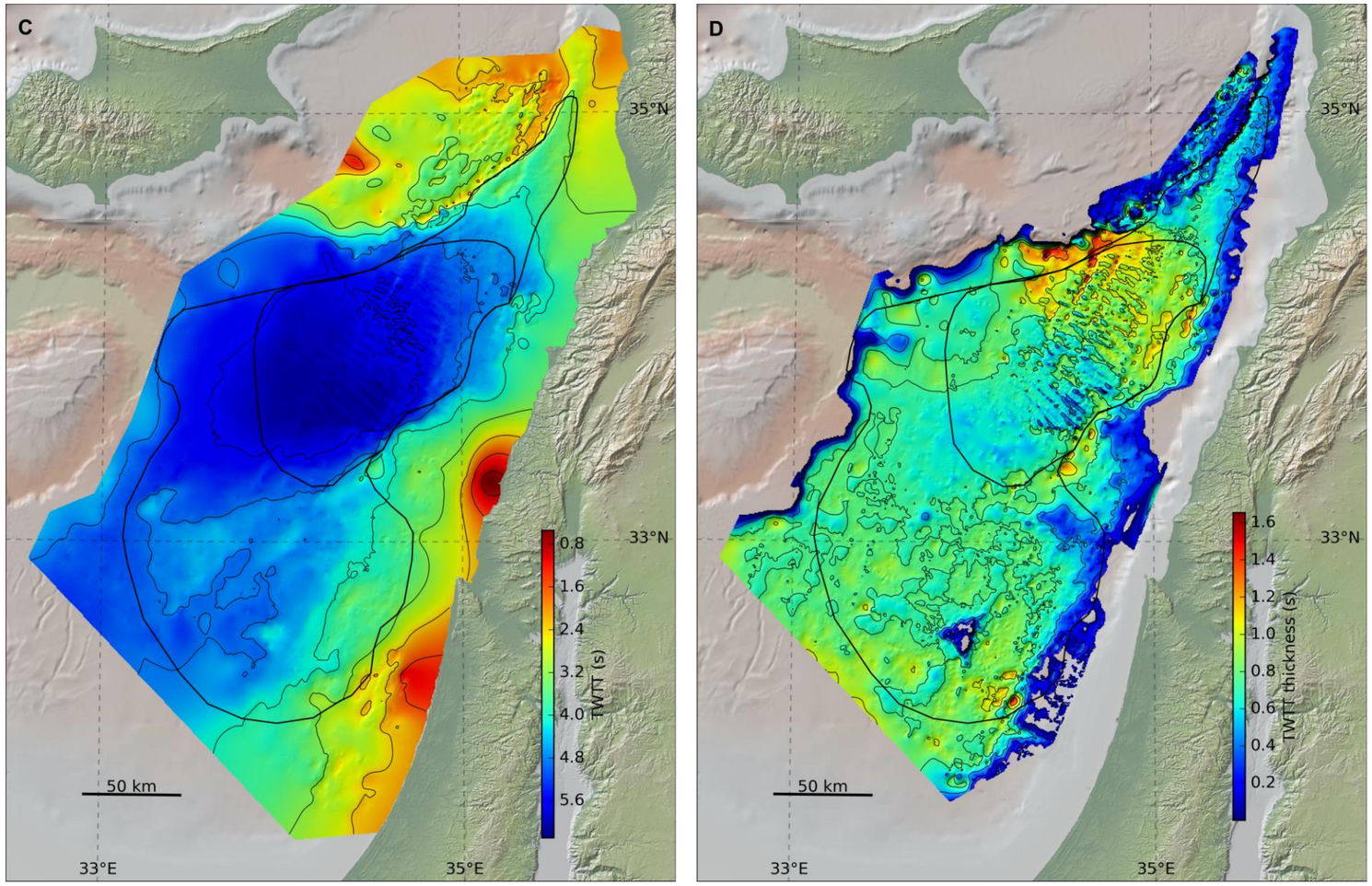
C
35°N
33°N
50 km
33°E
35°E
0.8
1.6
2.4
3.2
4.0
4.8
5.6
TWTT (s)
D
35°N
33°N
50 km
33°E
35°E
1.6
1.4
1.2
1.0
0.8
0.6
0.4
0.2
TWTT thickness (s)

It is possible that some of the proto-PKFs provided a fluid pathway for dissolution of underlying evaporites, but the underlying sediments do not fit the seismic characteristics of evaporites (Figure 6.5B). For mobile shales to be evacuated, an evacuation vector is required. Inspection of surrounding seismic data reveals only a single diapir of Oligo-Miocene age that could constitute this (Figure 3.19). The weld, and possible collapsed crest of the diapir suggests that at least some evacuation of the mobile material has occurred (Figure 3.19). The western edge of the Levantine Basin has few PKFs, if some evacuation occurred at the diapir and the occurrence of the PKFs is partly controlled by the presence of a mobile interval, then the reduced amount of material in the mobile interval may have contributed to this. However, the surrounding PKF-formation-age sediment reflectors appear subparallel in the direction of the PKFs (Figure 3.19; Figure 6.5B). This indicates that underlying lateral translation of a large amount of mobile shale has not occurred. Additionally, the PKFs cover a large area and even partial evacuation of a proportional volume of material might be expected to produce a more significant expression that a single diapir-although some might be located outside seismic coverage.

Consequently, this study favours preferential sediment deposition proximal to the Levant margin to explain that the thickest mobile interval is not in the deepest portion of the basin. A thicker interval is more likely to become mobile, even if its proximity to the Levant margin means it is prone to be coarser grained than the sediment further outboard. This assumes that the Levant margin is the sole source, as sediment may also be transported along the continental margin (Schattner and Lazar, 2016).

6.3 Perpendicular Folds

A series of folds may be observed approximately perpendicular to the PKFs in the LEB3D data (Figure 6.1C; Figure 6.6), in other seismic data immediately to the east (Figure 6.6B, G; Ghalayini et al., 2014), and to a lesser degree in seismic data to the west (Klimke and Ehrhardt, 2014). Thinning and in some cases erosion of the sediments over the folds indicates that they formed contemporaneously with the main PKFs (Figure 6.6; Ghalayini et al., 2014). Reflector terminations over the folds are uncertain and rare, however thinner sediment intervals at the anticlines between the Base MSC to Upper Miocene 2 (Figure 6.6C and D), but not between the Upper Miocene 2 to Base Middle Miocene interval (Figure 6.6E), indicates that this folding may have initiated slightly later than the PKFs. This is corroborated by compartmentalisation of some of the folds by some of the PKFs (Figure 6.6A, C, D). Other folds and inversion of the same age is also present at the Lebanese margin (Figure 6.6G, Section 3.6.2) that have been attributed to transpressive activity along the Lebanese restraining bend (Ghalayini et al., 2014). No late Miocene folding is known to this study offshore Israel, although there are large scale early to middle Miocene folds (Figure 6.6B; Section 3.6.5) that have previously been associated with the Syrian Arc II event (Gardosh et al., 2008b).

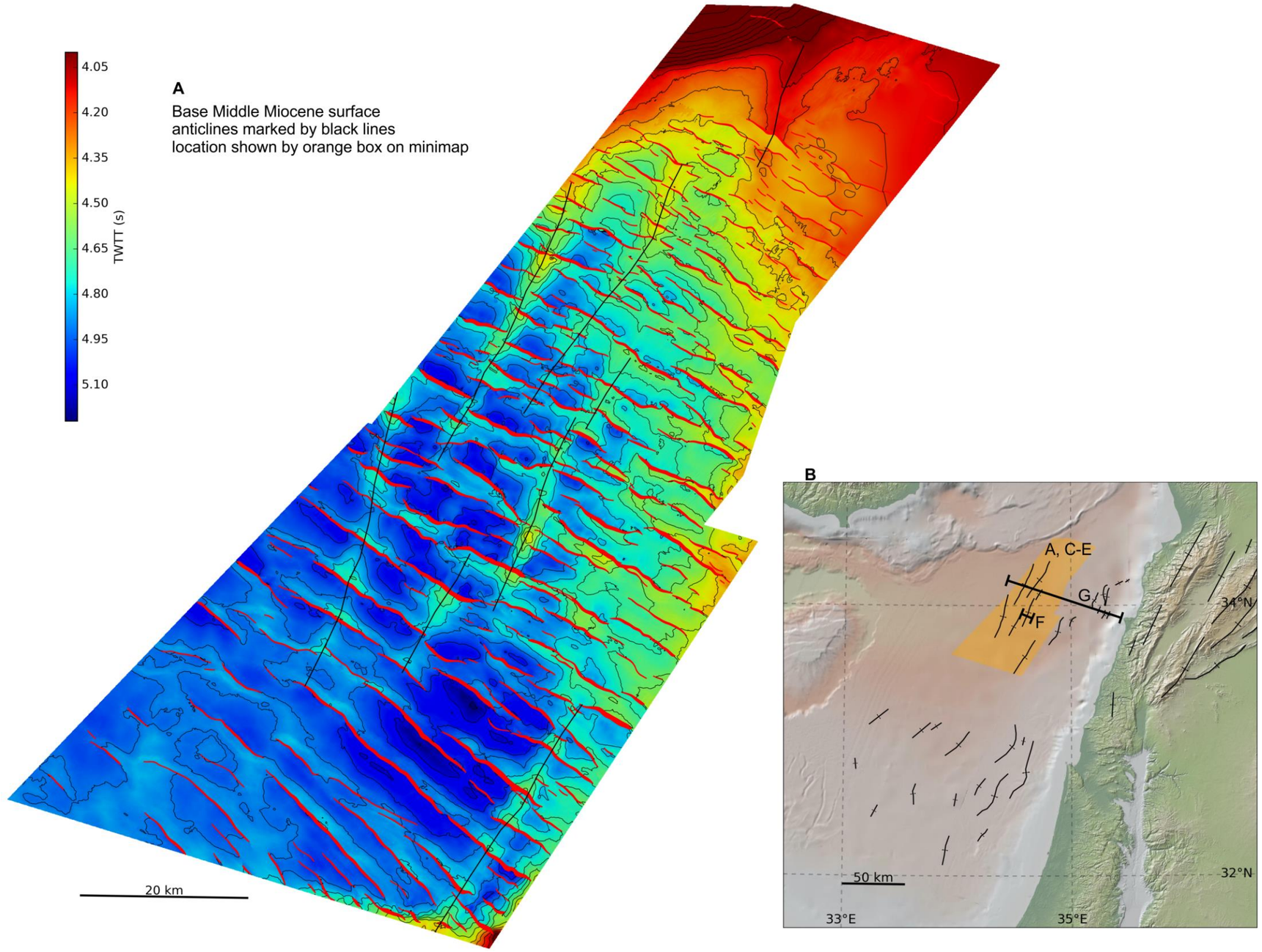

Figure 6.6-Summary of the folds perpendicular to the PKFs. A) Base Middle Miocene surface in time with anticlines marked; B) Map showing the locations of the other subfigures and late and early Miocene folds (Gardosh et al., 2008b; Ghalayini et al., 2014; Walley, 1998); Isopachs in time between the Base MSC, Upper Miocene 1 (C), Upper Miocene 2 (D) and Base Middle Miocene (E) horizons; F) seismic line across the steepest fold with the best examples of speculative reflector terminations marked; G) seismic line across the folds perpendicular to the PKFs and inverted normal faults adjacent to the Levantine margin. The global relief (Ryan et al., 2009) vertical scale on the minimap is shown on Figure 1.1 and the supplementary figure.

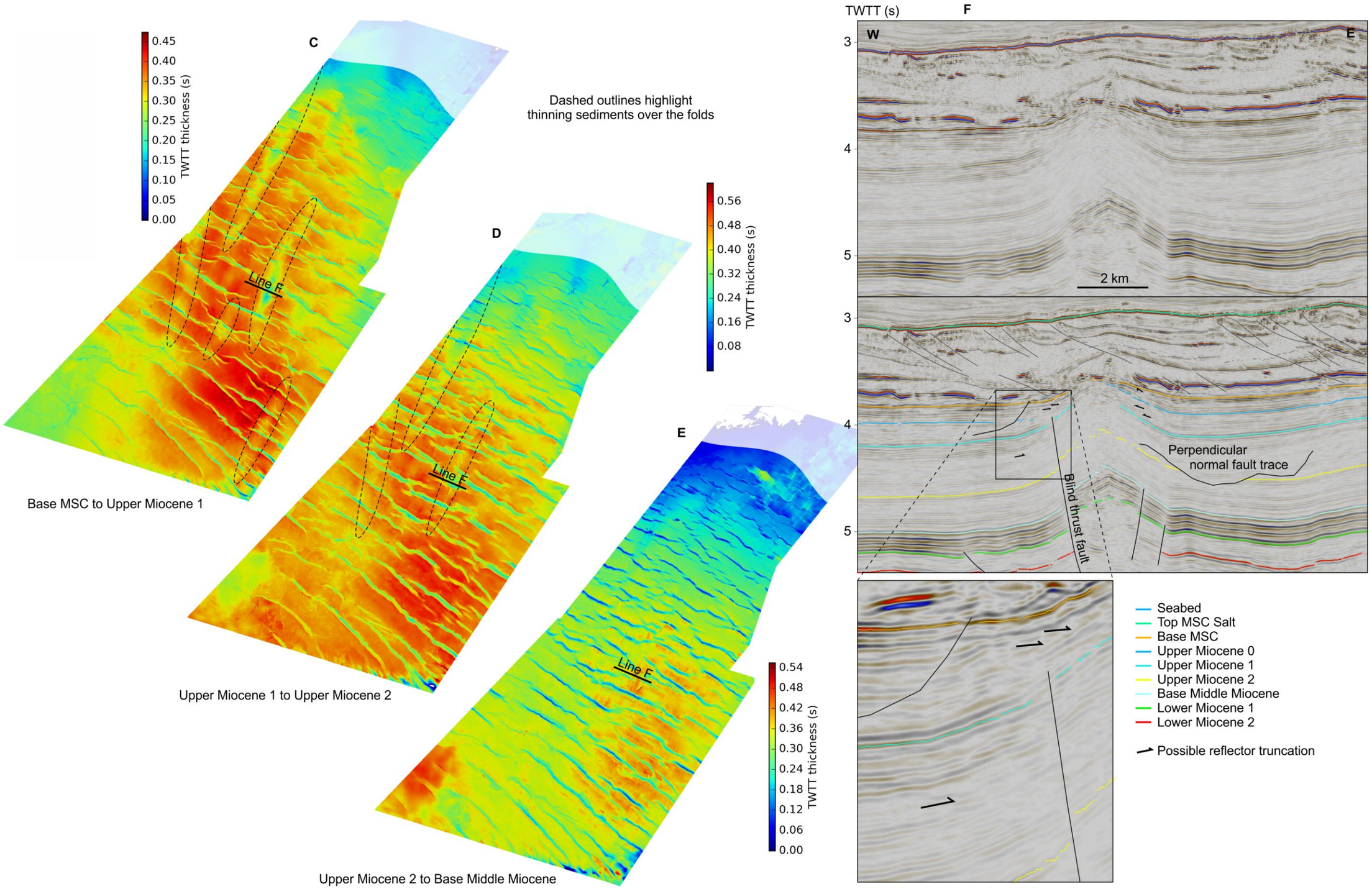
C
0.45
0.40
0.35
0.30
0.25
0.20
0.15
0.10
0.05
0.00
TWTT thickness (s)
Line F
Base MSC to Upper Miocene 1
D
Dashed outlines highlight
thinning sediments over the folds
Line F
Upper Miocene 1 to Upper Miocene 2
E
0.56
0.48
0.40
0.32
0.24
0.16
0.08
TWTT thickness (s)
Line F
0.54
0.48
0.42
0.36
0.30
0.24
0.18
0.12
0.06
0.00
TWTT thickness (s)
Upper Miocene 2 to Base Middle Miocene
TWTT (s)
F
W
E
3
4
5
2 km
3
4
5
Perpendicular
normal fault trace
Blind thrust fault
1
1
1
1
Seabed
Top MSC Salt
Base MSC
Upper Miocene 0
Upper Miocene 1
Upper Miocene 2
Base Middle Miocene
Lower Miocene 1
Lower Miocene 2
Possible reflector truncation

TWTT (s)

G

2
3
4
5
6
7
8

WNW

10 km

ESE

main PKF perpendicular folds

Inverted normal faults

Levantine Margin

?

?

Seabed
Top MSC
Base MSC
Base Middle Miocene
Base Miocene
Upper Eocene
Senonian Unconformity

The folds in the interior of the Northern Levantine Basin appear broadly symmetrical, and some blind shortcut thrusts are apparent in the flanks of the folds (Figure 6.6G). They appear to be cored by the same detachment interval as the PKFs (Figure 6.6G). These characteristics suggest they are not formed by inversion of underlying normal faults, and instead have formed in response to buckling of the sediments above the Oligocene mobile interval. This contrasts with the folds offshore Lebanon and Israel which are asymmetrical, suggesting they are inversion related thrust folds (Figure 6.6G; Figure 3.14B).

Some workers have interpreted both the NNE-SSW striking folds offshore Lebanon and those covered by the LEB3D volume as positive flower structures above strike-slip folds (Chbat et al., 2017). The folds within the LEB3D volume do not correlate to any offsets along the perpendicular faults (Figure 6.6A), despite their contemporaneous timing (Figure 6.6C-E), so they do not accommodate a component of transform motion. There may be a component of transform motion across the folds adjacent to the Lebanese continental margin, however primarily inversion can adequately explain the observed features, which concurs with earlier studies (Ghalayini et al., 2016, 2014).

A possible link between the PKFs and perpendicular folds has not been explored in published literature, however their contemporaneous formation suggests that they are key in understanding the PKFs. Possible mechanisms behind these perpendicular folds are explored in Section 6.6.4.

6.4 Numerical Analysis

Detailed analysis of the fault geometries has been cited as key in investigation of the genesis of the PKFs (Ghalayini et al., 2014). Interpretations of their seismic expression were made (Chapter 3) to facilitate the quantitative analysis presented in this section. Fault analysis software was written for purpose in Python (a coding language; Python Software Foundation, https://www.python.org) to generate this analysis from the interpretations. For those PKFs imaged on the 2D seismic data the only metric that could be accurately resolved was throw at the location of the seismic line, as this is independent of the lateral geometry of the fault. For those faults imaged by the 3D data many more metrics could be resolved. Because of this difference the following analysis focuses mainly on the portion of the main PKFs imaged by the LEB3D seismic volume. The interpreted faults were processed so each fault-horizon intersect is recorded as two lines of points in 3D space describing the footwall and hangingwall fault-horizon contact. Once the data were in this format various fault metrics could be calculated arithmetically. Calculable metrics include dip, azimuth, heave, throw, displacement and length. These metrics are spatially constrained and can be extracted, for example, as a fault average, fully spatially variant or as an average of a sub area.

Some numerical anaysis was undertaken by Ghalayini et al. (2016), however their analysis is restricted to the relationships between the displacement, length and timing for a smaller group of faults than what is used in this study. Thus, the location awareness of this analaysis and the amount of faults analysed is unprecidented for the PKFs.

6.4.1 Depth conversion

The LEB3D seismic volume is PSTM seismic data, and to correctly calculate fault metrics with a vertical distance component the fault analysis inputs need to be in depth. The initial depth conversion, referred to as the 'standard' depth conversion (shown on Figure 6.7 by the dashed lines), was achieved using a best estimate time-depth relationship (dashed line on Figure 6.8). This time-depth relationship was calculated for each contrasting stratigraphic package using Equation 6.1 and is based on typical linear compaction trends for the clastic sediments (k = 0.1) and typical fixed velocities for the salt and seawater (k = 0). The Spectrum EMED-00-047 PSDM seismic line provided calibration for this depth conversion, as in a previous study of the area (Reiche et al., 2014a). The PSDM line provided the best available constraint as it was depth migrated with stacking velocities which this study had no access to, and no alternative well data were available. Thus, this 'standard' depth conversion is as accurate as may be reasonably achieved given the limited data.

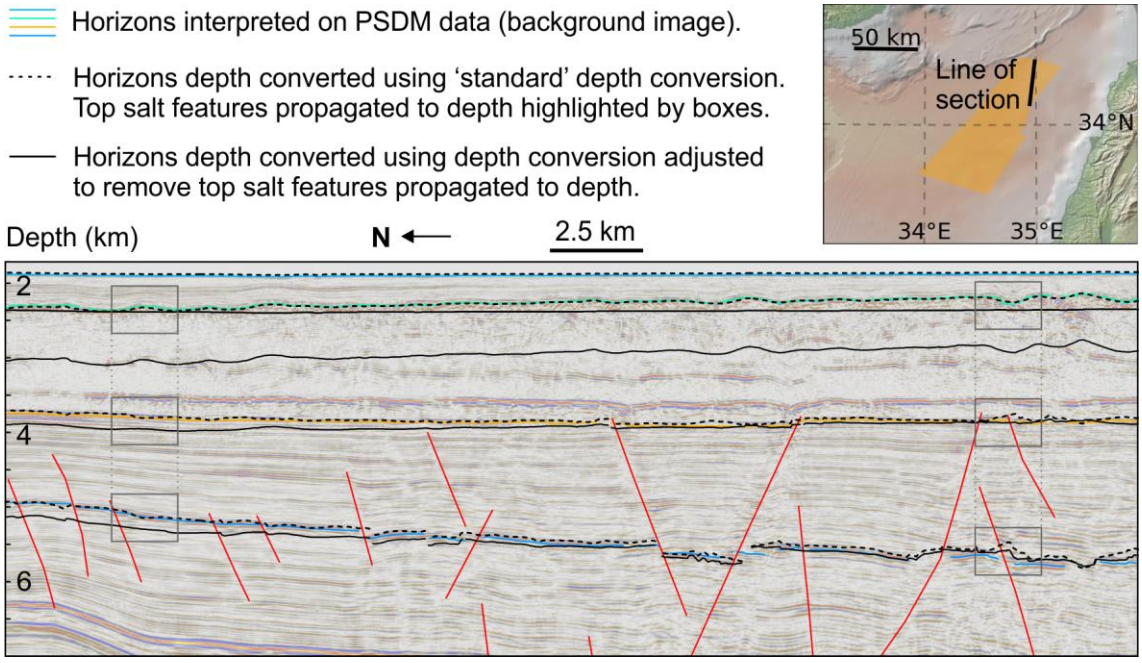

Figure 6.7-Section showing comparison of the different depth converted horizons. An example of the velocity profiles used in the depth conversions is shown in Figure 6.8. See text for discussion.

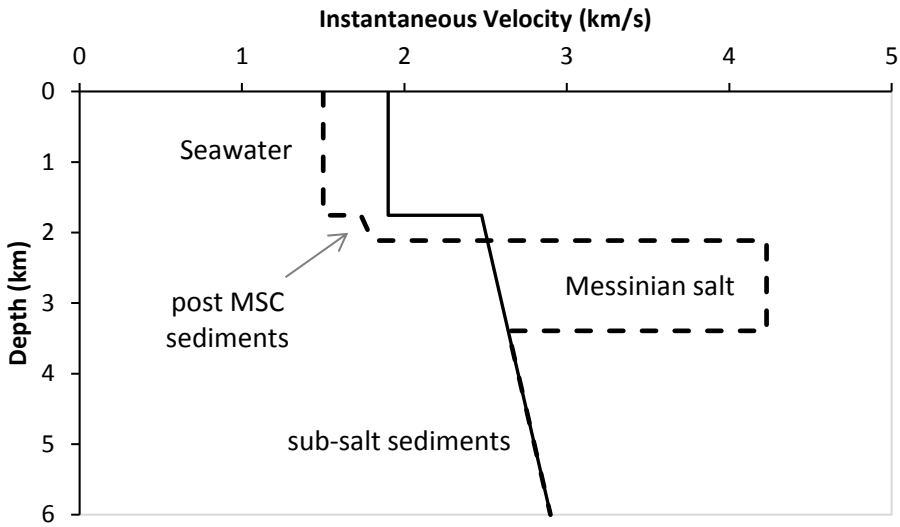

Figure 6.8-Example velocity profiles used in the two depth conversions. The dashed and non-dashed lines correspond to the depth conversions of the dashed and non-dashed black horizons on Figure 6.7. See text for discussion.

$$V = V_0 + k \cdot Z \qquad 6.1$$

V =instantaneous velocity at a point in an interval
V_0=velocity of stratigraphy at the datum (sea-level)
k =rate of change in velocity with increasing depth
Z=depth of the point

In the time domain and on the PSDM line, the Base MSC horizon is sub-planar where it is not faulted (Figure 6.7). The 'standard' depth conversion of the horizon sequence results in propagation of the folds in the top MSC surface through to the depth converted sub-salt horizons (Figure 6.7). Therefore, this 'standard' depth conversion does not produce depth converted horizons that will provide accurate horizons for the fault analysis. To achieve this another depth conversion was required that maintained the sub-planarity of the sub-salt horizons as on the PSDM seismic. The artificial propagation of the top MSC undulations occurs because during depth conversion of a point only the stratigraphic thicknesses directly above that point is taken into consideration. The anomalously high seismic velocity of the MSC salt means that small variations in its thickness in time result in large variations in its thickness in depth, with consequent impact on all horizons buried below the salt (Section 3.2.5). These variations do not appear in time as the source-receiver offset during acquisition of the seismic averages out the stratigraphic thickness variations of the overlying sediments, and the larger the distance to the thickness variations the wider the average is taken. During depth migration the source-receiver offsets are also taken into account so these variations also do not appear (Figure 6.7).

To eliminate these artificial horizon deformations, another depth conversion was accomplished by extrapolating the time-depth relationship of the sub-salt horizons to the seabed, removing the influence of the shape of the top and bottom of the salt body. On its own this change results in the PKF interval becoming artificially elevated, from the overall reduction in overlying velocities, and artificially thin, as the reduced depth means the sediments are simulated as being less

compressed and therefore as having reduced velocities. To tackle these errors, the velocity of the seawater was modelled as having a velocity of 1900 m/s. This increased velocity 'pushes' the depth converted Seabed and Top Salt reflectors artificially deep, but results in the Base Salt reflector being within <100 m of the 'standard' depth conversion. An exception to this is the high in the NW of the LEB3D survey (Figure 6.7), but as the PKFs are absent under the high (Figure 6.1C) this is inconsequential. As the Base salt reflector is in approximately the correct elevation and retains its correct geometry, and the underlying PKF interval is assigned 'standard' velocity values, this depth conversion permits analysis of the PKFs in depth without depth migration of the whole LEB3D volume.

Using these values depth conversion of the PKFs interpretations in the LEB3D volume was achieved using Equation 6.2 (Slotnick, 1936):

$$Z = \frac{V_0}{k} \cdot \left(e^{(k \cdot t)} - 1\right) \qquad 6.2$$

t=one-way travel time to the point

6.4.2 Orientation

The Upper Miocene 2 horizon is the youngest pre-kinematic surface that was interpreted. This means it is the most clearly imaged horizon that has experienced the full extension affecting the main PKFs. Consequently, it was selected as the exemplar horizon with which to demonstrate the orientation of the faults. The faults have a highly consistent orientation (Figure 6.9) but some change in strike from south to north may be observed (Figure 6.2). Figure 6.10 confirms this with the slope on the best fit line of orientation plotted against latitude, showing that the faults may be observed to fan slightly with a more EW strike to the NNE.

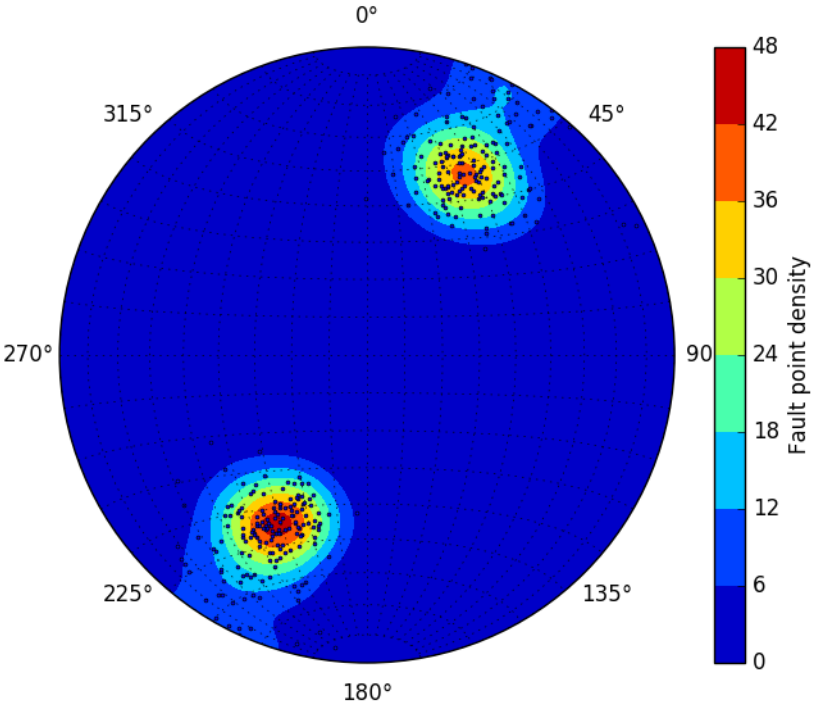

Figure 6.9-Contoured stereonet showing the tight distributions of fault orientations for the Upper Miocene 2 horizon.

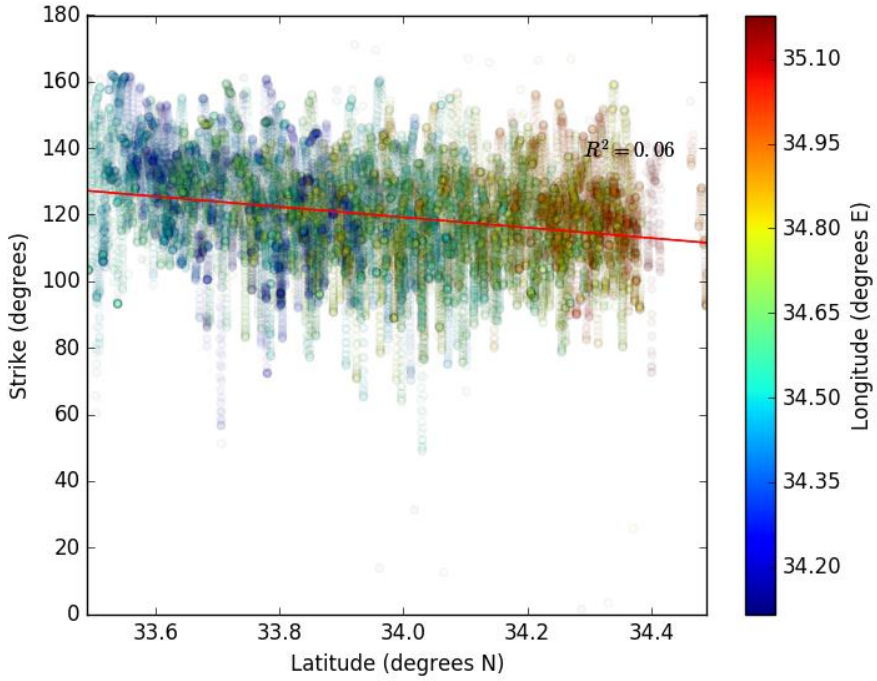

Figure 6.10-Graph showing strike of the PKF data points at the Upper Miocene 2 horizon plotted against Latitude. The red line indicates the trend of the data.

6.4.3 Displacement Trends

The Displacement-Length scatter plot shown on Figure 6.11 shows displacement length profiles that trend with a power constant of c. 0.6. During normal extensional fault growth this power constant would typically be between 1 and 1.5 (see refs. within Walsh et al., 2002). The lower power constant may indicate a lot of fault linkage has occurred (Fossen, 2010, p. 180), however as the PKFs are layer bound this may perturb the displacement length profiles from 'typical' trends (e.g. Cowie and Scholz, 1992; Walsh et al., 2002) as the displacements are restricted. This limits the applicability of typical displacement-length analyses. The average fault displacement profile is symmetrical (Figure 6.12). This indicates the locus of extension has not shifted laterally during the evolution of the faults. The 'shoulders' that may be observed on Figure 6.12 are the remnant off-centre peaks that remain after two faults have linked. These will be present in faults that are newly linked so their maximum displacement is not yet centred in the middle of the fault.

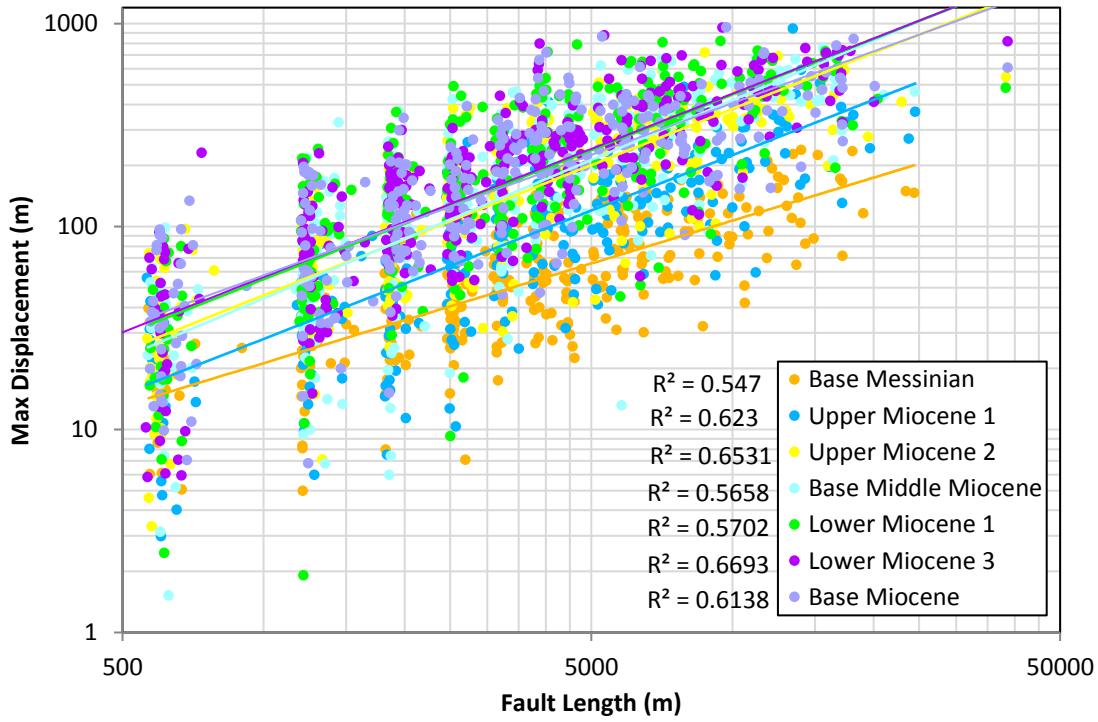

Figure 6.11-Log-log displacement-length plot of the faults in the different horizons.

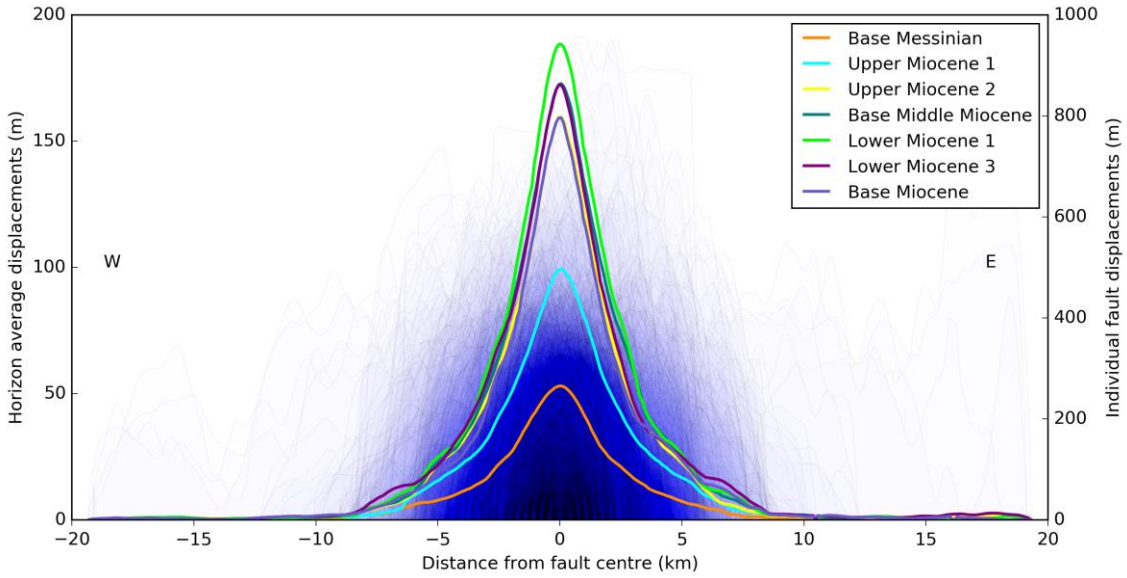

Figure 6.12-Graph showing horizon average and individual centred displacement-length profiles of the PKFs.

On Figure 6.11 the vertically elongate clusters of points at short fault lengths is due to the spacing of lines between which the faults were picked. This is an example of how picking faults at set seismic line intervals results in an artificial reduction in the length of the picked faults. No conclusions drawn from this analysis relies on variations in fault lengths at this resolution, so these artificial reductions in fault length are inconsequential.

Figure 6.13 shows that there is more displacement accumulated on the faults dipping out of the centre of the fault swarm. It also demonstrates that more of the younger displacement is accumulated to the south of the fault swarm. As this difference in displacement is not present on

the earlier horizons it follows that the older displacement must have accumulated to the north of the current centre of the fault swarm.

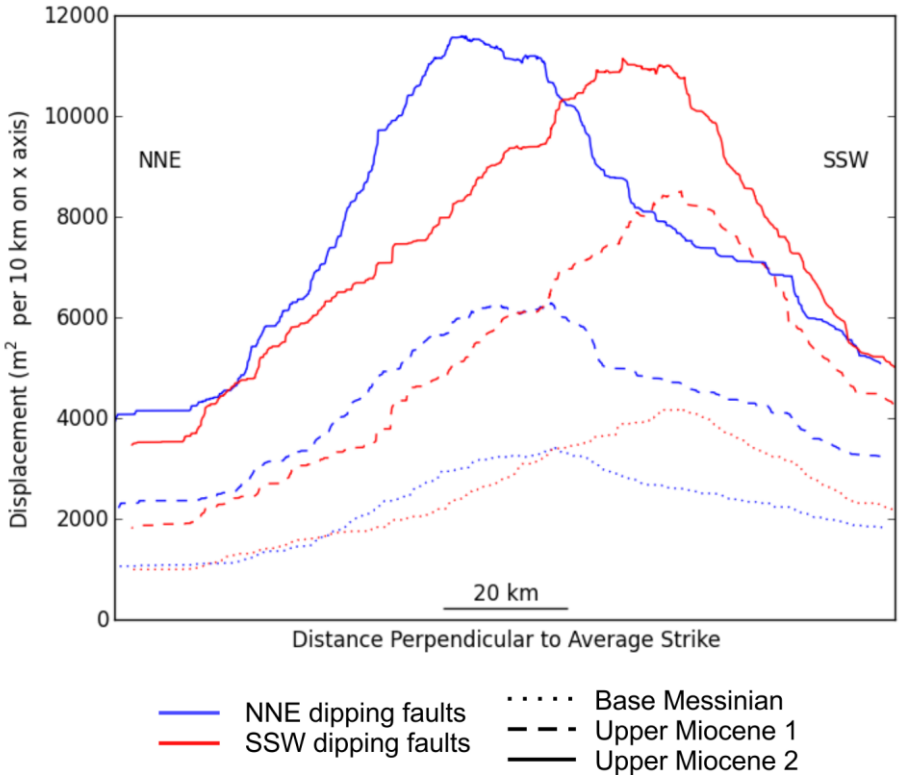

Figure 6.13-Graph showing a moving subtotal of displacement across the dip of the fault swarm. As the Upper Miocene 2 is the youngest pre-kinematic horizon it was selected as a representative horizon for this piece of analysis.

6.4.4 Timing

The initiation of the formation of the main PKFs has previously been interpreted as the start of the mid Miocene (16 Ma) on the basis of seismic interpretation (Reiche et al., 2014a), and the start of the Miocene on the basis of numerical analysis of seismic interpretations (Ghalayini et al., 2016). This section serves to further investigate this.

Only highly uncertain reflector terminations (i.e. syn-kinematic thinning of sediment packages) are observable in the blocks between faults. This could indicate low extension rates, and/or low sedimentation rates, however the fault block motion at the PKFs is largely vertical (Section 6.2) which would also result in limited reflector terminations. As on average the main PKFs dip out of the fault swarm (Figure 6.13), and the locus of these is in the centre of the Northern Levantine Basin (Figure 6.6A-D), much of the package thickening that is present in the fault blocks (Figure 6.1; Figure 6.14) may be attributed at least in part to increased sediment deposition in the centre of the basin. Where the sediment package thickness is more constant between blocks, and where faults dip into the basin, some slight thickening is consistently apparent in an upper Miocene interval (top set of arrows on Figure 6.14). In some rare locations there are examples of early Miocene sediment packages exhibiting syn-kinematic thickening (Figure 6.14B).

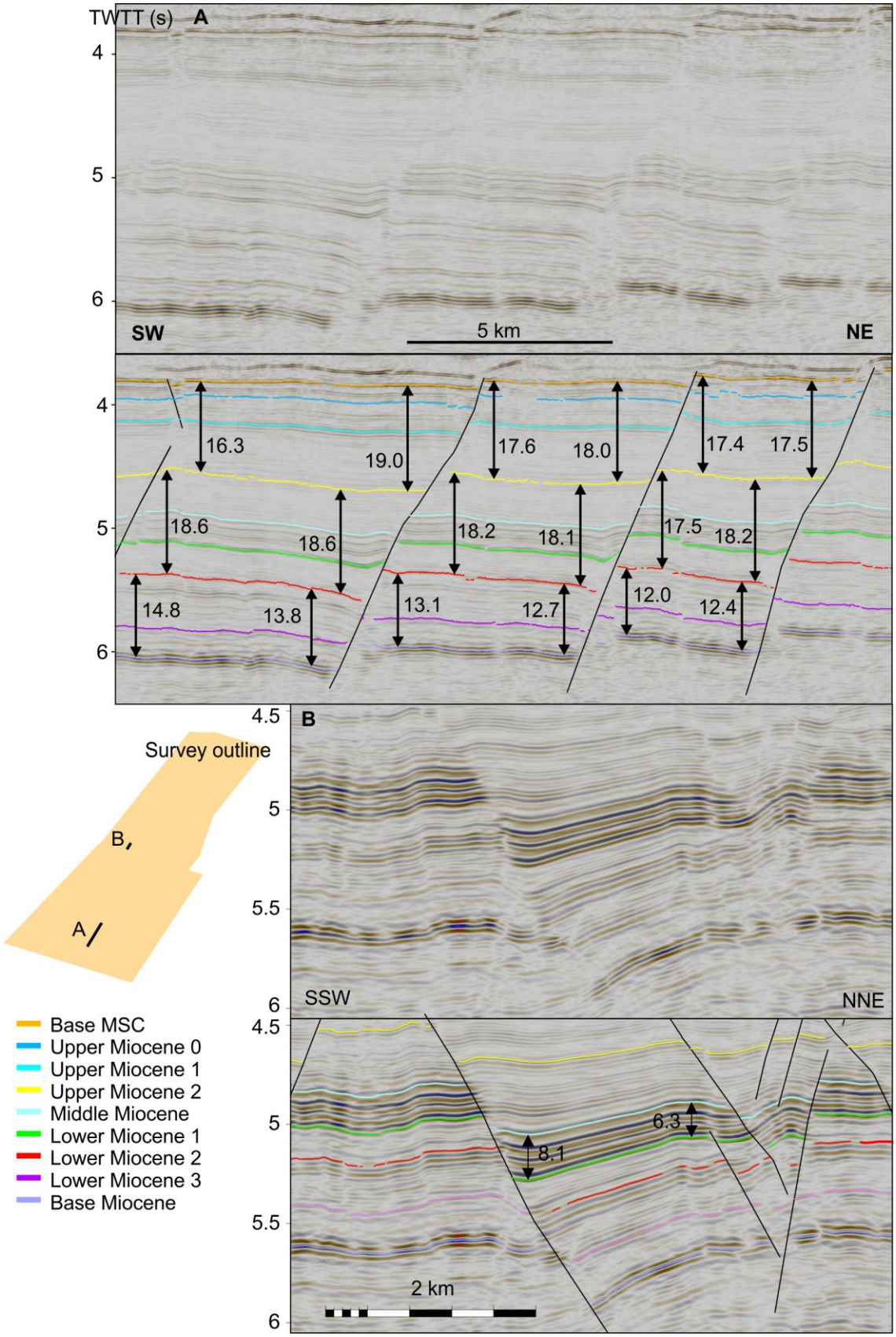

Figure 6.14-Seismic line displaying slight thickening of stratigraphic packages within fault blocks. The numbers indicate lengths (the units are arbitrary as the focus is relative lengths) measured vertically. On line A this does not take into account the block rotation, but for the upper interval the footwall side of the fault blocks has experienced more rotation, and as the arrows in the hangingwall side of the blocks are still longer the same relative conclusions may be drawn. On line B measurement points are selected where the horizon is horizontal so this is not an issue.

Isochore maps provide uncertain constraints on timing, due to the density of the faults, minor thickening in the fault blocks, and the lateral thickness variations of the sedimentary sequences.

The average displacement of the faults increases significantly between the Base MSC and the Upper Miocene 2 horizons and peaks in the lower Miocene 1 horizon (Figure 6.15; Figure 5.15; Figure 5.16). This is a good indicator that it was between these intervals that most displacement on the faults occurred. This trend could also appear if the total displacement of the different horizons was equal but there were more, smaller, faults on the younger horizons, however as the number of faults reduces in the youngest horizons this is not the case. Instead this reduction in the number of faults offsetting the younger horizons backs up the timing interpretation.

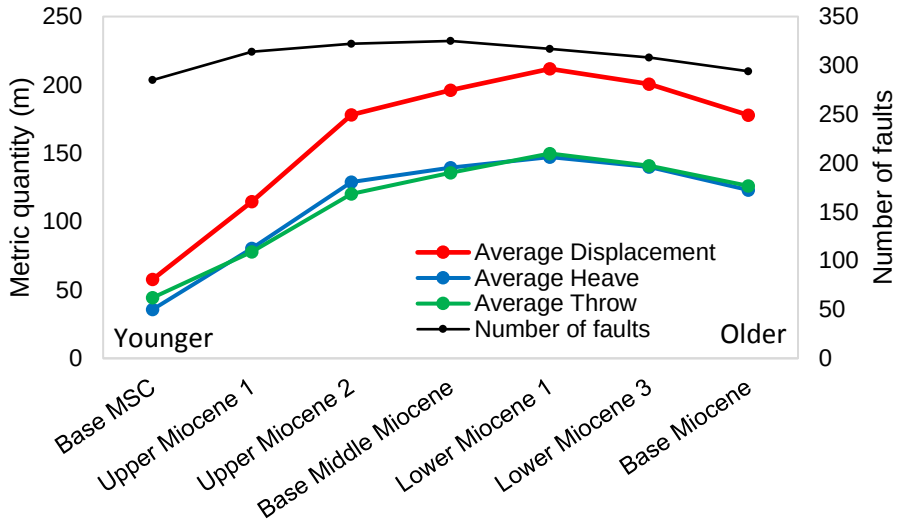

Figure 6.15-Graph showing the changes of the average fault metrics for horizons interpreted in the LEB3D volume.

The lack of reflector terminations and package thickening in the sys-sedimentary interval is likely to be partly due to the relatively high sedimentation rates during steady fault movement and/or primarily vertical (as opposed to rotational) block movement. Thus, the observations of this section are non-conclusive but appear to corroborate the timing of Reiche et al. (2014) who suggest the main PKFs started forming around the base of the middle Miocene. The following subsection provides a more detailed numerical analysis of the timing of the PKFs, in addition to the evolution of the extension location. This updated timing analysis, in conjunction with early Miocene PKFs in the southern Levantine Basin (Section 6.6.3) that we hypothesise share the same genesis (Section 6.6.1), corroborates the earlier timing of Ghalayini et al. (2016).

6.4.5 Beta Factors

'Beta factor' (β) is the term commonly used to denote and quantify the stretching an area has experienced and qualify the amount of extensional strain (stretched length / original length) along a section. Calculating the Beta factor for a given geological cross section results in a quantitative measure of the extension on that section. As this measure is quantitative, this permits more precise comparison with other sections, allowing confident observation of variations that otherwise may be too small to observe.

Figure 6.16A shows a plot of Beta values calculated across the Upper Miocene 2 horizon perpendicular to the PKFs. Figure 6.16F shows an example section showing how the beta values were calculated. For the beta plots in this document a ‘window’ of 30 km (orientated along the dip of the fault swarm) was used for which the stretched and original lengths were measured. Along dip fault spacing of the main PKFs is typically 2-5 km; consequently, a 30 km ‘window’ captures the extension of 6-15 faults (as in Figure 6.16A). This is large enough that the calculated betas are not overly affected by individual faults (as in Figure 6.16C) but not so many that there are not lateral variations in the calculated betas representative of the fault swarm (as in Figure 6.16D). The spacing between the points where beta values where calculated was 500 m, as a much smaller spacing meant along strike variations resulted in a noisy result (as in Figure 6.16E) and a much larger spacing did not resolve some of the trends in the beta values (as in Figure 6.16F).

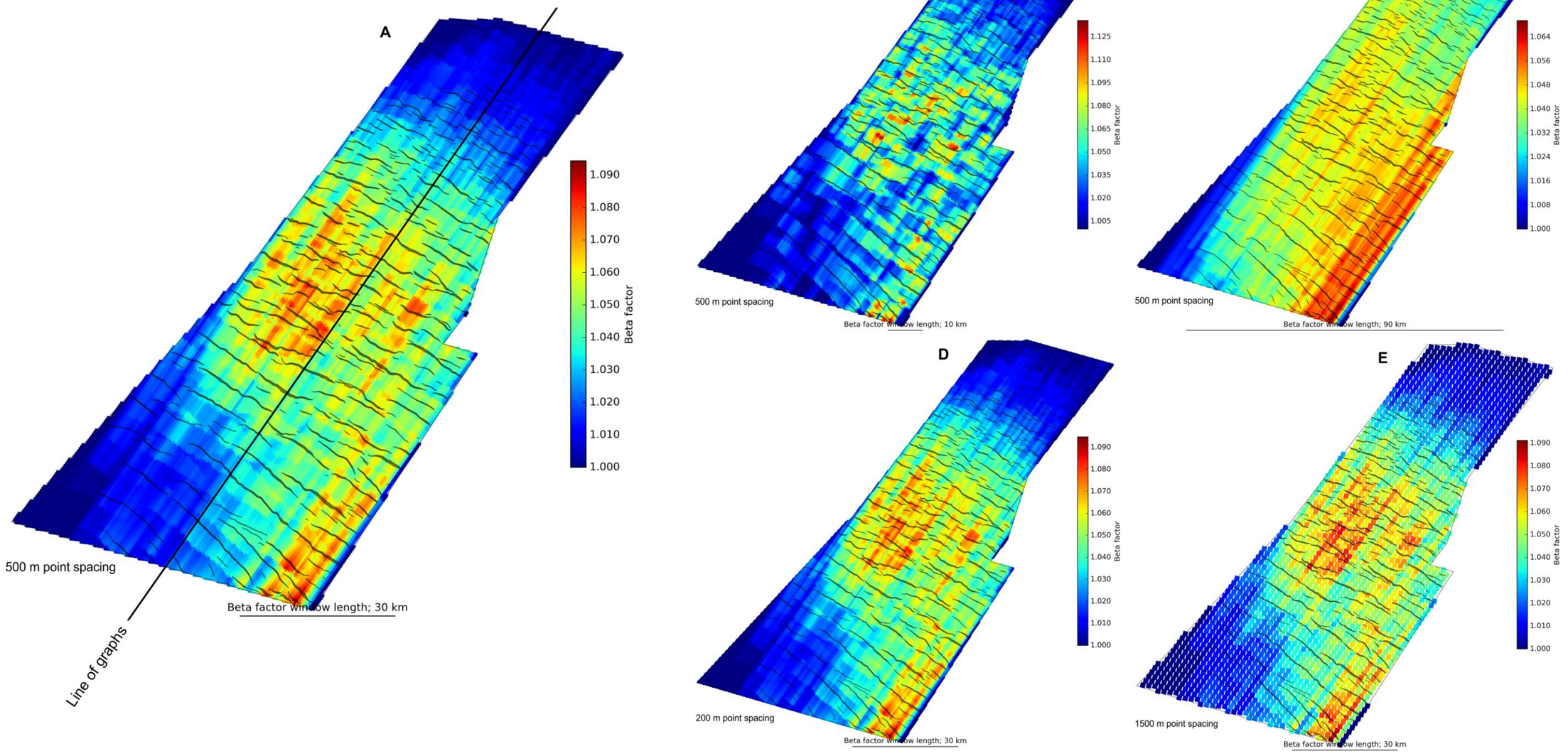

Figure 6.16-(A-E) Beta plots of three different window lengths and three different beta point spacings for the Upper Miocene 2 Horizon, to illustrate why the chosen values were used. The traces of the faults at this horizon are overlaid in black. (B) The graphs demonstrate how the beta values relate to the surface and fault data, shown in the parallel seismic line. The bold yellow line is the horizon for which the graphs and beta plots were calculated. See Figure 6.1A for a key for the seismic line.

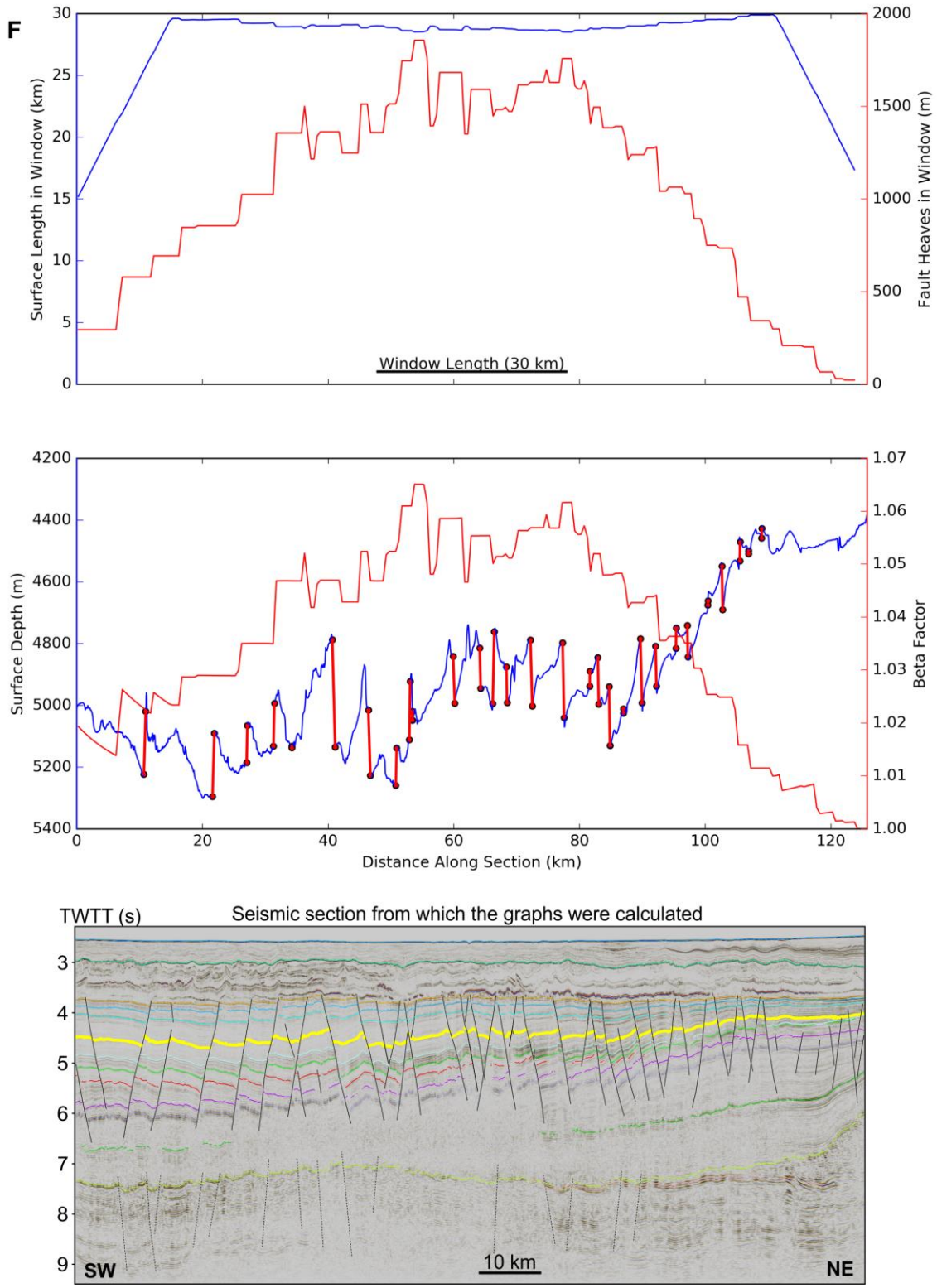

By cumulatively subtracting the extension observable on surfaces younger than a subject surface (Equation 6.3) it is possible to resolve the extension attributable to the time interval between a subject horizon and a younger horizon.

$$\beta_{t_n \rightarrow t_{n-1}} = \beta_{t_n} - \beta_{t_{n-1} \rightarrow t_{n-2}} + 1 \qquad 6.3$$

t_n=a point in time where the subscript denotes age (corresponds to the interpreted surfaces).

Where there are reductions in extension in progressively lower horizons, this produces 'interval' beta values that are <1. These reduced amounts of observed fault extension can be attributed to ductile deformation (Ghalayini et al., 2016) and typical fault offset patterns (Fossen, 2010). Typical fault offset patterns have reduced observed extension both up and down stratigraphy either side of a horizon with the maximum displacement, if the fault forms in a pre-existing sediment sequence (i.e. pre-kinematic sediment deposition), due to incremental sub-seismic resolution accommodation of the extension (Fossen, 2010). By capping the lower limits of the plotted beta values at 1, and subtracting the amount that was capped from the beta values from progressively older stratigraphy, it is possible to produce plots that represent the observed increases in beta value down through the stratigraphy. This technique was applied to seven intervals within the LEB3D volume to produce Figure 6.17.

These typical fault offset patterns mean that the beta factor plot method of analysis detailed above would indicate an erroneously early timing of fault movement. Three pieces of evidence suggest this is not the case for the PKFs:

- The faults are layer bound, meaning that the ductile layers above and below could more readily accommodate displacement than sub-seismic fractures.
- Progressively more extension may be confidently observed almost all the way down through the faulted sequence (Figure 6.17A-F).
- Some speculative syn-kinematic wedges may be observed in the upper portion of the faulted sequence (Figure 6.14A), matching the timing indicated by the beta plots.

Figure 6.17 indicates minor extension occurred during the lower Miocene, corroborating the PKF timing suggested by Ghalayini (2016), before a main pulse of extension in the middle Miocene, after which it and tailed off with the locus of extension moving ~30 km south until cessation of faulting during the MSC. The localisation and relatively reduced strength of the signal of extension prior to the middle Miocene (Figure 6.17D-G) contrasts with that after the middle Miocene (Figure 6.17A-C). This indicates the pre-middle Miocene signal of extension could be noise generated by inaccuracies in seismic imaging and interpretation. However, many of the PKFs in the southern Levantine Basin formed in the early Miocene, and earlier speculative syn-kinematic wedges are present in the Northern Levantine Basin (Figure 6.14B), so it is likely the earlier beta signal is due to some earlier faulting within the main PKFs.

Figure 6.17 also demonstrates that the signal of extension locus migration in Figure 6.13 is amplified by the south corner fault. This fault has had steady movement since the middle Miocene, in contrast to the reduction in fault movement of the main body of faults since the middle Miocene.

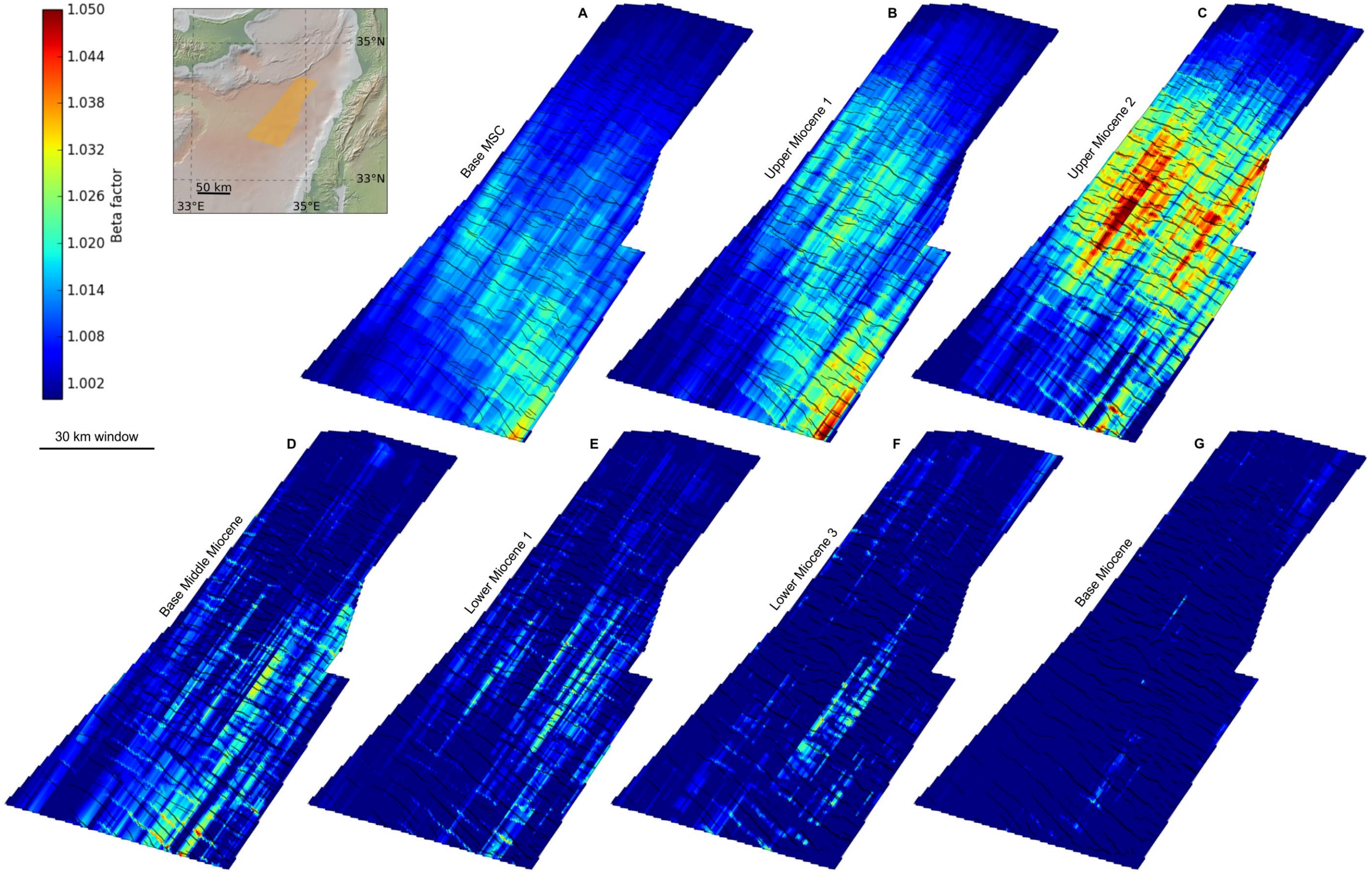

Figure 6.17-Beta factors attributable to the interval between each horizon and the one stratigraphically overlying. See the text for discussion on the production of these plots. The global relief (Ryan et al., 2009) vertical scale on the minimap is shown on Figure 1.1 and the supplementary figure.

6.4.6 Analysis Evaluation

The Miocene interval deformed by the PKFs is clearly imaged by the LEB3D volume. The horizons interpreted to investigate the PKFs may be traced between the PKFS, and the horizons selected for interpreting the PKFs are continuous over the area of the LEB3D volume deformed by the PKFs. Consequently, only negligible errors are likely to have been introduced into this analysis during the interpretation of the horizons.

The faults were interpreted by hand, and where the exact location of the fault plane is ambiguous (e.g. Figure 6.14) there will be some interpretation errors introduced (± <30 m lateral). The horizons between the faults are generally sub-planar, this means that a slight offset of the fault interpretation will generally have a very small effect on the displacement of the interpreted fault, reducing the potential for errors. As the analysis uses multiple faults, and these interpretation errors are random errors, a normally distributed error pattern (i.e. an even amount of positive and negative errors) means these errors will be further reduced. If the fault interpretation has resulted in a systematic errors, then these errors will be consistent for both the footwall and hangingwall fault/horizon intersections. This will further reduce the effect of the errors for the analyses. The change in the location of the faults (± <30 m) will be negligible on the scale of the faults (c. 10's of km).

The analyses presented here are only used quantitatively in relation to each other, except for the extension estimate used in Section 6.6.5. However, this extension estimate could be double or half its value and the same conclusions could still be confidently drawn.

As errors in the depth conversion will be consistent across the depth converted interpretations, any errors in the depth conversion will not have had any effect on the conclusions drawn by this study. For example, depth converting the interpretations assuming V0 and k values of 2300 m/s and 0.1 respectively results in a mean and max change in beta value of 1.6E-5 and 7.6E-5 respectively (for the Upper Miocene 2 Horizon, using the same 30 km window).

6.5 Hypotheses Testing

This study has considered many possibilities for the genesis of the PKFs; these are outlined in the subsections below. Some were discounted by earlier studies (e.g. Reiche et al., 2014a) and others at early stages of this investigation based on observations of the seismic data, but all are discussed here for comprehensive consideration of the PKFs. None of the hypothesis in Sections 6.5.1 and 6.5.2 explain the folding that has occurred contemporaneously and perpendicularly to the PKFs.

6.5.1 Thin-skinned Local Extension

Evacuation of a mobile substrate (discussed in Section 6.2.3)

The main PKFs are underlain by an interval interpreted as mobile shale (Section 6.2.3). Evacuation of a mobile substrate could cause faulting (Figure 6.18), however a single diapir is the only vector for the evacuation of shale known to this study, and it is a minor feature compared to

the scale of evacuation required to explain the formation of all the PKFs (Section 3.6.2). Additionally, no evidence of significant lateral transport of underlying shale is observed proximal to the diapir (Section 3.6.2). The seismic characteristics of the interval is non-indicative of an evaporite that could have dissolved and used the PKFs as an expulsion vector (Figure 6.1A). Crucially, evacuation of a mobile substrate cannot explain the consistent orientation of the faults (Section 6.4.2).

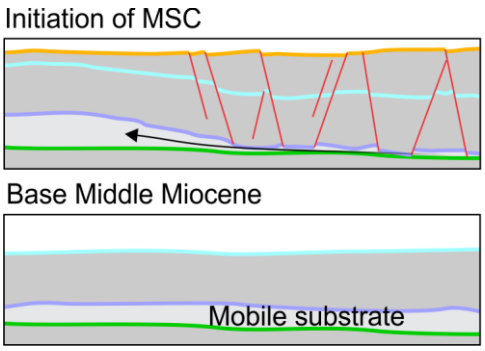

Figure 6.18-Sketch demonstrating the concept of evacuation of a mobile substrate as an explanation for the formation of the PKFs.

Polygonal faulting

Polygonal faulting is the name given to swarms of layer bound normal faults with stochastic variations in orientation (Cartwright et al., 2003; Ghalayini et al., 2016). They can form due to various mechanisms including volumetric contraction, compaction, diagenetic shear failure and pressure variations (Cartwright et al., 2003; Ghalayini et al., 2016). Ghalayini et al. (2016) note an area of the main PKFs with low throws offshore Lebanon that display stochastic geometries (Figure 6.19A), although this contrasts with the majority of the PKFs (Figure 6.9). The south-west corner of the seismic volume available to this study also images low throw faults with orientations more stochastic than the majority of the PKFs (Figure 6.19B). Ghalayini et al. (2016) suggest these stochastic orientations are evidence that polygonal faulting mechanism formed all the PKFs. They accredit the consistent orientation of the majority of the PKFs (Section 6.4.2) to an overlying perpendicular compressive stress field, a hypothesis is discussed further in Section 6.5.3. The amount of displacement on the PKFs is significantly greater than that typically observed on polygonal faults, and if the PKFs were formed via the same mechanisms as polygonal faults the PKFs would be the largest example of this phenomenon documented so far (Ghalayini et al., 2016).

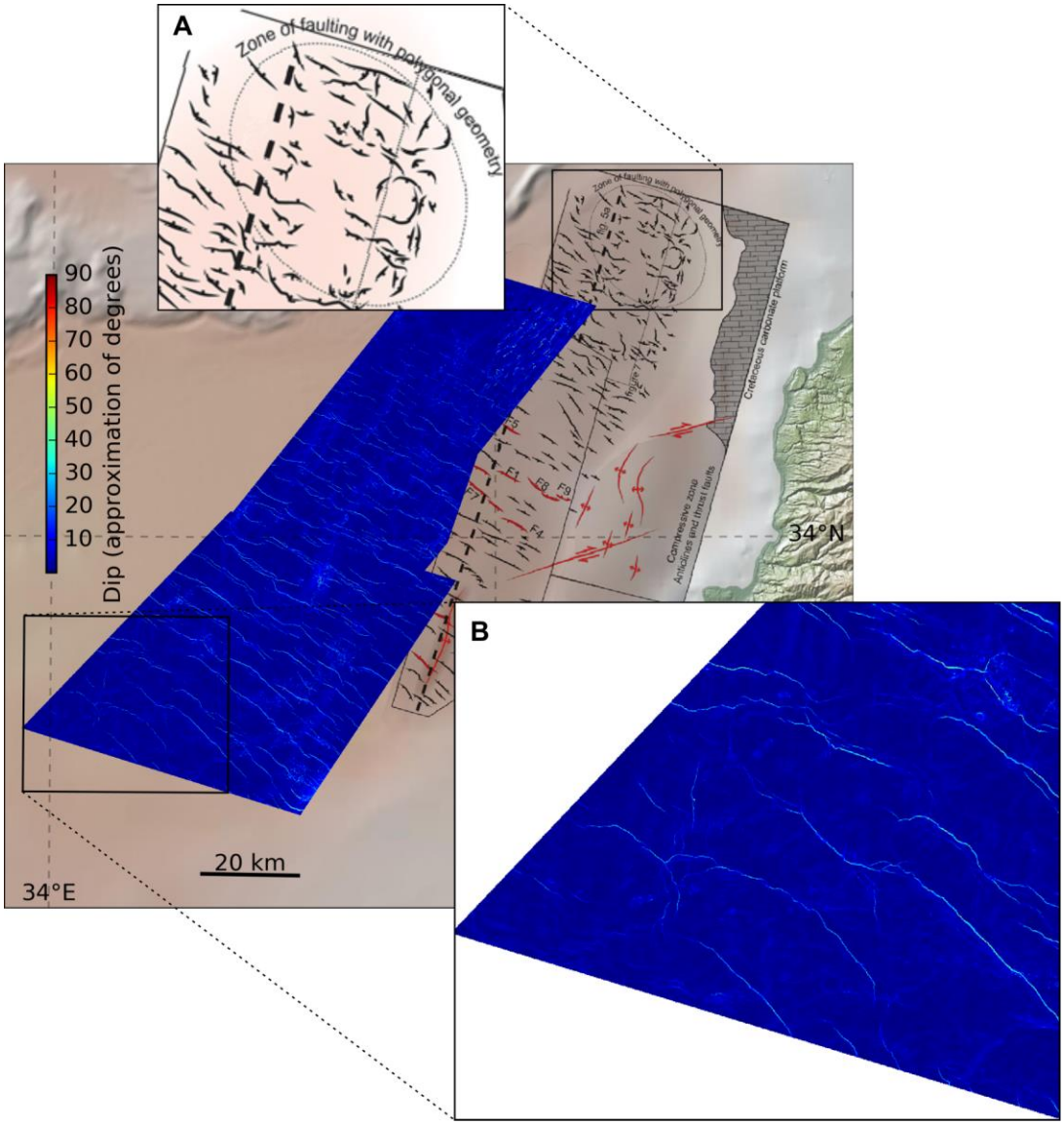

Figure 6.19-Map showing locations where the PKFs display more stochastic orientations than the majority of the faults swarm. A is adapted from Ghalayini et al. (2016) and B is the dip attribute of the Base MSC surface. The global relief (Ryan et al., 2009) vertical scale is shown on Figure 1.1 and the supplementary figure.

MSC water unloading

Kosi et al. (2012) suggest the formation of the PKFs was triggered by a pressure drop during MSC sea level drawdown. However seismic data reveal the main PKFs initiated in the middle Miocene (Reiche et al., 2014a; this study), as opposed to the late Miocene when the MSC occurred (Section 2.5.4). Additionally, displacements measuring in the hundreds of metres could be considered to be rheologically infeasible as a consequence of relaxation of <3 km of rock, and this would also not explain the consistent orientation of the PKFs.

Down-slope migration

Reiche et al. (2014) suggest that the PKFs could be a result of gravity driven failure down a slope which was produced or enhanced by a combination of convergence across the Cyprus Arc (Hall et al., 2005b), basin subsidence (Hawie et al., 2013), Lebanese continental margin uplift (Hawie et al., 2013) and LSZ stress release amplifying topography offshore Israel (Steinberg et al., 2014).

Some analogies for this exist. The Canyonlands of Utah, US, are a fault swarm with analogous geometries to the PKFs, and an analogous underlying mobile horizon (Kosi et al., 2012). The western central North Sea also has documented examples of gravity-driven thin-skinned extension above mobile evaporites (Bishop et al., 1995).

Gravity driven failure requires translation of the fault blocks to produce extension. Accordingly, this requires matching space accommodation at the base of the slope; for example in the Canyonlands the erosion of the Colorado River provides the 'gap' that the translated rocks can move into (Kosi et al., 2012). In the Levantine basin there is not an equivalent gap, so one might expect compressional features downslope. There is a hiatus in the compression affecting the Cyprus Arc during the period when the PKFs formed (Chapter 4), but crucially the Cyprus Arc is upslope of the PKFs (Figure 6.1D).

Figure 6.20 shows Base Miocene and Upper Eocene surfaces in time and depth converted using the 'accurate' depth conversion in Section 6.4.1. It may be observed that these surfaces have no consistent slope which might lend a gravity driven explanation for the formation of the PKFs. Additionally, gravity driven extension does not aid explanation of the peripheral PKFs. These arguments indicate that downslope translation cannot explain the genesis of the PKFs.

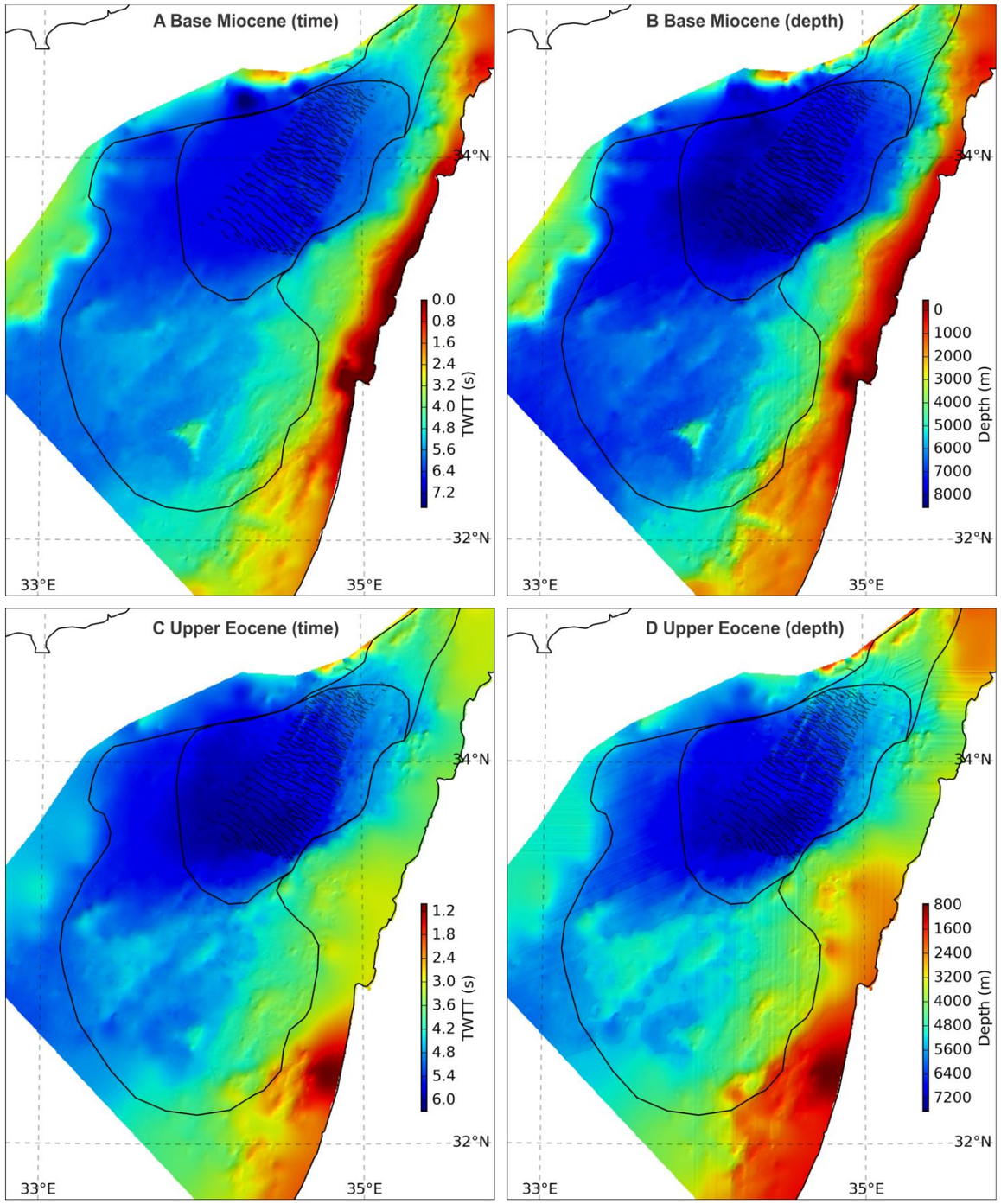

Figure 6.20-Depth converted surfaces demonstrating the lack of slope beneath the PKFs.

6.5.2 Subduction-Related Processes

Flexural bend/Outer Arc Extension

Extensional faulting proximal to convergent plate boundaries has been related to “flexural extension where bending due to subduction creates extensional forces within the upper and compressional forces within the lower part of the downgoing plate” (Bradley and Kidd, 1991; Hirano et al., 2006; quote: Reiche et al., 2014a; Zhou et al., 2015), as illustrated in Figure 6.21 Subduction has been inactive on the Eastern Cyprus Arc since the Cretaceous (Section 5.8.1), indicating this explanation does not apply to the PKFs. It is possible that significant underthrusting might achieve the same effect, however the seismic data suggest that significant underthrusting has not occurred adjacent to the main PKFs (Figure 5.27). Additionally this explanation would not provide a mechanism for the southerly peripheral PKFs, the locus of normal faulting would be expected to be adjacent to the subduction zone (Zhou et al., 2015)-which is not the case (Section 6.4.5).

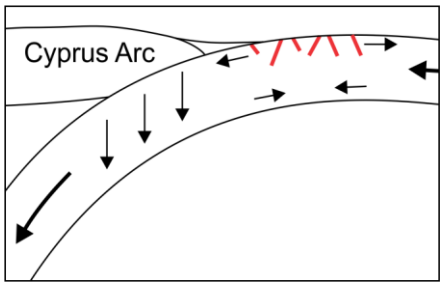

Figure 6.21-Sketch cross-section illustrating how bending of the lithosphere beneath the Cyprus Arc could lead to extension in the crust adjacent to the Cyprus Arc.

Slab pull

Slab pull of a subducting plate subjects the downgoing plate to significant tension (Zhou et al., 2015). This could result in subduction proximal extension (Figure 6.22). As with the flexural bend mechanism the lack of contemporaneous subduction discounts this potential mechanism (Chapter 4).

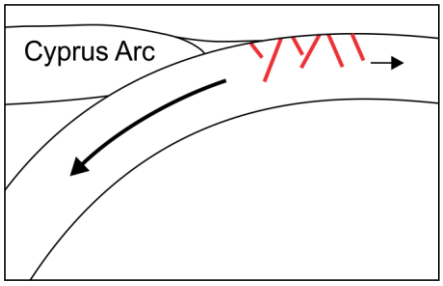

Figure 6.22-Sketch cross-section illustrating how slab pull from the subduction of lithosphere beneath the Cyprus Arc could lead to extension in the crust adjacent to the Cyprus Arc.

Slab break off

If slab break off occurred beneath the Cyprus Arc and the underlying lithosphere rebounded then this could form extension in the sediments overlying the rebounding plate, adjacent to the overriding plate (Figure 6.23; Fossen, 2010, sec. 17.11) Tomographic evidence suggests that at

least part of the subducted slab beneath Cyprus is still attached (Figure 5.29). This reduces confidence in this potential mechanism but does not discount it. If the PKFs did form from slab break off then an explanation would be required as to the delay between the cessation of subduction in the latest Cretaceous, and the proposed slab break off in the late Miocene. Additionally, no evidence is observed of the detachment this would require between the subduction decollement and interval in which the PKFs decol. This is discussed in Section 6.6.8.

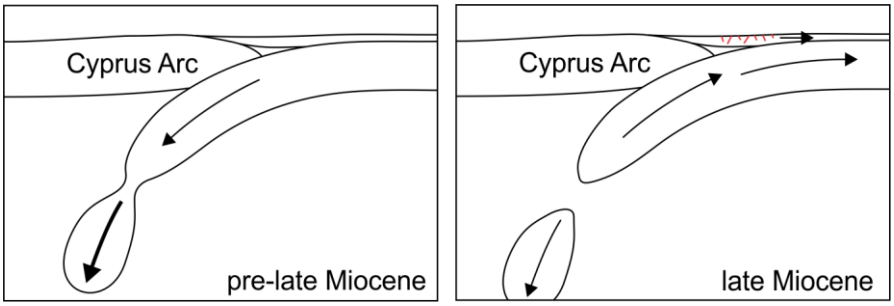

Figure 6.23-Sketch cross-section illustrating how slab break off beneath the Cyprus Arc could lead to extension in the crust adjacent to the Cyprus Arc.

6.5.3 Stress Field Anomalies

Compression causing perpendicular extension

Deforming a plastic volume by compression in one orientation can cause extension of the volume of the volume in a perpendicular orientation (Figure 6.24). The folds perpendicular to the PKFs (Figure 6.6) formed contemporaneously with the PKFs (Section 6.3), supporting this hypothesis as a mechanism for the formation of the PKFs (Ghalayini et al., 2016). However, this requires space for the volume to extend into (i.e. σ3 lateral as opposed to vertical), and in the context of geology and the PKFs the space would have to have been generated by contemporaneous extension, which would exclude the perpendicular compression as the main factor behind formation of any normal faults (Figure 6.24).

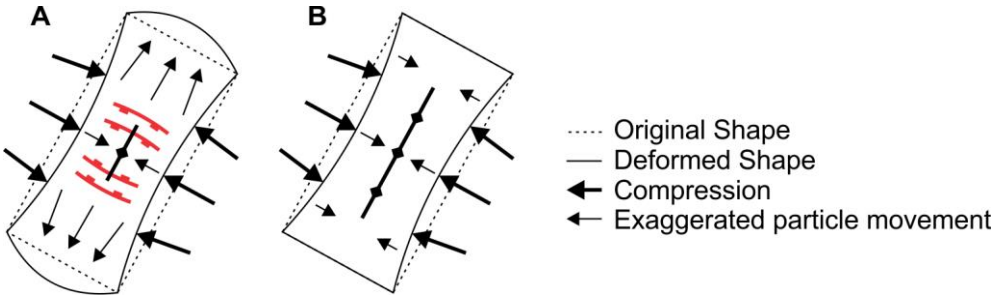

Figure 6.24-Sketch showing how compression in one orientation can cause A) parallel compression and perpendicular extension given free block movement and B) only parallel compression given constrained block movement.

Perpendicular compression orientating deformation associated with volume reduction

Ghalayini et al. (2016) suggest that this could have occurred due to volume reduction as with polygonal faults (Section 6.5.1). However, four arguments may be posed against this, Ghalayini et al. (2016) themselves acknowledge the first two:

- In the majority of cases where isotropic horizontal stress fields result in a more consistent orientation of polygonal faults, it is structure-proximal faults that become orientated, and more basin-ward faults retain classic polygonal (stochastic) orientations (Ghalayini et al., 2016). This is the opposite of what is observed for many of the PKFs (Figure 6.19), although some very minor faults immediately adjacent to leading thrusts of the Latakia Ridge appear perpendicular to the thrusts (Khairallah et al., 2017).
- The basin scale highly consistent strikes of the majority of the PKFs (Figure 6.9) are more consistent than any other documented examples of stress-field-orientated polygonal faults (Ghalayini et al., 2016).
- The distribution of the faults appears to be controlled by changes in the decollement interval, as opposed to changes in the faulted interval that might be linked to lithology (Section 6.2.3).

And the main argument against this hypothesis:

- That if volume reduction had occurred to an extent that produces normal faults, then it would also have accommodated the shortening that has produced the perpendicular folds (Section 6.3).

Despite these discrepancies this hypothesis cannot be entirely discredited as a secondary mechanism, as some minor offset faults with polygonal geometries do exist in the Northern Levantine Basin (Figure 6.19).

Transtensional pull-apart Basin

The synchronous timing of the PKF formation and movement on the proximal LSZ (Section 2.5.3) introduces the possibility of the PKF being transtensional and would also explain the contemporaneous perpendicular folds (Figure 6.6; Section 6.3). However, the strain ellipse that would fit the orientation of the PKFs and perpendicular folds does not match the orientation of the LSZ (Figure 5.18).

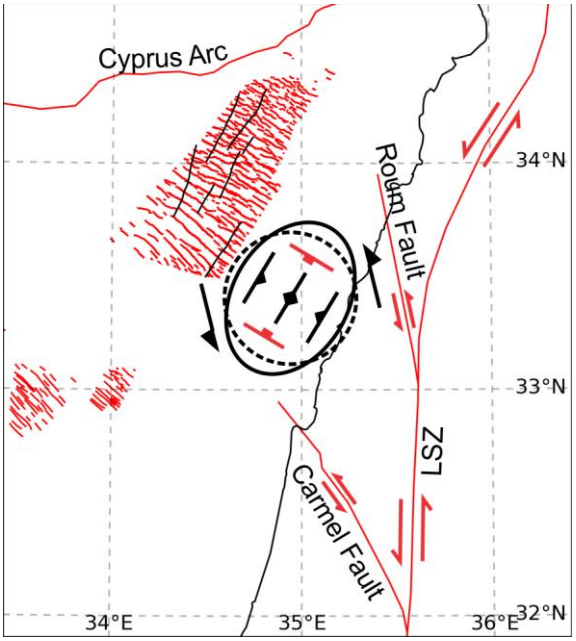

Figure 6.25-Figure showing the orientation of the Wilcox et al. (1973) type strain ellipse orientated to the PKFs and perpendicular folds relative to the orientation of the LSZ and the Carmel and Roum offshoots.

There is an unexplained >25 km discrepancy between the offsets of the southern and northern portions of the LSZ that has not been resolved, and an offshore continuation of the LSZ has been posed as a possible explanation (Section 2.6.8). The Carmel and Roum faults, offshoots of the LSZ hypothesised to continue offshore, do match the orientation of the PKF strain ellipse (Figure 6.25). However, no offshore continuation of these faults has been observed (Ghalayini et al., 2014; this study). To form faults with offsets the size of the main PKFs via transtension might be expected to require large strike slip faults to facilitate transfer of displacement from the LSZ to the main PKFs. Thus the PKFs may not be considered to be part of a pull-apart basin, but this study does favour a link between the shear system of the LSZ and the PKFs, discussed in Section 6.6.1

Extension across the Cyprus Arc

A hiatus in compression is observed at the Cyprus Arc during the late Miocene and Pliocene (Chapter 4). If the plate configuration at the time could generate a complete reduction in compression across the Cyprus Arc during a period of ongoing convergence between the African and Eurasian Plates, it is feasible that this could also produce a period of extension. This hypothesis is explored in more detail in the following section.

6.6 Discussion

In summary, the main PKFs are a set of normal faults that are layer-bound between MSC and Oligocene mobile intervals. The faults formed from sometime in the late Miocene until shortly after the initiation of the MSC. A set of perpendicular folds formed contemporaneously, possibly with a slightly later initiation. The periphery PKFs are a set of normal faults around the edge of the main PKFs with significantly smaller offsets. Periphery PKFs in the Southern Levantine Basin (southern periphery PKFs) appear to decol in the Eocene interval (as opposed to the shallower Oligocene

interval in the Northern Levantine Basin) and some do not offset the horizons of the upper Miocene. This suggests the southern periphery PKFs have formed earlier than the main PKFs, and is discussed in Section 6.6.2.

The following hypothesis is the only explanation known to this study that can explain these observations of the PKFs that cannot be strongly argued against using the evidence presented in the previous section.

6.6.1 Hypothesis

Chapter 4 concluded that there was a hiatus in compression along the eastern limb of the Cyprus Arc between the late Miocene to the latest Messinian or Pliocene. This is contemporaneous with the formation of the PKFs (Section 6.4.4) and introduces the possibility of regional extension at this time, including across the previously convergent tectonic boundary of the Cyprus Arc. To understand how this may have occurred a detailed understanding of the relative plate movements is required.

To recap from Section 2.5.3, the formation of the PKFs in the late Miocene initiated when the rifting of the Gulf of Suez had ceased, but the Red Sea spreading was ongoing, with a transfer of the strain onto the proto-LSZ at the Gulf of Aqaba. This allowed the Arabian Plate to move north faster than the Sinai Plate, with the differential movement facilitated by the propagation of the proto-LSZ to the Bitlis Suture. Published estimates document 60 km of mid to late Miocene sinistral slip on the LSZ south of the Palmyrides and latest Miocene to Pliocene sinistral slip partitioned into ~45 km along the Dead Sea segment and ~20-25 km along the Ghab Fault (Section 2.5.3). This means that the PKFs formed contemporaneously with northward propagation of the LSZ. Depending on the precise timing of the formation of the LSZ relative to the PKFs, two potential mechanisms can explain their formation from shear processes related to the LSZ.

(1) During the formation of the LSZ, a shear system would have existed around the propagating tip of the proto-LSZ. On one side of the strike-slip fault this results in compressional forces parallel to the shear system, and on the other extensional. The sinistral offset of the broadly NS LSZ is mechanically compatible with extension to the west of the LSZ (and compression to the east). Thus extensional faults may form during fault-propagation of the LSZ. This is referred to in subsequent sub-sections as the 'shear mechanism'.

    Two issues exist if this mechanism is used to explain the formation of all the PKFs. Firstly, some of the PKFs are large distances from the LSZ; for example, some of those southern peripheral PKFs are c. 150 km from the LSZ. Secondly, the orientation of the PKFs has only minor variability north to south, despite the change in orientation of the LSZ at the Palmyrides. The second of these issues could be explained if the PKFs formed during a short-lived episode, however the beta factor plots (Section 6.4.5) indicate this is not the case. It is possible that the relatively small magnitude of later extension means they inherit the previous trends instead of forming new ones.

(2) Despite ongoing convergence between the African, Sinai and Arabian Plates with Eurasia, the Arabian Plate (Figure 6.26A) has been moving north at a faster rate than the Sinai Plate

(Figure 6.26B) since the cessation of rifting at the Gulf of Suez, Red Sea spreading and the formation of the LSZ. During the tectonic indentation the Anatolian Plate (Figure 2.25), before its westward tectonic escape, and given sufficient coupling between the southeast edge of the Anatolian Plate (Figure 6.26C) and Sinai Plates (Figure 6.26B), net divergence could have resulted between the two (Figure 6.26). Thus, extension could have occurred across the eastern limb of the Cyprus Arc after the formation of the LSZ. This is referred to in the subsequent sections as the 'tectonic dragging mechanism'. In effect, it is an application of the 1st proposed mechanism on a larger scale and spanning the Anatolian Plate boundary. Key to the valid additional consideration for this hypothesis is the documented episode of early Miocene extension observed in the Misis Mountains (Figure 2.24; Robertson et al., 2004).

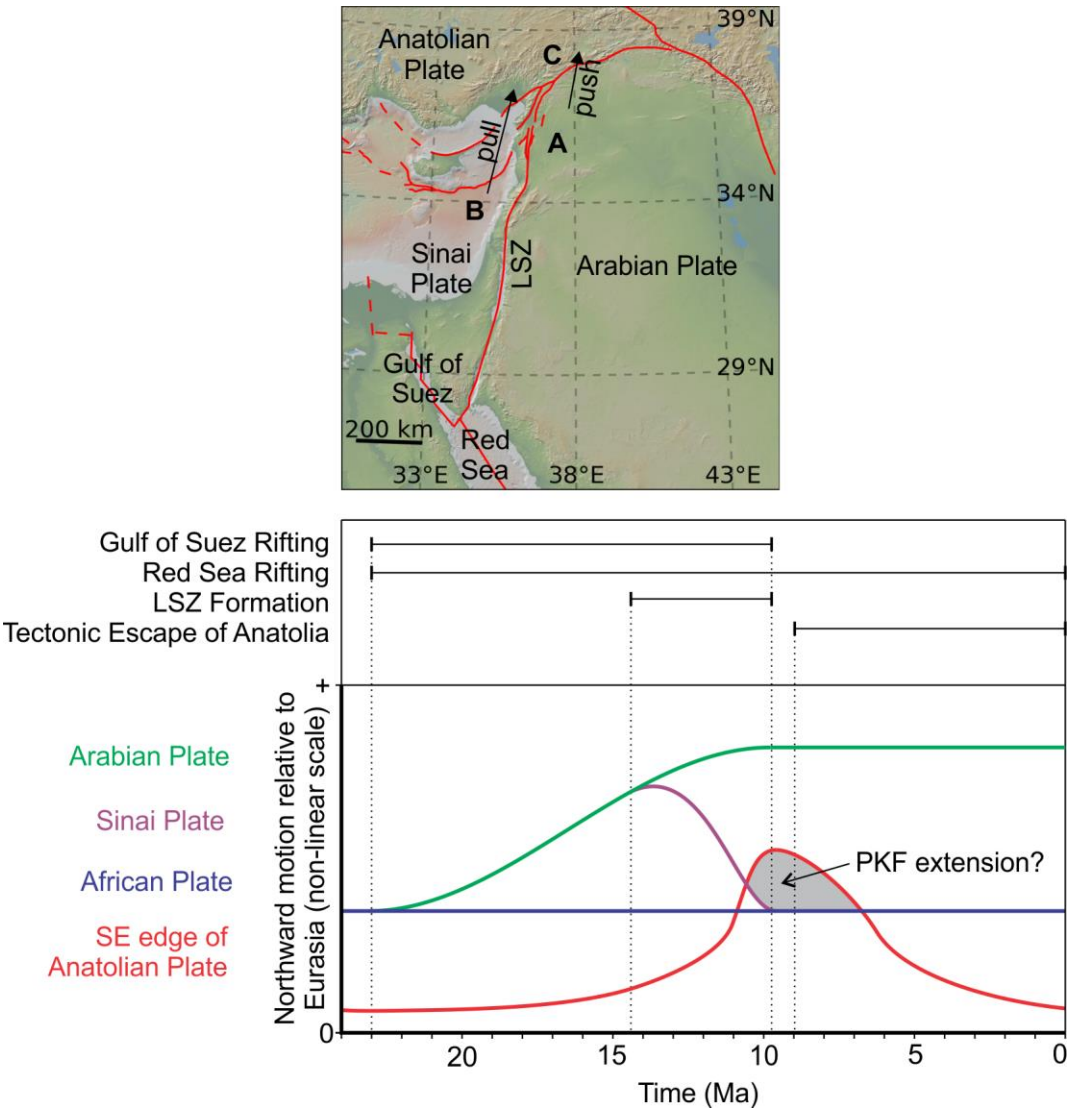

Figure 6.26-Graph showing the northward components of the plate motions of the African, Arabian, Sinai and Anatolian Plates relative to the Eurasian Plate. The global relief (Ryan et al., 2009) vertical scale on the minimap is shown on Figure 1.1 and the supplementary figure.

Several issues need to be addressed for this hypothesis and the proposed mechanism to remain valid; these are addressed in the following subsections.

6.6.2 Distributed faulting

The PKFs exhibit laterally distributed offsets (Figure 6.2). This might be interpreted to favour the tectonic dragging mechanism over the shear mechanism, as the latter might be expected to lead to localisation of fault offsets proximal to the LSZ.

The underlying mobile horizon may have contributed to the distributed larger (>200 m) offsets of the main PKFs, even if the shear mechanism formed the faults. As the displacement of the faults offset the faulted blocks they would have displaced the mobile interval. With ongoing extension, the downthrown blocks would eventually thin the mobile interval such that movement of the mobile interval becomes restricted. It might then have been mechanically easier for faults to form where additional offsets could be accommodated by thicker portions of the mobile interval. This feedback mechanism could lead to distributed faults of comparably larger (>200 m) offsets.

Where the mobile horizon is absent or reduced, as for many of the peripheral PKFs, their spatial distribution favours the tectonic dragging mechanism as the far field forces are predisposed to result in dispersed deformation.

6.6.3 Southern Periphery Piano Key Fault Timing

Many, but not all, of the southern periphery PKFs do not offset the late Miocene horizons, but do offset the Upper Eocene Unconformity (Figure 6.27). This contrasts with the main and northern periphery PKFs, and suggests that some of the southern periphery PKFs may have formed earlier. Three mutually inclusive explanations exist; 1) concurrent initial formation for all the PKFs but earlier formation termination of the periphery PKFs, 2) a locus of extension that shifts northward, and 3) a separate episode of extension.

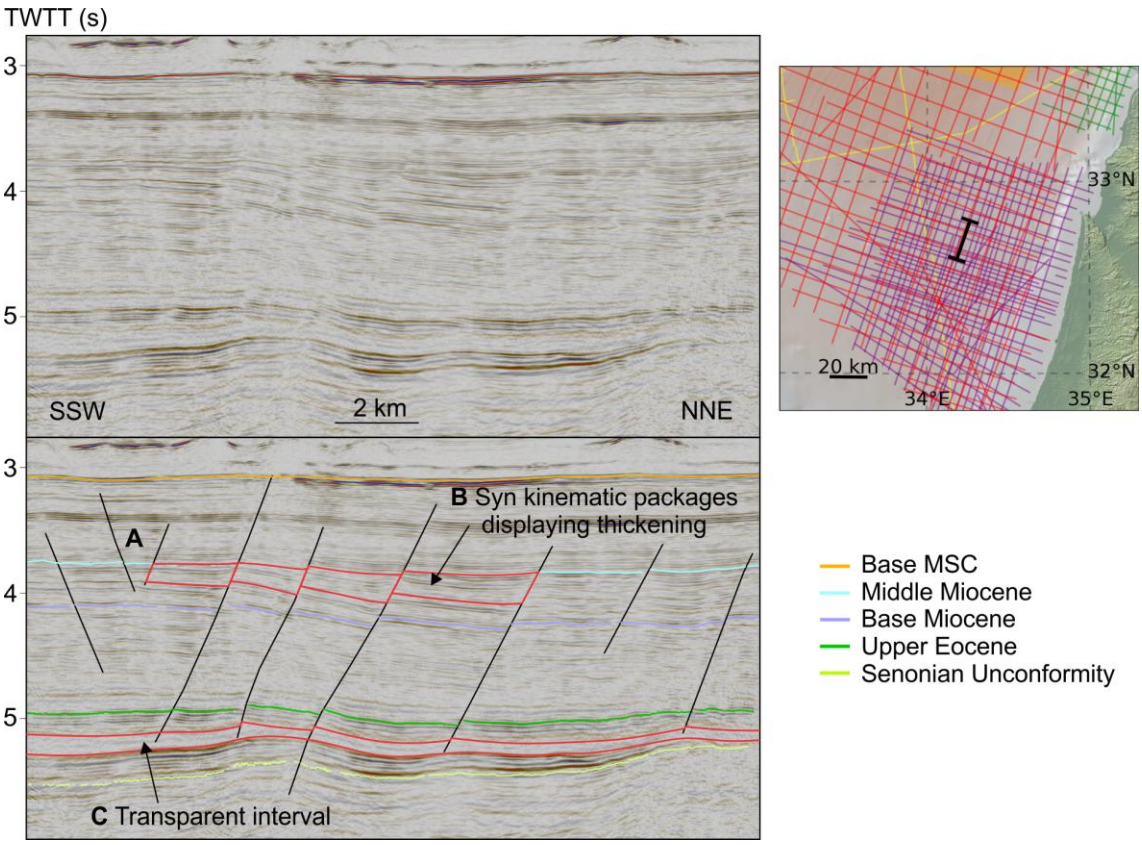

Figure 6.27-Seismic line over some earlier periphery PKFs offshore Israel. The global relief (Ryan et al., 2009) vertical scale on the minimap is shown on Figure 1.1 and the supplementary figure.

The presence of some southern periphery PKFs with apparent ages that match the main PKFs supports the foremost option over the latter (Figure 6.2). The earlier termination and comparatively reduced offsets of the periphery PKFs (both those in the Northern and Southern Levantine Basins) may be explained by the absence of the underlying Oligocene mobile horizon that is present at the main PKFs (Figure 6.27). This could mean offsets initially formed in the early Miocene across all the PKFs, but the shale interval underlying the area of the main PKFs accommodated fault block movement with comparatively reduced mechanical resistance, preferentially localising extension.

The early Miocene syn-kinematic (thinning) packages observable adjacent to some of the faults (Figure 6.27) is strong evidence that there was extension occurring at this time at the southern peripheral PKFs. However, these faults offset horizons younger than the syn-kinematic packages, demonstrating additional later extension, so this does not discount the former options. The southern portion of the LSZ formed in the early Miocene due to the continued opening of the Red Sea whilst the Gulf of Suez Rifting had ceased (Section 2.5.3); this could have generated the extension that formed these earlier offsets.

It is conceivable that the horizons have been inaccurately traced so that the ages of the picked intervals are incorrect, so that the syn-kinematic packages at the main PKFs are earlier than has been described here. However, the picking error would have to be c. 0.5 s TWTT for this to be the case and given the coherency of the seismic imaging this possibility may be discounted (Figure 3.14). It is also possible that the orientation of the earlier southern peripheral PKFs varies

from that of the rest of the PKFs, as the published images used to constrain the orientation of the southern peripheral PKFs are of the reservoir interval, which is upper Oligocene to early Miocene in age (Gardosh, 2013). However, in the absence of any evidence to the contrary and the matching apparent dips (on a given orientation of seismic line) with the rest of the PKFs (Figure 6.27; Figure 6.1A), the orientation of the earlier extension was assumed to be at least comparable with that of the main PKF extension.

Based on all the points discussed in this sub-section, it may be concluded that these faults formed as a combination of all three of the given options. As most of the southern peripheral PKFs have at least a portion of their displacement forming concurrently with the rest of the PKFs, they remain referred to as part of the PKFs.

Many of the southern peripheral PKFs that offset the Upper Eocene horizon either do not offset, or have greatly reduced offsets at, the Senonian unconformity (Figure 6.27). There is a seismically transparent interval between these two horizons that appears to be mobile on the basis of these fault offset and seismic characteristic observations (Figure 6.27C). As with the main PKFs (Section 6.2.3), it is likely that the presence of this mobile horizon has some control over the occurrence of the southern peripheral PKFs.

The presence of some early Miocene PKFs in the Southern Levantine Basin could also indicate that the beta factor signals prior to the formation of the majority of the main PKFs in the late Miocene (Figure 6.17D-F) could represent more minor early Miocene PKFs in the Northern Levantine Basin.

6.6.4 Perpendicular Compression

Several possible factors can be used to explain the folding perpendicular to the PKFs, all related to the LSZ. These are (A) a manifestation of strike-slip deformation related to the formation of the LSZ (Figure 6.28A), (B) Arabian Plate motion that results in a transpressive component across the LSZ once it had formed (Figure 6.28B), and (C) transpression related to the Lebanese restraining bend (Figure 6.28C; Ghalayini et al., 2014). To recap, two sets of PKF perpendicular folds exists; early Miocene folds in the Southern Levantine Basin (Figure 3.14B; Figure 6.6B; Section 3.6.5), and late Miocene folds offshore Lebanon (Section 6.3; Figure 6.28).

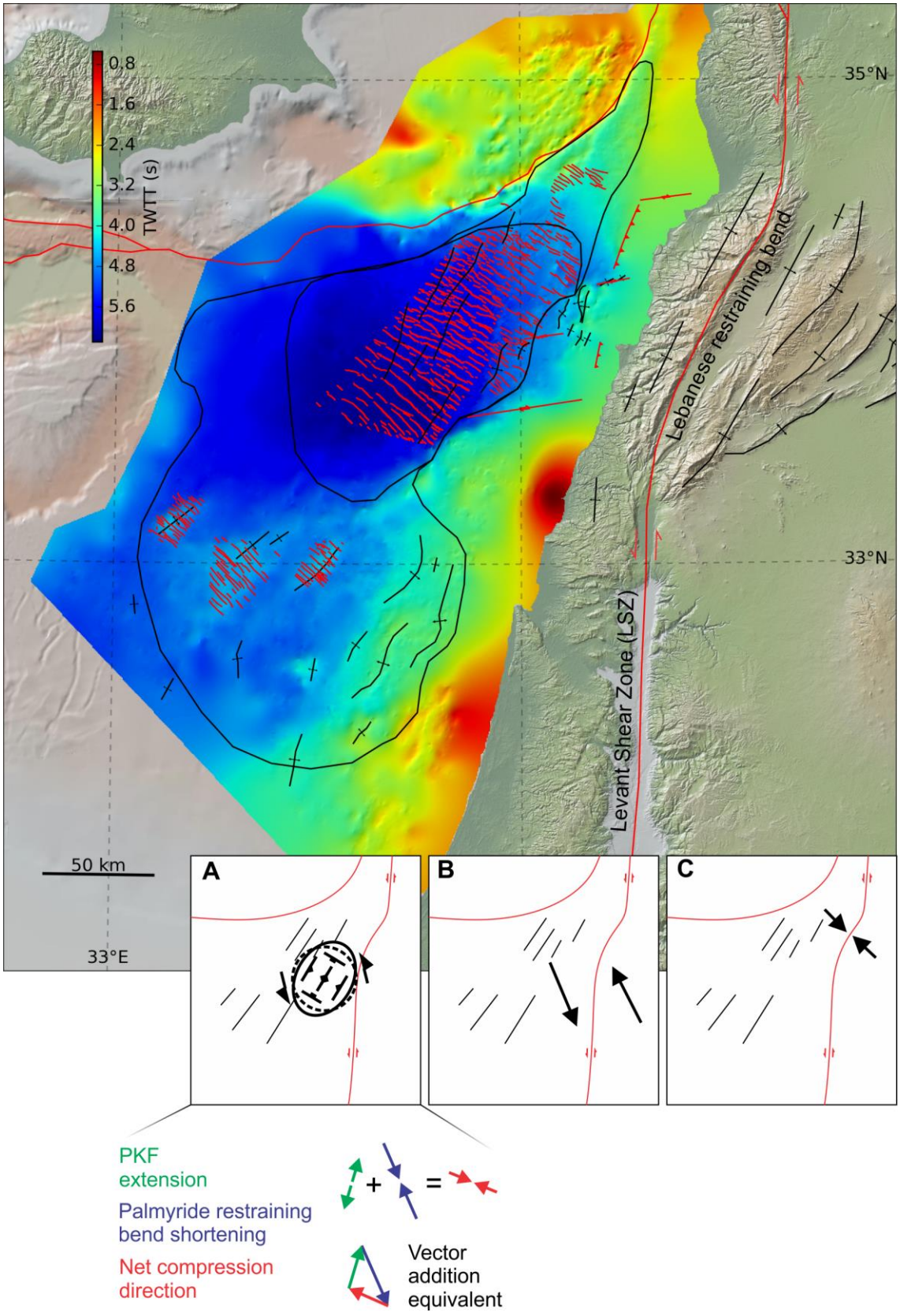

Figure 6.28-Map showing the Base Miocene surface, PKFs and perpendicular folds, and folds of the Syrian Arc II compression event, and sketches (A-C) of concepts discussed in the text. Features outside the area of the LEB3D survey are after Ghalayini at al. (2013; 2014). The global relief (Ryan et al., 2009) vertical scale is shown on Figure 1.1 and the supplementary figure.

Key in resolving the validity of the three possible factors is the timing of the formation of the LSZ. During its formation the LSZ propagated south to north. The southern segment formed in the mid

Miocene, and the northern segment formed in the latest Miocene. The timing of the folds appears to match with this formation; the Syrian Arc II compression is contemporaneous with the formation of the southern LSZ segment, and the formation of the folds perpendicular to the PKFs is contemporaneous with the formation of the northern segment of the LSZ.

A. The strain ellipse appears to indicate that the orientation of the proximal portion of the LSZ does not match the orientation of the PKFs and perpendicular folds (Figure 6.28A). However, if the area was also being subject to a component of tectonic-drag derived extension at the time (Section 6.6.1) then the relative orientation of the features matches (Figure 6.28A). NW verging compression in addition to NNE-SSW extension results in the observed WNW compression (Figure 6.28A).
B. Seafloor magnetic anomalies and the bathymetric relief of spreading ridges in the Gulf of Aden can be used to resolve the relative motion between the Arabian and African Plates (Leroy et al., 2013). When these relative motions are applied on a sphere some restorations result in some convergence between the Arabian and Sinai Plates, in addition to the transform motion (Seton et al., 2012). However, the low resolution of reconstructions at this scale, and the widespread possibilities of intraplate deformation means this conclusion is not definitive.
C. The Lebanese restraining bend gives a good explanation as to the formation of folds offshore Lebanon, as onshore folds associated with the feature are parallel to the structure. However, it does not help explain the folds offshore Israel, as these are at a distance and orientation that it is mechanically infeasible for the Lebanese restraining bend to have formed them.

Based on the evidence available to this study, a locally dependant combination of these three factors may be considered the most likely explanation for the folds perpendicular to the PKFs.

These forces would also be expected to act on the eastern side of the LSZ, however folding only appears to be present there in the Palmyrides (Ryan et al., 2009). This is likely due to the cratonic crust of the Arabian Plate being more mechanically resistant to deformation than the Palmyride Basin and sediments in the offshore Levant.

6.6.5 Extension Rates

The plots of beta-values suggest extension at the main PKFs underwent an abrupt pulse in the late Miocene before reducing more steadily (Figure 6.17). By considering this in relation to the components of the proposed genesis mechanism, it can inform on the mechanisms validity.

The relatively fast cessation of rifting in the Gulf of Suez once the LSZ was established matches the initial sudden initiation the main episode of extension that formed the PKFs (Section 6.4.5). The cessation of this extension could have occurred due to either changes in the direction of the movement of the African/Sinai Plates, or when the transition from northward to westward tectonic escape of the Anatolian Plate meant the net movement between the Anatolian and Sinai Plates was no longer divergent. Either option could match the progressive reduction in extension rate of the PKFs (Section 6.4.5).

If the PKFs did initiate with formation of the LSZ, then as the timing of formation of the LSZ is known more precisely than that of the PKFs, the former can give a more precise estimate on the

initiation of the PKFs. In combination with the beta plots this also permits rough estimation of the rate of extension across the main PKFs. The estimate makes many simplifications, but it serves as a test of the proposed mechanisms feasibility.

Assuming near-instantaneous initiation of full extension and linear reduction of extension until cessation of faulting permits estimation of the extension rate profile shown in Figure 6.29. This is based on the ~3.5 km extension observed along the dip of the fault body (Section 6.4.5) and corresponds to a maximum extension rate of ~1.3 mm/yr. This is a low velocity rate extension in comparison the velocities of the surrounding plates and is within the error bars of the techniques used (Reilinger et al., 2006) and thus accords with the hypothesis.

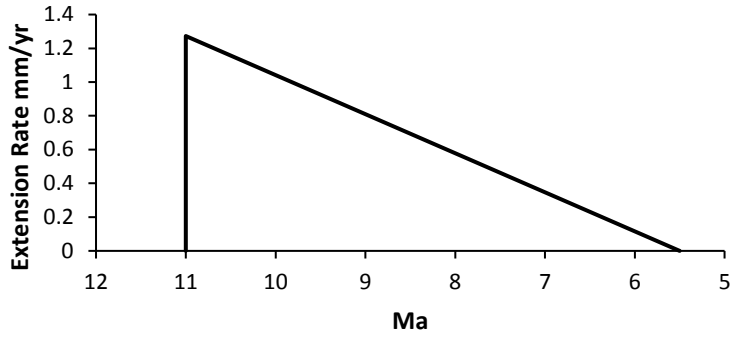

Figure 6.29-Graph showing the estimate extension profile for the PKFs.

The change in strike of the PKFs (Figure 6.10) may be associated with changes in the direction of extension as the locus of extension moved SW through time. An anticlockwise change in the direction of movement of the African Plate could provide the necessary stress changes, however the change in strike is small enough to introduce difficulties in resolving its cause.

6.6.6 Deformation at the Bitlis Suture

If the 2nd proposed mechanism is valid, then the signature of this deformation might be expected around the collision zone between the Arabian and Eurasian Plates. At the Bitlis Suture, continuing convergence since the formation of the PKFs has likely destroyed resolvable geological record of this. However, immediately west of the Bitlis suture lies the Misis-Andırın complex. Robertson et al. (2004) summarise the evolution of this feature as:

1) Diachronous collision that was complete by earliest Miocene time in the east;
2) Early Miocene basinal deposition in a setting that varied from compressional in the east to more extensional or transtensional in the west;
3) Post-suture tightening, accompanied by southward thrusting in Mid–Late Miocene time (Langhian–Serravallian);
4) Late Miocene (Tortonian) locally variable thrusting, folding and transpression;
5) Plio-Quaternary dominantly left-lateral strike-slip coupled with localised compression mostly in the east).

Key in this is the early Miocene easterly compression and westerly extension, which is what might be expected if the area had been subject to the 2nd PKF formation mechanism. The thrusting in

the remainder of the Miocene might be considered to be at odds with the mechanism however, especially as the formation of the main PKFs, the main period of PKF extension, occurred in the late Miocene. A counter argument to this may be reached after consideration of the ongoing collision between Arabia and Eurasia, as explained in the following paragraph.

The northernmost limit of the Arabian promontory is, and was during the Miocene, east of the Misis-Andırın complex. This means that the western limit of the suture has propagated west from this point since the initial collision. The location of the Misis-Andırın complex relative to this propagating suture limit could be such that during the early Miocene the experienced compression in the east to extension in the west. As the suture continued to propagate west, the region subject to extension propagated with it, so that the whole of the Misis-Andırın complex was then subject to compression, with extension then focused further west. Late Miocene subsidence and possible extensional faulting is observed in the Kyrenia Range during the mid to late Miocene, both preceded and followed by well evidenced compression (McCay and Robertson, 2012; Robertson and Kinnaird, 2015), matching a westward shift of extension.

Thus, the deformation at the Misis-Andırın complex is compatible with the proposed PKF formation mechanism. At the onshore portion of the easternmost Cyprus Arc, extensional (or transtensional) basin formation is observed in Syria in the mid Miocene (Hardenberg and Robertson, 2007), and transtensional basin formation in Turkey in the Pliocene (Boulton et al., 2006; Boulton and Robertson, 2008). These observations of extension to the west of the LSZ are also compatible with, and to a certain extent corroborate, the proposed PKF formation mechanism.

6.6.7 Trans-Subduction Zone Extension

The southern edge of the Cyprus Arc is a relic subduction zone upon which subduction ceased at the end of the Cretaceous (Chapter 4). At the initiation of the Miocene compression hiatus, it would have constituted the relic crustal scale low angle detachment with numerous overlying thrusts (Section 5.6.8). There are three end-member possibilities for deformation if this compressional plate boundary was subject to extension:

A) Extension is accommodated on the thrusts decollements. This is termed negative inversion after Williams et al. (1989).
B) No negative inversion occurs, and the plate boundary compartmentalises stresses so extension is accommodated on normal faults on the northern side of the plate boundary adjacent to where the extension is derived from.
C) The compressional plate boundary has no direct effect on how the extension manifests.

Negative inversion appears to be less common in the geological record than reactivation of extensional features in compression (positive inversion; Williams et al., 1989). This could be as a result of only partial decollement reactivation during negative inversion, however fundamental mechanics mean that low angle decollements do not provide pathways for lateral extension that are less effort than the formation of new high angle fault planes (Faccenna et al., 1995; Fossen, 2010; Williams et al., 1989). This means that where compressional structures are subject to

extensional forces it is common for new normal faults to form which bypass thrust planes entirely, or alternatively partial negative inversion occurs on higher angle thrust planes which are more conducive to extensional reactivation (D'Agostino et al., 1998; Faccenna et al., 1995 and refs. within; Powell and Williams, 1989; Tavarnelli, 1999).

This means that negative inversion of the low angle relic subduction zone thrusts may be deemed unlikely to accommodate all the extension that it is subject to. This also suggests that there is no reason for the compressional plate boundary to act as a buttress which might limit the effect of any extension. Thus, a realistic intermediary between the end members outlined above might be extension on both sides of the southern edge of the Cyprus Arc, with some partial negative inversion of higher angle thrust faults at the Cyprus Arc.

No definitive negative inversion was observed in the seismic data available to this study (Chapter 3). This could indicate that the Cyprus Arc was not subject to extension in the Miocene. However, there are several points which inhibit this conclusion:

A) There is a group of normal faults that are late Miocene in age immediately behind the thrusts of the Tartus Ridge (Section 6.2).
B) The southern edge of the Cyprus Arc is underlain by oceanic crust that has been thickened by overthrusting (Chapter 4). Thus, pre-existing fault planes notwithstanding, it is mechanically stronger than the adjacent Northern Levantine Basin which constitutes thinned continental crust overlain by non-crystalline sediments. Any expression of deformation might therefore be expected to manifest in the Northern Levantine Basin as opposed to the Cyprus Arc.
C) The Cyprus Arc has undergone a period of compression, with a component of strike-slip motion on the eastern limb, after the PKF extension period (5.6.8). The associated deformation may have obscured evidence of any negative inversion at the Cyprus Arc.
D) To-reiterate, the base-MSC parallel reflectors demonstrate that there was no compression at the eastern limb of the southern edge of the Cyprus Arc during a period of the Miocene (Section 5.6.5). If a given reconfiguration of stresses could result in the plate boundary between converging plates to cease to be subject to compression for a period, then it would be a relatively small step for the same reconfiguration of stresses to cause slight extension during that period.

Based on the points outlined in this subsection it is concluded that transmission of late Miocene regional tectonic extension across the Cyprus Arc subduction zone is geologically feasible. The subduction-front parallel deformation at the Indo-Burmese hyper-oblique subduction zone demonstrates that subduction decollements can compartmentalise stresses and the resulting deformation (Nielsen et al., 2004). However, this does not apply to the Cyprus Arc subduction zone as it is extension that is being transmitted. Additionally, both the docking of thinned continental crust in the subduction zone, and possible dehydration of the relic decollement in the c. 50 Myr since subduction, could cause the decollement to become restricted in its ability to slip.

6.6.8 Extension at Depth

If as postulated it was tectonic forces that formed the PKFs one might expect some expression of extension in the deeper stratigraphy. Three mutually inclusive potential explanations exist for the lack of extensional faults in the deeper stratigraphy; 1) ductile deformation of the deeper stratigraphy, 2) displacement along the leading decollements of the remnant subduction zone and 3) deeper faulting not resolved on seismic data. These potential explanations are discussed below.

1) Ductile deformation is challenging to interpret on seismic data with any degree of confidence as it requires the relative deformation of a non-ductile interval to be resolved. In the case of the PKFs, the late Miocene horizons that the PKFs displace is the non-ductile interval. Consequently, any ductile deformation of the underlying formations cannot be isolated.
2) If the displacement occurred along decollements in advance (to the south) of the Cyprus Arc subduction zone then the stratigraphy underlying the PKFs could diverge from the younger sediments at the leading edge of the overriding plate (Figure 6.30), producing thin-skinned tectonically derived extension. This also fits the southward migration of the locus of PKFs extension, as the faults would have initially formed closer to where the overlying plate at the Cyprus Arc is transferring the extension. As the downthrown fault blocks are such that the underlying mobile horizon is almost completely evacuated, it would have been mechanically easier for faults to form where additional offsets could be accommodated by the underlying mobile horizon, even if this was further from the buttress. The Palaeocene interval through which a décollement would have had to have formed to reach the mobile interval is well imaged in the seismic data available to this study (Figure 6.1A, Figure 6.30), but no decollement is resolvable. However, the low angle of such a feature and the low fidelity of reflectors in this Palaeocene interval mean a component of inversion on the subduction zone cannot be discounted.

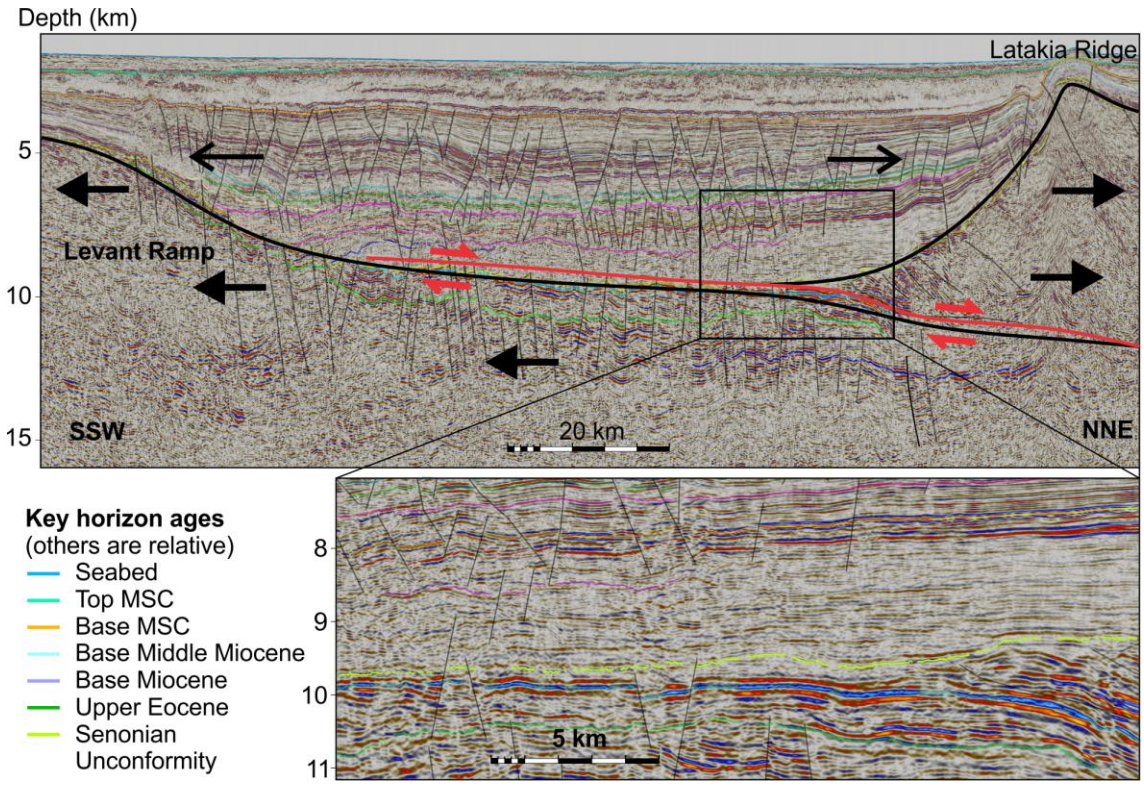

Figure 6.30-Sketch section overlain on a condensed image of Figure 6.1D showing how inverted reactivation of a laterally expanded Cyprus Arc subduction decollement (red line) during regional extension of the area (black filled arrows) could lead to extensional deformation localising in the Northern Levantine Basin (black unfilled arrows). The inset highlights an example of how no evidence of the extension of the hypothesised laterally expanded subduction decollement may be observed on the seismic data available to this study.

3) There are some uncertain offsets of the Senonian Unconformity horizon observable in the seismic data (Figure 6.1A, D; Reiche et al., 2014a). Tracing of the Senonian faults is challenging as the overlying deformation of the PKFs combined with the depth that is being imaged decreases the coherency of the offset reflectors. Consequently, underneath the centre of the main PKF swarm few deeper faults may be interpreted. Where the deeper faults may be observed they are sub-parallel to the PKFs (Figure 6.31). However, they do not appear to be deeper continuations of the fault planes of the main PKFs (Figure 6.1A, D). In the PSTM 3D volume the fault offsets appear minor in comparison to the main PKFs (Figure 6.1A). However, when one considers the depths of these faults and the increased seismic velocity that goes with the depth then the true, larger, fault offsets become apparent. On the PSDM line the throws of these deeper faults may be observed to have comparable offsets to the main PKFs (Figure 6.1D; Figure 6.30). These deeper faults are also resolved more clearly on the PSDM line than the PSTM data, and coherent reflectors may be traced between the Senonian unconformity and the Base Miocene. The faults appear to be a continuation of those pre-Senonian Faults that formed with the Levant Ramp (Section 3.6.4), and not deformation that occurred later. Considering all these factors together the deeper normal faults may have been reactivated to accommodate some of the extension of the PKFs at depth, however the amount of possible reactivation does not appear to be able to account for all the PKFs extension.

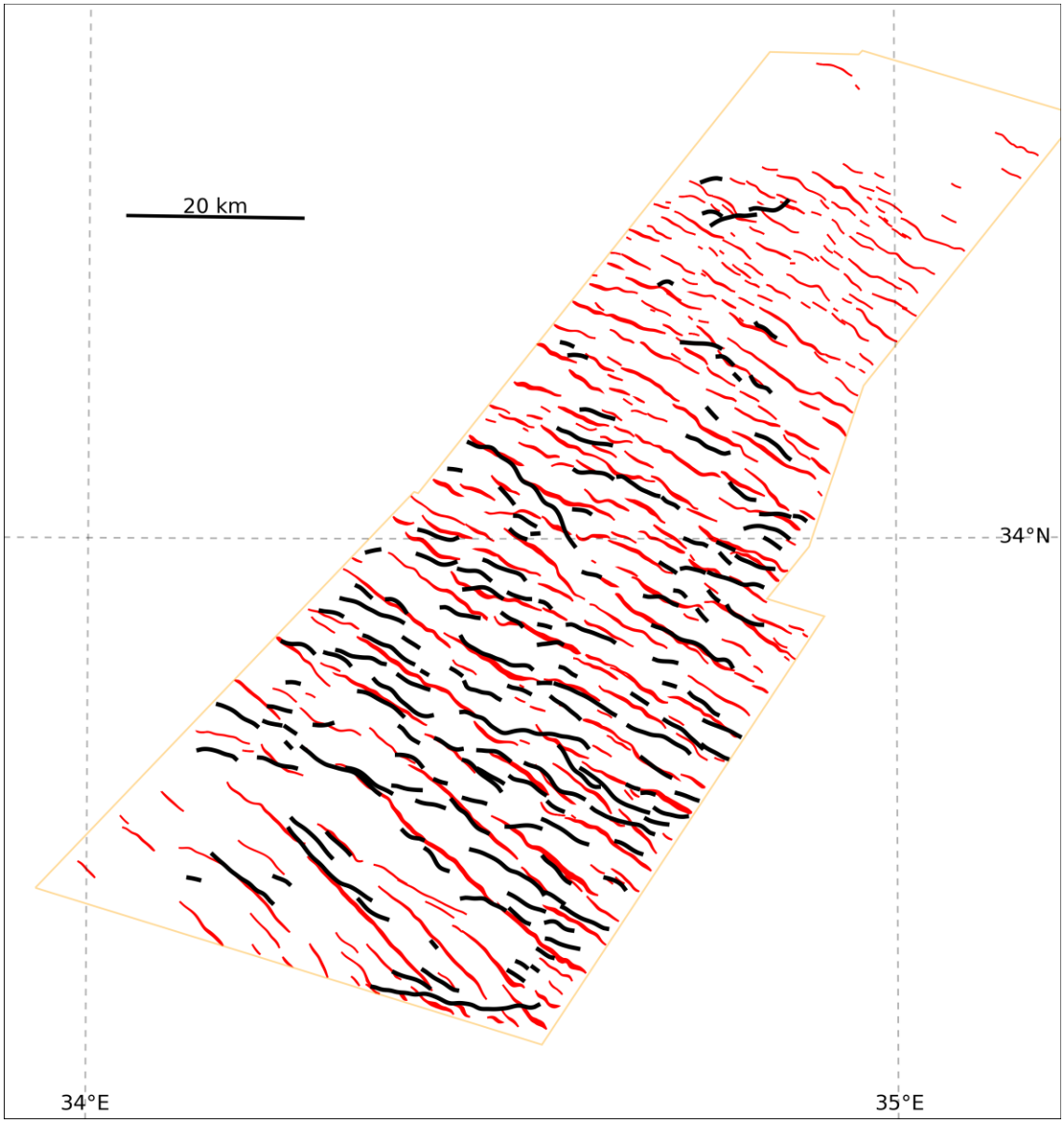

Figure 6.31-Comparison of the traces of the main PKFs (red) with the underlying normal faults of the Senonian Horizon (black) in the LEB3D seismic volume (orange).

6.7 Conclusions

To explain the formation of the PKFs, and on the basis of the discussion in the previous section, this study favours a combination of both shear forces related to the northward propagation of the LSZ and tectonic dragging of the Anatolian Plate from the collision of the Arabian Promontory (Section 6.6.1). A combination of these two mechanisms can explain the distribution and orientation of the PKFs, and the folding perpendicular to the PKFs (Figure 6.32). As both these mechanisms are related to the formation of the LSZ, it could be argued that they are part of the same single large shear system. The precise direction of tectonic forces around a large shear system such as the LSZ, especially considering the Palmyride restraining bend and possible components of transpressive motion across the LSZ, is complex, convoluted, and challenging to resolve accurately with confidence. The precise mechanics of this shear system are therefore speculative, but the net result of such a system is compatible with published literature and

observations of deformation in the seismic data available to this study, and with the hypothesised genesis for the PKFs and perpendicular folds.

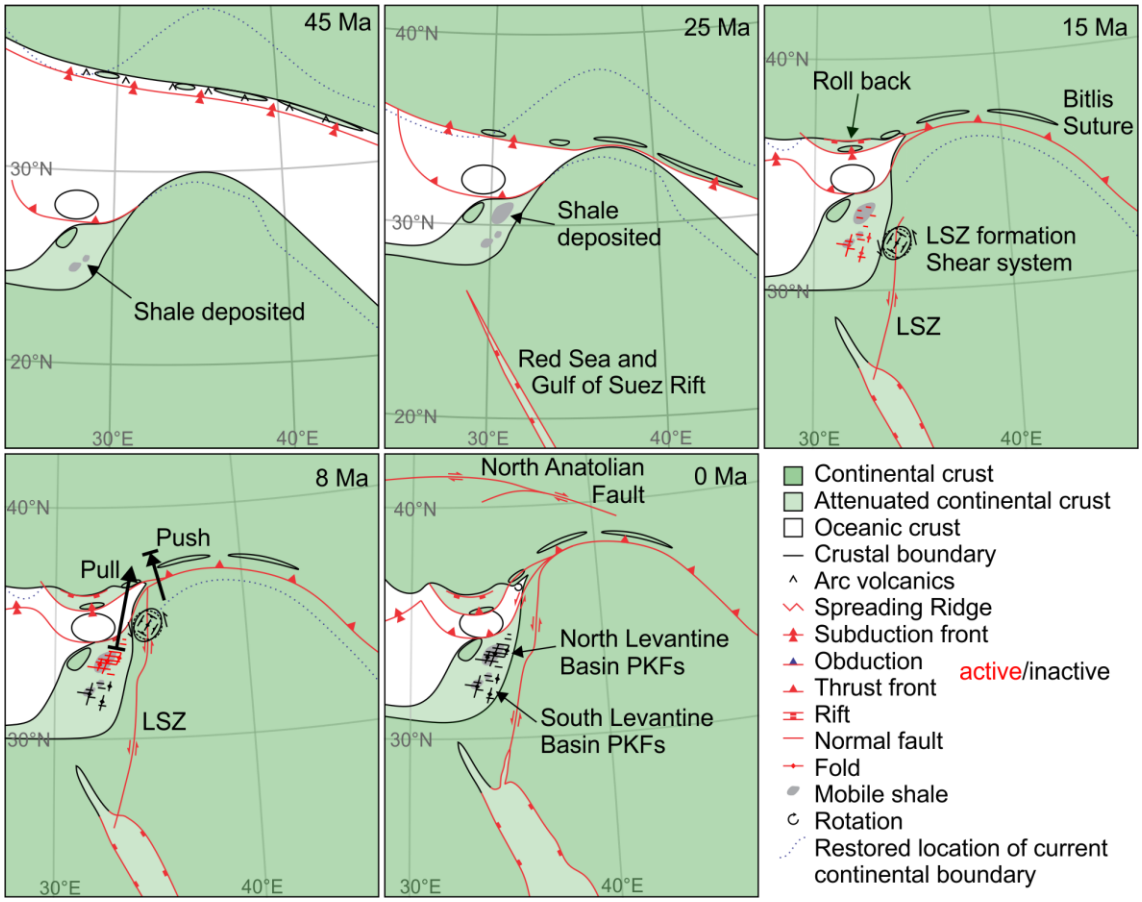

Figure 6.32-Summary sketch evolution of the formation of the PKFs as hypothesised by this study.

Based on the evidence and discussion presented in this Chapter, the earlier, generally more southerly PKFs formed in the proximal shear system of the northward LSZ propagation and the later, more northerly PKFs formed by a larger application of the same shear system that manifested as tectonic drag. The amount of throw of the PKFs in a specific area is a combination of two factors; positioning relative to the locus of tectonic dragging (the eastern limb of the Cyprus Arc) and the presence and/or thickness of an underlying mobile interval. The northerly folding perpendicular to the PKFs was interpreted to be due to a combination of the NW verging compression at the Palmyride restraining bend coupled with the NNE-SSW extension resolving to ~EW compression. The southerly folding perpendicular to the PKFs was interpreted to be part of the same shear system that formed the more southerly PKFs, orientated by reactivation of pre-existing folds and geological trends. This has two implications for the Syrian Arc II compression event; it suggests its genesis is the reconfiguration of plate forces during the formation of the LSZ, and extends its duration into the late Miocene.

This conclusion entails that the PKFs are a thin-skinned expression of tectonic forces. To avoid a space problem, two mechanisms are suggested to have combined to deform the underlying rocks. The first is a small amount of ductile deformation. This is the only available explanation for low throw peripheral PKFs in the Southern Levantine Basin, and if there is a minor component of this here, then it follows that there is an equivalent component beneath the main PKFs and other

peripheral PKFs. The other mechanism is the formation, or reactivation, of Cretaceous age normal faults in the underlying sediment sequence. The throws on these deeper faults are only apparent in depth data such as the PSDM line available to this study, as the >10 km depth of these sediments means the matching high seismic velocities reduces the signal of the offsets on PSTM seismic data. The strain partitioning beneath the mobile shales means that there are three main 'layers' of deformation in the Northern Levantine Basin; the Cretaceous sediments, the Oligo-Miocene sediments offset by the PKFs, and the post-MSC sediments. At least two additional minor 'layers' of deformation may be observed within Palaeogene sediments on the PSDM data (Figure 6.1D).

The offshore extension of the PKFs also provides a possible explanation for a portion of the 'missing' offset on the segment of the LSZ north of the Palmyrides (Section 2.6.8), although this would require deformation resulting in rotation of the intermediate lithosphere.

The validity of much of the more detailed analysis in this chapter is dependent on the input to the analysis including all the majority faults in the pertinent stratigraphic sequence. Given the size of the seismic volume and the number of faults it is possible that some minor faults have been missed, however care was taken to ensure interpretation of all confidently resolvable faults.

Chapter 7 Forward Modelling of Halokinesis

7.1 Introduction

The Eratosthenes 'Seamount' (ESM) is a spectacular bathymetric feature located in the SE Mediterranean Sea ~100 km South of Cyprus (Section 2.3.4). Although originally interpreted to represent a volcanic seamount more recent analysis suggests that it is a continental fragment capped by a drowned carbonate platform (Section 2.3.4). The bathymetric high is bordered on 3 sides by a depression that is defined by an external escarpment (Figure 7.1). This depression (moat) has been interpreted by various workers to have formed by normal faulting (Garfunkel, 1998; Kempler, 1998), strike-slip faulting (Aal et al., 2000), gravity sliding of supra-evaporite sediments causing thrusting (Loncke et al., 2006), dissolution of underlying evaporites (Major et al., 1998), kinematic evacuation of underlying evaporites (Montadert et al., 2014), and inflation of an evaporite body around the seamount uplifting the surrounding sediments (Reiche et al., 2015). As demonstrated in the following section all but the latter of these hypotheses may be discounted by interpretation of seismic and bathymetric data around the seamount. To further test this hypothesis, this chapter details the construction of a numerical model to simulate the hypothesised moat formation.

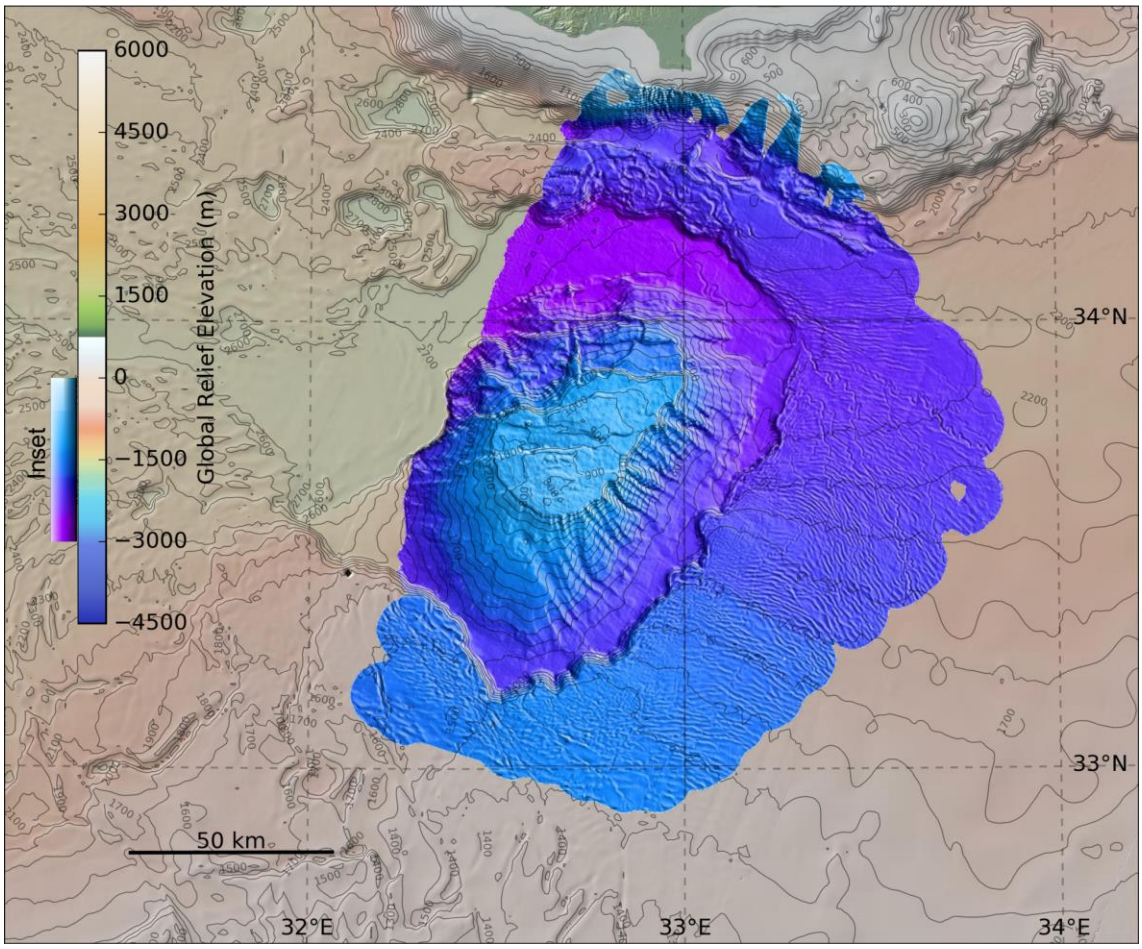

Figure 7.1-Map of the bathymetry around the ESM (GEBCO) with the ESM highlighted (Ehrhardt et al., 2011).

7.1.1 Moat Formation Hypotheses

PSTM seismic lines in the area reveal seismic pull-up by the (high seismic velocity) salt that could be interpreted to be faulting (Figure 7.2A-C). However, when this pull up is accounted for no offsets are observable in the pre-MSC reflectors (Figure 7.2D). The non-linear trace of the moat escarpment (Figure 3.25A) is also not indicative of faulting. Thus faulting can be discounted as having formed the ESM moat.

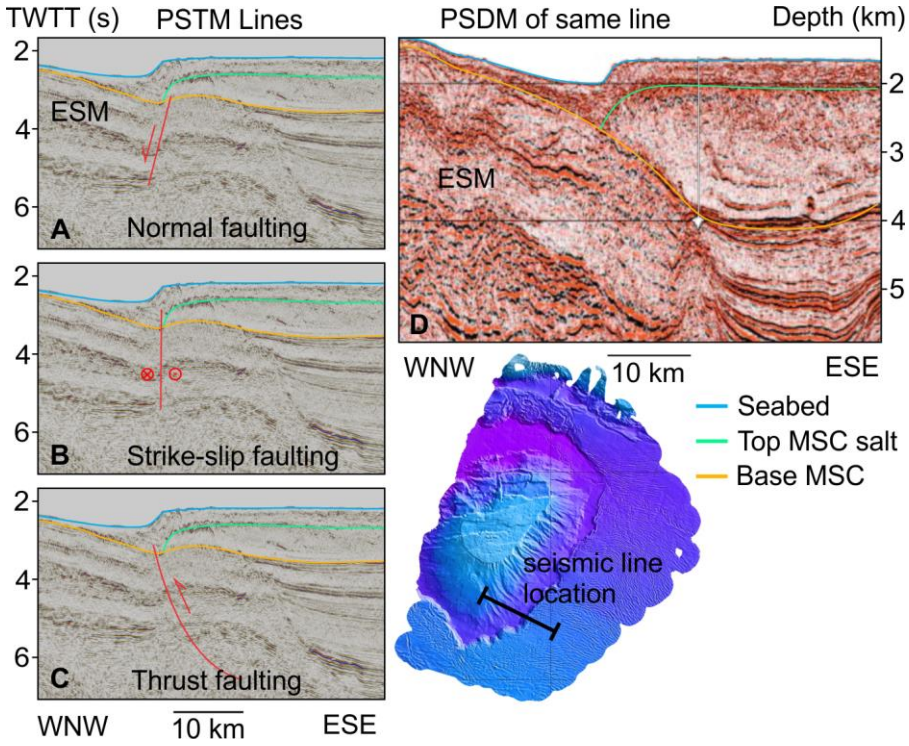

Figure 7.2-A, B, C: Sketches overlaid on a PSTM seismic line showing hypothesised faulting that could have formed the ESM moat. D: The same seismic line (Roberts et al., 2010) shown as PSDM data displaying no reflector offsets below the moat escarpment and planar sediments in the moat. The inset bathymetry vertical scale is shown on Figure 7.1.

Dissolution of evaporites is documented elsewhere in the Mediterranean (Jongsma et al., 1983), and halokinesis from differential loading is widespread in the EMR (Section 3.7). Formation of the moat by evacuation of underlying MSC salt by dissolution or halokinesis (Figure 7.3 A, B) are therefore possible mechanisms of moat formation that must be considered. Both these mechanisms would result in deformed and/or syn-kinematic sediments in the moat, but the seismic data reveal these sediments are planar and largely undisturbed (Figure 7.3C). Additionally, the remnant evaporites present in salt welds means that when shallow they typically image with high amplitude reflectors (Section 3.2.5), something not observed under the moat. For these reasons, kinematic evacuation and dissolution of evaporites may be discounted as having formed the ESM moat.

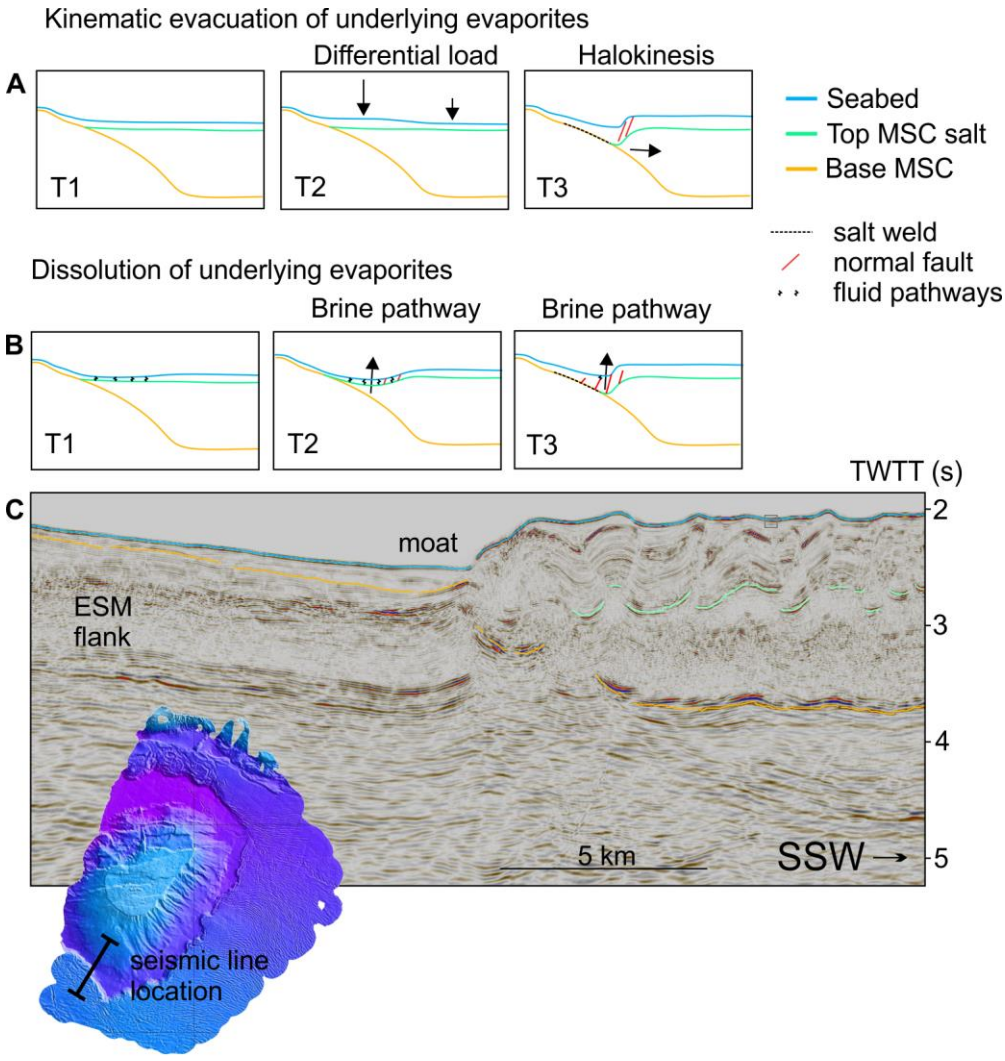

Figure 7.3-Sketches displaying two hypothesised mechanisms for formation of the ESM moat via evaporite evacuation; kinematic evacuation (A) and dissolution (B) of evaporites, and a seismic line on the southern portion of the ESM moat displaying undisturbed sediments in the moat (C). T1-3 indicates timesteps, with T3 being the present and T1 furthest back in time. The labels indicate the meaning of the arrows. The seismic line the sketches are based on is shown in Figure 7.2D. The inset bathymetry vertical scale is shown on Figure 7.1.

A key observation that supports gravity sliding as a mechanism for formation of the ESM moat is the presence of extensional structures upslope from the moat along the Levant continental margin and Nile Cone margin, and the compressional structures around the periphery of the moat (Figure 2.28; Figure 3.8; Figure 3.29; Figure 3.34B). However, lateral translation of only the supra-salt sediment cannot explain the dip on the moat-side edge of the evaporite body, and consequently gravity sliding of the supra-salt sediments may be discounted as the mechanism of formation for the ESM moat (Figure 7.4A). Gravity sliding of the evaporite body along a basal decollement, with rafting of the overlying sediments on the evaporite body, presents another possible moat formation mechanism (Figure 7.4B). However, if one considers the geometry of the top and bottom of the evaporite body this hypothesis may also be discounted. The sloped base of the evaporite body around the moat periphery means that attempting kinematic reversal results in a non-planar and non-level top to the evaporite body. As thick evaporite bodies such as this are deposited with planar and level tops this is geologically unrealistic. Attempting forward geometric

modelling of gravity sliding of the salt body and overlying sediment with an initially planar and level top to the salt body results in a salt body with a non-planar and non-level top to the evaporite body (Figure 7.4B). Although the slope at the moat-side edge of the salt body is consistent with observations in seismic, the non-planar and non-level top to the salt body over the rest of the salt body is not.

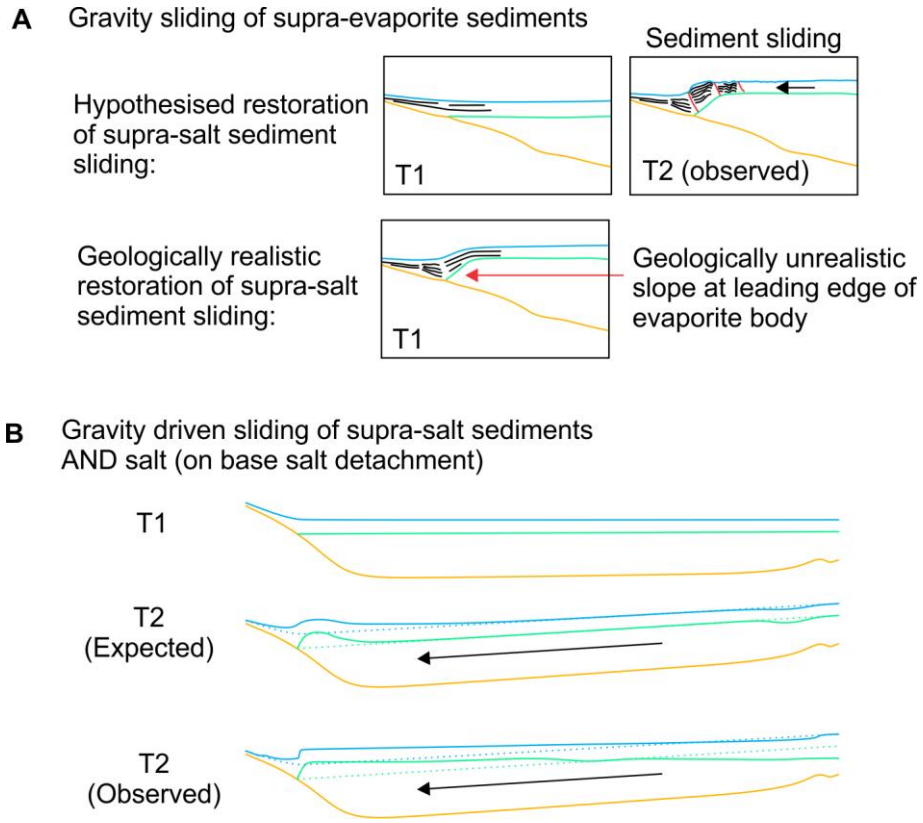

Figure 7.4-Sketches displaying two hypothesised mechanisms for formation of the ESM moat via gravity driven kinematics of A) supra-evaporite sediments and B) supra-evaporite sediments and underlying salt. T1-T2 indicates timesteps, with T2 being the present and T1 prior to the gravity driven kinematics.

Another potential explanation for the formation of the ESM moat is preferential erosion and deposition due to water currents; contourites and the plunge pools of overbank flows. Contourites have been documented to form elongate base-of-slope depressions (Faugères et al., 1993; Hernández-Molina et al., 2012; Stow et al., 2002; Surlyk and Lykke-Andersen, 2007) similar in bathymetric cross section to the ESM moat (Figure 7.5A vs. Figure 7.2D and Figure 7.3C). Analysis of currents in the EMR have also revealed a surface gyre centred on the ESM (Hayes et al., 2010; Menna et al., 2012) that could potentially indicate a deeper gyre around the ESM (Figure 7.5B). Another current-related process that could contribute to the formation of a moat is density cascading, which has been documented adjacent to the Bahama Bank (Figure 7.5C).

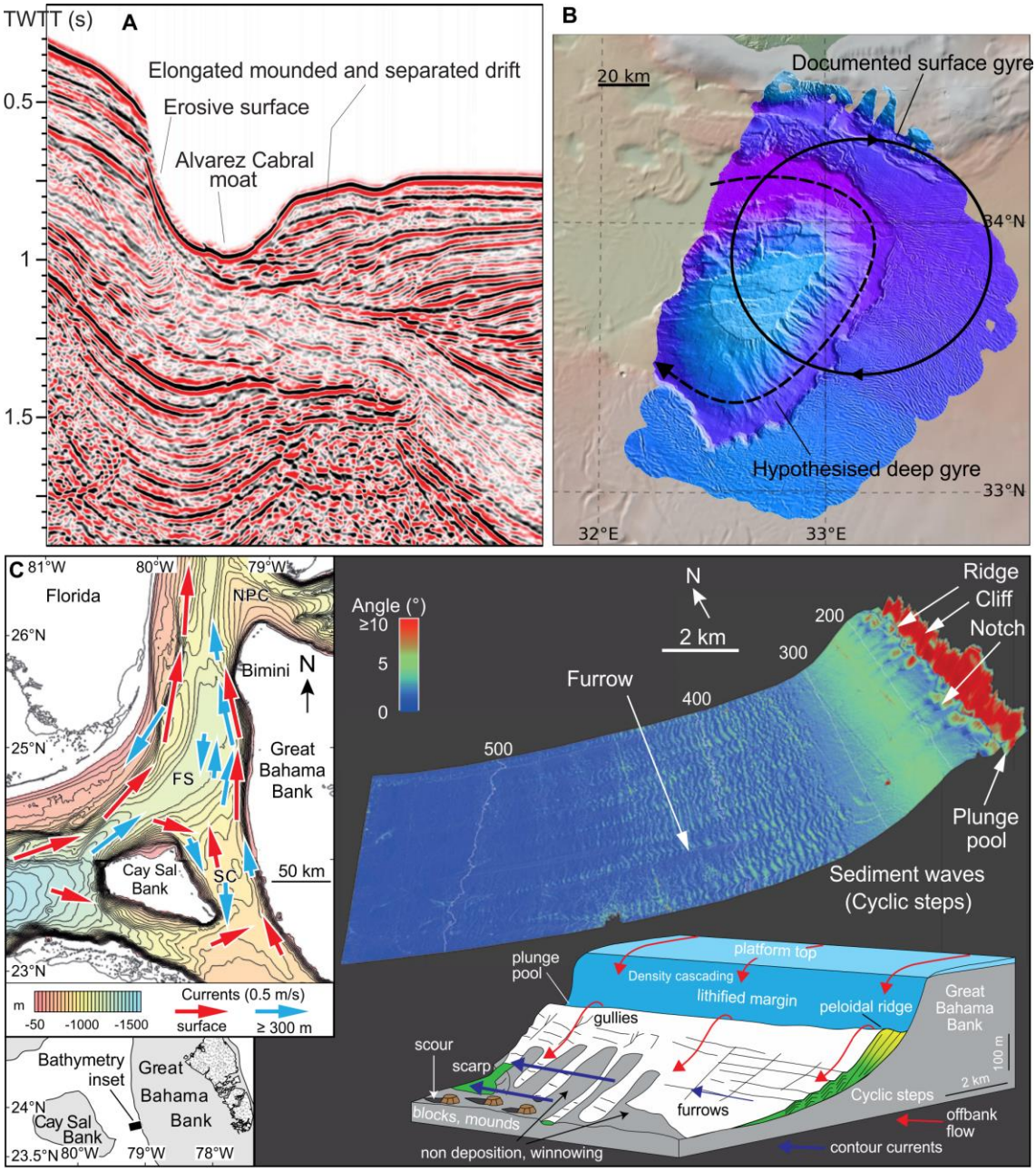

Figure 7.5-A) Seismic line across a contourite channel in the Gulf of Cádiz (adapted from Hernández-Molina et al., 2012); B) Bathymetry around the ESM overlaid by a documented surface Gyre (Hayes et al., 2010; Menna et al., 2012) and a hypothetical sea-floor Gyre, the vertical scales are the same as those on Figure 7.1.; C) Pereplatform drift process of adjacent to the Bahama Bank (adapted from Betzler et al., 2014).

There are several arguments that may be made against water current related formation of the ESM moat. The seismic packages that might be expected to result from these processes are absent; instead the reflectors are often laterally continuous when they are not thrusted (Figure 7.2; Figure 7.3). The bathymetric relief of the moat is also jaggedly undulant; not indicative of fluid flow (Figure 7.5B). The mechanisms behind the hypothetical flows are also uncertain, the surface gyre is offset from the required deeper gyre (Figure 7.5B), and the carbonate platform of the ESM has been drowned since the MSC (Section 2.5.4) so carbonate production sufficient to produce significant density flows is infeasible.

Based on the considerations made earlier in this section all the hypothesised mechanisms for the formation of the ESM moat have been effectively discounted apart from inflation by evaporite flow of the evaporite body around the ESM. This potential mechanism is discussed in the following section.

7.1.2 Salt Flow Hypothesis

It has been hypothesised that it was inflation of the evaporite body around the ESM (Reiche et al., 2015) that formed the moat. This uplifted the sediments on the exterior of the moat, as opposed to any mechanism that draws down the interior of the moat. The properties of evaporites means that in most geological scenarios salt flux may be simulated to occur via flow like a liquid, as opposed to translation of a rigid body (Fossen, 2010). The inflation of the salt body around the ESM is suggested to have occurred by 'flow' of the salt, a combination of gravity sliding and gravity gliding (Rowan et al., 2012), as it explains the geometries that may be observed (Figure 7.6).The driver of this flow is thought to vary on the different sides of the ESM:

- To the north of the ESM, tectonic shortening between the Cyprus Arc and ESM (Section 5.10) has compressed the salt body (Figure 7.6A). This compression explains why the portion of the moat escarpment at the north side of the ESM still produces a moat escarpment comparable to the rest of the moat (Figure 7.1), despite the adjacent salt body being much narrower (Figure 3.31).
- To the east of the ESM basin subsidence has formed a slope that is the primary driver and sediment loading at the Levant continental margin constitutes a minor secondary driver (Figure 7.6B).
- To the south of the ESM the Nile Cone forms a large sediment load and basin subsidence forms a slope (Figure 7.6C). The relative proportions of salt flow driven by subsidence or sediment load is discussed later.

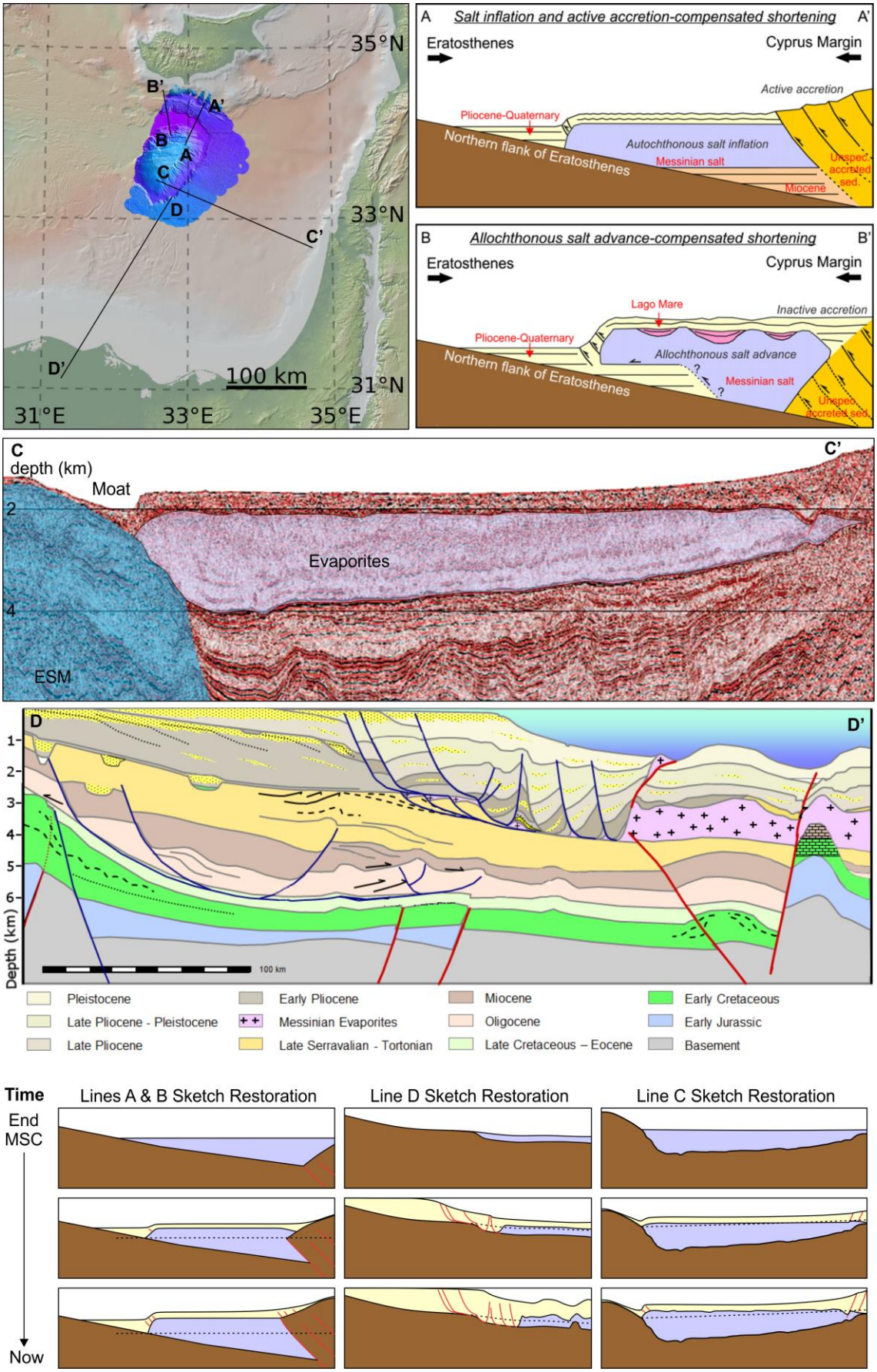

Figure 7.6-Cross sections illustrating the hypothesised drivers for the formation of the ESM moat (adapted from: D: Bertello et al., 2016; A & B: Reiche et al., 2015; C: Roberts et al., 2010). The minimap vertical scales are the same as those on Figure 7.1.

Truncation of reflectors within the salt body by the Top MSC Unconformity (Figure 3.33) indicate that a large amount of halokinesis occurred prior to the end of the MSC, demonstrating not all the internal deformation of the salt occurred after the MSC (Section 3.7.1). It could be argued that intra-MSC halokinesis could have generated salt body geometries that may have impacted the formation of the moat. However, the same reflector truncations combined with sub-parallel overlying reflectors indicates that the salt body was peneplained at the end of the MSC.

7.1.3 Issues with the Salt Flow Hypothesis

The salt flow hypothesis is compatible with the observations of the seismic data discussed in the previous section. However, there are some issues that need to be addressed to test this hypothesis:

1. Extensional structures upslope and compressional structures downslope are observed in the supra-salt sediments, indicating some translation of supra-salt sediment has occurred (Figure 7.6C, D, Section 3.7.4).
2. The top and bottom of the supra-salt sediments are planar in the Levantine Basin, at basin scale (Figure 7.2). For the salt flow hypothesis to remain valid the salt body would have had to have deformed such that the overlying surface remained sub-horizontal. This is likely linked to the salt body and overburden in the Levantine Basin not being thick enough to spontaneously initiate diapirism, and most the Levantine Basin salt body not having enough morphological variation to initiate diapirism via halokinetic localisation (Section 3.7.4).
3. Dividing the salt overburden into kinematic packages based on reflector terminations suggests that most halokinesis related deformation in the Levantine Basin adjacent to the ESM occurred when around half the sediment overburden had been deposited (Figure 7.7A; Figure 3.8B). The apparent delay before halokinesis has three possible explanations;
    - It was only with later supra-salt sediment translations that deformation occurred.
    - Strain-related viscosity reductions restrained earlier halokinesis (van Keken et al., 1993; Wagner, 2010).
    - Subsidence was insufficient to mobilise the evaporites until deformation is apparent.

    Based on observations syn-kinematic packages above diapirism in the Nile Cone (Figure 7.7B) the first option is the explanation favoured by this study.

To address the first issue a numerical model of salt flow was constructed to test whether a moat can form without supra-salt sediment translation.

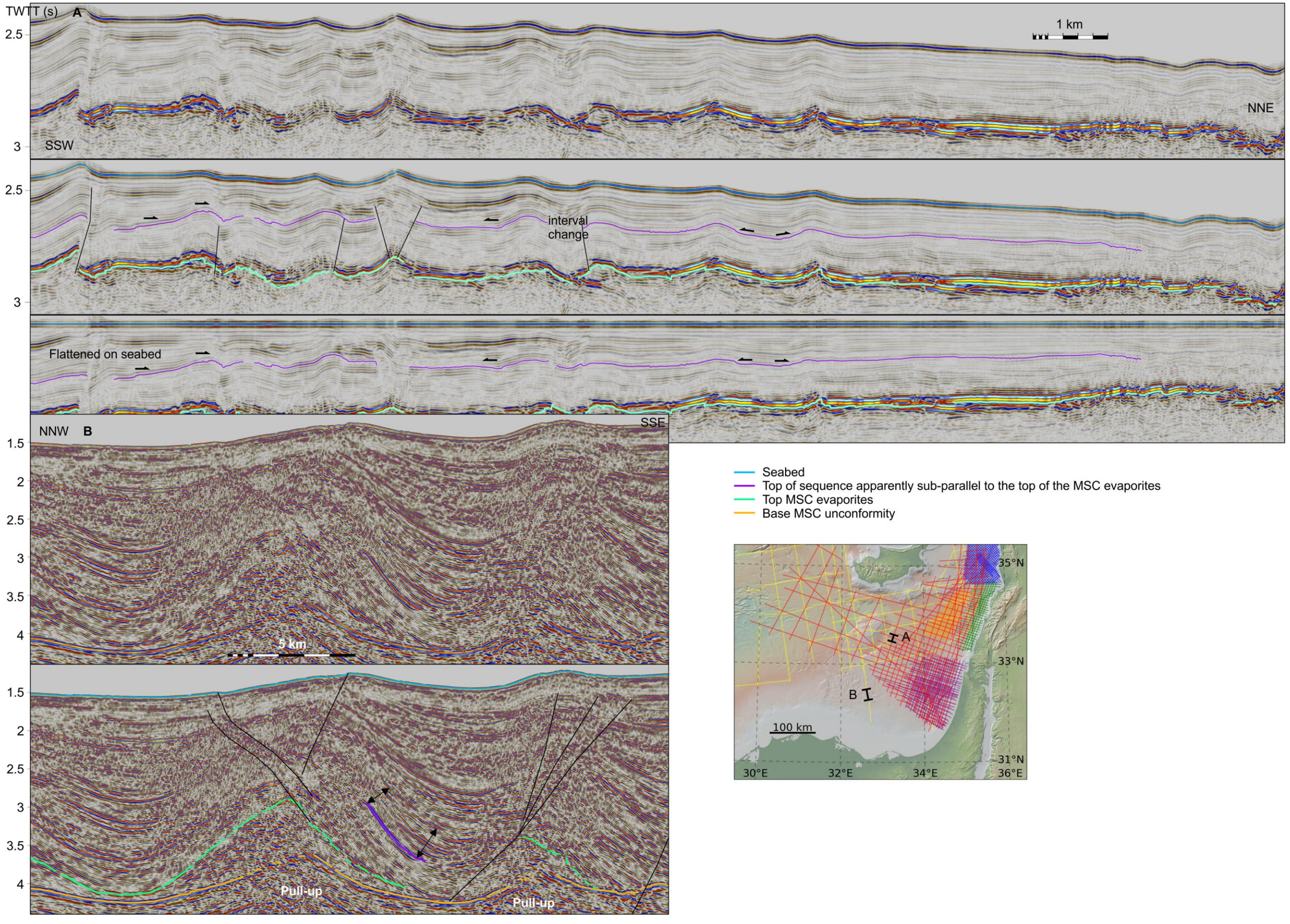

Figure 7.7-Seismic lines showing the stratigraphic interval in which reflectors non-parallel to the top of the evaporites appear, illustrating delayed halokinesis as discussed in the text. The global relief (Ryan et al., 2009) vertical scale on the minimaps is shown on Figure 1.1 and the supplementary figure.

7.2 Model Method

The aim of this numerical model is to test potential salt body and overburden geometries that may be created via evaporite translation but not sediment translation. For brevity this model is named the Pressure Model for Evaporite Kinematics (PMEK). The mechanical underpinnings that PMEK uses to simulate halokinesis are derived from a numerical model published by Peel (2014) that is termed DRAWL. Full simulations of salt flow are not attempted; instead a basic flow law is applied so lateral pressure gradients drive salt flux. Salt flux and sedimentation are calculated iteratively so that the simulated changes are taken into account in subsequent calculations. DRAWL simulations are 1D; PMEK simulations can be 1D or 2D.

In contrast to DRAWL PMEK attempts to account for sediment strength, similarly to DRAWL PMEK makes the following assumptions:

- Inertia and momentum are negligible.
- Sediments have uniform, user-defined density.
- No sediment compaction is considered.
- The salt has uniform viscosity.

These simplifications demand that the same caveat is given for PMEK as for DRAWL:

"While none of [the assumptions used in the model] are true representations of nature, they vastly simplify the process.... The model results are geologically realistic in appearance, indicating that the simplifications have not severely compromised the usefulness of the simulation" (Peel, 2014).

7.2.1 Translating Pressures into Salt Flux

Each modelled point in PMEK is referred to as an 'element'. These elements make up an evenly spaced 2D grid. The components of PMEK's calculations involving lateral variations in a variable refer to the neighbouring element in N-S or E-W directions.

Equation 7.1 shows how PMEK calculates salt flux from lateral pressure gradients.

$$F_e = \frac{\left(g \cdot \rho_e \cdot \Delta E_e + \Delta P_{eff}\right) \cdot {T_e}^{\mathrm{L}}}{X \cdot V} \qquad 7.1$$

The Δ prefix signifies lateral change in that variable.
F_e=salt flux
g=gravity
ρ_e=density of salt
E_e=elevation of top salt
P_{eff}=pressure acting on salt
T_e=thickness of salt
L=flow law exponent
X=distance that salt flux is being modelled over
V=viscosity of salt

The value of L represents the flow law of the model. There are two flow laws that can be used to simulate the flow of salt, termed Poiseuille and Couette. Flow by the processes simulated by these

laws is mutually inclusive as they simulate different modes of deformation. Couette flow corresponds to simple shear in the direction of flux. The amount of shear increases linearly from zero at the constrained base to the salt to its maximum at the top of the salt body. This maximum matches the translation of the overlying medium at the top of the salt body. Thus, applying Couette flow results in salt flux that is linearly proportional to the thickness of the salt body. Poiseuille flow is the standard model for representing laminar flow of a Newtonian viscous fluid between two parallel plates driven by a potentiometric gradient (Peel 2014; Figure 7.8). This law simulates flux that increases from zero at the edges of the salt body to a maximum in its centre, corresponding to constrained boundaries at the edges of the salt body. This results in a salt flux that is proportional to the cube of the thickness of the evaporate body.

Thus, as the moat formation hypothesis does not require translation of supra-salt sediments Poiseuille flow may be deemed the appropriate flow law for the salt flux. This flow law simulates that the fastest salt flow will be in the vertical middle of the salt body and it corresponds that the corresponding maximum deformation will also be in the vertical middle of the salt body.

A key difference between DRAWL and PMEK is the value of L used. A value of 3 represents Poiseuille flow, however Peel (2014) used a value of 1, which represents Couette flow, in order to produce geologically realistic simulations of salt minibasins using DRAWL.

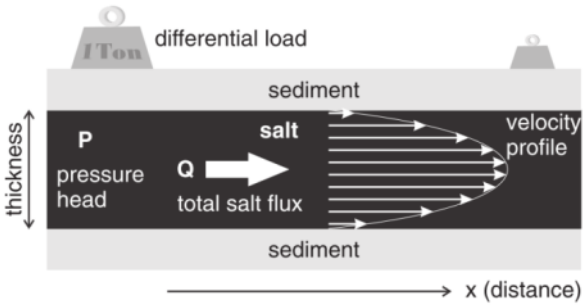

Figure 7.8-Theoretical plane Poiseuille flow from Peel (2014).

Both top salt topography and overburden are accounted for in the calculation of pressures acting on the salt. '$g \cdot \rho_e \cdot \Delta T_e$' in Equation 7.1 represents the lateral pressure difference generated by a difference in top salt elevation. The salt below the lowest elevation of top salt being considered need not be considered in this pressure difference. An analogy that may help understand why is to consider a bowl of water with a curved base; although the bottom of the bowl is curved no movement of water results.

The effective viscosity of evaporites is very high, estimated as 10^{17} to 10^{20} Pa s for rocksalt, strongly dependant on grain size and weakly dependant on temperature (van Keken et al., 1993). This means that very little salt flow occurs between each iteration of the model. To achieve practical computation times the viscosity was decreased, which when used in Equation 7.1 in the model is the equivalent of increasing the time simulated between iterations.

7.2.2 Sedimentation

Sedimentation that is controlled by the slope and angle of the underlying bathymetry was incorporated into PMEK. This means that the slight depression formed by the proto-moat will be subject to preferentially more sediment deposition. This will restrict intrusion of underlying salt, a positive feedback mechanism for the formation of the moat. To produce geologically reasonable sedimentation at the simulated continental margins, sediment supply and water depth also play roles in determining how much simulated sedimentation occurs. The following section documents the method by which the numerical model simulates this slope, source and depth controlled sediment deposition.

Assuming sea level may be approximated as constant, the amount of sediment overburden is the largest externally derived varying variable in PMEK. Due to the contrasting timescales of sediment and salt flux, simulation of the full sediment system was not attempted, instead calculations that produce geologically reasonable sedimentation during PMEKs iterative timesteps were constructed. These are shown in equations 7.2-7.8.

At each iteration of the simulation PMEK calculates the amount of sediment trying to settle at each element.

$$S_{tts} = S_{ptts} + S_{ms} + S_{fs} \quad 7.2$$

S_{tts}=sediment trying to settle
S_{ptts}=sediment trying to settle that did not settle in the previous model iteration
S_{ms}=marine sediment
S_{fs}=fluvially derived sediment

In reality the marine sediment (S_{ms}) will be a combination of both biogenic, aeolianaly derived, and fluvially derived sediment. For modelling purposes this sediment 'appears' at each submarine ($H_w > 0$) element of the model in a fixed amount each iteration.

The fluvially derived sediment (S_{fs}) is added at the edge of the modelled area also in a fixed amount each iteration. In this study this happens in two places and in two amounts, these represent the Nile point source and along the terrestrial margin.

As may be inferred by the presence of S_{ptts} in equation 7.2 not all the sediment settles each iteration:

$$S_s = S_{tts} \cdot F_s \cdot F_{wd} \cdot F_f \quad 7.3$$

S_s=amount of sediment settling this iteration
F_s=slope factor
F_{wd}=water depth factor
F_f=fining factor

The angle of repose (AOR) refers to the steepest angle that a slope of loose material remains stable. The critical AOR (*AORc*) is defined here as the proportion of the AOR below which the

slope of the sediment does not affect the amount of sediment settling. Where the slope of the sediment is greater than the *AORc* and the slope is away from the element the slope factor is calculated as:

$$F_s = 1 - \left(\frac{AORr - AORc}{1 - AORc}\right)^2 \quad 7.4$$

Where the slope is greater than the AOR no sedimentation is permitted (F_s is zero).

AORr is the AOR ratio; the ratio between the change in sediment height that would result in the AOR being reached on a level surface and the change in sediment height at the subject point. This is defined as:

$$AORr = \frac{\Delta S_e}{\tan(AOR) \cdot X} \quad 7.5$$

S_e=sediment elevation

With the discussed limits equation 7.4 produces the curve shown in Figure 7.9.

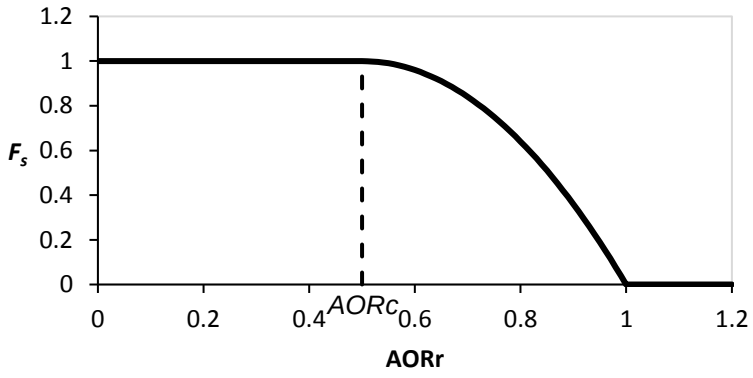

Figure 7.9-Graph showing the relationship between the AOR ratio (*AORr*) and slope factor (F_s) when *AORc*=0.5. The dashed line represents *AORc*.

The water depth factor is calculated as:

$$F_{wd} = \left(\frac{H_w}{CD}\right)^3 \quad 7.6$$

H_w=water depth
CD=critical depth

The CD is set to a value that represents the maximum depth affected by river processes. F_{wd} is capped at 1. This produces the curve shown in Figure 7.10.

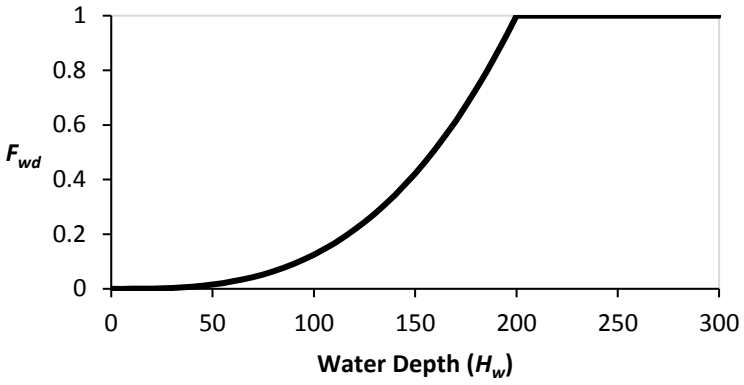

Figure 7.10-Graph showing the relationship between the water depth (H_w) and the water depth factor (F_{wd}).

The fining factor is calculated as:

$$F_f = \frac{1}{\sqrt{CS}} \tag{7.7}$$

CS=distance to the closest sediment source

This simulates the fining of sediment the further from the source. This method does not take into account the effect progradation of deltas will have in extending the transport distance of higher energy fluvial systems and their ability to transport larger sediment particles, but it is a lot less computationally expensive than doing so and produces reasonably geologically realistic results.

Sediment that has not settled ($S_{tts} - S_s$) is then distributed according to the slope of the surrounding sediments and the water depth. The greater the sediment slope away more sediment will be transported in that direction and the greater the water depth the less difference sediment slope makes. The amount of sediment going in each direction is calculated according to a slope transport multiplier. This multiplier is calculated as show in equation 7.8.

$$T_s = 1 + \frac{T_{sl}}{1 + \frac{H_w}{X}} \tag{7.8}$$

T_s=Sediment transport multiplier
T_{sl}=Slope transport multiplier

The resolution of the model is incorporated into this equation as the larger the resolution of the model the larger the effect of a given slope (in a given water depth) over the distance of the resolution of the model. This is because the larger the resolution the larger the drop in height for a given resolution.

The slope transport multiplier is the cube of *AORr* capped where the slope is greater than the AOR ($|AORr| > 1$). This produces the graph shown in Figure 7.11.

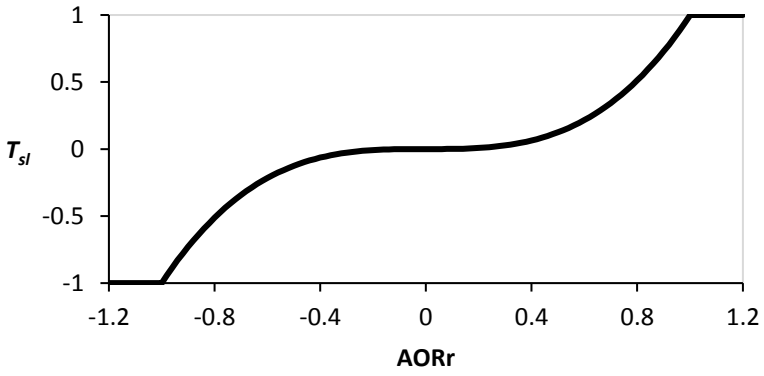

Figure 7.11-Graph showing how sediment slope (*AORr*) corresponds to sediment transport (*Ts*). Positive and negative AORrs correspond to slopes going down and up respectively.

It may be observed that some sediment transport occurs up slope ($1 + T_{sl}$ in equation 7.8). This spreads un-settled sediment out, simulating processes like sediment erosion, changing river paths and sediment transport in the marine water column. Thus it aids production of geologically reasonable outputs. This method was selected over inclusion of additional 'realistic' sediment transport processes (e.g. Gvirtzman et al., 2014) as it is significantly less computationally expensive.

Changes in sediment and evaporite height are taken into account in the calculations of the next iteration.

7.2.3 Sediment Strength

As the simulated sediment overburden deforms by vertical shear, and preferential evacuation of salt will occur where there is more overburden, a feedback loop can occur where some elements undergo significant overburden subsidence and adjacent elements undergo significant overburden uplift. This section details how PMEK simulates sediment strength in order to avoid this feedback loop, up to a certain point until faulting is simulated to have occurred.

P_{eff}, the variable driving salt flux, at a given element in PMEK is calculated as a combination of geostatic pressure and pressures that are transmitted via the internal strength of the sediment overburden. This is demonstrated in equations 7.9-7.14. Thicknesses and heights of sediment and water refer to the points halfway between elements, in order to take account of changes in these mediums.

$$P_{eff} = P_{geo} + P_{tra} \quad 7.9$$

P_{geo}=geostatic pressure
P_{tra}=pressure transferred laterally via sediment strength

$$P_{geo} = g \cdot (H_w \cdot \rho_w + T_s \cdot \rho_s) \quad 7.10$$

H_w=height of water column
ρ_w=density of water

T_s=thickness of sediment
ρ_s=density of sediment

$$P_{tra} = DA \cdot \mu_c \cdot \left(P_{geo} + \Delta P_{geo}\right) \quad 7.11$$

DA =displacement area
μ_c=shear modulus constant

The shear modulus constant (μ_c) is a multiplier used to calculate a useable value for the lateral transmission of forces from the pressure the sediment is under and the amount of offset between elements. This value is derived by trial and error. Using calculations based on shear moduli are invalid as the sediments are plastically deforming.

The displacement area (DA) is the sum of the sediment thicknesses deposited in previous iterations multiplied by the amount they have been offset:

$$DA = \sum_{i=1}^{n} Ts_i \cdot (Es_i - Es_{n-1}) \quad 7.12$$

Ts_i=thickness of sediment deposited in the ith iteration
Es_i=elevation of the base of the sediment in ith iteration
Es_{n-1}=elevation of the base of the sediment in the last iteration

In order to reduce the computational cost of calculating this variable the following method is used:

$$DA = DA_p + Ts_p \cdot \Delta Fe_p \quad 7.13$$

DA_p=displacement area from previous iteration
Ts_p=thickness of sediment from the previous iteration
Fe_p=evaporite flux from the previous iteration
This means that PMEK only needs to keep track of variables from one previous iteration.

If P_{tra} is greater than the shear strength of the sediment, then faulting is considered to have occurred. Sediment (shear) strength is defined according to the Mohr-Coulomb failure criterion:

$$\tau = \tan(\varphi) \cdot \left(\sigma - P_{pf}\right) + c \quad 7.14$$

τ=shear strength
φ=slope of the failure envelope
σ=normal stress
P_{pf}=pore fluid pressure
c=cohesion

As this criterion is a straight line σ may be approximated as the geostatic pressure half way through the sediment volume.

If faulted, then the lateral pressure transfer is set to zero. Although real faults do transmit some force, for the qualitative purposes of the simulation it produces geologically reasonable results.

7.3 Simulation Inputs

Various input values were required in order to construct the simulation. These include values for the equations detailed in the previous section, and the geometries of the salt body.

7.3.1 Variables

Table 10 shows single value inputs used by PMEK during simulations for this study. Sea level was assumed to be constant.

Parameter	Value	Source
Simulated time	5.3 Myr	Approximate age of Zanclean flooding (Section 2.5.4)
Seawater density	1024 kg/m³	Price et al. (1993, see note 5)
Sediment density	2400 kg/m³	Bar et al. (2013)
Marine sediment deposition	0.08 mm/year	calculated from overburden thickness
Nile sediment input	28 km³/year	calculated from the isopach of Nile Cone sediment
Angle of repose of sediments	6°	observed from bathymetry
Salt viscosity	10^{21} Pa·s	Wagner (2010)
Salt density	2165 kg/m³	Ellis and Singer (2007)
AORc	0.1	Produced geologically realistic results in testing (Section 7.2.2)
Critical depth (CD)	200 m	
Angle of internal friction (φ)	30°	Koloski et al. (1989)

Table 10-Table showing input values used by PMEK during simulations for this study.

The salt within the Levantine Basin is understood to be almost pure halite, albeit with internal claystone horizons (Feng et al., 2016). The seismic character of the MSC salt interval in the Levantine Basin has relatively little variation (Section 3.7.1) the salt properties were modelled as constant. The seismic character of the salt changes in the deep Herodotus Basin, however as the focus of the modelling is elsewhere this is relatively inconsequential.

Marine sediment deposition was approximated from the ~400 m of sediment deposited above the MSC salt in the ~5 Ma since the MSC. This simulates the lighter fluvially derived and biogenic sediments that are deposited away from the continental margins.

$$\frac{400\ m}{5 \times 10^6\ yrs} = 8 \times 10^{-5}\ m/yr = 0.8\ mm/yr \qquad 7.15$$

The volume of post-MSC Nile Cone sediment is estimated from seismic data as ~ 1.4E14 m³. This estimate is calculated from the area defined by the foot of the Nile Cone slope. This approximates to $28 \times 10^6\ m^3/yr$ of Nile derived sediment being deposited in the basin.

$$\frac{14 \times 10^{13}\ m^3}{5 \times 10^6\ yrs} = 28 \times 10^6\ m^3/yr \qquad 7.16$$

The area to be simulated was selected on the basis of its proximity to the ESM moat and factors that may potentially affect the halokinesis at the moat. The area is shown in Figure 7.12 and includes:

- The full ESM moat.
- All the massive MSC evaporites in the Northern and Southern Levantine Basin.
- Most of the Nile Cone.
- The portion of the Herodotus Basin adjacent to the ESM.

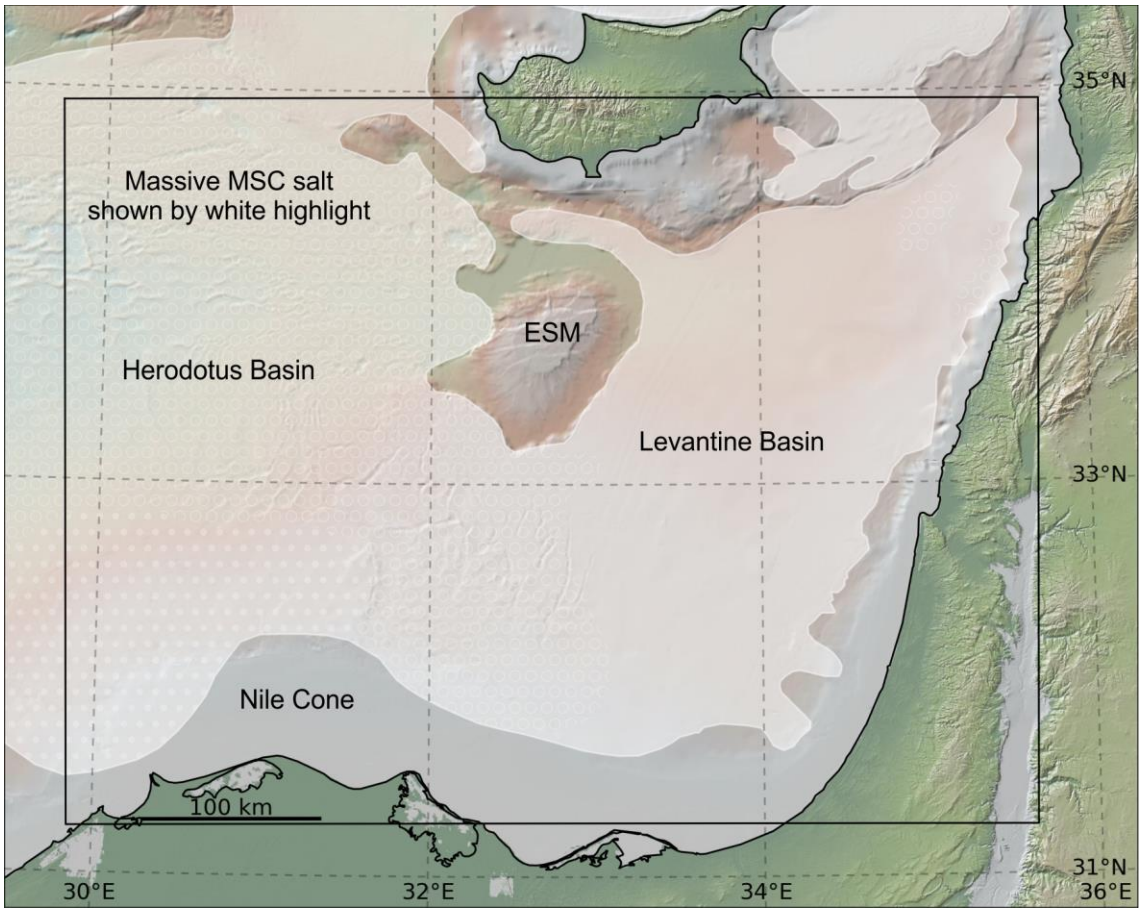

Figure 7.12-Map showing the location of the modelled area, with features potentially effecting the formation of the moat shown. The global relief (Ryan et al., 2009) vertical scale is shown on Figure 1.1 and the supplementary figure.

The model inputs required grids of the pre-halokinetic geometry of the salt body, and post MSC subsidence. These surfaces are calculated from the seismic data available to this study published maps of the Base MSC surface and salt isopachs over the Nile Cone (Allen et al., 2016). To obtain approximations of the true geometries of the Base MSC depth conversion was carried out. This depth conversion used the same velocity constraints as the 'typical' depth conversion detailed in Section 6.4.1, and is consistent with PSDM and well data. In order to calculate the pre-halokinetic geometry of the salt body the post-MSC subsidence was required, detailed in Section 7.3.2. Finally, the pre-halokinetic salt body and the underlying surface used in the simulations is shown in Section 7.3.3.

7.3.2 Subsidence

The pre-kinematic extent and depth (disregarding subsidence) of the salt body may be observed from the location of remnant salt rollers at the landward salt body margins, and the 'foot' of the salt body beneath the moat. The PSDM seismic lines available to this study and published constraints in depth permitted construction of the surface shown in Figure 7.13 which approximates the amount of relative subsidence that has occurred in the modelled area since the EMR. The shallowest subsidence constraint, the most landward salt rollers on the Levantine margin at 2000 m depth, is the datum for this relative subsidence. The absolute subsidence values will be larger than this as there will be subsidence on the margin, but this is inconsequential for the purposes of the model.

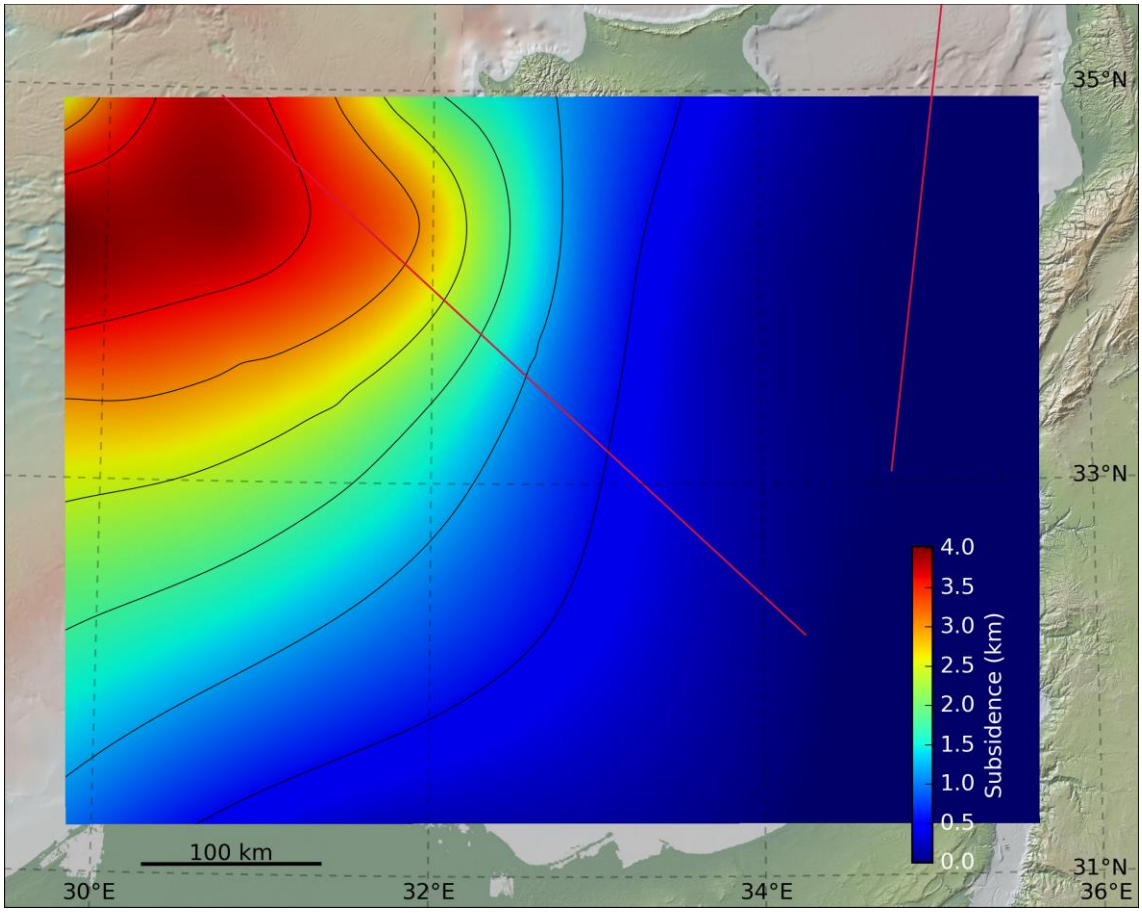

Figure 7.13-Map of the subsidence used in the simulation of the EMR. The global relief (Ryan et al., 2009) vertical scale is shown on Figure 1.1 and the supplementary figure.

Several basin modelling studies exist offshore Israel, but these rely on, and are focused around, well data close to the continental margin (Bar et al., 2013; Daher et al., 2015; Fattah et al., 2014; Gvirtzman et al., 2014; Tibor and Ben-Avraham, 2005). Consequently, they provide little constraint on the post-MSC subsidence in the farshore EMR. Their results are however compatible with those shown in Figure 7.13.

In the area of the Herodotus basin sufficient subsidence was assumed such that the pre-kinematic salt thickness (assuming salt deposition up to 2000 m depth) was slightly lower than the minimum thickness observed in the centre of the basin today. This is a highly uncertain constraint for the

Herodotus basin. However, as most of the moat borders the Levantine basin side of the ESM, constraints on the pre-kinematic geometry of the Levantine basin salt are the key inputs for this investigation. The Herodotus Basin was retained in the model as it provides more accurate edge values than a border to the simulation.

Investigation into the ESM revealed that significant subsidence had occurred on the flanks of the seamount carbonate platform relative to the summit. This was not incorporated into the subsidence model here, as the geometry of the summit of the seamount is inconsequential to the simulation output.

Some subsidence calculations have been made of the isostatic response of the events of the MSC, but low resolution inputs and a maximum evaporite are used which result in an inaccurate salt body geometry in the EMR (Govers et al., 2009). Consequently, these calculations are not used here.

7.3.3 Pre-Halokinetic Salt Distribution

The surface representing the base of the salt body where the salt body exists, and the MSC unconformities where the salt body is absent, was the base for the simulated salt body. This base of salt body surface is termed the Base Salt surface. The version of this surface used in the simulation underwent significant smoothing, in order to remove depth conversion errors in diapiric areas (Figure 7.14). It also results in less chaotic simulated halokinesis.

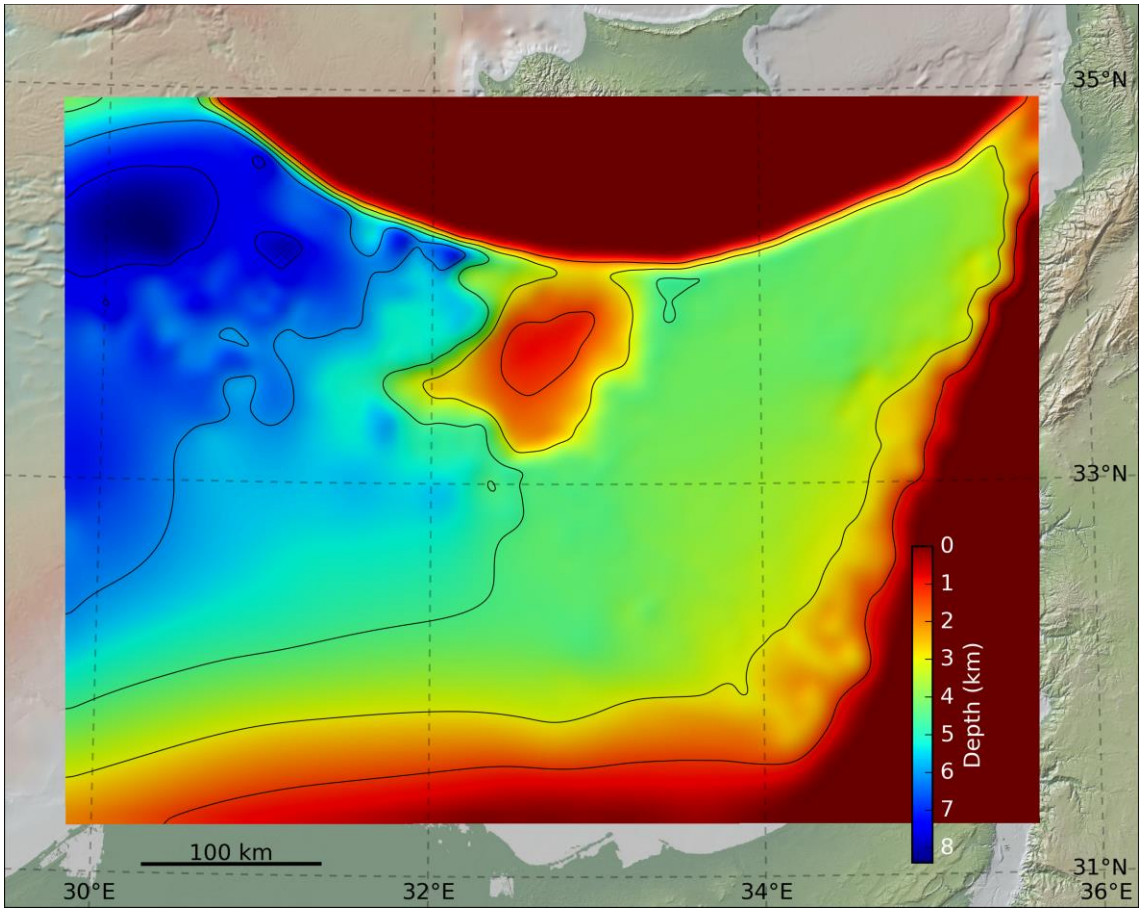

Figure 7.14-Surface representing the base of the MSC sequence used in PMEK simulations. The global relief (Ryan et al., 2009) vertical scale is shown on Figure 1.1 and the supplementary figure.

The location of the ‘tip’ of the salt body around the EMS margins provides a maximum estimate for the pre-halokinetic extent of the salt body. This may be assumed because this ‘tip’ is the downslope end of the salt body. Whether the MSC salt was deposited at a constant depth or at a constant thickness is debated (Govers et al. 2009). However, assuming either scenario results in the same configuration of pre-kinematic salt: a salt body that slopes into the centre of the Herodotus basin.

Consequently, generating the grid of salt thicknesses required subtracting the subsidence from the Base Salt surface, and filling the depressions in the resulting surface up to the elevation of the most landward salt rollers. The resulting pre-halokinetic salt body geometry is termed the Salt Height surface (Figure 7.15A). Comparison with the current evaporite body isopach demonstrates this simulated salt body is reasonable, although there are some differences (Figure 7.15B). Foremost among these is the reduced thickness of salt in the Herodotus Basin. This reduced thickness was chosen as thicker bodies of evaporites require longer computation times. As this portion of the evaporite body is away from the location of the moat, and is downslope of it, there will be negligible impact on the moats formation. Not simulating this portion of the model would have decreased the realism of the simulation, as evaporites evacuated from upslope require a destination. There are numerous small scale uncertainties concerning the pre-kinematic geometry of the salt. However, the qualitative function of the PMEK means that the approximation achieved is sufficient for the purposes of the model.

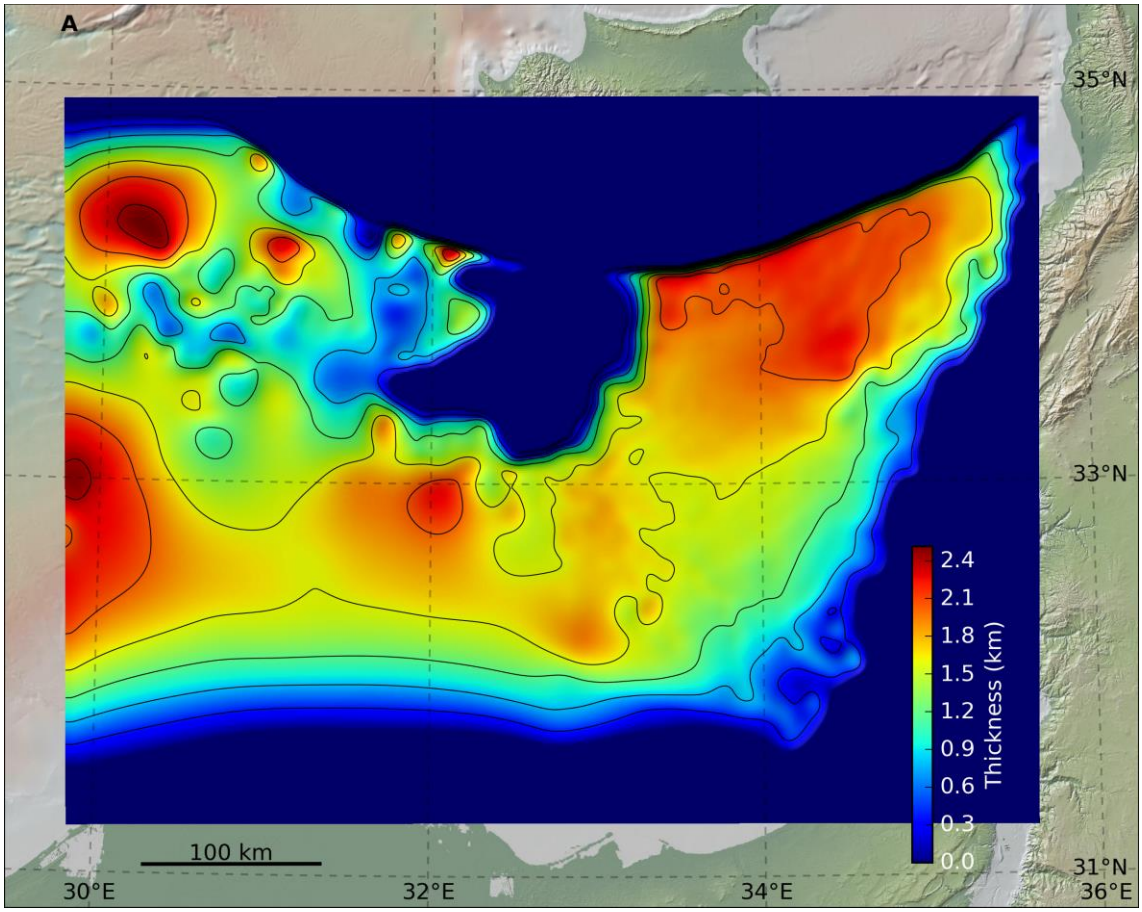

Figure 7.15-A) Isochore used in PMEK simulations representing the thickness of the salt body; B) isochore in time of the evaporite body as interpreted in the seismic data available to this study. The

global relief (Ryan et al., 2009) vertical scale on the maps is shown on Figure 1.1 and the supplementary figure.

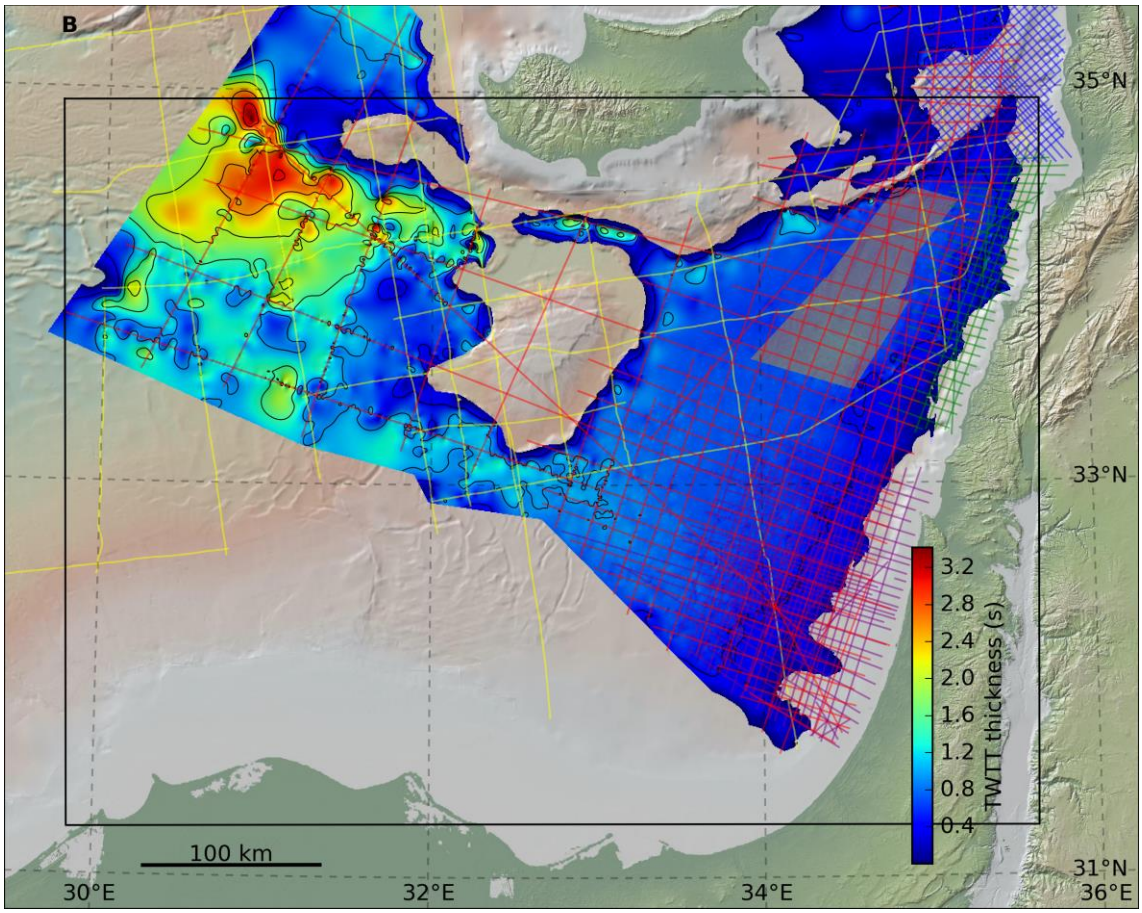

7.4 Sensitivity Analysis

The following figures show the results of the sensitivity analysis carried out for PMEK. As might be expected, the simulated evaporite viscosity is the key control on evaporite flow. It may be observed that higher viscosities resulted in an evaporite body the top of which was less level away from contrasting overburden thicknesses, and more level beneath contrasting overburden thicknesses (Figure 7.16A, B). This is geologically unrealistic based on what may be observed from seismic data in the EMR. Simulated viscosities at the lower end of those tested resulted in reductions in the elevation change across the simulated moat (Figure 7.16A, B). This occurs as evaporites intrude beneath where the moat would have otherwise formed. This does not happen at higher viscosities, as there is time for preferential deposition of sediment within the proto-moat to restrict intrusion of underlying evaporites. Consequently, a simulated evaporite viscosity of 1.8×10^{21} Ps was selected as a middle ground.

It may be observed that without simulation of sediment strength, vertical block motion occurs in areas with thicker sediments (Figure 7.16C). This affirms the necessity of including this mechanism in the simulation. Simulated instantaneous subsidence at the start of the simulation enhances the formation of the moat (Figure 7.16A, D). Instantaneous subsidence is unrealistic, so a subsidence curve where the rate of subsidence drops off was selected (Figure 7.16E)

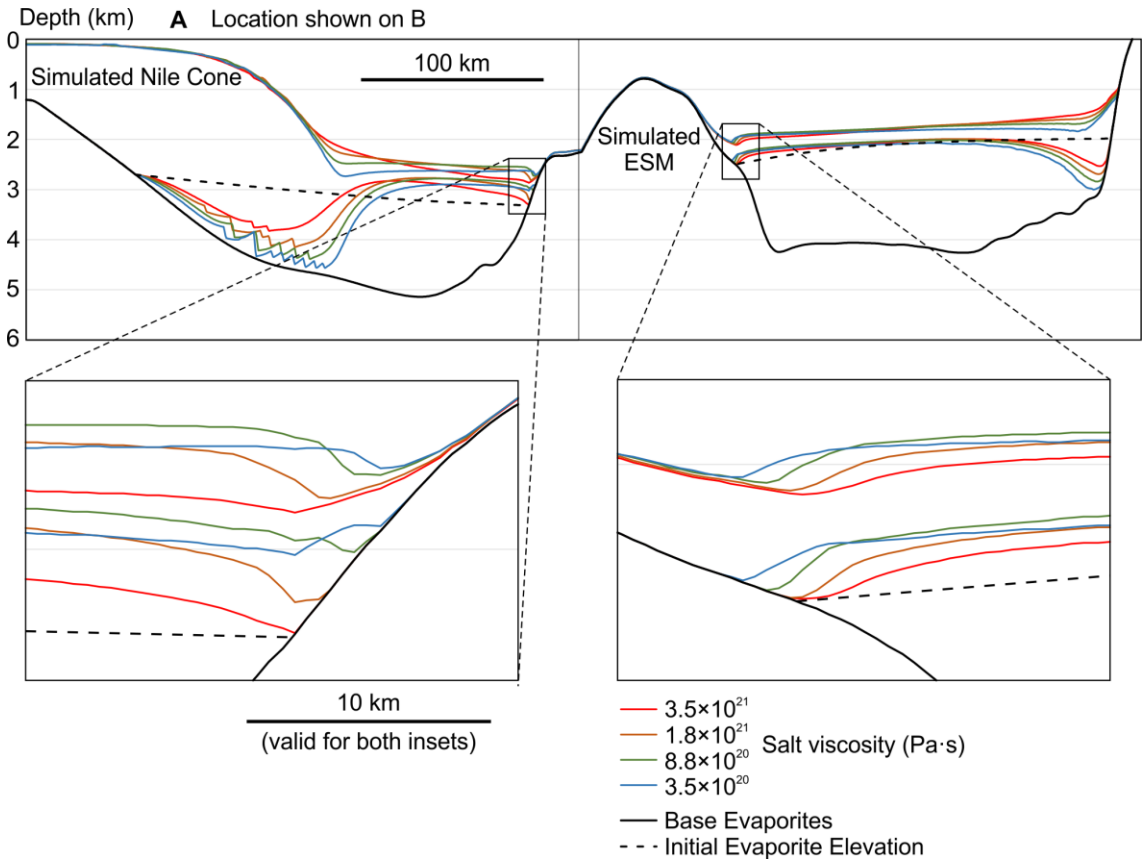

Figure 7.16-Simulation outputs illustrating points of the sensitivity analysis discussed in the text.

B

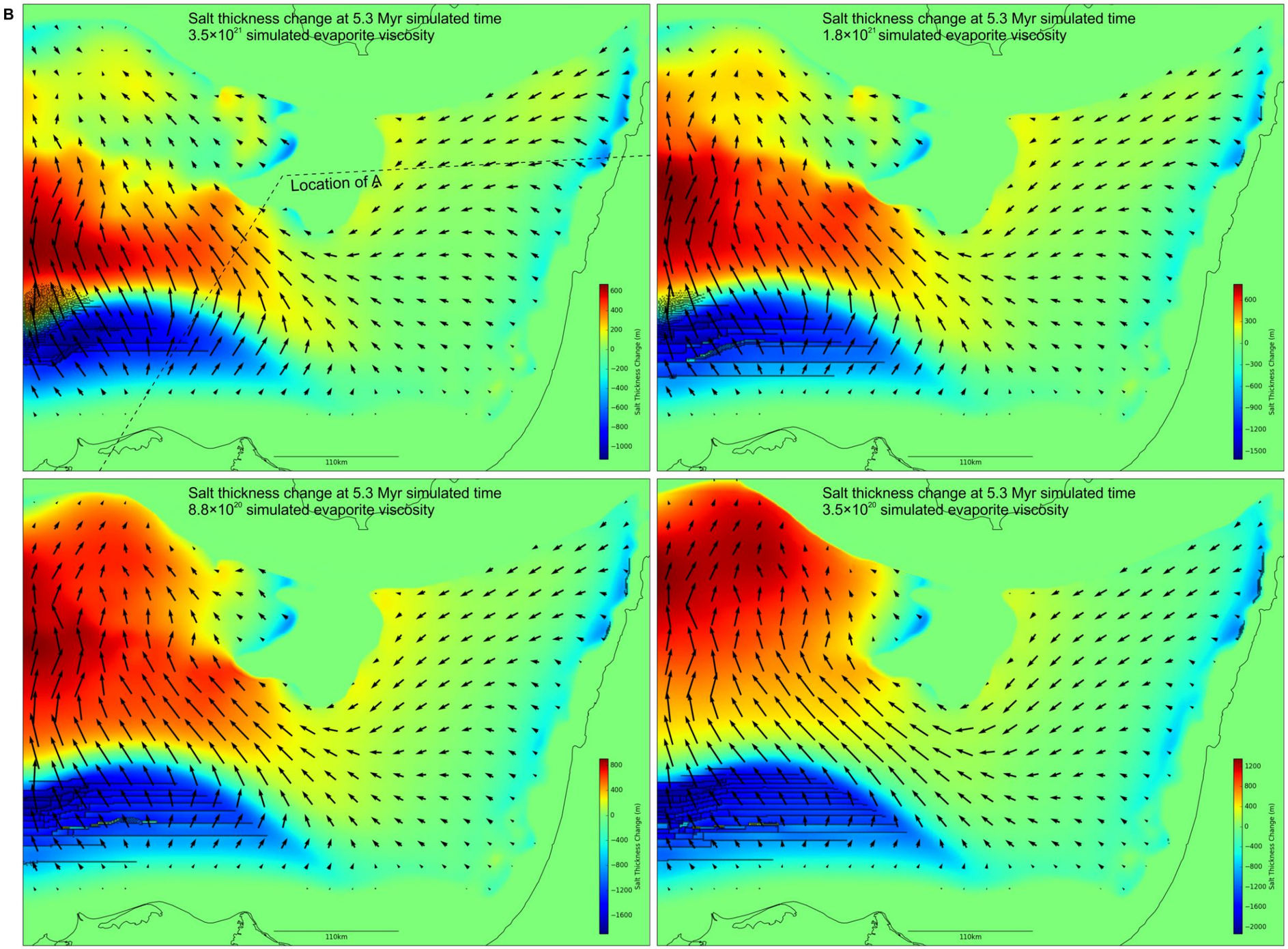
Salt thickness change at 5.3 Myr simulated time
3.5×10^21 simulated evaporite viscosity
Location of A
Salt Thickness Change (m)
600
400
200
0
−200
−400
−600
−800
−1000
110km
Salt thickness change at 5.3 Myr simulated time
1.8×10^21 simulated evaporite viscosity
Salt Thickness Change (m)
600
300
0
−300
−600
−900
−1200
−1500
110km
Salt thickness change at 5.3 Myr simulated time
8.8×10^20 simulated evaporite viscosity
Salt Thickness Change (m)
800
400
0
−400
−800
−1200
−1600
110km
Salt thickness change at 5.3 Myr simulated time
3.5×10^20 simulated evaporite viscosity
Salt Thickness Change (m)
1200
800
400
0
−400
−800
−1200
−1600
−2000
110km

C

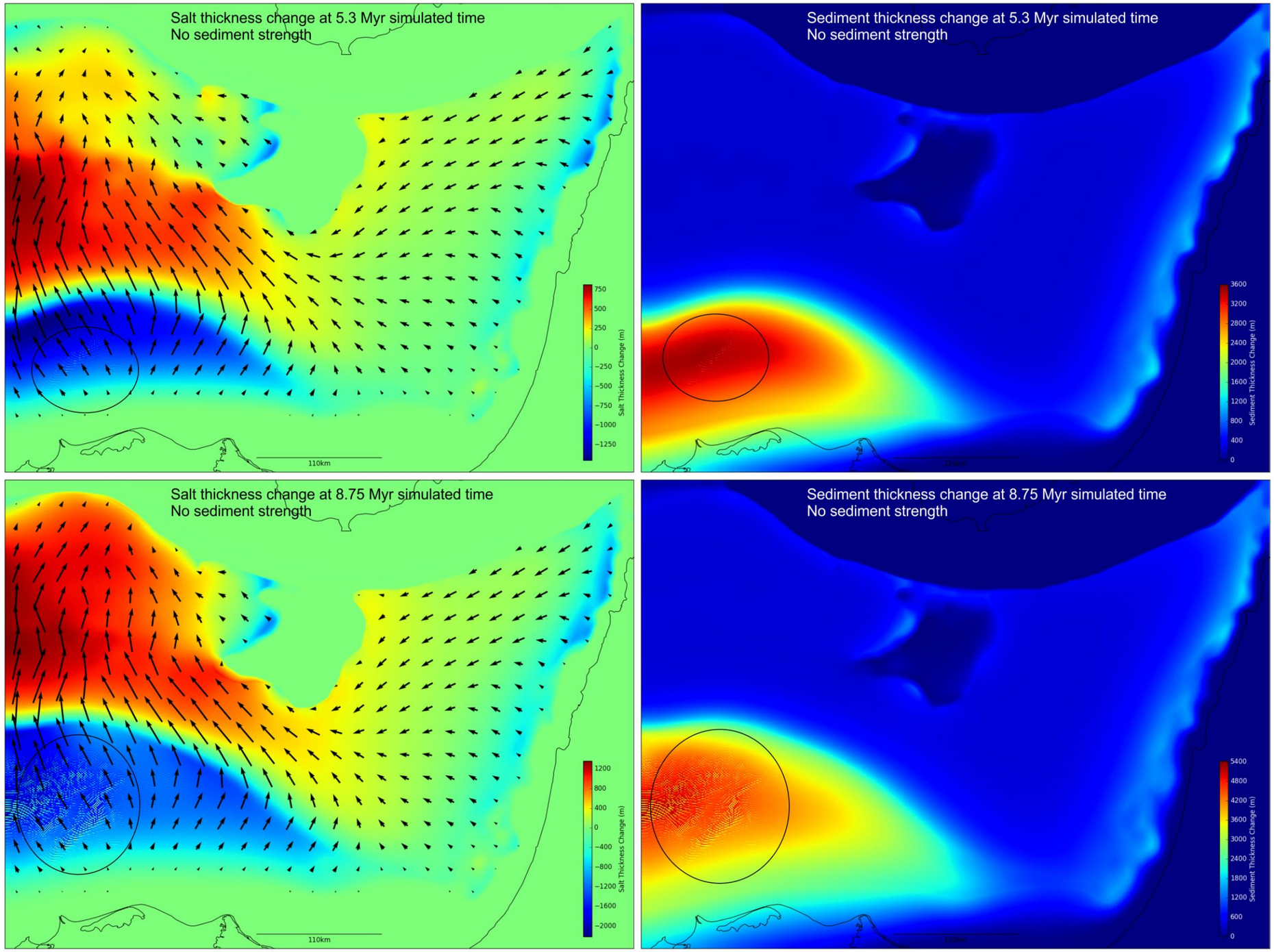
Salt thickness change at 5.3 Myr simulated time
No sediment strength
750
500
250
0
−250
−500
−750
−1000
−1250
Salt Thickness Change (m)
110km
Sediment thickness change at 5.3 Myr simulated time
No sediment strength
3600
3200
2800
2400
2000
1600
1200
800
400
0
Sediment Thickness Change (m)
Salt thickness change at 8.75 Myr simulated time
No sediment strength
1200
800
400
0
−400
−800
−1200
−1600
−2000
Salt Thickness Change (m)
110km
Sediment thickness change at 8.75 Myr simulated time
No sediment strength
5400
4800
4200
3600
3000
2400
1800
1200
600
0
Sediment Thickness Change (m)

D

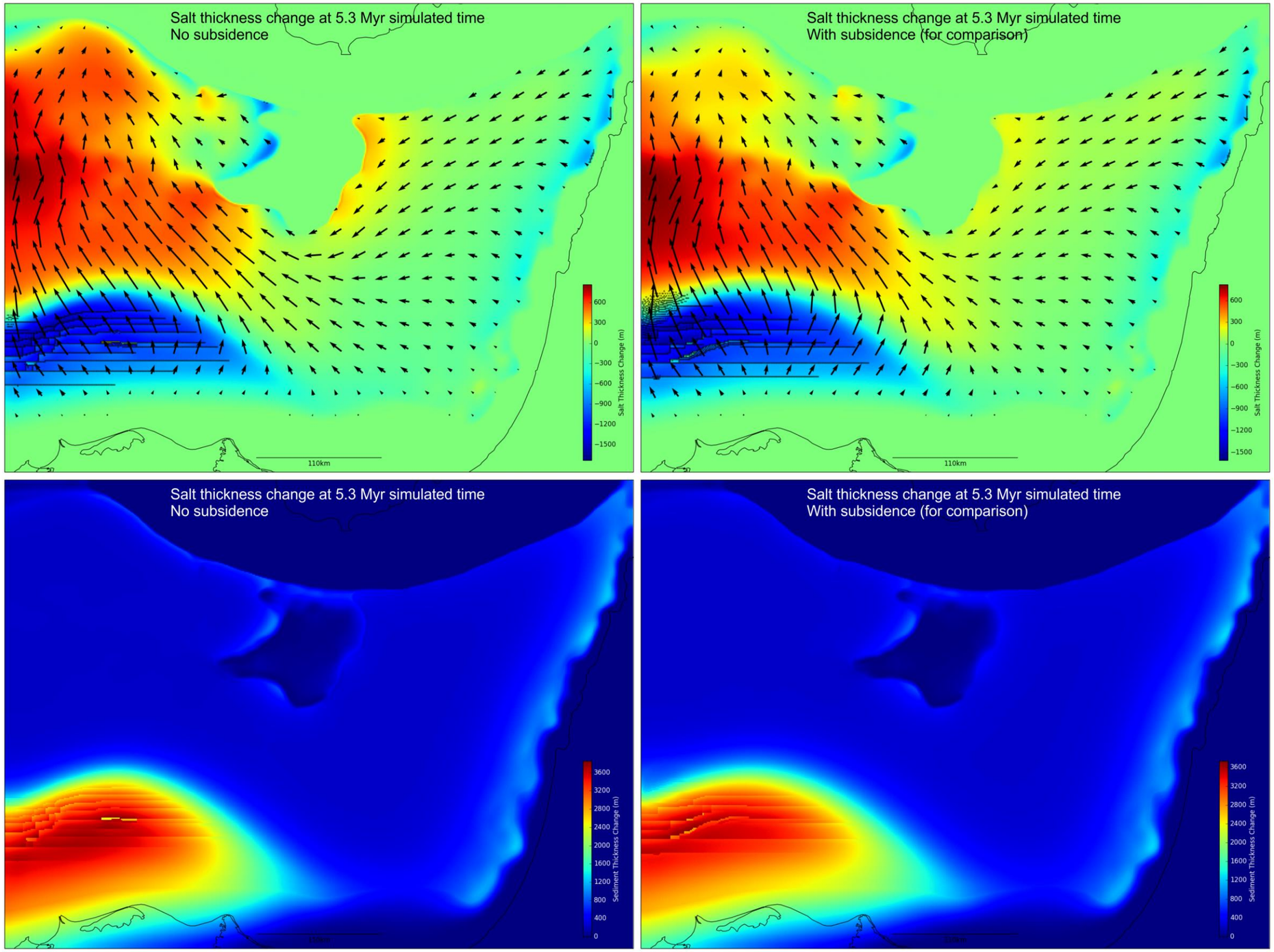
Salt thickness change at 5.3 Myr simulated time
No subsidence
Salt thickness change at 5.3 Myr simulated time
With subsidence (for comparison)
600
300
0
−300
−600
−900
−1200
−1500
Salt Thickness Change (m)
110km
Salt thickness change at 5.3 Myr simulated time
No subsidence
Salt thickness change at 5.3 Myr simulated time
With subsidence (for comparison)
3600
3200
2800
2400
2000
1600
1200
800
400
0
Sediment Thickness Change (m)

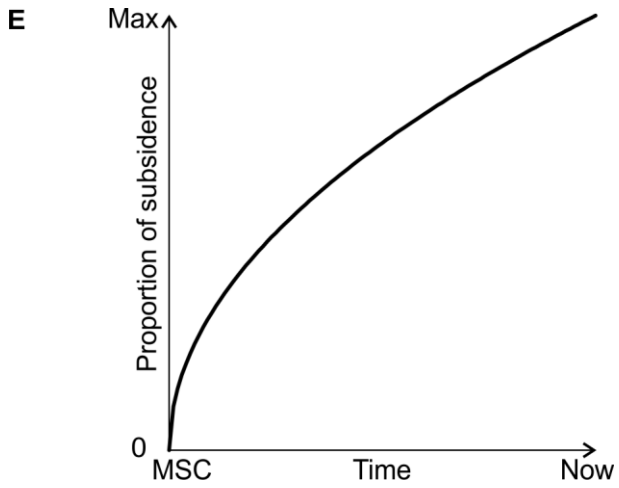

7.5 Results

Figure 7.17 shows simulated changes in salt and sediment thicknesses at the start and end of the model run. A build-up of evaporites around the flanks of the ESM may be observed from the start of the simulation, which gets progressively larger throughout the simulation. Sedimentation along the Levant Margin and under the Nile Cone may also be observed. Minor faulting is simulated at the Levantine Margin, and the Nile Cone faulting produces larger fault blocks. For the simulated fault blocks to have formed in the way they have, with some separation and following the curve of the Nile Cone requires the feedback between sediment strength, faulting and sedimentation to be operating in a way comparable to what may be observed in nature.

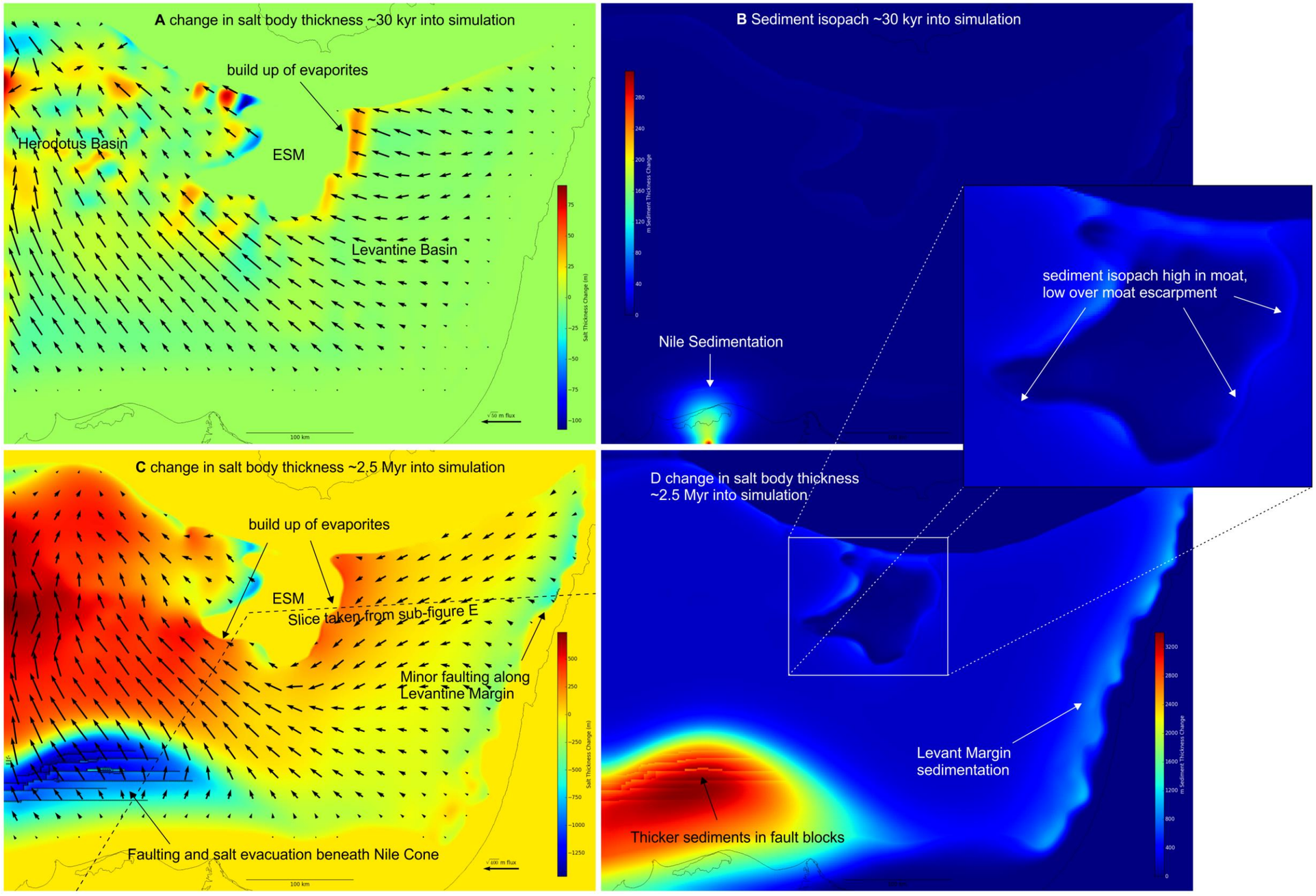

Figure 7.17-A-D) Model outputs at the start and end of the simulation, with features discussed in the text annotated. The arrows on A and C illustrate the direction of salt flux at the time of the model output. E) 3D visualisation of model output.

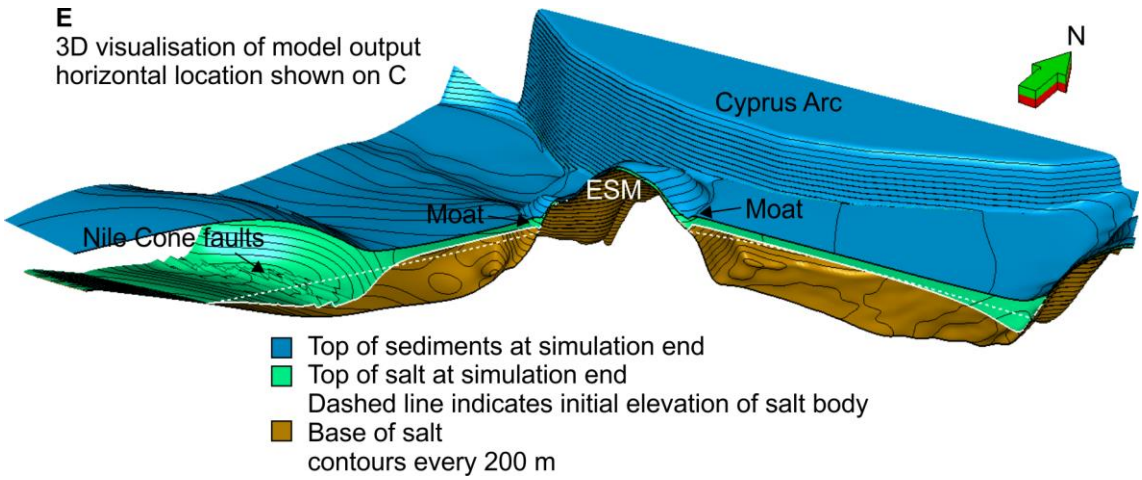

Initial salt fluxes in the Herodotus Basin contrast with those at the end of the simulation (Figure 7.17A, C). These changes occur as net salt movement from beneath the Nile Cone and Levantine Basin fill up the smaller scale depressions in the basin sediments, until the signal from the larger basin trends, the low in the Herodotus Basin, masks the other smaller scale signals.

In the Levantine Basin it may be observed that initial evaporite build up occurs along the ESM flank, before net evaporite height gain spreads out to cover more of the basin. This is an effect of interplay between reductions in salt flux at the edge of the evaporite body, and feedbacks keeping the top of the evaporite body level.

7.6 Discussion and Evaluation

The simulation outputs indicate that a moat around the EMS can be simulated to form from salt flux without lateral translation of overlying sediments. However, there are several issues with the numerical model inputs that introduce inaccuracies in the model outputs.

- The geometry of the initial evaporite body is uncertain.
- Subsidence, and the timing of subsidence, is poorly constrained.
- The viscosity of the evaporite body is only constrained to within a couple of orders of magnitude.

The lateral extent of the evaporite body is reasonably well constrained around the Levant Margin and ESM due to the coverage of the seismic data. However, depth conversion uncertainties, and a lack of data over the Nile Cone will have introduced inaccuracies in the pre-halokinetic salt body. These uncertainties will cause inaccuracies in the model outputs, but non-quantitative results will not be adversely effected. Access to data offshore Egypt could improve on this, however accurate depth conversion in areas with significant salt tectonics, such as between the Nile Cone and the ESM, is challenging and time consuming.

There are several changes that could be made to the numerical model in order to improve some of the uncertainties:

- Sediment densities based on compaction, and potentially calibrated by well data, could be used to generate more accurate overburden pressures. For example, where there is

thick overburden, such as the Nile Cone, the sediment will be denser and therefore cause more evacuation of underlying evaporites, for a given thickness of sediments.

- Modelling subsidence at its fullest extent is inaccurate. Further work to incorporate subsidence into the numerical model could help resolve this. However, this would require estimation and approximation of the subsidence curve in the modelled area. Without well data, typical estimates would have to be used.
- PMEK assumes Poiseuille flow within the salt (Figure 3b); thus salt flux drastically reduces where the salt body thins. This is consistent with the theoretical flow law, and aids formation of the ESM moat as it as the edge of the salt body, but means a salt weld (near zero thickness) is not achieved even under large sediment overburden. The focus of this investigation is at the downslope edge of the salt body, where Poiseuille flow results in a narrow zone of salt thinning, matching observations from seismic data (Figure 2). The upslope results are less geologically realistic (Figure 7.17E). Incorporation of salt 'block' motion could be simulated or approximated to aid resolution of this inaccuracy, but unless a proxy may be found this is likely a 3D pressure problem, which would require significant changes to the structure of the numerical model.
- Variations in sediment density and evaporite viscosity are not simulated. Vertical salt and sediment heterogeneities would also present a 3D problem, and would require a large amount of data in order to be accurately constrained in an area the size of which is involved in the formation of the ESM moat.
- The calculations undertaken to simulate sediment strength, and the effect of faulting, are approximations that appear to produce geologically reasonable results. Calculations that are mechanically more accurate could be undertaken that may produce more geologically realistic results.
- The moat produced by the numerical model is approximately half the amplitude of what may be observed in seismic data. This may be due to an overly high simulated evaporite viscosity. However, model limitations meant that decreasing the evaporite viscosity resulted in erroneously high salt fluxes in areas with thick salt. These large fluxes are the result of too much flux moving in a single iteration, such that on the next iteration the net flux is in the opposing direction. In nature, continuous as opposed to discrete time intervals means that feedbacks mediate this issue, but for numerical modelling the only solution is to reduce the simulated timestep. This means increasing the computation time. The practical time limitations of this study means this has not been carried out here, but further work to carry out the longer computations, or further refinement of the model to reduce computation time by other methods, could aid resolution of this issue. Another alternative for the reduced simulated moat size is that lateral translation of the sediment overburden may have thickened the sediment sequence adjacent to the moat, restricting intrusion of salt under the moat. Combined with more mobile salt, this would enhance the relief of the simulated moat. This last option is the favoured conclusion of this study with regards to the premise of the modelling.

On the basis of the points discussed above, the results of this modelling are not valid for use in quantitative applications. However, for qualitative purposes, the results appear to be consistent with what may be observed in nature. This matches the precursor to PMEK:

“It is not the purpose of this research program to provide rigorously scaled models: given the vast uncertainty on halite viscosity and flow laws at depth over geological timescales, predictive scaling adds little value. Instead, the purpose is to create models that appear realistic in form and evolution; the more closely they resemble real structures, the more likely it is that their evolution is applicable to natural examples, and the more value we can derive from this approach” (Peel, 2014).

The components of the results that are demonstrably inaccurate may be improved with further refinement of the numerical model. Access to regionally distributed well data would significantly improve many of the uncertainties in the model inputs for this case study.

Chapter 8 Summary and Conclusions

8.1 Introduction

The majority of the conclusions of this study are dependent on, corroborate, and are self-consistent with other conclusions made by this study in different geographical locations. Thus, these conclusions cannot be made, or cannot be made with as much confidence, without the regional scale of both the dataset and remit of this study. Often where this study may have revised a conclusion drawn by a previous study, the conclusion of the previous study is at the same spatial scale as the data upon which it is based. These points highlight the importance of considering the regional context of a given conclusion, crucially at a scale larger than that of the conclusion. Data and data access limitations mean this is not always possible, and this is the case for some of the conclusions drawn by this study. Effort has been made to allow and account for this, but it is acknowledged that the confidence in some conclusions could be increased by a wider range of input information.

The following sub-sections describe:

8.2: An evaluation of the general methods of this study.

8.3: Suggested resolutions to some of the controversies outlined in Section 2.6.

8.4: Conclusions which hypothesise amendments to previously undisputed understanding.

8.5: A summary of observations previously undocumented in the literature available to this study.

8.6: A self-consistent summary of the evolution of the area, drawing together all the pertinent conclusions of this study.

8.7: Recommendations for further work.

8.2 Evaluation

Limited stratigraphic constraints from the minimal well data available to this study (Section 3.2.5) had several effects on the methods undertaken:

- Depth conversion was limited to parts of the seismic interpretations for which relatively reliable velocity data was available (Sections 5.6.1, 6.4.1 and 7.3.3). The limited velocity constraints meant only low resolution geometric changes to most the interpreted surfaces would have resulted from depth conversion of all the seismic data. The most obvious change that would have resulted from depth conversion of all the seismic data would be removal of pull-up caused by lateral velocity contrasts associated with the MSC evaporites (Section 3.2.5). Instead, pull-up was accounted for during interpretations by noting areas with contrasting thicknesses of MSC evaporites. These pull-ups are harder to observe on TWTT maps without an awareness of where overlying evaporites exist, so overlays of the limits of the salt bodies were included on pertinent surface maps in this study.

- Chronostratigraphic analysis was limited in its lithological detail (Figure 3.13).
- The ages assigned to many of the interpreted horizons, intervals and events outside the Levantine Basin are speculative (Table 6).

The coverage of the seismic data available to this study was key in selecting the focus of the study. Consequently, the level of detail in the pertinent figures and discussion is also linked to this coverage. Because of this, some geologically complex areas with limited seismic coverage, such as the Hellenic Arc and Isparta Angle to the NW of the EMR, are not documented as completely as other locations in the EMR. It is therefore possible that some errors in illustration or discussed context may be present in this document. All reasonable effort has been made to avoid this, but the wealth of available literature and complex and distinct geological history of the areas surrounding the EMR (Africa, Arabia, Turkey) means there is some scope for error.

Where multiple examples of a phenomenon exist in the seismic data the best example is presented. The use of best examples, as opposed to an average example, may infer that features described or mapped across multiple seismic lines are clearer than they actually are. Consequently, effort has been made to describe these uncertainties where they exist.

8.3 Controversy Resolution

By integrating interpretations of regional seismic data with critical analysis of pertinent literature, this study aims to enhance our understanding of the geological evolution of the EMR. The review of literature pertinent to the geological evolution of the EMR concluded by describing multiple large-scale controversies within the documented understanding of the area (Section 2.6):

A. The genesis of the Mesozoic Palmyride basin.
B. The direction of Mesozoic rifting in the EMR.
C. The age of sea floor spreading following the Mesozoic rifting.
D. The location of the COB in EMR.
E. The location of the Sinai Plate boundaries.
F. The timing of subduction at the Cyprus Arc.
G. How enigmatic late Miocene extension occurred in the Northern Levantine Basin.
H. The accommodation vector of missing displacement on the LSZ.
I. The timing of MSC evaporite deformation.
J. The timing of MSC erosion.

The preferred explanations for these controversies are outlined below. Critical review of literature has resulted in preferred explanations for controversies A and B. Interpretations of the seismic data available to this study combined with critical review of literature provided preferred explanations for controversies D, E and H. Original work in this thesis, interpretations of the seismic data available to this study and critical review of literature have provided preferred explanations for F, G, I and J.

A. Controversy over the genesis of the Palmyride Basin has arisen from a lack of observed basin bounding faults (Section 2.6.1). Other basins exist outside the EMR where shallow seismic data presents analogous geometries without bounding faults, but deeper seismic data reveals

the underlying faults (Section 2.6.1). This is likely the case in the Palmyride basin where the equivalent deeper seismic data do not exist. Collection and interpretation of such data would provide the most concrete resolution of this controversy.

B. The depth of the reflectors pertinent to the timing and location of the rift features in the EMR means that little new constraints were resolved on the direction of the Mesozoic rifting in the EMR. Based on publically available data, and critical evaluation of published analysis of these data, a NW rift direction appears to best fit available evidence, with gravity and seismic reflection data taking the primary role in this (Section 4.6). Collection and analysis of new refraction data could assist in resolving this controversy.

C. No new constraint could be resolved on the age of seafloor spreading beneath the Herodotus Basin, due mostly to the lack of well data dating the pertinent sediments. The relevant sediments are also in >2 km deep water, and overlain by c. 6 km of sediments, decreasing the likelihood that penetration of these sediments will be undertaken (Section 2.3.8).

D. On the basis of the same gravity data that aids definition of the direction of Mesozoic rifting in the EMR and recently published magnetic data (Granot, 2016), the COB is located according to the interpretation of Longacre et al. (2007); to the west of the ESM (Figure 4.12). This location is corroborated by speculative interpretations on seismic data (Section 4.5) and regional geological data (Figure 4.12).

E. The seismic data available to this study provides strong evidence against hypotheses for Sinai Plate boundaries extending north-eastward from the north end of the Gulf of Suez, and through the Levantine Basin (Section 4.3). A commonly drawn boundary, extending directly north from the end of the Gulf of Suez, crosses an onshore area with no documented rift deformation (Section 4.2). The only alternative boundary, extending west and then north of the Gulf of Suez via a set of faults for which the published documentation is limited, is therefore deemed the likely vector that accommodated most the relevant deformation (Section 4.4). Discussion of plate vectors concludes that the deformation along the northern portion of this western Sinai Plate boundary would have been small in relative magnitude and with a large, if not primary, component of transform motion (Section 4.5).

F. Largely undeformed Palaeogene sediments extending over the relic accretionary wedge at the southern edge of the Cyprus Arc demonstrates subduction ceased there in the latest Cretaceous and did not restart, in contrast to a pervasive older interpretation that assumes ongoing subduction at the southern edge of the Cyprus Arc (Section 5.8.1). This observation implies that the geometry of this relic subduction zone has remained largely unchanged during the Cenozoic. This constraint necessitates a major reconfiguration in the published understanding of the evolution of the area (Section 5.9). This is described in detail in the following section as other observations of seismic data become key in constructing this new tectonic evolution.

G. The most recent published hypothesis for the formation of the PKFs suggests lithological volumetric reduction normally associated with polygonal faulting was orientated by perpendicular compression (Section 6.4.6). However, the authors of this hypothesis discuss several caveats that suggest their conclusion is at least partially a result of the exclusion of possible alternatives (Ghalayini et al., 2016). The seismic data over the convergent boundary

of the Cyprus Arc reveals a hiatus in compression that is contemporaneous and proximal to these faults (Section 5.6). This introduces the possibility that regional tectonic extension has formed the PKFs. Analysis of the tectonic configuration during the PKFs formation suggest the formation of the LSZ adjacent to the PKFs could explain their formation (Section 6.6.1). A key uncertainty of this hypothesis is that the PKFs are layer bound despite the suggested tectonic extension. An underlying shale interval in which the PKFs detach is suggested to have partitioned brittle deformation above form more ductile deformation below (Section 6.6.8). There are some previously undocumented underlying sub-parallel normal faults, however they are not sufficiently well imaged on the seismic data available to this study to confidently constrain their timing in relation to the PKFs, although they may have accommodated at least some extension (Section 6.6.8).

H. The PKFs, and their association with the large scale transpressive system of the LSZ, suggests that they could accommodate at least part of the missing displacement on the northern segment of the LSZ (Section 2.6.8, 6.7). However, for this to be the case this would require rotation and extension of the intermediate continental crust.

I. Post MSC halokinesis is well documented (Section 2.5.4). Some studies have interpreted an episode of halokinetic deformation during the MSC (Bertoni and Cartwright, 2007; Gvirtzman et al., 2013; Hodgson, 2012), however a more recent study disputes this (Allen et al., 2016). Based on the 3D seismic volume available to this study, deformation of internal reflectors within the salt body defy explanation of a genesis that does not involve intra-MSC deformation (Section 3.7.1).

J. A channel eroded prior to the onset of MSC evaporite deposition exists in the Southern Levantine Basin (Section 3.6.5). The location of the channel in the deepest portions of the basin, and its continuity over 200 km, suggest that draw down did occur at the onset of the MSC (Figure 3.24).

Points D and E also corroborate the most recent interpretations on the crust-type distribution in the EMR, as shown in Figure 2.1.

8.4 Amendments to Published Understanding

The data set offshore Syria has provided an abundant source of new observations that necessitated the modification of the published understanding of the evolution of the area. Foremost among these is the assertion that subduction at the southern edge of the Cyprus Arc ceased in late Cretaceous (Section 5.8.1). Although this was originally observed by Bowman (2011) it is yet to be widely integrated into published literature.

The regional seismic data set and gridded 2D data offshore Lebanon and Syria permitted amendments to be made of the published limits of the MSC evaporites in these areas (Section 3.7). Regional seismic data also constrained the true depth of the MSC evaporites in the Herodotus Basin (Section 3.7.1).

The region documented as being affected by the late Miocene PKF extension event was extended in the Northern Levantine Basin based on the data available to this study (Section 6.2; Figure

6.2). Careful examination of seismic data also revealed equivalent strike early Miocene normal faults extending over much of the Southern Levantine Basin that were previously undocumented (Section 6.2). Timing analysis revealed that contemporaneous folding exists perpendicular to these normal faults in both the Southern and Northern Levantine Basin (Section 6.3). Regional scale interpretations allowed the distribution of fault throws to be linked with a mechanically weak underlying interval, as opposed to the thickness of the faulted sediment sequence as previously suggested (Ghalayini et al., 2016). Interpretations of the Cyprus Arc revealed a hiatus in the compression across this convergent plate boundary that coincides with the formation of the PKFs, leading to a new hypothesis for the formation of the PKFs that links to the shear system around the northward propagation of the LSZ (Section 6.6.1).

Based on the observations and discussions in Chapter 6, the Syrian Arc II event first termed as such by Walley (1998), can be attributed to the reconfiguration of plate stresses during the formation of the LSZ. The locus of compression shifted northwards in parallel with the propagating LSZ system. Previously interpreted as ending in the middle Miocene (Gardosh et al., 2008b), the late Miocene folding is postulated here to be a continuation of the Syrian Arc II event (Section 6.6.4), which would extend the duration of the event.

Many studies in the EMR have extrapolated trends based on limited or uncertain data. Inevitably, some of these trends are subsequently shown to be incorrect because of new information. Sometimes however, particular inaccuracies persist despite evidence to the contrary. This can occur for several reasons including limited circulation of amendments, poor incorporation of the amendments into an accessible form such as a summary figure, or incomplete integration of the amendment with other relevant information. Examples of this in the EMR include fault maps of the Nile Cone, with inaccuracies at the ESM demonstrated but still persisting, and regional scale maps selected for republication as basemaps despite numerous documented inaccuracies and updated alternatives. Regional scale data aids the critical assessment of these figures and identification of the inaccuracies.

The nomenclature used by published studies for bathymetric features between Cyprus and Syria is highly inconsistent (Table 8). Collation of the different nomenclatures and consideration of their pertinence provided a revised set of terminologies used in this study (Figure 5.2).

8.5 Summary of New Observations

Regional Scale Surfaces

Gridding of the interpretations of the regional coverage seismic data available to this study permitted generation of continuous regional scale horizons over the EMR (Figure 3.12). Such subsurface coverage of the EMR is unprecedented in published literature. These interpreted horizons, and the understanding of the geological evolution of the area that they permit, facilitated many of the conclusions drawn by this study. Their exceptional coverage allows for better integration of the conclusions within their geological environment. The regional scale also permits more extensive tracing of large features, such as the Base MSC channel in the Southern Levantine Basin (Figure 3.24).

The Eratosthenes Seamount Carbonate Platform

Few new insights have been documented regarding the ESM since the ODP drilling on the structure in the late '90s. Some studies have been published but limited imaging constrained new observations (Klimke and Ehrhardt, 2014; Montadert et al., 2014). The data set available to this study imaged features below the MSC unconformities on the ESM that permitted new observations to be drawn. The interpretation of these observations led to an updated evolution of the feature. Key in this new evolution were the implications of the summit plateau being an erosional as opposed to reefal feature (Section 3.6.6).

The ESM is often drawn as an ovoid on palaeoreconstruction diagrams, although more precise outlines exist in published literature (Section 3.6.6). Although its current bathymetric expression is ovoidal, seismic data and the uplift of Cyprus reveals the underlying carbonate platform includes embayments and promontories. It was not possible to trace the continuation of the carbonate platform underneath Cyprus, but given the uplift of Cyprus it likely extends further north than the limits of the seismic data available to this study and forms the lead indentor associated with this collision (Figure 3.25; Figure 3.26).

Evolution of the Eastern Cyprus Arc

Access to data offshore Syria permits the documentation of a series of new observations regarding the Palaeogene and Miocene evolution of the Cyprus Arc. They are summarised in the restoration of the region (Figure 6.32) but a key highlight is the observation of a punctuated hiatus in the compression across the eastern Cyprus Arc during the late Miocene. This hiatus was key in the formulation of a new hypothesis for the genesis of late normal faulting in the Levantine Basin (the PKFs).

Cessation of subduction at the southern edge of the Cyprus Arc in the Cretaceous means that this feature has been close to its current location during the Cenozoic. This requires a reconfiguration of plate models, a highlight of which is the formation of the northern edge of the Cyprus Arc. This is believed to have been a subduction zone on which subduction ceased in the Miocene (Section 5.9; Figure 2.24). A new hypothesis was required to explain how the northern edge of the Cyprus Arc geometry parallels that of the subduction zone at the southern edge of the Cyprus Arc. The hypothesis developed was that the relatively thickened crust behind a subduction zone could restrict subduction, thereby causing the orientation of one subduction zone to match that of another (Section 5.8.4).

Interpretation and collation of deformation styles observable in seismic data across the Cyprus Arc suggests a current convergence direction of ~345° (Sections 5.8.2 and 0).

Piano Key Faults

The early Miocene low throw normal faults in the Southern Levantine Basin that are hypothesised here to represent an earlier stage of the PKFs were previously undocumented. The hypothesis for the formation of the PKFs is based on observation of a hiatus in compression on the adjacent convergent plate boundary (Section 6.7). The relative size of vectors for accommodation of extension at depth remains uncertain.

Levant Ramp

The Levant Ramp, although named by Hodgson (2012) has not been formally described as a single entity. This may be due to the transection of the boundary between Israeli and Lebanese waters by the Levant Ramp. Consequently, workers focussing on national interests are not predisposed to resolve the feature as a whole. The description of this feature in this study (Section 3.6.4) is therefore original.

Herodotus Basin

The pre-MSC stratigraphy of the Herodotus Basin has only limited interpretations in published literature. Interpretations included in this study, such as 1) mapping of the base of the MSC interval, 2) speculative mapping of a Senonian age horizon, and 3) interpretations of possible COB rift faulting on seismic data, have no precedent known to this study (Section 3.6.7).

8.6 Tectonic Evolution of the EMR

The following figures aim to illustrate the understanding of the evolution of the EMR developed in this study, based on new insights provided by this study, and their integration with published studies of the area. The information on Figure 8.1A was collated from the preceding portions of this study and drawn here according to their grouped age. They were then isolated at key intervals, extrapolated where appropriate, and drawn as palinspastic sketches that highlight the relevant structural features and depositional environment of the time (Figure 8.1B-G). This also serves as a verification that each component illustrated is mutually compatible.

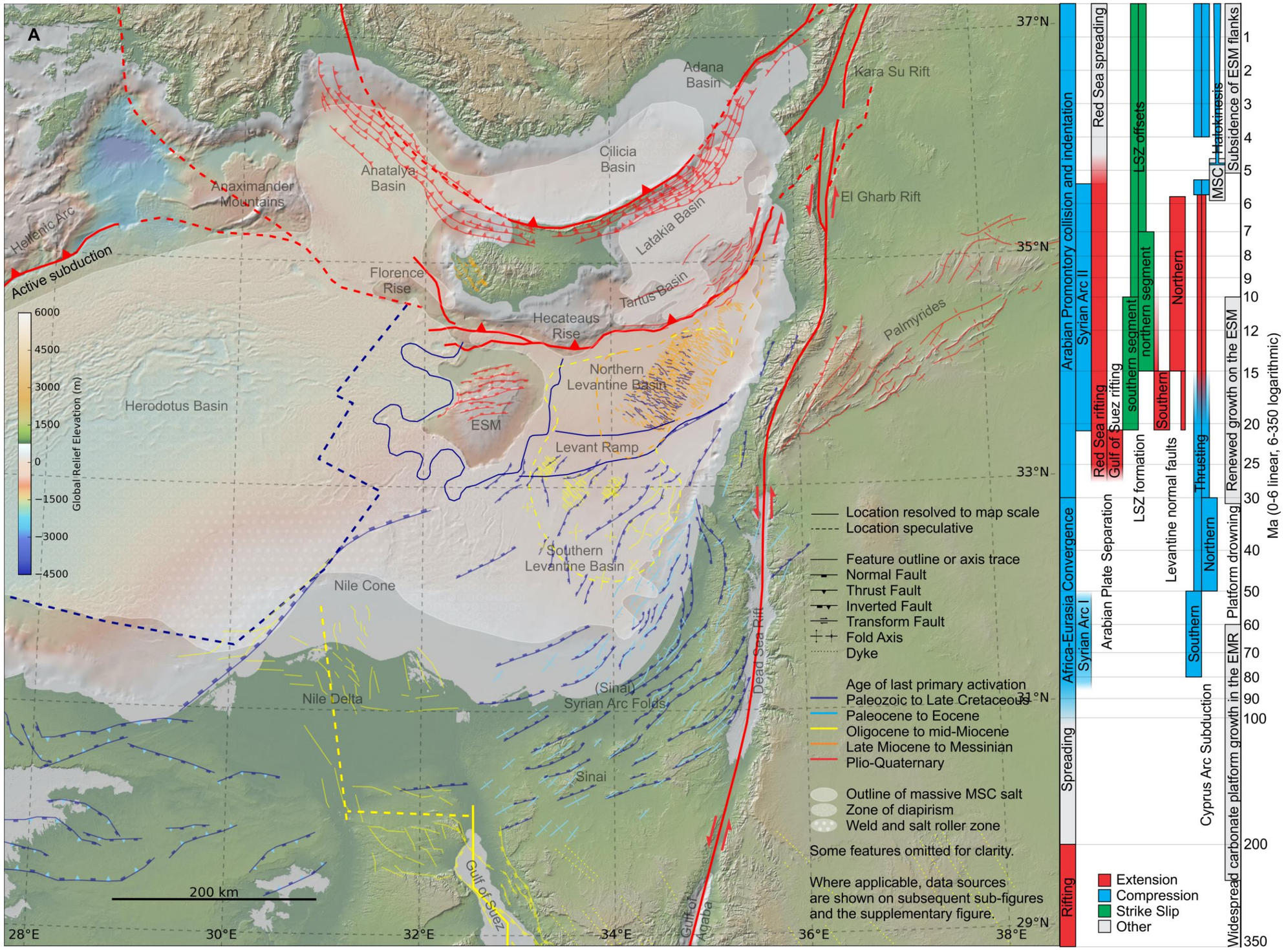

Figure 8.1-Summary of the tectonic evolution of the Easternmost Mediterranean. A) Map illustrating the location, age and nature of structural features in the region with a timeline of events; B-G, palinspastic sketches based on these structural features, the observations of seismic data, analysis and discussion described in this study, and integration of information in published literature. The colour of the feature indicates when it was last active, as opposed to when it formed. Please see sections 8.3, 8.4, and 8.5 for summaries of where this study has contributed to the understanding illustrated in this figure.

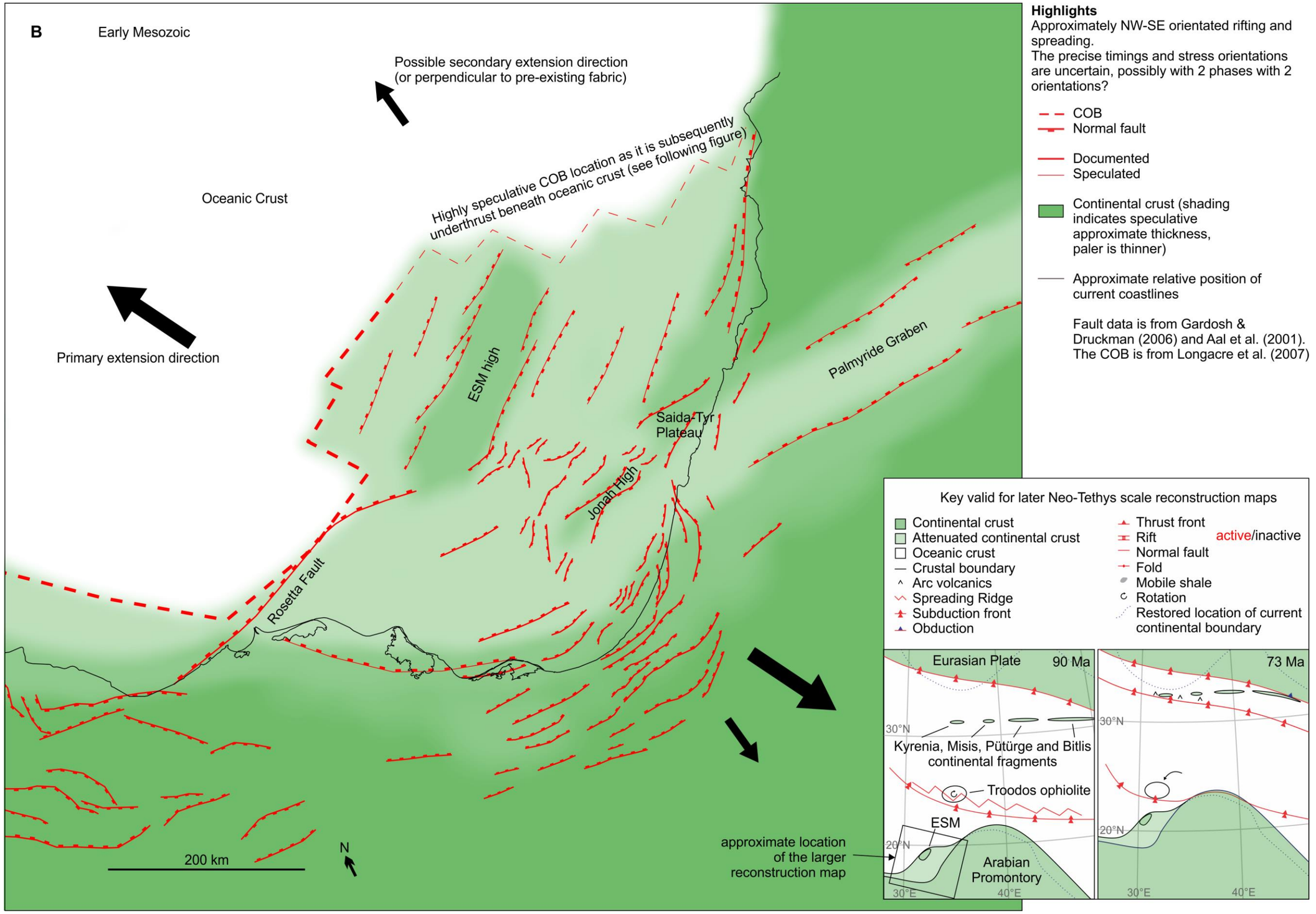
B
Early Mesozoic
Possible secondary extension direction
(or perpendicular to pre-existing fabric)
Oceanic Crust
Highly speculative COB location as it is subsequently underthrust beneath oceanic crust (see following figure)
Primary extension direction
ESM high
Saida-Tyr Plateau
Palmyride Graben
Jonah High
Rosetta Fault
200 km
N
Highlights
Approximately NW-SE orientated rifting and spreading.
The precise timings and stress orientations are uncertain, possibly with 2 phases with 2 orientations?
COB
Normal fault
Documented
Speculated
Continental crust (shading indicates speculative approximate thickness, paler is thinner)
Approximate relative position of current coastlines
Fault data is from Gardosh & Druckman (2006) and Aal et al. (2001). The COB is from Longacre et al. (2007)
Key valid for later Neo-Tethys scale reconstruction maps
Continental crust
Attenuated continental crust
Oceanic crust
Crustal boundary
Arc volcanics
Spreading Ridge
Subduction front
Obduction
Thrust front
Rift
active/inactive
Normal fault
Fold
Mobile shale
Rotation
Restored location of current continental boundary
approximate location of the larger reconstruction map
Eurasian Plate
90 Ma
73 Ma
30°N
20°N
30°E
40°E
Kyrenia, Misis, Pütürge and Bitlis continental fragments
Troodos ophiolite
ESM
Arabian Promontory

C End Cretaceous

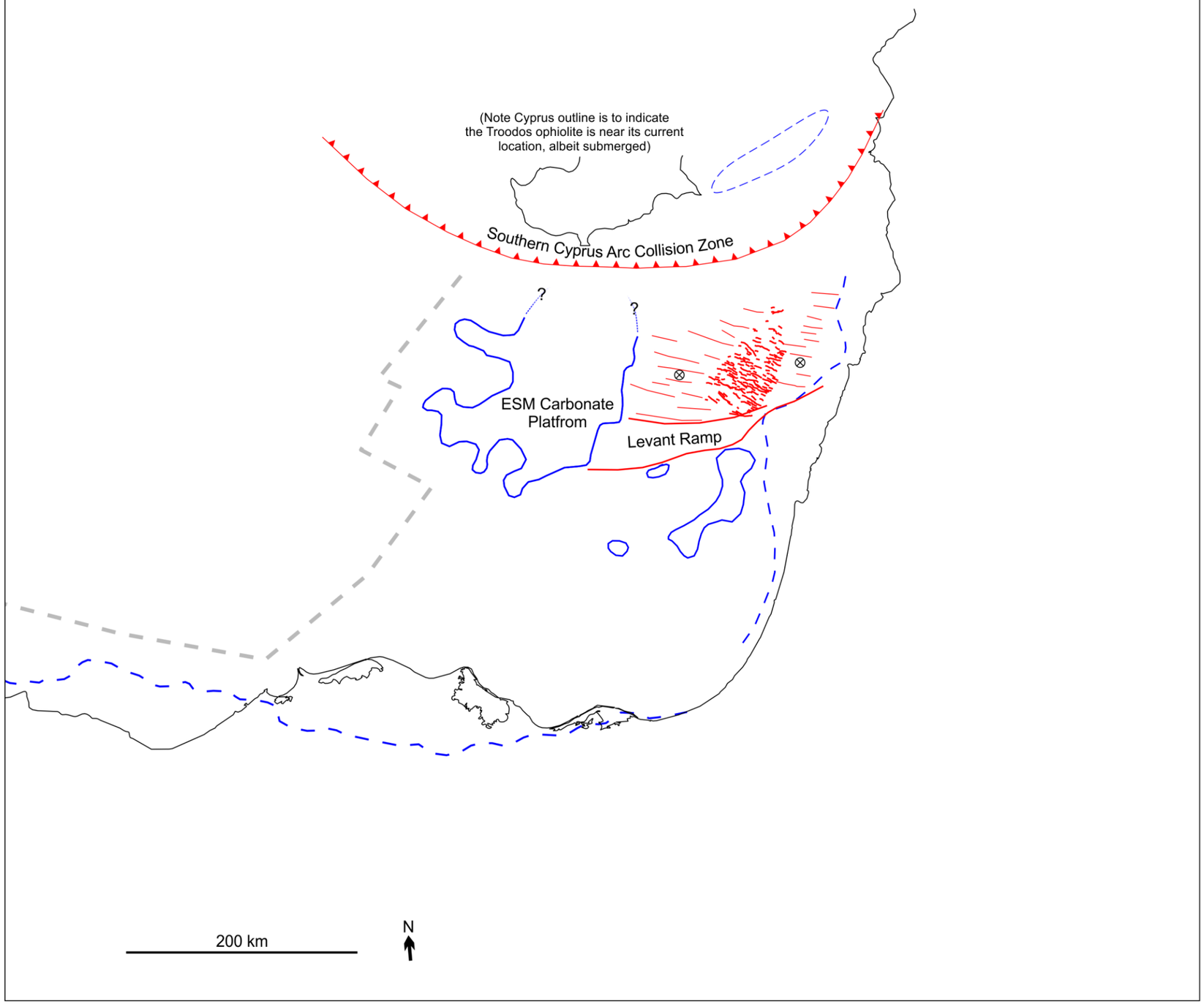

Highlights
Carbonate platforms have formed on basement highs in the EMR.

The subduction zone at the southern end of the Cyprus Arc arrives at close to its current location, bringing the Cypriot oceanic crust to close to its current location.

Subsidence of the Northern Levantine Basin, linked to the arrival of the adjacent subduction zone, forms the Levant Ramp and [Cretaceous] normal faults in the Northern Levantine Basin.

Subduction/collision zone
Carbonate platform outline
Carbonate platform margin outline/ shelf break

Documented normal fault
Speculated normal fault trend

⊗ Subsidence

Approximate relative position of current coastlines

Inactive pre-existing features shown in gray.

Carbonate platform outlines are from this study, Kassinis (2011), Klimke and Ehrhardt (2014) and Tassy et al. (2015).

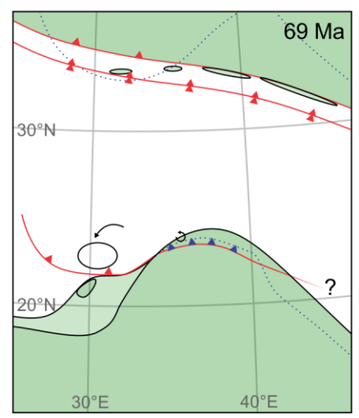

D Upper Eocene (c . 55 Ma)

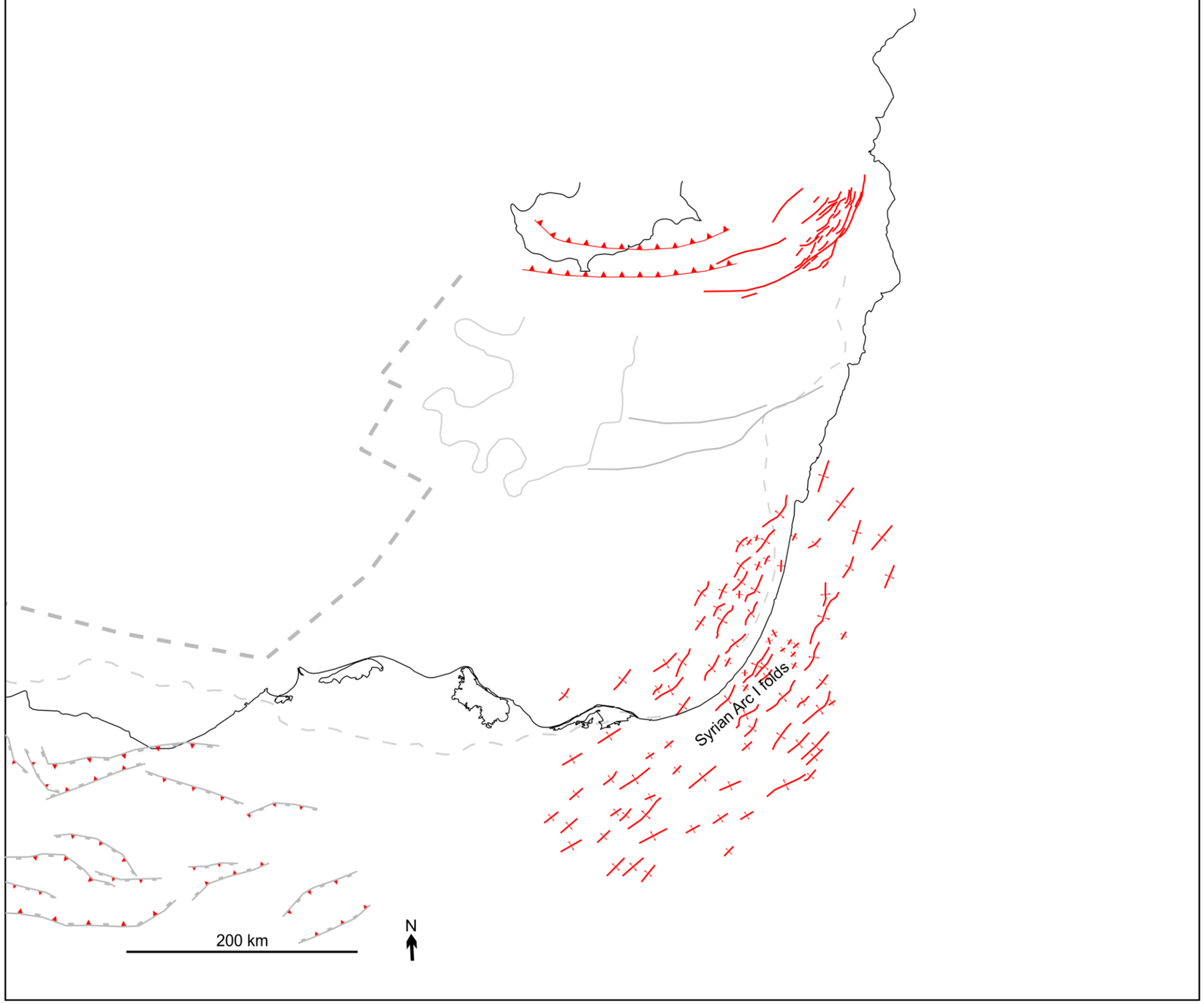

Highlights
The Syrian Arc I compression event occurred around the Palaeocene, likely due to far field forces from the initiation of convergence of the Neo-Tethys.

Thrusts formed at the southern edge of the Cyprus Arc behind the relic subduction front.

The carbonate platforms have drowned.

- Speculated thrusts
- Traced thrusts
- Anticline
- Inversion of normal fault
- Approximate relative position of current coastlines

Inactive pre-existing features shown in gray.

Syrian Arc folds are from Gardosh and Tannenbaumn (2014).
Inverted faults are from Bosworth et al. (1999).

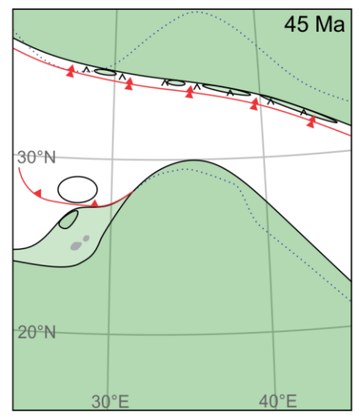

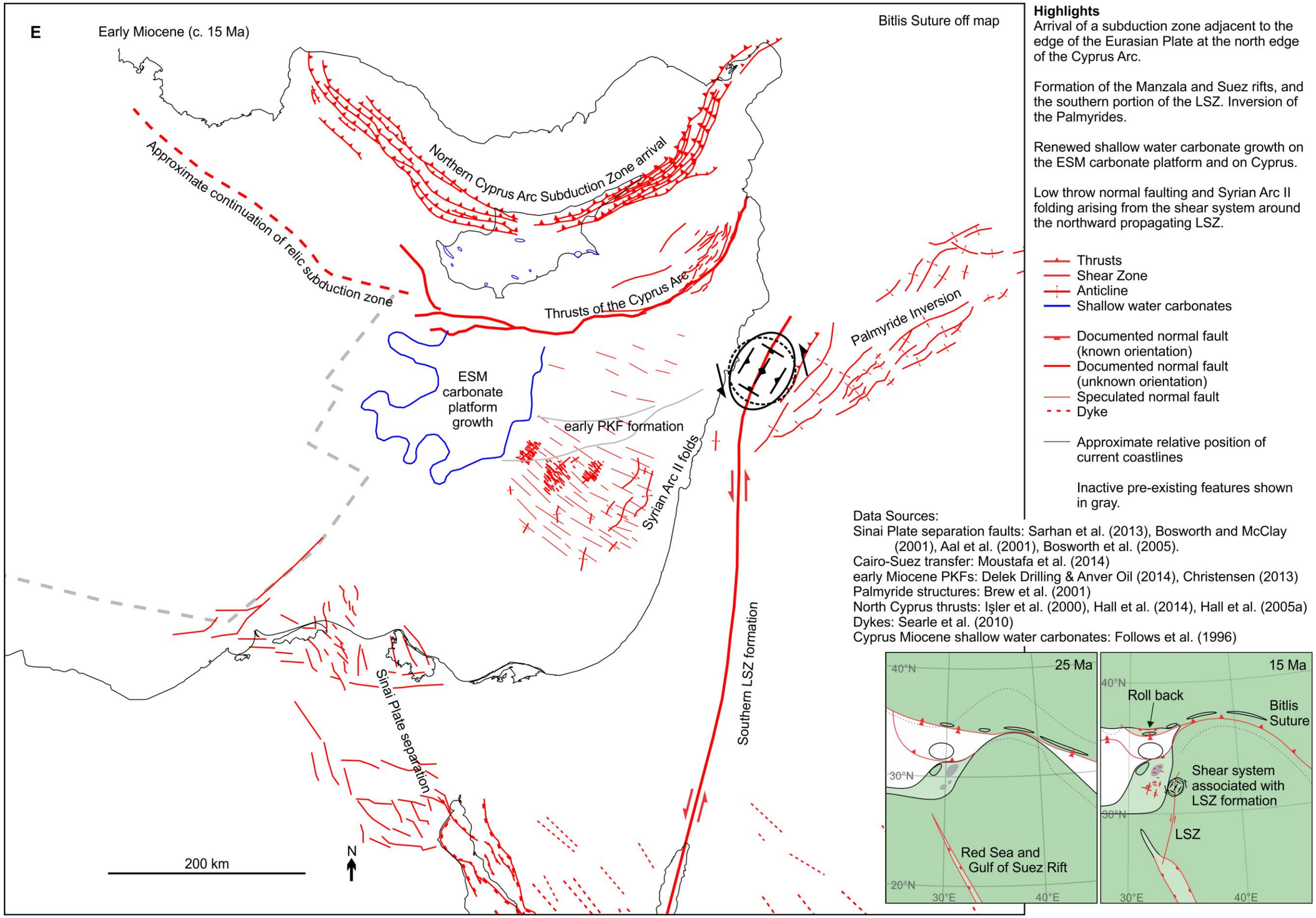
E
Early Miocene (c. 15 Ma)
Bitlis Suture off map
Approximate continuation of relic subduction zone
Northern Cyprus Arc Subduction Zone arrival
Thrusts of the Cyprus Arc
ESM carbonate platform growth
early PKF formation
Syrian Arc II folds
Palmyride Inversion
Sinai Plate separation
Southern LSZ formation
200 km
N
Highlights
Arrival of a subduction zone adjacent to the edge of the Eurasian Plate at the north edge of the Cyprus Arc.
Formation of the Manzala and Suez rifts, and the southern portion of the LSZ. Inversion of the Palmyrides.
Renewed shallow water carbonate growth on the ESM carbonate platform and on Cyprus.
Low throw normal faulting and Syrian Arc II folding arising from the shear system around the northward propagating LSZ.
Thrusts
Shear Zone
Anticline
Shallow water carbonates
Documented normal fault (known orientation)
Documented normal fault (unknown orientation)
Speculated normal fault
Dyke
Approximate relative position of current coastlines
Inactive pre-existing features shown in gray.
Data Sources:
Sinai Plate separation faults: Sarhan et al. (2013), Bosworth and McClay (2001), Aal et al. (2001), Bosworth et al. (2005).
Cairo-Suez transfer: Moustafa et al. (2014)
early Miocene PKFs: Delek Drilling & Anver Oil (2014), Christensen (2013)
Palmyride structures: Brew et al. (2001)
North Cyprus thrusts: Işler et al. (2000), Hall et al. (2014), Hall et al. (2005a)
Dykes: Searle et al. (2010)
Cyprus Miocene shallow water carbonates: Follows et al. (1996)
25 Ma
40°N
30°N
20°N
30°E
40°E
Red Sea and Gulf of Suez Rift
15 Ma
Roll back
Bitlis Suture
Shear system associated with LSZ formation
LSZ

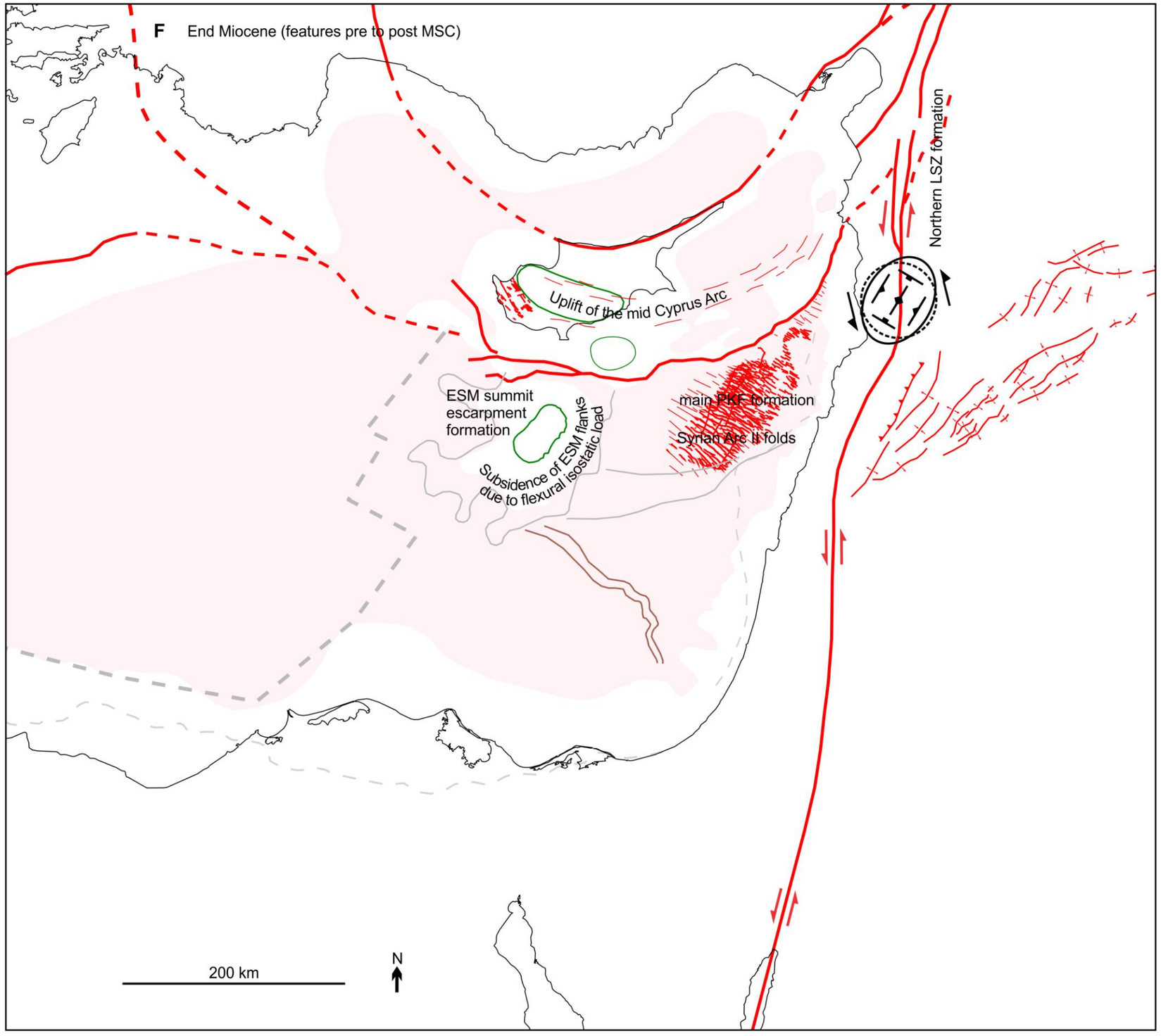

Highlights
pre MSC:
The shear system around the northward propagation of the LSZ forms normal faults and perpendicular folds in the northern Levantine Basin.

MSC:
Deposition of MSC evaporites.

Widespread erosion at the start and end of the MSC, and down slope movement of evaporites during the MSC.

Post MSC:
The flanks of the ESM subside due to the load of the evaporites.

The ongoing convergence at the Cyprus Arc causes uplift of the Arc. Normal faults form due to outer arc extension.

- Large scale tectonic boundary
- Large scale tectonic boundary (uncertain location)
- Anticline
- Documented normal fault
- Speculated normal fault trend
- Channel eroded at MSC onset
- Massive evaporite body
- Palaeo-coastline (not necessarily contemporaneous)
- Approximate relative position of current coastlines

Inactive pre-existing features shown in gray.

Palmyride structures are from Brew et al. (2001), and late Miocene PKFs outside the LEB3D survey from Ghalayini et al. (2014).

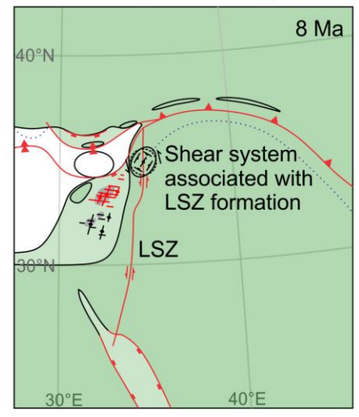

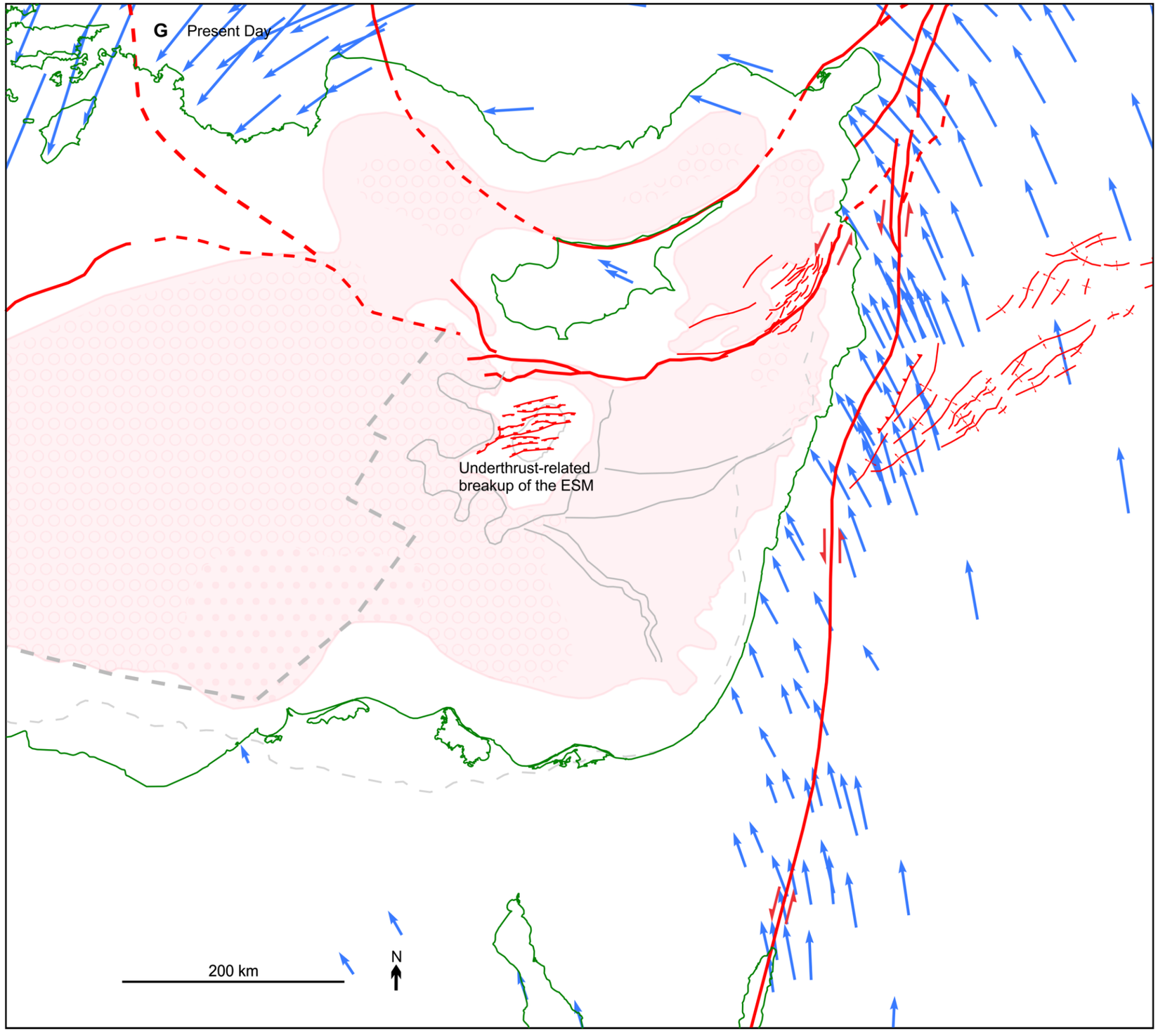

Highlights
Continued convergence across the Cyprus Arc.

Continued displacement on the LSZ and inversion of the Palmyrides.

Widespread halokinesis.

Further uplift of Cyprus, and subsidence and breakup of the ESM platform.

Large scale tectonic boundary
Large scale tectonic boundary (approximate location)
Anticline
Normal fault
Current coastlines
Outline of massive MSC salt
Zone of diapirism
Weld and salt roller zone

Inactive pre-existing features shown in gray.

Relative motion to Eurasia (Reilinger et al., 2006)
20 mm/yr

Palmyride structures are from Brew et al. (2001)

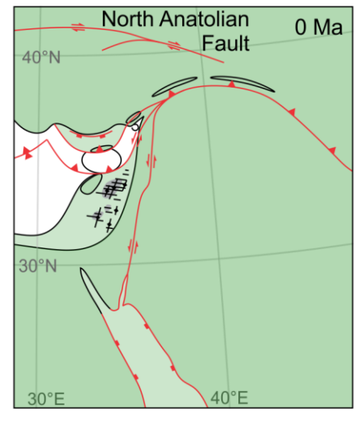

The evolution depicted in Figure 8.1 is summarised in text below:

- The passive continental margin that now forms the Levant and North African margin formed via rifting orientated broadly NW-SE, suggested to have initiated in the late Palaeozoic or early Mesozoic (Gardosh et al., 2010). However, a more recent estimate for subsequent spreading in the Neo-Tethys is around 340 Ma (Granot, 2016). The rifting resulted in a broad area of thinned crust beneath what is now the Levantine Basin, with outer highs spread across the thinned crust. An earlier, or polyphase of the rift produced the Palmyride Basin onshore Syria.
- In the Late Cretaceous, shallow water carbonate platforms formed on the margins of the un-attenuated continental cratons and the fault block highs of the attenuated continental crust in the EMR.
- Atlantic isochrons indicate closure of the Neo-Tethys initiated between 120 and 83 Ma.
- At the end of the Cretaceous, the carbonate platforms in the area drowned, and the subduction zone that is now the southern edge of the Cyprus Arc initiated continental collision at what is now the northern margin of the Levantine Basin. When the eastern extension of the same subduction zone collided with the Arabian Platform obduction occurred. The northern Levantine Basin faulted and subsided prior to the arrival of the subduction zone, forming the Levant Ramp.
- Between the end of the Cretaceous and Eocene, convergence of the African and Eurasian Plates was accommodated on subduction zones to the north of the EMR. This resulted in thrusting at the relic subduction zone at the northern margin of the Levantine Basin but relative tectonic quiescence elsewhere in the EMR.
- By the Eocene, the Syrian Arc I compression event had initiated, resulting in the inversion of normal faults and generation of folds in the Palmyride Basin and on the Israel continental margin. The source of the compression is believed to be far-field stresses from the northern margin of the Neo-Tethys; arc volcanism is widespread there during this time consistent with significant convergence.
- In the late Eocene to mid Miocene, a subduction zone arrived at what is now the northern edge of the Cyprus Arc. This marked the subduction of the last of the oceanic crust in the Neo-Tethyan cross section between southern Turkey and Egypt. Partially restricted subduction adjacent to oceanic crust thickened by thrusting behind the more southerly relic subduction zone meant that the shape of the more northerly subduction had modified to match that of the relic subduction zone to the South. Subsequently, convergence between the Eurasian and African Plates has been accommodated on thrusting in the relic subduction zones. An absence of well data, and difficulties associated with tracing contemporaneous reflectors near unconformities means it is unclear if the locus of thrusting shifted during this period, however the seismic data available to this study tentatively suggests there may have been minor northward migration of thrusting. This thrusting initiated uplift at the Cyprus Arc.
- In the late Oligocene, the Gulf of Suez and Red Sea rifted, separating what is now the Arabian Plate and Sinai Peninsula from the African Plate.

- During the early Miocene, shallow water carbonate growth returned on the ESM platform. Uplift in the centre of the Cyprus Arc also resulted in shallow water carbonate growth.
- In the early Miocene, extension had stopped in the Gulf of Suez but was continuing in the Red Sea, with the differential separation accommodated by the formation of the LSZ. This separated the Arabian Plate from the 'Sinai Plate' (this may also be considered a partly rifted crustal promontory of the African Plate).
- The shear zone around the northward propagating tip of the LSZ caused widespread low-throw normal faulting in the Levantine Basin where underlying shale provided a detachment surface. Perpendicular compression from the same shear zone forces generated the Syrian Arc II compression event which formed and reactivated perpendicular folds in the Southern Levantine Basin.
- In the late Miocene, the LSZ had propagated to its current extent. Numerous normal faults and perpendicular folds formed in the Northern Levantine Basin due to the shear system associated with the formation of the LSZ. The occurrence of these normal faults is controlled by a mobile shale interval in which the faults detach. The extension associated with the shear system also caused a hiatus in the compression on the eastern limb of the Cyprus Arc.
- Up to 4 km of evaporites, primarily massive halite, were deposited in the deep basins of the EMR during the MSC. Sea level draw-down at the start and end of the MSC resulted in erosive unconformities on the continental margins of the EMR, Cyprus, the Hecataeus Rise and formed the ESM summit escarpment. Gravitational collapse of the evaporite sequence occurred prior to the final erosion event.
- Basin subsidence from the isostatic load of the MSC evaporites and sediment deposition at the basin flanks has resulted in widespread gravity driven salt flow since the MSC. Diapirism has also occurred where the thickness of the salt and overburden are sufficiently thick. Supra-salt sediments have also undergone translation detaching and rafting on the MSC salt interval. These salt tectonics formed the ESM moat via inflation of the evaporite body around the ESM.
- The ongoing convergence between African and Eurasia is now accommodated by the collision of the attenuated continental crust of the Sinai continental promontory and the Cyprus Arc. This has uplifted the Arc, resulting in rapid uplift and exposure of Cyprus Island and less extreme uplift of the offshore Arc. Outer arc extension associated with this uplift can explain widespread normal faults that maybe observed in the Cyprus Arc, both onshore and offshore.

8.7 Recommendations for Further Work

The reconstructions, and conclusions they are generated from, have highlighted some of the remaining uncertainties in the tectonic evolution of the EMR. These are described below.

The onshore geology of Cyprus represents an opportunity to view areas of the Cyprus Arc with a level of detail and age constraint not possible in offshore seismic data. The relationships between offshore and onshore observations may therefore offer reciprocal insights. Reconsideration of the

current understanding of onshore Cyprus geology in the light of interpretation of adjacent offshore seismic data may provide a new understanding of the evolution of the island.

The absence of newer-vintage or densely spaced seismic data available north and west of Cyprus means that the pre-MSC structure of this region, including the Cyprus Arc Posterior, is very poorly documented and understood. Consequently, the formation of the Cilicia Basin, the connection between the Misis-Kyrenia Thrust Complex with the Isparta Angle, and the deep structure of the Florence Rise is highly speculative. These areas represent potentially key components of the evolution of the EMR and are therefore worthy of further study, however this would require substantial investment in data collection.

Although the Lebanese portion of the Levant continental margin is well imaged in the seismic data available to this study, a wealth of other data meant these data were not interpreted to the same level of detail in this study as other portions of the EMR such as the Cyprus Arc. Consequently, there are likely aspects of the Lebanese margin geology that could be investigated further using this dataset. A comparison of this margin relative to the Egyptian continental margin adjacent to the Western Desert could provide further insight into the rifting that formed these margins.

The trend of the Levant Ramp matched that of the northern limit of the Palmyride Basin prior to the offset along the LSZ (Section 3.6.4). Both features show evidence of late Cretaceous rifting, and both features are likely to have formed along pre-existing trends (Section 3.6.4; Figure 2.4). Further studies are recommended to test if these features are linked by an underlying, possibly Hercynian, basement trend.

Chapter 9 Bibliography

Aal, A.A., Barkooky, A. El, Gerrits, M., Meyer, H., Schwander, M., Zaki, H., 2000. Tectonic evolution of the Eastern Mediterranean Basin and its significance for hydrocarbon prospectivity in the ultradeepwater of the Nile Delta. Lead. Edge, 19, 1086–1102.

Aal, A.A., El Barkooky, A., Gerrits, M., Meyer, H.-J., Schwander, M., Zaki, H., 2001. Tectonic evolution of the eastern Mediterranean Basin and its significance for the hydrocarbon prospectivity of the Nile Delta deepwater area. GeoArabia, 6, 363–384.

Aksu, A.E., Calon, T.J., Hall, J., Mansfield, S., Yaşar, D., 2005a. The Cilicia-Adana basin complex, Eastern Mediterranean: Neogene evolution of an active fore-arc basin in an obliquely convergent margin. Mar. Geol., 221, 121–159. doi:10.1016/j.margeo.2005.03.011

Aksu, A.E., Calon, T.J., Hall, J., Yaşar, D., 2005b. Origin and evolution of the Neogene Iskenderun Basin, northeastern Mediterranean Sea. Mar. Geol., 221, 161–187. doi:10.1016/j.margeo.2005.03.010

Aksu, A.E., Hall, J., Yaltırak, C., 2009. Miocene–Recent evolution of Anaximander Mountains and Finike Basin at the junction of Hellenic and Cyprus Arcs, eastern Mediterranean. Mar. Geol., 258, 24–47. doi:10.1016/j.margeo.2008.04.008

Aksu, A.E., Walsh-Kennedy, S., Hall, J., Hiscott, R.N., Yaltırak, C., Akhun, S.D., Çifçi, G., 2014. The Pliocene–Quaternary tectonic evolution of the Cilicia and Adana basins, eastern Mediterranean: Special reference to the development of the Kozan Fault zone. Tectonophysics, 622, 22–43. doi:10.1016/j.tecto.2014.03.025

Albora, a. M., Sayın, N., Uçan, O.N., 2006. Evaluation of tectonic structure of İskenderun Basin (Turkey) using steerable filters. Mar. Geophys. Res., 27, 225–239. doi:10.1007/s11001-006-9002-5

Allaby, M. (Ed.), 2008. Oxford Dictionary of Earth Sciences3rd,ed. “Oxford University Press.” doi:10.1093/acref/9780199211944.013.0498

Allen, H., Jackson, C.A.-L., Fraser, A.J., 2016. Gravity-driven deformation of a youthful saline giant: the interplay between gliding and spreading in the Messinian basins of the Eastern Mediterranean. Pet. Geosci., petgeo2016-034. doi:10.1144/petgeo2016-034

Allen, M., Jackson, J., Walker, R., 2004. Late Cenozoic reorganization of the Arabia-Eurasia collision and the comparison of short-term and long-term deformation rates. Tectonics, 23. doi:10.1029/2003TC001530

Andersen, T.B., Jamtveit, B., Dewey, J.F., Swensson, E., 1991. Subduction and eduction of continental crust: major mechanisms during continent-continent collision. Terra Nov., 3, 303–310. doi:10.1111/j.1365-3121.1991.tb00148.x

Avedik, F., Nicolich, R., Hirn, A., Maltezou, F., McBride, J., Cernobori, L., 1995. Appraisal of a new, high-energy and low-frequency seismic pulse generating method on a deep seismic reflection profile in the central Mediterranean Sea. First Break, 13, 277–290.

Avigad, D., Abbo, A., Gerdes, A., 2016. Origin of the Eastern Mediterranean: Neotethys rifting along a cryptic Cadomian suture with Afro-Arabia. Geol. Soc. Am. Bull., B31370.1. doi:10.1130/B31370.1

Badawy, a, Horvath, F., 1999. The Sinai subplate and tectonic evolution of the northern Red Sea region. J. Geodyn., 27, 433–450. doi:10.1016/S0264-3707(98)00023-4

Bar, O., Gvirtzman, Z., Feinstein, S., Zilberman, E., 2013. Accelerated subsidence and sedimentation in the levant basin during the late tertiary and concurrent uplift of the arabian platform: Tectonic versus counteracting sedimentary loading effects. Tectonics, 32, 334–350. doi:10.1002/tect.20026

Baroz, F., 1979. Étude géologique dans le Pentadaktylos et la Mesaoria (Chypre septentrionale). Université de Nancy.

Barrier, E., Vrielynck, B., 2008. Palaeotectonic Maps of the Middle East: Tectono-sedimentary-palinspastic Maps from Late Norian to Pliocene : Atlas of 14 Maps. Commission for the Geological Map of the World (CGMW/CCCGM).

Bartov, Y., Steinitz, G., Eyal, M., Eyal, Y., 1980. Sinistral movement along the Gulf of Aqaba [mdash] its age and relation to the opening of the Red Sea. Nature, 285, 220–222.

Baudon, C., Cartwright, J.A., 2008. Early stage evolution of growth faults: 3D seismic insights from the Levant Basin, Eastern Mediterranean. J. Struct. Geol., 30, 888–898. doi:10.1016/j.jsg.2008.02.019

Bear, L.M., Morel, S.., 1960. The Geology and Mineral Resources of the Agros-Akrotiri Area.

Ben-Avraham, Z., Ginzburg, A., Makris, J., Eppelbaum, L., 2002. Crustal structure of the Levant Basin, eastern Mediterranean. Tectonophysics, 346, 23–43. doi:10.1016/S0040-1951(01)00226-8

Ben-Avraham, Z., Kempler, D., Ginzburg, A., 1988. Plate convergence in the Cyprean Arc. Tectonophysics, 146, 231–240. doi:10.1016/0040-1951(88)90093-5

Ben-Avraham, Z., Shoham, Y., Ginzburg, A., 1976. Magnetic Anomalies in the Eastern Mediterranean and the Tectonic Setting of the Eratosthenes Seamount. Geophys. J. R. Astron. Soc., 45, 105–123. doi:10.1111/j.1365-246X.1976.tb00316.x

Ben-Avraham, Z., Tibor, G., Limonov, a. F., Leybov, M.B., Ivanov, M.K., Tokarev, M.Y., Woodside, J.M., 1995. Structure and tectonics of the eastern Cyprean Arc. Mar. Pet. Geol., 12, 263–271. doi:10.1016/0264-8172(95)98379-J

Ben-Avraham, Z., Woodside, J.M., Lodolo, E., Gardosh, M.A., Grasso, M., Camerlenghi, A., Vai, G.B., 2006. Eastern Mediterranean basin systems. Geol. Soc. London, Mem., 32, 263–276. doi:10.1144/GSL.MEM.2006.032.01.15

Ben-Gai, Y., Ben-Avraham, Z., Buchbinder, B., Kendall, C.G.S.C., 2005. Post-Messinian evolution of the Southeastern Levant Basin based on two-dimensional stratigraphic simulation. Mar. Geol., 221, 359–379. doi:10.1016/j.margeo.2005.03.003

Ben-Menahem, A., Nur, A., Vered, M., 1976. Tectonics, seismicity and structure of the Afro-Eurasian junction—the breaking of an incoherent plate. Phys. Earth Planet. Inter., 12, 1–50.

Bentham, P., Hanbal, I., Cotton, J., Longacre, M.B., Edwards, R., 2007. Crustal Structure and Early Opening of the Eastern Mediterranean Basin-Key Observations from Offshore Northern Egypt. 3rd North African/Mediterranean Pet. Geosci. Conf. Exhib., 26–28.

Berk Biryol, C., Beck, S.L., Zandt, G., Özacar, a. A., 2011. Segmented African lithosphere beneath the Anatolian region inferred from teleseismic P-wave tomography. Geophys. J. Int., 184, 1037–1057. doi:10.1111/j.1365-246X.2010.04910.x

Berra, F., Angiolini, L., 2014. The Evolution of the Tethys Region throughout the Phanerozoic: A Brief Tectonic Reconstruction. AAPG Mem. 106, 106, 1–28. doi:10.1306/13431840M1063606

Bertello, F., Harby, H., Brandolese, S., 2016. Egypt: Zohr, an Outstanding Gas Discovery in a New Deep-Water Hydrocarbon Play. 8th Mediterr. Offshore Conf., 1–10.

Bertoni, C., Cartwright, J.A., 2015. Messinian evaporites and fluid flow. Mar. Pet. Geol.,. doi:10.1016/j.marpetgeo.2015.02.003

Bertoni, C., Cartwright, J.A., 2007. Major erosion at the end of the Messinian Salinity Crisis: Evidence from the Levant Basin, Eastern Mediterranean. Basin Res., 19, 1–18. doi:10.1111/j.1365-2117.2006.00309.x

Bertoni, C., Cartwright, J.A., 2006. Controls on the basinwide architecture of late Miocene (Messinian) evaporites on the Levant margin (Eastern Mediterranean). Sediment. Geol., 188–189, 93–114. doi:10.1016/j.sedgeo.2006.03.019

Bertoni, C., Cartwright, J.A., 2005. 3D seismic analysis of circular evaporite dissolution structures, Eastern Mediterranean. J. Geol. Soc. London., 162, 909–926. doi:10.1144/0016-764904-126

Best, J. a., Barazangi, M., Al-Saad, D., Sawaf, T., Gebran, a., 1993. Continental margin evolution of the northern Arabian platform in Syria. Am. Assoc. Pet. Geol. Bull.,. doi:10.1306/BDFF8BBE-1718-11D7-8645000102C1865D

Betzler, C., Lindhorst, S., Eberli, G.P., Lüdmann, T., Möbius, J., Ludwig, J., Schutter, I., Wunsch, M., Reijmer, J.J.G., Hübscher, C., 2014. Periplatform drift: The combined result of contour current and off-bank transport along carbonate platforms. Geology, 42, 871–874. doi:10.1130/G35900.1

Bevan, T., 2012. Understanding Crustal Structure and the Early Opening History of the Eastern Mediterranean Basin, Offshore Northern Egypt and the Levant, in: New and Emerging Plays in the Eastern Mediterranean. Geological Society, pp. 18–19.

Beydoun, Z.R., 1999. Evolution and development of the Levant (Dead Sea Rift) Transform System: A historical-chronological review of a structural controversy. Geol. Soc. London, Spec. Publ., 164, 239–255. doi:10.1144/GSL.SP.1999.164.01.12

Beydoun, Z.R., 1993. Evolution of the Northeastern Arabian Plate Margin and Shelf: Hydrocarbon Habitat and Conceptual Future Potential. Oil Gas Sci. Technol. - Rev. IFP, 48, 311–345.

Beydoun, Z.R., 1977. Petroleum Prospects of Lebanon: Reevaluation. Am. Assoc. Pet. Geol. Bull., 61, 43–64. doi:10.1306/C1EA3BF4-16C9-11D7-8645000102C1865D

Beyreuther, M., Barsch, R., Krischer, L., Megies, T., Behr, Y., Wassermann, J., 2010. ObsPy: A Python Toolbox for Seismology. Seismol. Res. Lett., 81, 530–533. doi:10.1785/gssrl.81.3.530

Bilim, F., Aydemir, A., Ates, A., 2016. Crustal thickness variations in the Eastern Mediterranean and southern Aegean region. Mar. Pet. Geol., 77, 507.e9-507.e14. doi:10.1016/j.marpetgeo.2016.06.012

Bishop, D.J., Buchanan, P.G., Bishop, C.J., 1995. Gravity-driven thin-skinned extension above Zechstein Group evaporites in the western central North Sea: an application of computer-aided section restoration techniques. Mar. Pet. Geol., 12, 115–135. doi:10.1016/0264-8172(95)92834-J

Bosworth, W., 2015. Geological Evolution of the Red Sea: Historical Background, Review, and Synthesis, in: The Red Sea. Springer Berlin Heidelberg. doi:10.1007/978-3-662-45201-1

Bosworth, W., Guiraud, R., Kessler, L.G., 1999. Late Cretaceous (ca. 84 Ma) compressive deformation of the stable platform of northeast Africa (Egypt): Far-field stress effects of the “Santonian event” and origin of the Syrian arc deformation belt. Geology, 27, 633–636. doi:10.1130/0091-7613(1999)027<0633:LCCMCD>2.3.CO;2

Bosworth, W., Huchon, P., McClay, K., 2005. The Red Sea and Gulf of Aden Basins. J. African Earth Sci., 43, 334–378. doi:10.1016/j.jafrearsci.2005.07.020

Bosworth, W., McClay, K., 2001. Structural and stratigraphic evolution of the Gulf of Suez rift, Egypt: a synthesis. Mémoires du Muséum Natl. d’histoire,.

Boulton, S.J., 2009. Record of Cenozoic sedimentation from the Amanos Mountains, Southern Turkey: Implications for the inception and evolution of the Arabia–Eurasia continental collision. Sediment. Geol., 216, 29–47. doi:10.1016/j.sedgeo.2009.01.008

Boulton, S.J., Robertson, A.H.F., 2008. The Neogene–Recent Hatay Graben, South Central Turkey: graben formation in a setting of oblique extension (transtension) related to post-collisional tectonic escape. Geol. Mag., 145, 800–821. doi:10.1017/S0016756808005013

Boulton, S.J., Robertson, A.H.F., Unlugenc, U.C., 2006. Tectonic and sedimentary evolution of the Cenozoic Hatay Graben, Southern Turkey: a two-phase model for graben formation. Geol. Soc. London, Spec. Publ., 260, 613–634. doi:10.1144/GSL.SP.2006.260.01.26

Bowman, S. a., 2011. Regional seismic interpretation of the hydrocarbon prospectivity of offshore Syria. GeoArabia, 95–124.

Bradley, D.C., Kidd, W.S.F., 1991. Flexural extension of the upper continental crust in collisional foredeeps. Geol. Soc. Am. Bull., 103, 1416–1438. doi:10.1130/0016-

7606(1991)103<1416:FEOTUC>2.3.CO;2

Brew, G., 2001. Tectonic evolution of Syria interpreted from integrated geophysical and geological analysis. Cornell University.

Brew, G., Barazangi, M., Al-Maleh, A.K., Sawaf, T., 2001a. Tectonic and geologic evolution of Syria. GeoArabia, 6, 573–616.

Brew, G., Lupa, J., Barazangi, M., Sawaf, T., Al-Imam, A., Zaza, T., 2001b. Structure and tectonic development of the Ghab basin and the Dead Sea fault system, Syria. J. Geol. Soc. London., 158, 665–674. doi:10.1144/jgs.158.4.665

Bridge, C., Calon, T.J., Hall, J., Aksu, A.E., 2005. Salt tectonics in two convergent-margin basins of the Cyprus arc, Northeastern Mediterranean. Mar. Geol., 221, 223–259. doi:10.1016/j.margeo.2005.03.008

Bry, M., White, N., Singh, S.C., England, R., Trowell, C., 2004. Anatomy and formation of oblique continental collision: South Falkland basin. Tectonics, 23, 1–20. doi:10.1029/2002TC001482

Buchbinder, B., Zilberman, E., 1997. Sequence stratigraphy of Miocene-Pliocene carbonate-siliciclastic shelf deposits in the eastern Mediterranean margin (Israel): effects of eustasy and tectonics. Sediment. Geol., 112, 7–32. doi:10.1016/S0037-0738(97)00034-1

Butler, M., Pullan, C.P., 1990. Tertiary structures and hydrocarbon entrapment in the Weald Basin of southern England. Geol. Soc. London, Spec. Publ., 55, 371–391. doi:10.1144/GSL.SP.1990.055.01.19

Butler, R.W.H., McCaffrey, B., Torvela, T., 2016. Virtual Seismic Atlas [WWW Document]. Leeds Univ.,. URL http://see-vsa.leeds.ac.uk/ (accessed 1.8.16).

Butler, R.W.H., Spencer, S., Griffiths, H.M., 1998. The structural response to evolving plate kinematics during transpression: evolution of the Lebanese restraining bend of the Dead Sea Transform. Geol. Soc. London, Spec. Publ., 135, 81–106. doi:10.1144/GSL.SP.1998.135.01.06

Calon, T.J., Aksu, A.E., Hall, J., 2005a. The Neogene evolution of the Outer Latakia Basin and its extension into the Eastern Mesaoria Basin (Cyprus), Eastern Mediterranean. Mar. Geol., 221, 61–94. doi:10.1016/j.margeo.2005.03.013

Calon, T.J., Aksu, A.E., Hall, J., 2005b. The Oligocene-Recent evolution of the Mesaoria Basin (Cyprus) and its western marine extension, Eastern Mediterranean. Mar. Geol., 221, 95–120. doi:10.1016/j.margeo.2005.03.012

Camera, L., Ribodetti, a., Mascle, J., 2010. Deep structures and seismic stratigraphy of the Egyptian continental margin from multichannel seismic data. Geol. Soc. London, Spec. Publ., 341, 85–97. doi:10.1144/SP341.5

Capitanio, F.A., Morra, G., Goes, S., Weinberg, R.F., Moresi, L., 2010. India-Asia convergence driven by the subduction of the Greater Indian continent. Nat. Geosci, 3, 136–139.

Carew, J., Mylroie, J., 1997. Geology of the Bahamas. Geol. Hydrogeol. Carbonate islands, Dev. Sedimenetology, Ch. 3A, 91–139. doi:S0070457104800232

Carton, H., Singh, S.C., Tapponnier, P., Elias, A., Briais, A., Sursock, a., Jomaa, R., King, G.C.P., Daëron, M., Jacques, E., Barrier, L., 2009. Seismic evidence for Neogene and active shortening offshore of Lebanon (Shalimar cruise). J. Geophys. Res., 114, B07407. doi:10.1029/2007JB005391

Cartwright, J.A., Bolton, A.J., James, D.M.D., 2003. The Genesis of Polygonal Fault Systems: a Review 223–243. doi:10.1144/GSL.SP.2003.216.01.15

Cartwright, J.A., Jackson, M., Dooley, T., Higgins, S., 2012. Strain partitioning in gravity-driven shortening of a thick, multilayered evaporite sequence. Geol. Soc. London, Spec. Publ., 363, 449–470. doi:10.1144/SP363.21

Cartwright, J.A., Jackson, M.P. a, 2008. Initiation of gravitational collapse of an evaporite basin margin: The Messinian saline giant, Levant Basin, eastern Mediterranean. Geol. Soc. Am. Bull., 120, 399–413. doi:10.1130/B26081X.1

Chaimov, T. a., Barazangi, M., Al-Saad, D., Sawaf, T., Gebran, A.L.I., 1992. Mesozoic and Cenozoic deformation inferred from seismic stratigraphy in the southwestern intracontinental Palmyride fold-thrust belt, Syria. Geol. Soc. Am. Bull., 104, 704–715. doi:10.1130/0016-7606(1992)104<0704:MACDIF>2.3.CO;2

Chaimov, T. a., Barazangi, M., Al-Saad, D., Sawaf, T., Khaddour, M., 1993. Seismic fabric and 3-D structure of the southwestern intracontinental Palmyride Fold Belt, Syria. Am. Assoc. Pet. Geol. Bull.,. doi:10.1306/BDFF8FC4-1718-11D7-8645000102C1865D

Chaimov, T. a., Barazangi, M., Al-Saad, D., 1990. Crustal shortening in the Palmyride fold belt, Syria, and implications for movement along the Dead Sea fault system. Tectonics, 9, 1369–1386.

Chbat, W., Cherel, L., Montadert, L., Savva, D., Testelin, V., 2017. Prospectivity of the Continental Margin Offshore Lebanon from the Regional 3D Seismic Surveys and Petroleum System Modelling, in: AAPG Regional Larnaca.

Christensen, C.J., Powers, G., Energy, N., 2013. Formation Evaluation Challenges in Tamar Field, Offshore Israel. SPWLA 54th Annu. Logging Symp.,.

Clark, I., Cartwright, J.A., 2013. A Case Study of Three-dimensional Fold and Growth Sequence Development and the Link to Submarine Channel-structure Interactions in Deep-water Fold Belts. pp. 315–335. doi:10.1306/13351559M1003536

Clube, T.M.M., Creer, K.M., Robertson, A.H.F., 1985. Palaeorotation of the Troodos microplate, Cyprus. Nature, 317, 522–525.

Constantinou, G., 1995. Geological Map of Cyprus 1:250000.

Cowie, L., Kusznir, N., 2012a. Mapping crustal thickness and oceanic lithosphere distribution in the Eastern Mediterranean using gravity inversion. Pet. Geosci., 18, 373–380.

doi:10.1144/petgeo2011-071

Cowie, L., Kusznir, N., 2012b. Gravity inversion mapping of crustal thickness and lithosphere thinning for the eastern Mediterranean. Lead. Edge, 31(7), 810–814.

Cowie, P. a., Scholz, C.H., 1992. Growth of faults by accumulation of seismic slip. J. Geophys. Res., 97, 11085. doi:10.1029/92JB00586

Cross, N.E., Cunningham, A., Cook, R.J., Taha, A., Esmaie, E., El Swidan, N., 2009. Three-dimensional seismic geomorphology of a deep-water slope-channel system: The Sequoia field, offshore west Nile Delta, Egypt. Am. Assoc. Pet. Geol. Bull., 93, 1063–1086. doi:10.1306/05040908101

D'Agostino, N., Chamot-Rooke, N., Funiciello, R., Jolivet, L., Speranza, F., 1998. The role of pre-existing thrust faults and topography on the styles of extension in the Gran Sasso range (central Italy). Tectonophysics, 292, 229–254. doi:10.1016/S0040-1951(98)00070-5

Daher, S.B., Ducros, M., Michel, P., Nader, F.H., Littke, R., 2015. 3D thermal history and maturity modelling of the Levant Basin and Margin. Arab. J. Geosci., 17, 3161. doi:10.1007/s12517-016-2455-1

Delek Drilling & Anver Oil, 2014. Delek Drilling and Avner Oil presentation [WWW Document]. URL www.delekenergy.co.il/_Uploads/dbsAttachedFiles/public.pdf (accessed 3.3.16).

DeMets, C., Gordon, R.G., Argus, D.F., 2010. Geologically current plate motions. Geophys. J. Int., 181, 1–80. doi:10.1111/j.1365-246X.2009.04491.x

Dercourt, J., Ricou, L.-E., Vrielynck, B., 1993. Atlas Tethys palaeoenvironmental maps. Gauthier-Villars.

Dewey, J.F., Pitman, W.C., Ryan, W.B.F., Bonnin, J., 1973. Plate Tectonics and the Evolution of the Alpine System. Geol. Soc. Am. Bull., 84, 3137–3180. doi:10.1130/0016-7606(1973)84<3137:PTATEO>2.0.CO;2

Dhuime, B., Bosch, D., Bodinier, J.L., Garrido, C.J., Bruguier, O., Hussain, S.S., Dawood, H., 2007. Multistage evolution of the Jijal ultramafic-mafic complex (Kohistan, N Pakistan): Implications for building the roots of island arcs. Earth Planet. Sci. Lett., 261, 179–200. doi:10.1016/j.epsl.2007.06.026

Druckman, Y., Buchbinder, B., Martinotti, G.M., Tov, R.S., Aharon, P., 1995. The buried Afiq Canyon (eastern Mediterranean, Israel): a case study of a Tertiary submarine canyon exposed in Late Messinian times. Mar. Geol., 123, 167–185. doi:10.1016/0025-3227(94)00127-7

Dziewoński, A.M., Chou, T., Woodhouse, J.H., 1981. Determination of earthquake source parameters from waveform data for studies of global and regional seismicity. J. Geophys. Res. Solid Earth, 86, 2825–2852.

Eberli, G.P., Masaferro, J.L., Sarg, J.F., 2004. Seismic Imaging of Carbonate Reservoirs and Systems. AAPG Mem. , 376 pages.

Ehrhardt, A., Damm, V., Engels, M., Heyde, I., Lutz, R., Schnabel, M., Adam, J., Bargeloh, H., Behrens, T., Demir, Ü., Kallaus, G., Pitschmann, D., Schröder, P., Schrader, U., 2011. Eratosthenes Seamount / Eastern Mediterranean Sea - Cruise No. MSM14/2 - January 18 - February 25, 2010 - Limassol (Cyprus) - Limassol (Cyprus). DFG-Senatskommisssion für Ozeanogr., 66. doi:DOI:10.2312/cr_msm14_2

Ekström, G., Nettles, M., Dziewoński, A.M., 2012. The global CMT project 2004–2010: Centroid-moment tensors for 13,017 earthquakes. Phys. Earth Planet. Inter., 200, 1–9.

Elias, A., Tapponnier, P., Singh, S.C., King, G.C.P., Briais, A., Daëron, M., Carton, H., Sursock, A., Jacques, E., Jomaa, R., Klinger, Y., 2007. Active thrusting offshore Mount Lebanon: Source of the tsunamigenic A.D. 551 Beirut-Tripoli earthquake. Geology, 35, 755. doi:10.1130/G23631A.1

Ellis, D. V, Singer, J.M., 2007. Well Logging for Earth Scientists. Springer Science & Business Media.

Encyclopædia Britannica, 2010. Occam's razor, in: Encyclopædia Britannica Online.

Eppelbaum, L., 2011. Tectonic-Geophysical Mapping of Israel and the Eastern Mediterranean: Implications for Hydrocarbon Prospecting. Positioning, 2, 36–54. doi:10.4236/pos.2011.21004

Eppelbaum, L., Katz, Y., 2015. Eastern mediterranean: Combined geological-geophysical zonation and paleogeodynamics of the Mesozoic and Cenozoic structural-sedimentation stages. Mar. Pet. Geol., 65, 198–216. doi:10.1016/j.marpetgeo.2015.04.008

Erbek, E., Dolmaz, M.N., 2014. Geophysical researches (Gravity and Magnetic) of the Eratosthenes Seamount in the eastern Mediterranean Sea. Acta Geophys.,. doi:10.2478/s11600-013-0185-2

Ergün, M., Okay, S., Sari, C., Zafer Oral, E., Ash, M., Hall, J., Miller, H., 2005. Gravity anomalies of the Cyprus Arc and their tectonic implications. Mar. Geol., 221, 349–358. doi:10.1016/j.margeo.2005.03.004

Esestime, P., Hewitt, A., Hodgson, N., 2016. Zohr – A newborn carbonate play in the Levantine Basin, East-Mediterranean. First Break, 34, 87–93.

Euler, L., 1776. General formulas for the translation of arbitrary rigid bodies. Novi Comment. Acad. Sci. Petropolitanae, 20, 189–207.

Eyal, M., Eyal, Y., Bartov, Y., Steinitz, G., 1981. The tectonic development of the western margin of the Gulf of Elat (Aqaba) rift. Tectonophysics, 80, 39–66. doi:10.1016/0040-1951(81)90141-4

Eyal, Y., 1996. Stress field fluctuations along the Dead Sea rift since the middle Miocene. Tectonics,. doi:10.1029/95TC02619

Eyal, Y., Reches, Z., 1983. Tectonic analysis of the Dead Sea Rift Region since the Late-Cretaceous based on mesostructures. Tectonics, 2, 167–185.

Faccenna, C., Bellier, O., Martinod, J., Piromallo, C., Regard, V., 2006. Slab detachment beneath eastern Anatolia: A possible cause for the formation of the North Anatolian fault. Earth Planet. Sci. Lett., 242, 85–97. doi:10.1016/j.epsl.2005.11.046

Faccenna, C., Nalpas, T., Brun, J.-P., Davy, P., Bosi, V., 1995. The influence of pre-existing thrust faults on normal fault geometry in nature and in experiments. J. Struct. Geol., 17, 1139–1149. doi:http://dx.doi.org/10.1016/0191-8141(95)00008-2

Fattah, R.A., Verweij, H., Halstenberg, B., 2014. Modeling of Tectonic Heat Flow in the Levant Basin (Eastern Mediterranean). Implications for Basin and Petroleum System Assessment (Abstract). Geo 2014,.

Faugères, J.-C., Mézerais, M.L., Stow, D.A. V, 1993. Contourite drift types and their distribution in the North and South Atlantic Ocean basins. Sediment. Geol., 82, 189–203. doi:http://dx.doi.org/10.1016/0037-0738(93)90121-K

Feng, Y.E., Reshef, M., 2016. The Eastern Mediterranean Messinian salt-depth imaging and velocity analysis considerations. Pet. Geosci., petgeo2015-088. doi:10.1144/petgeo2015-088

Feng, Y.E., Yankelzon, A., Steinberg, J., Reshef, M., 2016. Lithology and characteristics of the Messinian evaporite sequence of the deep Levant Basin, eastern Mediterranean. Mar. Geol., 376, 118–131. doi:10.1016/j.margeo.2016.04.004

Finetti, I., 1985. Structure and Evolution of the Central Mediterranean (Pelagian and Ionian Seas), in: Stanley, D.J., Wezel, F.-C. (Eds.), Geological Evolution of the Mediterranean Basin: Raimondo Selli Commemorative Volume. Springer New York, New York, NY, pp. 215–230. doi:10.1007/978-1-4613-8572-1_10

Folkman, Y., Ben-Gai, Y., 2004. The “Jonah” buried seamount; intrusive structure in the southeastern Levant Basin offshore Israel. Isr. Geol. Soc. Annu. Meet., Hagoshrim, 29.

Follows, E.J., Robertson, A.H.F., Scoffin, T.P., 1996. Tectonic controls on Miocene reefs and related carbonate facies in Cyprus. Model. Carbonate Stratigr. from Miocene Reef Complexes Mediterr. Reg., 5, 295–315.

Fossen, H., 2010. Structural Geology. Cambridge University Press.

Freund, R., Garfunkel, Z., Zak, I., Goldberg, M., Weissbrod, T., Derin, B., Bender, F., Wellings, F.E., Girdler, R.W., 1970. The Shear along the Dead Sea Rift [and Discussion]. Philos. Trans. R. Soc. London A Math. Phys. Eng. Sci., 267, 107–130.

Frey-Martínez, J., 2005. 3D seismic interpretation of soft-sediment deformational processes offshore Israel: implications for hydrocarbon prospectivity. Cardiff University.

Frey-Martínez, J., Cartwright, J.A., James, D., 2006. Frontally confined versus frontally emergent submarine landslides: A 3D seismic characterisation. Mar. Pet. Geol., 23, 585–604. doi:10.1016/j.marpetgeo.2006.04.002

Frizon de Lamotte, D., Raulin, C., Mouchot, N., Wrobel-Daveau, J.-C., Blanpied, C., Ringenbach,

J.-C., 2011. The southernmost margin of the Tethys realm during the Mesozoic and Cenozoic: Initial geometry and timing of the inversion processes. Tectonics, 30, 1–22. doi:10.1029/2010TC002691

Fuhrmann, A.R., 2010. The Origin of the Lower Pliocene Deepwater Andromeda Mound Complex, Levant Basin, Eastern Mediterranean Sea, Offshore Israel. University of Colorado.

Galindo-Zaldívar, J., Nieto, L., Robertson, A.H.F., Woodside, J., 2001. Recent tectonics of Eratosthenes Seamount: an example of seamount deformation during incipient continental collision. Geo-Marine Lett., 20, 233–242. doi:10.1007/s003670000059

Garcia-Castellanos, D., Estrada, F., Jiménez-Munt, I., Gorini, C., Fernàndez, M., Vergés, J., De Vicente, R., 2009. Catastrophic flood of the Mediterranean after the Messinian salinity crisis. Nature, 462, 778–781. doi:10.1038/nature08555

Gardosh, M.A., 2013. Review of Petroleum Systems and Hydrocarbon Plays of the Levant Margin, Offshore Israel, in: New Understanding of the Petroleum Systems of Continental Margins of the World. Society of Economic Paleontologists and Mineralogists, pp. 573–597. doi:10.5724/gcs.12.32.0573

Gardosh, M.A., 2009. The Late Tertiary Deep-Water Siliciclastic System of the Levant Margin-An Emerging Play Offshore Israel. AAPG Search Discov. Artic., 90090.

Gardosh, M.A., Druckman, Y., 2006. Seismic stratigraphy, structure and tectonic evolution of the Levantine Basin, offshore Israel. Geol. Soc. London, Spec. Publ., 260, 201–227. doi:10.1144/GSL.SP.2006.260.01.09

Gardosh, M.A., Druckman, Y., Buchbinder, B., Calvo, R., 2008a. The Oligo-Miocene deepwater system of the Levant Basin.

Gardosh, M.A., Druckman, Y., Buchbinder, B., Rybakov, M., 2008b. The Levant Basin Off Shore Israel: Stratigraphy, Structure, Tectonic Evolution and Implications for Hydrocarbon Exploration.

Gardosh, M.A., Garfunkel, Z., Druckman, Y., Buchbinder, B., 2010. Tethyan rifting in the Levant Region and its role in Early Mesozoic crustal evolution. Geol. Soc. London, Spec. Publ., 341, 9–36. doi:10.1144/SP341.2

Gardosh, M.A., Tannenbaum, E., 2014. The Petroleum Systems of Israel, in: Marlow, L., Kendall, C.G.S.C., Yose, L. (Eds.), Petroleum Systems of the Tethyan Region. AAPG Memoir 106, pp. 179–216.

Gardosh, M.A., Weimer, P., Flexer, A., 2011. The sequence stratigraphy of Mesozoic successions in the Levant margin, southwestern Israel: A model for the evolution of southern Tethys margins. Am. Assoc. Pet. Geol. Bull., 95, 1763–1793. doi:10.1306/02081109135

Garfunkel, Z., 2014. Lateral Motion and Deformation Along the Dead Sea Transform, in: Garfunkel, Z., Ben-Avraham, Z., Kagan, E. (Eds.), Dead Sea Transform Fault System: Reviews. Springer Netherlands, Dordrecht, pp. 109–150. doi:10.1007/978-94-017-8872-

4_5

Garfunkel, Z., 2004. Origin of the Eastern Mediterranean basin: a reevaluation. Tectonophysics, 391, 11–34. doi:10.1016/j.tecto.2004.07.006

Garfunkel, Z., 1998. Constrains on the origin and history of the Eastern Mediterranean basin. Tectonophysics, 298, 5–35. doi:10.1016/S0040-1951(98)00176-0

Garfunkel, Z., 1981. Internal structure of the Dead Sea leaky transform (rift) in relation to plate kinematics. Tectonophysics, 80, 81–108. doi:http://dx.doi.org/10.1016/0040-1951(81)90143-8

Garfunkel, Z., Almāgōr, G., Arad, A., 1979. The Palmahim disturbance and its regional setting. Geological survey of Israel.

Garfunkel, Z., Bartov, J., Eyal, Y., Steinitz, G., 1974. Raham Conglomerate–new evidence for Neogene tectonism in the southern part of the Dead Sea Rift. Geol. Mag., 111, 55–64.

Garfunkel, Z., Derin, B., 1984. Permian-early Mesozoic tectonism and continental margin formation in Israel and its implications for the history of the Eastern Mediterranean. Geol. Soc. London, Spec. Publ., 17, 187–201. doi:10.1144/GSL.SP.1984.017.01.12

Gass, I.G., Masson-Smith, D., 1963. The Geology and Gravity Anomalies of the Troodos Massif, Cyprus. Philosphical Trans. R. Soc. London, 255, 417–467. doi:10.1098/rsta.1963.0009

Gauch, H.G., 2003. Scientific method in practice. Cambridge University Press.

Gaullier, V., Mart, Y., Bellaiche, G., Mascle, J., Vendeville, B.C., Zitter, T. a. C., 2000. Salt tectonics in and around the Nile deep-sea fan: insights from the PRISMED II cruise. Geol. Soc. London, Spec. Publ.,. doi:10.1144/GSL.SP.1999.174.01.07

Ghalayini, R., 2017. An Overview of the Tectonic Evolution of the Eastern Mediterranean and the NW Arabian Plate Since the Mesozoic, in: AAPG Regional Larnaca. Laranaca.

Ghalayini, R., Daniel, J., Homberg, C., 2014. Impact of Cenozoic strike-slip tectonics on the evolution of the northern Levant Basin (offshore Lebanon). Tectonics, 33, 2121–2142. doi:10.1002/2014TC003574.Received

Ghalayini, R., Homberg, C., Daniel, J.-M., Nader, F.H., 2016. Growth of layer-bound normal faults under a regional anisotropic stress field. Geol. Soc. London, Spec. Publ.,. doi:10.1144/SP439.13

Ginzburg, A., Ben-Avraham, Z., 1987. The deep structure of the central and southern Levant continental margin. Ann. Tectonicae, 1, 105–115.

Ginzburg, A., Kashai, E., 1981. Seismic measurements in the southern Dead Sea. Tectonophysics, 80, 67–80.

Gomez, F., Nemer, T., Tabet, C., Khawlie, M., Meghraoui, M., Barazangi, M., 2007. Strain partitioning of active transpression within the Lebanese restraining bend of the Dead Sea Fault (Lebanon and SW Syria). Geol. Soc. London, Spec. Publ., 290, 285–303. doi:10.1144/290.10

Gorini, C., Montadert, L., Rabineau, M., 2015. New imaging of the salinity crisis: Dual Messinian lowstand megasequences recorded in the deep basin of both the eastern and western Mediterranean. Mar. Pet. Geol., 1–17. doi:10.1016/j.marpetgeo.2015.01.009

Govers, R., Meijer, P., Krijgsman, W., 2009. Regional isostatic response to Messinian Salinity Crisis events. Tectonophysics, 463, 109–129. doi:10.1016/j.tecto.2008.09.026

Gradmann, S., Hübscher, C.P., Ben-Avraham, Z., Gajewski, D., Netzeband, G., 2005. Salt tectonics off northern Israel. Mar. Pet. Geol., 22, 597–611. doi:10.1016/j.marpetgeo.2005.02.001

Granot, R., 2016. Palaeozoic-aged oceanic crust preserved beneath the eastern Mediterranean. Nat. Geosci., in press, 1–6. doi:10.1038/ngeo2784

Guiraud, R., Bosworth, W., 1999. Phanerozoic geodynamic evolution of northeastern Africa and the northwestern Arabian platform. Tectonophysics, 315, 73–108. doi:10.1016/S0040-1951(99)00293-0

Guiraud, R., Bosworth, W., Thierry, J., Delplanque, a., 2005. Phanerozoic geological evolution of Northern and Central Africa: An overview. J. African Earth Sci., 43, 83–143. doi:10.1016/j.jafrearsci.2005.07.017

Gupta, S., Borah, K., Saha, G., 2016. Continental like crust beneath the Andaman Island through joint inversion of receiver function and surface wave from ambient seismic noise. Tectonophysics, 687, 129–138. doi:10.1016/j.tecto.2016.09.013

Gurnis, M., Turner, M., Zahirovic, S., DiCaprio, L., Spasojevic, S., Müller, R.D., Boyden, J., Seton, M., Manea, V.C., Bower, D.J., 2012. Plate tectonic reconstructions with continuously closing plates. Comput. Geosci., 38, 35–42. doi:10.1016/j.cageo.2011.04.014

Gvirtzman, Z., 2010. Gradual uplift and exposure of north Arabia and enhanced sedimentation in the Levant basin during Neo-Tethys closure. Geol. Surv. Isr., 24.

Gvirtzman, Z., Csato, I., Granjeon, D., 2014. Constraining sediment transport to deep marine basins through submarine channels: The Levant margin in the Late Cenozoic. Mar. Geol., 347, 12–26. doi:10.1016/j.margeo.2013.10.010

Gvirtzman, Z., Reshef, M., Buch-Leviatan, O., Ben-Avraham, Z., 2013. Intense salt deformation in the Levant Basin in the middle of the Messinian Salinity Crisis. Earth Planet. Sci. Lett., 379, 108–119. doi:10.1016/j.epsl.2013.07.018

Gvirtzman, Z., Reshef, M., Buch-Leviatan, O., Groves-Gidney, G., Karcz, Z., Makovsky, Y., Ben-Avraham, Z., 2015. Bathymetry of the Levant basin: interaction of salt-tectonics and surficial mass movements. Mar. Geol., 360, 25–39. doi:10.1016/j.margeo.2014.12.001

Gvirtzman, Z., Steinberg, J., 2012. Inland jump of the Arabian northwest plate boundary from the Levant continental margin to the Dead Sea Transform. Tectonics, 31, 1–13. doi:10.1029/2011TC002994

Gvirtzman, Z., Zilberman, E., Folkman, Y., 2008. Reactivation of the Levant passive margin during

the late Tertiary and formation of the Jaffa Basin offshore central Israel. J. Geol. Soc. London., 165, 563–578. doi:10.1144/0016-76492006-200

Hall, J., Aksu, A.E., Calon, T.J., Yaşar, D., 2005a. Varying tectonic control on basin development at an active microplate margin: Latakia Basin, Eastern Mediterranean. Mar. Geol., 221, 15–60. doi:10.1016/j.margeo.2004.05.034

Hall, J., Aksu, A.E., King, H., Gogacz, a., Yaltırak, C., Çifçi, G., 2014. Miocene–Recent evolution of the western Antalya Basin and its linkage with the Isparta Angle, eastern Mediterranean. Mar. Geol., 349, 1–23. doi:10.1016/j.margeo.2013.12.009

Hall, J., Calon, T.J., Aksu, A.E., Meade, S.R., 2005b. Structural evolution of the Latakia Ridge and Cyprus Basin at the front of the Cyprus Arc, Eastern Mediterranean Sea. Mar. Geol., 221, 261–297. doi:10.1016/j.margeo.2005.03.007

Hall, R., 2002. Cenozoic geological and plate tectonic evolution of SE Asia and the SW Pacific: Computer-based reconstructions, model and animations. J. Asian Earth Sci., 20, 353–431. doi:10.1016/S1367-9120(01)00069-4

Hall, R., Ali, J.R., Anderson, C.D., Baker, S.J., 1995. Origin and motion history of the Philippine Sea Plate. Tectonophysics, 251, 229–250. doi:10.1016/0040-1951(95)00038-0

Hanafy, S., Nimmagadda, S.L., Mahmoud, S.E., Mabrouk, W.M., Farhood, K., 2016. Regional integrated interpretation of the hydrocarbon prospectivity of the Nile Delta, Offshore Egypt. Arab. J. Geosci., 9, 376. doi:10.1007/s12517-016-2387-9

Hardenberg, M.F., Robertson, A.H.F., 2007. Sedimentology of the NW margin of the Arabian plate and the SW-NE trending Nahr El-Kabir half-graben in northern Syria during the latest Cretaceous and Cenozoic. Sediment. Geol., 201, 231–266. doi:10.1016/j.sedgeo.2007.02.009

Harding, T.P., 1990. Identification of Wrench Faults Using Subsurface Structural Data: Criteria and Pitfalls. Am. Assoc. Pet. Geol. Bull., 74, 1590–1609.

Hardy, C., Homberg, C., Eyal, Y., Barrier, É., Müller, C., 2010. Tectonic evolution of the southern Levant margin since Mesozoic. Tectonophysics, 494, 211–225. doi:10.1016/j.tecto.2010.09.007

Harrison, R.W., Newell, W.L., Batıhanlı, H., Panayides, I., McGeehin, J.P., Mahan, S.A., Őzhűr, A., Tsiolakis, E., Necdet, M., 2004. Tectonic framework and Late Cenozoic tectonic history of the northern part of Cyprus: implications for earthquake hazards and regional tectonics. J. Asian Earth Sci., 23, 191–210. doi:10.1016/S1367-9120(03)00095-6

Harrison, R.W., Tsiolakis, E., Stone, B.D., Lord, a., McGeehin, J.P., Mahan, S. a., Chirico, P., 2012. Late Pleistocene and Holocene uplift history of Cyprus: implications for active tectonics along the southern margin of the Anatolian microplate. Geol. Soc. London, Spec. Publ., 372, 561–584. doi:10.1144/SP372.3

Hart, B.S., 2011. Introduction to Seismic Interpretation, AAPG Discovery Series.

Hawie, N., Gorini, C., Deschamps, R., Nader, F.H., Montadert, L., Granjeon, D., Baudin, F., 2013. Tectono-stratigraphic evolution of the northern Levant Basin (offshore Lebanon). Mar. Pet. Geol., 48, 392–410. doi:10.1016/j.marpetgeo.2013.08.004

Hayes, D., Testor, P., Zodiatis, G., 2010. Glider transects in the Levantine Sea: a study of the warm core Cyprus Eddy. Rapp. Commun. Int. …, 2910.

Hempton, M.R., 1985. Structure and deformation history of the Bitlis suture near Lake Hazar, southeastern Turkey. Geol. Soc. Am. Bull., 96, 233–243. doi:10.1130/0016-7606(1985)96<233:SADHOT>2.0.CO;2

Hernández-Molina, F.J., Stow, D.A. V, Alvarez-Zarikian, C., Williams, T., Lofi, J., Acton, G.D., Bahr, A., Balestra, B., Ducassou, E., Flood, R.D., 2012. Integrated Ocean Drilling Program Expedition 339 Preliminary Report: Mediterranean Outflow: Environmental significance of the Mediterranean Outflow water and its global implications: 16 November 2011-16 January 2012. Integr. Ocean Drill. Progr. Exped. 339 Prelim. Rep. Mediterr. Outflow,.

Hinsbergen, D.J.J., Maffione, M., Plunder, A., Kaymakcı, N., Ganerød, M., Hendriks, B.W.H., Corfu, F., Gürer, D., Gelder, G.I.N.O., Peters, K., van Hinsbergen, D.J.J., 2016. Tectonic evolution and paleogeography of the Kırşehir Block and the Central Anatolian Ophiolites, Turkey. Tectonics, 35, 983–1014. doi:10.1017/CBO9781107415324.004

Hirano, N., Takahashi, E., Yamamoto, J., Abe, N., Ingle, S.P., Kaneoka, I., Hirata, T., Kimura, J.-I., Ishii, T., Ogawa, Y., Machida, S., Suyehiro, K., 2006. Volcanism in response to plate flexure. Science (80-.)., 313, 1426–1428. doi:10.1126/science.1128235

Hirsch, F., Flexer, A., Rosenfeld, A., Yellin-Dror, A., 1995. Palinspatic and crustal studies of the eastern Mediterranean. J. Pet. Geol., 18, 149–170. doi:10.1111/j.1747-5457.1995.tb00895.x

Hodgson, N., 2014. A seismic tool to reduce source maturity risk in unexplored basins. First Break, 32, 103–108.

Hodgson, N., 2013. Selecting a 3D Dataset for the 2013 Licence Round Offshore Lebanon. GeoExPro, 10, 38–40.

Hodgson, N., 2012. The Miocene hydrocarbon play in Southern Lebanon. First Break, 30, 93–98.

Hodgson, N.A., Karyna, K.R., 2015. Mediterranean Halokinesis and Hydrocarbon Plays - Much Ado about Everything. EAGE 2015 Abstr., 1–4.

Hsü, K., Cita, M.B., Ryan, W., 1973. The origin of the Mediterranean evaporites. Initial Reports Deep Sea Drill. Proj. 13, Part 2, 1203–1231. doi:doi:10.2973/dsdp.proc.13.143.1973

Hübscher, C.P., Tahchi, E., Klaucke, I., Maillard, a., Sahling, H., 2009. Salt tectonics and mud volcanism in the Latakia and Cyprus Basins, eastern Mediterranean. Tectonophysics, 470, 173–182. doi:10.1016/j.tecto.2008.08.019

Hudec, M.R., Jackson, M.P. a, 2007. Terra infirma: Understanding salt tectonics. Earth-Science Rev., 82, 1–28. doi:10.1016/j.earscirev.2007.01.001

Hurwitz, S., Garfunkel, Z., Ben-Gai, Y., Reznikov, M., Rotstein, Y., Gvirtzman, H., 2002. The tectonic framework of a complex pull-apart basin: seismic reflection observations in the Sea of Galilee, Dead Sea transform. Tectonophysics, 359, 289–306.

Hüsing, S.K., Zachariasse, W.-J., van Hinsbergen, D.J.J., Krijgsman, W., Inceoz, M., Harzhauser, M., Mandic, O., Kroh, A., 2009. Oligocene-Miocene basin evolution in SE Anatolia, Turkey: constraints on the closure of the eastern Tethys gateway. Geol. Soc. London, Spec. Publ., 311, 107–132. doi:10.1144/SP311.4

IHO, 2013. Standardization of Undersea Feature Names. Monaco.

Inati, L., Zeyen, H., Henri, F., Adelinet, M., Sursock, A., Elie, M., Roure, F., 2016. Tectonophysics Lithospheric architecture of the Levant Basin (Eastern Mediterranean region): A 2D modeling approach. Tectonophysics, 693, 143–156. doi:10.1016/j.tecto.2016.10.030

Inwood, J., Morris, A., Anderson, M.W., Robertson, A.H.F., 2009. Neotethyan intraoceanic microplate rotation and variations in spreading axis orientation: Palaeomagnetic evidence from the Hatay ophiolite (southern Turkey). Earth Planet. Sci. Lett., 280, 105–117. doi:10.1016/j.epsl.2009.01.021

Işler, F.I., Aksu, A.E., Hall, J., Calon, T.J., Yaşar, D., 2005. Neogene development of the Antalya Basin, Eastern Mediterranean: An active forearc basin adjacent to an arc junction. Mar. Geol., 221, 299–330. doi:10.1016/j.margeo.2005.03.006

Jolivet, L., Faccenna, C., 2000. Mediterranean extension and the Africa-Eurasia collision. Tectonics, 19, 1095–1106. doi:10.1029/2000TC900018

Jongsma, D., Fortuin, A., Huson, W., 1983. Discovery of an anoxic basin within the Strabo Trench, eastern Mediterranean. Lett. to Nat.,.

Kassinis, S., 2011. Offshore Cyprus, Geological Framework & Hydrocarbon Prospectivity, News & Emerging Plays in the East Mediterranean. Geological Society of London, London.

Katz, O., Reuven, E., Aharonov, E., 2015. Submarine landslides and fault scarps along the eastern Mediterranean Israeli continental-slope. Mar. Geol., 369, 100–115. doi:10.1016/j.margeo.2015.08.006

Kelling, G., Gökçen, S.L., Floyd, P.A., Gökçen, N., 1987. Neogene tectonics and plate convergence in the eastern Mediterranean: New data from southern Turkey. Geology, 15, 425–429. doi:10.1130/0091-7613(1987)15<425:NTAPCI>2.0.CO;2

Kempler, D., 1998. Eratosthenes Seamount: The Possible Spearhead of Incipient Continental Collision in the Eastern Mediterranean. Proc. Ocean Drill. Program, Sci. Results, 160, 709–721.

Kempler, D., 1994. Tectonic patterns in the Eastern Mediterranean. Hebrew University of Jerusalem.

Kempler, D., Garfunkel, Z., 1994. Structures and kinematics in the northeastern Mediterranean: A study of an irregular plate boundary. Tectonophysics, 234, 19–32.

doi:http://dx.doi.org/10.1016/0040-1951(94)90202-X

Kendall, C.G.S.C., Alsharhan, A.S., Marlow, L., 2014. Stratigraphy and depositional systems of the southern Tethyan region, in: Marlow, L., Kendall, C.G.S.C., Yose, L. (Eds.), Petroleum Systems of the Tethyan Region: AAPG Memoir 106. pp. 29–57.

Khair, K., Tsokas, G.N., Sawaf, T., 1997. Crustal structure of the northern Levant region: multiple source Werner deconvolution estimates for Bouguer gravity anomalies. Geophys. J. Int., 128, 605–616. doi:10.1111/j.1365-246X.1997.tb05322.x

Khairallah, C., Ghalayini, R., Chbat, W., 2017. Quantitative Analysis and Regional Restoration of The Oligo-Miocene Normal Fault Array of The Levant Basin, in: AAPG Regional Larnaca.

Kinnaird, T.C., 2008. Tectonic and sedimentary response to oblique and incipient continental-continental collision the easternmost Mediterranean (Cyprus). University of Edinburgh.

Kinnaird, T.C., Robertson, A.H.F., 2012. Tectonic and sedimentary response to subduction and incipient continental collision in southern Cyprus, easternmost Mediterranean region. Geol. Soc. London, Spec. Publ., 372, 585–614. doi:10.1144/SP372.10

Kirkham, C., Cartwright, J., Hermanrud, C., Jebsen, C., 2017. The spatial, temporal and volumetric analysis of a large mud volcano province within the Eastern Mediterranean. Mar. Pet. Geol., 81, 1–16. doi:10.1016/j.marpetgeo.2016.12.026

Klimke, J., Ehrhardt, A., 2014. Impact and implications of the Afro-Eurasian collision south of Cyprus from reflection seismic data. Tectonophysics, 626, 105–119. doi:10.1016/j.tecto.2014.04.002

Klitgord, K.D., Hutchinson, D.R., Schouten, H., 1988. US Atlantic continental margin; structural and tectonic framework. Geol. North Am., 2, 19–55.

Koloski, J.W., Schwarz, S.D., Tubbs, D.W., 1989. Geotechnical Properties of Geologic Materials. Washingt. Div. Geol. Earth Resour. Bull.,.

Kosi, W., Tari, G., Nader, F.H., Skiple, C., 2012. Structural analogy between the “piano key faults” of deep-water Lebanon and the extensional faults of the Canyonlands grabens, Utah, United States. Lead. Edge, 31, 824–830.

Krenkel, E., 1924. Der syrische bogen, zentralblatt fuer mineralogie. Geol. und Palaeontol., 9, 274–281.

Krijgsman, W., Hilgen, F.J., Raffi, I., Sierro, F., Wilson, D., 1999. Chronology, causes and progression of the Messinian salinity crisis. Nature, 400, 652–655.

Krogh, E.J., 1977. Evidence of Precambrian continent-continent collision in Western Norway. Nature, 267, 17–19.

Kurkin, A., Kuznetsov, V., Mitkalev, D., 2013. Structural and Stratigraphic Evolution of El Arish Block, Offshore North Sinai. 75th EAGE Conf. Exhib., 10–13.

Lawrence, R.D., Yeats, R.S., Khan, S.H., Farah, A., DeJong, K.A., 1981. Thrust and strike slip fault interaction along the Chaman transform zone, Pakistan. Geol. Soc. London, Spec.

Publ., 9, 363–370. doi:10.1144/GSL.SP.1981.009.01.33

Le Beon, M., Klinger, Y., Amrat, A.Q., Agnon, A., Dorbath, L., Baer, G., Ruegg, J.C., Charade, O., Mayyas, O., 2008. Slip rate and locking depth from GPS profiles across the southern Dead Sea Transform. J. Geophys. Res. Solid Earth, 113, 1–19. doi:10.1029/2007JB005280

Le Pichon, X., Gaulier, J.M., 1988. The rotation of Arabia and the Levant fault system. Tectonophysics, 153, 271–294. doi:10.1016/0040-1951(88)90020-0

Le Pichon, X., Kreemer, C., 2010. The Miocene-to-Present Kinematic Evolution of the Eastern Mediterranean and Middle East and Its Implications for Dynamics. Annu. Rev. Earth Planet. Sci., 38, 323–351. doi:10.1146/annurev-earth-040809-152419

Leroy, S., Razin, P., Autin, J., Bache, F., D'Acremont, E., Watremez, L., Robinet, J., Baurion, C., Denèle, Y., Bellahsen, N., Lucazeau, F., Rolandone, F., Rouzo, S., Kiel, J.S., Robin, C., Guillocheau, F., Tiberi, C., Basuyau, C., Beslier, M.-O., Ebinger, C., Stuart, G., Ahmed, A., Khanbari, K., Ganad, I.A.-, de Clarens, P., Unternehr, P., Toubi, K.A.-, Lazki, A.A.-, 2013. From rifting to oceanic spreading in the Gulf of Aden: A synthesis, in: Al Hosani, K., Roure, F., Ellison, R., Lokier, S. (Eds.), Lithosphere Dynamics and Sedimentary Basins: The Arabian Plate and Analogues. Springer Berlin Heidelberg, Berlin, Heidelberg, pp. 385–427. doi:10.1007/978-3-642-30609-9_20

Lewry, J.F., Hajnal, Z., Green, A., Lucas, S.B., White, D., Stauffer, M.R., Ashton, K.E., Weber, W., Clowes, R., 1994. Structure of a Paleoproterozoic continent-continent collision zone: a LITHOPROBE seismic reflection profile across the Trans-Hudson Orogen, Canada. Tectonophysics, 232, 143–160.

Li, C., Ronnier Luo, M., Li, C., Cui, G., 2012. The CRI-CAM02UCS colour rendering index. Color Res. Appl., 37, 160–167. doi:10.1002/col.20682

Li, C., van der Hilst, R.D., Meltzer, A.S., Engdahl, E.R., 2008. Subduction of the Indian lithosphere beneath the Tibetan Plateau and Burma. Earth Planet. Sci. Lett., 274, 157–168. doi:10.1016/j.epsl.2008.07.016

Libby, S., Underhill, J.R., 2015. ESM PMEK modelling, in: Tectonic Studies Group 2015 Conference. Edinburgh.

Lie, Ø., Fürstenau, J., Comstock, J., 2013. Will Lebanon Be the Next Oil Province? GeoExPro, 39–40.

Lie, Ø., Trayfoot, M., 2009. Seismic characterization of the first 3D surveys offshore Cyprus and Lebanon. Search Discov. Artic., 10194.

Litak, R.K., Barazangi, M., Brew, G., Sawaf, T., Al-Imam, A., Al-Youssef, W., 1998. Structure and evolution of the petroliferous Euphrates graben system, southeast Syria. Am. Assoc. Pet. Geol. Bull., 82, 1173–1190. doi:10.1306/1D9BCA2F-172D-11D7-8645000102C1865D

Lofi, J., Déverchère, J., Gaullier, V., Gillet, H., Gorini, C., Guennoc, P., Loncke, L., Maillard, A., Sage, F., Thinon, I., World, C. for the G.M. of the, 2011. Seismic Atlas of the Messinian Salinity Crisis markers in the Mediterranean and Black Seas. Mem. la Société Géologique

Fr., 179, p72.

Loncke, L., Gaullier, V., Mascle, J., Vendeville, B., Caméra, L., 2006. The Nile deep-sea fan: An example of interacting sedimentation, salt tectonics, and inherited subsalt paleotopographic features. Mar. Pet. Geol., 23, 297–315. doi:10.1016/j.marpetgeo.2006.01.001

Longacre, M., Bentham, P., Hanbal, I., 2007. New crustal structure of the Eastern Mediterranean basin: detailed integration and modeling of gravity, magnetic, seismic refraction, and seismic reflection data. Innov. EM, Grav Mag Methods 2007 Int. Work.,.

Lugli, S., Gennari, R., Gvirtzman, Z., Manzi, V., Roveri, M., Schreiber, B.C., 2013. Evidence of Clastic Evaporites In the Canyons of the Levant Basin (Israel): Implications For the Messinian Salinity Crisis. J. Sediment. Res., 83, 942–954. doi:10.2110/jsr.2013.72

Macgregor, D.S., 2012. The development of the Nile drainage system: integration of onshore and offshore evidence. Pet. Geosci., 18, 417–431. doi:10.1144/petgeo2011-074

Mahadevan, L., Bendick, R., Liang, H., 2010. Why subduction zones are curved. Tectonics, 29, 1–10. doi:10.1029/2010TC002720

Mahmoud, S., Reilinger, R., Mcclusky, S., Vernant, P., Tealeb, a, 2005. GPS evidence for northward motion of the Sinai Block: Implications for E. Mediterranean tectonics. Earth Planet. Sci. Lett., 238, 217–224. doi:10.1016/j.epsl.2005.06.063

Maillard, A., Hübscher, C.P., Benkhelil, J., Tahchi, E., 2011. Deformed Messinian markers in the Cyprus Arc: Tectonic and/or Messinian Salinity Crisis indicators? Basin Res., 23, 146–170. doi:10.1111/j.1365-2117.2010.00464.x

Main, C.E., Robertson, A.H.F., Palamakumbura, R.N., 2015. Pleistocene geomorphological and sedimentary development of the Akaki River catchment (northeastern Troodos Massif) in relation to tectonic uplift versus climatic change. Int. J. Earth Sci., 105, 463–485. doi:10.1007/s00531-015-1251-6

Major, C.O., Ryan, W.B.F., Jurado-Rodriguez, M.J., 1998. Evolution of paleoenvironments of Eratosthenes Seamount based on downhole logging integrated with carbonate petrology and reflection profiles, in: Proceedings of the Ocean Drilling Program. Scientific Results. Ocean Drilling Program, pp. 483–508.

Makris, J., Abraham, Z. Ben, Behle, A., Ginzburg, A., Giese, P., Steinmetz, L., Whitmarsh, R.B., Eleftheriou, S., 1983. Seismic refraction profiles between Cyprus and Israel and their interpretation. Geophys. J. R. Astron. Soc., 75, 575–591. doi:10.1111/j.1365-246X.1983.tb05000.x

Manzi, V., Gennari, R., Hilgen, F.J., Krijgsman, W., Lugli, S., Roveri, M., Sierro, F.J., 2013. Age refinement of the Messinian salinity crisis onset in the Mediterranean. Terra Nov., 25, 315–322. doi:10.1111/ter.12038

Manzi, V., Lugli, S., Roveri, M., Dela Pierre, F., Gennari, R., Lozar, F., Natalicchio, M., Schreiber, B.C., Taviani, M., Turco, E., 2014. The Messinian salinity crisis in Cyprus: a further step towards a new stratigraphic framework for Eastern Mediterranean. Basin Res., 1–30.

doi:10.1111/bre.12107

Marlow, L., 2014. Tectonostratigraphic History and Petroleum Potential of the Levantine Basin, Eastern Mediterranean, in: Petroleum Systems of the Tethyan Region: AAPG Memoir 106. AAPG Special Volumes.

Mart, Y., 2013. Geodynamics of the Middle East domain since the Oligocene: research summary. J. Geol. Soc. London., 170, 483–496. doi:10.1144/jgs2012-030

Mart, Y., Ryan, W.B.F., 2002. The complex tectonic regime of the Cyprus Arc: A short review. Isr. J. Earth Sci., 51, 117–134. doi:10.1560/DCF4-08Q2-UF1U-6QK5

Mart, Y., Vachtman, D., 2015. The internal grabens of the Levant Rifts and their geodynamic significance. Comptes Rendus Geosci., 347, 191–200. doi:10.1016/j.crte.2015.06.010

Mascle, J., Benkhelil, J., Bellaiche, G., Zitter, T. a. C., Woodside, J.M., Loncke, L., Prismed II Scientific Party, 2000. Marine geologic evidence for a Levantine-Sinai plate, a new piece of the Mediterranean puzzle. Geology,. doi:10.1130/0091-7613(2000)028<0779:MGEFAL>2.3.CO;2

Mascle, J., Sardou, O., Loncke, L., Migeon, S., Caméra, L., Gaullier, V., 2006. Morphostructure of the Egyptian Continental Margin: Insights from Swath Bathymetry Surveys. Mar. Geophys. Res., 27, 49–59. doi:10.1007/s11001-005-1559-x

Mascle, J., Zitter, T. a. C., Bellaiche, G., Droz, L., Gaullier, V., Loncke, L., 2001. The Nile deep sea fan: Preliminary results from a swath bathymetry survey. Mar. Pet. Geol., 18, 471–477. doi:10.1016/S0264-8172(00)00072-6

McCallum, J.E., Robertson, A.H.F., 1995. Sedimentology of two fan-delta systems in the Pliocene-Pleistocene of the Mesaoria Basin, Cyprus. Sediment. Geol., 98, 215–244. doi:http://dx.doi.org/10.1016/0037-0738(95)00034-6

McCay, G. a., Robertson, A.H.F., 2012. Upper Miocene-Pleistocene deformation of the Girne (Kyrenia) Range and Dar Dere (Ovgos) lineaments, northern Cyprus: role in collision and tectonic escape in the easternmost Mediterranean region. Geol. Dev. Anatolia Easternmost Mediterr. Reg., 372, 421–445. doi:10.1144/SP372.6

McClusky, S., Balassanian, S., Barka, A., Demir, C., Ergintav, S., Georgiev, I., Gurkan, O., Hamburger, M., Hurst, K., Kahle, H., Kastens, K., Kekelidze, G., King, R., Kotzev, V., Lenk, O., Mahmoud, S., Mishin, A., Nadariya, M., Ouzounis, A., Paradissis, D., Peter, Y., Prilepin, M., Reilinger, R., Sanli, I., Seeger, H., Tealeb, A., Toksöz, M.N., Veis, G., 2000. Global Positioning System constraints on plate kinematics and dynamics in the eastern Mediterranean and Caucasus. J. Geophys. Res., 105, 5695. doi:10.1029/1999JB900351

McCulloch, M.T., Cameron, W.E., 1983. Nd-Sr isotopic study of primitive lavas from the Troodos ophiolite, Cyprus: Evidence for a subduction-related setting. Geol. , 11, 727–731. doi:10.1130/0091-7613(1983)11<727:NISOPL>2.0.CO;2

McGregor, V.R., Friend, C.R.L., Nutman, A.P., 1991. The late Archaean mobile belt through Godthåbsfjord, southern West Greenland: a continent-continent collision zone. Bull. Geol.

Soc. Denmark, 39, 179–197.

McKenzie, D.P., 1970. Plate tectonics of the Mediterranean region. Nature, 226, 239–243.

Mechie, J., Abu-Ayyash, K., Ben-Avraham, Z., El-Kelani, R., Qabbani, I., Weber, M., 2009. Crustal structure of the southern Dead Sea basin derived from project DESIRE wide-angle seismic data. Geophys. J. Int., 178, 457–478. doi:10.1111/j.1365-246X.2009.04161.x

Meert, J.G., Van Der Voo, R., 1997. The assembly of Gondwana 800-550 Ma. J. Geodyn., 23, 223–235. doi:http://dx.doi.org/10.1016/S0264-3707(96)00046-4

Menna, M., Poulain, P.M., Zodiatis, G., Gertman, I., 2012. On the surface circulation of the Levantine sub-basin derived from Lagrangian drifters and satellite altimetry data. Deep. Res. Part I Oceanogr. Res. Pap., 65, 46–58. doi:10.1016/j.dsr.2012.02.008

Montadert, L., Lie, Ø., Semb, P.H., Kassinis, S., 2010. New seismic may put offshore Cyprus hydrocarbon prospects in the spotlight. First Break, 28, 91–101.

Montadert, L., Nicolaides, S., Semb, P.H., Lie, O., 2014. Petroleum Systems offshore Cyprus, in: Petroleum Systems of the Tethyan Region: AAPG Memoir 106. pp. 301–334. doi:10.1036/13431860M1063611

Morris, A., Robertson, A.H.F., Anderson, M.W., Hodgson, E., 2015. Did the Kyrenia Range of northern Cyprus rotate with the Troodos–Hatay microplate during the tectonic evolution of the eastern Mediterranean? Int. J. Earth Sci.,. doi:10.1007/s00531-015-1208-9

Moustafa, A.R., 2010. Structural setting and tectonic evolution of North Sinai folds, Egypt. Geol. Soc. London, Spec. Publ., 341, 37–63. doi:10.1144/SP341.3

Moustafa, A.R., Khalil, M.H., 1995. Superposed deformation in the northern Suez Rift, Egypt: Relevance to hydrocarbons exploration. J. Pet. Geol., 18, 245–266. doi:10.1306/BF9AB758-0EB6-11D7-8643000102C1865D

Moustafa, A.R., Khalil, M.H., 1994. Rejuvenation of the eastern Mediterranean passive continental margin in northern and central Sinai: new data from the Themed Fault. Geol. Mag., 131, 435–448.

Moustafa, a. R., Salama, M.E., Khalil, S.M., Fouda, H.G. a., 2014. Sinai hinge belt: a major crustal boundary in NE Africa. J. Geol. Soc. London., 171, 239–254. doi:10.1144/jgs2013-021

Mukasa, S.B., Ludden, J.N., 1987a. Uranium-lead isotopic ages of plagiogranites from the Troodos ophiolite, Cyprus, and their tectonic significance. Geol. , 15, 825–828. doi:10.1130/0091-7613(1987)15<825:UIAOPF>2.0.CO;2

Mukasa, S.B., Ludden, J.N., 1987b. Uranium-lead isotopic ages of plagiogranites from the Troodos ophiolite, Cyprus, and their tectonic significance. Geol. , 15, 825–828. doi:10.1130/0091-7613(1987)15<825:UIAOPF>2.0.CO;2

Nader, F.H., Browning-Stamp, P., Lecomte, J.-C., 2016. Geological Interpretation of 2D Seismic Reflection Profiles Onshore Lebanon: Implications for Petroleum Exploration. J. Pet. Geol., 39, 333–356. doi:10.1111/jpg.12656

Neev, D., 1977. The Pelusium Line—a major transcontinental shear. Tectonophysics,. doi:10.1016/0040-1951(77)90207-4

Netzeband, G.L., 2006. The Levantine Basin – a seismic investigation of the crustal structure and the evolution of the Messinian evaporites.

Netzeband, G.L., Gohl, K., Hübscher, C.P., Ben-Avraham, Z., Dehghani, G. a., Gajewski, D., Liersch, P., 2006a. The Levantine Basin—crustal structure and origin. Tectonophysics, 418, 167–188. doi:10.1016/j.tecto.2006.01.001

Netzeband, G.L., Hübscher, C.P., Gajewski, D., 2006b. The structural evolution of the Messinian evaporites in the Levantine Basin. Mar. Geol., 230, 249–273. doi:10.1016/j.margeo.2006.05.004

Nielsen, C., Chamot-Rooke, N., Rangin, C., 2004. From partial to full strain partitioning along the Indo-Burmese hyper-oblique subduction. Mar. Geol., 209, 303–327. doi:10.1016/j.margeo.2004.05.001

Nocquet, J.M., 2012. Present-day kinematics of the Mediterranean: A comprehensive overview of GPS results. Tectonophysics, 579, 220–242. doi:10.1016/j.tecto.2012.03.037

Omeru, T., Cartwright, J.A., 2015. Multistage, progressive slope failure in the Pleistocene pro-deltaic slope of the West Nile Delta (Eastern Mediterranean). Mar. Geol., 362, 76–92. doi:10.1016/j.margeo.2015.01.012

Orszag-Sperber, F., Caruso, A., Blanc-Valleron, M.M., Merle, D., Rouchy, J.M., 2009. The onset of the Messinian salinity crisis: Insights from Cyprus sections. Sediment. Geol., 217, 52–64. doi:10.1016/j.sedgeo.2009.03.006

Öztürk, B., Rovere, M., 2015. Seamounts and Seamount-like Structures of the Eastern Mediterranean. Atlas Mediterr. seamounts seamount-like Struct., 226–264.

Palamakumbura, R.N., Robertson, A.H.F., 2016a. Pleistocene terrace deposition related to tectonically controlled surface uplift: An example of the Kyrenia Range lineament in the northern part of Cyprus. Sediment. Geol., 339, 46–67. doi:10.1016/j.sedgeo.2016.03.022

Palamakumbura, R.N., Robertson, A.H.F., 2016b. Pliocene–Pleistocene sedimentary–tectonic development of the Mesaoria (Mesarya) Basin in an incipient, diachronous collisional setting: facies evidence from the north of Cyprus. Geol. Mag., 1–26. doi:10.1017/S0016756816001072

Palamakumbura, R.N., Robertson, A.H.F., Kinnaird, T.C., Van Calsteren, P., Kroon, D., Tait, J., 2016. Quantitative dating of Pleistocene deposits of the Kyrenia Range, northern Cyprus: implications for timings, rates of uplift and driving mechanisms. J. Geol. Soc. London.,. doi:10.1144/jgs2015-130

Papazachos, B.C., Papaioannou, C.A., 1999. Lithospheric boundaries and plate motions in the Cyprus area. Tectonophysics, 308, 193–204.

Payne, A.S., Robertson, A.H.F., 1995. Neogene supra-subduction zone extension in the Polis

graben system, west Cyprus. J. Geol. Soc. London., 152, 613–628. doi:10.1144/gsjgs.152.4.0613

Peck, J.M., 2008. Giant oil prospects lie in distal portion of offshore East Mediterranean basin. Oil Gas J., 4–9.

Peel, F.J., 2014. How do salt withdrawal minibasins form? Insights from forward modelling, and implications for hydrocarbon migration. Tectonophysics, 630, 222–235. doi:10.1016/j.tecto.2014.05.027

Pindell, J., Graham, R., Horn, B., 2014. Rapid outer marginal collapse at the rift to drift transition of passive margin evolution, with a Gulf of Mexico case study. Basin Res., 26, 701–725. doi:10.1111/bre.12059

Pindell, J., Kennan, L., 2001. Kinematic Evolution of the Gulf of Mexico. Pet. Syst. Deep. Basins, GCSSEPM Found. 21st Annu. Bob F. Perkins Res. Conf., 193–220. doi:10.5724/gcs.01.21.0159

Plummer, M., Belopolsky, A., Fish, P., Norton, M., 2013. Tectonostratigraphic Evolution and Exploration Potential of the Northern Levant Basin. AAPG Search Discov. Artic., 10516.

Poisson, A., Yagmurlu, F., Bozcu, M., Senturk, M., 2003. New insights on the tectonic setting and evolution around the apex of the Isparta Angle (SW Turkey). Geol. J., 38, 257–282. doi:10.1002/gj.955

Poole, A., Shimmield, G., Robertson, A.H.F., 1990. Late Quaternary uplift of the Troodos ophiolite, Cyprus: Uranium-series dating of Pleistocene coral. Geology, 18, 894–897. doi:10.1130/0091-7613(1990)018<0894

Poole, a. J., Robertson, A.H.F., 1991. Quaternary uplift and sea-level change at an active plate boundary, Cyprus. J. Geol. Soc. London., 148, 909–921. doi:10.1144/gsjgs.148.5.0909

Powell, C.M., Williams, G.D., 1989. The Lewis Thrust/Rocky Mountain trench fault system in Northwest Montana, USA: an example of negative inversion tectonics? Geol. Soc. London, Spec. Publ., 44, 223–234. doi:10.1144/GSL.SP.1989.044.01.13

Price, J.F., Baringer, M.O., Lueck, R.G., Johnson, G.C., Ambar, I., Parrilla, G., Cantos, A., Kennelly, M. a, Sanford, T.B., 1993. Mediterranean Outflow Mixing Dynamics. Science (80-.)., 259, 1277–1282. doi:10.1126/science.259.5099.1277

Quennell, A.M., 1984. The Western Arabia rift system. Geol. Soc. London, Spec. Publ. , 17, 775–788. doi:10.1144/GSL.SP.1984.017.01.62

Quennell, A.M., 1958. The Structural and Geomorphic Evolution of the Dead Sea Rift. Q. J. Geol. Soc., 114, 1–24. doi:10.1144/gsjgs.114.1.0001

Reiche, S., 2015. A seismic reflection study of salt tectonics and incipient continent-continent-collision in the easternmost Mediterranean Sea. University of Hamburg.

Reiche, S., Hübscher, C.P., 2015. The Hecataeus Rise, easternmost Mediterranean: A structural record of Miocene-Quaternary convergence and incipient continent-continent-collision at the

African-Anatolian plate boundary. Mar. Pet. Geol., 67, 368–388. doi:10.1016/j.marpetgeo.2015.04.021

Reiche, S., Hübscher, C.P., Beitz, M., 2014a. Fault-controlled evaporite deformation in the Levant Basin, Eastern Mediterranean. Mar. Geol., 354, 53–68. doi:10.1016/j.margeo.2014.05.002

Reiche, S., Hübscher, C.P., Ehrhardt, A., 2015. The impact of salt on the late Messinian to recent tectonostratigraphic evolution of the Cyprus subduction zone. Basin Res.,. doi:10.1111/bre.12122

Reiche, S., Hübscher, C.P., Ehrhardt, A., Klimke, J., 2014b. The fate of salt in the Cyprus subduction zone 16, 6050.

Reilinger, R., McClusky, S., Vernant, P., Lawrence, S., Ergintav, S., Cakmak, R., Ozener, H., Kadirov, F., Guliev, I., Stepanyan, R., 2006. GPS constraints on continental deformation in the Africa-Arabia-Eurasia continental collision zone and implications for the dynamics of plate interactions. J. Geophys. Res. Solid Earth, 111.

Replumaz, A., Negredo, A.M., Guillot, S., Villaseñor, A., 2010. Multiple episodes of continental subduction during India/Asia convergence: Insight from seismic tomography and tectonic reconstruction. Tectonophysics, 483, 125–134. doi:10.1016/j.tecto.2009.10.007

Ricou, L.-E., 1994. Tethys reconstructed: plates, continental fragments and their Boundaries since 260 Ma from Central America to South-eastern Asia. Geodin. Acta, 7, 169–218.

Roberts, G., Harmer, C., Peace, D., 2010. Plays and Prospectivity Offshore Lebanon, Syria and Cyprus: New Insights from Depth-Imaged Seismic Data. w.searchanddiscovery.com, 10262.

Roberts, G., Peace, D., 2007. Hydrocarbon plays and prospectivity of the Levantine Basin, offshore Lebanon and Syria from modern seismic data. GeoArabia, 12.

Robertson, A., 2000. Tectonic evolution of Cyprus in its easternmost Mediterranean setting. Third Int. Conf. Geol. East. Mediterr. Proc., 11–44.

Robertson, A.H.F., 2007. Overview of tectonic settings related to the rifting and opening of Mesozoic ocean basins in the Eastern Tethys: Oman, Himalayas and Eastern Mediterranean regions. Geol. Soc. London, Spec. Publ., 282, 325–388. doi:10.1144/SP282.15

Robertson, A.H.F., 2006. Sedimentary evidence from the south Mediterranean region (Sicily, Crete, Peloponnese, Evia) used to test alternative models for the regional tectonic setting of Tethys during Late Palaeozoic-Early Mesozoic time. Geol. Soc. London, Spec. Publ., 260, 91–154. doi:10.1144/GSL.SP.2006.260.01.06

Robertson, A.H.F., 1998a. Mesozoic-Tertiary tectonic evolution of the easternmost Mediterranean area: integration of marine and land evidence. Proc. Ocean Drill. Program., 160.

Robertson, A.H.F., 1998b. Tectonic significance of the Eratosthenes Seamount: a continental fragment in the process of collision with a subduction zone in the eastern Mediterranean

(Ocean Drilling Program Leg 160). Tectonophysics, 298, 63–82. doi:10.1016/S0040-1951(98)00178-4

Robertson, A.H.F., 1998c. Formation and destruction of the Eratosthenes Seamount, Eastern Mediterranean Sea, and implications for collisional processes. Proc. Ocean Drill. Program, Sci. Results, 160, 681–699.

Robertson, A.H.F., 1990. Tectonic evolution of Cyprus, in: Malpa, J., Moores, E., Panayiotis, A., Xenophontos, C. (Eds.), Proceedings of Symposium “Troodos 1987.” Geol Surv Dept Cyprus, pp. 235–253.

Robertson, A.H.F., 1977. Tertiary uplift history of the Troodos massif, Cyprus. Bull. Geol. Soc. Am., 88, 1763–1772. doi:10.1130/0016-7606(1977)88<1763:TUHOTT>2.0.CO;2

Robertson, A.H.F., Dixon, J.E., Brown, S., Collins, A.S., Morris, a., Pickett, E., Sharp, I., Ustaomer, T., 1996. Alternative tectonic models for the Late Palaeozoic-Early Tertiary development of Tethys in the Eastern Mediterranean region. Geol. Soc. London, Spec. Publ., 105, 239–263. doi:10.1144/GSL.SP.1996.105.01.22

Robertson, A.H.F., Eaton, S., Follows, E.J., Payne, A.S., 1995. Depositional processes and basin analysis of Messinian evaporites in Cyprus. Later Tertiary-Quaternary Mediterr. tectonics paleo-environments., 7; 2, 233–253. doi:-

Robertson, A.H.F., Emeis, D.K.-C., Richter, D.C., Blanc-Valleron, M.M., Bouloubassi, I., Brumsack, H.-J., Cramp, a., Di Stefano, G.J., Flecker, R., Frankel, E., Howell, M.W., Janecek, T.R., Jurado, M.-J., Kemp, a. E.S., Koizumi, I., Kopf, a., Major, C.O., Mart, Y., Pribnow, D.F.C., Rabaute, a., Roberts, a. P., Rullkotter, J., Sakamoto, T., Spezzaferri, S., Staerker, T.S., Stoner, J.S., Whiting, B.M., Woodside, J.M., 1998. Collision-related break-up of a carbonate platform (Eratosthenes Seamount) and mud volcanism on the Mediterranean Ridge: preliminary synthesis and implications of tectonic results of ODP Leg 160 in the Eastern Mediterranean Sea. Geol. Soc. London, Spec. Publ., 131, 243–271. doi:10.1144/GSL.SP.1998.131.01.16

Robertson, A.H.F., Kinnaird, T.C., 2015. Structural development of the central Kyrenia Range (north Cyprus) in its regional setting in the eastern Mediterranean region. Int. J. Earth Sci.,. doi:10.1007/s00531-015-1215-x

Robertson, A.H.F., Mccay, G.A., Tasli, K., Yildiz, A., 2014. Eocene development of the northerly active continental margin of the Southern Neotethys in the Kyrenia Range, north Cyprus. Geol. Mag., 151, 692–731. doi:Doi 10.1017/S0016756813000563

Robertson, A.H.F., Parlak, O., Ustaomer, T., 2013. Late Palaeozoic-Early Cenozoic tectonic development of Southern Turkey and the easternmost Mediterranean region: evidence from the inter-relations of continental and oceanic units. Geol. Soc. London, Spec. Publ., 372, 9–48. doi:10.1144/SP372.22

Robertson, A.H.F., Parlak, O., Ustaomer, T., 2012a. Overview of the Palaeozoic-Neogene evolution of Neotethys in the Eastern Mediterranean region (southern Turkey, Cyprus,

Syria). Pet. Geosci., 18, 381–404. doi:10.1144/petgeo2011-091

Robertson, A.H.F., Tasli, K., İnan, N., 2012b. Evidence from the Kyrenia Range, Cyprus, of the northerly active margin of the Southern Neotethys during Late Cretaceous–Early Cenozoic time. Geol. Mag., 149, 264–290. doi:10.1017/S0016756811000677

Robertson, A.H.F., Unlügenç, Ü.C., Inan, N., Tasli, K., 2004. The Misis-Andırın Complex: a Mid-Tertiary melange related to late-stage subduction of the Southern Neotethys in S Turkey. J. Asian Earth Sci., 22, 413–453. doi:Doi: 10.1016/s1367-9120(03)00062-2

Robertson, A.H.F., Xenophontos, C., 1997. Cyprus, in: Encyclopedia of European and Asian Regional Geology SE - 23, Encyclopedia of Earth Science. Springer Netherlands, pp. 160–171. doi:10.1007/1-4020-4495-X_23

Robertson, A.H.F., Xenophontos, C., 1993. Development of concepts concerning the Troodos ophiolite and adjacent units in Cyprus. Geol. Soc. London, Spec. Publ., 76, 85–119. doi:10.1144/GSL.SP.1993.076.01.05

Rosenbaum, G., Lister, G.S., Duboz, C., 2002. Relative motions of Africa, Iberia and Europe during Alpine orogeny. Tectonophysics, 359, 117–129. doi:10.1016/S0040-1951(02)00442-0

Rotstein, Y., Kafka, A.L., 1982. Seismotectonics of the southern boundary of Anatolia, eastern Mediterranean region: Subduction, collision, and arc jumping. J. Geophys. Res. Solid Earth, 87, 7694–7706. doi:10.1029/JB087iB09p07694

Roveri, M., Flecker, R., Krijgsman, W., Lofi, J., Lugli, S., Manzi, V., Sierro, F.J., Bertini, A., Camerlenghi, A., De Lange, G., Govers, R., Hilgen, F.J., Hübscher, C.P., Meijer, P.T., Stoica, M., 2014. The Messinian Salinity Crisis: Past and future of a great challenge for marine sciences. Mar. Geol., 352, 25–58. doi:10.1016/j.margeo.2014.02.002

Rowan, M.G., Peel, F.J., Vendeville, B.C., Gaullier, V., 2012. Salt tectonics at passive margins: Geology versus models–Discussion. Mar. Pet. Geol., 37, 184–194.

Rukieh, M., Trifonov, V.G., Dodonov, a. E., Minini, H., Ammar, O., Ivanova, T.P., Zaza, T., Yusef, a., Al-Shara, M., Jobaili, Y., 2005. Neotectonic map of Syria and some aspects of Late Cenozoic evolution of the northwestern boundary zone of the Arabian plate. J. Geodyn., 40, 235–256. doi:10.1016/j.jog.2005.07.016

Ryan, W.B.F., 1978. Messinian badlands on the southeastern margin of the Mediterranean Sea. Mar. Geol., 27, 349–363. doi:http://dx.doi.org/10.1016/0025-3227(78)90039-7

Ryan, W.B.F., Carbotte, S.M., Coplan, J.O., O'Hara, S., Melkonian, A., Arko, R., Weissel, R.A., Ferrini, V., Goodwillie, A., Nitsche, F., Bonczkowski, J., Zemsky, R., 2009. Global Multi-Resolution Topography synthesis. Geochemistry, Geophys. Geosystems, 10. doi:10.1029/2008GC002332

Rybakov, M., Goldshmidt, V., Hall, J.K., Ben-Avraham, Z., Lazar, M., 2011. New insights into the sources of magnetic anomalies in the Levant. Russ. Geol. Geophys., 52, 377–397. doi:10.1016/j.rgg.2011.03.001

Rybakov, M., Segev, A., 2004. Top of the crystalline basement in the Levant. Geochemistry, Geophys. Geosystems, 5. doi:10.1029/2004GC000690

Sage, L., Letouzey, J., 1990. Convergence of the African and Eurasian plate in the eastern Mediterranean. Pet. tectonics Mob. belts, 49–68.

Sagy, Y., Gvirtzman, Z., Reshef, M., Makovsky, Y., 2015. The enigma of the Jonah high in the middle of the Levant basin and its significance to the history of rifting. Tectonophysics, 665, 186–198. doi:10.1016/j.tecto.2015.09.037

Said, R., 1981. The geological evolution of the River Nile. Springer Science & Business Media.

Salamon, A., Hofstetter, A., Garfunkel, Z., Ron, H., 2003. Seismotectonics of the Sinai subplate - The eastern Mediterranean region. Geophys. J. Int., 155, 149–173. doi:10.1046/j.1365-246X.2003.02017.x

Salamon, A., Hofstetter, A., Garfunkel, Z., Ron, H., 1996. Seismicity of the eastern Mediterranean region: Perspective from the Sinai subplate. Tectonophysics, 263, 293–305. doi:10.1016/S0040-1951(96)00030-3

Saleh, S., 2013. 3D Crustal and Lithospheric Structures in the Southeastern Mediterranean and Northeastern Egypt. Pure Appl. Geophys., 170, 2037–2074. doi:10.1007/s00024-013-0673-y

Samuel, A., Kneller, B., Raslan, S., Sharp, A., 2003. Prolific deep-marine slope channels of the Nile Delta, Egypt. Am. Assoc. Pet. Geol. Bull., 4, 541–560.

Sandvol, E., Turkelli, N., Barazangi, M., 2003. The Eastern Turkey Seismic Experiment: The study of a young continent-continent collision. Geophys. Res. Lett., 30. doi:10.1029/2003GL018912

Sandwell, D.T., Garcia, E., Soofi, K., Wessel, P., Chandler, M., Smith, W.H.F., 2013. Toward 1-mGal accuracy in global marine gravity from CryoSat-2, Envisat, and Jason-1. Lead. edge, 892–899. doi:10.1190/tle32080892.1

Sandwell, D.T., Müller, R.D., Smith, W.H.F., Garcia, E., Francis, R., 2014. New global marine gravity model from CryoSat-2 and Jason-1 reveals buried tectonic structure. Science, 346, 65–7. doi:10.1126/science.1258213

Sandwell, D.T., Smith, W.H.F., 2009. Global marine gravity from retracked Geosat and ERS-1 altimetry: Ridge Segmentation versus spreading rate. J. Geophys. Res., 114. doi:10.1029/2008JB006008

Sarhan, M.A., Collier, R.E.L., Basal, A., Abdel Aal, M.H., 2013. Late Miocene normal faulting beneath the northern Nile Delta: NNW propagation of the Gulf of Suez Rift. Arab. J. Geosci., 7, 4563–4571. doi:10.1007/s12517-013-1089-9

Sawaf, T., Brew, G., Litak, R., Barazangi, M., 2001. Geologic evolution of the intraplate Palmyride basin and Euphrates fault system, Syria, in: Ziegler, P., Cavazza, W., Robertson, A., Crasquin-Soleau, S. (Eds.), PeriTethys Memoir #6. pp. 441–467.

Schattner, U., 2010. What triggered the early-to-mid Pleistocene tectonic transition across the entire eastern Mediterranean? Earth Planet. Sci. Lett., 289, 539–548. doi:10.1016/j.epsl.2009.11.048

Schattner, U., Ben-Avraham, Z., 2007. Transform margin of the northern Levant, eastern Mediterranean: From formation to reactivation. Tectonics, 26, 1–17. doi:10.1029/2007TC002112

Schattner, U., Ben-Avraham, Z., Lazar, M., Hübscher, C.P., 2006. Tectonic isolation of the Levant basin offshore Galilee-Lebanon – effects of the Dead Sea fault plate boundary on the Levant continental margin, eastern Mediterranean. J. Struct. Geol., 28, 2049–2066. doi:10.1016/j.jsg.2006.06.003

Schattner, U., Lazar, M., 2016. Hierarchy of source-to-sink systems - example from the Nile distribution across the eastern Mediterranean. Sediment. Geol., 343, 119–131. doi:10.1016/j.sedgeo.2016.08.006

Schattner, U., Lazar, M., 2014. Flip convergence across the Phoenician basin through nucleation of subduction. Gondwana Res., 25, 729–735. doi:10.1016/j.gr.2013.09.010

Schellart, W.P., Lister, G.S., Toy, V.G., 2006. A Late Cretaceous and Cenozoic reconstruction of the Southwest Pacific region: Tectonics controlled by subduction and slab rollback processes. Earth-Science Rev., 76, 191–233. doi:10.1016/j.earscirev.2006.01.002

Schildgen, T.F., Cosentino, D., Bookhagen, B., Niedermann, S., Yıldırım, C., Echtler, H., Wittmann, H., Strecker, M.R., 2012. Multi-phased uplift of the southern margin of the Central Anatolian plateau, Turkey: A record of tectonic and upper mantle processes. Earth Planet. Sci. Lett., 317–318, 85–95. doi:http://dx.doi.org/10.1016/j.epsl.2011.12.003

Schirmer, W., Weber, J., Bachtadse, V., BouDagher-Fadel, M., Heller, F., Lehmkuhl, F., Panayides, I., Schirmer, U., 2010. Fluvial stacking due to plate collision and uplift during the Early Pleistocene in Cyprus. Cent. Eur. J. Geosci., 2, 514–523. doi:10.2478/v10085-010-0023-6

Searle, M.P., Chung, S.-L., Lo, C.-H., 2010. Geological offsets and age constraints along the northern Dead Sea fault, Syria. J. Geol. Soc. London., 167, 1001–1008. doi:10.1144/0016-76492010-009

Segev, A., 2005. Phanerozoic Magmatic Activity Associated with Vertical Motions in Israel and the Adjacent Countries, in: Hall, J.K., Krasheninnikov, V.A., Hirsch, F., Benjamini, C., Flexer, A. (Eds.), Geological Framework of the Levant Volume II: The Levantine Basin and Israel. p. 836.

Selim, E.S., Abouad, E., Moustafa, S.S.R., Al-Arifi, N.S., 2016. Active tectonic trends and crustal modeling of the eastern Mediterranean Sea deduced from geophysical data. Environ. Earth Sci., 75, 1–13. doi:10.1007/s12665-016-5842-8

Selim, E.S.I., 2013. Subsurface structural trends of the offshore Nile Delta area, Egypt: Evidences from gravity and magnetic data. Environ. Earth Sci., 68, 1015–1032. doi:10.1007/s12665-

012-1804-y

Sellier, N.C., Loncke, L., Vendeville, B.C., Mascle, J., Zitter, T. a. C., Woodside, J.M., Loubrieu, B., 2013. Post-Messinian evolution of the Florence Ridge area (Western Cyprus Arc), Part I: Morphostructural analysis. Tectonophysics, 591, 131–142. doi:10.1016/j.tecto.2012.04.001

Şengör, A.M.C., 1979. Mid-Mesozoic closure of Permo-Triassic Tethys and its implications. Nature, 279, 590–593.

Sengör, A.M.C., Yilmaz, Y., 1981. Tethyan evolution of Turkey: A plate tectonic approach. Tectonophysics, 75, 181–241. doi:10.1016/0040-1951(81)90275-4

Seno, T., Rehman, H.U., 2011. When and why the continental crust is subducted: Examples of Hindu Kush and Burma. Gondwana Res., 19, 327–333. doi:10.1016/j.gr.2010.05.011

Seton, M., Müller, R.D., Zahirovic, S., Gaina, C., Torsvik, T.H., Shephard, G., Talsma, a., Gurnis, M., Turner, M., Maus, S., Chandler, M., 2012. Global continental and ocean basin reconstructions since 200Ma. Earth-Science Rev., 113, 212–270. doi:10.1016/j.earscirev.2012.03.002

Shipboard Scientific Party, 1978. Sites 375 and 376: Florence Rise. Initial Reports Deep. Drill. Proj.,.

Skiple, C., Anderson, E., Furstenau, J., 2012. Seismic interpretation and attribute analysis of the Herodotus and the Levantine Basin, offshore Cyprus and Lebanon. Pet. Geosci., 18, 433–442. doi:10.1144/petgeo2011-072

Skiple, C., Sortemos, T., Lie, O., Lowrey, C.J., Semb, P.H., 2011. Regional geological understanding of offshore Cyprus and Lebanon from interpretation of dual-sensor streamer data. SPE Middle East Oil Gas Show Conf., 1–19. doi:10.2118/142290-MS

Slotnick, M., 1936. On Seismic Computations, With Applications, I. Geophysics, 1, 9–22. doi:10.1190/1.1437084

Spezzaferri, S., Tamburini, F., 2007. Paleodepth variations on the Eratosthenes Seamount (Eastern Mediterranean): sea-level changes or subsidence? eEarth Discuss., 115–132.

Stampfli, G., Borel, G., 2004. The TRANSMED Transects in Space and Time: Constraints on the Paleotectonic Evolution of the Mediterranean Domain, in: Cavazza, W., Roure, F., Spakman, W., Stampfli, G., Ziegler, P. (Eds.), The TRANSMED Atlas. The Mediterranean Region from Crust to Mantle SE - 3. Springer Berlin Heidelberg, pp. 53–80. doi:10.1007/978-3-642-18919-7_3

Stampfli, G., Borel, G., 2002. A plate tectonic model for the Paleozoic and Mesozoic constrained by dynamic plate boundaries and restored synthetic oceanic isochrons. Earth Planet. Sci. Lett., 196, 17–33.

Stampfli, G., Borel, G., Cavazza, W., 2001. Palaeotectonic and palaeogeographic evolution of the western Tethys and PeriTethyan domain (IGCP Project 369). Episodes, 1–6.

Stampfli, G., Marcoux, J., Baud, A., 1991. Palaeogeography and Paleoceanography of Tethys Tethyan margins in space and time. Palaeogeogr. Palaeoclimatol. Palaeoecol., 87, 373–409. doi:http://dx.doi.org/10.1016/0031-0182(91)90142-E

Steckler, M.S., Brink, U.S. ten, 1986. Lithospheric strength variations as a control on new plate boundaries: examples from the Arabian Plate. Earth Planet. Sci. Lett., 79, 120–132.

Steckler, M.S., Feinstein, S., Kohn, B.P., Lavier, L.L., Eyal, M., 1998. Pattern of mantle thinning from subsidence and heat flow measurements in the Gulf of Suez: Evidence for the rotation of Sinai and along-strike flow from the Red Sea. Tectonics, 17, 903. doi:10.1029/1998TC900002

Steinberg, J., Gvirtzman, Z., Folkman, Y., Garfunkel, Z., 2011. Origin and nature of the rapid late Tertiary filling of the Levant Basin. Geology, 39, 355–358. doi:10.1130/G31615.1

Steinberg, J., Gvirtzman, Z., Garfunkel, Z., 2014. Flexuarl response of a continental margin to sedimentary loading and lithospheric rupturing: The mountain ridge between the Levant Basin and the Dead Sea Transform. Tectonics, 33, 166–186. doi:10.1002/2013TC003330

Steinitz, G., Bartov, Y., Hunziker, J.C., 1978. K-Ar age determinations of some Miocene–Pliocene basalts in Israel: their significance to the tectonics of the rift valley. Geol. Mag., 115, 329–340. doi:10.1017/S0016756800037341

Stern, R.J., 2010. The anatomy and ontogeny of modern intra-oceanic arc systems. Geol. Soc. London, Spec. Publ., 338, 7–34. doi:10.1144/SP338.2

Stern, R.J., Johnson, P., 2010. Continental lithosphere of the Arabian Plate: A geologic, petrologic, and geophysical synthesis. Earth-Science Rev., 101, 29–67. doi:10.1016/j.earscirev.2010.01.002

Stow, D.A.V., Faugères, J.-C., Howe, J.A., Pudsey, C.J., Viana, A.R., 2002. Bottom currents, contourites and deep-sea sediment drifts: current state-of-the-art. Geol. Soc. London, Mem., 22, 7–20. doi:10.1144/GSL.MEM.2002.022.01.02

Surlyk, F., Lykke-Andersen, H., 2007. Contourite drifts, moats and channels in the Upper Cretaceous chalk of the Danish Basin. Sedimentology, 54, 405–422. doi:10.1111/j.1365-3091.2006.00842.x

Tahchi, E., Urgeles, R., Hübscher, C.P., Benkhelil, J., 2010. Mass Wasting at the Easternmost Cyprus Arc, Off Syria, Eastern Mediterranean. Adv. Nat. Technol. Hazards Res., 28, 323–334.

Tapponnier, P., Peltzer, G., Le Dain, a Y., Armijo, R., Cobbold, P.R., 1983. Propagation extrusion tectonics in Asia: New insights from experiments with plasticine. Geology, 10, 611–616. doi:10.1130/0091-7613(1982)10<611:PETIAN>2.0.CO;2

Tari, G., Hussein, H., Novotny, B., Hannke, K., Kohazy, R., 2012. Play types of the deep-water Matruh and Herodotus basins, NW Egypt. Pet. Geosci., 18, 443–455. doi:10.1144/petgeo2012-011

Tassy, A., Crouzy, E., Gorini, C., Rubino, J.L., Bouroullec, J.L., Sapin, F., 2015. Egyptian Tethyan margin in the Mesozoic: Evolution of a mixed carbonate-siliciclastic shelf edge (from Western Desert to Sinai). Mar. Pet. Geol., 68, 565–581. doi:10.1016/j.marpetgeo.2015.10.011

Tavarnelli, E., 1999. Normal faults in thrust sheets: Pre-orogenic extension, post-orogenic extension, or both? J. Struct. Geol., 21, 1011–1018. doi:10.1016/S0191-8141(99)00034-6

Ten Veen, J.H., Kleinspehn, K.L., 2003. Incipient continental collision and plate-boundary curvature: Late Pliocene-Holocene transtensional Hellenic forearc, Crete, Greece. J. Geol. Soc. London., 160, 161–182. doi:10.1144/0016-764902-067

ten Veen, J.H., Woodside, J.M., Zitter, T. a. C., Dumont, J.F., Mascle, J., Volkonskaia, A., 2004. Neotectonic evolution of the Anaximander Mountains at the junction of the Hellenic and Cyprus arcs. Tectonophysics, 391, 35–65. doi:10.1016/j.tecto.2004.07.007

The Egyptian Geological Survey, 1981. Geological Map of Egypt 1:200000.

Tibor, G., Ben-Avraham, Z., 2005. Late Tertiary paleodepth reconstruction of the Levant margin off Israel. Mar. Geol., 221, 331–347. doi:10.1016/j.margeo.2005.03.005

U.S. Geological Survey, 2015. ANSS Comprehensive Earthquake Catalog [WWW Document]. URL http://earthquake.usgs.gov/earthquakes/search/ (accessed 8.3.15).

Unknown, 2005. Schematic presentation of the genesis of the Troodos Ophiolite and the evolution of the Island of Cyprus [WWW Document]. URL http://www.moa.gov.cy/moa/gsd/gsd.nsf/f6b12283222a96a3c225734000315725/a9e0eeb1c9dc2e5ec225734000329c12/MainText/0.8A? (accessed 9.13.16).

Van Couvering, J. a, Castradori, D., Cita, M.B., Hilgen, F.J., Rio, D., 2000. The base of the Zanclean Stage and of the Pliocene Series. Episodes, 23, 179–187.

Van der Voo, R., 2005. Paleomagnetism of the Atlantic, Tethys and Iapetus oceans. Cambridge University Press.

van Keken, P.E., Spiers, C.J., van den Berg, A.P., Muyzert, E.J., 1993. The effective viscosity of rocksalt: implementation of steady-state creep laws in numerical models of salt diapirism. Tectonophysics, 225, 457–476. doi:10.1016/0040-1951(93)90310-G

Vidal, N., Alvarez-Marron, J., Klaeschen, D., 2000a. The structure of the Africa-Anatolia plate boundary in the eastern Mediterranean. Tectonics, 19, 723–739. doi:10.1029/2000TC900011

Vidal, N., Klaeschen, D., Kopf, A., Docherty, C., Von Huene, R., Krasheninnikov, V.A., 2000b. Seismic images at the convergence zone from south of Cyprus to the Syrian coast, eastern Mediterranean. Tectonophysics, 329, 157–170. doi:10.1016/S0040-1951(00)00194-3

Wagner, B.H., 2010. An Analysis of Salt Welding. University of Texas.

Walley, C.D., 1998. Some outstanding issues in the geology of Lebanon and their importance in the tectonic evolution of the Levantine region. Tectonophysics, 298, 37–62.

doi:10.1016/S0040-1951(98)00177-2

Walsh-Kennedy, S., Aksu, A.E., Hall, J., Hiscott, R.N., Yaltırak, C., Çifçi, G., 2014. Source to sink: The development of the latest Messinian to Pliocene–Quaternary Cilicia and Adana Basins and their linkages with the onland Mut Basin, eastern Mediterranean. Tectonophysics, 622, 1–21. doi:10.1016/j.tecto.2014.01.019

Walsh, J.J., Nicol, A., Childs, C., 2002. An alternative model for the growth of faults. J. Struct. Geol., 24, 1669–1675. doi:10.1016/S0191-8141(01)00165-1

Watts, A.B., 2011. Isostasy, in: Gupta, H. (Ed.), Encyclopedia of Solid Earth Geophysics SE - 81, Encyclopedia of Earth Sciences Series. Springer Netherlands, pp. 647–662. doi:10.1007/978-90-481-8702-7_81

Wdowinski, S., Ben-Avraham, Z., Arvidsson, R., Ekström, G., 2006. Seismotectonics of the Cyprian Arc. Geophys. J. Int., 164, 176–181. doi:10.1111/j.1365-246X.2005.02737.x

Welford, J.K., Hall, J., Rahimi, A., Reiche, S., Hübscher, C.P., Louden, K., 2015. Crustal structure from the Hecataeus Rise to the Levantine Basin, eastern Mediterranean, from seismic refraction and gravity modelling. Geophys. J. Int., 203, 2055–2069. doi:10.1093/gji/ggv422

Westaway, R., 2004a. Kinematic consistency between the Dead Sea Fault Zone and the Neogene and Quaternary left-lateral faulting in SE Turkey. Tectonophysics, 391, 203–237. doi:10.1016/j.tecto.2004.07.014

Westaway, R., 2004b. Comment on “Late Cenozoic reorganization of the Arabia-Eurasia collision and the comparison of short-term and long-term deformation rates” by M. Allen, J. Jackson, and R. Walker. Tectonics, 23, 1–4. doi:10.1029/2004TC001674

White, R., McKenzie, D., 1989. Magmatism at rift zones: The generation of volcanic continental margins and flood basalts. J. Geophys. Res., 94, 7685. doi:10.1029/JB094iB06p07685

Wilcox, R.E., Harding, T.P., Seely, D.R., 1973. Basic Wrench Tectonics. AAPG Bull. , 57, 74–96.

Williams, G.D., Powell, C.M., Cooper, M.A., 1989. Geometry and kinematics of inversion tectonics. Invers. Tectonics, 3–15. doi:10.1144/GSL.SP.1989.044.01.02

Williams, S.E., Dietmar Müller, R., Landgrebe, T.C.W., Whittaker, J.M., 2012. An open-source software environment for visualizing and refining plate tectonic reconstructions using high-resolution geological and geophysical data sets. GSA Today, 22, 4–9. doi:10.1130/GSATG139A.1.THE

Wilson, J.T., 1966. Did the Atlantic Close and then Re-Open? Nature, 211, 676–681.

Wood, B., 2011. Whole Lithospheric Folding as a Mechanism of Basin Formation and Tectonic Implications for Gondwana Evolution: Evidence from the Palmyride Trough, Syria. AAPG search Discov., 30176.

Wood, B.G.M., 2015. Rethinking post-Hercynian basin development: Eastern Mediterranean Region. GeoArabia, 20, 175–224.

Woodside, J.M., 1977. Tectonic elements and crust of the eastern Mediterranean Sea. Mar.

Geophys. Res., 3, 317–354. doi:10.1007/BF00285658

Woodside, J.M., Mascle, J., Zitter, T.A.C., Limonov, A.F., Ergün, M., Volkonskaia, A., 2002. The Florence Rise, the western bend of the Cyprus Arc. Mar. Geol., 185, 177–194. doi:10.1016/S0025-3227(02)00194-9

Wortel, M.J.R., Spakman, W., Govers, R., Ben-Avraham, Z., 2006. Deep Structure and Evolution of the Cyprus Arc, With Implications for the Tectonic Evolution of Anatolia. Eos Trans. AGU, 87, Fall Meeting Supplements, Abstract T24A-07.

Xu, Q., Zhao, J., Yuan, X., Liu, H., Pei, S., 2015. Mapping crustal structure beneath southern Tibet: Seismic evidence for continental crustal underthrusting. Gondwana Res., 27, 1487–1493. doi:10.1016/j.gr.2014.01.006

Yilmaz, A., Adamia, S., Yilmaz, H., 2013. Comparisons of the suture zones along a geotraverse from the Scythian Platform to the Arabian Platform. Geosci. Front., 5, 855–875. doi:10.1016/j.gsf.2013.10.004

Yousef, M., Moustafa, a. R., Shann, M., 2010. Structural setting and tectonic evolution of offshore North Sinai, Egypt. Geol. Soc. London, Spec. Publ., 341, 65–84. doi:10.1144/SP341.4

Zak, I., Freund, R., 1981. Asymmetry and basin migration in the Dead Sea Rift. Tectonophysics, 80, 27–38.

Zhou, Z., Lin, J., Behn, M.D., Olive, J.-A., 2015. Mechanism for normal faulting in the subducting plate at the Mariana Trench. Geophys. Res. Lett., 42, 4309–4317. doi:10.1002/2015GL063917

Ziegler, M. a., 2001. Late Permian to Holocene paleofacies evolution of the Arabian Plate and its hydrocarbon occurrences. GeoArabia, 6, 445–504.

Ziegler, P.A., 1978. North Sea Rift and Basin Development, in: Ramberg, I.B., Neumann, E.-R. (Eds.), Tectonics and Geophysics of Continental Rifts: Volume Two of the Proceedings of the NATO Advanced Study Institute Paleorift Systems with Emphasis on the Permian Oslo Rift, Held in Oslo, Norway, July 27 -- August 5, 1977. Springer Netherlands, Dordrecht, pp. 249–277. doi:10.1007/978-94-009-9806-3_21

Zitter, T. a. C., Woodside, J.M., Mascle, J., 2003. The Anaximander Mountains: a clue to the tectonics of southwest Anatolia. Geol. J., 38, 375–394. doi:10.1002/gj.961

Zucker, E., Gvirtzman, Z., Steinberg, J., Enzel, Y., 2017. Diversion and morphology of submarine channels in response to regional slopes and localized salt tectonics, Levant Basin. Mar. Pet. Geol., 81, 98–111. doi:10.1016/j.marpetgeo.2017.01.002

Zverev, S.M., Ilinsky, D.A., 2005. The deep structure of Eratosthenes Seamount from seismic refraction data., in: Hall, J.K., Krasheninnikov, V.A., Hirsch, F., Benjamini, C., Flexer, A. (Eds.), Geological Framework of the Levant, Vol. II, the Levantine Basin and Israel. pp. 73–111.

Zverev, S.M., Ilinsky, D.A., 2000. Deep structure and possible nature of the Eratosthenes

Seamount (Eastern Mediterranean). Geotektonika, 4, 67–84.